Wind Calibration and Measurement Algorithms Document

Lynn B. Wilson III (Code 672)
NASA GSFC
Project Scientist
August 15, 2024

Table of Contents

1 The *Wind* Mission

Much of the following is taken directly or adapted from *Wilson III et al.* [2021a].

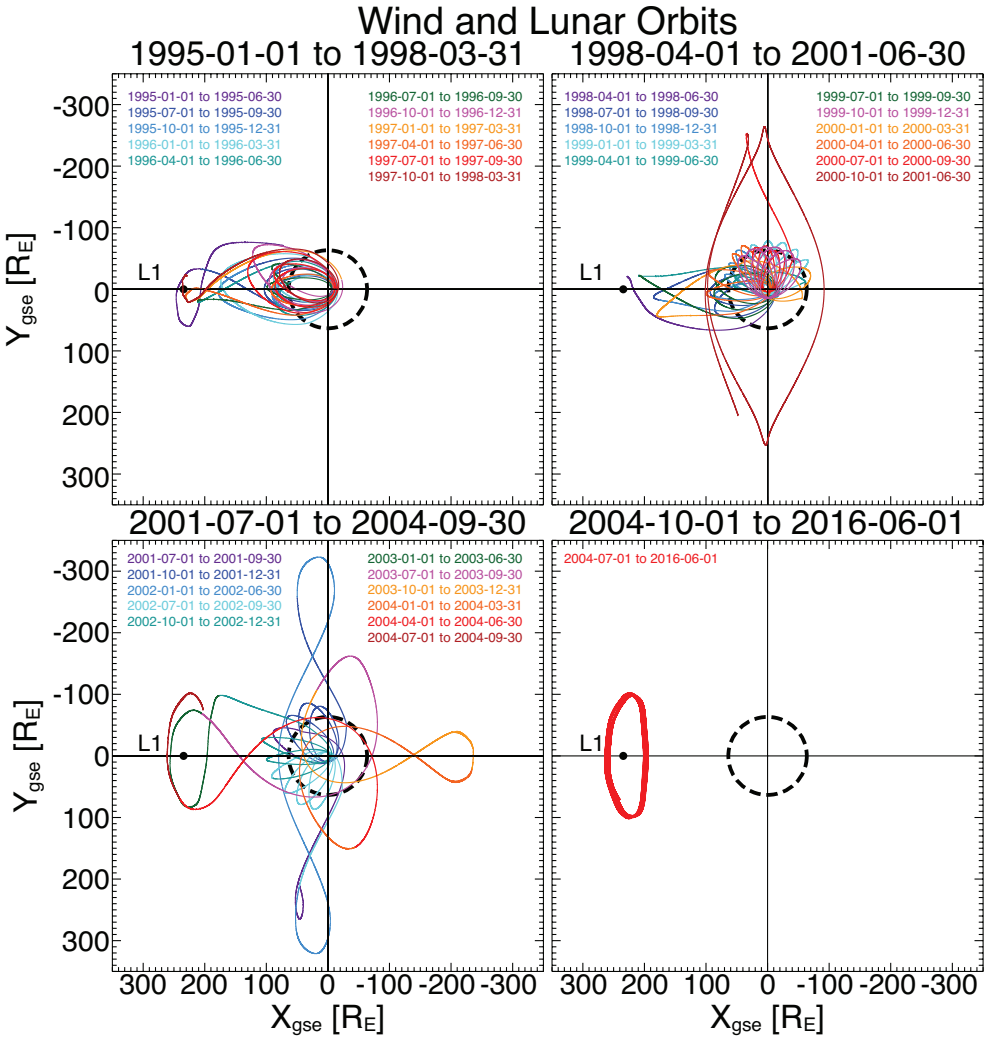

Figure 1: *Orbital trajectories of the* Wind *spacecraft in the GSE XY plane from 1 November 1994 to 1 June 2016. Colors denote time ranges as indicated. The dashed black circle indicates the Moon's orbit [Adapted from Figure 1 in Wilson III et al., 2021a]. Note that the orbit has not noticeably changed since 1 June 2016.*

NASA launched the *Wind* spacecraft on November 1, 1994. *Wind* and *Polar* [*Harten and Clark*, 1995] were part of the stand-alone Global Geospace Science (GGS) Program [*Acuña et al.*, 1995], a subset of the International Solar Terrestrial Physics (ISTP) Program [*Whipple and Lancaster*, 1995]. The ISTP Program included the additional missions *Geotail* [*Nishida*, 1994], the SOlar and Heliospheric Observatory or *SoHO* [*Domingo et al.*, 1995], and *Cluster* [*Escoubet et al.*, 1997]. The objective of the ISTP program was to study the origin of solar variability and activity, the transport of manifestations of that activity to the Earth via plasma processes, and the cause-and-effect relationships between that time varying energy transport and the near-earth environment.

Wind is a spin stabilized spacecraft – spin axis aligned with ecliptic south – with a spin period of ∼3 seconds. Prior to May 2004, *Wind* performed a series of orbital maneuvers *Franz et al.* [1998], as shown in Figure 1, that led to the spacecraft visiting numerous regions of the near-Earth enviroment. For instance, between launch and late 2002 *Wind* completed ∼67 petal orbits through

the magnetosphere and two lunar rolls out of the ecliptic in April and May of 1999. Between August 2000 and June 2002 *Wind* completed four east-west prograde 1:3–Lissajous orbits reaching $\gtrsim$300 R_E along the ±Y-GSE direction *Fränz and Harper* [2002]. From November 2003 to February 2004 *Wind* performed an excursion to the second Earth-Sun libration point, or Lagrange point, called L2[1].

During the magnetosphere passes, *Wind* also made several lunar flybys. *Wind* completed 10 wake crossings before entering a Lissajous orbit at L1 in 2004. Table 1 lists all crossings of the lunar optical wake *Ogilvie and Desch* [1997].

Table 1: Optical Lunar Wake Transits by *Wind*

Start time [UTC]	End time [UTC]
1994-12-01/15:04:07	1994-12-01/15:29:10
1994-12-27/14:36:30	1994-12-27/15:22:36
1996-03-24/05:19:43	1996-03-24/06:24:50
1996-11-13/01:43:16	1996-11-13/03:07:25
1999-04-01/20:38:02	1999-04-01/20:53:04
1999-05-12/20:52:12	1999-05-12/21:04:14
2000-08-19/15:35:45	2000-08-19/16:51:53
2001-12-05/16:48:53	2001-12-05/17:54:00
2002-07-18/17:46:39	2002-07-18/18:42:45
2002-11-30/11:30:28	2002-11-30/12:16:33

In May 2004, *Wind* made its final major orbital maneuver using a lunar gravitational assist to insert it into a Lissajous orbit about the first Earth-Sun libration point, labeled L1 by late June 2004. Note that *Wind*'s L1 orbit has a ±Y-GSE(±X-GSE) displacement about the sun-Earth line of ∼100 R_E(∼35 R_E), much larger than the other two NASA missions at L1 ACE and Deep Space Climate Observatory (DSCOVR). Note that the ±Z-GSE displacement from the ecliptic plane is $\lesssim$30 R_E for both ACE and *Wind*. On June 26, 2020, the *Wind* flight operations team (FOT) successfully completed the first halo orbit insertion maneuver and the second was successfully completed on August 31, 2020. The third maneuver was successfully completed on November 9, 2020. This orbital change was necessary to prevent the spacecraft trajectory from entering the solar exclusion zone – around the solar disk where solar radio emissions cause sufficient interference with spacecraft communications to prevent telemetry signal locks. The projection of the orbit in the ecliptic plane will not noticeably change, however the out-of-ecliptic projection will now be a stationary ellipse centered on the solar disk.

The original primary science objectives of the *Wind* mission are:

- Provide complete plasma, energetic particle and magnetic field for magnetospheric and ionospheric studies.
- Investigate basic plasma processes occurring in the near-Earth solar wind.
- Provide baseline, 1 AU, ecliptic plane observations for inner and outer heliospheric missions.

Since the spacecraft has been serving for >29 years and the diversity of environments explored (e.g., see Figure 1) is so broad, the areas of science investigated by the team and community using *Wind* over the mission lifetime have changed significantly. As a result of its longevity, diversity of instrumentation (e.g., see the *Wind* Project Data Management Plan or PDMP for details), and diversity of environments explored the *Wind* mission has amassed over 7295 refereed publications

[1]Note that L2 is located ∼233–235 R_E downstream of Earth and ∼500 R_E downstream of the Advanced Composition Explorer (ACE) *Stone et al.* [1998]. For reference, ACE launched in 1997 and was designed to study energetic particles and their composition. Unlike *Wind*, ACE was not designed to study kinetic physics or remote solar and astrophysical phenomena using electric fields.

between launch and Dec. 31, 2023, or an average of ∼252 publications per year. These publications have accumulated over 227,717 citations for an h-index of 173 and an i10-index of 4232 with over 1,377,048 reads on the *Wind* NASA ADS publication webpage[2]. These publications cover an expansive list of topics including (but not limited to) statistical solar wind trends, magnetic reconnection, large-scale solar wind structures, kinetic physics, electromagnetic turbulence, the Van Allen radiation belts, coronal mass ejection topology, interplanetary and interstellar dust, the lunar wake, solar radio bursts, solar energetic particles, and extreme astrophysical phenomena such as gamma-ray bursts.

As of August 15, 2024, there are ∼69 selectable data types with ∼1703 total data products (including OMNI data products) on SPDF CDAWeb. Below we will outline and describe these data products by instrument.

1.1 Spacecraft Health

Wind continues to operate in good health. The communication system was successfully reconfigured in 2000 to enhance the telemetry margins and reliance on a single digital tape recorder (with two tape units) since 1997 has never hindered operations. The flight operations team (FOT) took steps to minimize wear and extend the lifespan of the two tape units. Since the last Senior Review, the spacecraft has experienced the usual instrument latch-ups and single-event upsets (SEUs) that are likely caused by high energy particles. As in the past, the FOT was able to restore all instruments to fully operational within a day or two depending on Deep Space Network (DSN) scheduling. The automation of the recovery process for the WAVES instrument after latch-ups (i.e., due to SEUs) was successfully completed in October 2016 and the spacecraft command tables now include automated tests of the SWE electron instrument. Thus, *Wind* continues to maintain a fully operational status.

On Oct. 27, 2014 at 21:59:38 GMT, the *Wind* command and attitude processor (CAP) suffered two simultaneous SEUs. The redundant nature of the *Wind* spacecraft bus allowed the FOT to successfully switch to a second CAP, CAP2. The FOT began the recovery of CAP1 on Jan. 21, 2015 and finished Jan. 30, 2015, and the spacecraft was fully recovered at ∼17:50 UTC on Jan. 30, 2015.

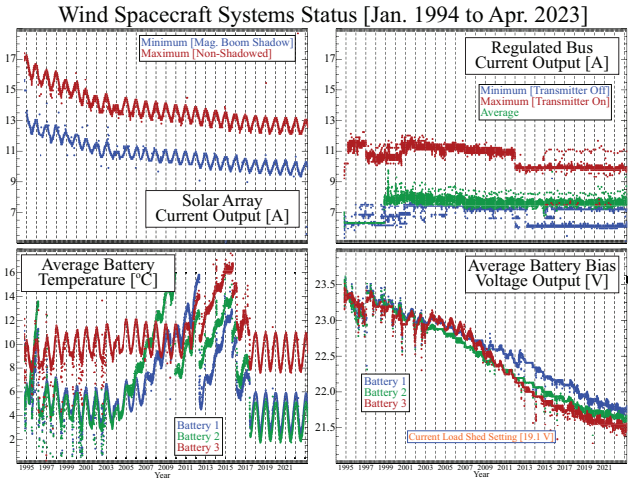

Figure 2: ***Summary of* Wind*'s Power System Status:*** *The* Wind *spacecraft systems status plotted from Jan. 1, 1994 to Apr. 1, 2023 as daily averages.*

The CAP1 anomaly resulted in a complete loss of data from October 27, 2014 until November 7, 2014 (i.e., 11 days or ∼3% annual total) and partial loss from all instruments between November 7–20, 2014 (i.e., 14 days or ∼4% annual total). The SWE instrument suffered complete data loss between October 27, 2014 and November 26, 2014 (i.e., 30 days or ∼8% annual total) and partial loss (HK only) from October 27, 2014 to December 1, 2014 (i.e., 35 days or ∼10% annual total). During the recovery process between Jan. 28–30, 2015 while CAP1 was in control, the attitude/telemetry information was invalid for ∼4 hrs 41 mins (i.e., <5% of those four days).

On April 11, 2016 one of the two tape units (TUA) began experiencing issues related to the read/write head causing ∼few percent data loss per day. The flight operations team successfully

[2]found at https://ui.adsabs.harvard.edu/public-libraries/DdelsbGYT5a8sM7CLujv_g

switched the primary record unit to TUB on May 6, 2016 to extend the life of TUA and reduce data loss. TUB is fully operational and averages >98.5% data recovery rates.

An examination of the spacecraft power systems (see Figure 2) shows that the batteries can maintain average bias voltages high enough to exceed the current load shed setting of 19.1 V until at least mid-2056 based on an extrapolation beyond the date range of the lower right panel. To cause a spacecraft reset, all three batteries must simultaneously fall below this load shedding voltage level which is commandable from the ground and will be changed when necessary to avoid a spacecraft reset. The load shedding can be safely reduced to at least 18.2 V (reached at least 20 years beyond 2056 based on present trends).

All three batteries went through mode changes prior to 2020 to reduce the maximum charge voltage. Each battery was experiencing excess charging, causing an increase in temperature (see lower-left-hand panel in Figure 2) and reduction in efficiency. The mode changes successfully reduced the temperatures to nominal ranges. The current trend shows that the battery temperatures will not exceed the critical threshold of ∼17°C until well after the year ∼2100.

The solar array output is producing more than enough current for spacecraft operations and will continue to do into early ∼2044, assuming that the maximum current drawn from the batteries (i.e., red line in upper right in Figure 2) does not exceed the average solar array output (not shown). The maximum solar array output (i.e., red line in upper left-hand panel) will not drop to the maximum regulated bus output until mid ∼2058, assuming current trends hold. Therefore, *Wind* can operate at current capacity for the next several decades.

Wind continues to maintain a large fuel reserve. As of August 7, 2024, the tanks contained ∼34.9 kg of fuel, which is equivalent to ∼70 m/s of radial delta-V assuming normal thruster operations. Typically only four station keeping maneuvers are performed each year, each requiring only ∼0.12 kg of fuel. Thus, *Wind* has enough fuel for ∼70 years.

1.2 Instrument Status

The *Wind* instrument names and acronyms are listed below in Table 2.

Table 2: *Wind* Instrument Names

Abbrev.	Instrument name	Reference
TGRS	Transient Gamma-Ray Spectrometer	*Owens et al.* [1995]
KONUS	Gamma-Ray Spectrometer	*Aptekar et al.* [1995]
EPACT	Energetic Particles: Acceleration, Composition, and Transport	*von Rosenvinge et al.* [1995a]
SMS	Solar Wind and Suprathermal Ion Composition Experiment	*Gloeckler et al.* [1995]
MFI	Magnetic Field Investigation	*Lepping et al.* [1995]
WAVES	The Radio and Plasma Wave Investigation	*Bougeret et al.* [1995]
3DP	Three-Dimensional Plasma and Energetic Particle Investigation	*Lin et al.* [1995]
SWE	Solar Wind Experiment	*Ogilvie et al.* [1995]

It is important to note that unlike most other missions, *Wind* was designed with significant redundancy in its measurements. For instance, there are at least five possible measurements of the solar wind number density (two from 3DP, two from SWE, one from WAVES, and one from SMS under certain conditions) and prior to 2000 there were two different gamma ray instruments. The MFI comprises two fluxgate magnetometers at different locations on a 12 meter boom (one closer at ∼8 m, the other at 12 m) which improves spacecraft noise/artifact removal. There are three

separate measurements of protons with energies >50 keV (one from 3DP, one from SMS, and one from EPACT). Finally, there are at least three separate measurements of heavy ions (i.e., ions more massive than alpha-particles).

Seven of the eight *Wind* instruments, including all of the fields and particles suites, remain largely or fully functional. The only instrument fully turned off is the TGRS γ-ray instrument that was designed for only a few years of operations (instrument off prior to ~January 2000). Aside from temporary data losses due to a command and attitude processor (CAP) and tape unit anomaly (both issues were resolved or mitigated, discussed in detail below), the instruments continue to return >98% of all captured data annually. The dates of significant spacecraft and instrumental issues are listed in Table 3 for reference.

Table 3: Wind Instrument and Spacecraft Anomalies

Date	**Part Affected**	**Impact**
January 19, 1995	GTM1[a]	failure
October 1995	APE-A/APE-B/IT HVPS[b]	suffered a loss of gain
April 30, 1997	CAP1[c]	Reed-Solomon encoder failure
December 13, 1997	DTR2[d]	power supply failure
January 2000	TGRS	γ-ray instrument turned off (planned coolant outage)
May 2000	SMS-SWICS	solar wind composition sensor turned off
June 2001	SWE-VEIS	thermal electron detectors HVPS failure
August 2002	SWE-Strahl	reconfigured to recover VEIS functionality
June 2009	SMS DPU	experienced a latch-up reset – MASS acceleration/deceleration power supply in fixed voltage mode
2010	SMS-MASS	experienced a small degradation in the acceleration/deceleration power supply
May 19, 2014	3DP-PESA Low	suffered an anomaly that affected only the telemetry HK[e] data
October 27, 2014	CAP1	anomaly at ~21:59:38 GMT
November 7, 2014	CAP2	set to primary while recovery starts on CAP1
November 26, 2014	SWE	full reset due to CAP1 anomaly
January 30, 2015	CAP1	fully recovered
April 11, 2016	DTR1 TUA	began experiencing read/write errors (~1% bit errors)
May 6, 2016	DTR1 TUB	FOT sets as primary recorder

[a] two GGS telemetry modules, GTM1 and GTM2 [b] high voltage power supply
[c] two command and attitude processors, CAP1 and CAP2 [d] two digital tape recorders, DTR1 and DTR2, each with independent tape units, TUA and TUB [e] house keeping

The instrument capabilities and current status are shown in Table 4 (see the Glossary and Acronyms Appendices for definitions). Below we discuss the instrument anomalies in more detail.

The EPACT APE-A/APE-B/IT high voltage power supply (HVPS) suffered a loss of gain in October 1995. The EPACT-APE detector only returns two energy channels of ~5 and ~20 MeV protons during enhanced periods. The EPACT-LEMT and -STEP telescopes continue to operate normally, providing crucial and unique observations of solar energetic particles up to 10 MeV in energy. The SMS-SWICS solar wind composition sensor had to be turned off in May 2000. The SMS DPU experienced a latch-up reset on 26 June 2009 causing the MASS acceleration/deceleration

Table 4: Operational Instruments on *Wind*

Name	Type	Cadence	Range	Status & Notes
MFI				**Nominal**
	3 $B_{o,j}$[a]	∼11–22 sps[b]	±4 – ±65,536 nT	±0.001 – ±16 nT
WAVES				**Nominal**
TDS Fast	2 δE_j	1.8–120 ksps	∼0.1–300 mV/m	∼80 μV rms
TDS Slow	1 or 3 δE_j	0.1–7.5 ksps	∼0.5–300 mV/m	∼300 μV rms
	1 or 3 δB_j	0.1–7.5 ksps	∼0.25 – $\gtrsim$30 nT	$\sim 10^{-9}$ nT^2 Hz^{-1} @ 100 Hz
TNR	1 δE_j	∼1 min	∼4–256 kHz	∼7 nV Hz$^{-1/2}$
RAD1	2 δE_j	∼1 min	∼20–1040 kHz	∼7 nV Hz$^{-1/2}$
RAD2	2 δE_j	∼1 min	∼1.1–14 MHz	∼7 nV Hz$^{-1/2}$
3DP				**Nominal**
EESA	e^-	∼3–22 s	∼0.003–30 keV	∼20% $\Delta E/E$[c], ∼5.6–22.5°
PESA	H^+, He^{2+}	∼3–75 s	∼0.003–30 keV	∼20% $\Delta E/E$, ∼5.6–22.5°
SST Foil	e^-	∼12 s	∼25–400 keV	∼30% $\Delta E/E$, $\gtrsim$22.5°
SST Open	H^+	∼12 s	∼25–6000 keV	∼30% $\Delta E/E$, $\gtrsim$22.5°
SWE				**VEIS Off**, **Strahl Reconf.**
FCs	H^+, He^{2+}	∼92 s	∼0.15–8 keV	∼6.5% $\Delta E/E$
Strahl	e^-	∼12 s	∼0.005–5 keV	∼3% $\Delta E/E$
				∼3° × 30°
SMS				**SWICS Off**, **MASS Reduced**
STICS	H – Fe	$\gtrsim$3 min	∼8–226 keV/e	∼5% $\Delta E/E$, ∼4° × 150°
			1–60 amu/e	∼12% $\Delta M/M$[d]
EPACT				**IT off**, **APE Reduced**
LEMT	He – Fe	$\gtrsim$5–60 min	∼2–12 MeV/n	$\gtrsim$20% $\Delta E/E$
			∼2–90 Z	$\gtrsim$2% $\Delta Q/Q$[e]
STEP	H – Fe	$\gtrsim$10 min	∼0.02–2.56 MeV/n	$\gtrsim$30% $\Delta E/E$
				∼17° × 44°
KONUS	photons	$\gtrsim$2 ms	∼0.02–15 MeV	**Nominal**
		$\gtrsim$3 s	∼0.02–1.5 MeV	$\gtrsim$5% $\Delta E/E$
				Background Mode
TGRS	photons	$\gtrsim$62 μs	∼0.025–8.2 MeV	**Off (out of coolant)**
				∼3 keV @ 1 MeV
				eff. ∼43% @ 511 keV

[a] three magnetic field vector components [b] samples per second [c] normalized energy resolution
[d] normalized mass resolution [e] normalized charge resolution

power supply to stay in a fixed voltage mode, rather than stepping through a set of voltages. The moderate risk of power cycling of the SMS DPU required to fix this issue was declined to protect the unique and fully functional SMS-STICS sensor. In 2010, MASS experienced a small degradation in the acceleration/deceleration power supply further reducing the instrument efficiency. However, the SMS-MASS sensor still returns science quality data.

The VEIS thermal electron detectors on the SWE instrument suffered high voltage power supply problems in June 2001. In August 2002 the SWE Strahl sensor was reconfigured to recover most of the original functions. Moreover, the 3DP instrument also covers the impacted electron

measurements making these observations still redundant and hence robust. The entire SWE instrument suite required a full reset due to the CAP anomaly (see Section 1.1 for details), which resulted in a complete loss of data from late Oct. 27, 2014 to Nov. 26, 2014, and partial loss until Dec. 1, 2014 when the instrument was returned to nominal operations.

On May 2014 the 3DP instrument (specifically PESA Low) suffered an anomaly that only affected the telemetry house keeping (HK) data. A quick investigation showed that while the telemetry information (e.g., micro-channel plate grid voltage) showed unreliable instrument operations information, the science data remained unaffected (i.e., no noticeable change in flux was observed during and after event). All the other detectors within the 3DP instrument suite continue to operate nominally. Thus, the anomaly resulted in no loss of scientific data.

1.3 Science Team

The *Wind* instrument/science team is a small but dedicated group of scientists. Due to the longevity of the mission, a number of the original instrument PIs have retired or passed away. The SWE instrument suite is currently headed by **Bennett A. Maruca (University of Delaware)** with Michael L. Stevens (Harvard Smithsonian) leading the SWE Faraday Cup team. **Stuart D. Bale (University of California, Berkeley SSL)** is the PI of 3DP. **Andriy Koval (University of Maryland, Baltimore County/Code 672)** took over as PI of the MFI instrument replacing Adam Szabo (GSFC), who moved on to other missions. **Susan T. Lepri (University of Michigan, Ann Arbor)** is the PI for SMS. **Keith Goetz (University of Minnesota, Twin Cities)** is the American PI for WAVES while the French PI is **Karine Issautier (Observatoire de Paris-Meudon)**[3]. Both the original and previous acting EPACT PIs, Tycho von Rosenvinge and Allen Tylka, respectively, retired so **Ian G. Richardson (University of Maryland, College Park/Code 672)** took over as the EPACT PI in late 2019. Finally, unfortunately Rafail Aptekar passed away in late December 2020 so **Dmitry Frederiks (Ioffe Institute, Laboratory for Experimental Astrophysics, St. Petersburg, Russia)** has taken over as the KONUS PI. Lynn B. Wilson III has been Project Scientist for *Wind* since June 2016. A summary of the instrument leads can be found in Table 5.

Table 5: The status of the *Wind* instruments

Instrument	Principal Investigator	Institution	Status
SWE	B.A. Maruca	Electrons: GSFC, UNH Ions: SAO	Strahl detector reconfigured Faraday Cup fully operational
3DP	S.D. Bale	UC Berkeley	Fully operational
MFI	A. Koval	GSFC/UMBC	Fully operational
SMS	S. Lepri	U. Michigan	SWICS turned off MASS reduced coverage STICS fully operational
EPACT	I. Richardson	GSFC/UMCP	IT turned off APE – only 5 and 20 MeV protons LEMT and STEP operational
WAVES	K. Goetz	U Minnesota	Fully operational
KONUS	D. Frederiks	Ioffe Institute, Russia	Fully operational
TGRS	B. Teegarden	GSFC	Intentionally turned off (ran out of coolant)

[3]The original PI was Jean Louis Bougeret of France, with a strong partnership between the French institutions and the University of Minnesota and NASA Goddard Space Flight Center. The previous American PIs were Michael Kaiser and Robert MacDowall (both at GSFC).

1.4 Mission Team

The current *Wind* mission management team is as follows. Lynn B. Wilson III (GSFC, Code 672) is the Project Scientist. Patrick Koehn (NASA HQ) is the Program Scientist. Robert F. Stone (GSFC, Code 584) is the Mission Director and Rich Burns (GSFC, Code 444) is the Program Manager. The flight operations team (FOT) is headed by Jacqueline M. Snell (GSFC/KBRwyle, Code 444) and the lead engineer is Eric S. Smith (GSFC/KBRwyle, Code 444).

2 General Instrument Theory

This section will provide some theoretical background on the fundamentals of how various instrument types work and on what principles the measurements are founded. We will refer back to this section throughout for generic reference.

2.1 Microchannel Plate Theory

A microchannel plate (MCP) consists of a series of small (5 μm to 0.25 mm diameter) holes (or channels) in a thin plate (typically 0.4–3.0 mm thick) made of a conducting material specially fabricated to produce signals similar to a secondary electron analyzer (e.g., lead-glass is common) [e.g., *Ladislas Wiza*, 1979; *Mackenzie*, 1977]. MCPs are often used in pairs where a cross-sectional cut through two connecting channels creates a v-shaped tube, called a chevron pair. This prevents incident particles from directly impacting the detector (e.g., anode) behind the plates. When a particle impacts the channel wall, if it has enough energy, it will produce a shower of electrons. The number of electrons per incident particle impact is referred to as the gain of the detector [e.g., *Fraser*, 1983; *Gershman et al.*, 2016; *Kanaya and Kawakatsu*, 1972; *Ladislas Wiza*, 1979; *Meier and Eberhardt*, 1993; *Paschmann and Daly*, 1998; *Rösler and Brauer*, 1988; *Sternglass*, 1957; *Wüest et al.*, 2007].

There is a fraction of particles which either strike the pore voids (spaces between channels) or those which do not generate an electron shower/avalanche which are undetected. These factors influence the *quantum efficiency* of the detector. Before going into too much theory, we should define a physical quantity of an MCP, which is called the open area ratio:

$$f_{OAR} = \left(\frac{\pi\sqrt{3}}{6}\right)\left(\frac{d}{p}\right) \tag{1}$$

where d is the diameter of the channels and p is the pitch or center-to-center spacing of the channels. A typical MCP[4] has a channel length-to-diameter ratio of 40:1 and $f_{OAR} \sim$ 60-70% [e.g., *Fraser*, 1983; *Fraser et al.*, 1991, 1993; *Mackenzie*, 1977]. MCP lead glass has an effective atomic number of ~11.24, effective atomic mass of ~22.47 amu, and number density of atoms of ~8.84 x 10^{28} m^{-3} [e.g., *Fraser*, 2002].

2.1.1 Microchannel Plate Efficiency

If we let T_{max} = the maximum emission coefficient, $\delta(E)$ is the secondary emission yield function, and E_{max} is the energy at which efficiency reaches its maximum value [*Bordoni*, 1971; *Goruganthu and Wilson*, 1984; *Kanaya and Kawakatsu*, 1972], then we have:

$$\varepsilon = \frac{1 - e^{-k\delta(E)/\delta_{max}}}{1 - e^{k}} \tag{2}$$

where $\delta(E)$ is given by:

$$\delta(E) = \delta_{max}\left[\frac{E}{E_{max}}\right]^{1-\alpha}\left[\frac{1 - e^{-T_{max}(E/E_{max})^{\alpha}}}{1 - e^{-T_{max}}}\right] \tag{3}$$

where δ_{max} is the maximum value of the secondary emission coefficient, k is an adjustable parameter

[4]Note that the *Wind* 3DP EESA Low detector [*Lin et al.*, 1995] was manufactured by Mullard (later called Photonis) had a channel length-to-diameter ratio of 80:1 and resistivities of ~400 $M\Omega\ cm^{-2}$. As of late 2003, an estimated ~8 $C\ cm^{-2}$ of charge was extracted from the MCPs with an estimated total available of ~100 $C\ cm^{-2}$ from the start [*Wüest, M., Evans, D. S., & von Steiger, R.*, 2007].

that depends upon δ_{max} and a complicated probability. If we assume the distribution of secondary electrons is Poissonian in nature, $P(n,\delta) = \frac{\delta^n}{n!}\ e^{-\delta}$, where $\delta = \delta(E)$ the secondary emission coefficient, then we can show that the extinction probability, X, of a chain process started by an electron of energy E_1 is given by the smallest root of:

$$X = e^{-[1-X]\delta(E_1)} \tag{4}$$

Therefore, the probability that a process started by an electron with energy E_o terminates is given by:

$$X_1 = \sum_{n=0}^{\infty} P[n, \delta(E_o)]\, X^n = e^{-[1-X]\delta(E_o)} \tag{5}$$

where we have used the known relationship:

$$\sum_{n=0}^{\infty} e^{nt} \left(\frac{\lambda^n e^{-\lambda}}{n!}\right) = e^{-l\left(1-e^t\right)} \tag{6}$$

We can simplify the right-hand side of this equation by using Equation 4 to get:

$$X_1 = \sum_{n=0}^{\infty} P[n, \delta(E_o)]\, X^n = \sum_{n=0}^{\infty} e^{n\ \{-[1-X]\delta(E_1)\}} \frac{\delta^n(E_o)\, e^{-\delta(E_o)}}{n!} \tag{7a}$$

$$= e^{+\delta(E_o)\left[e^{-[1-X]\delta(E_1)}-1\right]} \tag{7b}$$

$$= e^{-[1-X]\delta(E_o)} \tag{7c}$$

which we can see from Equation 4 shows that:

$$e^{-[1-X]\delta(E_1)} - 1 = -[1-X] \tag{8}$$

We can now show that:

$$X_1 = e^{-[1-X]\delta(E_o)} \tag{9a}$$

$$= \left[e^{-[1-X]\delta(E_o)}\right]^{\frac{\delta(E_1)}{\delta(E_1)}} \tag{9b}$$

$$= \left[e^{-[1-X]\delta(E_1)}\right]^{\frac{\delta(E_o)}{\delta(E_1)}} \tag{9c}$$

$$= X^{\delta(E_o)/\delta(E_1)} \tag{9d}$$

The next step is to determine the probability, X_2, that an incident electron with energy, E, does not produce any pulses. This is given by:

$$X_2 = \sum_{n=0}^{\infty} P[n, \delta(E)]\ \ {X_1}^n = e^{-\delta(E)} \cdot e^{\delta(E)\ X_1} \tag{10}$$

Therefore, the efficiency, ε, is given by:

$$\varepsilon = 1 - X_2 \tag{11a}$$
$$= 1 - e^{-\delta(E)} \cdot e^{\delta(E)\ X_1} \tag{11b}$$
$$= 1 - e^{-\delta(E)[1-X_1]} \tag{11c}$$
$$= 1 - e^{-\frac{k\ \delta(E)}{\delta_{max}}} \tag{11d}$$

where $k = \delta_{max}\,[1 - X_1]$ and δ_{max} is the maximum value of the secondary emission coefficient.

We now define $\varepsilon_1\,(E)$ as the relative efficiency value measured at fixed energy, E, and $\varepsilon\,(E)$ is the true efficiency then we can show that:

$$\alpha\ \varepsilon_1\,(E) = \varepsilon\,(E) = 1 - e^{-\frac{k\ \delta(E)}{\delta_{max}}} \tag{12}$$

Then the ratio between an experimental measurement relative to energy E and the energy at which the efficiency reaches a maximum, E_{max}, is given by:

$$\frac{\varepsilon_1\,(E)}{\varepsilon_1\,(E_{max})} = \frac{1 - e^{-\frac{k\ \delta(E)}{\delta_{max}}}}{1 - e^{-k}} \tag{13}$$

One can solve Equation 13 to determine the value of k, which then allows one to calculate the value of α for a detector.

As an example, the values for Equations 2 and 3 used by the *Wind*/3DP EESA Low detector[5] are: $T_{max} = 2.283$, $E_{max} = 325$ eV, $\alpha = 1.35$, $\delta_{max} = 1.0$, and $k = 2.2$.

2.1.2 Microchannel Plate Deadtime

This section discusses the effect of deadtime – time period when the detector is unable to measure incident particles due to the channel's discharge recovery time, preamp cycle rates, etc. [e.g., *Kanaya and Kawakatsu*, 1972; *Meeks and Siegel*, 2008; *Schecker et al.*, 1992]. For instance, if the count rates are high, then the channel cannot fully recharge causing smaller avalanches, thus less gain which translates to lower counts. The dead time is also defined as the minimum amount of time between two pulses necessary for the detector such that it records two distinct pulses. A detailed discussion can be found in Section 3.1.3 of *Wüest, M., Evans, D. S., & von Steiger, R.* [2007].

Let us define the following:

- $\tau \equiv$ dead time
- $c_r \equiv$ measured count rate
- $C_r \equiv$ corrected count rate
- $N_t \equiv$ total number of counts
- $P\,(t)\,\Delta t \equiv$ probability that a detector detects a particle between t and $t + \Delta t$
- $D_t \equiv$ delay time (assume $> \tau$)

From these definitions, we find that:

$$C_r = \frac{c_r}{1 - c_r\ \tau} \tag{14}$$

and the probability is given by:

[5] e.g., see routine **mcp_efficiency.pro** in *Wilson III* [2021]

$$P\left(t\right)\Delta t = C_r\ \Delta t\ e^{-C_r\ t} \tag{15}$$

which has a desireable property that the expectation value of t^m is given by the simple form:

$$\langle t^m \rangle = \int_0^\infty dt\ t^m\ C_r\ e^{-C_r\ t} = \frac{m!}{{C_r}^m} \tag{16}$$

One can see this implies that $\langle t \rangle = {C_r}^{-1}$, so we can also infer that:

$$\frac{\langle t^m \rangle}{\langle t \rangle^m} = m! \tag{17}$$

If the instrument is working properly and measurements are taken at times t_i, then discretely one should have:

$$\frac{\sum_{i=0}^{N_t-1} \frac{{t_i}^m}{N_t}}{\left(\sum_{i=0}^{N_t-1} \frac{t_i}{N_t}\right)^m} = m! \tag{18}$$

However, we know that there is statistical uncertainty due to finite N_t and an unknown τ. To try and estimate τ, we can take our times t_i and subtract off a delay time, D_t, until the moments match the expectation values derived from theory, thus we have:

$$\frac{\sum_{i=0}^{N_t-1} \frac{(t_i - D_t)^m}{N_t}}{\left[\sum_{i=0}^{N_t-1} \frac{(t_i - D_t)}{N_t}\right]^m} \rightarrow m! \tag{19}$$

where one varies D_t until Equation 19 actually equals $m!$.

The variance of the numerator in Equation 17 is given by:

$${\sigma_m}^2 = \langle t^{2m} \rangle - \langle t^m \rangle^2 \tag{20a}$$

$$\frac{\sigma_m}{\sqrt{N_t}} = \frac{\langle t \rangle^m\ m!}{\sqrt{N_t}} \sqrt{\frac{2\ m!}{\left(m!\right)^2} - 1} \tag{20b}$$

where Equation 20a is the standard deviation of the numerator in Equation 17. The uncertainty of the denominator is given by:

$$\left(\langle t \rangle \pm \frac{\langle t \rangle}{\sqrt{N_t}}\right)^m \approx \langle t \rangle^m \left(1 \pm \frac{m}{\sqrt{N_t}}\right) \tag{21}$$

The fractional uncertainties of the numerator and denominator cannot be added in quadrature because the same t_i appear in both expressions. We can, however, find a fractional uncertainty for Equation 17 by subtracting the squares of the fractional uncertainties of the numerator and denominator and taking the square root to give:

$$\sigma_{tm} = \frac{1}{\sqrt{N_t}} \sqrt{\frac{2\ m!}{\left(m!\right)^2} - (m^2 + 1)} \tag{22}$$

2.2 Silicon Solid-State Detectors

A silicon (Si) solid-state detector (SSD) is comprised of ultra-pure silicon crystals. They can be doped in multiple different ways but the basic response to an incident charged particle remains the same. As a charged particle moves through the material, it can promote valence band electrons to the conduction band energies, which allows them to move freely in response to an external electric field. Each promoted electron has a corresponding hole, which behaves like a free positive charge and also moves in response to external electric fields [the above and much of the following are from Section 2.2.5.2 of *Wüest, M., Evans, D. S., & von Steiger, R.*, 2007].

In a SSD, the Si crystals will each have electrodes on opposite sides of the thin wafer to operate as a reverse biased diode (i.e., current is allowed to flow in only one direction). The electrons move to one side while the holes move to the other, resulting in a net current (or net collection of charge on the electrodes). The total charge collected per wafer is proportional to the energy lost by the incident particle to the Si crystal. Roughly 3.6 eV of energy is required to generate a single electron-hole pair in pure Si.

The incident particle generates a tube-like path that behaves like a high-density ($\sim 10^{15}$–10^{17} cm^{-3}) plasma. The applied electric field is used to prevent the plasma constituents, called carriers (i.e., the electrons and holes), from recombining and neutralizing. The lifetime of the carriers is limited by recombination and trapping due to impurities or defects in the Si crystal. The typical carrier lifetimes are on the order of ~ 10 μs while the carrier collection times for a Si detector electrode can be as low as ~10–100 ns. That is, the experimentalist wants the carrier collection times to be shorter than the carrier loss time scales.

There are two additional sources of error/uncertainty in Si detectors. The first is due to the effect of a so called "dead layer," ~100 nm thick, on the surface of the Si crystal. It is called dead because the incident particle we wish to measure will lose energy in this region but will not generate charge carriers, i.e., no measureable signal. Therefore, proper calibration requires that one knows the energy loss characteristics through this dead layer and through the electrodes. This issue is much more significant for low than high energy particles, as will be explained in the next section.

The second issue is called the "mass defect" effect, which results because some of the energy lost by an incident ion will not result in the generation of charge carriers. This effect increases with increasing ion mass (i.e., this does not affect incident electrons). Therefore, the mass defect must be properly characterized during calibration to accurately determine the incident particle's energy.

SSDs usually pass the current, from the electron-collecting anode, to a charge sensitive preamp which converts the signal into a voltage tail pulse (i.e., fast/abrupt increase followed by slow decay). This voltage pulse is then sent to a linear amplifier which shapes the pulse while amplifying the signal to generate the short duration, peaked pulse that has an amplitude proportional to the collected charge (i.e., pulse height distribution or PHD). Properly designed SSDs will use amplifier discriminator electronics to reduce (avoid is possible) analyzer paralysis due to a high energy heavy ion or large fluxes of lower energy particles. The instrument can become paralyzed by these scenarios due to either the large charge generated or pulse pile-up.

SSDs have several strengths over some other particle detectors including compact size, energy resolution, fast time resolution, and tailorable crystal thickness to match measurement requirements. However, they also have several weaknesses including limited thickness of pure Si crystals[6], susceptibility to damage by incident particles (i.e., material fatigue from ionizing radiation), and a

[6]Without special techniques like lithium-drifted Si, or Si(Li), most pure Si crystals are limited to $\lesssim$1 mm in thickness. In contrast, a Si(Li) crystal can be upwards of ~1000 mm thick. The disadvantage of Si(Li) crystals is that they have coarser energy resolution (~30 keV) unless cooled to cryogenic temperatures. This is usually required for photon detecting instruments (down to ~200 eV resolution) but not so for high energy particle instruments.

relatively high energy threshold (typically ~20 keV) for particle detection. For additional details on SSDs, see *Kleinknecht* [1998], *Knoll* [2000], and/or *Lutz* [1999].

2.2.1 Bethe-Bloch Theory

For the purposes of this section alone, we define the following parameters (not already defined in Appendix 17.7) to discuss the theory of energy loss by charged particles propagating through a solid medium, known as Bethe-Bloch [*Janni*, 1982a,b; *Paul*, 1971; *Skyrme*, 1967; *Wüest, M., Evans, D. S., & von Steiger, R.*, 2007].

- $\beta = \frac{v}{c} \equiv$ normalized speed of incident particle
- $z \equiv$ charge state of incident particle (e.g., alpha-particle would be +2)
- $M_i \equiv$ rest mass of incident particle [e.g., kg]
- $Z \equiv$ atomic number of stopping medium (e.g., Si would be 14)
- $E \equiv$ kinetic energy of incident particle [e.g., eV]
- $A \equiv$ atomic weight of stopping medium (e.g., Si would be 28.085 amu)
- $I \approx k_1\ Z\left(1 - k_2\ Z^{-2/3}\right)$ (where $k_{1[2]} \sim 10.3$ eV[0.793]) $\equiv$ adjusted ionization potential or mean excitation potential of atoms in stopping medium, e.g., pure Si has been estimated to have $I \sim 174.5$ eV $\pm$ 6.49% [e.g., see *Janni*, 1982a,b, for more details]
- $\rho \equiv$ mass density of stopping medium [e.g., $g\ cm^{-3}$] (e.g., pure Si would have ~2.329 $g\ cm^{-3}$ or ~2329 $kg\ m^{-3}$)
- $N_e = \frac{N_A\ Z\ \rho}{A} \equiv$ number density of electrons in stopping medium [e.g., cm^{-3}] (e.g., pure Si would have ~4.99397 x 10^{22} cm^{-3})
- $W_{max} \equiv$ maximum kinetic energy that can be transferred to an at rest, unbound electron [e.g., eV], defined in Equation 24 [e.g., see *Janni*, 1982a,b, for more details]
- $\delta \equiv$ correction term for density effect due to polarization of the stopping medium, i.e., density correction that arises because stopping atoms are not free
- $\mathcal{C} \equiv$ shell correction term that arises because inner shell electrons do not participate equally in the stopping of incident particles

Then the theoretical approximation for the amount of energy lost by an incident particle is then given by:

$$-\frac{dE}{dx} \approx \frac{2\pi\ N_e\ z^2\ e^4}{m_e c^2\ \beta^2}\left[\ln\left|\frac{2\ m_e c^2\ \beta^2\ W_{max}}{I^2\left(1-\beta^2\right)}\right| - 2\beta^2 - 2\frac{\mathcal{C}}{Z} - \delta\right] \tag{23}$$

where W_{max} is given by:

$$W_{max} = \frac{2\ m_e\ c^2\ \beta^2}{1-\beta^2}\left[1 + \frac{2\ m_e}{M_i\ \sqrt{1-\beta^2}} + \left(\frac{m_e}{M_i}\right)^2\right]^{-1} \tag{24}$$

Note that for incident particle energies satisfying $E \leq \frac{{M_i}^2 c^2}{2 m_e}$, the terms in [ ]'s reduce to roughly unity and so can be neglected. Note that for protons this would correspond to ~861 GeV, i.e., nearly three orders of magnitude beyond the upper energy bound of all space-based SSDs (of which the author is aware).

3 Instrument Descriptions

This section discusses some more specific details of the physical specifications and measurements made by the *Wind* instruments.

3.1 MFI Instrument

The *Wind* SWE instrument consists of a dual, triaxial fluxgate magnetometer mounted on a ∼12 m deployable boom [*Lepping et al.*, 1995]. The outer sensor is mounted at the end of the boom while the inner at ∼2/3 of the length of the boom. The detector has eight dynamic ranges[7] from ±4 nT to ±65,536 nT using a 12-bit analog-to-digital-convert (ADC) corresponding to eight digital resolutions[8] varying from ±0.001 nT to ±16 nT. The sensor noise level is nominally $\lesssim$0.006 nT rms over ∼0–10 Hz. This results in a precision of ∼0.025% and a sensitivity of ∼0.008 nT/step quantization. The instrument returns one 3-vector magnetic field ∼10.9 times per second for most of the mission[9]. The onboard sun sensor and star trackers allow the instrument team to correctly calculate the spin phase of the spacecraft when in Earth's (or the Moon's) shadow throughout the early phase of the mission (i.e., prior to ∼May 2004). This is critical for properly calculating the magnetic field in these regions. The instrument also suffers from several extra harmonics above the expected spin tone harmonics due to power switching between the solar arrays and batteries turning on and off during rotation[10] [e.g., *Koval and Szabo*, 2013]. These are now removed through several automated processes but the user is still warned to be careful with data near the Nyquist frequency of the instrument.

[7] i.e., ±4 nT, ±16 nT, ±64 nT, ±256 nT, ±1024 nT, ±4096 nT, ±16,384 nT, and ±65,536 nT

[8] i.e., ±0.001 nT, ±0.004 nT, ±0.016 nT, ±0.0625 nT, ±0.25 nT, ±1.0 nT, ±4.0 nT, and ±16 nT

[9] That is, after ∼October 1997 the highest sample rate was ∼10.9 sps whereas before ∼November 1997 there were periods with ∼22 sps.

[10] There is also an issue of a ballast mass (copper plate placed outside thermal blankets) being installed near the end of the magnetometer boom shortly before launch that causes time-varying magnetic field signatures due to variation in exposure to sunlight and its rotation through a magnetic field. This is why the instrument team relies primarily upon the inner than outer magnetometer. Note that the MFI team did not find out about the addition until after launch when examining pre-launch photographs.

3.2 3DP Instrument

Physical Specs: The *Wind* 3DP instrument [*Lin et al.*, 1995] is comprised of four electrostatic analyzers (ESAs) and three arrays of double-ended semi-conductor solid state telescopes (SSTs). Below we describe the generic properties/parameters of each instrument type and then list the specific specs of each detector. Details come from the original instrument paper by *Lin et al.* [1995] and in-person (and/or email) discussions with Davin E. Larson, James (Jim) McFadden, and Robert (Bob) Lin.

The ESAs are spherical top-hat analyzers on top of microchannel plates (MCPs) that sit above anodes which measure current pulses generated by electron showers emitted from the MCPs. The ESAs are split into low (L) and high (H) energy ranges[11] and into electron (E) and ion (P) detectors. They are thus named EESA Low, EESA High, PESA Low, and PESA High. The two EESAs are mounted on a ∼0.5 m boomlet alone while the two PESAs and SSTs are on an opposing ∼0.5 m boomlet. The top-hat hemispheres are lined with gold black coating to reduce scattered light/glint within the detector. A grid at the analyzer exit prevents leakage fields from the MCP from entering the analyzer section (i.e., top-hat part). Both EESA High and PESA High have 24 discrete anodes while EESA Low and PESA Low only carry 16. The orientation of the detectors is such that the anodes define the poloidal (with respect to the spin axis of the spacecraft) angular resolution. They are arranged such that there are eight anodes with ∼5.625° resolution for the anodes within ±22.5° of the spin plane[12], four anodes (two on each side of the eight) with ∼11.25° resolution between ∼22.5° and ∼45° of the spin plane, and the remaining anodes all have ∼22.5° resolution. Although each ESA has at least 16 discrete anodes, they are often averaged onboard down to an eight anode equivalent. The charge pulses produced by the electron showers emitted from the MCPs hit an anode and are sent to a pre-amplifier-discriminator (specifically a AMPTEK A111) and then accumulated into a 24-bit counter (specifically a 8C24) mounted on the amplifier board. The MCPs are mounted in a chevron pair configuration and designed to produce a gain of $\sim 2\times10^6$ with a narrow pulse height distribution. Each of the two MCPs are ∼1 mm thick with a bias angle of ∼8°. The analyzers are swept logarithmically in energy and the counters are sampled 1024 times per spacecraft spin (∼3 ms sample period) Below we discuss each detector individually.

The SSTs consist of either a pair or triplet of closely-sandwiched silicon detectors. One SST end is covered by a thin lexan foil (SST Foil), to stop protons up to ∼400 keV, with 1500 Å of aluminum evaporated on each side to eliminate sunlight. The oposite end is not covered but open (SST Open) and is lined by a common broom magnet to sweep away electrons below ∼400 keV. The center detector of the triplet has an area of ∼1.5 cm^2 and is ∼0.5 mm thick (SST Thick), while all other silicon wafers are ∼1.5 cm^2 by ∼0.3 mm thick. Each double-ended telescope has two $36°\times20°$ fields-of-view (FOVs) at FWHM, thus each detector type acts like six telescopes (i.e., one SST Foil telescope has two sets of silicon wafer detectors). Therefore, five of the telescopes for each type can cover a 180° × 20° slice of the sky. The rotation of the spacecraft gives a complete 4π steradian coverage. Both ends of telescope 2 are covered with a drilled tantalum cover that acts as an attenuator for the most intense particle events (i.e., reduces the geometric factor by 10). The collimators on the SST Open sides prevent sunlight from directly hitting the silicon wafers on all six Open telescopes except 5. The inside of the collimators are blackened to reduce scattered light. The electronics were designed to recover quickly (within ∼130 ms) from the current pulse generated during exposure to the Sun, i.e., only 30° of rotation are lost for Open telescope 5. The ion-implanted silicon wafers were designed to have exceptionally low leakage currents of $\lesssim$10 nA at

[11] High and low also refer to the sensitivity of the instrument as the fluxes at low energies vastly exceed those at higher energy ranges.

[12] Note that the spin plane of *Wind* is always aligned to within $\lesssim1°$ of the ecliptic plane.

room temperature.

- **EESA Low (EL):** Measures electrons from ~3 eV to ~1 keV though after 2000 most times span ~5 eV to ~1.1 keV. The detector has a 180° × 14° FOV and 16 discrete anodes, i.e., the angular acceptance angle is ±7° (7.5° FWHM). The top-hat has an inner hemispherical radius of ~3.75 cm (R) with a separation of ~0.28 cm (ΔR) and a top-cap separation of ~0.56 cm. This gives an entrance opening half angle of ~19°. The energy resolution is $\Delta E/E$ ~ 20% FWHM. The electrons exiting the top-hat ESA are post-accelerated by at least a +500 V potential (commandable and changed over mission lifetime as MCPs slowly degrade) to increase the detection efficiency to ~70%. A single attenuator grid results in a total geometric factor of 1.26×10^{-2} E cm^2-sr (where E is energy in eV). All particle distribution returned by this instrument using the software[13] written by *Wilson III* [2021] have 15 energy bins and 88 solid angle bins, whether in burst or survey mode. The total integration time for this instrument is always one spin period (~3 s) but the time betwen distributions (i.e., between the center time of each) can vary between spin resolution in burst mode to ~24–78 s in survey mode. EL does not have an anti-coincidence detector. The nominal dynamic range is ~10^2–10^9 eV cm^{-2} sr^{-1} s^{-1} eV^{-1}.
- **EESA High (EH):** Nominally measures electrons from ~100 eV to ~30 keV but most distributions have energies varying from a minimum of ~137 eV to a maximum of ~28 keV. The detector has a 360° × 90° FOV and 24 discrete anodes, i.e., the angular acceptance angle is ±45°. Although EH has the same $\Delta R/R$ and opening angle as EL, electrostatic deflectors increase the FOV from ±7° to ±45°. Leakage fields from these deflectors are minimized by a pair of grids at the outer analyzer collimator. The top-hat has an inner hemispherical radius of ~8.0 cm with a separation of ~0.6 cm and a top-cap separation of ~1.2 cm. This gives an entrance opening half angle of ~19° like that of EL. The energy resolution is $\Delta E/E$ ~ 20% FWHM. The MCPs are surrounded by an L-shaped plastic anti-coincidence scintillator, thus allowing the detector to reject MCP pulses coincident with light pulses. The optical geometric factor of the analyzer is ~0.20 E cm^2-sr. Combining this with an MCP efficiency of ~70% and a grid transmission (3 separate grids) of ~73% results in a total geometric factor of ~0.1 E cm^2-sr. All particle distribution returned by this instrument using the software written by *Wilson III* [2021] have 15 energy bins and 88 solid angle bins, whether in burst or survey mode. The total integration time for this instrument depends upon whether its in survey or burst mode, varying between ~3 s in burst mode to several minutes in survey mode. Unlike EL, the time between EH center times is often the same as the total integration times. The nominal dynamic range is ~10^0–10^8 eV cm^{-2} sr^{-1} s^{-1} eV^{-1}.
- **PESA Low (PL):** Nominally measures ions from ~3 eV to ~30 keV but most times span either ~100 eV to ~10 keV or ~700 eV to ~6 keV. PL is nearly identical to EL and only differences will be listed here. After existing the top-hat analyzer, ions are post-accelerated by an electrostatic grid located ~1 mm above the MCP by voltages ≤ -2500 V (commandable and changed over mission lifetime as MCPs slowly degrade) to improve detection efficiency. Due to the intensity of the cold, fast solar wind beam, the PL detector has a collimator/attenuator to reduce the instrument response by a factor of 50. This collimator/attenuator has ~0.24 mm diameter holes uniformly spaced in a ~1 mm × ~2.25 mm grid pattern. This results in a total geometric factor of 1.62×10^{-4} E cm^2-sr but an identical energy-angle response to that of PH. The total integration time for this instrument depends upon whether its in survey or burst mode, varying between ~3 s in burst mode to several minutes in survey mode. All particle distribution returned by this

[13] reorganized and commented/documented versions of the original 3DP software libraries

instrument using the software written by *Wilson III* [2021] have 14 energy bins and 25(64) solid angle bins in survey(burst) mode. The nominal dynamic range is $\sim 10^{4}$–10^{11} eV cm^{-2} sr^{-1} s^{-1} eV^{-1}.

- **PESA High (PH):** Nominally measures ions from ∼3 eV to ∼30 keV but typically covers ∼500 eV to ∼28 keV. PH has the same physical top-hat schematics as PL except that PH has a 360° FOV and 24 anodes instead of 16. PH also has a post-acceleration grid above (before) the MCP to increase ion detection efficiency. Similar to EH, PH has an anti-coincidence scintillator surrounding the MCPs for rejecting light pulses. The optical geometric factor of the analyzer is 0.04 E cm^2-sr, combined with a MCP efficiency of 50% and a grid entrance post-transmission of 75%, while the total geometric factor is ∼0.015 E cm^2-sr. The total integration time for this instrument depends upon whether its in survey or burst mode, varying between ∼3 s in burst mode to several minutes in survey mode. All particle distribution returned by this instrument using the software written by *Wilson III* [2021] have 15 energy bins and five possible solid angle bin settings[14], commandable from ground, for both survey and burst mode. The nominal dynamic range is $\sim 10^{1}$–10^{9} eV cm^{-2} sr^{-1} s^{-1} eV^{-1}.
- **SST Foil (SF):** Nominally measures electrons from ∼25–400 keV but often spans ∼27–520 keV. Each of the telescopes has a geometric factor of ∼0.33 cm^2-sr for a combined value of ∼1.65 cm^2-sr for the five telescope set. The total integration time for this instrument depends upon whether its in survey or burst mode, varying between ∼3 s in burst mode to ∼12 s in survey mode. All particle distribution returned by this instrument using the software written by *Wilson III* [2021] have 7 energy bins and 48 solid angle bins in both survey and burst mode. The nominal dynamic range is $\sim 10^{-1}$–10^{6} eV cm^{-2} sr^{-1} s^{-1} eV^{-1}.
- **SST Open (SO):** Nominally measures protons from ∼20–6000 keV but often spans ∼70–6700 keV. Like SF, each of the telescopes has a geometric factor of ∼0.33 cm^2-sr for a combined value of ∼1.65 cm^2-sr for the five telescope set. The total integration time for this instrument depends upon whether its in survey or burst mode, varying between ∼3 s in burst mode to ∼12 s in survey mode. All particle distribution returned by this instrument using the software written by *Wilson III* [2021] have 9 energy bins and 48 solid angle bins in both survey and burst mode. The nominal dynamic range is $\sim 10^{-1}$–10^{6} eV cm^{-2} sr^{-1} s^{-1} eV^{-1}.
- **SST Foil+Thick (FT):** Nominally measures electrons from ∼400 keV to >1 MeV. There are two telescopes giving a $72° \times 20°$ FOV and total geometric factor of ∼0.36 cm^2-sr (one, telescope 6, has a geometric factor of ∼0.33 cm^2-sr the other, telescope 2, ∼0.03 cm^2-sr). The total integration time for this instrument depends upon whether its in survey or burst mode, varying between ∼3 s in burst mode to ∼12 s in survey mode. All particle distribution returned by this instrument using the software written by *Wilson III* [2021] have 7 energy bins and 16 solid angle bins in both survey and burst mode. The nominal dynamic range is $\sim 10^{-2}$–10^{6} eV cm^{-2} sr^{-1} s^{-1} eV^{-1}.
- **SST Open+Thick (OT):** Nominally measures protons from ∼6–11 MeV. OT has the same FOV and geometric factor as FT as they are on opposite ends of the same telescope pair. The total integration time for this instrument depends upon whether its in survey or burst mode, varying between ∼3 s in burst mode to ∼12 s in survey mode. All particle distribution returned by this instrument using the software written by *Wilson III* [2021] have 9 energy bins and 16 solid angle bins in both survey and burst mode. The nominal dynamic range is $\sim 10^{-2}$–10^{6} eV cm^{-2} sr^{-1} s^{-1} eV^{-1}.

[14] i.e., distributions can have one of the following number of solid angle bins: 121, 97, 56, 65, or 88

3.3 WAVES Instrument

Physical Specs: The *Wind* WAVES instrument is comprised of three orthogonal electric field antenna and three orthogonal search coil magnetometers. The electric field antenna are dipole antennas with two orthogonal wire antennas in the spin plane and one spin axis stacer antenna. The spin plane wire antennas have a diameter of ∼0.38 mm; are made of seven strands of BeCu with a mass density of ∼1.1 g/m; and are capped by a tip mass of ∼10.5 g. The spin axis stacer antennas have a diameter of ∼28.4 mm; are made of polished silver-plated BeCu with a mass density of ∼85.0 g/m; and are capped by a tip mass of ∼52.2 g. The spin plane antennas have mechanical, tip-to-tip lengths of 100 m (x-antenna) and 15 m (y-antenna). The spin axis stacer antennas have a mechanical, tip-to-tip length of 12 m (z-antenna) [*Bougeret et al.*, 1995; *Wilson III*, 2010; *Wilson III et al.*, 2010].

All conducting materials in a plasma will exhibit a sheath region due to the combination of plasma thermal currents and photoelectron currents due to incident ionizing radiation, resulting in non-zero spacecraft floating electric potential fields. These sheaths reduce the mechanical length of electric field antennas to what is called an *effective antenna length* that is usually shorter than the mechanical length. The initial effective antenna lengths are ∼41.1 m, ∼3.79 m, and ∼2.17 m for the x-, y-, and z-antenna, respectively. The electric field antennas on *Wind* operate as dipoles, thus one of the monopoles is assigned a positive and the other a negative value. The +x-antenna has broken twice since launch, once on August 3, 2000 around ∼21:00 UTC and September 24, 2002 around ∼23:00 UTC[15]. These breaks reduced the effective antenna length the x-antenna from ∼41.1 m to ∼27 m after the first break and ∼25 m after the second break [e.g., see discussion in *Malaspina and Wilson III*, 2016; *Malaspina et al.*, 2014].

The search coils contain a 4 mil supermalloy laminated bar with a radius and length of ∼4.7625 mm and ∼393.7 mm, respectively. The initial permeability was $\mu_i \sim 60{,}000$ at 100 Hz. The effective permeability of the rod was found to be $\mu_e \sim 1738$. The search coils contain 5715 turns of #44 AWG wire per section for a total of 40,005 turns per bobbin. There is an additional 1000 turns of #40 AWG wire in the eighth section of the bobbin for calibration [see *Hospodarsky*, 1992, for detailed discussion and calibration].

Measurements: The *Wind* WAVES instrument measures electric and magnetic fields in two ways: as a remote radio receiver for spectrograms and as an in situ instrument for time series vector fields. The WAVES radio receiver is comprised of four receivers: Low Frequency FFT receiver or FFT (∼few to ∼11 kHz), Thermal Noise Receiver or TNR (∼4–256 kHz), radio receiver band 1 or RAD1 (∼20–1040 kHz), and radio receiver band 2 or RAD2 (∼1.075–13.825 MHz). Unfortunately, the FFT receiver, which covers ∼few to ∼10 kHz is dominated by noise and therefore rarely used and not publicly available. The TNR, RAD1, and RAD2 receivers, however, are extremely well calibrated and highly utilized. The radio data are measured either with as a multi-channel, band-limited Fourier spectrum (TNR) or swept frequency response (RAD1 and RAD2). For details about the TNR bands, see Table 6.

The WAVES instrument contains two more receivers that record high cadence electric and magnetic fields in time series form. These are the time domain sampler (TDS) receivers. There are two of them, one fast (TDSF) and one slow (TDSS). The TDSF data are always comprised of two electric field components called channels. Channel 1 is always the x-antenna and Channel 2 can be commanded to be the y- or z-antenna. Nearly all TDSF waveform captures use the x- and y-antennas. The TDSS receiver returns four vector fields of three magnetic(electric) and one electric(magnetic) field components. Any combination of channels can be commanded to the

[15]The exact times of the break are not known due to the data products necessary to determine a break not having 100% coverage. These are the current best guesses.

Table 6: Wind WAVES TNR Specs

Band	Range (kHz)	Sampling Rate (kHz)	Measurement Time (ms)
A	4-16	64.1	320
B	8-32	126.5	160
C	16-64	255.7	80
D	32-128	528.5	40
E	64-256	1000.0	20

spacecraft provided there is three magnetic(electric) and one electric(magnetic) field components. Both TDSS and TDSF have commandable sample rates from ∼117 sps to 7500 sps for TDSS and from ∼1800 sps to 120,000 sps (see Table 7 for specific modes). All TDS waveform captures, called TDS events for brevity, have 2048 time steps per field component. When in its highest sampling rate, the TDSF data have little to no gain below ∼120 Hz so the data are high pass filtered at ∼150 Hz in the data documented by *Wilson III* [2023]. The search coils show a gain roll off ∼3.3 Hz, thus are not DC-coupled [e.g., see *Wilson III*, 2010; *Wilson III et al.*, 2010, 2012, 2013a, and references therein for more details]. The instrument related sections of this paper are reproduced at the *Wind* project webpage[16]. Some additional documentation exists also at the WAVES instrument webpage[17]. The content and format of the various WAVES data products are also described on the instrument webpage.

Table 7: Wind WAVES TDS Specs

Speed	Fast Sampler (sps)	Slow Sampler (sps)
A	120,000	
B	30,000	
C	7,500	7,500
D	1,875	1,875
E		468
F		117

[16] https://wind.nasa.gov
[17] https://spdf.gsfc.nasa.gov/pub/data/stereo/documents/websites/solar-radio/wind/index.html

3.4 SWE Instrument

The *Wind* SWE instrument consists of three separate detectors: two Faraday cup (FC) sensors; a vector electron and ion spectrometer (VEIS); and a strahl[18] sensor (Strahl). Nominally, both the FCs and the VEIS detectors can measure ions while the Strahl detector only electrons. However, the high voltage power supply failed on VEIS on May 31, 2001 reducing the SWE capabilities to the FCs for ions and Strahl detector for electrons. The discussion below will be taken from *Ogilvie et al.* [1995], *Kasper* [2002], and *Kasper et al.* [2006]. The detectors' specifications and nominal ranges are shown in Table 8.

Table 8: SWE Detector Specs [altered from Table II in *Ogilvie et al.* [1995]]

Comments	**FCs**	**VEIS**	**Strahl**
Energy/charge Range[a] [keV/e]	∼0.15–8.0	∼0.007–24.8	∼0.005–5.0
Resolution at FWHM			
$\Delta(E/Q)/(E/Q)$	∼6.5–13%	∼6%	∼3%
Total Instrument Geometry Factor			
GF [cm^2 sr]	∼110	∼0.00046	∼0.0007
FOV[b]	N/A	7.5° × 6.5°	≈ 3° × ±30°

[a] nominal and/or design values/measurements; [b] field-of-view;

VEIS: The *Wind* VEIS detector is comprised of two units each with three separate ESAs, i.e., six ESAs total. The instrument was nominally intended to measure ions and electrons over an energy-per-charge range of ∼0.005–24.8 keV/e with 16 logarithmically spaced energy bins and a resolution of $\Delta(E/Q)/(E/Q) \sim 6\%$. Ions and electrons were measured sequentially by flipping the sign of the electric potential in the ESAs. The particles were detected using channel electron multipliers. The FOV for each ESA, 7.5° × 6.5°, is determined entirely by a collimator at the entrance to the ESA and the sensitive area of the detector. Thus, each analyzer has geometric factor of ∼0.00046 cm^2-sr for a total geometric factor of ∼0.00276 cm^2-sr. The hemispherical plates have radii of ∼4.717 cm and ∼5.443 cm. Near the entrance, the outer hemispherical plate of the ESA has a mesh-covered hole to serve as a light trap. Between the exit of the ESA and the channeltron there is a high-transparency mesh grid to prevent electric field leakage between the two sections. These features help improve the accuracy of the solid angle knowledge and greatly reduce the responses resulting from photoelectrons produced inside the detector. Note, there two channeltrons per analyzer, one for electrons and one for ions. The gains of each of the six analyzers must be known to ∼1%. This was achieved using UV photons to excite each detector to provide a stable relative calibration for each.

FC: The *Wind* FCs are located on the top and bottom of the spacecraft bus, each pointed ∼15° away from the spin plane of the spacecraft, i.e., the FC normals are pointed ∼15° above and below the ecliptic plane. Each FC has nine grids, one acting as a square-wave modulator at 200 Hz, one biased to -130 V located just above the collecting plates and seven more grounded grids located on either side of the the modulator grid and the collecting plates (three above, four below). The modulator acts as to define the energy-per-charge of the incident ions and to discriminate between charged particles and the photoelectric currents generated by sunlight. The biased grid acts as the suppressor, i.e., to prevent the loss of secondary electrons from the collector plates. The outermost

[18] German for beam, the strahl is the magnetic field-aligned, anti-sunward (usually) electron population typically seen with E ∼ few 10s of eV.

grounded grids reduce the emission of time-varying electric fields near the front/aperture of the sensor. The gounded grids between the modulator and suppressor grids reduce the capacitively-coupled currents induced by the modulator electric fields. The collector plates are semi-circular in shape (i.e., hemispheres) and are connected to preamps to measure the net current incident on the plate. The currents are inverted to estimate a model reduced velocity distribution function for both protons and alpha-particles. Each of the FCs have a total collecting area of ∼34 cm^2 for normal incidence particles, a FOV of $\sim 121^\circ \times 121^\circ$, an energy-per-charge range of ∼0.15–8.0 keV/e over 64 logarithmically spaced energy bins and a resolution of $\Delta\left(E/Q\right)/\left(E/Q\right) \sim 6.5$–13%, and a total geometric factor of ∼110 cm^2-sr. When the detector is in a mode that uses a ∼30 ms integration time, the instrument can measure net currents in the range of $\sim 3 \times 10^{-7}$ to $\sim 3 \times 10^{-2}$ μA (i.e., $\sim 3 \times 10^{-7}$ μA is the thermal noise level for a ∼30 ms integration time).

Strahl: The *Wind* Strahl detector is a truncated, toroidal electrostatic analyzer that bends particles through ∼131° before they hit a MCP stack with anodes behind. The instrument's original design had a FOV of $\sim 3^\circ \times \pm 30^\circ$. There are two channel plates, with six anodes per plate, each covering ∼5° of the sky (i.e., ∼30° total per plate). The detector has an energy-per-charge range of ∼0.005–5.0 keV/e with a resolution of $\Delta\left(E/Q\right)/\left(E/Q\right) \sim 3\%$ using 16 logarithmically spaced energy bins. In its original configuration, the instrument would step the energy only once per spin, thus requiring 16 spins to complete the energy sweep. The detector has a geometric factor of ∼0.0007 cm^2-sr per anode, i.e., total of ∼0.0084 cm^2-sr. The two toroidal plates have inner radii of ∼5.40 cm and ∼14.4 cm while the outer radii are ∼6.60 cm and ∼15.6 cm.

After the failure of VEIS, Strahl was reconfigured to have 13 energy channels with eight azimuthal angle bins (each ∼45° wide) and six poloidal/elevation bins (each ∼9° apart) for a total of 624 measurements accumulated over three spacecraft rotations, i.e., ∼9 seconds in duration. The poloidal angles are defined by the anodes, the azimuthal by the spacecraft rotation, and the energy by the toroidal plate potentials. Assuming the spacecraft spin axis is directed exactly along the south ecliptic direction, then the mid-point look direction of the six poloidal angles relative to the ecliptic plane are: -26.55°, -17.10°, -7.34°, +7.63°, +17.10°, and +26.53°. The 13 energies were[19] as follows: 19.34 eV, 38.68 eV, 58.03 eV, 77.37 eV, 96.71 eV, 116.1 eV, 193.4 eV, 290.1 eV, 425.5 eV, 580.3 eV, 773.7 eV, 1006 eV, and 1238 eV. These values correspond to electron speeds ranging from ∼2608 km/s to ∼20,830 km/s.

[19]The past tense is used here because these energy bin values may change over time (for various reasons related to detector aging) and the documentation is specific to when the instrument was originally reconfigured.

3.5 SMS Instrument

The *Wind* SMS instrument consists of three separate detectors: the Solar Wind Ion Composition Spectrometer (SWICS), the high-resolution MASS spectrometer (MASS), and the Supra-Thermal Ion Composition Spectrometer (STICS). The SWICS and STICS detectors can measure ions from hydrogen (H) to iron (Fe) and MASS from helium (He) to neon (Ne). The SWICS and STICS detectors can determine mass-per-charge (M/Q) from 1–30 and 1–60, respectively. As discussed in Section 1.2, the SWICS detector was turned off in May 2000 so it's no longer producing data. The MASS detector has suffered a few incidents of degradation in its acceleration power supply, thus the publicly available data from this detector are limited. The majority of the science quality data produced by SMS comes from STICS, which is still actively producing new data and new data products. The discussion below will be taken from *Gloeckler et al.* [1995], *Gruesbeck* [2013], and *Chotoo* [1998]. The detectors' specifications and nominal ranges are shown in Table 9.

SWICS: The *Wind* SWICS detector is a time-of-flight (TOF) mass spectrometer, capable of measuring the mass (M), mass-per-charge (M/Q), and energy (E) of incident particles. Ions enter the electrostatic deflection analyzer through a large-area, conical, multi-slit collimator then pass through a TOF system. The entire assembly gives STICS an energy-per-charge, mass-per-charge, and mass resolution of $\Delta\left(E/Q\right)/\left(E/Q\right) \sim 6\%$ FWHM, $\Delta\left(M/Q\right)/\left(M/Q\right) \sim 4\%$ FWHM, and $\Delta M/M \sim 20\%$ FWHM[20], respectively. The SWICS detector covers the energy-per-charge range of ∼0.5–30 keV/e with a total geometric factor of ∼0.0023 cm^2-sr and a FOV of $4° \times 45°$.

The width of the collimator channels are designed such that they limit dispersion and flight path differences in the TOF system to $< 0.5\%$. The deflection system is conical in shape, has a small angle, and is pie-shaped with ∼45° deflection plates. These deflection plates are connected to a variable power supply that cycles through 60 logarithmic energy steps, separated by ∼7%, one step per spacecraft spin (i.e., once every ∼3 seconds). The deflection system uses a combination of serration, black-coating, and light traps to eliminate stray or reflected light and UV radiation. This deflection system defines the energy-per-charge resolution and is used for the mass versus mass-per-charge analysis.

Ions are post-accelerated by up to ∼30 kV after exiting the deflection system, before entering the TOF system. The post-acceleration energy gain after the collimator is necessary for depositing enough energy in the solid state detector (SSD), which typically have a ∼25–35 kV threshold. After this, the ions strike a thin (∼2 μg cm^{-2}) carbon foil[21], supported on an ∼85% transmission nickel grid, at the entrance to the TOF telescope. The ion will pass through and eject at least one secondary electron that strikes the start MCP detector. Behind the MCP are two discrete anodes to help provide elevation angle information. The ion propagates ∼10.5 cm to a SSD[22], the gold front surface of which acts as the electron source for the second, stop MCP. The electrons are deflected toward the start and stop MCPs by a common ∼1 kV power supply, which negligibly affects the ions. The difference in flight path between the secondary electrons only introduces a ∼0.5 ns FWHM timing uncertainty. Thus, the instrument measures or sets or knows the TOF time, τ, incident energy-per-charge, E/Q, residual energy, E_{res}, post-acceleration voltage, ϕ_a, TOF path length, d, energy-per-charge accounting for small loss at start foil, E'/Q, and the nuclear defect [e.g., see *Ipavich et al.*, 1978] in the SSDs, α. From these one can calculate the the mass (M), mass-per-charge (M/Q), charge state (Q), incident energy (E), and incident speed (V_{inc}):

[20] $\Delta M/M$ is species-dependent

[21] *Gruesbeck* [2013] shows an example estimate of the energy loss due to the carbon foil for an oxygen atom, with an initial kinetic energy of ∼78.81 keV, to be ∼4.42 keV for the STICS TOF system.

[22] The SSD is gold-silicon (Au-Si) wafer.

$$M = 2\left(\frac{\tau}{d}\right)^2 \left(\frac{E_{res}}{\alpha}\right) \tag{25a}$$

$$Q = \frac{E_{res}/\alpha}{\phi_a + E'/Q} \tag{25b}$$

$$\frac{M}{Q} = 2\left(\frac{\tau}{d}\right)^2 \left(\phi_a + E'/Q\right) \tag{25c}$$

$$E = Q\left(\frac{E}{Q}\right) \tag{25d}$$

$$V_{inc} \approx 438\sqrt{\frac{E}{M}} \tag{25e}$$

where the units of V_{inc} are km/s for E/M in units of keV/amu.

Table 9: SMS Detector Specs [altered from Table I in *Gloeckler et al.* [1995]]

Comments	**SWICS**	**MASS**	**STICS**
Ion Species[a]	H–Fe	He–Ni	H–Fe
Mass/charge Range[a] [amu/e]	1–30	N/A	1–60
Energy/charge Range[a] [keV/e]	∼0.5–30	∼0.5–11.6[b]	∼8–226
Resolution at FWHM			
$\Delta(E/Q)/(E/Q)$	∼6%	∼5%	∼5%
$\Delta(M/Q)/(M/Q)$	∼4%	N/A	∼15%
$\Delta M/M$ ∼20%[b]	∼1%[b]	∼12%[c]	
Total Instrument Geometry Factor			
GF [cm^2 sr]	∼0.0023	N/A	∼0.05
gf [cm^2]	∼0.018	∼0.35	N/A
FOV[d]	4° × 45°	4° × 40°	4.5° × 156°
Other Paramters			
Dynamic Range[a]	10^{10}	10^{10}	5×10^{10}
Min eflux[e,a] [cm^{-2} sr^{-1} s^{-1} $(keV/e)^{-1}$]	N/A	10^{-6}	N/A
Min iflux[f,a] [cm^{-2} s^{-1}]	10^{-2}	10^{-2}	N/A

[a] nominal and/or design values/measurements; [b] species-dependent; [c] STICS only measures mass above ∼30–100 keV, depending on species; [d] field-of-view; [e] energy flux [f] integrated number flux

The total residual kinetic energy, E_{res}, is measured by one of three low-noise, rectangular SSDs. The center SSD is used for bulk/thermal solar wind ions when the instrument points at the sun (i.e., once per spin) and for suprathermal ions for all other pointing directions. The two side detectors primarily measure suprathermal ions for all pointing directions. Together, the three SSDs have a combined FOV of ∼45° for one pointing direction. By sectoring the respective outputs, one can determine anisotropy information above, below, and in the ecliptic plane.

MASS: The *Wind* MASS detector is a mass spectrometer capable of distinguishing the elemental and isotopic solar wind ion composition. Like SWICS, MASS employs an electrostatic deflection system and a TOF mass analyzer system. However, the electrostatic deflection system for MASS is spherical in shape and operates as a UV trap and energy-per-charge discriminator/filter. The

entire assembly gives MASS an energy-per-charge and mass resolution[23] of $\Delta\,(E/Q)\,/\,(E/Q) \sim 5\%$ FWHM and $\Delta M/M \sim 1\%$ FWHM, respectively. The MASS detector has an energy-per-charge range[24] of ∼0.5–11.6 keV/e total integrated (over solid angle) geometric factor is ∼0.35 cm^2.

The ions enter the spherical hemispheres of the electrostatic deflection system, which has a mean radius of ∼107.75 mm with a separation of ∼4.50 mm, deflecting the original particle trajectory by ∼128°. The hemispheres have a voltage range from ∼ -0.077 kV to ∼ +1800 kV in 64 logarithmic energy steps. After passing through the the electrostatic deflection system the ions impact a thin carbon foil.

The ions retained their charge state through the electrostatic deflection system. At the start of the TOF system is a 4 x 15 mm, grid-supported, ∼2 μg cm^{-2} thin carbon foil. Unlike the ions passing through the foil in SWICS, these ions mostly reach a neutral or singly charged state, with a smaller fraction of incident ions retaining final charge states, Q^*, satisfying $Q^* \geq +2$ or $Q^* \leq$ -1. As the ion emerges from the foil, a few to a few tens of secondary electrons are ejected. These electrons are accelerated to a start MCP that begins the TOF system timing. Only those ions that have $Q^* \geq +1$ are accelerated in the opposite direction to their original incidence toward a large area (∼10.0 x 1.5 cm) stop MCP (i.e., ion path through electrostatic deflection system to the stop MCP has an S-shape).

The electric potential used to accelerate the particles in the TOF system is not a static, constant potential, but depends upon spatial position, z, normal to the carbon foil and stop MCP surface. That is, the ions enter the TOF system through the carbon foil at $z = 0$ (with a non-normal angle of incidence) and are deflected through an arc (with $z > 0$) returning to the stop MCP also at $z = 0$. The magnitude of the electric potential satisfies $\phi \propto z^2$. This profile is achieved by putting the TOF system between a positively charged, hyperbolically-shaped potential plate and a V-shaped, low potential plate. In such a potential, the TOF duration, τ, depends only upon the mass-per-charge, i.e., $\tau \propto \left(\frac{M}{Q^*}\right)^{1/2}$. Since τ is accurately measured to fractions of a nanosecond and the magnitudes of τ tend to satisfy ∼60–460 ns, the ion mass can be measured to a high degree of accuracy for Q^* = +1 ions.

The entire TOF system floats at an adjustable potential, $\phi_{A/D}$, relative to the electrostatic deflection system. This floating potential has 256 linearly-spaced values between ∼ -6.0 kV and ∼ +1.7 kV. The value of $\phi_{A/D}$ is adjusted once per spin, where negative values accelerate lower energy ions to increase the fraction of $Q^* = +1$ ions exiting the foil and postive values are used to decelerate higher energy ions to contain them within the TOF system (i.e., so they don't hit the surface opposite the stop MCP).

STICS: The *Wind* STICS detector is a TOF mass spectrometer, capable of measuring the mass (M), charge state (Z), and energy (E) of incident particles. The detector is composed of three telescopes, oriented to view latitude sectors[25] and rely on the spacecraft spin to map out nearly the full 4π steradian sky. Ions enter through an aperture opening and immediately pass through an ESA similar to the concept behind the 3DP top-hats but STICS has an angular acceptance angle of ∼4.8°. The ESA serves as a UV trap and an energy-per-charge discriminator/filter. The azimuthal sectors are divided into 16 equally sized bins, each spanning ∼22.5°. The STICS detector covers the energy-per-charge range of ∼6.2–223.1 keV/e with a total geometric factor of ∼0.05 cm^2-sr and a FOV of 4° × 156°.

[23] both energy and mass resolution are species-dependent

[24] energy range is also species-dependent

[25] The sector angles, relative the spacecraft spin plane (i.e., 0° is in spacecraft spin plane), are as follows: Telescope 1 covers +79.5° – +26.5°, Telescope 2 covers +26.5° – −26.5°, and Telescope 3 covers −26.5° – −79.5°.

The spherical hemispheres have a mean radius of ∼107.75 mm with a separation of ∼4.50 mm with a voltage range from ∼0.263 kV to ∼9.45 kV, deflecting the original particle trajectory by ∼125°. The hemisphere voltage difference is stepped through 30 times on a logarithmic scale allowing the detector to discriminate the particle's energy-per-charge over the range ∼6.2–223.1 keV/e for a resolution of $\Delta\left(E/Q\right)/\left(E/Q\right) \sim 5\%$ FWHM. The voltage is stepped once every two spins, which corresponds to ∼180 seconds for a full energy sweep. The STICS TOF assembly is very similar to that of SWICS described above except there is no post-acceleration grid after the ESA and the TOF path length is ∼10 cm instead of ∼10.5 cm. The lack of post-acceleration also implies the lower energy ions will not register in the SSD. Once the ions hit the SSD, two events will occur: (1) if the incident ion's total energy exceeds the threshold energy of the SSD, i.e., ∼30–35 keV, then the ion's energy can be measured; (2) the incident ion ejects another secondary electron from the SSD which is measured by a second MCP to determine the stop signal. The duration between start and stop times allows the instrument to calculate the particle speed since the telescope length is well defined at 10 cm. The entire assembly gives STICS a mass-per-charge and mass[26] resolution of $\Delta\left(M/Q\right)/\left(M/Q\right) \sim 15\%$ FWHM and $\Delta M/M \sim 12\%$ FWHM, respectively. Additional details of the instrument calibration, operation, and data products can be found in *Gruesbeck* [2013] and *Chotoo* [1998].

The properties of each observed particle (i.e., mass, mass-per-charge, and energy) are calculated onboard. This data is saved and sent to ground. The instrument also creates pulse height analyzed (PHA) words for a subset of the observed particles. Each PHA word contains the measured TOF, energy, and observation direction information. From this, the element, charge state, and velocity of the particle can be determined. Using the combination of this information, one can construct the phase space density distribution for each ionic species. The data products currently available (as of August 15, 2024) are H^+ and He^{2+}, both separated into observations made in the magnetosphere and those in the solar wind. Eventually, the following additional ion species data are to be released: He^+, C^+, C^{2+}, C^{5+}, O^+, O^{6+}, and Fe^{10+}.

[26] Only measures mass for ions with $E \gtrsim$ 30–100 keV, depending on species.

3.6 EPACT Instrument

The *Wind* EPACT instrument consists of three separate detectors: the Low Energy Matrix Telescope (LEMT); the Electron Isotope Telescope (ELITE); and the Suprathermal Energetic Particle (STEP) telescope. The ELITE system contains three separate telescopes comprising two Alpha-Proton-Electron (APE) telescopes (APE-A and APE-B) and one Isotope Telescope (IT). The LEMT system is also composed of three telescopes, but all measure the same particles. The STEP system contains two identical telescopes. All telescopes except STEP use the "dE/dx vs E" method to identify particles relying on solid state detectors (SSDs). The STEP telescopes measure time-of-flight (TOF) and energy using start and stop MCPs in combination with a SSD to measure the total energy (similar to the SMS STICS design discussed in Section 3.5). As discussed in Section 1.2, the ELITE system had a major failure in its HVPS in 1995 resulting in only APE-B returning one energy channel of protons between ∼5 and ∼20 MeV while IT and APE-A return nothing. The discussion below will be taken from *von Rosenvinge et al.* [1995b], *Chotoo* [1998], *Filwett et al.* [2017], and *Filwett et al.* [2019]. The detectors' specifications and nominal ranges are shown in Table 10.

Table 10: EPACT Detector Specs [altered from Table I in *von Rosenvinge et al.* [1995b]]

Comments	**LEMT**	**APE-A**	**APE-B**	**IT**	**STEP**
Ion Species[a]	H–U	e, H–Fe	e, H–Fe	He–Fe	He–Fe
Charge Range[a] [e]	+2 to 90	-1 to +26	-1 to +26	+2 to 26	+2 to 26
Energy Ranges					
Electrons [MeV][a]	N/A	∼0.2–2.0	∼1–10	N/A	N/A
Hydrogen [MeV][a]	∼1.4–10	∼4.6–25	∼19–120	N/A	∼0.1–2.5[b]
Helium [MeV/nucleon][a]	∼1.4–10	∼4.6–25	∼19–500	∼3.4–55	∼0.04–8.1
Iron [MeV/nucleon][a]	∼2.5–50	∼15–98	∼73–300	∼12–230	∼0.020–1.2
Total Instrument Geometry Factor					
GF [cm^2 sr]	∼3×17	∼1.2	∼1.3	∼9.0	∼2×0.4

[a] nominal and/or design values/measurements; [b] extra data product

STEP: The *Wind* STEP detector is a time-of-flight (TOF) mass spectrometer, capable of measuring the energy (E) and TOF duration of incident particles, which allows for the determination of mass (M). Ions enter a collimated sun shade and are incident on two thin (each ∼1000 Å thick) nickel foils. After emerging from the foils, ∼4–30 secondary electrons are ejected and are then deflected toward a start MCP by a ∼1 kV potential. The TOF system is ∼10.5 cm in length and it typically takes ions ∼2–100 ns to reach the SSD at the end of the TOF assembly. The nominal FOV is 17° × 44° (poloidal by azimuthal angles) with a total geometric factor of ∼0.4 cm^2-sr per telescope (two telescopes total). The two telescopes are pointed at ∼64° and ∼111° relative to the spacecraft spin axis[27]. The azimuthal scans of each telescope are divided into eight equal segments of ∼45°. STEP cannot distinguish the charge state of the ions but nominally measures charge states from ∼2–26 (though with careful effort hydrogen can be separated, as discussed below). The detector's energy range depends upon the species but can go well below 100 keV/nucleon for iron to over 8 MeV/nucleon for helium. The instrument is sensitive enough to distinguish the following ion populations: H^+, He^{2+}, CNO^{X+}, NeS^{X+}, and Fe^{X+}. That is, STEP can determine if an incident ion is in the carbon-nitrogen-oxygen group but cannot distinguish which of the three or its charge state. This diversity of ion groups is only available for longer integration times (i.e., ∼1 hr)

[27] The spin axis is pointed toward the south ecliptic pole

while the shorter integration times (i.e., ∼10 minutes) only allow for H^+, He^{2+}, CNO^{X+}, and Fe^{X+}.

LEMT: The *Wind* LEMT detector consists of three telescopes, each with 16 apertures covered by surface barrier detectors, SSDs, arrayed on a spherical dome. Each of these are ∼18 ± 0.34 μm thick and have surface areas of ∼1.75 cm^2. These top/outer detectors measure the dE/dx of the particle, i.e., its loss of energy with respect to spatial displacement through a solid material, the so called Bethe-Bloch effect[28] [e.g., see Chapter 13 of *Jackson*, 1998, for basic theory]. Each of the 16 surface SSDs have ∼0.3 mil (∼7.62 mm) kapton aluminum foil on inside surface and indium-tin-oxide foil (same thickness) on outside surface. Inside each of the three spherical domes, there is a residual energy, E, detector located directly behind (i.e., just under ∼6 cm from furthest dome inner surface) the spherical domes. This detectors, ion-implanted silicon (Si), are ∼1000 μm thick and have surface areas of ∼36 cm^2. They are subdivided into five ∼13.3 mm wide strips on each side (top and bottom), where strips are orthogonal on opposite sides. Each strip has its own, independent preamplifier. Behind the residual energy detector lies a ∼65 cm^2 x ∼1000 μm thick, ion-implanted Si, anti-coincidence detector. Each spherical dome has a total geometric factor of ∼17 cm^2-sr for a total of ∼51 cm^2-sr for the entire LEMT system. The instrument can nominally measure ions with charge states from ∼2–90 and particle energies from ∼1.4–50 MeV/nucleon. In practical use, the instrument usually measures helium to lead over ∼2–20 MeV/nucleon *Reames* [2017]. Each spherical dome has a nominal FOV of $126° \times 126°$ and the spin of the spacecraft allows for full 4π sr coverage. LEMT does not determine charge state but it does determine the element. The publicly available data includes hourly averaged omnidirectional spectra of He^{2+}, C^{X+}, O^{X+}, Ne^{X+}, Si^{X+}, and Fe^{X+}.

APE: The *Wind* APE detector consists of two telescope systems, APE-A and APE-B. APE-A is a single-ended telescope with a nominal FOV of $50° \times 50°$. The opening is covered by two thin foils to protect the detector from high count rates of lower energy particles and sunlight. The outer foil is ∼25 μm thick sheet of kapton. The inner foil is ∼12 μm thick sheet of aluminum. Below these foils are two silicon detectors, A1 and A2, and two lithium-drifted silicon detectors (LiDs), A3 and A4. The A1 and A2 detectors are silicon surface barriers that are each ∼8 cm^2 x ∼150 μm thick. The A3 and A4 detectors are circular LiDs that are each ∼17 cm^2 x ∼3000 μm thick. The geometry is defined by there being a coincidence between the A1 and A2 detectors combined with an anti-coincidence with the A4 detector. Much like LEMT, the detector uses the "dE/dx vs E" method to identify particles and cannot deduce the charge state. The total geometric factor of ∼1.2 cm^2-sr and the instrument nominally measures electrons and ions from hydrogen to iron, i.e., charge states satisfying $-1 \leq Q \leq +26$. Nominally, APE-A could measure electrons from ∼0.2–2.0 MeV, protons from ∼4.6–25 MeV, helium from ∼4.6–25 MeV/nucleon, and iron from ∼15–98 MeV/nucleon.

APE-B is a double-ended telescope with a nominal FOV of $54° \times 42°$. The larger (FOV-wise) opening is covered by two thin foils both made of ∼127 μm thick kapton. All of the LiDs in APE-B are silicon-based. Below these are two LiDs, B1 and B2, and each are ∼8 cm^2 x ∼2000 μm thick. Note that B1 is less than 1 cm from the foils but B2 is ∼6-7 cm below B1. Further, B1 and B2 are curved (mean radius of curvature ∼7.0 cm) to minimize pathlength variations of penetrating particles. Immediately below B2 are seven more LiDs. The first two, C1 and C2, are ∼17 cm^2 x ∼3000 μm thick. The remaining five, C3–C7, are ∼36 cm^2 x ∼3000 μm thick. Immediately following C7 is another LiD labeled D and is ∼17 cm^2 x ∼3000 μm thick. Below D are two more foils, from top(inner) to bottom(outer): ∼1020 μm thick aluminum foil and a ∼127 μm thick kapton

[28]The full corrections for real materials can be found in *Skyrme* [1967] and *Paul* [1971].

foil. Nominally, APE-B could measure electrons from ∼1–10 MeV, protons from ∼19–120 MeV, helium from ∼19–500 MeV/nucleon, and iron from ∼73–300 MeV/nucleon.

Particles entering on the B1-side are referred to as forwards particles and those on the D-side as backwards particles. Particles that pass through B1 and B2 but stop before C7 are called stopping particles and the total geometric factor for these particles is ∼1.3 cm^2-sr. Particles stopping in B2 are referred to as 2-D and those making it to C1–C6 are referred to as 3-D. Particles that pass through B1 and B2 and D are called penetrating particles. The total geometric factor[29] for penetrating particles is ∼1.95 x 1.08 cm^2-sr.

IT: The *Wind* IT detector consists of a single-ended telescope with a nominal FOV of $77° \times 77°$ with a total geometric factor of ∼9.0 cm^2-sr and charge states satisfying $+2 \leq Q \leq +26$. Similar to LEMT and the APE telescopes, IT uses the "dE/dx vs E" method to identify particles. The opening is covered by two thin foils to protect the detector from high count rates of lower energy particles and sunlight. The outer foil is a ∼19 μm thick sheet of kapton. The inner foil is ∼12 μm thick sheet of aluminum. Below these foils is a tungsten ring ∼380 μm thick with an inner radius of ∼5.61 cm. There are two tungsten rings, both immediately above a two-dimensional position sensitive detector (PSD), PSD1 and PSD2. The tungsten rings are vertically[30] separated by ∼7.02 cm. They sit ∼0.44 cm above each PSD. The PSDs are each ∼36 cm^2 x ∼150 μm thick of ion-implanted silicon. Each PSD is segmented into 125 strips with a pitch of ∼0.5 mm and an inter-strip gap of ∼35 μm. Preamplifiers are connected to strips 1, 32, 63, 94, and 125 to create four sections of 32 strips each on each PSD. If a particle is incident on a strip between 32 and 63, then the two preamps connected to those two strips will both measure pulse heights but the charge will be distributed between the two preamps proportional to the number of strips between impact location and the preamp strips (i.e., the closer preamp will measure more charge). Below the PSD2, there are three surface barrier (silicon) detectors, E1, E2, and E3. The separation between PSD2 and E1 and between E1 and E2 and E2 and E3 is ∼0.51 cm. These detectors have the following dimensions in order of E1, E2, and E3: ∼26 cm^2 x ∼110 μm thick, ∼34 cm^2 x ∼400 μm thick, and ∼70.3 cm^2 x ∼1000 μm thick. Below E3 by ∼0.35 cm is the first of four LiD detectors, E4, E5a, E5b, and E6[31]. The first three LiDs have dimensions of ∼57.3 cm^2 x ∼4000 μm thick. The last LiD, E6, has dimensions of ∼66 cm^2 x ∼3000 μm thick. There are a total of 26 preamplifiers attached to the stack of detectors, 10 for each of the two PSDs and one for each of surface barrier detectors (E1–E3) and one for each of the LiDs (E4–E6). Nominally, IT could measure helium from ∼3.4–55 MeV/nucleon and iron from ∼12–230 MeV/nucleon and the mass resolution was sufficient to easily distinguish the isotopes of helium and even those of magnesium.

[29] This accounts for the ∼5% view obstruction by the spacecraft bus on the backwards side of the telescope but ignores the possible obstruction due to the magnetometer boom in its FOV due to the small mass per unit area compared to the telescope detectors.

[30] Up is oriented here in such a way as to look along the telescope opening view direction, i.e., along the telescope axis.

[31] E6 acts as an anti-coincidence detector

3.7 KONUS Instrument

The *Wind* KONUS instrument consists of two identical sodium iodide (NaI) crystals activated with thallium (Tl), i.e., NaI(Tl) crystals [*Aptekar et al.*, 1995]. The KONUS instrument is controlled by the Astrophysics division and is a Russian instrument, thus not part of the Heliophysics data policies. The KONUS instrument does not receive any direct NASA funding through the project scientist, thus this section will be limited to just the instrument description and brief description of data products.

Each cylindrical NaI(Tl) crystal has a diameter of ∼127 mm and length of ∼76.2 mm. The crystals are housed in an aluminum case and the entrance aperture is covered by a beryllium (Be) window. The instrument has several measurement channels including two analog channels, A1 (∼10–750 keV) and A2 (∼0.2–10 MeV), four standard amplitude gamma ray channels, SG1 (∼10–50 keV) and SG2 (∼50–200 keV) and SG3 (∼200–750 keV) and SGZ (>10 MeV), and two enabled signal channels for controlling the operation of the pulse height analyzers, ES1 (∼10–750 keV) and ES2 (∼0.2–10 MeV). Nominally the burst mode can measure gamma rays covering ∼0.2–15 MeV at a cadence of $\gtrsim$2 ms with $\Delta E_\nu/E_\nu \gtrsim 5\%$ while the background mode covers ∼0.02–1.5 MeV at a cadence of $\gtrsim$3 s. The KONUS instrument was designed to measure GRBs and solar flares. Between November 1994 and mid-2019, it has measured $\gtrsim$2740 GRBs, $\gtrsim$1040 solar flares, ∼500 short GRBs, and ∼270 soft gamma repeaters (SGRs) [*Frederiks et al.*, 2019].

3.8 TGRS Instrument

The *Wind* TGRS instrument[32] has been powered off since January 2000, thus this section will be more brief than some other instrument descriptions. That is, this section will be a summary of the instrument papers [*Owens et al.*, 1991, 1995]. The instrument was designed to measure sources such as GRBs, bright galactic transient sources, the galactic center, the Crab Nebula, and solar flares.

The *Wind* TGRS instrument is a ∼215 cm^3 cylinder (∼6.7 cm diameter, ∼6.1 cm length) high purity n-type germanium (Ge) crystal with a 170° FOV FWFM[33]. The instrument measured photons with energies satisfying 25 keV $\lesssim E_\nu \lesssim$ 8.217 MeV and an energy resolution of ΔE_ν ∼ 3 keV at 1 MeV. The intrinsic time resolution is ∼62 μs but becomes ±1.5 ms after ground processing/calibration.

The instrument assembly is surrounded by a two-part radiative cooling system. A ∼30 mil (∼0.762 mm) beryllium-copper (BeCu) alloy passive-Sun-shield was included around the outside of the outer radiative cooler. Surrounding ∼90° of this Sun shield is a ∼13.5 mm thick molybdenum/lead (Mo/Pb), ∼1.5 mm of Mo and ∼12 mm of Pb, shield that acts as an occulter for ecliptic plane sources[34]. The outer radiative stage aperture is covered by fine ∼2 mil (∼0.0508 mm) BeCu wires to prevent stray fields due to spacecraft/instrument charging from interfering with onboard electric field measurements (i.e., WAVES). The outer stage was designed to operate at ∼164 K (∼ -109 °C). The inner radiator was designed to operate at ∼85 K (∼ -188 °C). Both radiators are constructed from Be and magnesium (Mg) to minimize weight and x-ray attenuation. The radiating surfaces of both the inner and outer stages, however, are constructed entirely of Be.

The instrument samples data in 8192 discrete energy channels (1 channel ≈ 1 keV). To reduce memory, the first 200 channels are read out as 500 count histograms. There is an event-by-event burst mode for enhancements above channel 200. These are digitized and time-tagged to ∼62.5 μs and stored directly in the onboard 2.75 Mbit burst memory buffer. The instrument also stores 128 sectored, 64 channel histograms (∼2.8° of spacecraft rotation for ∼3 s spin period). Finally, 1024 and 8192 channel histograms are accumulated over ∼3 and ∼24 minutes, respectively (accumulation times are commandable from ground), to determine background.

[32] An interesting note is that the surface finish of the WAVES z-antenna (spin axis) was specifically chosen to reduce the amount of reflected sunlight hitting the TGRS cooling unit. The antenna seams/joints were also oriented to be out of the TGRS FOV.

[33] Full Width Fiftieth Maximum ≃ 2.38 FWHM

[34] The Mo acts to passively shield fluorescent photons produced in the lead layer.

4 Thermal Electron Corrections

This section will discuss how to correct the thermal electron measurements for known artifacts and/or spacecraft-related phenomena that are not part of the velocity distribution which is of interest.

4.1 Total Electron Density

The *Wind* WAVES instrument [*Bougeret et al.*, 1995] can consistently and accurately measure the "upper hybrid line" (sometimes called the "plasma line"). The upper hybrid line is the most unambiguous measure of the total electron density, n_e (see Appendix 17.7 for symbol definitions), in any plasma where the magnetic field magnitude, B_o, can be well measured [e.g., *Meyer-Vernet and Perche*, 1989]. The reason being is that the upper hybrid frequency, f_{uh}, is given by:

$$f_{uh}{}^2 = f_{pe}{}^2 + f_{ce}{}^2 \tag{26}$$

where f_{ce} is the electron cyclotron frequency ($\sim 27.99249\ B_o$[nT]) and f_{pe} is the electron plasma frequency ($\sim 8978.66281\ n_e{}^{1/2}$[cm^{-3}]). Thus, one can see that f_{uh} only depends upon n_e and B_o, given by:

$$\left(\frac{2\pi\ \varepsilon_o\ m_e}{e^2}\right)\left[f_{uh}{}^2 - \left(\frac{e\ B_o}{2\pi\ m_e}\right)^2\right] = n_e \tag{27}$$

where ε_o is the permitivity of free space, m_e is the electron rest mass, and e is the fundamental charge. If an instrument measures f_{uh} directly through the observation of the upper hybrid line and a user combines that with measurements of B_o, the user can invert to calculate n_e. This is the most accurate method for measuring the total electron density in a plasma. Nearly all space environments accessible for in situ measurements will satisfy quasi-neutrality given by:

$$n_e = \sum_s Z_s n_s \tag{28}$$

where Z_s and n_s are the charge state and number density of ion species s (e.g., $s = p$ for protons). Therefore, both thermal electron and ion particle instruments can calibrate their measurements to satisfy Equation 28.

4.2 Spacecraft Potential Estimation

The *Wind* WAVES instrument does not continuously measure the quasi-static, DC-coupled electric field so it cannot directly measure the spacecraft potential, ϕ_{sc}, of the bus. However, there are numerous ways to determine ϕ_{sc} from various measurements [e.g., see *Pulupa et al.*, 2014; *Wilson III et al.*, 2019a, and references therein].

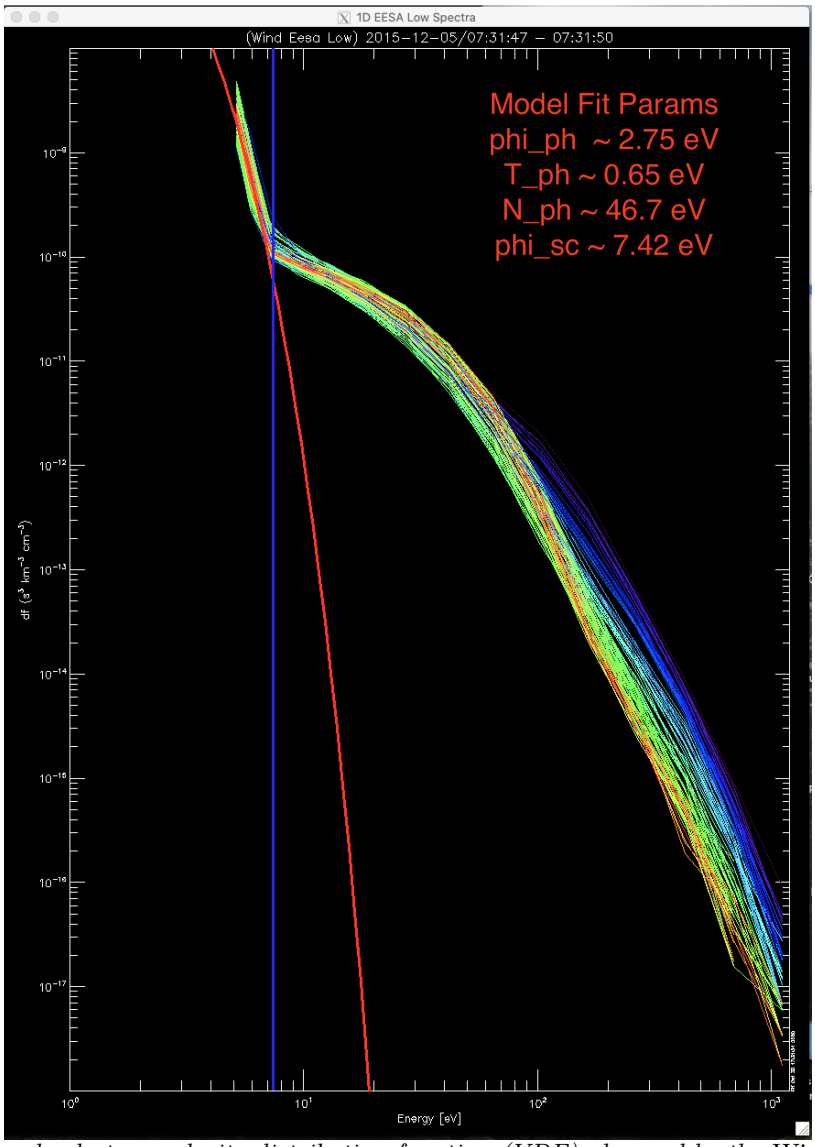

Figure 3: *An example electron velocity distribution function (VDF) observed by the* Wind *3DP instrument [Lin et al., 1995] that has not removed the photoelectrons. The data are shown in the spacecraft frame of reference in units of phase space density [s^{+3} km^{-3} cm^{-3}] versus kinetic energy [eV] The thin rainbow colored lines correspond to the 88 solid angle look directions of the VDF. The thick blue line (at ~7.42 eV) is a rough estimate of the spacecraft potential, ϕ_{sc}, while the thick red line shows a one-dimensional Maxwellian model of the photoelectrons for energies below the thick blue line. The fit parameters of this model are shown in the upper right-hand corner of the plot with the subscript ph for photo.*

Figure 3 shows an example electron VDF measured by the *Wind* 3DP EESA Low instrument. The data are shown as one-dimensional energy spectra in units of phase space density in the spacecraft frame of reference. Each of the thin, rainbow colored lines represents a different solid angle look direction. The thick blue line is indicates the discontinuity in phase space density at

a given energy, which marks a rough cutoff between photoelectrons and ambient electrons [e.g., *Lavraud and Larson*, 2016], i.e., the spacecraft electric potential, ϕ_{sc}. The thick red line shows a model fit to the photoelectron population.

There are two methods for removing photoelectrons from the data. The first is the easiest and somewhat kludgy. The user simply "kills" the data at energies below ∼130% of the vertical blue line then shifts the energies by ϕ_{sc} (after converting to phase space density or flux etc.). The use of 130% instead of 100% can be seen from examining the thick red line. While photoelectrons should not have more kinetic energy than $e\,\phi_{sc}$ if they started with zero during emission from a conductive surface on the spacecraft, there is a thermal spread and ambient electric fields etc. that alter the boundary slightly. The bigger effect is that the estimate of ϕ_{sc} from the discontinuity in phase space density is not the true ϕ_{sc}, as it would vary based upon the density and temperature of the ambient electrons[35].

The second method involves fitting the photoelectrons to some model function, like what is shown by the thick red line in Figure 3, and subtracting that model from the data then "killing" data below ϕ_{sc} then shifting the energies accordingly. This more sophisticated approach helps remove photoelectrons at energies higher than the ϕ_{sc} estimated from the discontinuity and doesn't do so in a discontinuous manner (i.e., more realistic). If done properly, there should be fewer photoelectrons remaining in the final VDF.

All of the above requires that the thermal electron detector measures a low enough energy to capture the photoelectron peak. This does not always occur. For instance, early in the *Wind* mission, the lowest energy bin of the 3DP EESA Low instrument, E_{min}, was set to ∼11 eV and later[36] dropped down to ∼5 eV. During periods when $E_{min} > \phi_{sc}$, one can approximate the spacecraft potential using the measured ion density [e.g., see *Wilson III et al.*, 2019a, and references therein]. This provides an initial guess value for ϕ_{sc}. If the detector geometric factor and anode-specific efficiencies are all well known, then one adjusts ϕ_{sc} until the integrated n_e matches the calculated n_e from the upper hybrid line (see Section 4.1). If the detector geometric factor and anode-specific efficiencies are not well known or well calibrated by time[37], then the derived ϕ_{sc} will be a proxy for the true ϕ_{sc} and will nonlinearly include the anode-specific corrections within as a sort of fudge factor. This later result is the most common thing occuring in research involving the *Wind* 3DP EESA Low instrument.

A database of ϕ_{sc} values [*Wilson III et al.*, 2023a], determined from the EESA Low data similar to that shown in Figure 3, can be found on Zenodo[38]. The data spans from January 1, 2005 to January 1, 2022.

[35] That is, in hotter plasma with similar densities, the ambient electron VDF profile would be broader and also lower in phase space density magnitude. Therefore, the energy where the photoelectrons start to dominate would be higher.

[36] around February 1999

[37] The latter will change over time as the instrument ages.

[38] https://zenodo.org/records/8364797

4.3 3DP Anode Corrections

After knowing/calculating n_e following Section 4.1 and calculating ϕ_{sc} following Section 4.2, one then needs to correct the efficiencies of each anode. These corrections are actually a way that electrostatic analyzers (ESAs) with MCPs often use to adjust the geometric factor for unit conversion and science analysis. That is, there is a total geometric factor determined from optical ray tracing analysis done during design, build, and testing. If everything worked perfectly according to theory with perfect sources, the calibration would be complete. However, the MCP material degrades over time requiring higher and higher initial impact energy. This is mediated by an pre-acceleration grid above the first MCP chevron pair that has a commandable electric potential. Even so, there are other issues within the instrument that lead to gain corrections for which one must account. A further complication specifically with the AMPTEK A111 preamps used in the *Wind* 3DP instrument is that the electronic deadtime and PHD depend upon the PHD of the previous pulse, i.e., it has some form of hysteresis (personal communication with J.P. McFaddon on July 18, 2011). That is, the A111 deadtime depends upon the amplitude of both the initial and trailing charge pulse. Larger pulses require longer recovery times before a second pulse can be registered [*Wüest, M., Evans, D. S., & von Steiger, R.*, 2007]. Therefore, the instrument must be calibrated in space again.

Just to clarify jargon as many will have different definitions, we will refer to the efficiency adjustments here though some would call this a modification of the geometric factor for each anode or a deadtime correction or some combination of these plus other effects. We use efficiency for brevity but know that changing this correction factor will alter the unit conversion process because the practical implication is a modification of the geometric factor for each anode.

The general procedure is to first calculate n_e following Section 4.1 and calculate ϕ_{sc} following Section 4.2. Then to model the VDF according to assumed "known" parameters. The use of a nonlinear, least-squares fit approach with free parameters is often employed [e.g., *Markwardt*, 2009; *Moré*, 1978]. The free parameters depend on the model used, but at 1 AU, it is often assumed that there is a two-component electron VDF because the fit is performed on the 1D VDFs like those shown in Figure 3. So the free parameters are the core and suprathermal electron densities, temperatures, drift speeds, and an exponent if the suprathermal part of the VDF is assumed to be a kappa distribution [e.g., see *Wilson III et al.*, 2019a, and references therein]. The fits are performed iteratively while modifying the efficiencies for every solid angle bin until closure is reached. To help reduce numerical instability [e.g., *Liavas and Regalia*, 1998] and increase the likelihood of a stable, closed solution, the user often reduces the number of free parameters depending upon what they can assume in any given region. Note that the adjusted efficiencies will alter the unit conversion for every energy-angle bin during each iteration so the data starts in units of raw counts at the start of each iteration.

The above method is somewhat circular but there are physical constraints that can be imposed to improve the accuracy of the corrections. For instance, we know $n_e = n_{ec} + n_{es}$, where $n_{ec(s)}$ is the core(suprathermal) electron density. So those two free parameters are tied together. The sum of the two model functions for these components are tied together by the data, i.e., $f_{obs} \geq f_{ec} + f_{es}$. One can also use statistical trends to constrain the bounds on the suprathermal-to-core temperature ratios [e.g., see *Feldman et al.*, 1975; *Skoug et al.*, 2000; *Wilson III et al.*, 2019b, and references therein] and density ratios [e.g., see *Maksimovic et al.*, 2005; *Štverák et al.*, 2009; *Wilson III et al.*, 2019b, and references therein]. One can also use statistical trends to constrain the bounds on the suprathermal and core temperatures [e.g., see *Feldman et al.*, 1978; *Maksimovic et al.*, 2005; *Skoug et al.*, 2000; *Wilson III et al.*, 2019b, and references therein], densities [e.g., see *Maksimovic et al.*, 1997; *Skoug et al.*, 2000; *Štverák et al.*, 2009; *Wilson III et al.*, 2019b, and references therein],

etc. Note that Section 4.4.5 in *Wüest, M., Evans, D. S., & von Steiger, R.* [2007] describes this process in more detail.

5 *Wind* TGRS

The TGRS detector is fully described in the instrument paper [*Owens et al.*, 1995] and will not be discussed in detail as it has not generated data since pre-Jan. 2000.

6 *Wind* KONUS

The KONUS detector is fully described in the instrument paper [*Aptekar et al.*, 1995] and will not be discussed in detail as it is a Russian instrument that is not funded by the Heliophysics Science Division.

7 *Wind* EPACT IT

The IT detector is fully described in the EPACT instrument paper [*von Rosenvinge et al.*, 1995a] and will not be discussed in detail as it has not generated data since pre-Oct. 1995.

8 *Wind* EPACT STEP

The STEP detector is fully described in the EPACT instrument paper [*von Rosenvinge et al.*, 1995a] and further discussed by *Filwett et al.* [2017] and *Filwett et al.* [2019].

Species identification from STEP data is enabled from the measured TOF vs residual E tracks determined during pre-flight calibration (e.g., see Figure 3.4-4 in instrument paper). Once an ion falls onto a specific track, we know its mass in AMU, which can be used, along with the measured TOF and energy losses, to calculate the incident energy. The proton track is not shown in Figure 3.4-4 in *von Rosenvinge et al.* [1995a] and was not calibrated pre-flight. Protons generate fewer secondary electrons from the start foils, and so their measurement efficiency is significantly lower than the heavier ions. So STEP is mostly for heavy ions but one can recover some proton data as evidenced by the publicly available data products.

The SSD energy threshold sets the total measurable energy for each species. If there are no energy losses through the foils and the SSD dead layer, then a threshold of ∼100 keV, would ideally allow us to measure protons just above ∼100 keV, alphas just above ∼25 keV/nucleon, and so on. However, energy losses are proportionally larger at lower energies and for heavier ions, and so the lowest total energy that can be measured also increases with species. Thus, a ∼100 keV threshold does not allow us to measure Fe from above ∼2 keV/nucleon but from ∼25 keV/nucleon which is ∼1400 keV total energy. Note that the STEP mass resolution is not sufficient to separate carbon, nitrogen, and oxygen, thus the CNO data products.

The STEP calibration software can be found in the *Wind* lz decommutation softare *Wilson III et al.* [2021c] and is thus not further discussed.

9 *Wind* EPACT LEMT

The LEMT detector is fully described in the EPACT instrument paper [*von Rosenvinge et al.*, 1995a] and further discussed by *Reames* [2017] (and references therein).

The LEMT calibration software can be found in the *Wind* lz decommutation softare *Wilson III et al.* [2021c] and is thus not further discussed.

10 *Wind* SMS SWICS

The SWICS detector is fully described in the SMS instrument paper [*Gloeckler et al.*, 1995] and will not be discussed in detail as it has not generated data since pre-May 2000.

11 *Wind* SMS MASS

The MASS detector is fully described in the SMS instrument paper [*Gloeckler et al.*, 1995] and by *Hamilton et al.* [1990]. More details can be found in parts of *Ho* [1998] found below.

11.1 *Ho*, (1998) Chapters 2 and 3

CHAPTER 2: INSTRUMENTATION

2.1 The Solar Wind and Suprathermal Ion Composition Experiment

The Solar Wind and Suprathermal Ion Composition (SMS) Experiment on WIND consists of three separate sensors that measure ion species from H to Fe with energies between 0.5 to 230 keV/e. A summary of the three sensors' capabilities is given in Table (2.1). The Solar Wind Ion Composition Spectrometer (SWICS) uses an energy per charge analyzer with post-acceleration up to 30 keV/e. SWICS was designed to measure the mass per charge and mass of ions from 0.5 to 30 keV/e. Unfortunately, a power supply failed which prevents SWICS from meeting its full designed capability. The Supra-Thermal Ion Composition Spectrometer (STICS) measures the supra-thermal ion population with a relatively large geometrical factor. It measures three-dimensional distribution functions for H to Fe from 30 to 230 keV/e in interplanetary space to make direct comparison with ion populations inside the Earth magnetosphere.

The MASS instrument was added to be part of the SMS experiment in 1988 [Gloeckler *et al.*, 1995]. MASS features a new solar wind composition measurement technique and is the first of its kind being flown in space. It measures the elemental and isotopic abundance of solar wind ions with high mass resolution. A detailed description of the MASS sensor is given in the following two sections.

Table 2.1. Capabilities of the three SMS instruments. (Table from Gloeckler *et al.*, 1995).

	SWICS sensor	MASS sensor	STICS sensor
Ion species	H–Fe	He–Ni	H–Fe
Mass/charge range (amu/e)	1–30	–	1–60
Energy range (keV/e)	0.5–30	0.5–11.6[a]	8-226
Mean speed range (km s^{-1})			
H^+	310–2400	–	–
O^{+6}	190–1470	200–900	–
Fe^{+10}	130–1010	200–500	–
Resolution (FWHM)			
Energy, $\Delta(E/Q)/(E/Q)$	0.06	0.05	0.05
Mass/charge, $\Delta(M/Q)/(M/Q)$	0.04	–	0.15
Mass, $\Delta M/M$	0.2[a]	0.01[a]	0.12[b]
Total instrument geometrical factor			
cm^2 sr	2.3×10^{-3}	–	0.05
cm^2	1.8×10^{-2}	0.35	–
Field of View (FOV)			
Pointing direction is	22.5° wrt	22.5° wrt	0°
perpendicular to spin axis	STICS	STICS	
FOV is fan-shaped	4° by 45°	4° by 40°	4.5° by 156°
Dynamic range	10^{10}	10^{10}	5×10^{10}
Minimum flux			
$(cm^2\ s\ sr\ keV/e)^{-1}$	–	10^{-6}	
$(cm^2\ s)^{-1}$	10^{-2}	10^{-2}	–

[a] Species dependent.

[b] STICS measures the mass of ions only above about 30-100 keV (depending on species).

2.2 MASS Principle of Operation

The SWICS instrument on Ulysses (launched in 1990) introduced a technique for solar wind ion composition measurement using an electrostatic analyzer to select the energy per charge (E/Q) of the ion that enters a time-of-flight (TOF) region in which the mass per charge ratio (M/Q) can be measured. If the energy of the ion exceeds the threshold of the solid state detector that is located at the end of the TOF path, the energy (E) of that ion can be measured and hence the mass (M) and charge (Q) of the ion can be separately determined [Gloeckler, 1990].

What makes MASS unique from SWICS and STICS is the design of its TOF region. A specially designed electric field is set up in the TOF region of MASS by placing the equipotential plates in the configuration shown in Figure (2.1). The upper, hyperbolic surface in Figure (2.1) holds a positive potential, V_{hps}, and the V-shaped lower surface is held at an accelerate/decelerate voltage (more on this later). This configuration provides an electric field that increases linearly with distance z from the vertex. A positive ion that starts out at the vertex of the "vee" and travels in this field region along the center line undergoes harmonic motion and will have a TOF proportional to the square root of the M/Q^* ratio, where Q^* is the ion's charge state after passage through a thin carbon foil. The TOF value is totally independent of the ion's energy. Therefore, we can directly measure the ion's mass, assuming $Q^* = 1$, with high resolution and with no energy dependence. The start TOF signal is generated from secondary electrons emitted when an ion passes through the thin (~2.2 μ g/cm^2) carbon foil located at one end of the vertex of the "vee". The

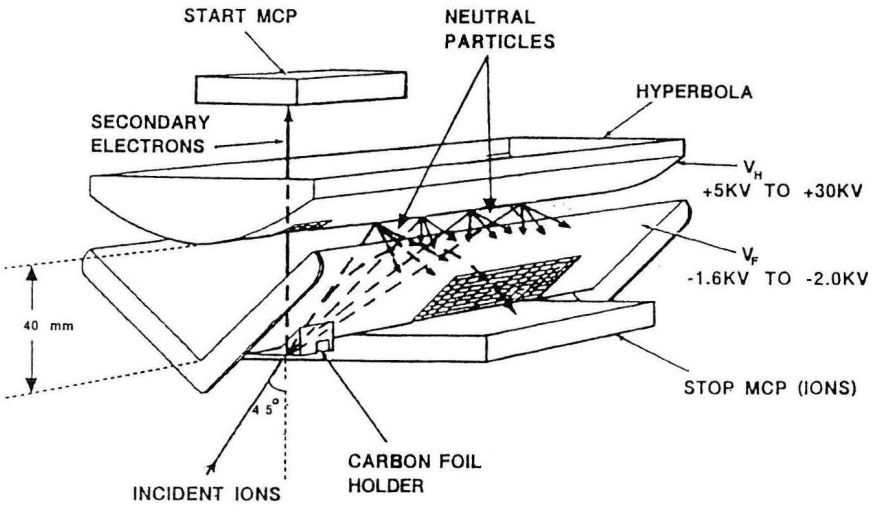

Figure 2.1. MASS TOF equipotential configuration. The hyperbolic top surface has a positive voltage of V_H = 5-30 kV (23.2 kV in flight configuration) and the lower V-shaped surface is held at an acceleration/deceleration potential V_F = 1.6 to –2.0 kV (1.7 to –3.0 in flight configuration). Ions that start out at the carbon foil and travel along the center will hit the stop MCP and have TOF proportional to the ions' $\sqrt{M/Q^*}$ value.

electrons are accelerated through the hyperbola and collect at the start mico-channel plate. A stop signal is obtained when the ion terminates its trajectory directly onto the stop micro-channel plate (MCP) surface, just below the vertex of the "vee". The measured TOFs range from 58.6 ns for protons to 432 ns for iron for V_{hps} = 23 kV. The TOF resolution of the instrument is approximately 1 ns, so that high mass resolution can be obtained. Hamilton *et al.* [1990] reported $\frac{m}{\Delta m}$ of over 100 from their MASS prototype model.

2.3 WIND/SMS/MASS

We show a schematic of the MASS instrument in Figure (2.2). A positive ion enters MASS through the spherical segment deflection system that was built by the University of Bern, Switzerland. The curved path of the ion though the analyzer is out of the plane of the figure. The pointing direction of the aperture of the deflection system relative to the spacecraft x-axis is shown in Figure (2.3). Only ions that have a specified *E/Q* ratio will pass through the analyzer. The *E/Q* is determined by the voltage (V_{dpps}) applied to the inner plate of the analyzer. The V_{dpps} potential is stepped once per spacecraft spin, completing a 60 step cycle, logarithmically spaced from -0.076 kV to -1.467 kV, in three minutes. These steps correspond to *E/Q* ratios of 0.52 to 9.89 keV/e with an energy passband of approximately 4%.

After the selected ions pass through the deflection analyzer, they are accelerated (decelerated) by a negative (positive) potential difference, V_{adps}, between

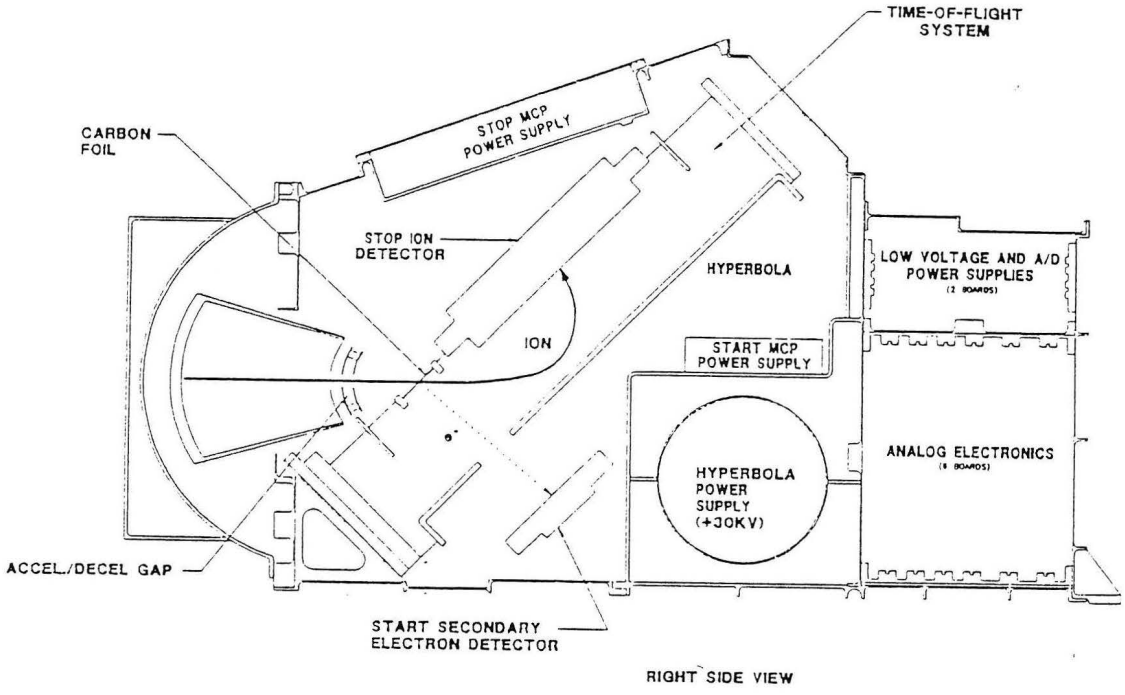

Figure 2.2. A cross sectional view of the WIND/MASS instrument. At the left of the figure is the spherical segment electrostatic analyzer built by the University of Bern. The thick solid line is a typical ion trajectory. The dashed line labeled "e" is the path of the secondary electrons as they accelerate towards the start micro-channel plate.

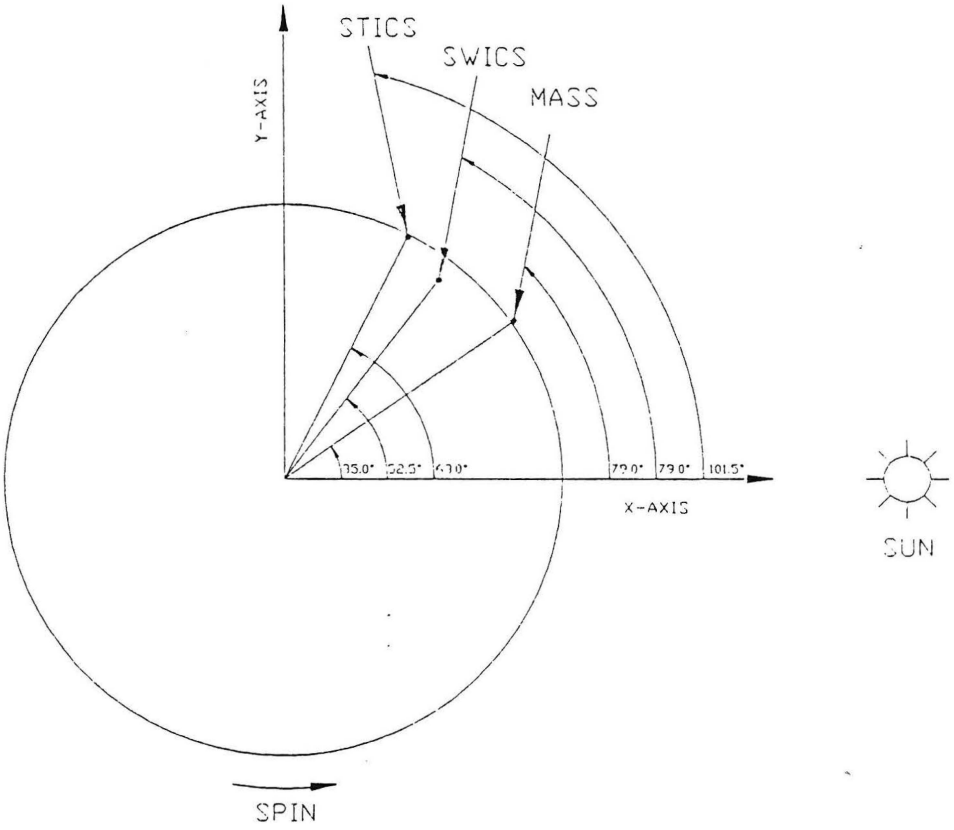

Figure 2.3. The pointing directions of the three SMS sensors on WIND [Gloeckler *et al.*, 1995].

the analyzer and the harmonic TOF region (as shown in Figure 2.2). The purpose of the V_{adps} potential is twofold. The potential accelerates low energy ions to an energy of ~35 keV in the TOF region to increase the yield of singly charged ions after passage through the carbon foil. At low energies, the percentage of +1 ions emerging from the foil increases as a function of the ion's energy [Gonin *et al.*, 1991]. Second, the potential decelerates those ions that have energies too high to be contained within the TOF region.

The exact V_{adps} voltage is determined by an on-board algorithm using data obtained two-science records (120 spacecraft spins, or 120 V_{dpps} steps) prior. MASS determines the solar wind velocity through detecting at which V_{dpps} step the maximum peak in the Front SEDA Rate (FSR, where SEDA stands for Secondary Electron Detection Assembly) occurs. It is assumed this maximum results from solar wind protons. The FSR rate counts pulses from the start MCP. The SMS Data Processing Unit (DPU) then uses this information to determine the solar wind velocity, and uses Equation (2.1) to set the V_{adps} voltage for each of the 60 *E/Q* steps in order to meet the two goals listed above as well as possible.

$$V_{adps} = 2.054 - 0.0322 \cdot L_{adps} \tag{2.1}$$

where L_{adps} is the V_{adps} level, and is given by

$$L_{adps} = A_0 + A_1 \cdot S_H + A_2 \cdot S + A_3 \cdot S_H^2 + A_4 \cdot S_H \cdot S + A_5 \cdot S^2 \tag{2.2}$$

and $A_0 = 215.68$; $A_1 = 7.8900$; $A_2 = -2.2700$; $A_3 = 0.1620$, $A_4 = -0.1870$, $A_5 = -0.0602$

V_{hps} is the hyperbola voltage in kV, S is the current *E/Q* step number (0-59), and S_H is the *E/Q* step corresponding to the solar wind proton peak.

The values of the V_{adps} range from -6.0 kV (accelerating the positive ions) to +1.7 kV (decelerating the ions). However, we limit the V_{adps} range from -3.0 kV to +1.7 kV in flight (L_{adps} from 11 to 160) to avoid possible high-voltage discharge.

The selected ions after passage through the potential V_{adps} will enter the harmonic TOF region at an 45^{O} angle in the symmetry plane (as shown in Figure 2.1). After going through the V_{adps} potential, they will pass through a thin (~2.2 μ g/cm^2) carbon foil. The secondary electrons produced as a result of ions passing through the carbon foil are accelerated upward toward the start MCP that is placed above a hole in the hyperbola. The ions will continue their original path at an 45^{O} angle entering the MASS TOF section if there is no scattering in the carbon foil. A TOF is measured when the ions travel through the harmonic field region and hit the stop MCP placed just below the "vee". The hyperbola voltage and ion energy determine the exact trajectory of the ions in the TOF region. If the energy of the ion is too high, or if the ion exits the foil as a neutral, it will strike the hyperbola. A hyperbola voltage of V_{hps} = 23.2 kV has been used since launch. Assuming the ion has not been scattered from the initial angle after passage through carbon foil, the maximum energy an ion can have inside the TOF region is approximately 46 keV/e (for V_{hps} = 23.2 kV). If we take V_{adps} into account, MASS can measure Fe^{12+} up to a maximum solar wind velocity of 478 km/s (see Table 2.1).

We mentioned in the previous section that the ion's TOF is proportional to the square root of the mass to charge ratio ($\sqrt{M/Q^*}$). The charge, Q^*, is the charge state of the ion after passage through the carbon foil. Gonin *et al.* [1994] have shown that at low energies (~keV/nuc), the most common charge states after the foil

are 0 or +1 (see Figure 2.4). The TOF pulse height analyzer on MASS has 4096 channels covering the range 0-515 ns . The conversion of TOF channel to M/Q^* is given by

$$M^* \equiv M/Q^* = (1.9781\times10^{-7})\cdot(TOF\ \text{Channel})^2 \cdot V_{hps} \qquad (2.3)$$

where the V_{hps} is in kV, and the units of the constant are $amu/e\cdot kV$.

In summary, MASS is one of three sensors of the WIND/SMS instrument package. It features a new measurement technique enabling it to make high mass resolution solar wind composition measurements. In the next chapter we will discuss the analysis of MASS data.

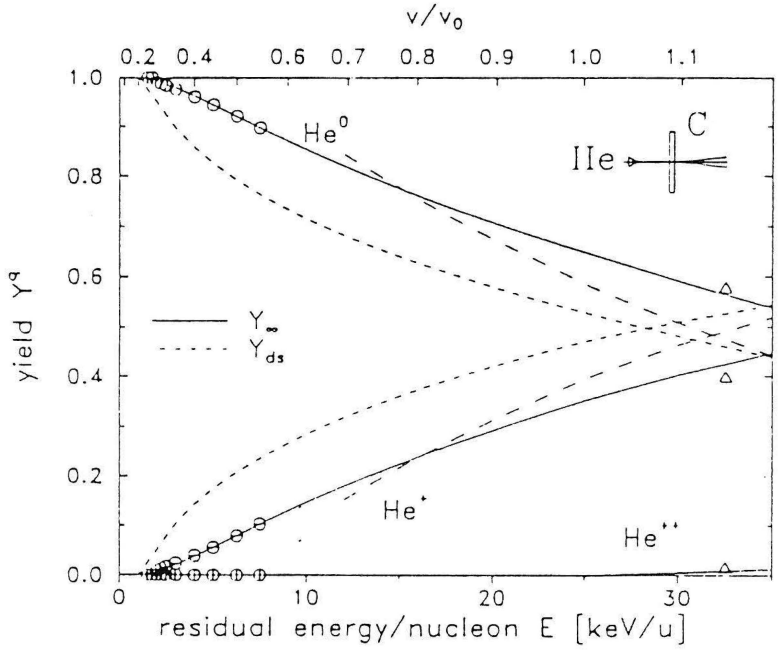

Figure 2.4. The charge state yields of helium after passage through a 1.1 μg/cm^2 foil. The open circles are the experimental results from Bürgi *et al.* [1993], and the different dashed lines are theoretical calculations by Gonin *et al.* [1994].

CHAPTER 3: DATA ANALYSIS

3.1 Data Format

A common Data Processing Unit (DPU) is used for all three SMS sensors. It handles all on-board data processing, command processing, telemetry formatting and alarm monitoring. The on-board data processing involves executing fast classification algorithms using look up tables stored in Random Access Memory (RAM) and generating Basic Rates, Matrix Rates and Pulse Height Analyzed (PHA) data. The DPU then stores all the science and housekeeping data and compresses them into the available spacecraft telemetry. The telemetry can be divided into two modes: science and maneuver. In science mode, telemetry can be further sub-divided into fast telemetry (high bit rate) and slow telemetry (low bit rate).

The WIND spacecraft spins at three seconds per revolution with its spin axis normal to the ecliptic plane. During each spacecraft spin, the electrostatic deflection voltages (*E/Q*) on all three sensors are held constant, with a step occurring at spin boundaries. The normal MASS deflection voltage sequence covers 60 steps. Science data gathered from each spin form an Experiment Data Block (EDB). The spacecraft allocates 800 (400) bytes per EDB during high (low) bit rate for the SMS experiment. An EDB consists of three data blocks: the EDB header, the Core data and the PHA words stored separately for the SWICS, STICS and MASS sensors. Descriptions of each data block for MASS are given below.

a) EDB header

The EDB header consists of 11 bytes of data at both high and low bit rates. It contains essential housekeeping data from the three SMS sensors (e.g., spin counter, discharge counter and instrument on/off indicator). Other housekeeping data are stored in the Fixed Housekeeping (HK) data and Housekeeping Data Block (HDB) in the telemetry not within the header. The housekeeping data are used to monitor the health and state of the sensors.

b) MASS core data

The MASS core data consists of Basic Rates (BRs), Matrix Rates (MRs), deflection voltage step and engineering rates.

Unlike SWICS and STICS, the MASS BRs classification algorithm involves only the Time-of-Flight PHA and the hyperbola voltage (SWICS and STICS classification algorithms use both TOF and Energy from the solid state detector). The MASS BRs classification algorithm uses Equation (3.1) to classify BRs.

$$M^* = T_m^2 \cdot \frac{V_{hps}}{C_1^2} \tag{3.1}$$

M^*	mass in amu
T_m	measured TOF in nanoseconds
V_{hps}	hyperbola voltage in kV
C_1	286.1

Hyperbola voltage is given by

$$V_{hps} = C_2 L_H$$

L_H	hyperbola power supply level (0 to 255)
C_2	0.1302

Four BR "boxes" are used for MASS: the BR0s and BR1s for both the sun and nonsun sectors. The BR0s have mass range from 0 to 11 amu, and BR1s mass range covers from 11 amu to the maximum detectable mass on MASS (77 amu for current hyperbola voltage setting). The BRs are used in determining the range for PHA events (see Chapter 3.3). In addition, the instrument divides the spin plane into 16 equally spaced sectors (see Figure (3.1)). Two sectors (9 and 10) are classified as sun sectors (45°) and the other 14 sectors are nonsun sectors (315°). The sun and nonsun "supersectors" each have a corresponding BR0 and BR1. The DPU classifies each particle into its appropriate BR box using Equation (3.1) and the direction information. The boundaries of the BR boxes can be changed by command.

Besides the coarse resolution BR boxes, there are ten MR boxes that correspond to the counting rates of selected ion species. They are not sectored like the BRs. Table (3.1) lists the mass ranges of the MR boxes that have been used since launch. The MASS core data also include engineering rates: Front SEDA Rate (FSR), Rear SEDA Rate (RSR) and Double Coincidence Rate (DCR). These rates are used primarily for in-flight instrument diagnostics. However, the FSR can be used for simple data analysis when detailed particle classification is not required. Further discussion of how to use FSR for data analysis is given in Chapter 3.1.1.

c) PHA words

The PHA words contain the most detailed information about a particle's time-of-flight and arrival direction. They are sectored and ranged just like the BR boxes. Each MASS PHA word is 16 bits long and contains the particle's TOF

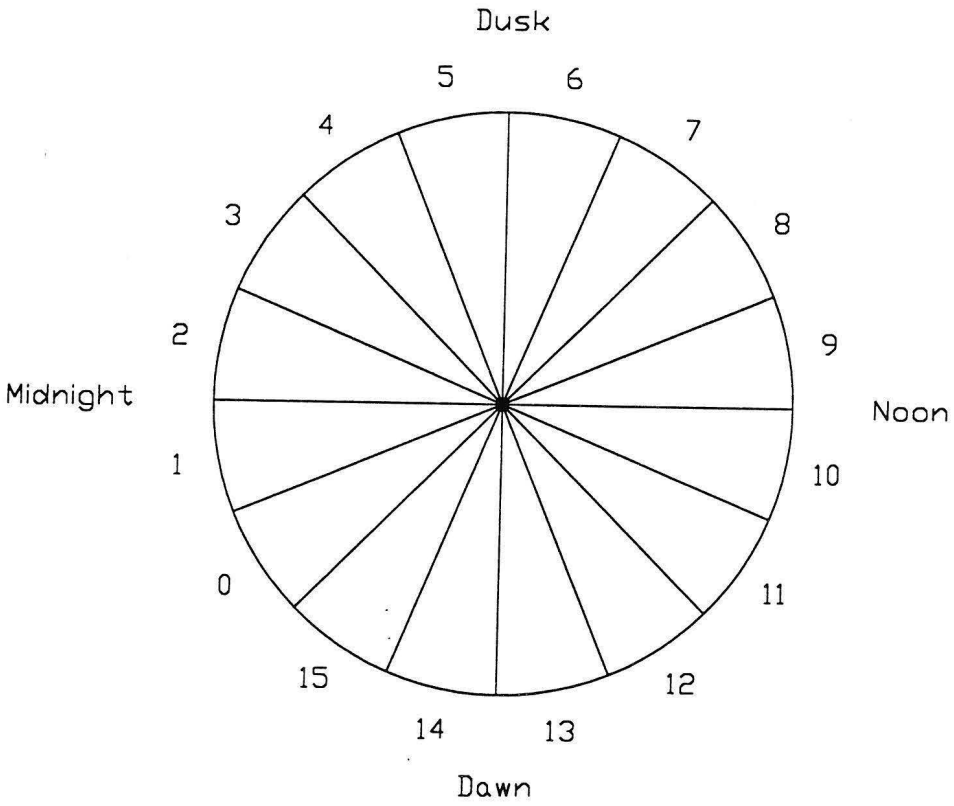

Figure 3.1. The DPU divides the spin plane into 16 equal angular sectors. The sun sector includes both sectors 9 and 10. The rest are classified as non-sun sector. We show the relative positions of all 16 sectors in the spin plane of the spacecraft.

Table 3.1. The ten MR boxes that are used by MASS.

MASS core data location	Matrix rate	Ion
Byte 15	MR 0	H
Byte 16	MR 1	^{3}He
Byte 17	MR 2	^{4}He
Byte 18	MR 3	C
Byte 19	MR 4	N
Byte 20	MR 5	O
Byte 21	MR 6	Ne
Byte 22	MR 7	Mg
Byte 23	MR 8	Si
Byte 24	MR 9	Fe

channel number, mass range and sector information (see Figure 3.2). PHA words are first accumulated in memory before they are transmitted in telemetry by the DPU. A maximum of 64 PHA words for each sector and range can be stored for every spin. Hence for every spin, the DPU is able to collect 64x16x2 = 2048 PHA words. However, because spacecraft telemetry is limited, only a small fraction of these PHA words are transmitted.

The number of MASS PHA words to be transmitted depends on the telemetry mode, the spin rate, and the number of PHA words currently allocated for all SMS sensors. If all sensors have collected at least the nominal number of PHA words, the DPU calculates the number of PHA words from each sensor to include in the telemetry. If one sensor can not fill its nominal PHA area, then the remaining space will be distributed to the other sensors.

Within the MASS PHA area, the DPU allocates telemetry space for each sector and range. This allows the transmission of a significant fraction of rare events (such as solar wind C, N, O, Fe) in range 1, while not completely excluding the more abundant ion species (protons and heliums) in range 0. The detailed MASS PHA distribution is given in Appendix D.

3.2 Science Data

In this dissertation we have used two kinds of science data from MASS: FSR and PHA data. We will discuss in detail how we make use of each type of data in the following sections.

	MSB															
bits of the PHA word	15	14	13	12	11	10	9	8	7	6	5	4	3	2	1	0
bits of the subgroup	0	0	1	0	11	10	9	8	7	6	5	4	3	2	1	0
subgroup	S	R	Anode		Time of Flight											

Figure 3.2. Each MASS PHA word is 16 bits long. The low order 12 bits are the TOF information. Bits 12 and 13 are the MCP anode information (not used because a planned split start anode was replaced by a one-piece anode before launch). Bits 14 and 15 are the range and sector information, respectively.

3.2.1 FSR Data

Ions that pass through the electrostatic analyzer and penetrate the 2 μg/cm^2 carbon foil at the start of the TOF section will be counted in the FSR (Front Secondary electron detection assembly Rate). These data are not sectored and are equivalent to that from a standard hemispherical *E/Q* solar wind ion instrument.

An example of the daily time series FSR stack graph is given in Figure (3.3). Time runs vertically from bottom to top, and the horizontal axis gives energy per charge. Each spectrum corresponds to one instrument cycle (three minutes) that covers 60 logarithmically *E/Q* steps from 0.5 to 10 keV/e. Ions will enter the spherical segment analyzer at different steps according to their *E/Q* values. The largest peaks at the left of the plot indicate the solar wind protons. The second largest peaks to the right of the protons indicate solar wind alpha particles. All the other peaks to the right of the alphas are heavier ions (Z>2) in the solar wind. These kinds of *E/Q* spectra provide an overview of the MASS data set and are useful for identifying interesting events. The location of the proton peaks at different *E/Q* values indicate the changing solar wind velocity and the width of the peaks indicates the kinetic temperature of the solar wind. In particular, these spectra can be used to detect any enhanced ^{3}He event. The ^{3}He peaks will show up between the solar wind proton and alpha peaks.

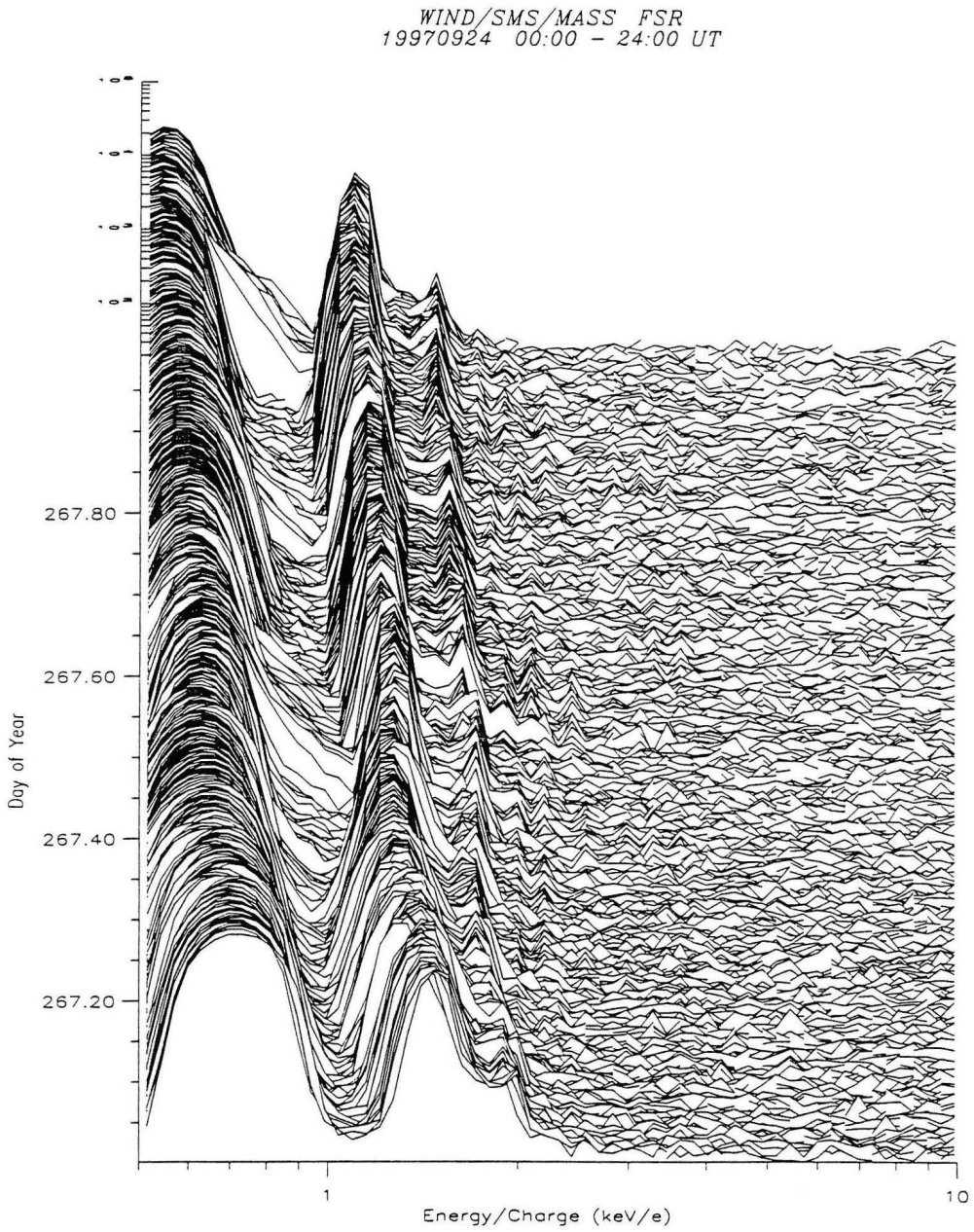

Figure 3.3. Daily time series FSR stack plot. Each spectrum corresponds to approximately 3 min of measurement. Time is running from bottom to the top of the plot.

3.2.2 PHA Data

PHA data provide the most detailed measurements from MASS. Each PHA word contains an individual particle's TOF and sector information. Figure (3.4) shows the raw sun sector PHA data plotted in *M/Q* vs. *M** (*M** = mass per charge after foil). The conversion from TOF to *M** is done using Equation (3.1). Since most low energy ions are either neutral or singly charged after the foil, *M** is usually equivalent to ion's mass. Neutral particles are not deflected by the TOF electric field and those that impact the hyperbola and scatter back to the stop MCP produce the major source of background (see Appendix A.3). There are some cases in which the fraction in the +2 or even +3 charge state can be significant and must be taken into account.

The conversion from *E/Q* to incident *M/Q*, however, is more involved. First we fit the solar wind alpha peak in the FSR rate as a maxwellian function in *E/q* and determine the speed of the alpha particles. Assuming the alphas and other heavy ions in the solar wind move at a common bulk velocity [Schmidt *et al.*, 1980; von Steiger, 1995a], we derive the *M/Q* associated with each *E/Q* step. MASS has a total of 60 logarithmically spaced *E/Q* steps. Depending upon the given solar wind velocity, which varies from 200 to 1000 km/s, the 60 *E/Q* steps will correspond to different *M/Q* values. Therefore we define 200 logarithmically spaced *M/Q* bins from 0.8 to 32.0 amu (Equation 3.2).

$$Bin\_no = \frac{\ln\left(\frac{M/Q}{0.8}\right)}{0.018444} \tag{3.2}$$

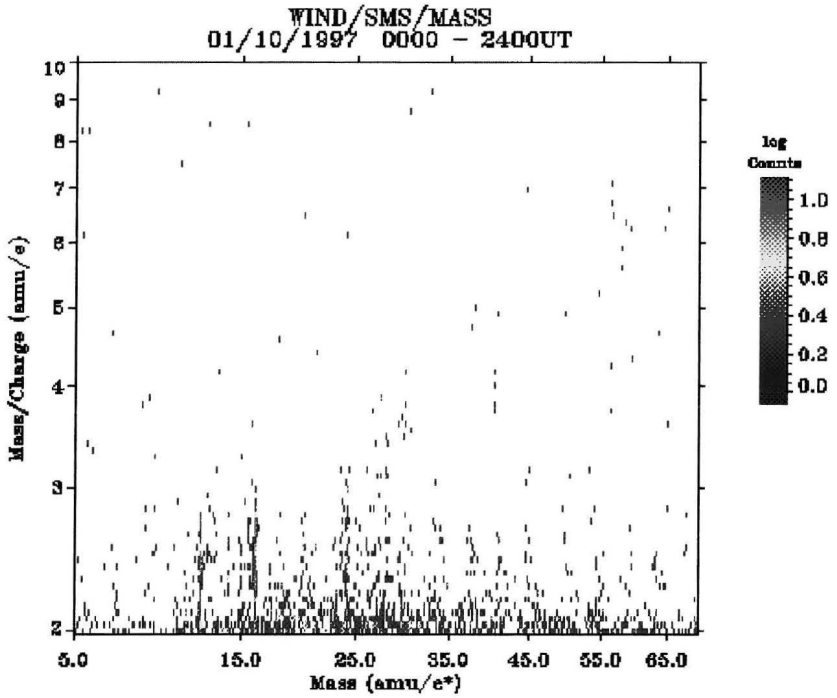

Figure 3.4. Color display of the MASS PHA data. The y-axis is the 200 M/Q bins as described in Chapter 3.2.2 (plotted only from 2 to 10 amu/e). The x-axis plots the 4096 TOF channels (binned by two) after being converted into M^* using Equation (3.1). The color spectra qualitatively show the overall solar wind ion composition for a broad mass range. Using this plot, we can identify the various charge states of carbon ($M^* = 12$), nitrogen ($M^* = 14$), oxygen ($M^* = 16$). Different charge states of one element will show a vertical spread in the y-direction.

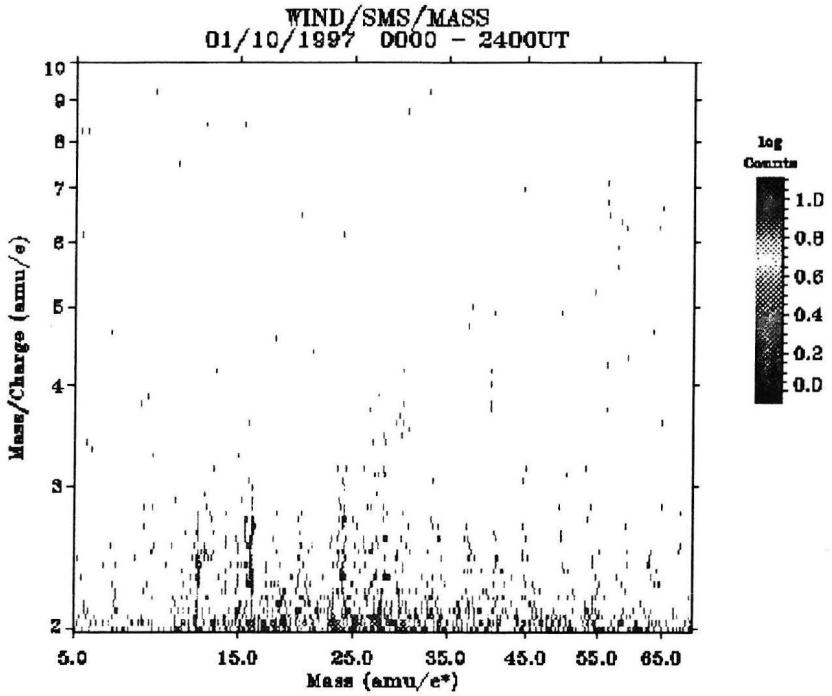

Figure 3.4. Color display of the MASS PHA data. The y-axis is the 200 *M/Q* bins as described in Chapter 3.2.2 (plotted only from 2 to 10 amu/e). The x-axis plots the 4096 TOF channels (binned by two) after being converted into M^* using Equation (3.1). The color spectra qualitatively show the overall solar wind ion composition for a broad mass range. Using this plot, we can identify the various charge states of carbon ($M^* = 12$), nitrogen ($M^* = 14$), oxygen ($M^* = 16$). Different charge states of one element will show a vertical spread in the y-direction.

Counts are accumulated in those bins. The counts in each of the 200 *M/Q* bins are weighted according to the number of times any energy per charge step was mapped into it.

3.3 Flux Calculation

We define the particle flux, *J,* to be the number of ions per unit area per unit time, and the unit is $(cm^2\text{-}s\text{-}sr\text{-}keV/e)^{-1}$. We calculate the flux in the following manners:

$$J = \frac{Corrected\ Counts}{Weight_x \cdot G \cdot \eta_{total} \cdot dt \cdot \Delta(E/Q)} \tag{3.3}$$

where *Corrected Counts, Weight, G,* η_{total}, *dt,* and $\Delta(E/Q)$ will be discussed in details in the following sections.

3.3.1 Box Selection

To obtain the *Corrected Counts* of a targeted ion species, we have to unambiguously identify it within the PHA data. First, we select data that have TOF values within the range of the targeted species. The TOF ranges of selected species are listed in Appendix B. This 1-D cut in the PHA data effectively excludes events that originate from ions that have different M^* values. When we plot the TOF selected PHA data vs. *M/Q*, different charge states of the selected species will fall into different *M/Q* peaks (as shown in Figure 3.5). The widths of the different *M/Q* peaks represent the thermal spread of the ion distributions. To calculate the flux of

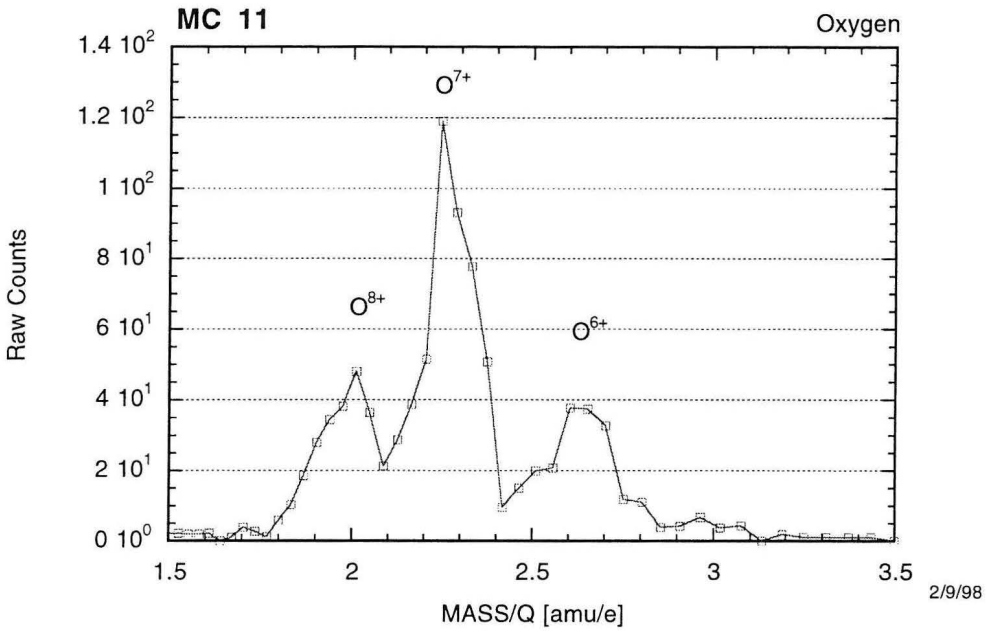

Figure 3.5. We can select PHA data based on a restricted range of TOF channels. This figure shows the PHA data from TOF channels corresponding to 15.91 to 16.1 amu. It shows the three charge states of oxygen with very little background.

the different charge states, we then sum up a range of *M/Q* steps. The ranges of *M/Q* for different species' charge states were found by fitting gaussian distributions to a long period of slow speed (<400 km/s) data. The entire selection process is similar to summing *Corrected Counts* in a box range within the 2-D *M/Q* vs. M^* in MASS PHA data.

However, different species can still fall into the same TOF and/or *M/Q* ranges. Since MASS's TOF scales with M^*, those ions that have the same M/Q^* (Q^* is the charge state after the foil) value will fall into the same TOF peak. Summing only the appropriate*M/Q* ranges of the targeted species can eliminate the majority of this contamination from other species.

For those species that have the same M^* and *M/Q* ratios, we can estimate their individual contributions using: (a) a standard solar system abundance table [e.g. Anders and Grevesse, 1989]; (b) MASS pre-flight calibrated data; (c) measured charge state composition after passage through a carbon foil [Kallenbach *et al.*, 1995 and reference within]. Considering the C^{6+} ion, Mg^{12+} will fall into the C^{6+} M^* and *M/Q* ranges if the charge state of Mg^{12+} is +2 after foil. Since carbon is five times more abundant than magnesium in the interstream solar wind, we expect a similar abundance ratio to enter MASS [Anders and Grevesse, 1989].

In addition, with an assumed freezing-in temperature of 2.0 MK in the solar wind, Mg^{12+} contributes only 6×10^{-7} % of the total magnesium (more than 92 % of the magnesium is in Mg^{10+} form). Figure (3.6) shows the relative ionic ratios of magnesium for a 2 MK freezing-in temperature. Although at 1.0 keV/nuc the predicted magnesium detection efficiency is three times higher than the carbon

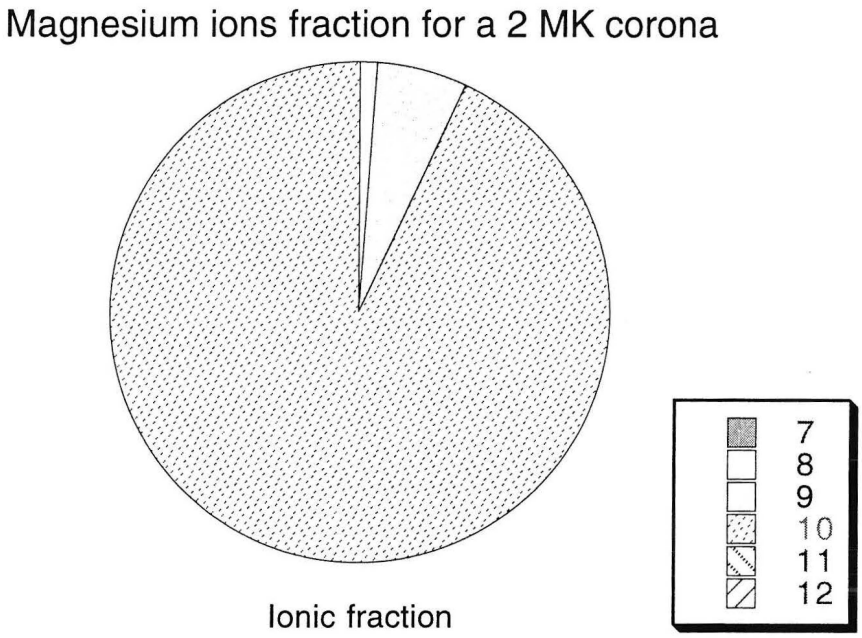

Figure 3.6. The predicted magnesium ionic fraction based on Arnaud and Rothenflug [1995]. Over 90% of the magnesium is in the +10 state at a temperature of 2.0 MK.

detection efficiency (see Appendix A), the total contamination of C^{6+} by Mg^{12+} will be negligible. We list the amount of contamination from other species for all measured charge states in this study in Table (3.2). It is clear that contributions from other species are negligible.

3.3.2 Efficiency

The flux calculation requires information on the MASS response functions for detecting ions as a function of species and energy. Prior to launch, we calibrated MASS extensively to obtain the detection efficiencies for selected ion species. The calibration was done at the University of Bern low energy accelerator. A list of the pre-launch calibrated ion species and energies is given in Table (3.3).

The MASS efficiency is defined as followed:

$$\eta_{total} = \eta_{deflection} \cdot \eta_{start} \cdot \eta_{stop} \cdot \eta_{+} \tag{3.4}$$

where,

$$\eta_{deflection} = \frac{FSR}{Beam\ Flux \cdot Geometric\ Factor \cdot \eta_{start}} \tag{3.5}$$

is the deflection analyzer efficiency;

$$\eta_{start} = \frac{DCR}{RSR}, \text{ and} \tag{3.6}$$

$$\eta_{stop} = \frac{DCR}{FSR} \tag{3.7}$$

are the start and stop efficiencies, respectively; and

$$\eta_{+} = \frac{Counts\ in\ +1\ PHA\ Peak}{Total\ PHA\ Counts} \tag{3.7}$$

Table 3.2. Contributions from other species to the targeted species' *M/Q* and *M**. The first column is the species intended to be measured, the second column lists those species that fall into the same *M/Q* and *M** ranges if their charge state after the foil is +2. The third column gives the fraction of the contaminating species expected to be in the appropriate charge state to produce the same *M/Q* value as the target species. The efficiency ratios are determined as discussed in Appendix A. The +2/+1 ratios are the ratios of doubly charged to singly charged ions after passage through a 2.2 μg/cm^2 carbon foil [Gonin, 1991].

Target species	Contaminant species	Contaminant species charge state fraction*	Efficiency ratios†	+2 / +1††	Average abundance ratio†††	Contribution of contaminating species
C^{4+}	Mg^{8+}	9.83×10^{-3}	0.26	0.28	0.22	1.6×10^{-4}
C^{5+}	Mg^{10+}	9.29×10^{-1}	0.30	0.28	0.22	1.7×10^{-4}
C^{6+}	Mg^{12+}	6.16×10^{-9}	0.29	0.28	0.22	1.1×10^{-10}
N^{6+}	Si^{12+}	4.51×10^{-1}	0.35	0.24	1.46	5.5×10^{-2}
N^{7+}	Si^{14+}	1.35×10^{-3}	0.32	0.24	1.46	1.5×10^{-4}
O^{6+}	S^{12+}	9.72×10^{-3}	0.26	0.24	0.04	2.4×10^{-5}
O^{7+}	S^{14+}	5.21×10^{-3}	0.26	0.047	0.04	2.5×10^{-6}
O^{8+}	S^{16+}	2.51×10^{-20}	0.23	0.047	0.04	1.1×10^{-23}

* From Arnaud and Rothenflug [1985], calculated at 2 MK.

† Ratios of targeted species over contaminating species at 1 keV/nuc.

†† Predicted ratios of the species charge states after passage of 2.2 μg/cm^2 carbon foil at 1 keV/nuc [Gonin, 1991].

††† Average ratios determined in ecliptic solar wind [Shafer, 1995].

Table 3.3. List of all different ion species and energies that were used during MASS calibration at the University of Bern low energy accelerator. The run number corresponds to the file number that was used to store the calibration data.

Run number	Ion beam type	Energy/Charge (kev/e)
76-79	H^+	5, 7, 9, 11
96-100	$^3He^+$	5, 8, 11, 14, 17
15-21	$^4He^+$	5, 7, 9, 11, 13, 16, 19
59-63	C^+	15, 20, 25, 30, 35
70-74	N^+	15, 20, 25, 30, 35
53-57	O^+	15, 20, 25, 30 , 35
41-47	Ne^{2+}	8, 10, 15, 18, 20, 25, 30
27-32	Ar^{2+}	10, 15, 20, 25, 30
33-37	Kr^{3+}	15, 20, 25, 30, 34

is the +1 ion fraction in TOF spectrum efficiency. Detailed explanations for each efficiency and a summary of the efficiency results are given in Appendix A.

3.3.3 PHA Weighting

The available spacecraft telemetry for SMS is inadequate to transmit all detected PHA events. Therefore, in order to transmit PHA data on rare as well as abundant species, the DPU must uses a priority scheme (see Appendix D). Basically, the DPU divides available telemetry for MASS PHA into four boxes. The four boxes are for the PHA data in range 1 and range 0 in both the sun and nonsun sectors, just like the four BR "boxes" as defined in Chapter 3.1. Therefore, the more abundant solar wind protons and alphas will be limited to range 0 and will use telemetry allocated to the heavier ions in range 1.

In order to recover the prioritization being done to the PHA data, we use data from the BRs. The four Basic Rates count all analyzed events except when on-board electronics cannot handle the high number of counts.

Assuming the PHA data are distributed in the same manner as the BR rate counts in each box, the PHA events should be weighted according to

$$Weight_x = BRi_x/PHAi_x \tag{3.9}$$

where i is the range 0 or 1, and x is sun or nonsun sector.

However, there are times when the on-board electronics could not handle the high rate. This is true when the abundant solar wind proton and alpha distributions are entering the instrument. Since the solar wind propagates approximately radially outward from the sun, all solar wind ions will enter MASS in 1 or 2 out of 16 look

directions. This amounts to a high number of counts in a short period of time, especially for the *E/Q* steps for solar wind protons and alphas. The maximum rate of analyzed events is limited by the transfer rate of the optocoupler between the TOF assembly and the main MASS electronics. In particular, the maximum transfer rate of the MASS optocoupler is 15625 analyzed events per second. Therefore, BRs can not possibly count all the events for abundant species (protons and alphas). Fortunately, this is only a problem for the solar wind protons and alphas; all heavier species counting rates will be low enough to be handled by the on-board electronics. We will discuss how we can use the double coincidence rate from MASS to recover some of the lost alpha information in Chapter 4.3.

3.3.4 Accumulation Time and Geometric Factor

In order to convert counts per EDB to rates, we need to determine the exact time per measurement (EDB). As we discussed, MASS's electrostatic analyzer goes through 60 energy per charge steps during every science record. The deflection voltage is optimized for any given species at one *E/Q* step (or at two or three steps if the kinetic temperature is high) for only 3 s of every three-minute period. In addition, because the spacecraft is spinning, MASS is not exposed to the solar wind during the entire spin. For a single *E/Q* step, a spin rate of once every 3s, and an angular acceptance of 4°, this corresponds to

Δt = 0.033 s (for a collimated beam)

for every science record of data collected.

The geometric factor is a measurement of the effective area-solid angle product of the instrument in sampling the particle flux. If I is the absolute intensity of an isotropic particle distribution in (sec^{-1}-cm^{-2}-sr^{-1}), and C is the counting rate in (counts sec^{-1}), then

$$C = GI \tag{3.10}$$

where G is the isotopic geometric factor and it is assumed that detection efficiency is 100%. And

$$G = \int_{\Omega}\int_{S} (\cos\theta \cdot dA) d\Omega \tag{3.11}$$

where θ is the angle between the incident particle trajectory and the normal to the element of area dA, $d\Omega$ is the element of solid angle, and S represents the domain of dA [Gloeckler, 1970].

If the area, A, of the detection surface is normal to the incident flux, then Equation (3.11) becomes

$$G = A \cdot \Delta\Omega \tag{3.12}$$

where $\Delta\Omega$ is the effective solid angle subtended by the aperture.

If we assume the solar wind is an narrow beam with no width, the angular dependence drops out, it is useful to use an "effective area" rather than an isotropic geometric factor in flux calculations. With the MASS sensor, this area is the effective area of the carbon foil (the 4° by 20° field-of-view of the deflection analyzer is mapped entirely onto the carbon foil surface), which is approximately 5 x 7 mm^2. The effective area is then the ratio of counting rate (s^{-1}) to directed flux in $(cm^2\text{-}s)^{-1}$.

3.3.5 Energy Passband

The energy passband is defined as the Full-Width at Half Maximum (FWHM) of the energy per charge that will pass through the deflection analyzer. We determined the MASS's deflection system passband during the calibration period to be $\frac{\Delta(E/Q)}{E/Q} = 4\%$.

3.2.6 Background Contribution

The major source of background in the TOF section of MASS comes from neutrals reflecting off the hyperbola producing real PHA events. These neutrals are produced from ions picking up extra electrons while passing through the carbon foil. Because they are electrically neutral, the harmonic electric field in the MASS TOF spectra will not affect to them. These neutrals would follow the ions' initial trajectories and strike the hyperbolic surface on the top of the TOF section. Most of these neutrals will reflect from the hyperbolic surface and then strike the stop MCP producing TOF signals that are longer than those associated with singly charged ions.

In particular, solar wind doubly charged helium is a problem for MASS because it is abundant in the solar wind and produces neutrals that interfere with other heavy ion measurements. Figure (3.7) shows the broad neutral helium peak is a major background problem for heavy species with $M/Q^* = 2$, although C^{6+}, N^{7+}, O^{8+}, and Mg^{12+} are still visible. Fortunately, since MASS has an energy per charge

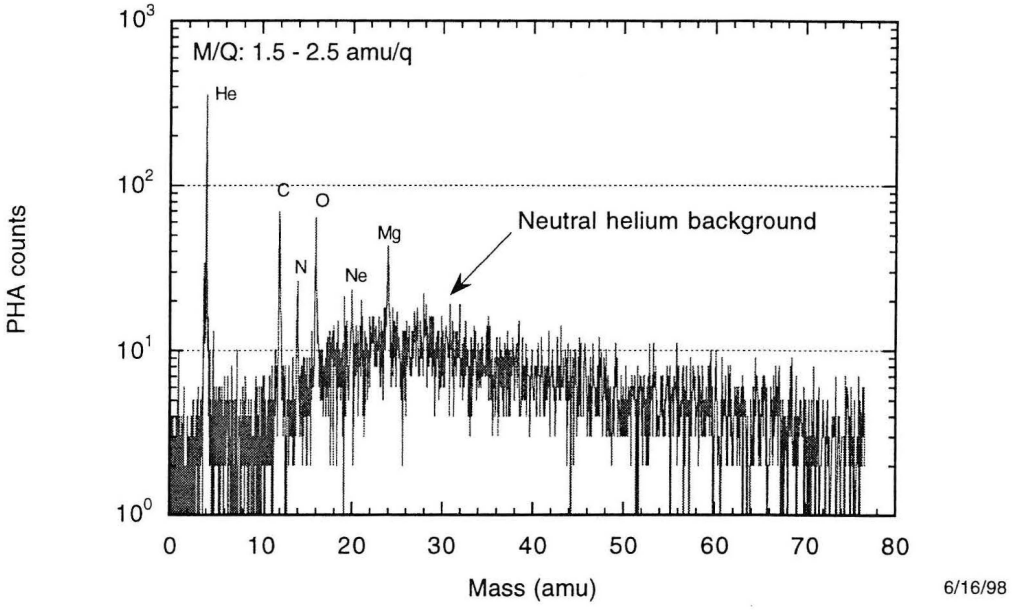

Figure 3.7. The neutralized helium produces the highest background in MASS PHA data. The neutralized helium atoms reflect from the hyperbola surface and produce TOF signals in the same range as those produced by singly ionized carbon to iron. Fortunately, we can select *E/Q* steps to avoid those in which the solar wind alpha particles enter.

analyzer, we can select V_{dpps} steps in which the helium does not enter the instrument. In addition, the background can be evaluated and subtracted by examining TOF channel ranges below and above the range of the targeted species if the background is not too large. Other types of background are discussed in Appendix A.

11.2 *Ho*, (1998) Appendices A and B

APPENDIX A: PARTICLE DETECTION EFFICIENCIES

A.1 MASS Calibration

The MASS flight instrument was calibrated at the University of Bern low energy accelerator facilities during 2 weeks of November 1993. The MASS instrument was calibrated with 9 different types of ions in the energy range 0.3 to 11.0 keV/nuc. Essentially all available ion species were used and the energy range was chosen to provide a sufficiently broad range to cover all solar wind conditions, to the extent possible. For a few selected ion species and energies, the MCP bias voltage and hyperbola voltage were also varied.

The Bern accelerator produces ion beams with energy from 5 keV/e to ~60 keV/e. A feedback control loop using beam monitor sensors at different locations in the accelerator guarantees the ion beam to have constant intensity within ±5 %. Ghielmetti *et al.* [1983] gave a full description of the accelerator facility.

A.2 Calibration Overview

A.2.1 Calibrated Species and Energies

During the calibration at Bern, all available ion species from the accelerator were used. A list of the ion species and approximate energy of each run is given in Table 3.2.

A.2.2 Types of Runs

In addition to varying the species and energy for a fixed V_{hps} and V_{adps} setting, other types of runs were performed to determine the instrument response function under different sensor configurations. Table A.1 lists these additional instrument performance tests.

Table A.1. Different types of tests that were done during MASS Bern calibration. Not shown are the tests listed in Table 3.3.

Beam Species	Beam Energy (keV/e)	Varying sensor parameter	Comments
None	None	V_{hps} level	Background rates vs. V_{hps} level test
N^+ (On and off)	30.0	Stop MCP bias level	Stop MCP level test
N^+	30.0	Start MCP bias level	Start MCP level test
N^+	30.0	V_{adps} level	Efficiency vs ADPS level test
He^+	9.0	Start MCP bias level	Start MCP level test
He^+	9.0	Stop MCP bias level	Stop MCP level test
All nine calibrated species	Selected	V_{adps} level	V_{adps} level test
All nine calibrated species	Selected	Wide and narrow angles	MASS angular response test

A.3 Efficiency Analysis

A.3.1 Background

In order to appropriately analyze either calibration or flight data, certain forms of background in the data must be accounted for or subtracted. This section discusses the various types of background.

A.3.1.1 Electronic Noise

There are three counting rates that we used in our calibration data analysis. The Universal Front Seda (Secondary Electron Detection Assembly) Rate (UFSR) indicates counts that open the TOF window. The Rear Seda Rate (RSR) closes the TOF window and the Double Coincidence Rate (DCR) indicates counts that have a valid TOF.

The electronic noise in the UFSR, RSR and DCR rates are generated in both analog and digital components of the instrument (thermal noise, amplifier noise, etc.). This type of electronic noise should vary mainly as a function of temperature but not as a function of instrument setting (i.e. hyperbola voltage).

A.3.1.2 ADC Noise

MASS uses a 12-bit "Sample and Hold" Analog to Digital Converter (ADC) to convert the analog Time-to-Amplitude Converter (TAC) output into a digital signal to be used in the DPU. During the initial calibration that was done at GSFC, two types of "noise" were identified that were attributed to the ADC. The first one was the "low bit" noise, that appears as ripple in the TOF histogram, as shown in Figure (A.1). This noise was believed to be caused by voltage fluctuations in the ADC and/or the TAC output. As the ADC reads an analog signal, it needs to hold the signal for a brief time (5-10 microseconds) in order to compare its value to a reference voltage to set in the appropriate bits. Therefore if there were a slight fluctuation during the

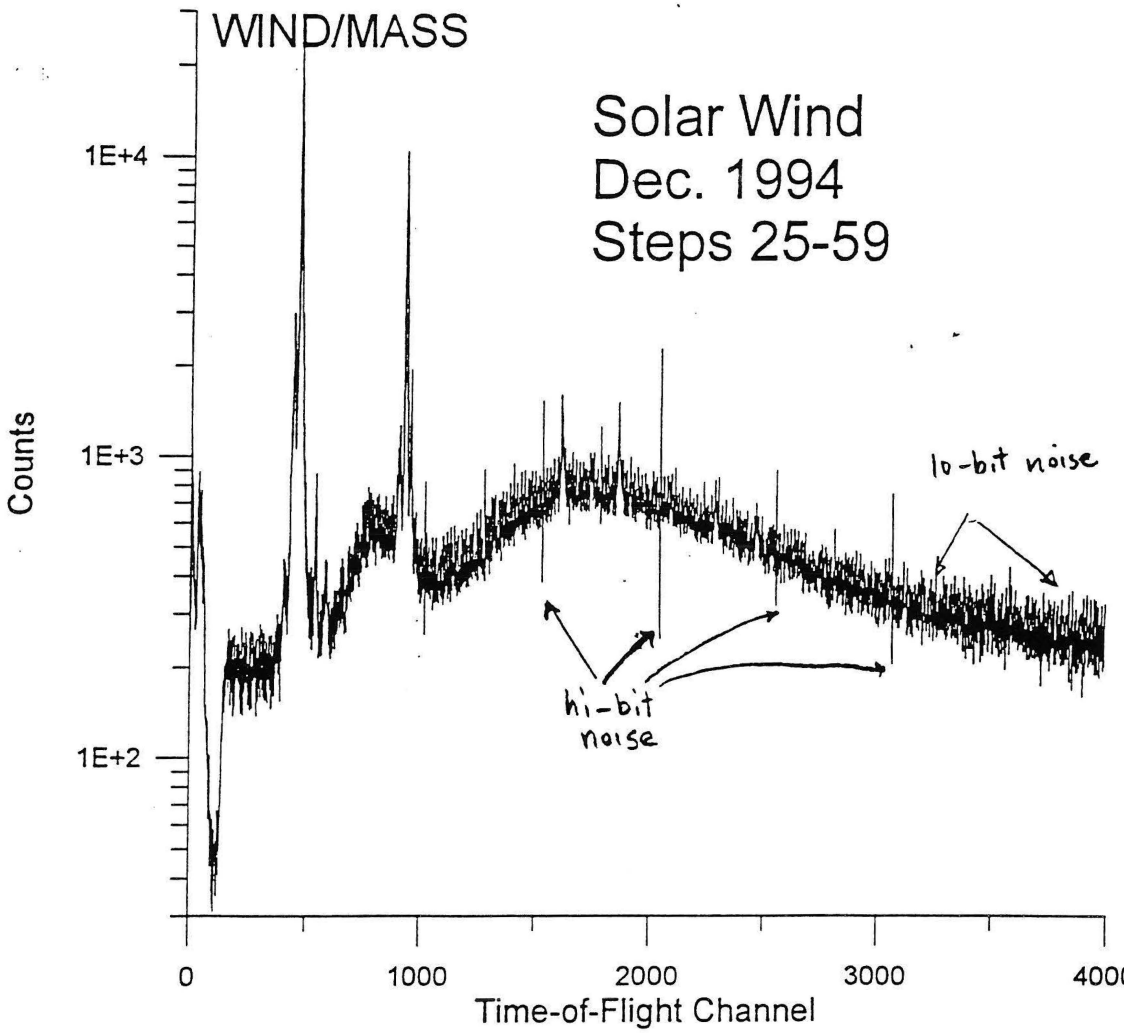

Figure A.1. Two types of noise were identified in the TOF histogram. The first one was the "low-bit" noise, which appears as ripple in the TOF histogram. The second type of noise is the "high-bit" noise. A large spike in the TOF spectra can be seen at almost every 2^n channel.

voltage comparison process, either on the reference voltage (ADC) or input voltage (TAC output), the lowest bit would be misplaced by one bit (upper or lower) depending on the direction of the fluctuations at that instant of time. This kind of noise will only affect the lowest bit.

The second type of noise that is caused by the ADC is the "high-bit" noise. A large spike in the TOF spectra can be seen at almost every 2^n (where n is an integer) channel. This noise is believed to be caused by underdamping in the ADC's sampling switches, which generates a ringing peak on the "sample and hold" capacitor [Sheldon, 1995]. When the ringing in the capacitor decays during conversion, it affects only the most significant bit and shows up in the 2^n channel in the TOF spectra.

Re-binning the data more coarsely (e.g. in 2-channel bins) eliminates most of the "low-bit" noise. Bining the data will decrease the resolution of the instrument, but 2-channel binning maintains sufficient resolution. In addition, combining 2-4 channels around the 2^n spikes seems to get rid of the "high-bit" noise.

A.3.1.3 TOF Background

A close examination of the PHA data will reveal that the mass peak is not a perfect gaussian. From the Bern calibration, we found that the mass peak departed from a gaussian distribution with a high TOF tail, as shown in Figure (A.2). This high TOF tail is believed to contain genuine events, and is attributed to TOF paths that deviated from the nominal. Ions whose paths deviate from the central axis of the instrument have longer times-of-flight (see Appendix F).

In addition to the high TOF tail, we have also observed "Ringing" peaks in our calibration and flight data. The cause of the ringing peak has been linked to the pick-up of a signal inside the TAC board during the analog to digital conversion process. However, a detailed explanation of this noise has yet to be found. The first

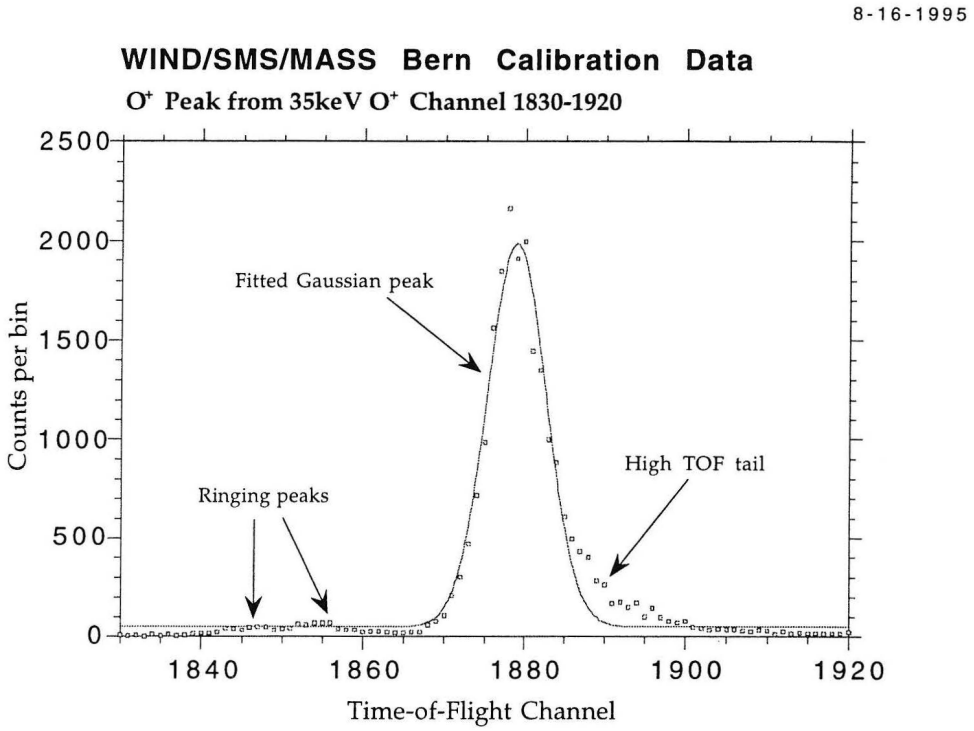

Figure A.2. One of the oxygen calibration data sets that was taken in Bern. As shown in the data, both the ringing peaks and high TOF tail distorted the otherwise gaussian distribution. The solid line is a fitted gaussian. Despite the noise features, the fitted function still gave a good estimate on the sigma of such a TOF peak.

ringing peak appears approximately 23 channels (~ 3 ns) below the main peak. In some cases an additional peak appears 64 channels below the main peak. The first ringing peak is always the largest and contains from a few to 20% of the main peak counts. A typical number is 10%. The second ringing peak typically is down by another factor of two.

Aside from the above two TOF backgrounds, the major background comes from ions neutralized in the carbon foil reflecting off the hyperbola producing a real TOF event. We discuss that process in the main section of this paper.

A.3.2 Calibrated Ion Efficiencies

There are two different ways for deriving the efficiencies for the MASS instrument. The first method uses the efficiencies that are calculated independently for the deflection analyzer, start detection, stop detection, and +1 ion yield. The total efficiency for the MASS instrument is the product of all four efficiencies. The advantage of this method is that we can derive the efficiency curves for species that were not calibrated in the accelerator, but are observed in space, by interpolating from the calibrated efficiency curves.

The second method for calculating the efficiencies is to treat the MASS instrument as a whole "black box". We need not concern ourselves about the individual efficiencies from the deflection analyzer, start, stop and +1 ion yield. All we use in this method is the number of ions going into the instrument and how many of them show up in the appropriate TOF channels.

This second method of calculating the efficiency will theoretically give the same total efficiency as is done by the individual efficiency method. However, this method will not give any insight into the efficiency curves for species that were not

calibrated in the accelerator. Therefore we have decided to use the individual efficiencies method in calculating the instrument's overall efficiency.

A.3.2.1 Individual Efficiencies

The definitions of deflection analyzer, start, and stop efficiencies are listed below:

Deflection analyzer efficiency:

$$\eta_{deflection} = \frac{UFSR}{Flux \cdot G \cdot \eta_{start}} \tag{A.1}$$

where *Flux* is defined as number of particles per unit area per second in the beam as determined by the beam monitors and *G* is the MASS aperture in cm^2

Start efficiency:

$$\eta_{start} = \frac{DCR}{RSR} \tag{A.2}$$

Stop efficiency:

$$\eta_{stop} = \frac{DCR}{UFSR} \tag{A.3}$$

A.3.2.2 Deflection Analyzer and Start Efficiencies

The definition of the deflection analyzer efficiency is given in Equation (A.1). It gives the probability of an incident ion of appropriate energy passing through the analyzer and entering the TOF section. We have found different values of the deflection analyzer efficiency (shown in Figure (A.3)) in the calibration data depending on whether we used the Faraday Cup (FC) measurement or the Channel Electron Multiplier (CEM) measurement as the beam monitor. We will include both sets of data in this paper until the problem can be resolved.

Start efficiency is defined in Equation (A.2). This efficiency includes the effects of secondary electron production in the carbon foil and detection of those

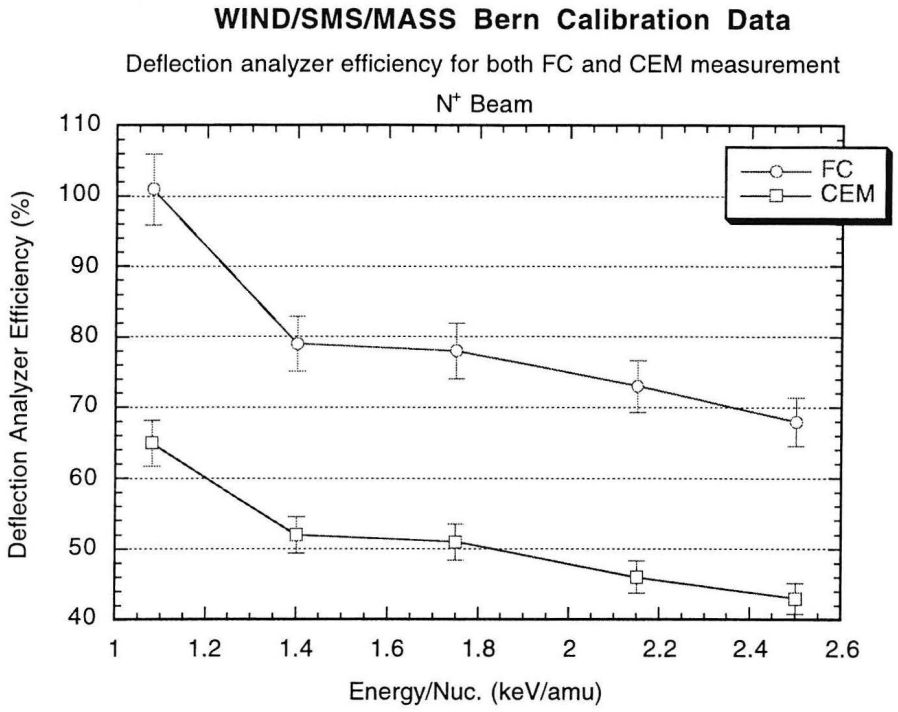

Figure A.3. Two deflection analyzer efficiencies are shown here. Both efficiencies were calculated from the same nitrogen beam over the same time. The open circles are the efficiencies derived from the flux measured by the Faraday Cup (FC) beam monitor. The open squares are the efficiencies derived from the flux measured by the Channel Electron Multiplier (CEM). The efficiencies that were calculated from the FC measurement are about 60% larger than the values that were obtained by the CEM measurement. It has been pointed out that FC measurement are in general more accurate than the CEM readings.

electrons by the start MCP. It also includes the effect of holes in the carbon foil since an ion passing through a hole can produce an RSR count but never a UFSR or DCR count. In order to give a mechanical support for the thin carbon foil, the foil is mounted on a ~90% transparent nickel mesh grid. The grid has cell size of ~0.3 mm. Individual cells can be lost due to acoustic and vibration tests. Right after the Bern calibration, we did a visual inspection of the foil, and it was discovered that approximately 10% of the cells were gone. Therefore it is more than likely we would lose more cells during the harsh launch environment. Figure (A.4) shows the start efficiency of all nine calibrated ion species as a function of total energy in keV along with their respective polynomial fits.

The calculated values of $\eta_{deflection}$, sometimes exceeded unity. This tells us that the beam monitor rates have given us values that were lower than the actual beam rates. However, if we use the product of the deflection analyzer and start efficiencies, the results are always below unity. Therefore we have chosen to use the product of these efficiencies as our new start efficiency, Combined Start Efficiency (CSE).

$$\eta_{cse} = \eta_{deflection} \times \eta_{start} \tag{A.4}$$

Furthermore, because of the inconsistency of the two beam monitor rates, we will include both sets of efficiency results in this paper until the problem can be resolved. Accelerator personnel suggest that Faraday cup measurements are more reliable.

A.3.2.3 Stop Efficiency

Equation (A.3) gives the stop efficiency. Many factors can affect it. In order to generate a stop signal in MASS, ions have to exit the foil positively charged and remain near the center of the TOF region (see discussion in Appendix F). If they exit

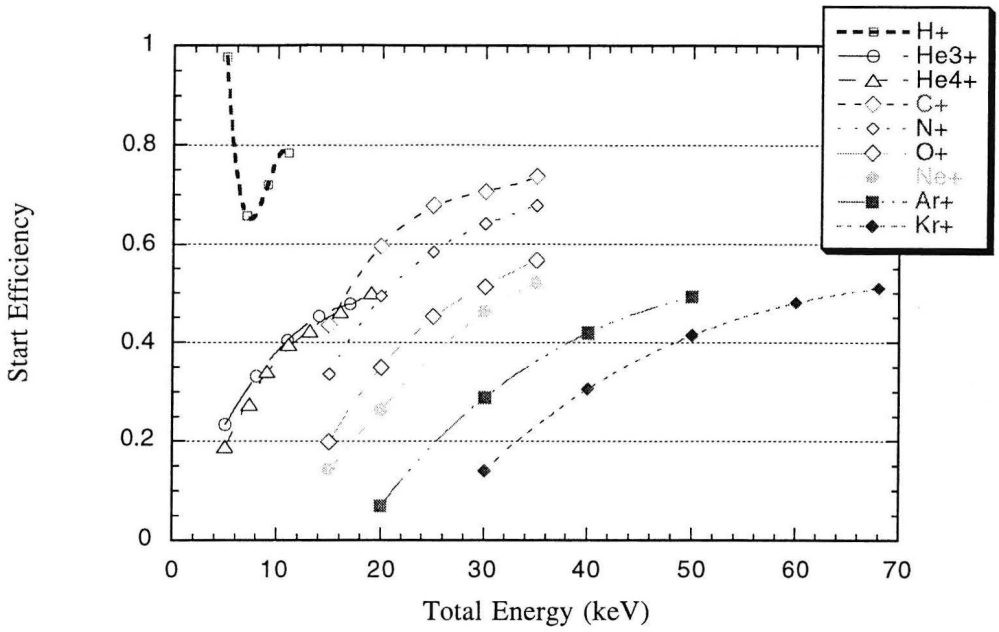

Figure A.4. Start efficiencies for all nine calibrated species are shown here. Plotted on the x-axis is the total kinetic energy of the ion beams. The lowest energy measurement (5 keV) for proton is most likely due to beam uncertainity.

the foil neutral, they will impact the hyperbola. If they scatter away from the center line, they will miss the narrow 16x101 mm^2 stop MCP (see discussion in Sheldon, 1995). In addition, based on the literature, an MCP is not as responsive to single ions as it is to multiple electrons. Thus we could expect the stop efficiency to be much smaller than the start efficiency. We can clearly see that by comparing the stop efficiency in Figure (A.5) to start efficiency in Figure (A.4). The stop efficiencies are smaller by about two orders of magnitude than the start efficiencies.

A.3.2.4 +1 Ion Fraction in TOF Spectrum

There is a final efficiency that is important in analyzing the MASS TOF PHA data. Not all ions entering the TOF section of the instrument produce a TOF appropriate to the +1 charge state of that element. The TOF may lie outside the appropriate peak because of scattering inside the instrument, and will be counted as part of the background (e.g. neutralized helium shown in Figure 3.7). Also, a certain fraction of the ions emerges in the +2 (or even +3) charge state after the foil passage and lies in a separate well-defined peak. We define the +1 ion fraction in TOF spectrum efficiency as

$$\eta_+ = \frac{\text{Counts in the } +1 \textit{ PHA} \text{ Peak}}{\text{Total } \textit{PHA} \text{ Counts}} \qquad \text{(A.5)}$$

where (Total *PHA* Counts) are from an accelerator run with a single ion species. In defining the peak channel range, we immediately ran into difficulty with various types of backgrounds. First, looking into the calibration data (Figure (A.2) for example), we noticed both the ringing peaks and high TOF tail features. Decisions were made not to include the ringing peaks and high TOF tail as part of the peak. The ringing peaks were excluded because they are relatively small and are frequently obscured by other background or other mass peaks. The high TOF tail part of the PHA peak was

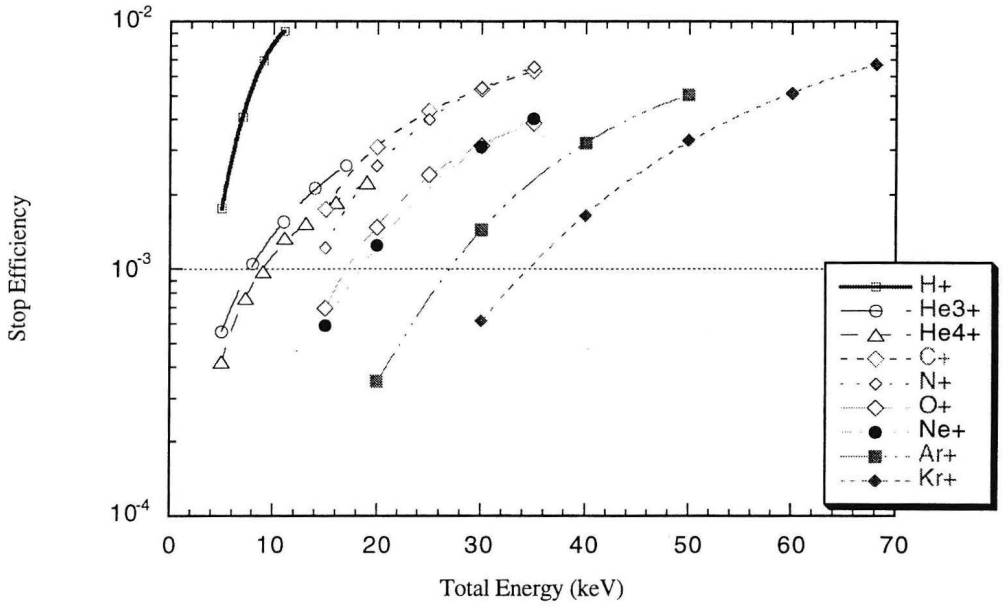

Figure A.5. The stop efficiencies for the nine calibrated species. Comparing with the start efficiencies in Figure (A.4), the stop efficiencies are orders of magnitude lower than start efficiencies.

initially included as part of the peak in the calibration data. However, they have been excluded now after further investigation. Calibration data usually shows the high TOF tail feature clearly, but in early flight data, it was hard to pick these features out distinctively from the general background. In order to reduce the risk of including too many background counts, we have limited the accepted TOF range to ±2 sigma of the center of the PHA peak. This range excludes most of the high TOF tail and also the ringing peaks. The sigma of the peak was found by fitting the data (with the tail) with a gaussian functional form. We have found that the fitted sigmas well describe the upper half of the PHA peak. Figure (A.6) shows the +1 ion fraction efficiencies for all nine calibrated species.

A.3.2.5 Total Efficiencies for Calibrated Ions

Two sets of start efficiency are given; one is denoted as Combined Start Efficiency (FC), which is the product of the deflection analyzer efficiency from the Faraday Cup measurement and the start efficiency. The other Combined Start Efficiency (CEM) is the product of the deflection analyzer efficiency from the Channel Electron Multiplier (CEM) measurement and the start efficiency.

The total efficiency for MASS is then the product of three individual efficiencies for every ion species and energy,

$$\eta_{total} = \eta_{cse} \times \eta_{stop} \times \eta_{+} \qquad \text{(A.6)}$$

Figure (A.7) shows all nine calibrated species total efficiency plotted against total energy along with fitted third order polynomial fits using the Combined Start Efficiency (FC). Figure (A.8) shows the total efficiency using the Combined Start Efficiency (CEM). All the polynomial fit coefficients for both total efficiencies (FC and CEM) are listed in Table (A.2).

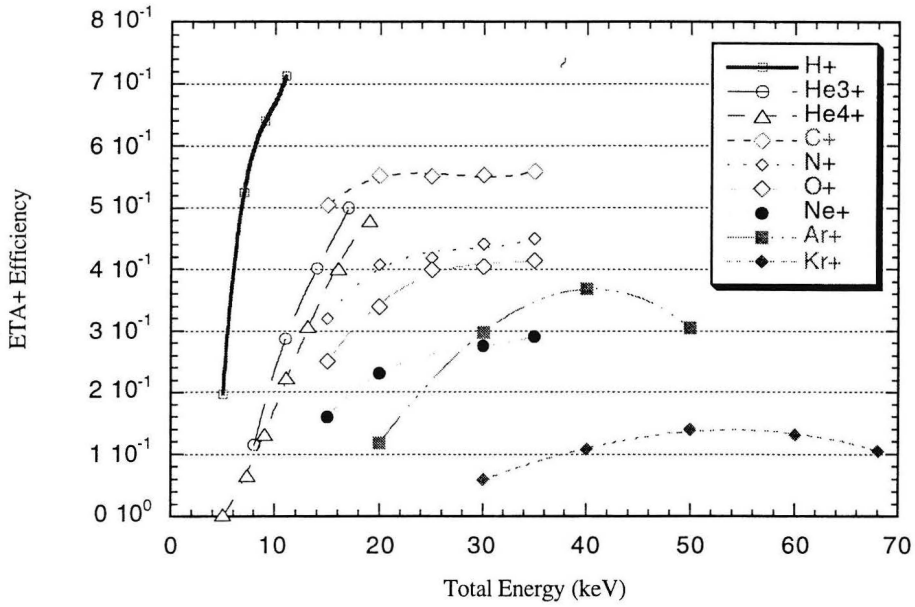

Figure A.6. +1 ion fraction efficiencies (Counts in the +1 PHA peak divided by the total PHA counts), as defined in Equation (A.5), for all nine calibrated species.

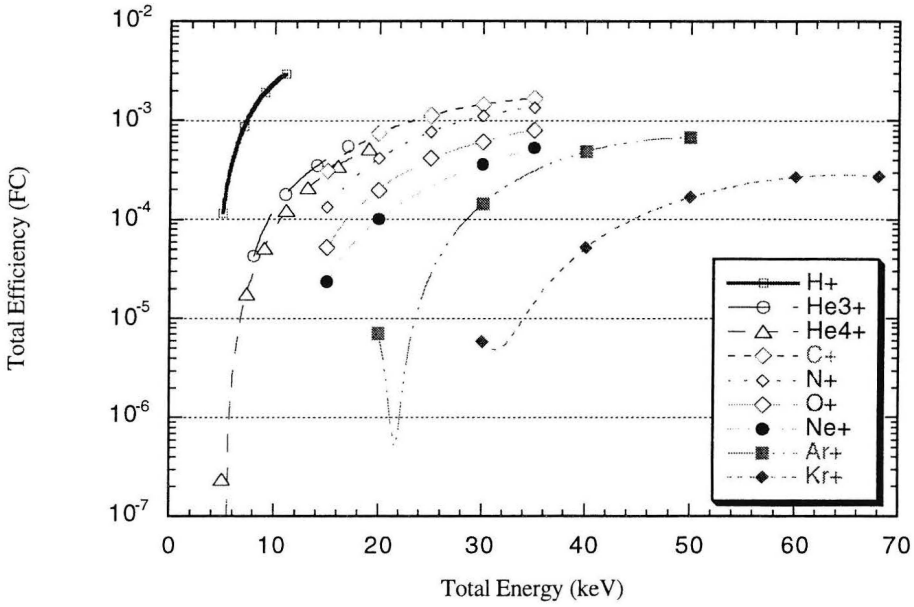

Figure A.7. Total efficiencies plotted against total energy along with fitted third order polynomial fits using the Combined Start Efficiencies (FC).

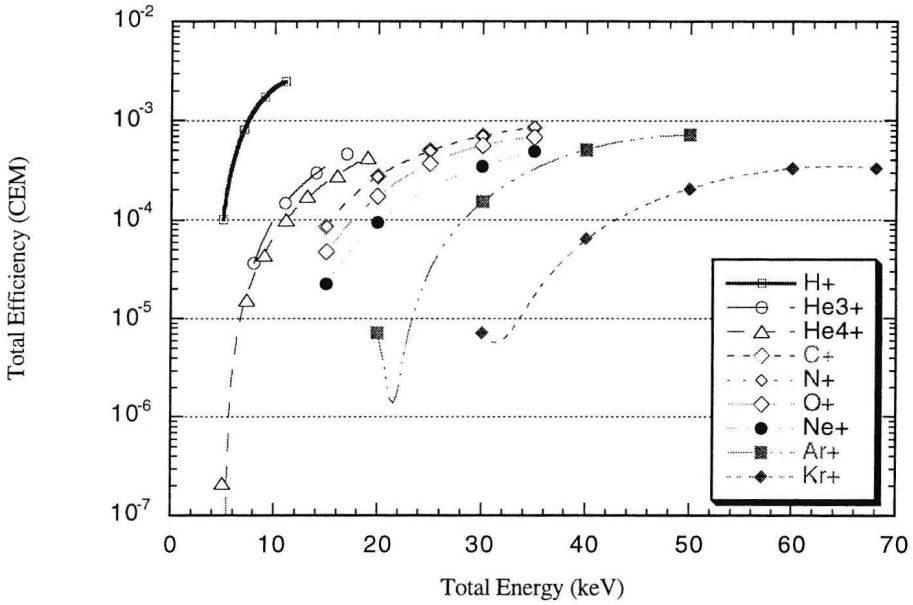

Figure A.8. Total Efficiencies using the Combined Start Efficiency (CEM) for the calibrated species.

Table A.2. Coefficients for the polynomial fits to the calibrated ion efficiencies.

Ions	Combined Start Coefficients				Combined Stop Coefficients			
	P0	P1	P2	P3	P0	P1	P2	P3
H+	-9.36e-2	1.37e-1	-1.22e-2	3.83e-4	2.06e-3	-1.71e-3	3.41e-4	-1.35e
He3+	-1.39e-1	1.11e-1	-7.55e-3	1.74e-4	-8.28e-5	-5.20e-5	1.13e-5	-2.03e
He4+	1.72e-2	6.36e-2	-2.90e-3	4.40e-5	2.11e-4	-9.60e-5	1.19e-5	-2.35e
C+	-9.01e-2	4.10e-2	-7.94e-4	2.51e-6	-3.72e-3	4.46e-4	-1.11e-5	1.22e-
N+	2.83e-1	-8.94e-3	1.20e-3	-2.28e-5	-9.96e-4	4.84e-5	3.80e-6	-5.63e
O+	-3.37e-1	6.91e-2	-2.11e-3	2.34e-5	2.37e-5	-6.30e-5	6.16e-6	-8.81e
Ne+	-1.56e-1	3.79e-2	-7.68e-4	5.29e-6	3.42e-5	-4.93e-5	4.31e-6	-5.72e
Ar+	-5.91e-1	5.66e-2	-1.06e-3	6.89e-6	1.83e-3	-2.26e-4	8.41e-6	-7.99e
Kr+	-6.28e-1	3.77e-2	-4.08e-4	1.08e-6	2.10e-3	-1.66e-4	4.11e-6	-2.90e

In order to use the table we will have,

$$\eta_{\text{Combined Start}} = P0 + P1 \cdot (E / Nuc) + P2 \cdot (E / Nuc)^2 + P3 \cdot (E / Nuc)^3$$

Similarly,

$$\eta_{\text{Combined Stop}} = P0 + P1 \cdot (E / Nuc) + P2 \cdot (E / Nuc)^2 + P3 \cdot (E / Nuc)^3$$

using their respective coefficients.

A.3.3 Non-calibrated Species Efficiencies

The nine different species that we calibrated MASS with are only a subset of the species that MASS will analyze during its mission in space. For those species for which MASS has no pre-flight calibration, we must estimate their efficiencies by interpolating between the existing calibration data points. The first step in creating those non-calibrated ion efficiencies is to find the underlying organizing variables (mass, energy per nucleon, atomic properties) in the existing efficiency data. Then we can construct the efficiency curves for those non-calibrated ions using the underlying organizing variables.

A.3.3.1 Combined Start Efficiency

Figure (A.9) plots the Combined Start efficiencies (FC) versus mass for different total energies using existing calibration data. W can see the data are reasonably well organized by total energy and mass. The shown fits in Figure (A.9) are all linear functions with slopes and intercepts plotted in Figure (A.10) and Figure (A.11), respectively. Figure (A.10) shows that the intercepts of the linear fits for all different ion energies are 0.522±0.001.

Hence if we want to construct the combined start efficiencies for the non-calibrated ions, we have

$$\eta_{\text{Combined Start}} = 0.522 + Slope \cdot mass; \tag{A.7}$$

where

$$Slope = -1.3008 \cdot (E_{total}^{-1.6625}); \tag{A.8}$$

and *mass* is the atomic mass in amu and E_{total} is the total energy of the ion in keV. The lowest energies for different species for which we can obtain Combined Start efficiencies using the above equations are listed in Table (A.3).

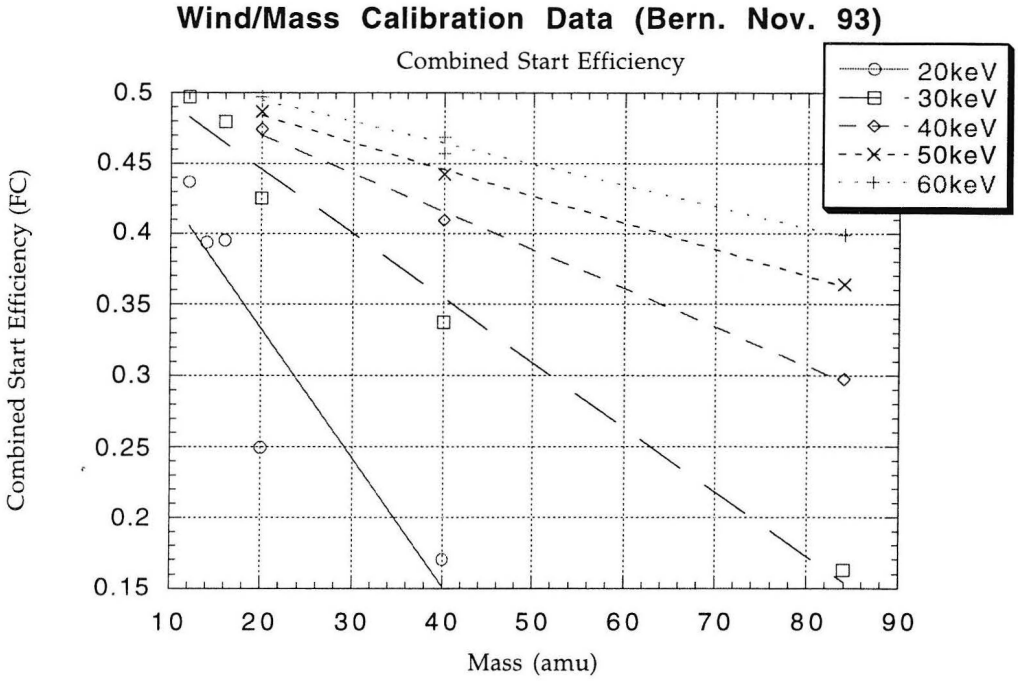

Figure A.9. Combined start efficiencies organized by total energy for all heavy calibrated ions (where mass > 4 amu) are plotted against the species' mass in amu. Data from He^+ and H^+ are not included because they do not follow the same pattern as the heavier ions. We can clearly see that they are very well organizied by total energy and mass. The fitted lines are all linear functions with their respective slopes and intercepts plotted in Figure A.10 and Figure A.11.

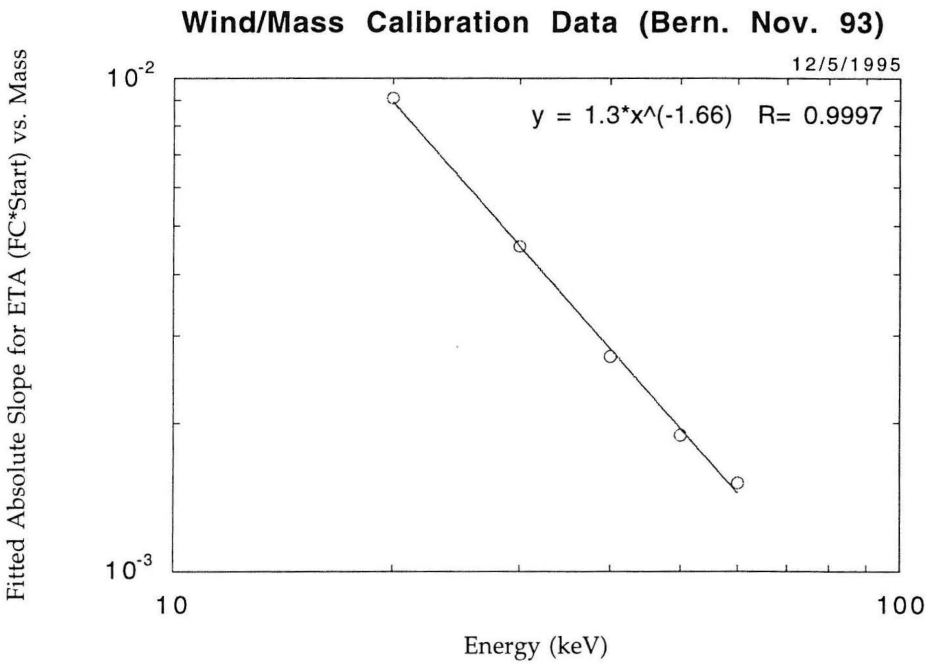

Figure A.10. The slopes of the linear fits to the Combined Start efficiencies, which are plotted in Figure A.9, are shown here plotted vs. total energy in keV in a log-log plot. The slopes are fitted well using a power law function as shown in the figure along with its functional form printed.

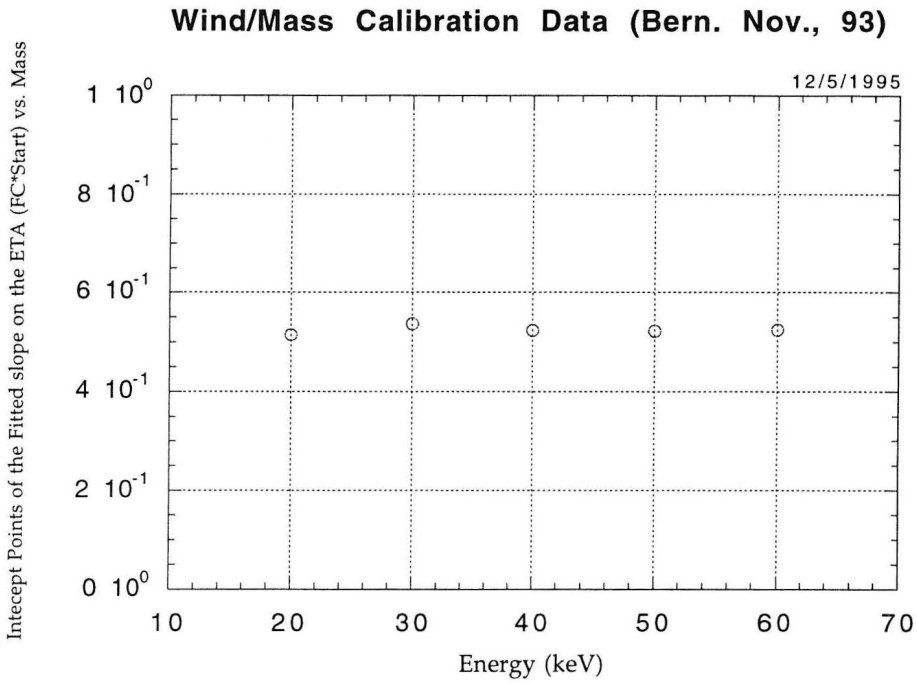

Figure A.11. The y-intercept points of the linear functions that are plotted in Figure A.9 are shown here. As demonstrated in this figure, the intercepts points showed a consistent values for different energies.

Table A.3. The minimum energies for which the fit to the data is valid for selected non-calibrated ions.

Ions	B	F	Na	Mg	Al	Si	S	Cl	K	Ca	Ti	Cr	Fe	N
Energy (keV/nuc)	0.67	0.54	0.50	0.49	0.47	0.46	0.44	0.42	0.40	0.40	0.37	0.36	0.35	0.34

A.3.3.2 Combined Stop Efficiency

Similar to the method used in producing combined start efficiencies, we have also used the product of the stop and +1 ion fraction efficiencies and treated it as combined stop efficiency while seeking underlying organizing variables. The measurement of the +1 ion fraction in the MASS TOF spectrum should be directly related to the production of +1 charge state ions after the ion passes through the carbon foil. Hence we have used the data obtained by Gonin *et al.* [1991] and their subsequent papers in measurement of charge state yields for different energetic ion species passing through a carbon foil. Figure (A.12) shows the absolute logarithm of the combined stop efficiency divided by the +1 ion yield fraction (obtained from a subroutine provided by Dr. R. Kallenbach at University of Bern that utilizes Gonin *et al.* [1991] results) versus energy per nucleon along with its fourth order polynomial fit. The polynomial fit characterizes the data reasonably well over this energy range, but there is considerable scatter in the data. We will use this fit to construct the combined stop efficiency data for the non-calibrated ions. The combined stop efficiency is given as:

$$\eta_{\text{Combined Stop}} = \eta_{\text{Stop Universal}} \cdot Yield \tag{A.9}$$

where

$$\eta_{\text{Stop Universal}} = 10^{Poly(\ln(E/nuc))}; \tag{A.10}$$

and *ploy((ln(E/nuc))* is the fourth order polynomial fit to $\eta_{\text{Stop Universal}}$ with *ln (E/nuc)* as its independent variable. *Yield* is the +1 charge yield (fractional) for ions after they pass through a $2.2\,\mu$ g/cm^2 of carbon foil as predicted by Gonin *et al.* [1991].

The total efficiency for the non-calibrated ion species is given as

$$\eta_{\text{Total}} = \eta_{\text{Combined Start}} \cdot \eta_{\text{Combined Stop}} \cdot \tag{A.11}$$

The total efficiencies for some selected non-calibrated and all calibrated ion species are shown in Figure (A.13).

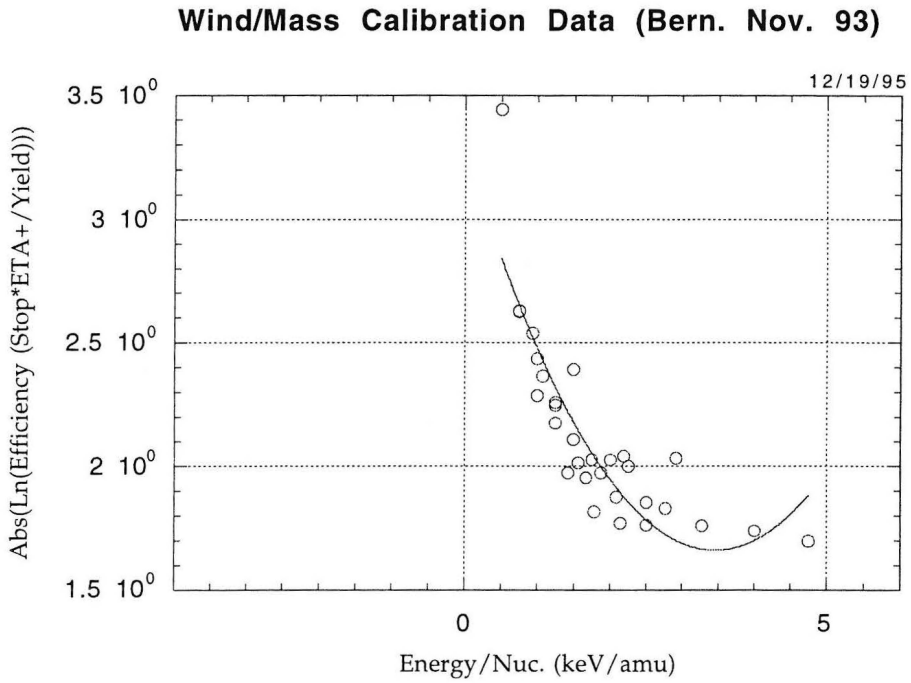

Figure A.12. The absolute natural log of combined stop efficiencies divided by the +1 ion yield fraction obtained from Gonin *et al.* [1991] ($\eta_{\text{Stop Universal}}$) versus the energy per nucleon along with its fourth order polynomial fit. We can see that polynomial fit characterizes the data reasonably well.

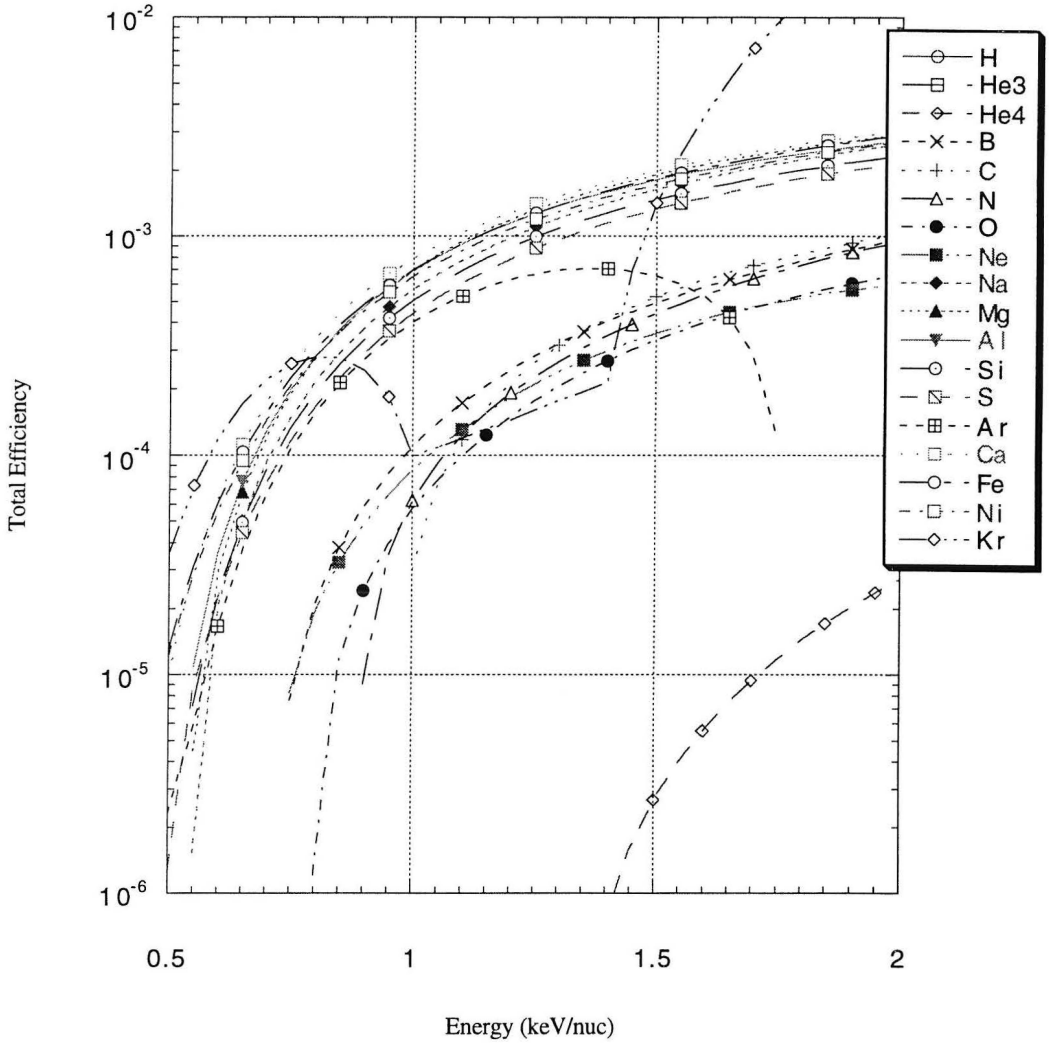

Figure A.13. Total efficiencies for all calibrated (H, ^{3}He, ^{4}He, C, N, O, Ne, Ar, and Kr) and some selected non-calibrated ions (B, Na, Mg, Al, Si, S, Ca, Fe, Ni) are plotted here versus energy per nucleon.

A.4 V_{adps} Defect

The term "V_{adps} defect" refers to an observed decrease in the MASS start efficiency (at equal total energy) with increasing post-acceleration or, equivalently, increasingly negative V_{adps} voltage. We hypothesize the effect is due to secondary electrons missing the start MCP. During the Bern calibration, we discovered the effect in our start rate and found that the side plate near the start MCP, with an intended voltage V_{adps}, was actually floating. Shown in Figure (A.14) are start efficiency data from the Bern calibration for two ion species, He^{+} and Ar^{+2}. The ratio of the measured start efficiency at non-zero V_{adps} to that at $V_{adps} = 0$ decreases from about unity at 2 kV to about 80% at –4 kV. After the calibration and before launch, the floating plate was set to V_{adps} using conductive epoxy to establish contact and correct the problem.

Unfortunately, as a result of routine post-launch instrument checks, it was discovered that the problem had apparently not been corrected. Figure (A.15) shows MASS in-flight He^{2+} and O^{6+} data, which clearly still exhibit a V_{adps}-dependent start efficiency (Note that V_{adps} and V_f, for "floating" potential are used interchangeably). Interestingly enough, the in-flight start efficiency appears to be about 80% of the value measured during the Bern calibration (compare Figures (A.15) and (A.14) at equal V_{adps}), although the shape of the defect (observed efficiency/calibrated start efficiency (V_{adps} =0) at a given energy) curve as a function of V_{adps} appears to be the same.

We believe the V_{adps} -defect is due to defocusing by the electrostatic lens formed in the post-acceleration gap of the mass instrument. The 80% offset is believed due to two factors. The first is the possible loss of cells in the carbon foil during the transport and launch of the instrument. The second, and likely more important effect, is the angular spread of the actual solar wind in comparison to the

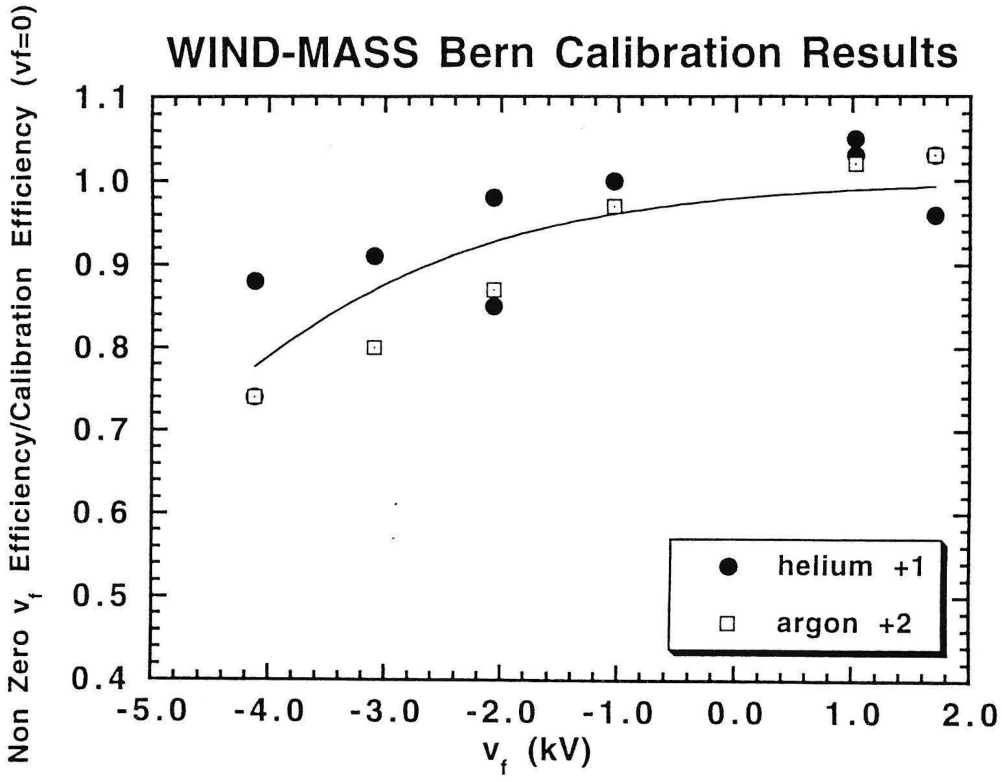

Figure A.14. Start efficiency data from Bern calibration for He^+ and Ar^{2+}. The ratio of the measured start efficiencies at non-zero $V_{adps}(V_f)$ to that at $V_{adps}(V_f) = 0.0$ decreases from about unity at 2 kV to about 80% at –4 kV.

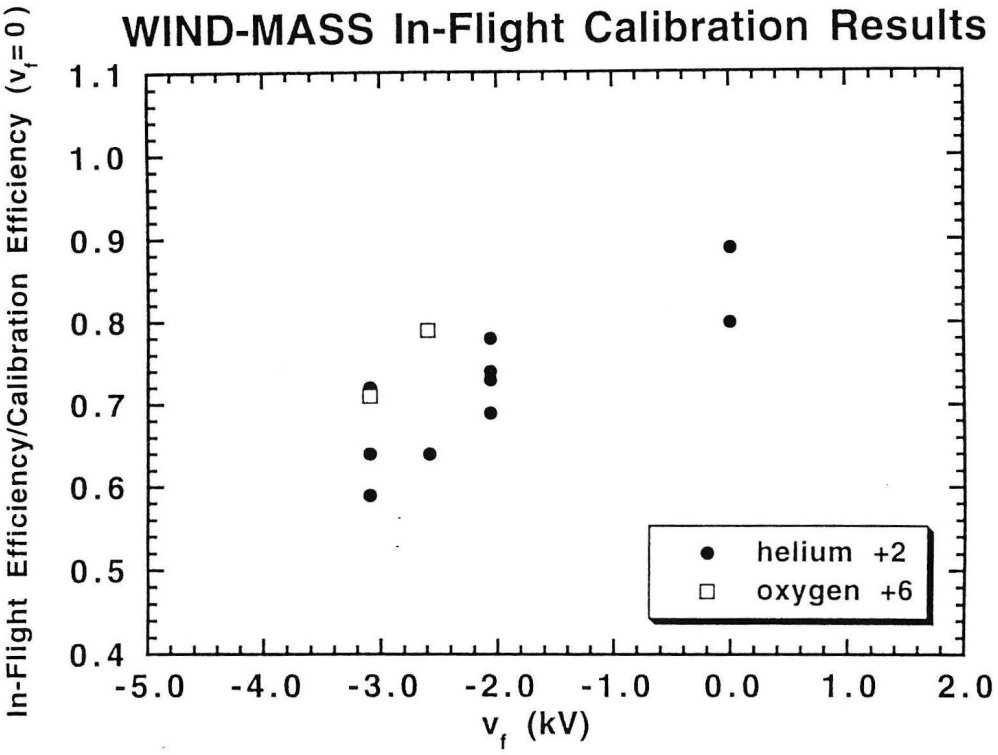

Figure A.15. Ratio of the measured in-flight start efficiencies at various $V_{adps}(V_f)$ values to Bern calibration start efficiencies at $V_{adps}(V_f) = 0.0$ for He^{2+} and O^{6+}.

beam-like conditions during the Bern calibration. Figure (A.16) shows the start efficiency as a function of azimuthal angle, θ, during the Bern calibration.

A.5 Correcting V_{adps}

Figure (A.17) shows the combined in-flight and Bern calibration data with the Bern V_{adps} -defect values multiplied by a factor of 0.8 to account for differences in calibration and space situations. These data were fit to an offset gaussian to characterize the V_{adps} defect as a function of V_{adps}.

However, it was noted that there appears to be a smaller, second order dependence on the incident ion energy per nucleon. This type of energy per nucleon dependence does not seem unreasonable if the process responsible for the V_{adps} defect depends in part on the energy of the start secondary electrons liberated from the foil. Figure (A.18) shows the ratio of the observed V_{adps} defect to the predicted V_{adps} defect based on the simple gaussian fit in the post-acceleration voltage. Clearly at high energy per nucleon values (> about 3 keV/nuc), the gaussian fit tends to underestimate the degree of defect. The energy per nucleon dependence shown in Figure (A.18) was fit to an exponential in energy per nucleon plus a constant offset. Because the minor ions entering the MASS instrument tend to be below 3 keV/nucleon, this correction is usually small.

The final expression for the V_{adps} defect is as follows:

$$\frac{\eta_{start}}{\eta_{start}(V_{adps}=0)} = 0.82 \cdot e^{-(V_{adps}-1.21)^2/91.94} \cdot \left[0.959 + 1.88\times10^{-4} \cdot e^{1.64 \cdot E/A}\right] \qquad \text{(A.12)}$$

Figure (A.19) shows the agreement for both in-flight and calibration data between the observed start efficiency defect and that given by the expression above. The largest derivations are for He^{2+} and O^{6+}, solar wind ions, and may be due to the difficulties associated with in flight determinations of the start efficiencies, especially

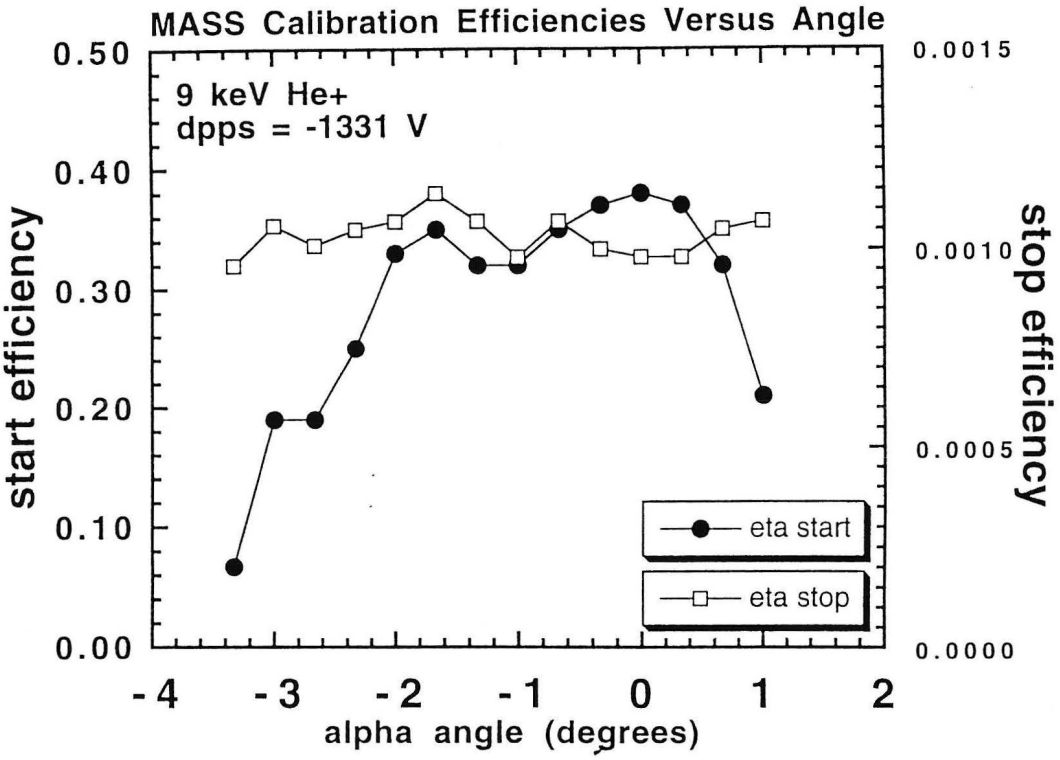

Figure A.16. The solar wind has a much wider spread compared to the beam-like conditions during the calibration. The figure shows the start efficiency as a function of the azimuthal angle during the Bern calibration.

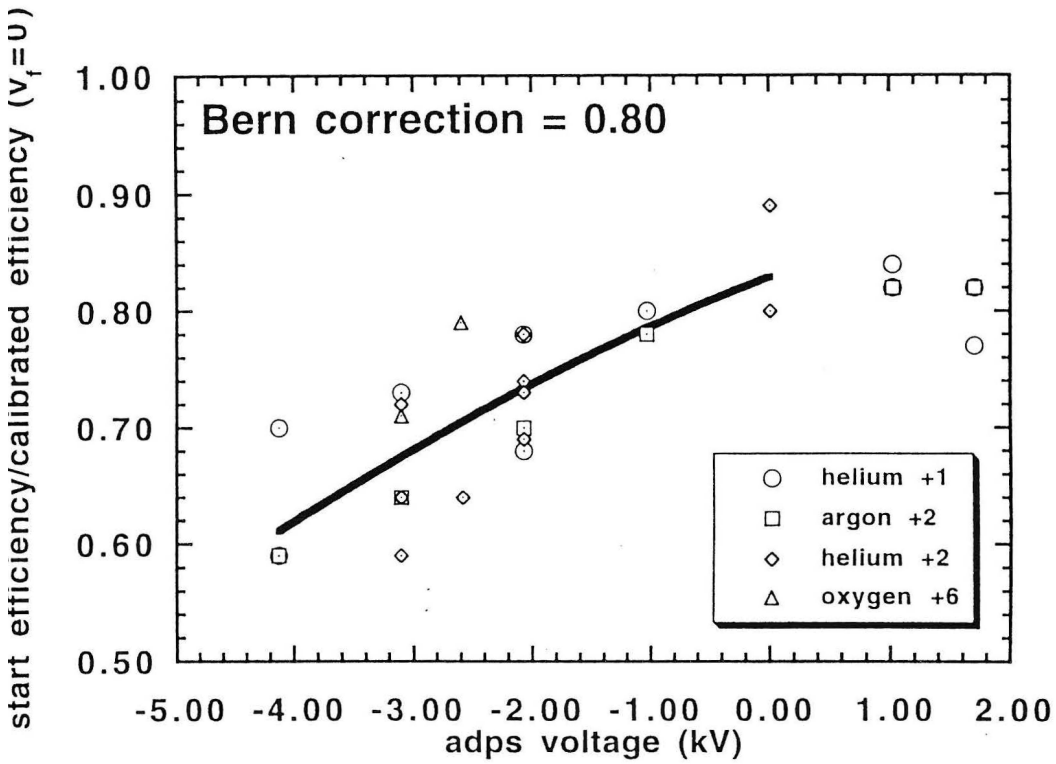

Figure A.17. This figure shows the combined in-flight and Bern calibration data with the Bern $V_{adps}(V_f)$ –defect values multiplied by a factor of 0.8 to account for the losses due to passage through carbon foil and the width of the beam in the solar wind.

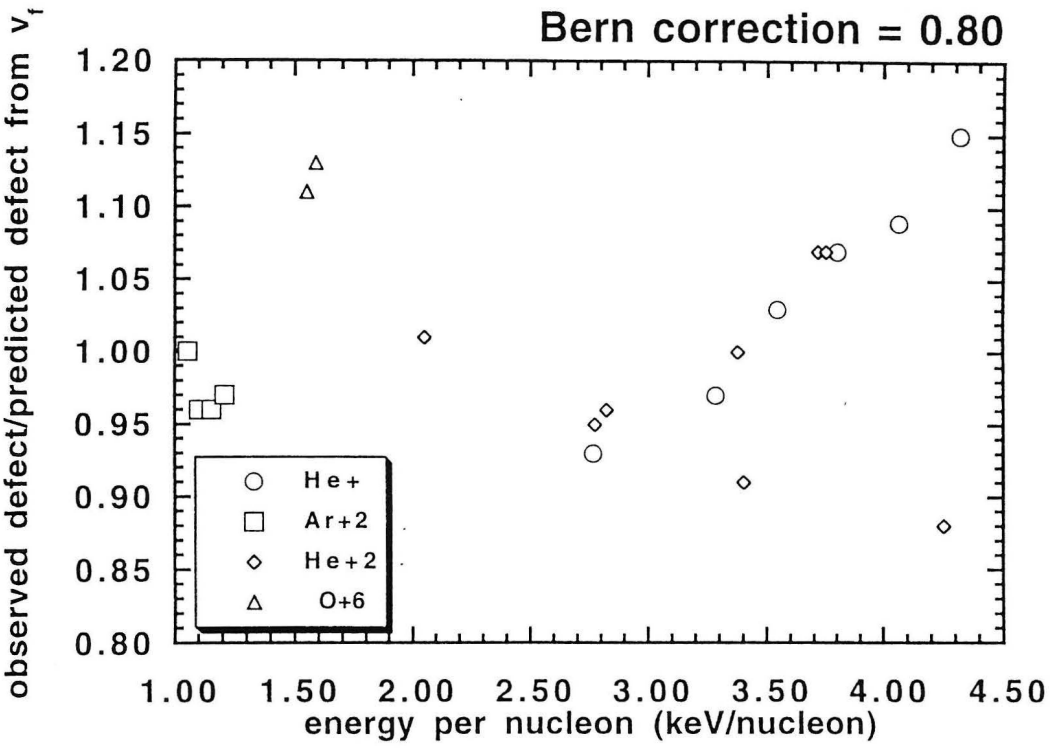

Figure A.18. The ratio of the observed $V_{adps}(V_f)$ defect to the predicted V_{adps} defect. The agreement is acceptable. But at high energy per nucleon values (> about 3 keV/nuc), the gaussian fit tends to underestimate the degree of defect.

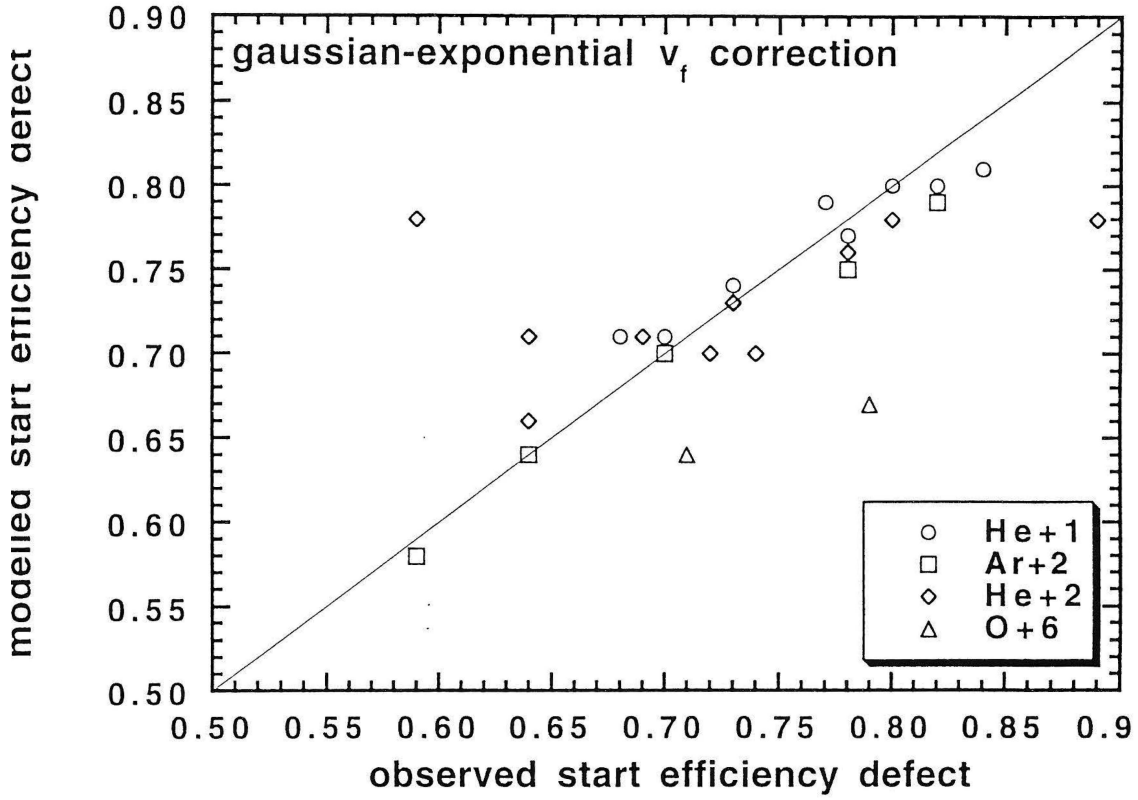

Figure A.19. This figure shows the agreement for both in-flight and calibration data between the observed start efficiency detect and that given by the fitted functional form as stated in section A.4.1. The largest deviations are for He^{2+} and O^{6+}.

for O^{6+}. In any case, it appears that the V_{adps} defect given by the above expression is good to typically better than 10%. In addition, in this dissertation data are in the form of ratios so as to cancel instrumental effects that are common to the different species.

APPENDIX B: TOF CHANNEL RANGES

WIND/MASS has total of 4096 channels for TOF measurement. Depending on different V_{hps} settings, Equation (3.1) gives the relationship between channel number and actual mass in amu. All the calibrated species' TOF ranges were determined prior to launch by fitting their TOF peaks in gaussian form (as discussed in Appendix A.3). The V_{hps} voltage was 23.0 kV during calibration and 23.2 kV in-flight. The calibrated TOF ranges have been changed to reflect the difference. In addition, we also have to determine the TOF ranges for non-calibrated species. This is done by fitting the actual TOF data for long slow speed solar wind events. The actual TOF and background ranges that we used in this dissertation are given in Table B.1.

Table B.1. TOF and background channel ranges for selected species.

Mass (amu)	TOF ranges (Channel number)	Background TOF ranges	
		Lower TOF background (Channel number)	Upper TOF background (Channel number)
4	932 – 946	908 - 922	956 – 970
12	1612 – 1632	1584 – 1604	1637 – 1657
14	1738 – 1766	1700 – 1728	1771 – 1799
16	1862 – 1882	1800 – 1820	1910 – 1930
20	2082 – 2100	2000 – 2018	2140 – 2160
22	2176 – 2190	2139 – 2153	2209 – 2221
23	2234 – 2254	2200 – 2220	2258 – 2278
24	2282 – 2300	2259 – 2279	2308 – 2326
25	2334 – 2340	2307 – 2313	2350 – 2356
26	2380 – 2390	2355 – 2365	2411 – 2421
27	2426 – 2438	2411 – 2423	2442 – 2454
28	2466 – 2486	2526 – 2546	2580 – 2614
32	2624 – 2658	2672 – 2720	2580 – 2614
40	2946 – 2988	3000 – 3042	2880 – 2922
56	3490 - 3536	3622 - 3668	3400 - 3446

11.3 *Ho*, (1998) Appendix D

APPENDIX D: MEMORY ALLOCATION OF PHA WORDS AMONG THREE SMS SENSORS

The number of PHA words allocated to STICS, MASS and SWICS depends on telemetry mode (LBR = Low Bit Rate, HBR = High Bit Rate), the spin rate (subframes per EDB) and the sensor status. We show the distribution in Table D.1.

In cases when one of the three sensors does not use up its allocated PHA space, MASS will use the remaining space. The default distribution for un-used PHA space (in 10% steps) is listed in Table D.2.

Within MASS, the distribution among different ranges and sectors is given in Table D.3. If the number of PHA words is more than 12, the DPU will use Table D.3 as a look up table for PHA word allocation. For example, if the number of PHA words is 29, the DPU will take the distribution of two times 12 and one times 5 events from Table D.3. Therefore:

The number of PHA words of range 0 (sun) is: 2x4+1 = 8

The number of PHA words of range 0 (non-sun) is: 2x1+1 = 3

The number of PHA words of range 1 (sun) is: 2x6+2 = 14

The number of PHA words of range 1 (non-sun) is: 2x1+1 = 3

If the sector can not fill up its allocated space, the remaining space will be distributed to other sectors. In addition, the DPU will try to format PHA words from every azimuthal sector.

Table D.1. Number of MASS PHA words to be transmitted.

Telemetry Mode Number of subframes per EDB	SWICS OFF STICS OFF MASS ON	SWICS ON STICS OFF MASS ON	SWICS OFF STICS ON MASS ON	SWICS ON STICS ON MASS ON
LBR 6SF/EDB	101	36	28	9
LBR 7SF/EDB	121	46	38	17
LBR 8SF/EDB	141	56	48	25
LBR 9SF/EDB	161	66	58	27
LBR 10SF/EDB	181	76	68	37
LBR 11SF/EDB	201	86	78	43
LBR 12SF/EDB	221	96	88	49
LBR 13SF/EDB	241	91	61	46
LBR 14SF/EDB	261	101	69	52
LBR 15SF/EDB	281	111	77	58
LBR 16SF/EDB	301	121	85	64
LBR 17SF/EDB	321	131	93	70
LBR 18SF/EDB	341	141	101	76
LBR 19SF/EDB	361	151	109	82
LBR 20SF/EDB	381	161	117	88

Table D.2. Distribution of remaining PHA allocation.

SWICS additional PHA space (10%)	MASS additional PHA space (10%)	STICS additional PHA space (10%)	SWICS sensor status	MASS sensor status	STICS sensor status
3	4	3	ON	ON	ON
4	6	0	ON	ON	OFF
5	0	5	ON	OFF	ON
10	0	0	ON	OFF	OFF
0	6	4	OFF	ON	ON
0	10	0	OFF	ON	OFF
0	0	10	OFF	OFF	ON
0	0	0	OFF	OFF	OFF

Table D.3. MASS PHA word distribution for ranges and sectors in telemetry.

Number of PHA events	Events of BR0 (sun)	Events of BR0 (non-sun)	Events of BR1 (sun)	Events of BR1 (non-sun)
0	0	0	0	0
1	0	0	1	0
2	1	0	1	0
3	1	0	1	1
4	1	1	1	1
5	1	1	2	1
6	2	1	2	1
7	2	1	3	1
8	2	1	4	1
9	3	1	4	1
10	3	1	5	1
11	3	1	6	1
12	4	1	6	1

11.4 *Ho*, (1998) Appendix F

APPENDIX F: MASS TIME OF FLIGHT CALCULATION

The MASS TOF unit defines a region with a harmonic potential field, Φ. The equations of motion for ions within this region are well known. We define the coordinate system within the MASS TOF in Figure (F.1). The x-axis is from the vertex of the "vee" to the hyperbola, the y-axis is horizontal distance measured from the vertex. If the hyperbola surface has a voltage of $V = U_h$ and the "vee" is $V = 0$, the potential field is then equal to:

$$\Phi(x,y,z) = \frac{U_h}{d^2}(x^2 - y^2) \tag{F.1}$$

whereas d is the x-distance of the hyperbola from the origin. The motions for ions with mass, m; and charge, q, entering the TOF with initial energy $E_o = \frac{1}{2}mv_o^2$ are given as:

$$x(t) = x_o \cos(\omega t) + \frac{v_o \cos\alpha}{\omega}\sin(\omega t)$$

$$y(t) = y_o \cosh(\omega t) + \frac{v_o \sin\alpha}{\omega}\sinh(\omega t) \tag{F.2}$$

whereas x_o and y_o are the initial position and the frequency ω is given by:

$$\omega^2 = \frac{2U_h q}{d^2 m}$$

We can study the deviation from an ideal period, Δt, if we assume particle begin at x,y = (0, 0) and make a small angle, ε, deviation ($v_x/v_y = tan(\varepsilon) << 1$) from the angle α. We substitute $\alpha' = \alpha + \varepsilon$ into Equation (F.2) and solve for Δt, using small angle approximation, and findΔt such that

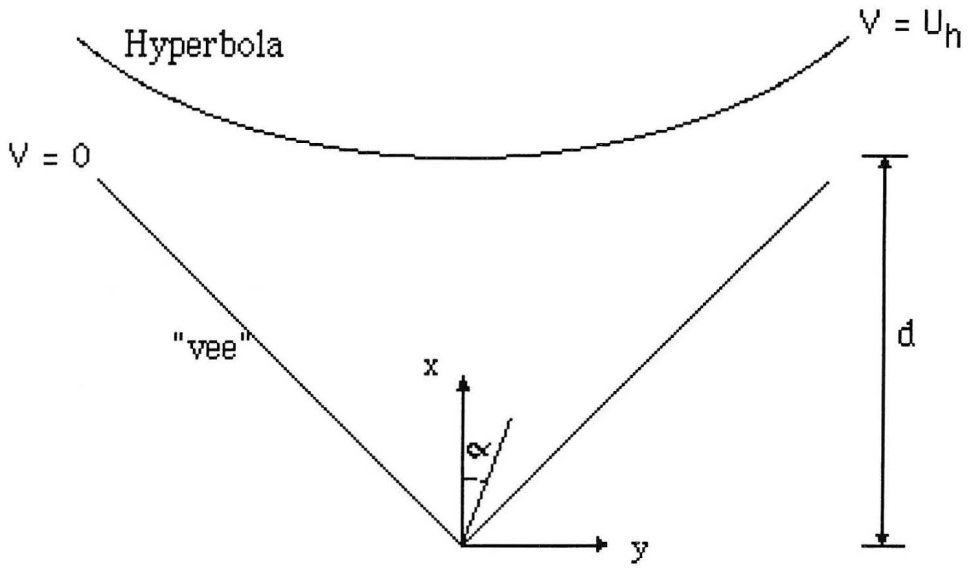

Figure F.1. Coordinate system that we will use for solving the equations of motions for ions within MASS TOF.

$$\Delta t \equiv \frac{1}{\omega}\left(\frac{1}{3}\varepsilon^3 + \frac{2}{15}\varepsilon^5 + \vartheta(\varepsilon')\right) \tag{F.3}$$

whereas the deflection in the y-axis, depends on the angular deviation such that,

$$\Delta y = \frac{v_{yo}}{\omega}\left(\varepsilon + \varepsilon^2 + \vartheta(\varepsilon')\right). \tag{F.4}$$

Therefore to lowest order, the time delay is proportional to:

$$\Delta t \propto \Delta y^3 \tag{F.5}$$

And this deviation occurs only on one side of the peak towards longer TOF, producing a "tail" in the TOF distribution [Sheldon, 1995].

To conclude, for ions that start out at $\alpha \neq 0$, they will produce a longer TOF than ions that travel at $\alpha = 0$.

12 *Wind* SMS STICS

This section will include pieces from *Chotoo et al.* [1998] and *Gruesbeck* [2013] as well as documentation provided by the instrument team.

12.1 *Chotoo*, (1998)

CHAPTER 2: INSTRUMENTATION

This Chapter contains a description of the instrument used in this study. The chapter is introduced with a brief overview of the WIND mission followed by a summary of the Solar Wind, Mass, and Suprathermal Ion Composition (SMS) investigation on WIND. The main instrument used in this work is the suprathermal SMS sensor (STICS). The way STICS works and its angular resolution are discussed in Section 2.3. The STICS data transmitted from the spacecraft to the Earth are reviewed in Section 2.4.

2.1 The WIND Mission

The WIND spacecraft was sucessfully launched on November 1, 1994. It is the first of two missions in the Global Geospace Science (GGS) initiative, the other being POLAR (launched February 24, 1996). The main focus of GGS is to greatly improve the understanding of the flow of energy, mass, and momentum in the solar-terrestrial environment with particular emphasis on the near-Earth region (Acuna et al., 1995). While WIND is mainly concentrating on the region upstream of the Earth's magnetosphere and bow shock, POLAR is focusing on the Earth's magnetosphere with a 2 x 9 Earth radii (R_e) polar orbit.

The GGS program is part of the US contribution to the International Solar Terrestrial Physics (ISTP) program. ISTP is a joint effort by the United States, Europe, Russia, and Japan to understand the physics of the behavior of the solar-terrestrial system in order to predict how the Earth's atmosphere will respond to changes in the solar wind. The Japanese Institute of Space and Astronautical Science (ISAS) launched GEOTAIL, which has been collecting data in the Earth's geomagnetic tail since 1992. The SOHO and CLUSTER Programs are the European Space Agency's (ESA) contribution to the ISTP effort. SOHO was successfully launched in December 1995, but CLUSTER was destroyed during its launch in June 1996.

CLUSTER is now being rebuilt by the ESA. The InterCosmos Agency (IKI) of the former USSR and Eastern European countries contributed its INTERBALL set of four spacecrafts (Whipple and Lancaster, 1995). INTERBALL-TAIL was launched on August 3, 1995 and INTERBALL-AURORA, on August 29, 1996.

The WIND mission was designed to measure the properties of the solar wind before it reaches the Earth. The initial orbit consisted of a series of lunar swingbys causing the spacecraft to move quickly in and out of the Earth's magnetosphere (Figure 2.1). This allows WIND to study the Earth's bow shock, magnetosheath, magnetosphere, and the corresponding boundary layers. WIND spent several months in 1995 and 1997 in a halo orbit around the Lagrangian point (L1) between the Earth and the Sun, about 240 Earth radii (1 R_e = 6380 km) from the Earth, where it continuously monitored the solar wind. There are eight instruments on the spacecraft which consists of twenty-four separate sensors. These state-of-the-art instruments are optimized for measuring waves, fields, and particle distributions of space plasmas. Table 2.1 gives a summary of these instruments. The spacecraft itself is cylindrical in shape with a diameter of 2.4 m and a height of 1.8 m and spins at a rate of ~20 rpm (Harten and Clark, 1995), see Figure 2.2. Throughout the entire mission the spin axis will be normal to the ecliptic plane with the spacecraft +z axis (Figure 2.2) pointing in the -z Geocentric Solar Ecliptic (GSE) direction.

2.2 The Solar Wind, Mass, and Suprathermal Ion Composition Experiment (SMS)

The Solar Wind, Mass and Suprathermal Ion Composition (SMS) investigation is making major contributions to the global objectives of ISTP. It is designed to measure, under all conceivable solar wind flow conditions, (1) the elemental and isotopic composition of solar wind ions, and (2) the differential energy spectra, abundances and charge states of all dominant species from H to Fe with energies

between 0.5 to 230 keV/e (Gloeckler et al., 1995). This experiment consists of three separate sensors: the Solar Wind Ion Composition Spectrometer (SWICS), the high-resolution MASS spectrometer (MASS), and the Supra-Thermal Ion Composition Spectrometer (STICS), serviced by a common data processing unit (DPU).

SWICS uses electrostatic deflection followed by a time-of-flight (TOF) and energy measurement. After particles pass through the SWICS deflection system, they are accelerated in order to increase the energy of the solar wind ions above the 30 keV threshold of the low-noise solid-state detector in the time-of-flight system. SWICS was designed to measure the abundances of about forty different ions in the solar wind and to give their speed and kinetic temperature.

MASS uses electrostatic deflection followed by a time-of-flight measurement but does not require an energy measurement. The MASS sensor is the first instrument flown that can routinely measure the isotopes of the solar wind elements heavier than helium because of its high-mass resolution ($M/\Delta M > 100$). MASS is characterizing in detail the matter entering the magnetosphere by measuring the elemental and isotopic composition of the solar wind.

STICS also uses electrostatic deflection followed by a time-of-flight (TOF) and energy measurement, but has no post acceleration. STICS characterizes the interplanetary suprathermal ion populations by measuring the three-dimensional distribution functions of H, He, C, O, Si, and Fe for direct comparision with ion populations inside the magnetosphere. STICS is also used for pick-up ion studies.

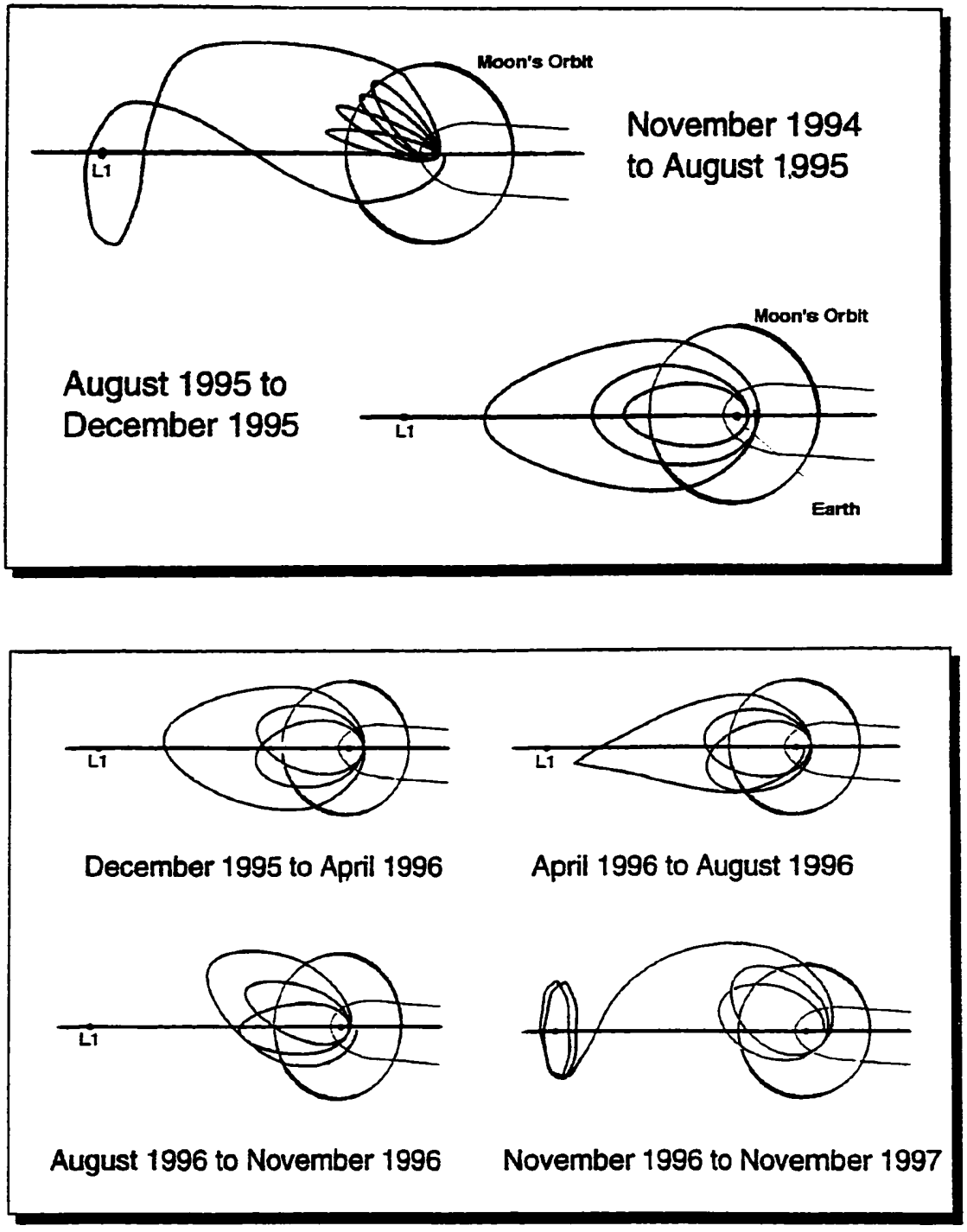

Figure 2.1. The WIND trajectory at different stages during the mission (GSE X-Y projection).

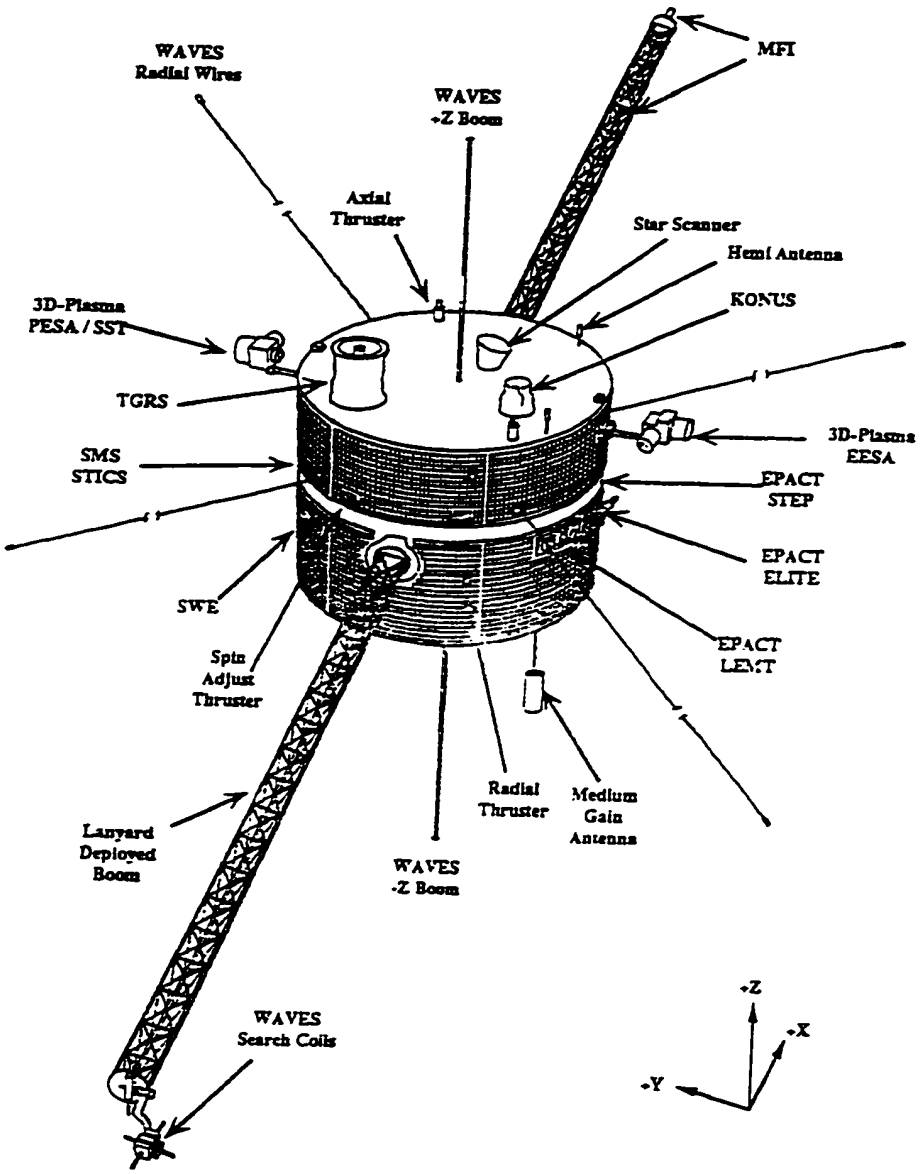

Figure 2.2. The WIND spacecraft and its sensors (Harten and Clark, 1995).

Table 2.1. Summary of the different instruments on the WIND spacecraft, the principal investigator (P.I.) for each instrument, and the P.I.'s institution (Harten and Clark, 1995).

Instrument	Description	Principal Investigator
Magnetic Field Investigation (MFI)	d/c magnetic fields	R. Lepping (NASA/GSFC)
Radio and plasma wave experiment (WAVES)	a/c electric/magnetic fields 8 Hz-16 MHz	J. Bougeret (Obs. de Paris) M. Kaiser (NASA/GSFC)
Solar Wind Experiment (SWE)	Mass, energy, direction of low energy ions and electrons 7 eV - 22 keV	K. Ogilvie (NASA/GSFC)
3-D Plasma (3-DP)	Distribution and energy of ions and electrons in range 3 eV-30 keV and 20 keV-11 MeV (SST)	R. Lin (U.C. Berkeley)
Energetic Particles: Accelertaion, Composition Transport (EPACT)	Mass, energy, direction of ions in range 0.2-500 MeV	T. von Rosenvinge (NASA/GSFC)
Solar wind/Mass Suprathermal ion composition studies (SMS)	Mass, energy with angular resolution of ions in range 0.5-230 keV/e	G. Gloeckler (U. of Maryland)
Transient Gamma-Ray Spectrometer (TGRS)	High spectral resolution gamma-ray detector in range 15 keV to 10 MeV	B. Teegarden (NASA/GSFC)
KONUS (Russian instrument)	High time resolution gamma-ray detector	E. Mazets (IOFFE Institute Russia)

2.3 The Supra-Thermal Ion Composition Spectrometer

STICS can determine the mass, charge state, and mass per charge of the ions, their arrival directions both in and out of the ecliptic plane, and their energy-per-charge (E/Q). STICS uses an electrostatic deflection system to select ions of a given energy-per-charge value followed by a time-of-flight (TOF) measurement of the ions. The total ion energy is then measured with a solid state detector. The combination of these measurements allows the determination of the mass, charge, and energy of the incoming ions. Due to its angular resolution and the large angular acceptance, STICS can therefore determine the full three-dimensional distribution functions of suprathermal ions in the energy range 6.2 - 223.1 keV/e.

Physically, STICS is made up of two units: the STICS sensor and the Analog Electronics (AE) Box (Figure 2.3). The sensor contains the deflection system, three time-of-flight telescopes, high voltage (HV) power supplies for the deflection system, the microchannel plates, and the detector pre-amplifiers. The remainder of the analog electronics, including the shaping amplifiers, discriminators, time-of-flight circuits, analog-to-digital converters (ADC), valid-event logic circuits (for the pulse height), and the low voltage power supply are located in the separate Analog Electronics Box. This separation frees the mechanical and thermal design of these circuits from the constraints imposed by the odd shape of the sensor package. Outputs from the Analog Electronics Box are sent to the SMS Data Processing Unit (DPU) where they are processed then submitted to the spacecraft telemetry (Galvin, 1991).

2.3.1 Principle of Operation

Figure 2.4 shows a simplified cross-sectional view of the STICS sensor. For a more detailed description see Gloeckler et al. (1995). Particles enter the spherical electrostatic deflection system through a simple aperture which includes a light trap. The light trap is important because the TOF section is senstive to ultraviolet radiation.

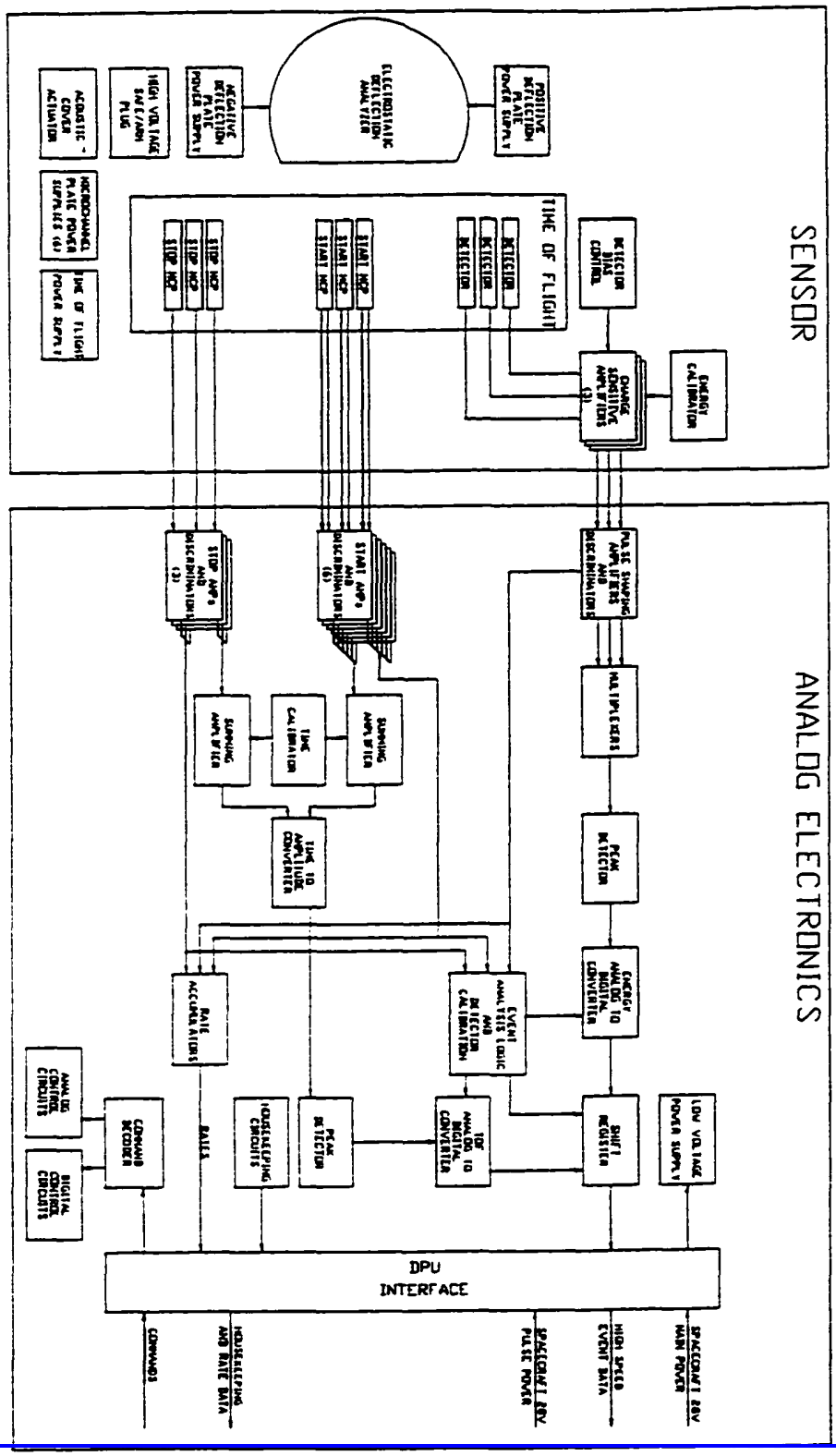
SENSOR
ANALOG ELECTRONICS
TIME OF FLIGHT
DPU
INTERFACE
COMMANDS
HOUSEKEEPING
AND RATE DATA
SPACECRAFT PULSE POWER
HIGH SPEED
EVENT DATA
SPACECRAFT
MAIN POWER

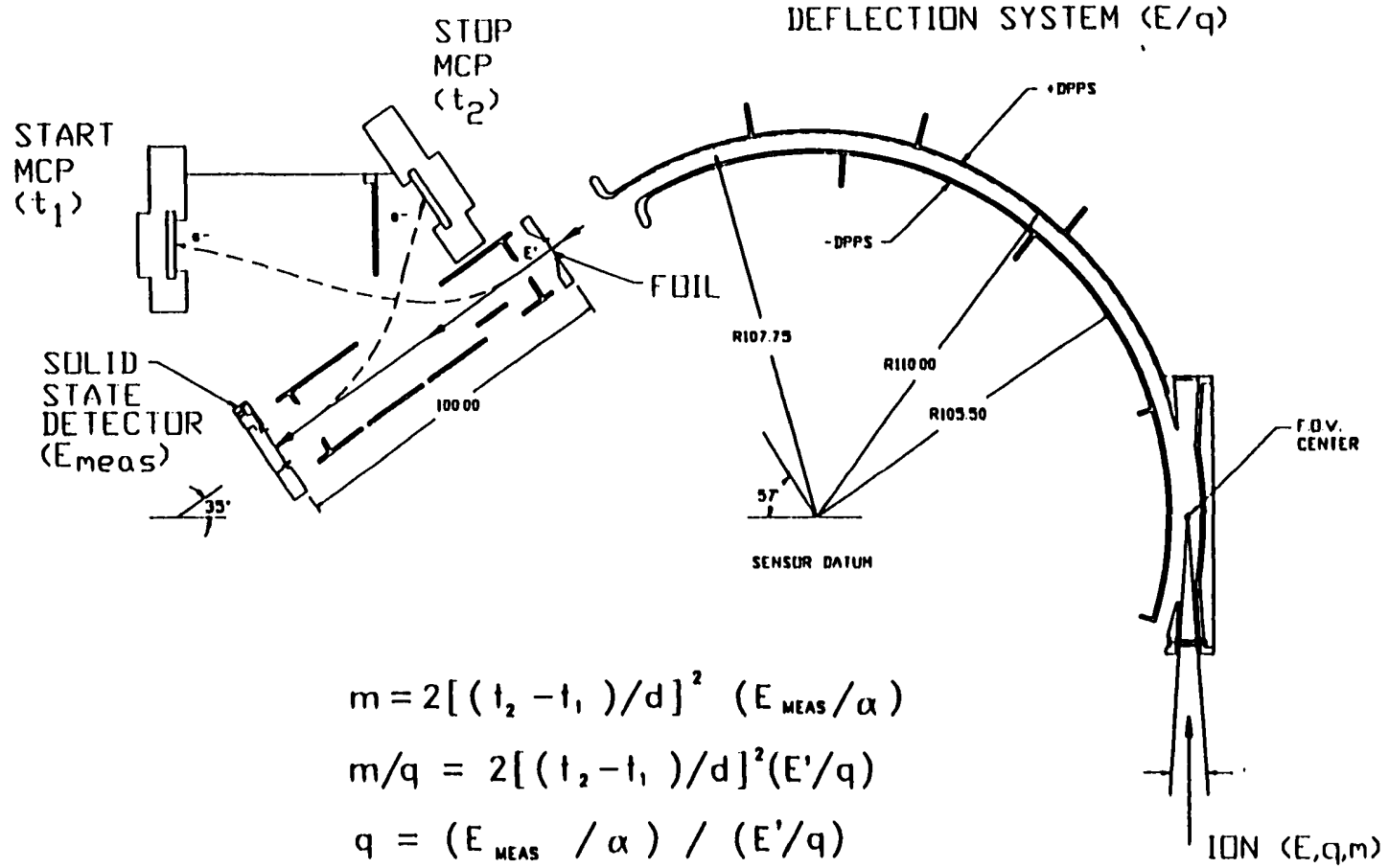

$$m = 2[(t_2 - t_1)/d]^2 \ (E_{MEAS}/\alpha)$$

$$m/q = 2[(t_2 - t_1)/d]^2 (E'/q)$$

$$q = (E_{MEAS}/\alpha) / (E'/q)$$

$$E = q \cdot (E/q)$$

Only those ions with a specific E/Q determined by the voltage U on the analyzer make it through to the time-of-flight system. A pair of high voltage power supplies step the voltage on the deflection plates once every spin or every two spins depending on the telemetry rate. Thirty-two deflection voltage steps (DVS 0 - 31) are logarithmically spaced to take the plates from a minimum of ±260 volts to a maximum deflection voltage of ±10 kilovolts in order to cover the entire E/Q range of the sensor (6.2-223.1 keV/e). Since STICS became fully operational on December 21, 1994, DVS 2-31 were used for the first sixteen days. From January 6, 1995, onwards, DVS 0-30 (excluding DVS 26) have been used.

After passing through the deflection system, the particles strike a thin (~2μg/cm^2) carbon foil at the entrance of the TOF telescope. As the particles pass through the foil, they knock off secondary electrons, but the particles themselves continue on through the TOF chamber relatively undisturbed. The secondary electrons are detected by the front secondary electron detector assembly (SEDA), which consists of a Start microchannel plate (MCP), two discrete front anodes, and a system of accelerating gaps and deflection electrodes for accelerating and guiding the electrons onto the MCP. This generates a START signal for the TOF analysis. Each front MCP has two anodes, which give additional information on the angle of the ions entering the instrument.

When the particles reach the end of the telescope, they strike a solid-state detector knocking out secondary electrons. These electrons are detected by the rear SEDA creating the STOP signal. If the energy of the particle is greater than the threshold of the solid-state detector, an energy measurement is also obtained.

The TOF system consists of three identical telescopes stacked vertically in the STICS sensor. The middle telescope (2) measures particles in the ecliptic plane within ±26.5°. Telescope 1 looks above the ecliptic from 26.5° to 79.5°, and telescope 3 scans below the ecliptic from -26.5° to -79.5°.

If both a START and a STOP signal (double coincidence) are generated, the time, t, for the particle to travel a known distance (d = 10 cm) can be determined. For triple coincidence must be three signals, the START, STOP, and energy measured (E_{meas}) by the solid-state detector. Along with the E/Q from the deflection system we can calculate the mass (M), ionic charge state (Q), and the incident energy (E) of each ion using the following equations:

$$\begin{aligned} M &= 2(t/d)^2(E_{meas}/\gamma) \\ M/Q &= 2(t/d)^2(E'/Q) \\ Q &= (E_{meas}/\gamma)/(E'/Q) \\ E &= Q \bullet (E/Q) \end{aligned} \qquad (2.1)$$

E'/Q takes into account the small energy loss of the ions passing through the thin carbon foil, and γ is a number less than one that takes into account the pulse height defect in the solid-state detectors. If the energy of the incident particle is not large enough to trigger the SSD and only t is measured, then only M/Q can be determined, and the mass is colloquially called "mass zero" events. If both E_{meas} and t are obtained, then the mass and M/Q can be calculated.

Besides composition measurements, the particle's direction can be determined. The six discrete Start anodes (two each per Start MCP) provide the polar entrance angle of the incident particle. The polar angle of +79.5° to -79.5° out of the ecliptic is divided into six equal sectors, and each START anode represents one of these polar sectors, nominally 26°. The anodes are labeled from top to bottom: anodes 1 and 2 are in telescope 1, anodes 3 and 4 in telescope 2, and anodes 5 and 6 in telescope 3 (Figure 2.5a). For the azimuthal angle, the DPU uses information from the sector/spin clock of the spacecraft. The spacecraft spin axis is perpendicular to the eclipitic plane, and one complete spin is divided up into sixteen 22.5° azimuthal sectors labelled 0-15. The direction of the sun is typically in azimuthal sector 9 (Figure 2.5b).

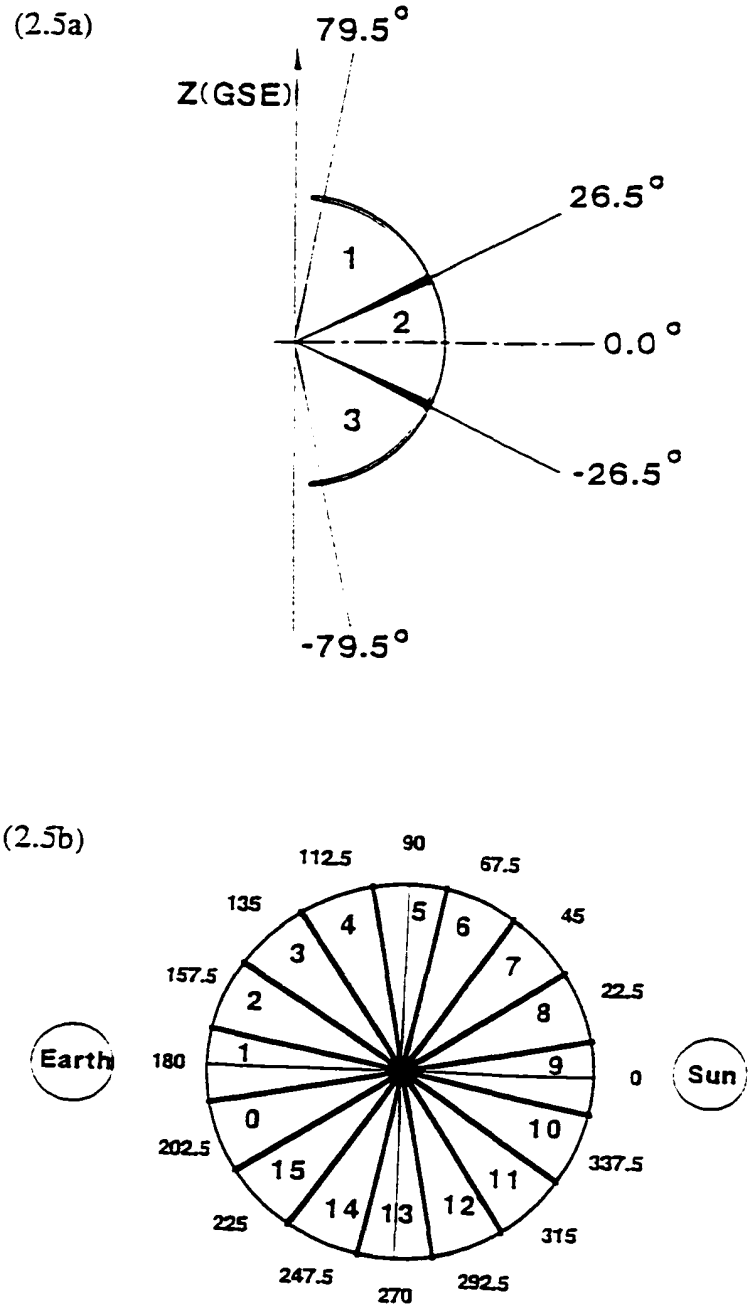

Figure 2.5. (a) STICS polar *look* directions for TOF telescopes 1, 2, and 3. (b) STICS *look* direction in the ecliptic plane consists of sixteen azimuthal sectors (0-15). The view from the north looking downwards shows the spacecraft spinning clockwise. The look angle for the center of each sector is indicated in degrees. Solar wind ions are typically detected in sector 9 of telescope 2.

2.3.2 Angular Apertures

Polar (α) Direction: The nominal polar acceptance angle is 159 ($\pm$79.5° from the ecliptic plane). However, certain angular ranges were blocked due to mechanical considerations in assembling the instrument (Figure 2.6). Because the carbon foil used in the time-of-flight chamber is very thin, it had to be mounted in four sections for each telescope leading to three blocked angular ranges per telescope. The effective polar acceptance angle, $\Delta\alpha$, for the entrance aperture of each telescope is about 44.44° with telescope 1, 2, and 3 looking above, in, and below the ecliptic, respectively.

Azimuthal (ß) Direction: Figure 2.7 shows a cross-sectional view of the entrance aperture. Only the particles entering from +2.6° to -2.2° of the center line are focused to the center field of view (FOV) where they are then channeled into the deflection system.

The effective area of the physical opening, through which particles can be detected, has an azimuthal acceptance angle, $\Delta ß = 4.8°$ and radius, $r = 3.594$ cm. Therefore, the area of the entrance aperture, A_e, for each telescope is as follows:

$$A_e = r^2 \Delta\alpha \Delta ß$$

$$A_{e1} = A_{e2} = A_{e3} = 0.84 \text{ cm}^2 \qquad (2.2)$$

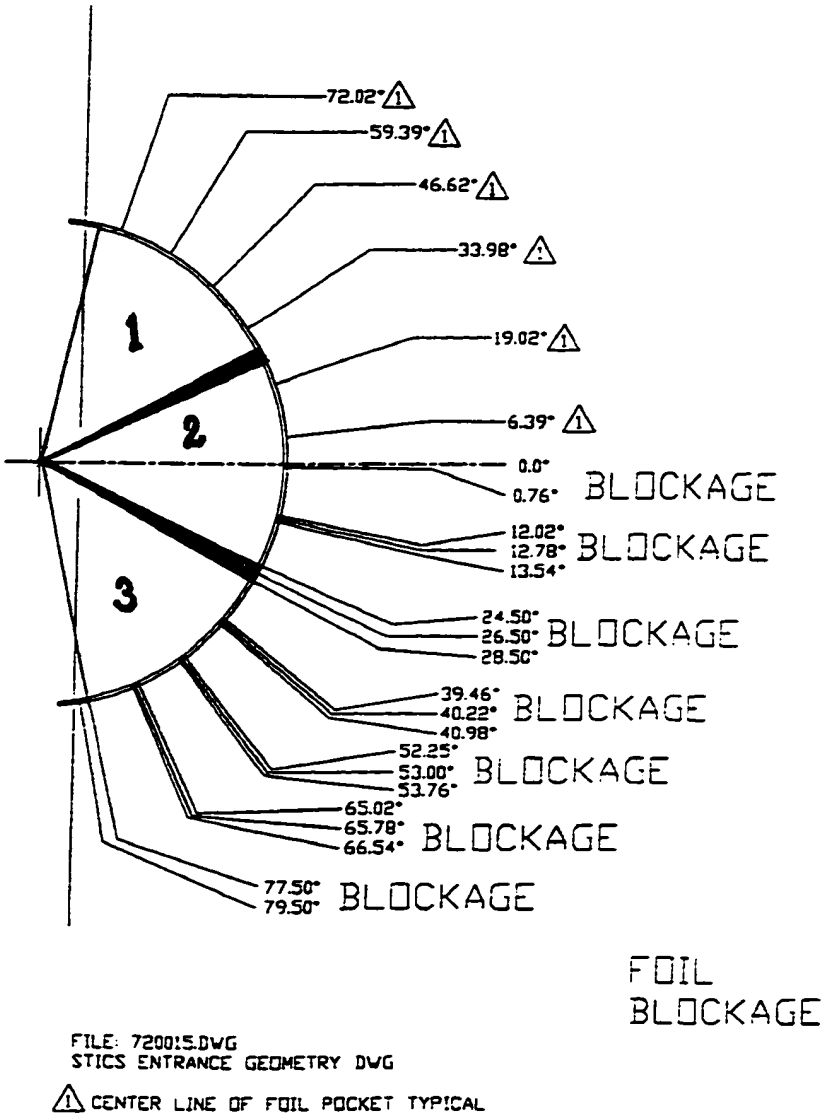

Figure 2.6. Physical blockages result in a reduced polar acceptance angle for telescopes 1, 2 and 3.

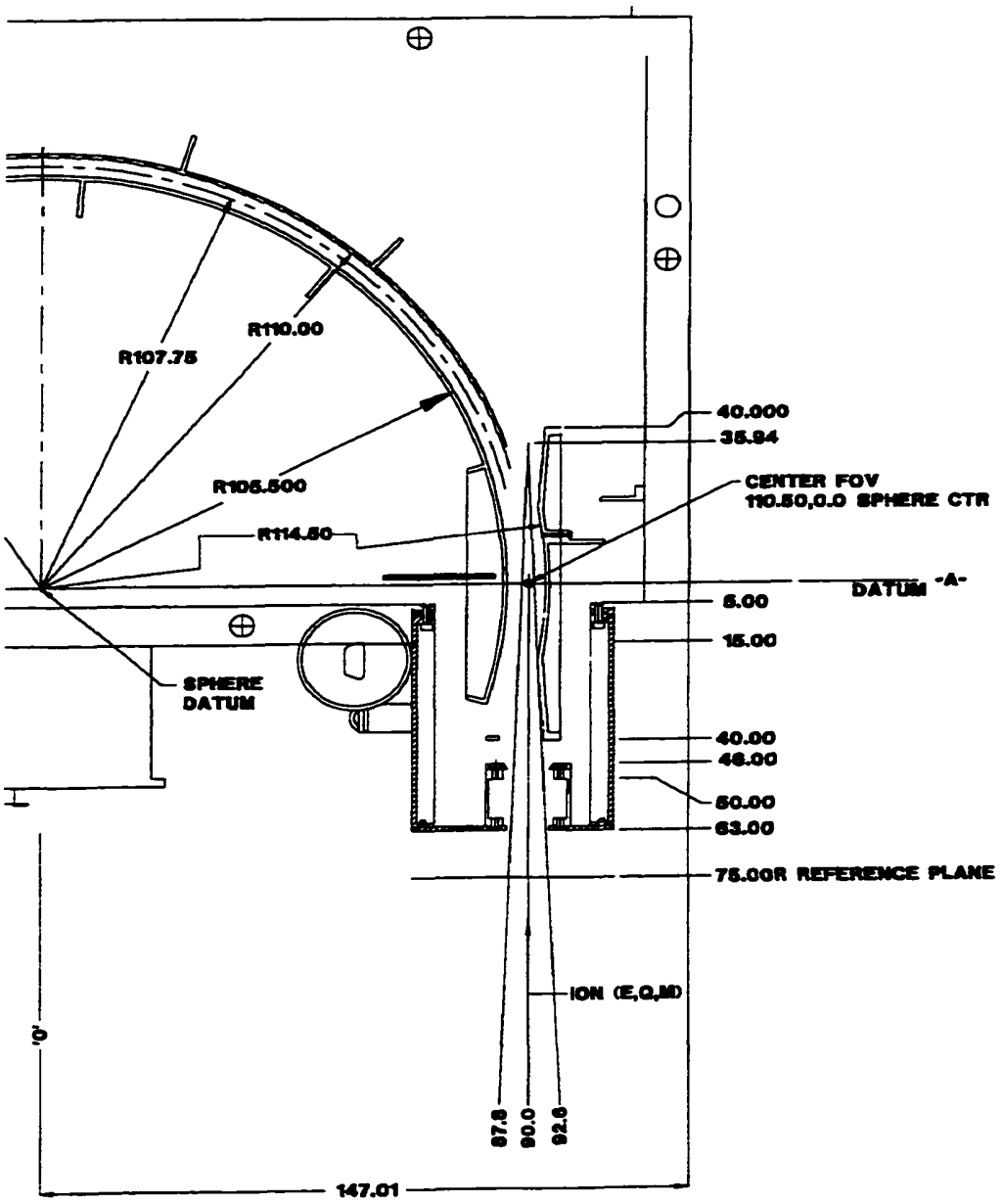

Figure 2.7. A cross-sectional view of the entrance aperture showing the azimuthal acceptance angle.

2.4 Telemetry

The spacecraft transmits data back to Earth at two different telemetry rates: high bit rate (HBR) and low bit rate (LBR). In high bit rate the STICS telemetry allocation is 720 bits per second and in low bit rate, 360 bits per second . When WIND is in the near Earth region, the telemetry is sent at high bit rate. As the spacecraft moves away from Earth in interplanetary space, the data are transmitted at low bit rate. The telemetry received from the spacecraft consists of Housekeeping (HK) Data, Direct Sensor Rates, Science Rates, and Pulse Height Analyzed (PHA) Words. In high bit rate, the STICS deflection voltage is held constant for one spin (~3 secs) and in low bit rate, for two spins (~6 secs) . All STICS counting rates are given in terms of counts at each voltage step. A detailed description of the STICS telemetry can be found in the DPU document (Gerlach and Wiewesiek, 1994).

2.4.1 Housekeeping Data

This data basically contains information on the operating status of the instrument. For example, the ON/OFF status of the power supplies, the deflection voltage step number, the SSD threshold levels, the MCP levels, compression codes, trigger modes, etc., are all part of the housekeeping data. The current and voltage of all power supplies can also be found in the HK data.

2.4.2 Direct Sensor Rates

These rates are read from the different counters in the time-of-flight section for each telescope, e.g., the front SEDA rates (FSR's), the rear SEDA rates (RSR's), the solid-state detector rates (SSD's), the double coincidence rates (DCR's), the triple coincidence rates (TCR's), etc. The FSR is the most sensitive rate, and it is our best indicator for when a particle event has occurred.

2.4.3 Science Rates

The M-M/Q space is divided-up into three different regions, Range 0, 1 and 2. The Basic Rates (BR0, BR1 and BR2) count the total number of particles in each Range (R0, R1 and R2, respectively). Within these regions there are pre-defined boxes (see Figure 2.8) representing charge states of different elements, e.g., H^+, He^+, He^{2+}, O^+, O^{6+}, O^{7+}, Fe^{8+}, Fe^{9+}, Fe^{10+}, etc. The He^{2+} rate is the High-resolution Matrix Rate (HMR) which contains full directional information (6 polar sectors x 16 equatorial sectors). The medium-resolution Sectored Matrix Rate (SMR) contains only partial directional information (3 polar x 8 equatorial sectors). The H^+ rate is the SMR. There are twenty Omnidirectional Matrix Rates (OMR0-19) which are accumulated over all polar and equatorial sectors and contain no directional information. Table 2.2 gives a list of all the science rates along with their boundaries in M-M/Q space as currently defined in the DPU. The H^+, He^+, and He^{2+} rates all include both triple coincidence and double coincidence data ("mass zero (mz)" events), whereas OMR1-19 contain only triple coincidence data. The rate boundaries are changeable by command.

2.4.4 PHA Words

The analog electronics generates an Event Word for every detected particle and sends it to the DPU. The Event Word contains the measured time-of-flight, measured energy and detector/telescope identification. All Event Words are classified by the DPU for placement into Basic Rate bins and possible placement into other Science Rate bins. In addition, a limited number of Event Words are selected by the DPU for formatting into the STICS PHA Words. Each PHA word consists of the STOP MCP identification, START and Range identification, the measured energy channel number, azimuthal sector number, SSD number, and time-of-flight channel number. The

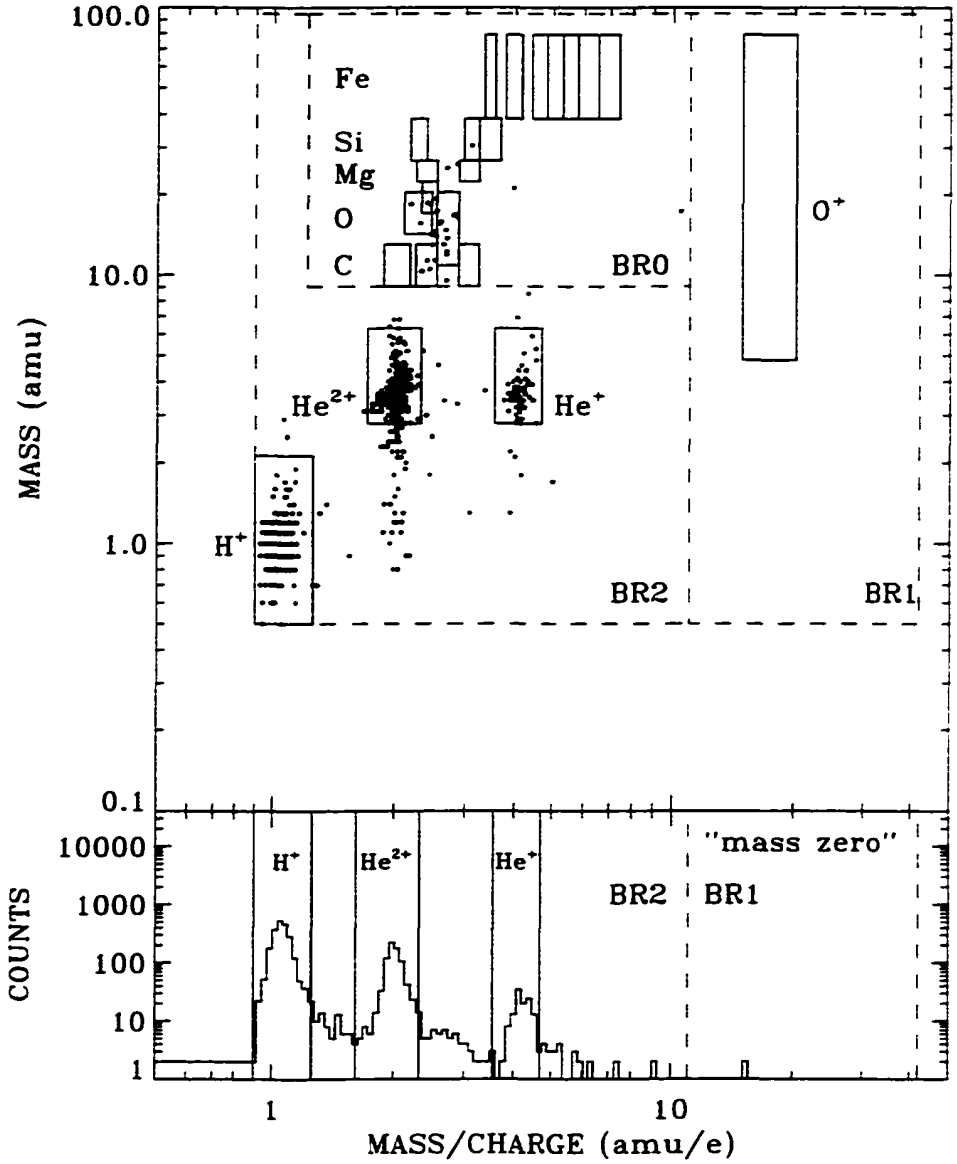

Figure 2.8. Raw PHA data plotted in M-M/Q space for April 7, 1995 15:00-20:00 UT from the out-of-ecliptic telescopes (1 and 3) when WIND was in interplanetary space ~223 R_e upstream of the Earth. The Basic Rate and Matrix Rate boundaries are shown. The horizontal "stripes" in the H^+ box appears because the mass values are rounded-off to 1 decimal place. The size of the boxes give an indication of the allowable spread in the data.

Table 2.2 Default Matrix Rate definitions in M-M/Q space as defined in the DPU.

Rate Designation	Species	Mass Range (amu)	M/Q range (amu/e)
HMR	*He^{2+}	2.79-6.30	1.71-2.32
		mz†	1.61-2.32
SMR	H^{+}	mz† - 2.13	0.90-1.26
OMR0	*He^{+}	2.79-6.30, mz	3.55-4.67
OMR1	C^{6+}	9.04-12.99	1.87-2.18
OMR2	C^{5+}	9.04-12.99	2.25-2.54
OMR3	C^{4+}	9.04-12.99	2.87-3.24
OMR4	O^{7+}	14.21-20.41	2.11-2.46
OMR5	O^{6+}	10.83-20.41	2.54-2.87
OMR6	O^{+}	4.80-79.30	14.89-20.20
OMR7	Ne^{8+}	17.03-22.34	2.32-2.54
OMR8	Mg^{10+}	22.34-26.77	2.25-2.54
OMR9	Mg^{8+}	22.34-26.77	2.87-3.24
OMR10	Si^{12+}	26.77-38.44	2.18-2.39
OMR11	Si^{9+}	26.77-38.44	2.96-3.24
OMR12	Si^{8+}	26.77-38.44	3.24-3.66
OMR13	Fe^{16+}	38.45-79.28	3.34-3.55
OMR14	Fe^{14+}	38.45-79.28	3.77-4.14
OMR15	Fe^{12+}	38.45-79.28	4.40-4.82
OMR16	Fe^{11+}	38.45-79.28	4.82-5.28
OMR17	Fe^{10+}	38.45-79.28	5.28-5.78
OMR18	Fe^{9+}	38.45-79.28	5.78-6.53
OMR19	Fe^{8+}	38.45-79.28	6.53-7.38

*See Table 3.2 for revised helium M and M/Q boundaries in ground-based PHA analysis. †Mass zero (mz) or double coincidence events.

energy and time information given in the PHA word is the same as that in the Event word, except that the energy is compressed to 9 bits in the PHA word.

The Start anodes are used to define the incident polar direction of each particle (see section 2.3.1). There are 10 START states which identify the anode that fired. States 1-6 indicate which single front anode fired. State 7 indicate a simultaneous firing by anodes 1 and 2, state 8 simultaneous firing by anodes 3 and 4, and state 9 simultaneous firing by anodes 5 and 6. State 0 means that no anode fired. The START state and Range of a particle are combined into one number (ID) using the following relation:

$$ID = START*3 + Range \qquad (2.3)$$

where START = 0-9 and Range = 0-2. This gives the following Truth Table (2.3) for ID:

Table 2.3. Truth table for the ID states of the the combined START and Range values stored in the PHA words. States 30 and 31 are undefined.

Range	START									
	0	**1**	**2**	**3**	**4**	**5**	**6**	**7**	**8**	**9**
0	0	3	6	9	12	15	18	21	24	27
1	1	4	7	10	13	16	19	22	25	28
2	2	5	8	11	14	17	20	23	26	29

Because of the limited telemetry, the DPU cannot send every Event Word down as a PHA word. Hence the Event Words are prioritized and a limited number that meet pre-defined criteria are incorporated into the telemetry. STICS is allotted 22 PHA words for the duration of each voltage step (one spin in high bit rate, and two spins in low bit rate). If there are 22 particles or fewer detected during one voltage step, then all the corresponding PHA words are transmitted by the DPU to the spacecraft

telemetry. In this case unused STICS PHA slots are assigned to SWICS or MASS. otherwise the slots are filled with zeros. If there are more than 22 particles detected during one voltage step. then an attempt is made to sample all azimuthal directions and all ranges with Range 0 having highest priority and Range 2, lowest. There are 8 PHA slots for Range 0, and 7 each for Ranges 1 and 2. Any spare slots in any Range are allotted according to range priority.

2.5 Summary

The STICS instrument uses electrostatic deflection. followed by a time-of-flight measurement, and an energy measurement with a solid state detector to determine the mass. mass-per-charge, and energy of ions from H - Fe in the energy-per-charge range of 6.2 - 223.1 keV/e. In flight, the electrostatic deflection voltage is stepped in 30 logarithmically spaced steps covering 6.2-198.8 keV/e. The arrival directions of the ions can also be obtained. There are six polar sectors covering ±79.5° relative to the ecliptic plane, and sixteen azimuthal sectors covering 360°.

The STICS telemetry consists of Housekeeping Data, Direct Sensor Rates. Science Rates, and Pulse Height Analyzed (PHA) Words. The Housekeeping Data contain information on the operating status of the instrument, and the Direct Sensor Rates are read from the different counters in the time-of-flight section. Each Science Rate gives the number of counts falling within a specified range of mass and mass-per-charge values representing a given ion (H^+, He^{2+}, He^+, O^{6+}, etc.) or range of ions. All STICS counting rates are given in terms of counts per deflection voltage step. The PHA words contain the measured energy, measured flight time. and directional information for each detected ion. STICS is allotted 22 PHA words per voltage step.

CHAPTER 3: DATA ANALYSIS

In this chapter, the algorithms used in extracting the mass and mass-per-charge information from the STICS science telemetry data are first given in Section 3.1. The number of measured counts for a given ion at a given energy-per-charge channel can be converted to differential flux or distribution function using the instrument response function in order to get an energy spectrum or velocity distribution, respectively. The different factors that make-up the instrument response function are explained in Section 3.2. The method used to bin the data and the equations used to calculate the differential flux and distribution function are discussed in Section 3.3 and 3.4. A summary of the information is presented in the last section.

3.1 Data Extraction

The STICS data basically consists of Matrix Rates and pulse height analyzed (PHA) data for each deflection voltage step (DVS) or equivalently each energy-per-charge (E/Q) channel, (see section 2.4). Only two of the Matrix Rates (H^+ and He^{2+}) contain directional information, whereas the rates for the other ions are averaged over all directions by the data processing unit (DPU). The Matrix Rate for each ion keeps track of all the counts detected by STICS that fall into pre-defined boxes in M-M/Q space. On the other hand, the PHA data have full information for each detected particle: the energy channel number, the time-of-flight channel number, both azimuthal and polar directions. However, the number of PHA words may be less than the number of detected particles. Because of the limited telemetry, STICS is only allowed 22 PHA words per DVS. When the number of particles exceeds 22 for any DVS, the data are normalized by the Basic Rates to take this into account (see Section 3.2.2).

The PHA data is preferred over the Matrix Rates when studying STICS data in-depth because they contain all the information for each particle, and they are less

susceptible to being corrupted during transmission from the spacecraft to the Earth (telemetry hits). With the PHA data, the ion identification is not limited to the pre-defined Matrix Rate M-M/Q boxes as defined in the DPU. New box definitions may be created and old ones redefined to classify ions as needed. More thorough checks can be made on the PHA data to ensure that they are not corrupted.

Each STICS PHA word is stored in 4 bytes (32 bits) of telemetry. The time-of-flight channel number, the solid-state detector (SSD) identification, the azimuthal sector, the compressed energy channel number, the Start anode identification and Range combined into ID (see equation 2.3 and Table 2.2), and the Stop MCP identification. The Start anode and Range information can be separated using the following equation:

$$\begin{aligned} &START = ID/3 \qquad \{\text{integer division}\} \\ &Range = ID - 3*START \end{aligned} \tag{3.1}$$

The time-of-flight channel number, T_{ch}, is converted to time, τ, in nanosecond (ns) using the following relation as determined from pulser calibrations (see Appendix A.3):

$$\tau\ \{ns\} = [T_{ch} - 44]/2.372530695 \tag{3.2}$$

The compressed energy channel number, E_c, is first decompressed to E_d using

$$\begin{aligned} &E_d = E_c && \text{for } E_c < 256 \\ &E_d = 2E_c - 256 && \text{for } 256 \le E_c < 384 \\ &E_d = 4E_c - 1024 && \text{for } 384 \le E_c < 1024 \end{aligned} \tag{3.3}$$

Then E_d is converted to the measured energy, E_{meas}, in units of kiloelectronvolts (keV) using the following equation:

$$E_{meas}\ \{keV\} = [E_d + 6]/0.37654782 \tag{3.4}$$

The energy-per-charge can be determined using:

$$E/Q\ \{keV/e\} = 6.190722 * (1.1225857)^{DVS} \tag{3.5}$$

The mass-per-charge and mass are calculated using the following algorithms

$$M/Q\ \{amu/e\} = 1.9159E\text{-}05 * [E/Q - C_1] * \tau^2 \tag{3.6}$$

where $C_1 = 1.5$ for $M/Q < 11$ and $C_1 = 2.5$ for $M/Q \geq 11$, and

$$\ln(M) = A_1 + A_2*X + A_3*Y + A_4*XY + A_5*X^2 + A_6*Y^3 \quad (3.7)$$

where $A_1 = 2.69575$, $A_2 = -0.843766$, $A_3 = -2.38009$, $A_4 = 0.385641$, $A_5 = 0.0513127$, $A_6 = 0.0690096$, $X = \ln(E_{meas})$, and $Y = \ln(\tau)$. If $E_{meas} < E_{min} = 21$ keV, then $M = 0$, commonly called "mass zero" events since the M/Q can still be determined from the time of flight.

The M-M/Q space is subdivided into 58 mass bins (N_m) and 126 mass-per-charge bins (N_q) that are logarithmically spaced between the minimum and maximum values. The boundaries of the N_m bins are defined by the following relations:

Mass Range {amu} = 0.5 - 95.0

N_m Range = 1 - 58

$k_m = (95.0/0.5)^{1/58}$

$$M \{\text{lower bound of } N_m \text{ in amu}\} = 0.5 * k_m^{(Nm - 1)} \quad (3.8)$$

For the "mass zero" events, $N_m = 0$. Similarly, the boundaries of the N_q bins are defined as follows:

Mass/Charge Range {amu/e} = 0.9 - 42.0

N_q Range = 1 - 126

$k_q = (42.0/0.9)^{1/126}$

$$M/Q \{\text{lower bound of } N_q \text{ in amu/e}\} = 0.9 * k_q^{(Nq - 1)} \quad (3.9)$$

Classifying the ions into these small N_m-N_q bins is extremely useful when studying charge states. For example, for ^{56}Fe ions at energy 78 keV, charge state 9+ will enter during DVS 3, whereas charge state 10+ will enter during DVS 2.

3.2 Instrument Response Function

After identifying the element and its charge state from the PHA data, further analysis may involve calculating the distribution function, f(v), over a given time period. In order to do so, the instrument response function must be applied to the accumulated raw counts. The instrument response functions includes the Duty Cycle and Deadtime Correction, the Basic Rate Normalization to the PHA data, the Box Efficiency in M-M/Q space, Geometric Factor, the time-of-flight telescopes efficiencies, and the Energy Passbands.

3.2.1 Duty Cycle and Deadtime Corrections

Duty Cycle (or Accumulation Deadtime): Nominally, the spacecraft spin rate is one rotation every 3 seconds. Since each spin is divided into sixteen azimuthal sectors, the accumulation time for each sector is 187.5 ms. At the beginning of each of sectors 1-15, there is a deadtime in the DPU of 12 ms during which no STICS data are accumulated. This time is allotted to the DPU for various functions, including reading the different counters and classifying the data for each sector. The deadtime for sector 0 is 100 ms in order to avoid accumulating data while the deflection voltage step is changing at the beginning of this sector, a transition which takes about 50 ms. Even when the deflection voltage step is held constant for two consecutive spins (during low bit rate), sector 0 maintains the 100 ms deadtime for convenience in the DPU programming. The overall deadtime is 0.28 sec for each spin. The deadtime correction is a factor (Table 3.1) by which the accumulated counts for a given sector are multiplied in order to compensate for the time the instrument is not collecting data. For example, the correction factor for sector 0 is given by 187.5/(187.5 - 100) = 2.143.

Table 3.1. Accumulation deadtime corrections factors.

	Deadtime Correction
Sector 0	2.143
Sector 1,...,15	1.068
Entire Spin	1.103

Electronic Deadtime Correction: The Electronic Deadtime can be at two levels: sensor electronics and DPU classification. At the sensor level, the MCP can saturate if the incident flux is too high. A cloud of electrons from more than one particle hits the MCP, but the MCP cannot tell that the cloud came from several particles, so it counts it as "one" event. The time signal uses "fast electronics", but there is an "analysis window (~409 ns)", and if another particle comes in during that window, it will not get measured for a PHA event. The energy pulse height measurement is slowed-up by the analysis time (~20 μs) of the current in the SSD. If another particle enters while the energy from the first is being measured, it may not be detected as a separate event. These effects occur at the sensor level and would affect the Direct Sensor Rates.

At the DPU level, the PHA event words are classified by the DPU using fast look-up table techniques to establish a relation between the energy and time-of-flight. When the incident flux of particles becomes too great, not all the particles are processed. The DPU look-up time is not relevant to the Direct Sensor Rates, only to the Science Rates (Basic Rates and Matrix Rates). Therefore, the Science Rates begin to saturate before the Direct Sensor Rates. When a counting rate (Direct Sensor or Science rate) begins to saturate, there is no longer a linear relation between the incident flux and the rate (see Section A.2). For the first three years of the WIND mission, the particle intensities encountered both in the magnetosphere and in interplanetary were not large enough to make the electronic deadtime significant.

3.2.2 Basic Rate Normalization

As previously discussed (section 2.4.4), not all the PHA Words may have been transmitted because of the limited telemetry. To get around this problem, the Basic Rates are used for normalization. There are three Basic Rates (BR0, BR1, and BR2) that count the total number of particles in each of the respective Ranges (Range 0, 1, and 2). For STICS, each Basic Rate is sectored into eight bins. Bin 1 counts all the particles accumulated in azimuthal sectors 0 and 1 for all three telescopes combined, bin 2 counts all the particles accumulated in azimuthal sectors 2 and 3 for all three telescopes combined, bin 3 counts all the particles in azimuthal sectors 4 and 5 for all three telescopes, etc. The Range of each particle is contained in the PHA word. All the PHA words for a given spin can be grouped according to their assigned Ranges into PHA0, PHA1, and PHA2 over the same sectors and all telescopes combined as the corresponding Basic Rate sectored bin. Each PHA group is a selected subset of the events counted by the Basic Rates. The Basic Rate Normalization is performed by multiplying the number of measured counts in a given sector by the corresponding weighting factor $[BRi_{norm} = BRi/PHAi]_{sector}$ where i = 0, 1, or 2.

When the spacecraft is in interplanetary space upstream of the Earth's bow shock, the number of particles detected by the instrument is typically less than 22 for each DVS. However, in the near Earth region (magnetosheath and magnetosphere), the number is usually greater than 22 making the Basic Rate normalization of the PHA data more important in that region.

3.2.3 Box Efficiency

Sometimes all the counts for a given ion may not fall into its pre-defined box in M-M/Q space (see Figure 3.1). Or, boxes that are close together, e.g., the Fe charge state bins, may have counts spilling over into neighboring boxes. The Box Efficiency must be determined and used to correct for the number of measured counts. The ions

examined in this dissertation are H^+, He^{2+}, and He^+. Upon examining flight data, about 8% of the H^+ raw counts fall outside its box causing its efficiency to be ~92%.

The He^+ and He^{2+} boxes were increased because the original ones missed about 10% of the counts. The original He boxes, which are still used by the DPU, do a good job in that they are centered on the two peaks, and the bulk of the counts for both the "mass zero" and triple coincidence events are obtained. However, they clearly do not contain all the He triple coincidence events, as can be seen from the M-M/Q plot (Figure 3.1). The new He boxes, shown as dashed lines drawn around the old ones, are about 98% efficient.

When the solar wind speed rises above 600 km/s during high speed streams, the tails of the solar wind ion spectra are measured by the lower energy-per-charge steps mainly as "mass zero" events in telescope 2 (middle). The mass-per-charge range of the He^{2+} box is reduced for DVS 0-8 to decrease the number of heavy ions spilling into this box (see Table 3.2 and Figure 3.1). The fraction of energy lost by the ions in passing through the carbon foil at the entrance of the time-of-flight is greater for the lower energy ions resulting in lower mass and mass-per-charge resolution. This means that the box efficiency for the lower energy ions would be slightly less.

Table 3.2. Box definition and efficiency for H^+, He^+ and He^{2+}.

Ion	Mass Range (amu)	Mass/Charge Range (amu/e)	Box Efficiency
H^+	mz-2.13	0.90-1.26	0.90 for DVS < 15 0.99 for DVS ≥ 15
He^+	1.77-6.89#, mz	3.55-4.67	0.98
He^{+2}	1.77-6.89# mz	1.71-2.32 1.61-2.32 (1.61-2.11)*	0.98

*Only used for events measured by telescope 2 DVS 0-8 during high-speed streams.
#Values different from those used by the on board DPU given in Table 2.3.

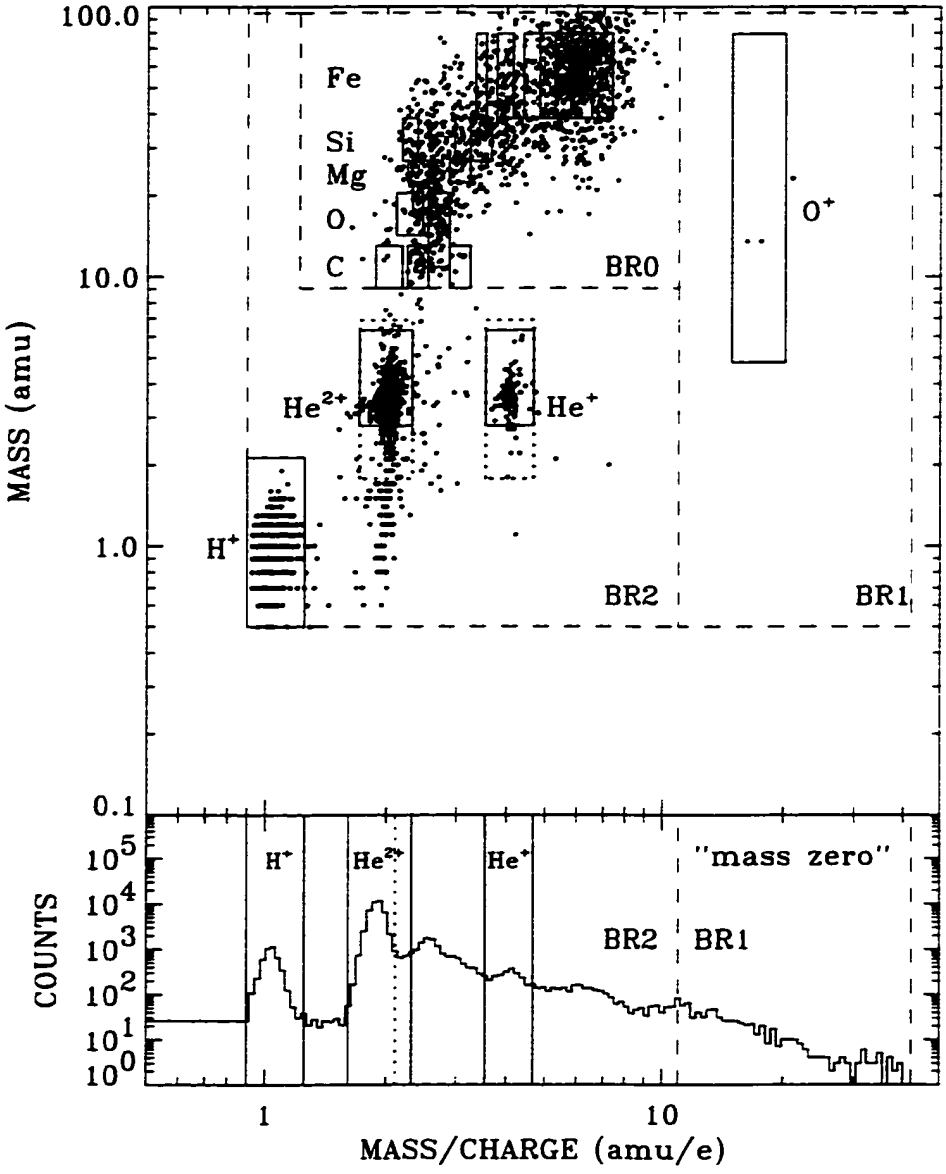

Figure 3.1. A plot of the M-M/Q PHA data is shown for the period May 30, 1995, 10:00 - 22:30 UT during a CIR event. The new triple coincidence He^{+} and He^{2+} boxes are indicated by dashed lines around the old boxes. The dashed lines in the "mass zero" He^{2+} box shows the reduced box used for DVS 0-8 when measuring solar wind ions with telescope 2.

3.2.4 Geometric Factor

The Geometric Factor relates the instrument's counting rate to the flux of the incident radiation and is solely dependent on the dimensions of the aperture and the sensitive area of the detector system. Consider the case of an ideal telescope, whose efficiency for detecting particles is 100%, measuring an isotropic particle distribution with absolute intensity I (units of counts sec^{-1} cm^{-2} sr^{-1}). The counting rate, C with units of counts sec^{-1}, is given by

$$C = \int_{\Omega A}\int (\cos\theta * dA)\, d\Omega\, I$$

Since I is isotropic, then

$$C = Ig$$

and

$$g = \int_{\Omega A}\int (\cos\theta * dA)\, d\Omega \qquad (3.10)$$

where g is the isotropic Geometric Factor, θ is the angle between the incident radiation and the normal to the element of area dA, $d\Omega$ is the element of solid angle, and A represents the domain of dA (Gloeckler, 1970). If the area, A, of the detection surface is normal to the incident flux, then equation (3.10) becomes

$$g = A*\Delta\Omega \qquad (3.11)$$

where $\Delta\Omega$ is the effective solid angle subtended by the aperture.

For a parallel beam of particles incident perpendicular to the aperture (e.g., the solar wind), there is no angular dependence, and in this case the Geometric Factor, G, is simply given by

$$G = A \qquad (3.12)$$

With the STICS sensor, this area is the effective area of the carbon foil, A_C, through which the particles pass.

From the pre-flight calibration data and inflight cross-calibrations (Appendix A.4) with WIND-SMS-MASS at the lower end of the STICS energy range and with WIND-EPACT-STEP at the higher end, the geometric factors for each telescope are as follows:

Table 3.3. Geometric factors determined from pre-flight and inflight calibrations.

Telescope	Parallel Beam Geometric Factor, G_i, {cm^2}	Isotropic Geometric Factor, g_i, {cm^2 sr}
1	0.72 ± 0.18	0.031 ± 0.002
2	0.68 ± 0.18	0.029 ± 0.002
3	0.74 ± 0.18	0.029 ± 0.002

3.2.5 TOF Telescope Efficiencies

As particles travel through the instrument, some get lost in the deflection system, some do not pass through the carbon foil at the entrance of the time-of-flight (TOF) telescope, and some are not detected when the reach the end of the TOF chamber. The TOF telescope efficiencies are given in two parts, the Start (η_1) and Stop (η_2) efficiencies. They are defined as follows:

$$\eta_1 = \frac{FSR}{CFR} = \frac{DCR}{RSR} \qquad (3.13)$$

$$\eta_{2a} = \frac{DCR}{FSR} \qquad \eta_{2b} = \frac{TCR}{FSR} \qquad (3.14)$$

where the Carbon Foil Rate (CFR) is the rate at which the particles pass through the carbon foil, FSR is the Front SEDA Rate (where SEDA stands for secondary electron

detector assembly as explained in Section 2.3.1). RSR is the Rear SEDA Rate. DCR is the Double Coincidence (time signal obtained) Rate, and TCR is the Triple Coincidence (both time and energy measurements made) Rate. There is no direct sensor reading for CFR so the Start efficiency will be determined by DCR/RSR. Since triple coincidence (mass and mass/charge measured) results in more accurate identification of particles, TCR/FSR would be used for the Stop efficiency. But in the case when there is no energy measurement, i.e., only DCR, then the DCR/FSR would be used. The DCR/FSR Stop Efficiencies are used for H^+, He^{2+}, and He^+ because all three ion boxes include the "mass zero" events. Figure 3.2 shows the smoothed TOF efficiencies curves for the calibrated ions (see Appendix A.2.4).

3.2.6 Energy Passband ($\Delta E/Q$)

When the deflection voltage is at a given value, the spherical deflection system will allow only those particles with a specific E/Q value to enter the instrument. However, there is some allowable spread in these E/Q values. From calibration data (see Appendix A.2.3), the average E/Q passband, $\frac{\Delta(E/Q)}{E/Q}$, was found to be 1.9% (FWHM) of the central energy, which is about 2.5 times less than the design goal of 5%.

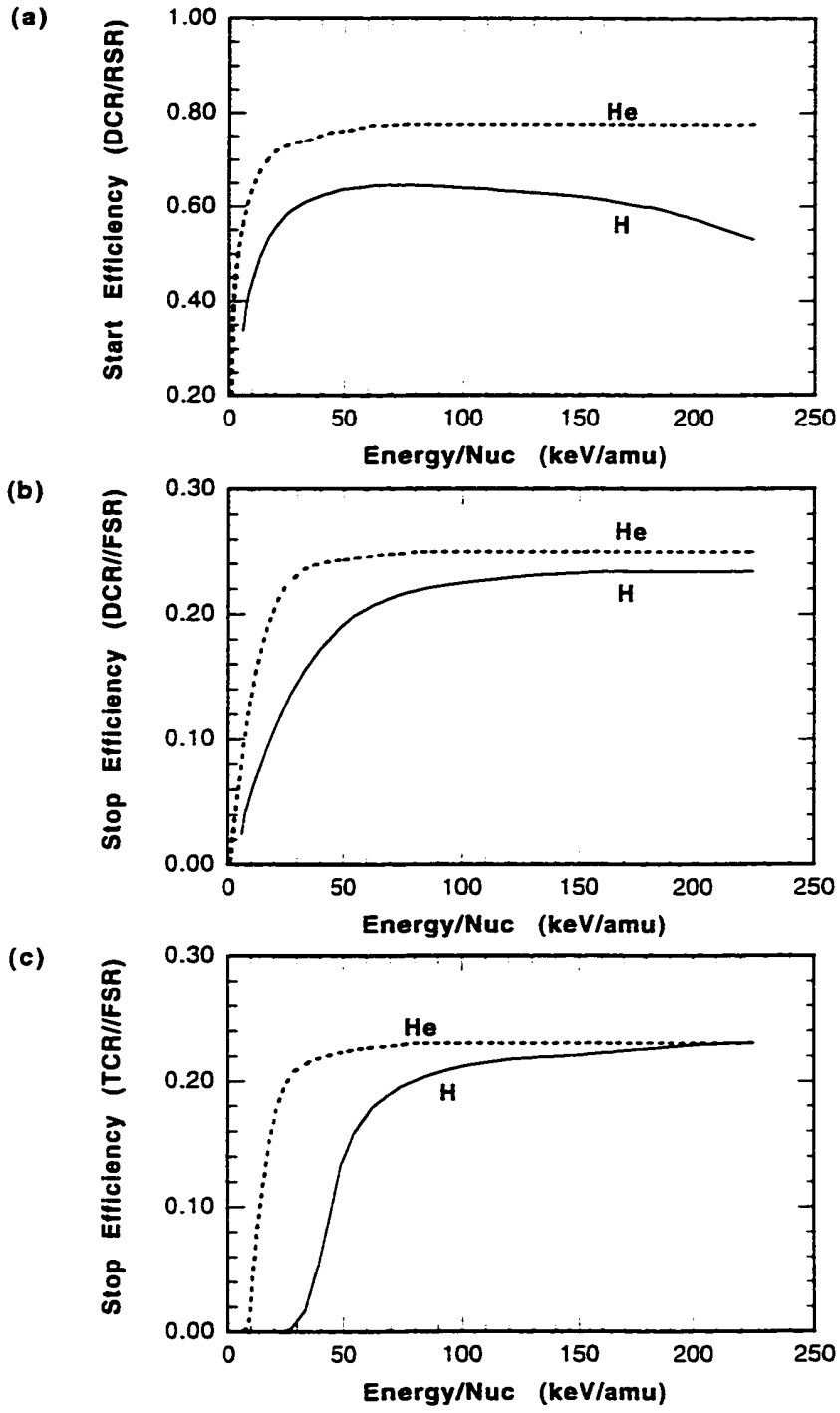

Figure 3.2. Smoothed H and He TOF efficiency curves.

3.3 Binning the Data

The STICS instrument selects ions by energy-per-charge (E/Q) using electrostatic deflection. There are 32 deflection voltage steps (DVS 0-31) that are logarithmically spaced from 6.19-223.12 keV/e with a passband of 1.9% (FWHM) of the mean E/Q value (see Table 3.4). Therefore, the data are naturally binned by E/Q. After identifying the mass and charge of the ions, the bins can be converted to E/M using

$$E/M\ \{keV/amu\} = E/Q\ *\ Q/M \tag{3.15}$$

Since the lower end of the STICS E/Q range may include the tail of the solar wind ion spectra, it is sometimes necessary to bin the data by V_{ion}/V_{sw} where V_{ion} is the ion speed and V_{sw} the solar wind bulk speed. The normalized velocity bins are also logarithmically spaced such that there is a one-to-one mapping from E/Q to V_{ion}/V_{sw}. The velocity bin number, VBN, for each ion at each DVS is given by

$$V_{ion}\ \{km/s\} = 437.74\sqrt{E/M} \tag{3.16}$$

$$VBN = \text{integer}\left[\frac{\log_{10}(V_{ion}/V_{sw})}{VBS}\right] \tag{3.17}$$

where VBS = 0.025 is the logarithmic size of the bins.

3.4 Differential Flux and Distribution Function

If *dN* is the number of particles passing through an area element *dA* at location **r** made over the time interval *t* and *t* + *dt* with energy between *E* and *E* + *dE* whose direction of incidence is within the solid angle cone $d\Omega$, then the differential flux, *dJ/dE*, is defined by

$$dN = \frac{dJ}{dE} dA\ dE\ d\Omega\ dt \tag{3.18}$$

The distribution function, *f*, is defined as the number of particles, *dN*, in an infinitesimal coordinate-space volume (***r*** to ***r*** + ***dr***) and an infinitesimal velocity-space volume (***v*** to ***v*** + ***dv***) at a time *t*, i.e.,

$$f = \frac{dN}{d^3r\ d^3v} \tag{3.19}$$

Table 3.4. The corresponding energy-per-charge and passband for each deflection voltage step. The E/Q value is obtained from equation 3.5 and the passband (FWHM) is 0.019E/Q.

DVS	E/Q {keV/e}	ΔE/Q {keV/e}
0	6.19	0.12
1	6.95	0.14
2	7.80	0.16
3	8.76	0.18
4	9.83	0.20
5	11.04	0.22
6	12.39	0.25
7	13.91	0.28
8	15.61	0.31
9	17.53	0.35
10	19.68	0.39
11	22.09	0.44
12	24.80	0.50
13	27.84	0.56
14	31.25	0.62
15	35.08	0.70
16	39.38	0.79
17	44.21	0.88
18	49.62	0.99
19	55.71	1.11
20	62.54	1.25
21	70.20	1.40
22	78.81	1.58
23	88.47	1.77
24	99.31	1.99
25	111.49	2.23
26	125.16	2.50
27	140.50	2.81
28	157.72	3.15
29	177.05	3.54
30	198.76	3.98
31	223.12	4.46

From equations 3.18 and 3.19, and using $dv^3 = v^2\, dv\, d\Omega$ and $dr^3 = dt\, A\, v$, it follows that

$$\frac{dJ}{dE} dA\, dE\, d\Omega\, dt = f\, d^3r\, d^3v = f\, v^2\, dv\, d\Omega\, v\, dt\, dA$$

$$\Rightarrow \quad f = \frac{m^2}{2E}\frac{dJ}{dE} \qquad (3.20)$$

where we used $E = 0.5mv^2$ and $dE = mvdv$. Equation 3.20 is only true for non-relativistic particles, and is appropriate for the STICS energy range. The differential flux for STICS at any given energy E is

$$\frac{dJ}{dE} = \frac{\text{counts}}{g\, \Delta E\, \eta_1\, \eta_2\, \Delta t}\frac{DC \times BR_{norm}}{Box_{eff}} \qquad (3.21)$$

where g is the geometric factor, ΔE the energy passband, η_1 and η_2 the TOF efficiencies, Δt the accumulation time, DC the deadtime correction factor, BR_{norm} the Basic Rate Normalization, and Box_{eff} the box efficiency. The units of dJ/dE is $[cm^2\ s\ sr\ keV/amu]^{-1}$. With m measured in units of amu and E in keV along with the units of dJ/dE, the units of f can be converted to s^3/km^6 by multiplying the right hand side of equation 3.20 by 1.076, i.e.,

$$f\ \{s^3 / km^6\} = 1.076\ \frac{m^2}{2E}\frac{dJ}{dE} \qquad (3.22)$$

For an omni-directional distribution, the accumulation time, Δt, per spin is ~3.0 s and the and the isotropic geometric factor, g, is used. However, when measuring the uni-directional solar wind distribution, the parallel beam geometric factor, G, is used, and the time per spin when the instrument observes the parallel beam solar wind is given by

$$\Delta t\ \{s\} = \frac{3^o}{360^o} \times \text{Spin Period} \qquad (3.23)$$

where 3° is the effective azimuthal acceptance angle of the instrument (Appendix A.2.2), and the spacecraft spin period is ~3.0 s.

3.5 Summary

The PHA data are preferred over the Matrix Rates because the PHA words contain all the information on the detected particles, and more thorough checks can be made on the PHA data to ensure that the data are valid. The mass and mass-per-charge can be obtained from the measured time and energy channel numbers using equations 3.2 - 3.7. Since STICS uses electrostatic deflection, the incident ions are naturally selected and binned by their energy-per-charge. The energy-per-charge bins can be easily converted to energy-per-nucleon or, equivalently, velocity bins. The differential flux and distribution function of a given ion can be determined by applying the instrument response function (Table 3.5) to the measured counts as seen equations 3.21 and 3.22.

Table 3.5. Summary of instrument response function parameters.

Instrument Response Function	
Accumulation Deadtime: Sector 0 Sector 1,....15 Entire Spin	Correction Factor 2.143 1.068 1.103
Basic Rate Normalization	$[BRi_{norm} = BRi/PHAi]_{sector}$ Range, i, = 0, 1, or 2.
Box Efficiency	See Table 3.2
Energy-per-charge Passband Δ(E/Q) [FWHM]	$(0.019 \pm 0.001)E/Q$
Geometrical Factor: Isotropic: $g_{1,2,3}$ Parallel Beam, G_2	 0.031, 0.029, 0.029 $\pm$ 0.002 cm^2 sr 0.68 $\pm$ 0.18 cm^2
Time-of-flight Efficiencies: Error Limits: Start, η_1 Stop, η_2	See Tables A.2-3 for H, He $\pm$5%; $\pm$15%

12.2 *Gruesbeck*, (2013)

CHAPTER V

The Wind/STICS Data Processor

In this chapter, we will discuss the method we use to process data from the Suprathermal Ion Composition Spectrometer (STICS) onboard the Wind spacecraft. We first provide an overview of the satellite's mission, followed by details of the instrument itself. Then, we discuss the process we employ to calculate distribution functions for various ionic species from the particle counts observed by the instrument. Finally, we discuss a novel method we have begun to use to contend with the intermittent nature of the data.

5.1 The Wind Mission

The Wind spacecraft began operating nearly 20 years ago. It was launched on November 1, 1994 and started its data collection shortly thereafter. Wind is one of two missions that make up the Global Geospace Science (GGS) initiative, the United States contribution to the International Solar Terrestrial Physics (ISTP) program. Prior to this, many spacecraft missions worked independently to make observations with different individual focuses. Wind, combined with its sister spacecraft POLAR, were designed to investigate the solar-terrestrial system together, with a main emphasis on the flow of energy, mass, and momentum in the geospace environment (*Acuña et al.*, 1995). Geospace refers to both Earth's magnetosphere and the nearby helio-

spheric environment. To accomplish a thorough investigation of this environment, Wind observes the upstream region of the magnetosphere and bow shock while POLAR observes the Earth's magnetosphere via a polar orbit. In addition to these two spacecraft, the ISTP program includes contributions from a number of international space agencies. The European Space Agency (ESA) provided SOHO and CLUSTER, the Japanese Institute of Space and Astronautical Science (ISAS), now combined with the Japanese Aerospace Exploration Agency (JAXA), provided GEOTAIL, and the Russian Space Agency provided INTERBALL (*Acuña et al.*, 1995; *Chotoo*, 1998). These missions combined to provide a global view of the entire solar-terrestrial system, ranging from remote observations of the Sun, to *in situ* measurements in the deep tail of the Earth's magnetosphere.

Wind, as seen in Figure 5.1, is equipped with a series of instruments to investigate the magnetic field, waves and the plasma environment, including solar wind and energetic particles. Wind is a cylindrical spin-stabilized spacecraft, with its spin axis oriented perpendicular to the ecliptic plane. The spacecraft spins at an angular speed of twenty rotations per minute (*Harten and Clark*, 1995). Initially, Wind launched with a three year mission plan, composed of a series of orbits enabling observations both upstream and downstream of the Earth's bowshock. This was accomplished through a number of petal orbits, utilizing lunar swingbys (*Acuña et al.*, 1995). The initial mission orbits are shown in Figure 5.2.

In 1997, the spacecraft was originally planned to enter into a halo orbit about the 1st Langragian Point (L1), approximately 240 Earth radii upstream from the Earth, along the Sun-Earth line. Here it would begin to monitor the solar wind environment continuously. This plan was changed however, and Wind continued sampling the magnetosphere and upstream conditions with another series of petal orbits, taking the spacecraft through the magnetosheath and bow shock and eventually further downstream the magnetotail. Beginning in 2001 and lasting until late 2003, Wind

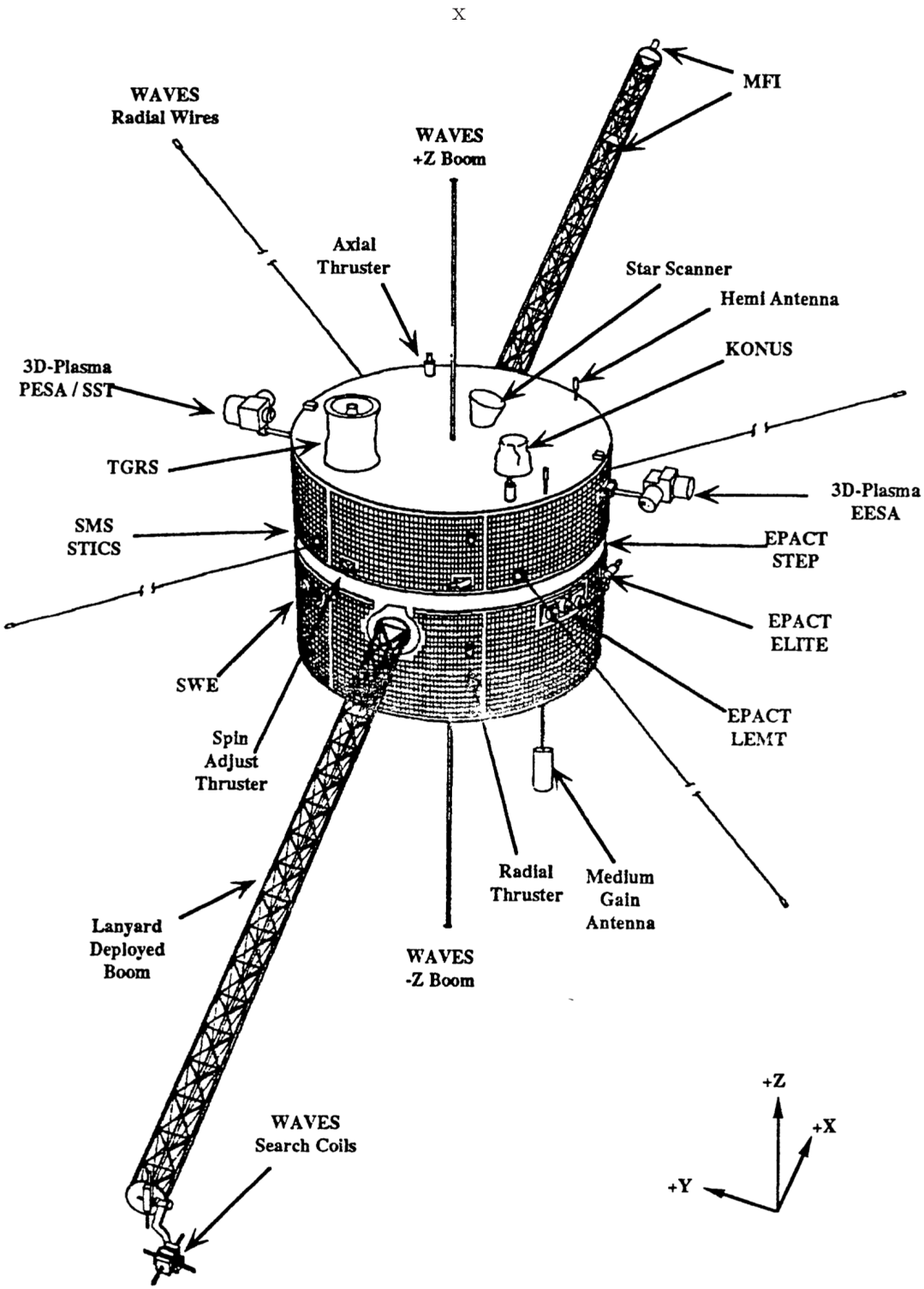

Figure 5.1: Illustration of the Wind spacecraft. The location of its instruments are indicated. Published in *Harten and Clark* (1995)

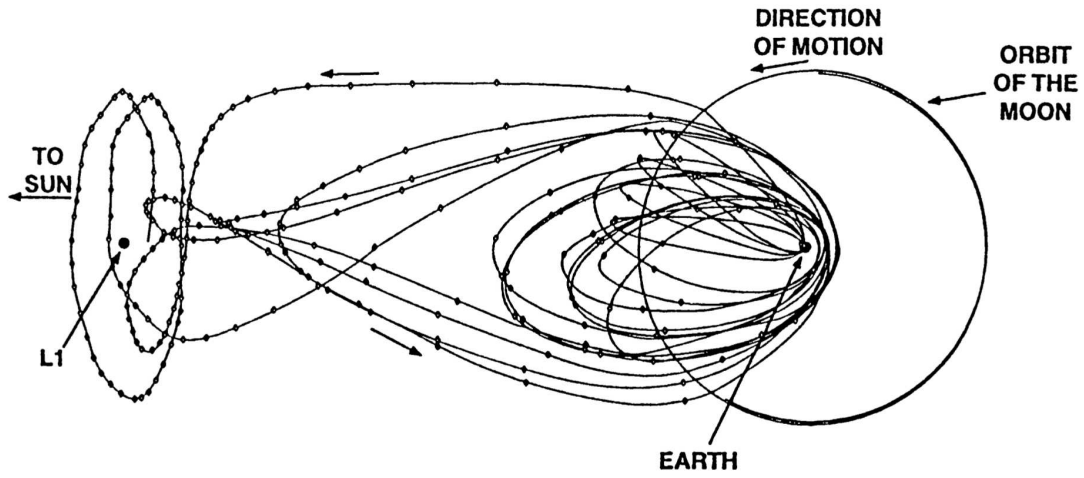

Figure 5.2: Illustration of the initially planned orbit for Wind. Shown, is the orbit projected on the GSE X-Y plane. Published in *Acuña et al.* (1995)

began prograde orbits, taking it far from the Earth along a direction perpendicular to the Sun-Earth axis. A diagram of this orbital phase is shown in Figure 5.3. In late 2003, the Wind spacecraft performed a deep magnetotail transit, traveling further than 200 Earth radii downstream in the magnetotail, before finally moving out to orbit L1 in mid 2004. Since then, Wind has continually monitored the solar wind upstream of the Earth.

As previously mentioned, for nearly 20 years the Wind spacecraft has been providing a number of different observations from a variety of plasma environments and solar conditions using eight different instruments, composed of twenty-four different sensors (*Acuña et al.*, 1995; *Chotoo*, 1998). The magnetic field is observed using the Magnetic Field Investigation (MFI) instrument (*Lepping et al.*, 1995). Radio and plasma waves, that occur throughout the geospace environment, are observed with the Radio and Plasma Waves Investigation (WAVES) (*Bougeret et al.*, 1995). Particles are measured over a large range of energies from the six other instruments. Low energy bulk plasma, from 7 ev to 22 keV, is observed by the Solar Wind Experiment (SWE) (*Ogilvie et al.*, 1995) while the 3-D Plasma (3DP) instrument (*Lin*

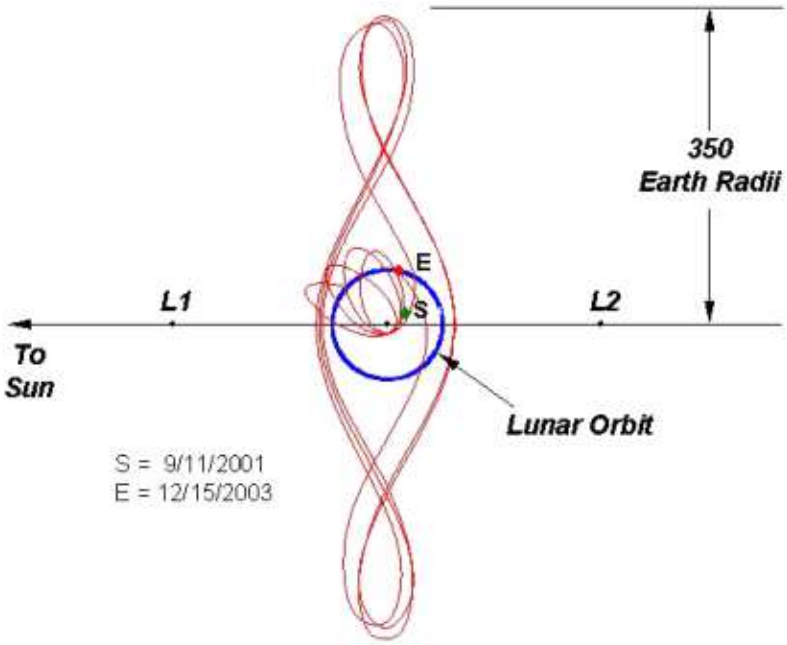

Figure 5.3: Illustration of the Wind prograde orbit from mid-2001 to late 2003. Shown, is the orbit projected on the GSE X-Y plane. Plot obtained from the wind.nasa.gov/orbit.php site.

et al., 1995), provides three-dimensional distribution information for plasma in this energy range. Energetic particle distributions are observed between the energies of $0.2 - 500$ MeV with the Energetic Particles: Acceleration, Composition Transport (EPACT) instrument (*von Rosenvinge et al.*, 1995). Gamma-rays are observed onboard Wind from two separate instruments: the Transient Gamma-Ray Spectrometer (TGRS) (*Palmer et al.*, 1995) and the Konus experiment (*Aptekar et al.*, 1995). Finally, the composition of the heliospheric plasma from the bulk solar wind through the suprathermal tail is observed with the Solar wind/Mass Suprathermal ion composition studies (SMS) instrument suite (*Gloeckler et al.*, 1995). For the remainder of this chapter, we focus on the data from the suprathermal ion population observed from the Suprathermal Ion Composition Spectrometer (STICS), which is part of SMS (*Gloeckler et al.*, 1995).

5.2 The Suprathermal Ion Composition Spectrometer (STICS

STICS is a time-of-flight (TOF) mass spectrometer, capable of measuring independently an incoming particle's mass, charge state, and energy. A diagram of the instrument is shown in Figure 5.4. Particles enter through the instrument aperture and immediately pass through an electrostatic deflection system. Here, an electric potential is imposed on two curved plates which the particle passes between. This potential causes the particle's path to be deflected, allowing only ions with a specific energy-per-charge (E/Q) through. The deflection plates step through thirty logarithmically spaced voltages, allowing ions to pass through with energies ranging between $6.2-223.1$ keV/e. This curved deflection system not only selects the E/Q of incoming particles but also helps to prevent any stray light from making it into the instrument.

Once through the deflection system, the particle impacts a very thin carbon foil ($\sim 2\,\mu g/cm^2$), at the beginning of the TOF telescope. The carbon foil is thin enough for an energetic ion to pass through, but it will knock off one or more secondary electrons as it does. This secondary electron is then detected by the front secondary electron detector assembly (SEDA), which causes a start signal for the TOF calculation. The front SEDA consists of a microchannel plate (MCP), which generates the start signal, and two discrete anodes, which help to provide the elevation angle information of the ion. The ion does lose some energy as it passes through the carbon foil which can be estimated, as described later. Once inside the TOF telescope, the ion travels a distance of 10.0 cm until it strikes a solid state detector (SSD). Here, two things happen. First, if the incident ion has an energy that is greater than the measurement threshold of the SSD, $\sim$ 30 keV, then the energy of the ion can be measured. And second, on impact with the SSD, the ion knocks another secondary electron off of the detector. This electron is then detected by the rear SEDA, causing a stop signal for the TOF analysis. With both the start and stop signals, the duration the ion spent in the TOF telescope can be determined. Since the length of the telescope is known,

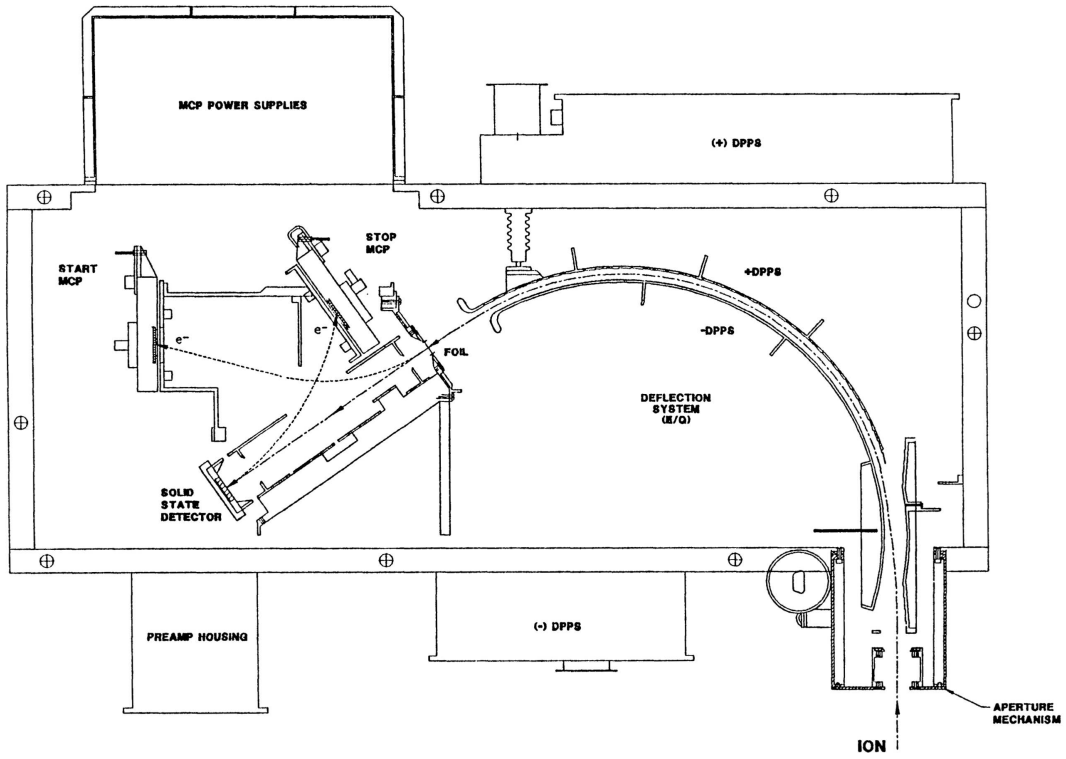

Figure 5.4: Simplified cross-section of the STICS instrument. It shows the path of a particle as it enters the detector and travels through the system. Published in (*Gloeckler et al.*, 1995).

the velocity of the particle can also then be obtained (*Gloeckler et al.*, 1995; *Chotoo*, 1998). Figure 5.4 shows these components of the STICS instrument which an ion encounters during its path through the system.

The entrance aperture of STICS is oriented such that it is perpendicular to the spin axis of Wind. This allows observations over all azimuthal angles. The instrument itself consists of three TOF telescopes. Oriented such that observations spanning from 79.5° above the ecliptic plane to −79.5° below the ecliptic plane can be made, split into three sectors, one for each telescope 53° in span. These three sectors are shown in the top portion of figure 5.5. Two 53° telescopes look above and below the ecliptic plane, while one 53° telescope looks directly along the plane. Since the instrument look direction is perpendicular to the spin axis, STICS can observe all azimuthal directions

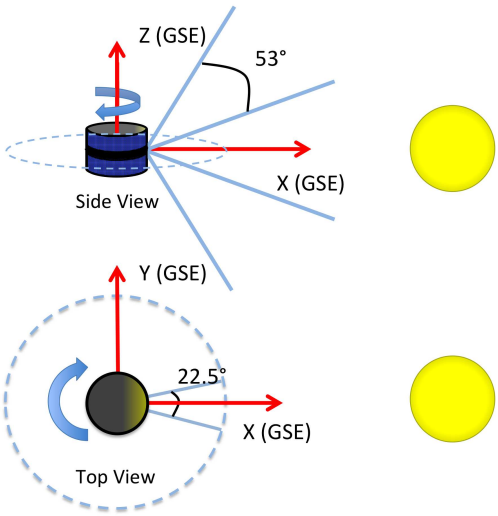

Figure 5.5: Field-of-View (FOV) of STICS. The top picture shows the off-ecliptic FOV, in the GSE X-Z plane. The bottom picture shows the azimuthal acceptance angle for STICS for 1 observational sector, in the GSE X-Y plane. Sectors not to scale.

as the spacecraft spins. The angular acceptance angle of the instrument is 4.8° and continually observes particles as the spacecraft spins, observing all azimuthal angles. The azimuthal observations are divided into sixteen equally sized bins, each having a span of 22.5°. These are numbered from 0-15, with sector 0 denoting when the deflection system's voltage changes. The bottom portion of figure 5.5 demonstrates the azimuthal span of the STICS instrument. These individual observation bins combine to give nearly three-dimensional compositional analysis of the suprathermal plasma (*Chotoo*, 1998).

STICS is optimized to make high cadence observations of the suprathermal plasma population. As previously mentioned, the Wind spacecraft rotates at speed of 20 rpm, equivalent to 3 seconds per spin. Each deflection voltage step is held for 2 spins in order to make observations in all sixteen azimuthal sectors at each voltage. To step through all of the voltage steps it takes 60 spins, or 3 minutes. Therefore, STICS

is able to make a single E/Q and direction observation with a time resolution of 3 seconds, and can sample the full distribution of energies, in all directions, every 3 minutes.

Properties of each observed particle, such as mass, mass-per-charge (M/Q), and energy are calculated onboard the spacecraft. The particle data is then finally transmitted to Earth in two forms. In the first form, the data is binned onboard into previously set bins based on ion mass and M/Q. The particles are accumulated in each bin over the amount of time it takes for the instrument to cycle through all voltage steps, creating matrix rates for each ionic species. For the He^{2+} matrix rate, the full directional information is retained. While for the H^{+} rate, only half of the directional information is preserved, as each returned rate is the combination of two observational sectors. Finally, for twenty other ionic species, which represent a number of heavy ions (such as C^{4+}, O^{6+}, and Fe^{10+}), the returned matrix rate is accumulated over all observation directions, retaining no directional information. In addition to the matrix rates, STICS also creates a number of Pulse Height Analyzed (PHA) words for a subset of the particles observed by the instrument. Each PHA word contains the measured time-of-flight, energy, and observation direction information. This allows the element, ionic state, and velocity of the particle to be determined. With this information, the phase space distribution for each ionic species can be calculated.

5.3 From PHAs to the Phase Space Distribution Function

In order to maximize the scientific uses of the suprathermal plasma observations from STICS, we often need more information than the counting rate of particles alone. PHA words make it possible to produce the phase space distributions for each ionic species. A phase space distribution describes the density of particles, from a given parcel of plasma, as a function of velocity of the particles. In other words, we can

see how the particles in a plasma are distributed over a range of energy and space. As with any distribution, we can then take moments of this distribution in order to determine the bulk parameters of the plasma. For instance, the zeroth moment determines the density of the plasma, the first moment determines the bulk velocity, and the second moment determines the thermal velocity. The process to convert an instrument's counting rates to a phase space distribution is well understood (*von Steiger et al.*, 2000). For the STICS instrument, we follow a process similar to that presented in *Chotoo* (1998).

5.3.1 Calculating Physical Properties from the PHA Word

To begin, we first need to identify the ionic species that created each PHA word. As previously mentioned, each PHA consists of the time-of-flight, energy, and directional information. This information can be used to determine the identity of the ion. However, since this information is encoded into digital channel numbers to preserve memory space, we first need to convert these to physical units. *Chotoo* (1998) describes this process, using the following equations.

To calculate the time-of-flight, in ns, of the the particle, τ, from the digital channel number, T_{CH}, we use the following equation.

$$\tau = (T_{\mathrm{ch}} - 44)/2.372530695 \tag{5.1}$$

To determine the measured energy, in keV, from the SSD, E_{meas}, from the compressed energy channel, E_{c}, we use the process described in *Chotoo* (1998). Due to the memory constraints on the size of each PHA word, only 1024 different energy channels are able to be used. However, in order to represent the full span of energies for the many different ionic species of the solar plasma, the telemetered channel number is compressed from the actual energy channel number E_{d}. This allows a greater span of energy bins. Therefore, we need to first decompress the channel.

$$E_{\mathrm{d}} = E_{\mathrm{c}} \text{ for } E_{\mathrm{c}} < 256 \tag{5.2}$$

$$E_{\mathrm{d}} = 2E_{\mathrm{c}} - 256 \text{ for } 256 \leq E_{\mathrm{c}} \leq 384 \tag{5.3}$$

$$E_{\mathrm{d}} = 4E_{\mathrm{c}} - 1024 \text{ for } 384 \leq E_{\mathrm{c}} < 1024 \tag{5.4}$$

Then the measured energy can be obtained from the following relation.

$$E_{\mathrm{meas}} = (E_{\mathrm{d}} + 6)/0.37654782 \tag{5.5}$$

We can determine the E/Q, in keV/e, of the ion based on the the deflection voltage step number, DVS, that the instrument is set to when the particle passes through the deflection system. This step number is contained within the PHA word. To determine the E/Q, from the step number, DVS we can use the following equation.

$$E/Q = 6.190722 * (1.1225857)^{DVS} \tag{5.6}$$

As previously discussed, the STICS instruments steps through a total of thirty separate voltages which are applied across the deflection plates, allowing ions with energies ranging from $6.2-223.1$ keV/e. In order to fully sample all sixteen azimuthal directions at each voltage step, the deflection voltage is currently held constant for two spins. This allows for an ample observation time while in the heliosphere. Therefore, it takes a total of sixty spins to step through all the defined voltage steps once. One full sequence of all the voltage steps is defined as a cycle. The order in which the voltage is applied can be defined at any time. Currently, STICS uses a triangular stepping sequence. In other words, the deflection plates begin at the lowest possible voltage and steadily increase to the maximum voltage over the next thirty spins, holding each step constant for two spins. After the plates reach the maximum voltage of the

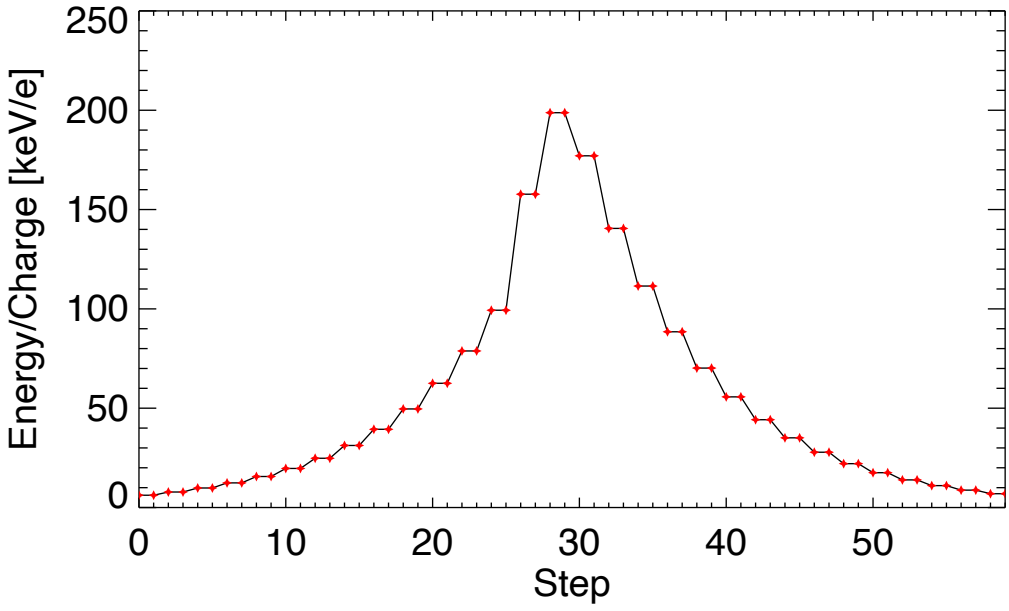

Figure 5.6: Typical E/Q stepping sequence for the STICS deflection system.

stepping table, STICS steadily steps back down to its minimum voltage over the next thirty spins. The voltages applied during the first thirty steps are different from those applied during the last thirty steps, allowing different ion E/Q through on either side of the voltage maximum. An illustration of the triangular stepping sequence is shown in figure 5.6.

5.3.2 Ion Identification

Once the TOF, E/Q, and energy of a PHA are determined, identification of the ionic species is possible. This can be accomplished in a few different ways. First, we will discuss using the time-of-flight and the energy-per-charge of the particles. Figure 5.7 shows the distribution of PHAs, accumulated over the entire year of 2004, versus the time-of-flight and the E/Q of the measured ion. It can be seen that there are a number of distinct tracks that are enhanced over the background. These tracks correspond to individual ion species. The three bright tracks on the left side of the

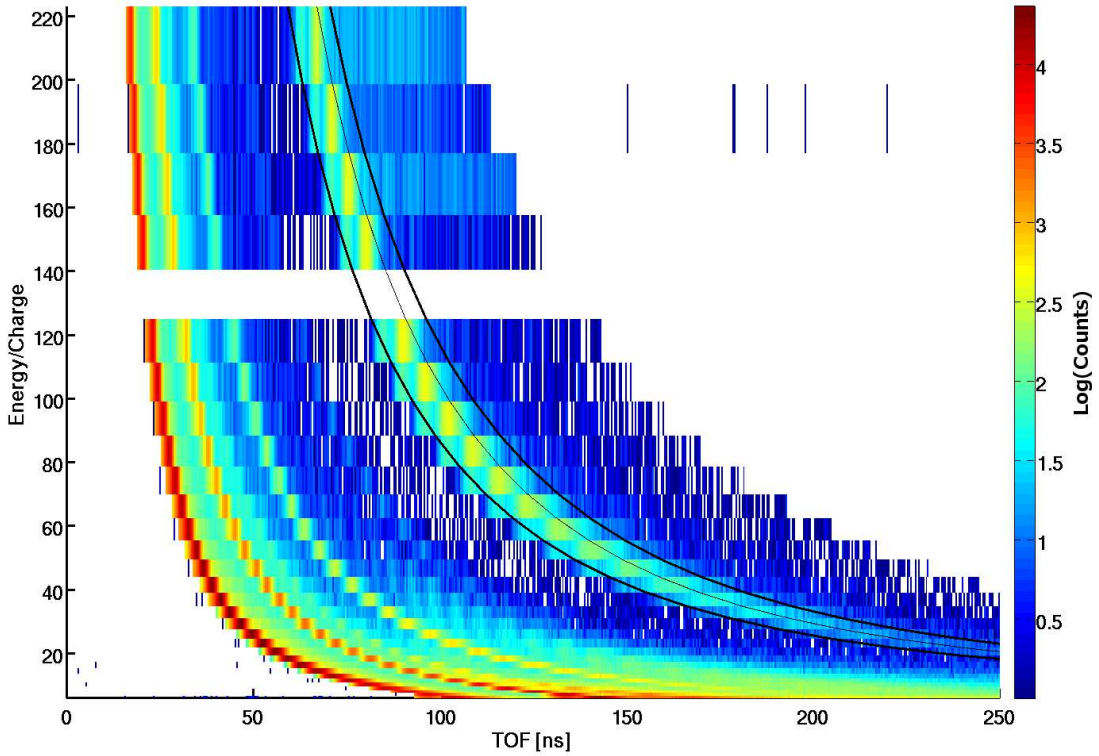

Figure 5.7: Distribution of the particles over the time-of-flight and energy-per-charge measured by STICS. The data shown is an accumulation of PHAs over the entire year of 2004. The thin black line is the predicted location of O^+, while the two thick black lines indicates the bin used for O^+ identification.

data correspond to H^+, He^{2+} and He^+. In early 2004, Wind was finishing its deep magnetotail orbit, spending a portion of time sampling the Earth's magnetosphere, resulting in a large O^+ track appearing in the data, to the right of the previously mentioned three tracks. We will use this track as an example of identification using the TOF and E/Q distribution.

To ensure that the TOF track is composed of $O+$ ions, we first predict the time-of-flight for an $O+$ ion at all the energy-per-charge steps of STICS. We do this by calculating the velocity an ion would have after it passes through the carbon foil, V_{ion} in km/s, entering the STICS TOF telescope during energy-per-charge step, E/Q in keV/e, using the following relation.

$$V_{\text{ion}} = 439.36 * \sqrt{((E/Q) * (Q/M) - (E_{\text{loss}}/M))} \tag{5.7}$$

In the above equation, Q/M represents the ratio of the charge to mass of a specific ion. To improve the accuracy of the ion's predicting velocity in the TOF telescope, we must account for the energy lost by the ion when it passes through the carbon foil, E_{loss}. This can be estimated by using the Transport of Ions in Matter (TRIM) software (part of the Stopping and Range of Ions in Matter (SRIM) software package, *www.srim.org*). TRIM calculates the kinetic energy a particle loses when passing through some material from collisions with the atoms of the material. By performing a monte carlo simulation of atoms of a specific energy impacting a defined material one can estimate the average loss of energy for a particle passing through that material. Figure 5.8 shows one such calculation we performed for an oxygen atom with an energy of 78.81 keV impacting a layer of carbon 89 angstroms thick, similar to the carbon foil in STICS. The energy loss has a gaussian distribution, due to the randomness of the scattering of the particle in the material. Therefore, we can determine the energy loss for a particular energy-per-charge step by calculating the mean of the distribution. This calculation is carried out for all E/Q steps of the instrument to characterize the energy loss for all possible ion observations.

Once the velocity of the ion has been determined, it is trivial to determine the ion's time-of-flight, τ in ns, through the TOF system. Since the distance the ion travels in the TOF telescope, $d = 10.0$ cm, is known, τ is simply the ratio of distance to velocity. The following equation shows this relation, where the leading factor of 10000 performs the necessary unit conversion.

$$\tau_{\text{ion}} = 10000 * \frac{d}{v_{\text{ion}}} \tag{5.8}$$

Combining Equation 5.7 and Equation 5.8 results in the relation for the predicted

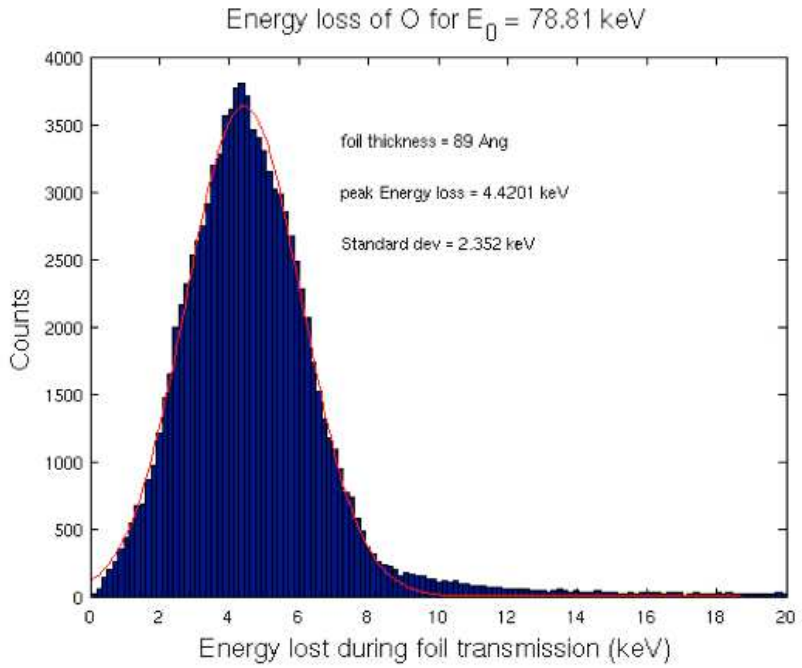

Figure 5.8: Results of the TRIM calculation for a number of oxygen atoms, with an energy of 78.81 keV, impacting a carbon foil of thickness of 89 angstroms, the same thickness as the carbon foil on STICS. The red curve is a gaussian curve fit to the histogram, with the mean energy loss and standard deviation displayed.

time-of-flight of an ion determined by its E/Q, as measured by STICS.

$$\tau = \left[\frac{439.36}{10,000 * d} * \sqrt{((E/Q) * (Q/M) - (E_{\text{loss}}/M))} \right]^{-1} \tag{5.9}$$

In Figure 5.7, the predicted time-of-flight, using Equation 5.9, of an O^+ ion is plotted as the thin black line. It can be seen that this predicted track lines up with the bright track in the data. For each voltage step, a range of potential E/Q of the incident ions are capable of passing through the deflection system. This is referred to as the energy passband, $\Delta E/Q$. Calibration data has shown that the average passband is $\frac{\Delta E/Q}{E/Q} = 1.9\%$ (*Chotoo*, 1998). Considering this spread in E/Q we can create a TOF band, centered on the predicted track, for a given ion. This band is shown in Figure 5.7, by the two thick black lines. Any PHA landing in this band we then classify as an O^+ ion. As can be seen, the entire bright track in the data lies within these bounds. For any ion which we can create a track for, we can then classify using the time-of-flight and energy-per-charge information of the PHA.

The TOF-E/Q method works well for ions that have distinct mass-per-charge ratios, but for many of the heavy ions, these tracks would overlap each other, making it harder to classify the ions. Instead we can use the mass and mass-per-charge calculated from each PHA word. From the E/Q, energy, and time-of-flight of the PHA, we can calculate the mass and M/Q. This method is similar to the one used onboard the spacecraft to create the matrix rates previously discussed. *Chotoo* (1998) provides the equations used for these conversions.

$$M = 2 * (\tau/d)^2 * (E_{\text{meas}}/\gamma) \tag{5.10}$$

$$M/Q = 2 * (\tau/d)^2 * (E/Q) \tag{5.11}$$

We then create a distribution of PHAs, accumulated over a length of time, in

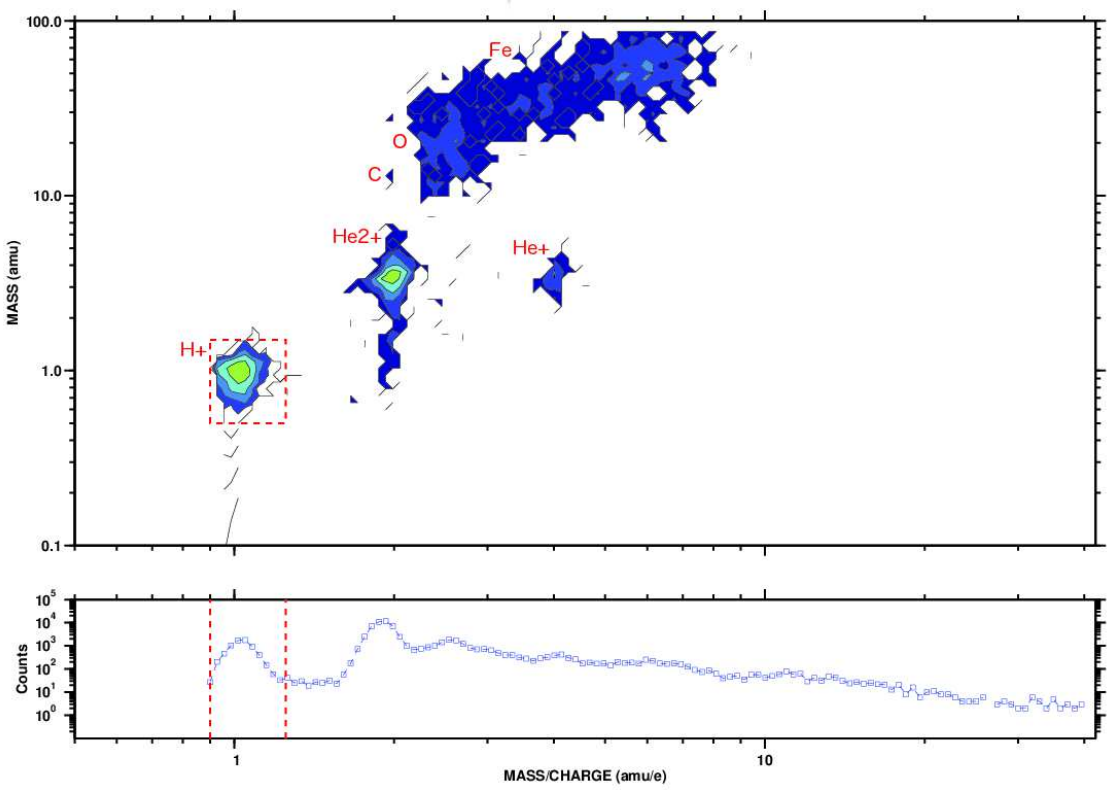

Figure 5.9: The top panel shows a distribution of PHA words from May 30, 1995 versus M/Q and mass. The bottom panel shows the distribution of counts integrated over all masses as a function of M/Q. The Mass-M/Q box boundaries for $H+$ ions is shown, as well as the general location of the $He2+$ ions, $He+$ ions, C group, O group, and Fe group.

Mass-M/Q space. Figure 5.9 shows one such distribution, accumulated on May 30, 1995, similar to the Figure in *Chotoo* (1998). Compared to Figure 5.7, individual ions appears as distributions spread around a single point, determined by the ion's mass and M/Q, instead of tracks. The top panel of Figure 5.9 displays the distribution of particles that created PHA words, while the bottom panel shows the number of particles per M/Q. The bottom panel is created by integrating over all masses for each M/Q bin in the distribution.

Based on the mass and M/Q of each species, the identification of the ionic species is possible for each particle. To do this, we create boxes in Mass-M/Q space, centered

Ionic Species	Mass Low (amu)	Mass High (amu)	M/Q Low (amu/e)	M/Q High (amu/e)
H^+	0.0	2.13	0.90	1.26
He^+	2.79	6.30	3.55	4.67
He^{2+}	2.79	6.30	1.61	2.32
C^{4+}	9.04	12.99	2.87	3.24
C^{5+}	9.04	12.99	2.25	2.54
C^{6+}	9.04	12.99	1.87	2.18
O^+	4.80	79.30	14.89	20.20
O^{6+}	10.83	20.41	2.54	2.87
O^{7+}	14.21	20.41	2.11	2.46
Fe^{8+}	38.45	79.28	6.53	7.38
Fe^{9+}	38.45	79.28	5.78	6.53
Fe^{10+}	38.45	79.28	5.28	5.78
Fe^{11+}	38.45	79.28	4.82	5.28
Fe^{12+}	38.45	79.28	4.40	4.82
Fe^{14+}	38.45	79.28	3.77	4.14
Fe^{16+}	38.45	79.28	3.34	3.55

Table 5.1: Mass and M/Q boundaries for ionic species measured by Wind/STICS. Published in *Chotoo* (1998).

on the mass and M/Q for each species. These boxes account for any spread of the ions in the space due to energy loss of the ion in the system and the energy passband of the instrument allowing ions with energies ranging about the E/Q step to enter the system. In Figure 5.9 we show one such box, in the top panel, for selecting protons. Any particle that falls within this box is classified as a proton. Using the same mass and M/Q box definitions which STICS uses onboard to create the matrix rates for heavy ions, as described earlier, we can then classify a number of the ions. In Figure 5.9 we have indicated the distribution of both the $He+$ and $He2+$ ion as well as the general location of the C, O, and Fe groups of ions.

Table 5.1 shows the boundaries of these boxes in both dimensions for the heavy ions which we can currently identify, provided by *Chotoo* (1998). If an incoming particle does not have enough energy to overcome the SSD energy threshold, then its mass can not be determined. These events are called double coincidence events, as only a start and stop signal can be made, as opposed to a triple coincidence event,

when both timing signals and an energy measurement can be made. The mass of a double coincidence particle can not be determined, and will then have a mass of zero amu. These events can still be included in analysis for some ions, by only considering the M/Q ranges from Table 5.1. The bottom panel of Figure 5.9 illustrates the M/Q range for H^+. Inside these bounds we can see a clear peak, corresponding the large contribution of proton measurements. Additionally, we can see a significant peak near $M/Q \sim 2$, corresponding to the He^{2+} observations. Further identification in this manner can be difficult however, as many heavy ions have a very similar M/Q. For example, the M/Q of O^{7+} is $\sim$ 2.4 while the M/Q of C^{5+} is $\sim$ 2.3. The distribution for an ion is spread out in mass-M/Q space, making it difficult to discriminate between two ions in the region where they may overlap.

5.3.3 Calculating Differential Flux

In order to minimize the observational error of a specific ion, we accumulate the observations over a duration of time. With the number of ions observed over this time period known, we can then calculate the phase space distribution of the sampled plasma, following the methodology of *Chotoo* (1998). The first step, is to convert the counts into differential flux. The differential flux describes the flux of particles, per unit of energy, incident on the instrument's detectors. The conversion from the number of counts of a particular ion identified by STICS to flux, is straightforward. *Chotoo* (1998) gives the relation as

$$\frac{dJ}{dE} = \frac{counts}{g\,\Delta E/Q\,\eta_1\,\eta_2\,\Delta t}\frac{DC\,BR_{\text{norm}}}{Box_{\text{eff}}} \tag{5.12}$$

The differential flux has units of $[cm^2\ s\ sr\ keV/amu]^{-1}$ and is denoted as $\frac{dJ}{dE}$ in the above equation, while *counts* is the number of ions that we have identified by one of the identification previously discussed for a particular E/Q step. The accumulation time of the observation is denoted by Δt. The remaining terms in the above equation

Telescope	**Parallel Beam**	**Isotropic**
	Geometric Factor (cm^2)	**Geometric Factor** ($cm^2\,sr$)
1	0.72 ± 0.18	0.031 ± 0.002
2	0.68 ± 0.18	0.029 ± 0.002
3	0.74 ± 0.18	0.029 ± 0.002

Table 5.2: Geometric factors for STICS determined from calibration. As published in *Chotoo* (1998).

describe the efficiency of the STICS instrument's ability to observe an ion from the incident flux and will be described in further detail.

The geometric factor of the instrument is represented by g in Equation 5.12. As not every particle is able to make it into the instrument due to scattering in the electrostatic analyzer and the particle's angle of entry, the geometric factor represents the relationship between the counting rate of particles in the instrument and the actual incident flux from the heliosphere on the aperture.. This factor represents the effective aperture size that particles can enter the system through. The values for the geometric factors of STICS are published in *Chotoo* (1998) and shown in Table 5.2. These values were determined from pre-flight calibration and in-flight cross calibration (*Chotoo*, 1998). If the radiation is from a beam of particles entering the instrument perpendicular to the aperture, then the geometric factor is only dependent on the area of the aperture. If, however, the particles are isotropically distributed and impacting the aperture at a number of different angles, then the geometric factor is dependent on the full solid angle acceptance range of the aperture (*Chotoo*, 1998). This results in smaller geometric factors, seen in Table 5.2, for isotropic particle distributions compared to that from the parallel beam case. The parallel beam approximation is appropriate for particle populations originating from a single source, such as the solar wind, while the isotropic factor is used for particle populations which are evenly distributed in velocity space, such as the suprathermal particles or pick-up ion distribution.

As previously discussed, the deflection system of STICS is designed to allow only

particles with a particular E/Q to enter the instrument. However, the E/Q of particles that do make it through the deflection system spread over a small range about this value. This is called the energy passband, $\Delta E/Q$, as described in the previous section. From calibration data, this has been found to have a value of $\frac{\Delta E/Q}{E/Q} \sim 1.9\%$ (*Chotoo*, 1998).

Not all the particles that make it through the deflection system become measured by the TOF telescope. The likelihood of a particle of a particle in the TOF telescope to pass through the carbon foil and then trigger a measurement at the SSD detector is referred to as the efficiency and is denoted by the η_X terms in Equation 5.12. The efficiency of a particle passing through the carbon foil and triggering a start signal is referred to as the start efficiency, η_1. The efficiency denoted by η_2 can refer to two different situations. If we are considering triple coincidence particles, then η_2 refers to the triple efficiency. The triple efficiency describes the ability for a particle to produce both the stop signal and the SSD energy measurement. If however, we also choose to consider double coincidence events in the analysis, then η_2 refers to the stop efficiency. The stop efficiency illustrates the ability of a particle, that has triggered a start signal, to trigger a stop signal. These efficiencies have been determined during the calibration of the instrument, and are provided by *Chotoo* (1998). Figure 5.10 shows a sample efficiency curve for protons. The top panel shows the start efficiency, η_1, and the middle panel shows the triple efficiency, η_2. Since, the calculation for differential flux uses the product of these efficiencies, we show this in the bottom panel. This represents the overall efficiency of a particle that passes through the deflection system to be measured by the TOF system.

The value DC, in Equation 5.12, is the deadtime correction for the instrument. Each spin of the Wind spacecraft takes 3 seconds, however the instrument does not make observations for this entire time. This is due to a number of reasons as the instrument requires time for flight software to classify ions which it has previously

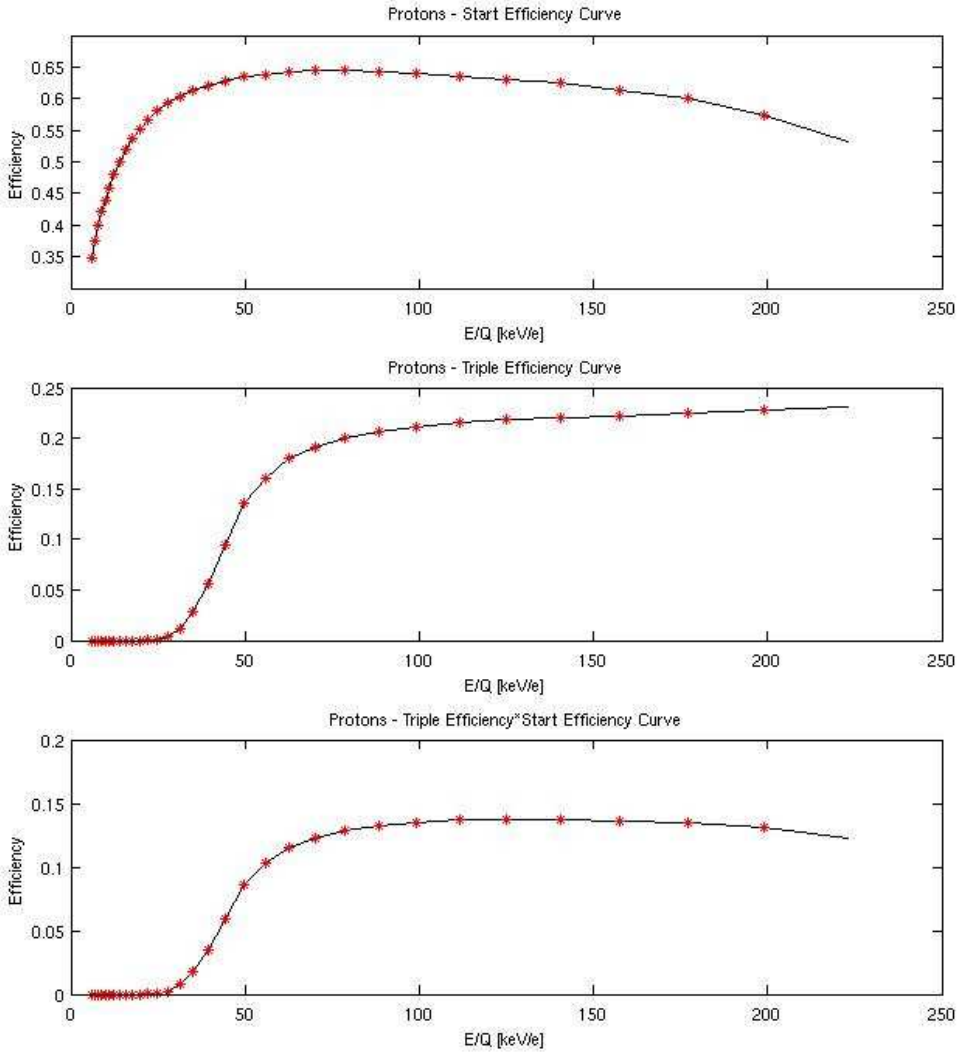

Figure 5.10: Efficiency curves for protons. The top panel shows the efficiency of an incoming particle to trigger a start signal. The middle curve shows the efficiency of a particle that has triggered a start signal also triggering a stop signal and a measured energy from the SSD. The bottom curve shows the combination of these first two curves. Curves are determined from calibration data, and published in *Chotoo* (1998). The red asterisks represent the E/Q steps from the deflection system.

Sector	Deadtime Correction Factor
0	2.143
1-15	1.068
Full Spin	1.103

Table 5.3: The deadtime correction factors for STICS. As published in *Chotoo* (1998).

observed, read counters, and perform other housekeeping chores. These things happen between every observation sector. There is a longer deadtime period for the first observation sector of each spin. The voltage in the deflection system is changed at the beginning of the spin and more time is required for the stepping voltages to settle. As there are sixteen observation sectors, each one lasting 187.5 ms. The instrument has a deadtime of 12 ms between each sector, and an additional 100 ms of deadtime for sector 0 (*Chotoo*, 1998). Sector 0 will always have a deadtime of 100 ms, as a convince for the data processing unit, regardless of whether the voltage has been changed. The deadtime correction is simply a factor to account for this lost observation time, and is determined by the ratio of total available time to actual observation time. Table 5.3 shows the deadtime correction factors for sector 0, the first observation sector, and the other sectors. Additionally, the deadtime correction factor for an entire spin is shown. This is used when we use considering one of the counting rates that does not have directional information. These factors were published in *Chotoo* (1998).

The BR_{norm} term represents the basic rate normalization applied to the observed counts. Since STICS cannot return a PHA word for every measured particle, three basic rates (BR), for eight azimuthal directions, are returned accounting for particles falling within 3 separate mass-M/Q regions. The PHAs are then created for a portion of particles in each of these bins, distributed based on the priority assigned to each mass-M/Q region. One bin encompasses H^+, He^+, and He^{2+}, which composes a majority of the observed heliospheric plasma.

To ensure that all the telemetered PHA words are not created from protons, this region is given the lowest priority. In other words, the smallest number of PHAs are

Ion	Box Efficiency
H^+	0.90 for $DVS < 15$
	0.99 for $DVS \geq 15$
He^+	0.98
He^{2+}	0.98

Table 5.4: The box efficiency for the M-M/Q boxes of H^+, He^+, and He^{2+}. The efficiencies for H^+ are dependent on the deflection voltage step number, DVS. This were published in *Chotoo* (1998).

created per number of measured particles.

Multiply charged heavy ions constitute the next highest priority, and singly charged pick-up heavy ions have the highest priority. The basic rate then describes the total amount of particles that were observed by STICS. Thus, the basic rate normalization is simply the ratio $BR_{\mathrm{norm_i}} = BR_{\mathrm{i}}/PHA_{\mathrm{i}}$ for each azimuthal sector, where i represents the basic rate region and PHA_{i} refers to the number of PHA words created from particles falling in that region (*Chotoo*, 1998).

The final term in Equation 5.12 represents the efficiency of the mass-M/Q box to include all observed ions of the particular box, Box_{eff}. The ion distribution can spread beyond the bounds of the mass-M/Q box that is defined. The box efficiency is meant to correct for the number ions that are observed by STICS but are not properly identified due to the limitations of the mass-M/Q box used. *Chotoo* (1998) has characterized this value for the H^+, He^+, and He^{2+} boxes, while further ion box efficiencies have yet to be characterized. As seen in *Chotoo* (1998) and table 5.4, this correction is very small and should not alter the resulting differential flux much. For the ions not yet characterized, we use an efficiency of 1.0. Table 5.4 shows that there are two separate efficiencies for $H+$. As *Chotoo* (1998) describes, this is due to a larger amount of energy being lost in the carbon foil for the less energetic protons. Protons, due to their lighter mass and momentum, suffer from a greater energy loss in the carbon foil when the protons are slower. This causes the distribution to spread more, resulting in more protons falling outside of the classification box.

5.3.4 From Differential Flux to a Phase Space Distribution

Finally, we can obtain a phase distribution for a given ionic species, by calculating the phase space density from the differential flux. The phase space density, f in units of s^3/km^6, is the density of particles occurring in a volume of velocity space. This can be written in the same manner as *Chotoo* (1998).

$$f = \frac{dN}{d^3r\, d^3v} \tag{5.13}$$

The density of the particles is defined as the number of particles, dN, present in a volume of space, d^3r. The d^3v represents the volume of velocity space that the particles inhabit. Velocity space is another way of describing the energy range of a particular population of particles. To obtain the density of particles passing through the instrument, we relate it to the differential flux observed by STICS, using the following relation from *Chotoo* (1998).

$$dN = \frac{dJ}{dE}\, dA\, dE\, d\Omega\, dt \tag{5.14}$$

In the above equation, dJ/dE is the differential flux measured by STICS. The other terms describe how the observation was obtained. The dA term represents the unit area which particles are flowing through, dE represents the range of energies of the incident particles, $d\Omega$ is the solid angle acceptance cone of the aperture, and dt is the accumulation time of the measurement. Combining these two equations, we can get to a relation between differential flux and phase space distribution, as derived in *Chotoo* (1998).

$$dN = f\, d^3r\, d^3v \tag{5.15}$$

$$\frac{dJ}{dE}\, dA\, dE\, d\Omega = f\, d^3r\, d^3v \tag{5.16}$$

We can simplify this relation further. First, we transform the differential velocity space into spherical coordinates, by $d^3v = v^2\,dv\,d\Omega$. Next, since $dr = v\,dt$, we can re-write the differential space term as, $d^3r = v\,dt\,dA$. Substituting these two relations into the above equation gives the following equation.

$$\frac{dJ}{dE}\,dA\,dE\,d\Omega = f\,v^3\,dv\,d\Omega\,dA\,dt \tag{5.17}$$

Canceling like terms from this equations, yields

$$\frac{dJ}{dE}\,dE = f\,v^3\,dv \tag{5.18}$$

Since, the energy appearing in the above equation is simply the kinetic energy of the particle, we can then write the energy as $E = 0.5\,m\,v^2$ which makes the differential energy, $dE = m\,v\,dv$. Substituting these relations into the above equations, yields our final equation which we can use to obtain the phase space density for a given ionic species from the observed differential flux.

$$\frac{dJ}{dE}\,m\,v\,dv = f\,v^3\,dv \tag{5.19}$$

$$\frac{dJ}{dE} = \frac{v^2}{m}\,f \tag{5.20}$$

$$\text{Since, } v^2 = \frac{2\,E}{m} \tag{5.21}$$

$$\frac{dJ}{dE} = \frac{2E}{m^2}\,f \tag{5.22}$$

$$\Longrightarrow f = \frac{m^2}{2E}\,\frac{dJ}{dE} \tag{5.23}$$

However, as previously stated, the units of differential flux are $[cm^2\,s\,sr\,keV/amu]^-$ while the phase space distribution is commonly given in units of s^3/km^6. To perform the unit conversion, we multiply the right hand side of the above equation by 1.076 (*Chotoo*, 1998). This yields our final relation for the phase space density of an ionic

species, as a function of particle energy.

$$f = 1.076 \frac{m^2}{2E} \frac{dJ}{dE} \tag{5.24}$$

We can then create the phase space distribution of a ion from this relation. The measurement error for the phase space density can be estimated from the Poisson counting error from the instrument, or $\sigma_{\text{counts}} = \sqrt{counts}$. We can then propagate the error through the above equations to determine the error of the phase space density, σ_{f}. This is shown in the following equations.

$$\sigma_{\text{counts}} = \sqrt{counts} \tag{5.25}$$

$$\sigma_{\frac{\text{dJ}}{\text{dE}}} = \frac{\sigma_{\text{counts}}}{g\,\Delta E/Q\,\eta_1\,\eta_2\,\Delta t} \frac{DC\,BR_{\text{norm}}}{Box_{\text{eff}}} \tag{5.26}$$

$$\sigma_{\text{f}} = 1.076 \frac{m^2}{2E}\,\sigma_{\frac{\text{dJ}}{\text{dE}}} \tag{5.27}$$

To calculate full phase space distribution function, the data needs to be accumulated over a set period of time. Because of Wind's spin configuration, STICS observes particles coming from all azimuthal directions. In order to calculate the 3-dimensional phase space density, the distribution function is then accumulated and calculated individually for each observation sector. If the distribution function is accumulated over all of the sectors, only a 1-dimensional distribution is able to be calculated. The 1-dimensional function can be determined with smaller measurement error when accumulated over shorter cadences than the 3-dimensional observation, but lacking any directional information. Figure 5.11 shows an example of a calculated phase space distribution function for alpha particles over a 14 hour observation period during DOY 150 of 2003 accumulated over all observation sector. The poisson counting errors are shown as the red vertical bars.

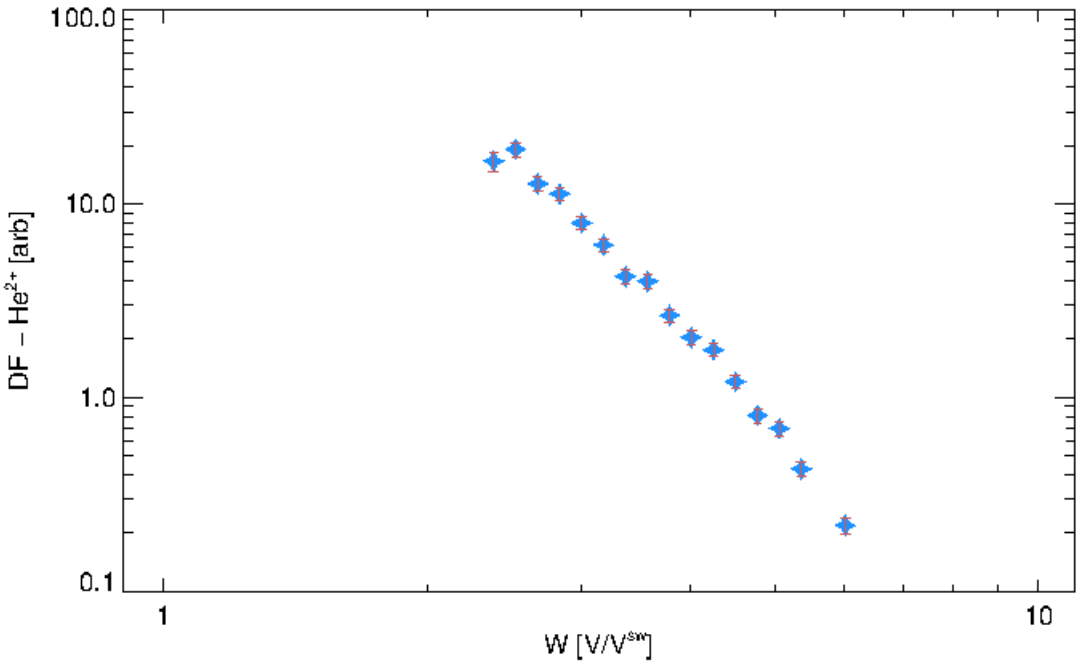

Figure 5.11: Phase space density, DF versus particle speed W, normalized by solar wind bulk speed, for alpha particles. Distribution was accumulated over DOY 150.083 – 150.67 of 2003, and all sixteen view directions. The red error bars signifies the Poisson counting error.

5.4 Adaptive Cadence - Solution to Intermittent Periods of Observations

Normally, to create phase space distribution functions of solar wind plasma, as described in the previous sections, we accumulate the PHAs for a set amount of time, usually on the order of hours. This accumulation takes places in order to obtain enough counts to minimize the errors of the measurement. For the STICS data, even with two hour accumulations, the error bars can at times be very large because of the very small amount of incident particles. To accommodate these intermittent periods of measurements we have developed a method of an adaptive cadence.

The adaptive cadence method allows the accumulation time of the phase space distribution to vary, while processing long periods of data. To do this, we first set a desired counting error threshold and the number of energy bins of the distribution function to exceed this threshold. Typically we run the adaptive cadence method requiring 10 energy bins in order to ensure that at least $\sim 30\%$ of the total energy bins contain an observation satisfying the set error threshold. Initially, we choose an error threshold of $\sim 50\%$. This value was settled on as it requires that the distribution function is computed from more than only 1 or 2 counts.

After the number of energy bins and error threshold are determined, we begin to step through each measurement cycle and accumulate the number of STICS counts for a particular ion in each energy bin. At the end of each cycle, we compute the distribution function from the current accumulated counts and compute the measurement errors. Then we test each measurement error versus the desired error threshold which had been set. If the total number of energy bins achieving the desired error is greater than or equal to the number of bins we set, then the distribution function is outputted and accumulation for the next observation begins. However, if the number of energy bins satisfying the our desired measurement error is not large enough,

the next measurement cycle is accumulated into the current distribution function measurement and the error threshold is tested once again. This procedure continues over the time period which we wish to process, allowing each calculated distribution function to be accumulated over a different amount of time, but all satisfying a set measurement error.

Figure 5.12 shows one such example of the adaptive cadence method. The top panel shows the accumulation time required to ensure that 10 energy bins had an error less than 50% for the three ions C^{4+}, C^{5+}, and C^{6+}. The next three panels shows the distribution function as it evolves in time for the three ions. The magenta dashed line shows the start time of an ICME as determined by *Richardson and Cane* (2010). As can be seen over the course of the three days, the accumulation time required to produce a distribution function varies from 1 day to 0.5 hours, for both C^{5+} and C^{6+}.

Using the adaptive cadence method we have been able to pinpoint a wide array of periods when the measured phase space distribution from STICS is able to be computed at very high-cadences. These often occur near transitions in the heliospheric environments, such as at co-rotation interaction region (CIRs), interplanetary (IP) shocks, and interplanetary coronal mass ejections (ICMEs). During these transition events the cadence time required to calculate phase space distributions can be on the order of ten's of minutes, compared to quieter periods when it can take up to ten's of days. High-cadence measurements during these time periods enable the investigation of their impact on the suprathermal particles. It is not well understood whether transition events like these have a significant impact on the suprathermal population, such as further heating of the particles. We also find that high-cadence measurements can be produced upstream of the Earth's bow shock and inside the magnetosphere. Observations such as these, allow the exploration of the leakage mechanism of plasma into and out of the magnetosphere, and any possible energization of the plasma occur-

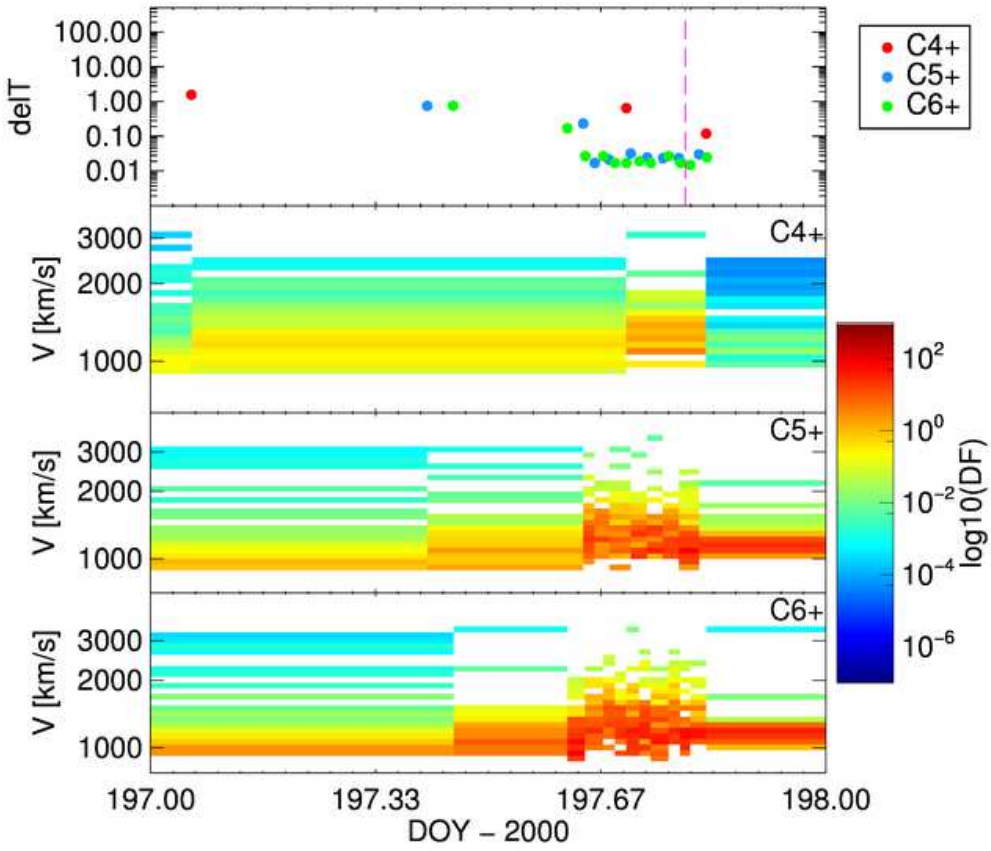

Figure 5.12: Spectrogram plot showing an example of the adaptive cadence ratio, for the carbon ions C^{4+}, C^{5+}, and C^{6+}. Top panel shows the accumulation time for each returned distribution function. The next three panels show the phase space distribution versus time. Particle velocity is along the y-axis. The magenta dotted line represents the beginning of an ICME, as determined from (*Richardson and Cane*, 2010).

ring at the bow shock. Using the ICME time periods determined from this method, we can explore the relationship between the suprathermal ionic composition and the bulk plasma, utilizing the unique compositional characteristics of ICMEs.

12.3 STICS Data Product Release Notes

The STICS calibration software can be found in the *Wind* lz decommutation softare *Wilson III et al.* [2021c] and is thus not further discussed.

WIND/STICS Level 2 Data Release Notes, revision D
Data Version 3.0

Susan T. Lepri, Jim M. Raines, Keeling C. Ploof, Patrick J. Tracy, Jacob R. Gruesbeck, Tyler J. Eddy and Jonathan W. Thomas

1 Overview

The Suprathermal Ion Composition Spectrometer (STICS) is a charge-resolving, time of flight – energy (TOF-E) ion mass spectrometer, capable of identifying mass and mass per charge for incident ions from 6-230 keV/e (Gloeckler et al., 1995). It uses an electrostatic analyzer to admit ions of a particular energy per charge (E/Q) into the TOF chamber. The E/Q voltage is stepped through 32 values, sitting at each value for approximately 6 sec., to measure ions over the full E/Q range of 6 - 230 keV/e. It completes one total E/Q scan every ~3 min (184 sec, 60 spacecraft spins). Ions then pass through a carbon foil and TOF chamber, before finally impacting on a solid-state detector (SSD) for total energy measurement. STICS combines these three measurements of E/Q, TOF and total energy, producing ion event words for each ion measured in "triple coincidence". (Ion event words are often referred to as pulse height analysis (PHA) words for historical reasons.) Triple coincidence measurements enable calculation of an individual ion's velocity, mass (M), and charge(Q), as described in Gloeckler et al (1992). These ion events are analyzed on the ground to assign them to individual ion species. This triple-coincidence technique greatly improves the signal to noise ratio in the data, significantly reducing background noise. If an ion's incident energy falls below the SSD low energy threshold (~35 keV), an ion's total energy cannot be recovered and therefore the ion's mass and charge state cannot be separately determined. These measurements of E/Q and TOF can still be used to determine ion mass per charge (m/q). These so-called "double-coincidence" measurements are characterized by improved counting statistics since they include both the triple coincidence ions, as well as additional double coincidence ions. Ion identification in double-coincidence measurements are completed in E/Q--TOF space where ions can be separated by M/Q and is limited to select ions that are well separated in E/Q – TOF (and M/Q) space.

The STICS instrument provides full 3D velocity distribution functions during each E/Q scan, by combining multiple telescopes and accumulating over multiple spacecraft spins. The instrument includes three separate TOF telescopes that view distinct elevation sectors in and out of the ecliptic plane. These telescopes have a native field of view (FOV) of 53 degrees, with shared boundaries, providing a 159° total FOV, as shown in Figure 1. As the Wind spacecraft spins, the 3 telescopes to trace out an approximately 3π steradian viewing area. The azimuthal (in ecliptic) scans (resulting from spacecraft spin) are divided into 16 sectors that are each 22.5 degrees wide (Figure 2). The solar direction is within sectors 8-10 while the earthward direction is in sectors 0-2.

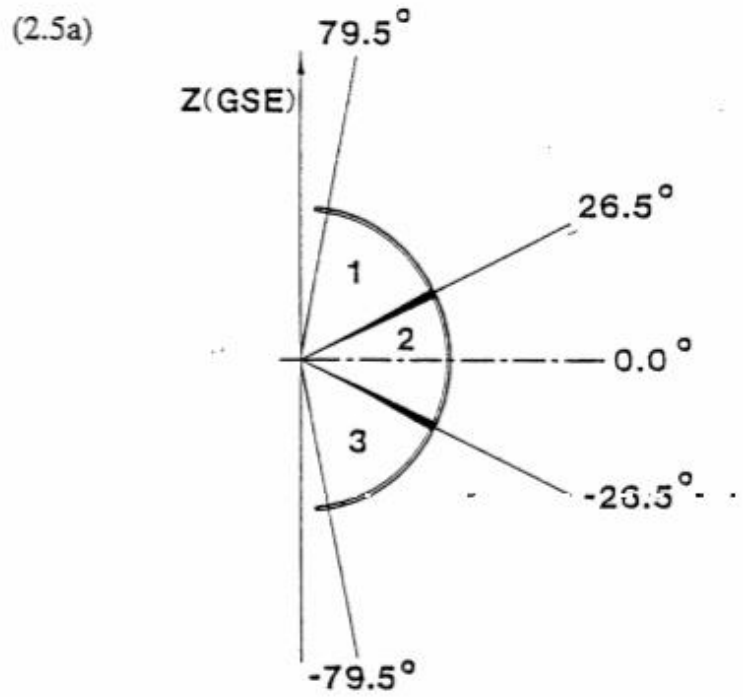

Figure 1. STICS is composed of 3 separate telescopes that view 3 different elevation ranges in and out of the ecliptic plane (Adapted from Chotoo et al. 1998).

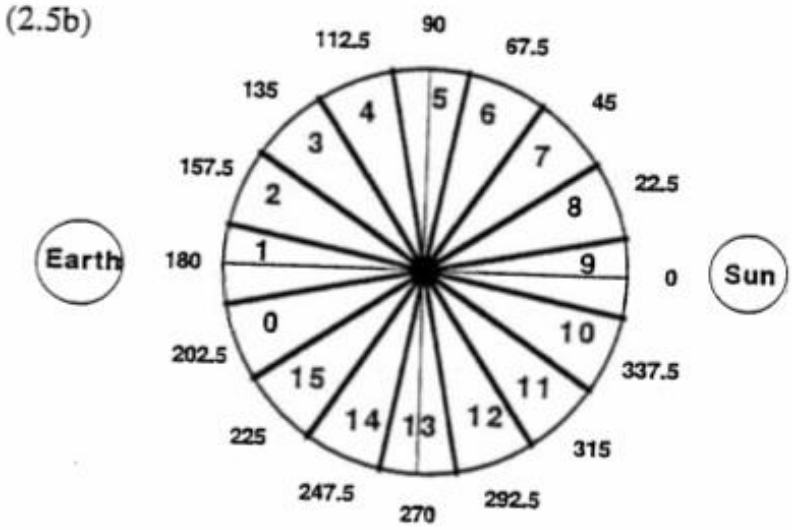

Figure 2. STICS spins through 360 degrees during one measurement cycle sweeping out 16 sectors in space in the ecliptic plane. Sectors 8-10 include the solar direction (Adapted from Chotoo et al. 1998).

2 Instrumental effects

STICS does not apply a post-acceleration voltage to boost ion energy (unlike Wind/SWICS see Gloeckler et al. 1992), so lower energy ions, regardless of charge, do not have enough kinetic energy at the lower E/Q steps to trigger the SSD (make sure it's defined above) and generate a full, triple-coincidence measurement. This results in a sharp cutoff in measured triple coincidence ions at E/Q values < 35 keV/e in the phase space density curve. The cutoff, being dependent on ion energy and number of nucleons, varies for each ion depending on the ions mass and velocity (total energy). The effect is less for highly-charged heavy ions — with more mass and therefore more energy, for a given E/Q and thus can be measured down to somewhat lower velocities (Gloeckler et al. 1995). This enables the VDF of heavy ions to extend down to lower ranges than their lighter counterparts. Ions that do not have sufficient energy to produce a triple-coincidence measurement often produce a double-coincidence measurement, allowing extension of STICS distributions to lower energy, at the expense of increased noise and difficulty of assignment to particular ions. Ions with the same mass per charge cannot be cleanly separated from each other in double-coincidence. The type of measurement, triple coincidence (TC) or double coincidence (DC) is indicated in the file name, described below.

As STICS is designed to measure ions in the suprathermal energy range, significantly above the normal solar wind energy range for low mass ions. The flux of particles in this range will vary considerably with solar wind density, velocity and thermal velocity, as well as due to many other solar phenomena (e.g. CMEs). Lower statistics of suprathermal populations frequently result in periods of time that have insufficient statistics for the calculation of distribution functions or parts of the distribution function. As a result, the distribution functions may not be continuous in velocity space and there may be gaps in time periods where there are insufficient counts from which to assemble quality distribution functions. It should be noted that the DC data has considerably higher statistics, at the expense of lower accuracy in species identification. The latter point means that in the DC data more noise counts may be attributed to ions and that more real ion events may be attributed to the wrong ions. The TC data has the opposite properties: species identification is more accurate, but statistics are lower. This is particularly true for observations made in the solar wind, where the flux of suprathermal particles is low enough under nominal solar wind conditions (e.g. ~440 km/s speeds) that there can very few TC counts for days on end, even some scans with zero counts. For observations made in the Earth's magnetosphere, especially the central plasma sheet, statistics, especially for protons and alphas, are usually quite good for both TC and DC data.

3 Method for assigning counts to ions

Since STICS does not measure mass and mass per charge directly, some interpretation of the measurements is required to assign individual event counts to particular ions. Full ion event words are accumulated for each E/q scan then assigned to individual ions via an inversion method, which preserves the statistical properties of the measurements (Gruesbeck, 2013). After assignment, these counts vs. E/Q arrays are transformed to distribution functions in units of phase space density (s^3/km^6) as a function of velocity.

This inversion/identification method is applied separately to the TC and DC data, since they have different parameters. Figure 3 (top) shows STICS TC measurements for a

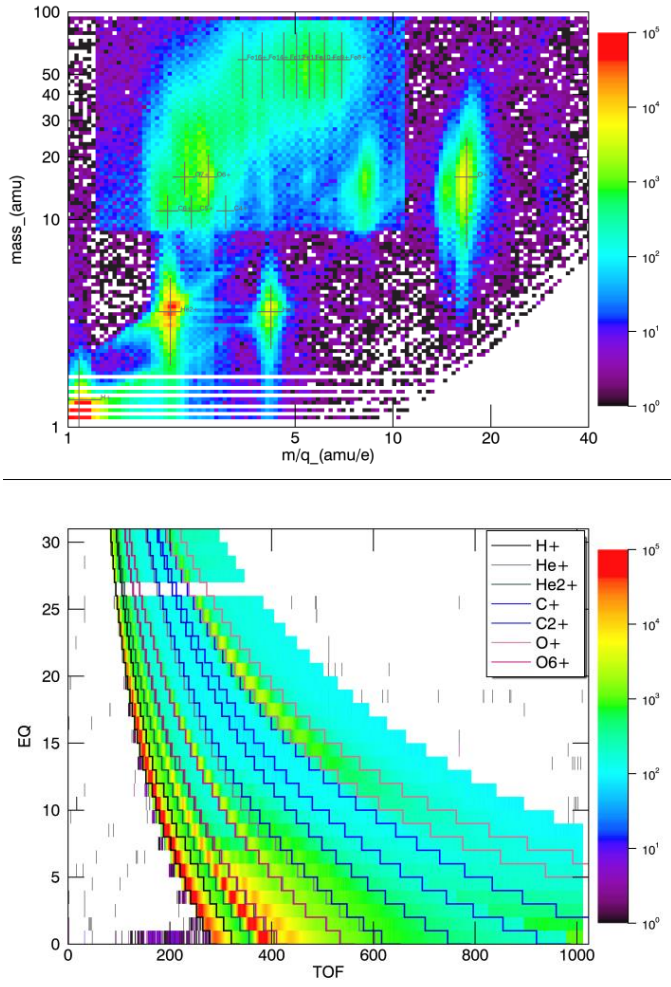

Figure 3. (top) STICS triple coincidence (TC) measurements for a single E/q step. Forward model positions for identified ions are indicated at black crosses. (bottom) STICS DC measurements with forward model tracks for indentified ions as colored curves.

single E/q step, with forward model positions for identified ions marked. This histogram of counts in energy – TOF space is known as an E-T slice. The TC inversion is applied independently for each E-T slice. Figure 3 (bottom) shows STICS DC measurements in E/q-TOF space. Different ion species group along curvesthat are then delineated into different species regions marked by the stair stepped lines, often called "tracks". The boundaries for each ion species are shown in the legend in Figure 3.

Though this analysis procedure is applicable to a wide range of ions, each requires independent validation to ensure usability for science. Users interested in ions shown in Figure 3 but not yet included in the public data release should contact the instrument team. More details can be found in Gruesbeck (2013).

4 Data Description

This dataset contains several different products for a range of ions. Work is ongoing to define, validate and release additional ion species. The current version includes the following ions:

TC: H+, He+, He2+, C5+, O+, O6+, and Fe10+.
DC: H+, He+, He2+, O+, O6+

The data is separated based on whether the measurements were accumulated in the magnetosphere (until 2004) or in the solar wind (full mission) using the Wind bow shock crossing list, https://wind.nasa.gov/mfi/bow_shock.html.

All data in this release is in the native STICS 3-minute time resolution. Users can build larger accumulations by simply accumulating over multiple time steps.

Values that cannot be properly calculated are filled with a value of -1.0 or left as 'nan' (not a number).

4.1 Velocity Distribution Functions (VDFs)

Velocity distribution functions (VDFs) provide the most information about a particular measured ion, separated by E/q, elevation angle and azimuthal angle bins at native resolution. Velocity space represents three of the six dimensions in phase space, the three velocity dimensions, as they are observed at one point in space. The three position coordinates can be retrieved from the Wind spacecraft orbit and attitude data from Space Physics Data Facility (SPDF).

The VDF files contain 3D velocity distribution functions in three units: phase space density, differential number flux and counts. There are 512 values for A(v) for each time step, corresponding to each directional sector (values 0-15 as shown above for a total of 16 look directions) and each Deflection Voltage Step (DVS) corresponding to a fixed E/q value (32 total voltage steps per sector). Subsequent time steps follow the same pattern.

Error values are based on counting/statistical error, √N/N, where N is the number of counts in a given step, propagated through the moment calculations.

The columns in these files are as follows:

Column	*Description*
Epoch	Time start of average interval (ms).
DF_dc_{ion}	(DC) 3D VDF in phase space density (s^3/km^6).
DF_error_dc_{ion}	(DC) Statistical VDF Error (s^3/km^6).
counts_dc_{ion}	(DC) 3D VDF in counts.
Counts_error_dc_{ion}	(DC) Statistical VDF Error, estimated assuming Poisson statistics.
dJ_dc_{ion}	(DC) 3D VDF in differential flux, dJ/dE $(cm^2\ s\ sr\ eV/eV)^{-1}$.
dJ__error_dc_{ion}	(DC) Statistical VDF Error in differential flux $(cm^2\ s\ sr\ eV/eV)^{-1}$.
DF_tc_{ion}	(TC) 3D VDF in in phase space density (s^3/km^6).
DF_error_tc_{ion}	(TC) Statistical VDF Error, in phase space density (s^3/km^6).
counts_tc_{ion}	(TC) 3D VDF in counts
counts_error_tc_{ion}	(TC) Statistical VDF Error, estimated assuming Poisson statistics.
dJ_tc_{ion}	(TC) 3D VDF in differential flux, dJ/dE $(cm^2\ s\ sr\ eV/eV)^{-1}$.
dJ__error_tc_{ion}	(TC) Statistical VDF Error in differential flux $(cm^2\ s\ sr\ eV/eV)^{-1}$.
eoq	Energy per charge (keV/e), 32 steps in total
SECTOR_labl	Sector labels provide the string 'Sector {index} {angle} deg' with quantities in brackets drawn from the sector variables described below. (See Figure 2)
SECTOR_index	Natural number referencing sectors (1-16).
SECTOR_angle	Center angle within each 22.5° wide sector (°).
SECTOR_number	List index referencing sectors (0-15).
Telescope_Labl	Telescope labels provide the string 'Telescope {index} ±{angle}deg' with quantities in brackets drawn from the telescope variables described below. (see Figure 2)
TELESCOPE_index	Natural number referencing the telescope (1-3).
TELESCOPE_angle	Center angle within the 53° wide telescope view {-53°, 0°, 53°}.
Telescope_number	List index referencing the telescope (1-3).
STEP_index	Step index used to identify the energy per charge step of each cycle (1-32).
delT	Accumulation time, 184 sec per scan.

Variables including '{ion}' are included for each individual ion delivered, e.g. counts_dc_he2 for He2+. To allow for future expansion without making extensive changes to the CDF format, placeholders for many additional ions are included. Ions not listed in this document (above) have not yet been delivered and will have only fill values.

4.2 Moments

Density and mean value of the energy distribution are provided to facilitate *browsing of the data*.
Due to the lower collecting power (geometric factor) of the instrument and the lower density of suprathermal tails (in both the solar wind and magnetosphere), STICS data values are often zero. Times with available data can be easily identified by their non-zero or non-fill density values. Searching through many days or years of data using the VDFs is complicated by the fact that the files are large in size (even when counts are low / zero), so that loading large ranges takes substantial computer memory and time. The moments, in contrast, are very small files so that years of data can easily be loaded and analyzed for periods of potential interest. Once identified, VDFs for these periods can can be studied in detail.

Density (0^{th} moment) and the mean value of the energy distribution (1^{st} moment) are the most appropriate moments for suprathermal ions as they do not assume any form of the distribution function, but simply provide a measure of its properties. They are formed by integrating the VDF over all three dimensions, E/q, elevation angle and azimuthal angle.

The columns in these files are as follows:

Column	*Description*
Epoch	Time start of average interval (ms)
n_dc_{ion}	Ion double coincidence number density (cm^{-3}).
n_err_dc_{ion}	Error in ion double coincidence number density assuming Poisson statistics (cm^{-3}).
E_ave_dc_{ion}	Ion mean double coincidence energy (keV)
E_ave_err_dc_{ion}	Error in ion mean double coincidence energy (keV).
n_tc_{ion}	Ion triple coincidence number density (cm^{-3}).
n_err_tc_{ion}	Error in ion triple coincidence number density assuming Poisson statistics (cm^{-3}).
E_ave_tc_{ion}	Ion mean triple coincidence energy (keV)
E_ave_err_tc_{ion}	Error in ion mean triple coincidence energy (keV).
V_dc_{ion}	Not used. Preserved for compatibility.
V_err_dc_{ion}	Not used. Preserved for compatibility.
V_tc_{ion}	Not used. Preserved for compatibility.
V_err_tc_{ion}	Not used. Preserved for compatibility.
DelT	Time difference since last time step (sec).

4.3 Angular Flux Maps (AFMs)

Angular Flux Maps (AFMs) give the flow direction of the measured plasma divided into 48 velocity vector components ranging over sixteen azimuthal sectors and three elevation bins . AFMs are formed by integrating the VDFs over E/q. Experience has shown that it is often easier to identify flow directions in this representation, since statistics are improved by integration over energy and since they are suited to 2D visualizations (such as Molleweide projections) which are intuitive to interpret. These are presented in the Geocentric Solar Ecliptic (GSE) coordinate system.

The columns in these files are as follows:

Column	*Description*
Epoch	Time start of average interval (ms).
AFM_dc_{ion}	(DC) Angular flux map of ion flux values for a given direction (cm^2 sr s)$^{-1}$.
AFM_tc_{ion]	(TC) Angular flux map of ion flux values for a given direction (cm^2 sr s)$^{-1}$.
SECTOR_index	Sectors are swept out by the spacecraft's spin motion within the ecliptic plane (see Figure 2). Sector numbers provide a natural number reference to the sector (1-16).
TELESCOPE_index	Three telescopes divide the 159° latitudinal coverage centered upon and ranging above and below the ecliptic plane (see Figure 2). Telescope index is the natural number referencing the telescope (1-3).
Telescope_Labl	Telescope labels provide the string 'Telescope {index} ±{angle}deg' with quantities in brackets drawn from the telescope variables described above and telescope angles {-53°, 0°, 53°}.

4.4 Energy-resolved pitch-angle distributions (ERPAs)

Energy-resolved pitch-angle distributions (ERPAs) organize the data by the angle relative to the magnetic field vector direction, in 7.5 degree bins. The energy separation is preserved at the native resolution of the E/q bins. Magnetic field data is from the Wind/MFI instrument. These are presented in the Geocentric Solar Ecliptic (GSE) coordinate system.

The columns in these files are as follows:

Column	*Description*
Epoch	Time start of average interval (ms).
ERPA_dc_{ion}	(DC) Energy-resolved pitch-angle distributions (s^3/km^6).
ERPA_tc_{ion}	(TC) Energy-resolved pitch-angle distributions (s^3/km^6).
SECTOR_angle	Sector angle.
SECTOR_index	Sector index.
PA 0-11	(TC) Phase space density in s^3/km^6 separated by pitch angle bin, 0-11, each 15 degrees wide. PA 0 is a 0-degree angle from the magnetic field.

5 File Naming Convention

There are two primary methods for downloading STICS data from the CDAWeb interface. The first method is to download the original daily comprehensive data files containing information on all available variables offered for a given data product. The second method for downloading data generates a single file covering a prescribed

temporal range containing data limited to a list of variables chosen by the user. The files are named as follows:

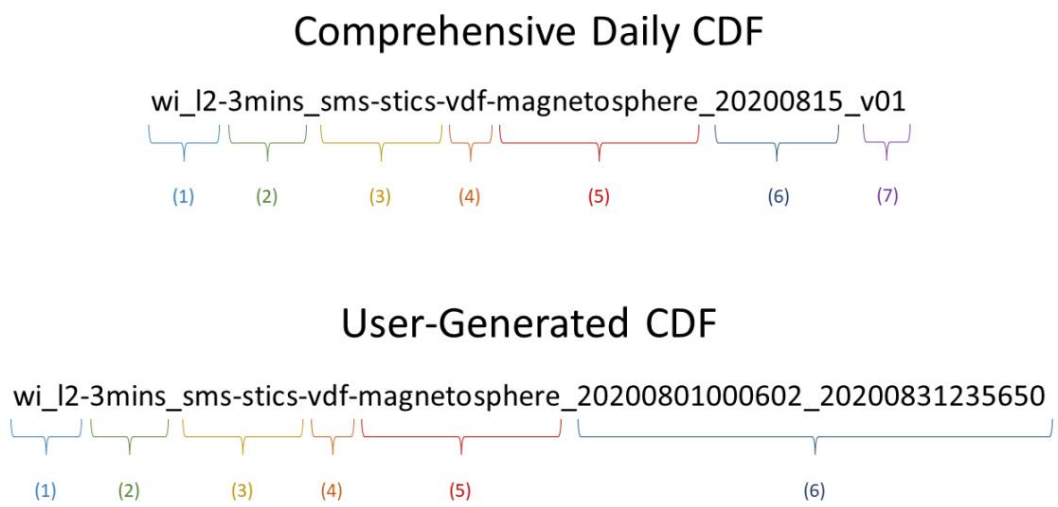

1. Mission and data level: We use the string 'wi_l2' to signify the type of data.
2. Cadence: The time interval between data values is three minutes.
3. Instrumentation: This file contains data from SMS suite's STICS instrument.
4. Data product: These are 3D velocity distribution functions ('vdf').
5. Region: This data was taken in the solar wind.
6. Time range: The filenames include the date of the observations, in yyyymmdd format. For the original daily files this comprises the date observations were made whereas user-generated files describe the range of time for which the data is provided. For example, measurements in the above files were collected on 15 August 2020 (comprehensive daily) and between 01 August 2020 and 31 August 2020. The first date is the start date; the second one is the stop date.
7. The version of the original daily data.

The files following the new naming convention files replace older versions, named wtdcLV2_distfunc*.dat wtlv2_deliv_distfunc*.dat files. Improvements in our analysis techniques have led to the latest release.

6 Calibration Notes

STICS was calibrated with an ion beam prior to launch at both NASA GSFC and at the University of Bern in Switzerland (facility details can be found in Ghielmetti et al.,1983). Goddard tests included measuring the instrument response to H+, He+, C+, C2+, N+, N2+, O2+, and Ne2+. Beam measurements at Bern included H+, He+, C+, O+, Ne+, Ne3+, Ar4+, and Kr5+. Post-launch, STICS was cross calibrated with helium solar wind data from Wind/MASS and Wind/EPACT-STEP. The Time-of-Flight efficiencies were

compared with those on Geotail/EPIC-STICS (heritage) and Ulysses/SWICS, which made similar measurements to Wind/STICS under 85 keV/e.

Further SMS calibration details can be found in Chotoo, 1998.

7 Contacts

For science questions relating to STICS, contact Sue Lepri (slepri@umich.edu), SMS Principal Investigator. For data and instrument operations questions, contact Jim Raines (jraines@umich.edu), SMS Instrument Scientist.

8 References

Gloeckler, G., et al. (1992), The Solar Wind Ion Composition Spectrometer, Astronomy and Astrophysics Supplement Series, 92, 267-289

Gloeckler, G. et. al., "The Solar Wind and Suprathermal Ion Composition Investigation on the WIND Spacecraft", Space Science Reviews, 71, p79-124, 1995.

Ghielmetti, A. G., et al., Calibration System for Satellite and Rocket-borne Ion Mass Spectrometers in the Energy Range from 5 eV/charge to 100keV/charge, Rev. Sci. Instr., 54(5), 425-436, 1983.

Chotoo, K., Measurements of H+, He2+, He+ in Corotating Interaction Regions at 1 AU, PhD Thesis, 1998.

Gruesbeck, J. R., Exploring the origin of coronal mass ejection plasma from in situ observations of ionic charge state composition, Ph.D. Thesis, 2013.

9 Revision History

Rev	Date	Author(s)	Description
	04Dec2007	JMR/STL	Initial writing.
A	18Dec2007	STL	Addition of calibration notes.
B	01Apr2010	STL/JMR	Release of double coincidence measurements.
C	10May2018	JMR/STL	Release of new data version and file format.
D	01Jun2019	JMR/STL	Release of additional data products (moments, AFM and ERPA) as well as heavy ions.
E	05Jul2022	TJE/JMR/STL	Updated to match new CDF files. Improved discussion of TC and DC data. Minor corrections made elsewhere.

13 *Wind* SWE Electrons

This section will include notes from the SWE electron sensors accumulated by the team to be used in conjunction with the SWE electron software [*Wilson III et al.*, 2021c].

13.1 SWE VEIS and Strahl Data Product Notes

WGGS

An Interactive Solar WIND/SWE Data Analysis Tool
(Completed new-mode modifications: 03/12/2004)

Richard J. Fitzenreiter
Interplanetary Physics Branch
Laboratory for Extraterrestrial Physics

Matt Holland
Advanced Data Management and Analysis Branch
Information Systems Division

Goddard Space Flight Center
Greenbelt, Maryland 20771

Contents

Chapter 1. Introduction

1a. Overview.

WGGS is an interactive software tool designed to facilitate the analysis of solar wind data from a variety of experiments. The tool utilizes widget interfaces and was originally intended for the analysis of experimental data from the ISTP Global Geospace (GGS) mission spacecraft, WIND and POLAR. Hence, the acronym WGGS. The tool provides access and display capability for multiple and diverse data sets on a common time scale and is not limited to any particular spacecraft or experiment. The tool is written in the IDL language and consists of analysis procedures interactively executed through the widget interfaces. It has the flexibility to simultaneously display and analyze data sets with different time scales. The time scales may range from multiday survey plots down to the highest time resolution detailed data. For example, 3sec electron velocity distribution function data can be viewed and analyzed in conjunction with 24 hour plots of electron plasma parameters such as density and temperature. The tool can be readily adapted to include new and specialized analysis modules as well as new data sets. All WIND/SWE data processing is also performed within the tool environment as outlined in Chapter 4.

Use of the interactive part of the tool begins with the main widget interface which accesses data and then displays the data versus time in panels stacked one upon the other. The data displayed in these plots are referred to as survey data and this widget interface is referred to as the *Survey Data Display*, which provides entry to the other tool functions, including the level zero data interfaces, which are additional, specialized widget interfaces to access and display the high time resolution data which may complement the survey data being displayed.

1b. How to use this document.

This document is intended to be read as the tool is being used. Chapters 2 and 3 are in tutorial form with specific instructions for commands to enter and buttons to push in the widget interfaces. This hands-on approach should facilitate learning the tool much faster than simply referring the reader to figures of widget buttons on paper. It is important therefore to follow the tool-use instructions exactly in the tutorial that follows. The widget interfaces covered by the tutorial have **HELP** buttons which bring up on-line documentation which also appears in Appendices 2 and 3. More detailed information about the tool functions are found in Appendices 4 - 7. Appendix 1 contains essential information on starting the tool and tailoring the startup file to the user's machine.

This document is also intended to be an overview of the SWE data processing methods and procedures associated with the conversion of SWE level zero data to the final data products accessed by the WGGS tool. The very important Chapter 4 provides an overview of the data processing system as well as instructions on maintaining the input level zero data and the final survey data files. Appendix 9 contains bar charts of the completed processed data coverage for the period 1995 – 2002.

Chapter 2. How to use the Survey Data Display: Tutorial.

In order to provide hands-on experience to a new user, the reader should now run the following tutorial session.

First, install the latest version of the WGGS tool, wggs00/ (where 00 designates version number), and the companion directory, wggs_tutor/, on the user machine directory from which you wish to run the tool. The directories wggs00/ and wggs_tutor/ can be found as tar files on the ftp site of machine leprjf:ftp/pub/exports/. Secondly, in file wggs_tutor/startup.pro, edit two lines at the beginning of the file, entering the name of the current version name of the tool, and the full path to the tool location. The lines to be edited for the user's particular machine in file wggs_tutor/startup.pro are

```
wggs_version  = 'wggs10'          ; name of current version of the WGGS tool
wggs_dir = '/export/home/rjf/'    ; path name of directory of wggs_version
```

Then follow these instructions:

1. cd to the directory in which wggs00/ and wggs_tutor/ are located and initiate an IDL session as follows:

   % *idl wggs_tutor/startup*

2. The WGGS tool is started by typing at the IDL prompt:

   IDL> *wanal*

   which brings up the main *Survey Data Display*.
   IMPORTANT: Position the *Survey Data Display* in the upper part of the screen and the command window used to start the tool at the bottom of the screen so that part of the command window can be seen at all times.

The set of instructions which follow are user actions on widgets in the *Survey Data Display:*

3. Type 19990510 in **yyyymmdd** field. (Data for this date are included in wggs_tutor/).
4. Click **swe_moments** and **swe_fpitch** in data types box.
5. Click **READ**
6. In pop-up widget, *click N density, T temperature, U flow speed, A anisotropy, Q heat flux, th_q, ph_q, B magnetic field, th_b, ph_b, cos(Q.B), Spin avg f(en,t), 94.3*
7. Click **Save 0**
8. Click **Plot 0** (Selected plot variables are plotted in stacked panels.)
9. Click left mouse button at any time on any plot panel.
10. Click middle mouse button at any *later* time.
11. In pop-up widget, click **Plot**. (The selected time interval is plotted.)

12. Click 5 in **Smooth** droplist widget. (Median smoothing.)
13. Click 0 in **Smooth** droplist widget.
14. Click **Minmax** in **Y-axis** droplist widget. (Y scale range changes to minmax.)
15. Click **Preset** in **Y-axis** droplist widget.
16. Click **On** in **Time mark** droplist widget.
17. Click left mouse button on plot panel. (Vertical line is plotted at selected time.)
18. Click **Off** in **Time mark** droplist widget.
19. Click left mouse button on plot panel. (No new vertical time mark line is plotted.)
20. Click **Remove** button. (Vertical time mark lines disappear.)
21. Click **Previous** in Time interval button set. (Previous time interval plotted.)
22. Click **Current** in Time interval button set. (Last time interval selected by mouse.)
23. Click **Original** in Time interval button set. (Original time interval is plotted.)
24. Click **Current** in Time interval button set. (Original has become current interval.)
25. Click 3 in **Nr days** droplist widget.
26. Click **swe_moments, swe_fpitch, and swe_strahl** in data types box.
27. Click **READ**. (Reading **swe_strahl** data will take a little longer than other types.)
28. In pop-up widget, click *strahl energy spectrum*, *strl_max_cts, strl_widthmx, 251, N density, B magnetic field, th_b, ph_b.*
29. Click **Save 1**.
30. Click **Plot 1** (Selected plot variables are plotted in stacked panels.)
31. Click 3 in **Smooth** droplist widget. (Removing noise pixcel changes color scale.)
32. Click **Quit** (Survey Data Display interface disappears and IDL prompt appears..)
33. Type *wanal* at the IDL prompt (Survey Data Display interface reappears.)
34. Click **Current** (Last plot reappears.)

A more detailed description of the *Survey Data Display* can be accessed by clicking on the **HELP** button. The on-line HELP documentation can also be found in Appendix 2.

Chapter 3. How to use the SWE Level Zero Data Interface: Tutorial.

3a. VEIS distribution function plots.

The tutorial continues in this section with access of the *SWE LZ Data Display* interface from the *Survey Data Display* in which survey data is plotted. SWE data is used in this tutorial, but any type of survey data that overlaps the time for which level zero data is desired may be used. The starting point for this part of the tutorial is step 34 of the previous section.

35. Click on the **SWE level zero** button of the *Survey Data Display* interface. (The *SWE LZ Data Display* interface appears with the *strahl energy spectrum* color image from the *Survey Data Display* plotted in the top panel.)
36. Click **Parent** to return to *Survey Data Display*.
37. Click **SWE levelzero** on *Survey Data Display* to return to *SWE LZ Data Display*.
38. Click on **Strahl** from the droplist (first widget, second row). (The strahl line plot replaces the strahl image in the top panel.)

39. Click on 19950511 in the date droplist (fourth widget, first row.)
40. Click **Open LZ**. (See Chapter 4a for details on the result of this action.)

Steps 41 – 46 are the various ways to select a time for a distribution function plot:

41. Click left mouse button on top panel at any time of date, 19950511.
    (Default plot, f contours and f cuts, appears in one lower plot windows.)
42. Click + and/or – buttons of the **Spin** group (second row).
    (Distributions appear sequentialy in lower three plot windows with each click.)
43. Click **auto** in **Spin** group. (Three consecutive plots appear.)
44. Click + and/or – buttons of the **Mfrm** group. (Increments major frame.)
45. Type 300 in **Mfrm**, hit return, then click in any of three windows. (Selecting mjf.)
46. Type 024850 in **hhmmss** field, hit return, then click in window. (Selecting time.)

47. Select each plot type in the droplist (third widget from the right, second row), clicking in a plot window after each selection to see the plot.
48. Select default plot type **f fcuts** and click in a plot window.
49. Click 10 in **vstps** droplist (second widget from right, second row) and click in a plot window.
50. Click 16 in **vstps** droplist (second widget from right, second row) and click in a plot window.
51. Click 3 in **pbin** droplist (last widget on right, second row) and click in plot window.
52. Click 15 in **pbin** droplist and click in plot window.
53. Click 9 (default) in **pbin** droplist and click in plot window

When a VEIS distribution function is plotted, then the VEIS raw counts spectrum and the STRAHL sensor data for the selected major frame and spin may also be displayed. Clicking on the **Veis data** brings up another widget interface, *SWE Veis Counts Data*, in which the VEIS raw counts are plotted vs electron speed. The *SWE Veis Counts Data* interface also provides various diagnostic and calibration functions on the data and which are explained Chapter 3b. Clicking on the **Strahl data** button brings up yet another widget interface, *SWE Strahl Counts Data*, which is described in Chapter 3c. The use and function of all the widget buttons in the *SWE LZ Data Display* are explained by clicking on the ***HELP*** button and also in described in Appendix 3.

3b. VEIS raw data counts spectra.

The tutorial continues with the *SWE Veis Counts Data* interface. The starting point is step 53 of the last section in the *SWE LZ Data Display.*

54. Click left mouse button on top panel at any time of date, 19950511 in the *SWE LZ Data Display*.
55. Click on the **Veis data** button which brings up the *SWE Veis Counts Data* interface. (Default plot of raw electron counts vs electron velocity step is displayed. Sun glint points are highlighted but are eliminated in final distribution function plots and in creation of daily moments and pitch angle files.)

56. Click (in turn) on buttons **Cts_sector, Cts_phi,** and **Cts_pitch**. (Raw data counts are plotted vs sector, sun phase angle, and pitch angle, respectively, at a single velocity step.)
57. Click on **Vstep** + or – to increment velocity step for any of the plots selected in previous step.
58. Click on **Spin** + or – to increment spin (seven spins per major frame).
59. Click on **Mfrm** + or – to increment major frame (major frame = record).
60. Click on **Sect** + or – .(No effect for plots of counts vs sector, sun phase angle, or pitch angle.)
61. Click **Det angles. (**Plots VEIS look angles phi (azimuth) and theta (elevation), and velocity sweep steps during one 3s spacecraft rotation.)
62. Click (in turn) **Cts_phi all steps** and **Cts_sun all steps.** (Plots raw counts for all velocity steps vs azimuthal look angle, phi, and vs sun phase angle, respectively.)
63. Click **Cts_step (def).** (Plots raw counts.)
64. Click **Cts_step /correctd**. (Plots counts corrected for relative gain factors, removal of sun glint samples, and background adjustments.)
65. Click **f_step.** (Plots phase density converted from corrected counts.)
66. Click **f w/ patch, scpot**. (Plots distribution function with Adolfo Vinas fitted 3D gaussian patch over thermal core using coefficients from moments file which also corrects for spacraft potential.)
67. Click **f w/ new patch**. (Same as previous step except fitted patch coefficients are computed on-line.)
68. Click **Cts_step (def)**. (returns to default plot.)
69. Click **Sect** + six times and observe the spin count advance.
70. Click **Spin** + seven times and observe the major frame count advance.
71. Click **Mfrm** + and observe the major frame count advance
72. Click on **Parent** to bring forward the *SWE LZ Data Display*.
73. Click on **Veis data** which brings back the *SWE Veis Counts Data* interface.
74. Click on **Parent** to return to the *SWE LZ Data Display*.

3c. Strahl electron distribution data display.

The tutorial continues with the *SWE Strahl Counts Data* interface. The starting point is step 74 of the last section in the *SWE LZ Data Display.*

75. Enter 112 in the **Mfrm** widget field in the *SWE LZ Data Display* and hit Return (keyboard).
76. Click in one of the three lower plot windows.
77. Increment **Spin** + or – to 1.
78. Click **Strahl data.** (SWE *Strahl Counts Data* interface appears with STRAHL image at 154 eV.)
79. Click (in turn) **Counts vs phi, f vs phi,** and **Count vs pa, f vs pa** ,where pa = pitch angle. (These plots are for strahl detectors 0 2 4 6 8 10.)
80. Click the **1 3 5 7 9 11** button and repeat the previous step.
81. Click **f vs pa (all detectors)**.

82. Click **Counts vs phi index**.
83. Click **Compare strahl & veis**.
84. Click **Increment spin** + or – and watch **Spin** field change and plot at next energy appear.
85. Click **f(phi, theta) (def)** .
86. Click **Search for current strahl step** + or **-** . (The next occurrence of major frame and spin with the same energy step as the current one is plotted.)
87. Enter 209 in the **Increment recn** field and hit Return. (Strahl image should appear with Sun showing as intense image at 180 degrees.)
88. Toggle **Sun mask** button and watch strahl appear when Sun mask is **On**.
89. Click on **Parent** return to *SWE LZ Data Display*.
90. Click **Strahl data** in *SWE LZ Data Display* to bring back SWE *Strahl Counts Data* interface.

This ends the tutorial.

Chapter 4. SWE Electron Data Processing in the WGGS Environment.

4a. Converting level zero data to distribution functions.

This section outlines the data processing steps performed by the WGGS tool in converting the raw level zero data into VEIS and STRAHL distribution function plots. When a level zero file is opened by clicking on the **Open LZ** button in te *SWE LZ Data Display*, procedure lzinput.pro is called which reads or makes available the following:

1. lzinput.pro
   a.) telemetry index map which unpacks the science and housekeeping data blocks from the level zero data file;
   b.) spin phase look angles of each detector, energy step, and sector and the corresponding unit vectors;
   c.) relative gains for the set of six detectors for the current date;
   d.) definition of swest.patch_include(n_vdets,n_sectors,n_vesteps), which determines which detector, sector, and energy steps are to be omitted (in cases of very low or unreliable detector response) from the calculation of the A. Vinas' gaussian patch over the core of the distribution function (see documentation in lzinput.pro);
   e.) magnetic field data for the entire day from the MFI experiment (first preference is 3s data, which if not available, then key parameter data used);
   f.) WIND orbit and attitude data for the entire day;
   g.) SWE ion key parameter data for the entire day;
   h.) level zero file header for the current day;
   i.) which science mode (determined by reading the first level zero record);
   j.) background counts data file (only for dates prior to 26 October, 1997);
   k.) sun glint map appropriate for the current date.

Each time a VEIS or STRAHL data plot is made, raw data corresponding to the selected input time is unpacked from the levelzero file record and converted to the appropriate plot variables. Selecting a time by any of the various methods described in the previous section (e.g., clicking on a plot window, etc) initiates execution of the following sequence of procedures:

2. proc_fw.pro :
    a.) The selected levelzero file major frame and spin number are determined from the selected input time (there are seven spin blocks of data per major frame; the terms major frame and level zero record are used interchangeably).
    b.) The procedure proc_rec.pro unpacks the selected major frame of data from the level zero file and stores the VEIS and STRAHL data in the structure, *vsmjf*, as described below in Cahapter 4b.
    c.) The magnetic field data is obtained for the selected time.
    d.) The VEIS distribution function array, *fblk(ndets, nvsteps, nsectors)*, for the selected time is formed, where *ndets* = number of detectors, *nvsteps* = number of velocity steps, *nsectors* = number of sectors. The gaussian patch over the thermal core of the electron distribution function is determined (using a method by Adolfo Vinas).
    e.) The procedure fparr.pro prepares the data for display, such as contouring.
    f.) The procedure do_lzplot.pro calls the actual plot procedures.

3. proc_rec.pro
    a.) The selected major frame (containing seven spins) is read. Since only one spin per major frame is time-tagged, the next major frame is also read for the purpose of computing spin period using the number of spacecraft rotations between time tags.
    b.) The science mode of the instrument is determined for the selected record.
    c.) The unpacking of the selected major frame of level zero data is done by procedure mode1.pro for science mode = 1 and science mode = 4, and by procedure mode6.pro for science mode = 6 in which the data structure, *vsmjf*, is formed. Data structure *vsmjf* contains the selected major frame (seven spins) of unpacked levelzero data in both raw counts and phase density form, as well as necessary conversion and calibration data, and is described in Chapter 4b.

4b. Description of the Level Zero Data Structure, *vsmjf*.

The structure *vsmjf* is defined in the procedure wggs00/swelz/mode1.pro or wggs00/swelz/mode6.pro, depending on science mode, and contains all the raw data counts, the converted phase densities, and the instrument conversion factors for a single major frame of data, which is seven spacecraft rotations. Also included are the sweep energy steps and phase angles for all data samples. The structure *vsmjf* is shared with other program elements through the *common* statement (given below) and the

help,vsmjf,/str describes the tags to *vsmjf*. Detailed information can be found in the documentation included in the programs, mode1.pro or mode6.pro.

```
IDL> common lzstuff,lzfile,lundat,recn,fh,lz,ihk,sp,vsmjf,veis_hvtbl
IDL> help,vsmjf
VSMJF (LZSTUFF) STRUCT    = -> <Anonymous> Array[1]
IDL> help,vsmjf,/str
** Structure <801850>, 68 tags, length=322936, refs=1:
   DESCR           STRING    'veis-strahl data samples'
   TJD             LONG              1308
   SEC             DOUBLE          79860.701
   HOUR            LONG              22
   MIN             LONG              11
   ISEC            LONG              0
   MS              INT           701
   MJFCNT          LONG              216
   SCIMODE         INT               6
   SPINP           DOUBLE          3.0630667
   N_VDETS         LONG              6
   N_VESTEPS       LONG              16
   N_SECTORS       LONG              6
   N_SPINS         LONG              7
   N_STRDETS       LONG              12
   N_STRPHIS       LONG              28
   DELTASP         DOUBLE       0.0097656250
   DEADTIM_ELE     DOUBLE          0.0000000
   DEADTIM_ION     DOUBLE          0.0000000
   DELT_ELE        DOUBLE        0.025912760
   DELT_ION        DOUBLE        0.025912760
   GEOMF           FLOAT     Array[6]
   LZRECN          LONG              870
   VEIS            INT       Array[6, 16, 6, 7]
   VEIS_B          FLOAT     Array[6, 16, 6, 7]
   CVEIS           FLOAT     Array[6, 16, 6, 7]
   CVEIS_B         FLOAT     Array[6, 16, 6, 7]
   FVEIS           FLOAT     Array[6, 16, 6, 7]
   FVEIS_B         FLOAT     Array[6, 16, 6, 7]
   VEISTEP         BYTE      Array[16, 7]
   ELEION_SWEEP    INT       Array[7]
   ELEION          INT       Array[7]
   ALTSPIN_ENABLED INT       Array[7]
   PRIMALT_TBL     INT       Array[7]
   SECVEIS         DOUBLE    Array[16, 6, 7]
   PHIVEIS         DOUBLE    Array[6, 16, 6, 7]
   THEVEIS         DOUBLE    Array[6]
   VUNIT           DOUBLE    Array[6, 16, 6, 3, 7]
   STRL            BYTE      Array[12, 28, 7]
   FSTRL           FLOAT     Array[12, 28, 7]
   STRLSTEP        BYTE      Array[7]
   NUMSTRLSTPS     INT           32
   IBCI_STRL       INT       Array[28, 7]
   SECSTRL         DOUBLE    Array[28, 7]
   PHISTRL         DOUBLE    Array[28, 7]
   THESTRL         DOUBLE    Array[12]
   VUNITSTRL       DOUBLE    Array[12, 28, 3, 7]
```

```
BXYZ_STATUS     BYTE      Array[7]
BXYZ_IND        BYTE      Array[7]
BXYZ_RANGE      INT       Array[7]
BXYZ_PHASE      INT       Array[7]
BXYZ_BX         INT       Array[7]
BXYZ_BY         INT       Array[7]
BXYZ_BZ         INT       Array[7]
SUNSEC_VSBL     DOUBLE    Array[7]
SUNTIM_VSBL     DOUBLE    Array[7]
PB5TIM_VSBL     LONG      Array[3, 7]
VQLTY           LONG      Array[7]
SQLTY           LONG      Array[7]
XVEIS           INT       Array[6, 16, 6, 7]
RELGAIN         FLOAT     Array[6]
BDATE           STRING    '00000000'
BCTS            FLOAT     Array[6, 16, 6, 7]
RELGAIN_BACKG   FLOAT     Array[6]
CTS_FACTOR      FLOAT     Array[6, 16, 7]
STRL_CTS_FACTOR FLOAT     Array[12, 7]
BACKGROUND_TEST INT           0
SET_DET2_EQ_DET3  INT       =       0
```

4c. Creation and storage of daily survey files of electron moments, strahl detector data, and electron pitch angle distributions.

The end product of SWE data processing consists of 1) daily survey files, such as moments, VEIS pitch angle distributions, and STRAHL data versus time, which are displayed by the WGGS tool as described in Chapter 2, and 2) detailed distribution function data collected over a single 3s spacecraft rotation which are processed and displayed directly from the raw level zero data as described in Chapter 3. While distribution function data are processed and displayed interactively using the WGGS tool, the survey data files are created in a batch mode in the WGGS tool environment. Both interactively plotted distributuions and daily survey plots both use the same analyses and tool procedures described in Chapter 4a to form the data structure, *vsmjf,* described in Chapter 4b, on which both data products are based.

These are the steps to follow in creating the daily survey files from level zero data files:

1) Start an IDL session using wggs_startup.pro as described in Appendix 1.

% *idl wggs_startup*

2) Run the procedure

IDL> .r *lzdates_to_process*

and follow the prompts. The program lzdates_to_process.pro does the following:

a) reads the dates of the levelzero files in the *swe_levelzero* data path that you specify in the pop-up widget that appears;
b) creates a file of those dates to be processed **(for "mode7" it's the lzpitch_dates file mentioned in the "new operational-mode note" below)**;
c) prompts you to choose which type of processing and then prompts you with the name of the processing program to run, i.e., **(see below)**

moments :	*mom*	.r lzmom
pitch angle distribution at each energy:	*pitch*	.r lzpitch
strahl:	*strahl*	.r lzstrahl
60 degree pitch angle average:	*pitchavg*	.r lzpitchavg

New operational-mode (mode7) note: All "old-mode" (before mode7) data products have been **finalized** as of the printing of this WGGS documentation-version. When processing "new-mode" (mode7) data products, select the 'pitch' processing-type when running the *lzdates_to_process* procedure (or, for small processing runs, directly create/modify the lzpitch_dates file in your WGGS-registered [via startup file] sav_dir directory by listing the *yyyymmdd* values of the dates-to-process—one per line, **no extraneous characters** [headers, spaces, extra newlines, etc].) This is due to the unification of all new-mode data-product processing into a *single* processing routine (based upon the original old-mode lzpitch.pro code) called lzswenewmode.pro. After selecting the dates-to-process, simply execute:

'.r lzswenewmode' from the IDL command-line (follow prompts).

The result is a *.mom, *.pit, and *.str data-product file for each selected date.

The processing program names, the corresponding data type names, output file name extensions, and the output file data paths are as follows:

Processing program	Data type	Extension	leprjf.gsfc.nasa.gov:data path
lzmom.pro	swe_moments	.mom	/data7/swe/moments/
lzpitch.pro	swe_fpitch	.pit	/data9/swe/ptch/
lzstrahl.pro	swe_strahl	.strahl	/data8/swe/strl/
lzpitchavg.pro	swe_fparaperp	.pitavg	/data5/swe/ptchav/

New-mode (mode7) processing: (see note above)

lzswenewmode.pro	**all new-mode**	**all ext.**	**/data3/swe/<*data-type*>**

The files created by these processing programs are all saved in the subdirectory mpnew whose full path is specified in the user's startup file wggs_startup.pro. This is a temporary staging location. After processing, the files must be moved to the locations on the data server machine given by the data path names in the table above.

Each processing program listed above contains documentation and is located in subdirectory wggs00/swelz , where wggs00 is the top directory of the WGGS tool.

Data calibration files used by these programs in processing the raw counts, such as relative detector gains and sun glint maps, are included within the WGGS tool.

Other ancillary data required by one or more of these processing programs are:

Ancillary data type	Description
swe_ionkp	SWE ion key parameter density and bulk flow speed
mfi_mag3s	MFI 3s magnetic field data
mfi_magkp	MFI key parameter data (used only if 3s data unavailable)
wind_orbit	WIND spacecraft orbit and attitude data

The data paths for these ancillary data are given in the startup file wggs_startup.pro. The WGGS tool accesses the MFI data files by mounting a disk exported by MFI Co-Investigator Adam Szabo. The SWE key parameter data files, the WIND orbit and attitude files, and the SWE levelzero data files are sent electronically to the server machine leprjf.gsfc.nasa.gov each day. Periodically (approximately once each week) these files must be moved from the anonymous ftp site to their permanent location on leprjf.gsfc.nasa.gov. This is done automatically by running the following program on machine leprjf.gsfc.nasa.gov and following the program prompts:

leprjf.gsfc.nasa.gov% *idl wggs_startup*
IDL> .r *move_wind_files*

The SWE levelzero files received electronically may be removed from leprjf.gsfc.nasa.gov *only after* the CD-ROMs containing the SWE LZ data have been received and checked.

4d. Maintaining the SWE data files and processing system.

There are three critical functions that must be performed periodically.

1. A copy of the current version of the WGGS tool should be kept on the server machine leprjf.gsfc.nasa.gov as well as any other machine on which the tool is to be used. Current backups of the tool should be kept.

2. The ancillary files discussed in the previous section and the SWE levelzero files, all of which are currently sent to the anonymous ftp site on machine leprjf.gsfc.nasa.gov each day should be moved to their permanent disk location on leprjf.gsfc.nasa.gov by running the program move_wind_files.pro as discussed in the previous section.

3. Backups should be maintained of the following file systems containing SWE data and necessary ancillary data on leprjf.gsfc.nasa.gov using the DLT IV ½ inch cartridge tapes: (See next page for complete new-mode listing.)

leprjf.gsfc.nasa.gov file system	Program leprjf.gsfc.nasa.gov:/opt/local/Backup/
/data7	data7_moments_dump0
/data8	data8_strahl_dunp0
/data9	data9_pitch_dump0
/data5	**data5_swe_ancil_dump0**
/data2	**data26_dump0 (level zero data)**
/data3	**data13_dump0 (new-mode data)**

4e. Timeline of SWE instrument mode and bias level changes and other events affecting SWE electron data processing.

Date	Mode	Significant changes	
19941130 – 19950801	1		
		19950510	VEIS bias increase.
19950802 – 19950807	2		
19950808 - 19950916	1		
19950917 – 19950918	2		
19950919 – 19951127	1		
		19951121	VEIS bias increase.
19951128 – 19960125	2		
19960126 – 19960321	1		
19960322 – 19960513	2		
		19950513	VEIS bias increase.
19960514 – 19960813	1		
		19960813	VEIS bias increase.
19960814 – 19961108	2		
19961109 – 19961113	1		
19961114 – 19970114	2		
19970115 – 19971014	1		
19971015 – 19990125	4		
		19971028	VEIS detector response degrades more rapidly.
		19980514	VEIS bias increase.
		19980728	VEIS bias increase.
		19980811	VEIS bias increase.
		19981026	Lowest energy steps of detectors 0, 2 unusable; cause unknown.
		19981124	VEIS bias increase.
19990126 – 20020715		19990326	VEIS bias increase.
		19990405	VEIS bias increase.

20001023	VEIS bias increase.
20001023	STRAHL bias increase.
20011029	VEIS bias increase to highest possible level.

20011119 VEIS bias supply fails.

20020815 VEIS turned off; new STRAHL operational-mode implemented. This marks the beginning of "new-mode" (mode7) mission operation.

Chapter 5. ISEE-1 Data Access and Display with the WGGS Tool.

<No documentation yet for this partially-developed tool functionality.>

Chapter 6. SWE/Strahl New Science-mode ("mode7") in the Absence of VEIS Data.

6a. Basics of new-mode operation.

Background Facts:

1) WIND is a spinning spacecraft with a spin-period of about 3 seconds. The spin-axis is oriented in the –Z GSE direction (s/c spin-phase given in the –ϕ GSE direction). Each successive spin is assigned a successive spincount value (0-255, "rolling over" periodically) and one spin per major-frame (LZ record) recieves a time-tag reference.
2) A sun-pulse is generated by the spacecraft's on-board processor when the s/c +X-axis points at the Sun (+X GSE direction)—the absolute s/c spin-phase (= 0^o) reference.
3) A pseudo sun-pulse is then generated by the SWE DPU at a programmable angle with respect to this reference. All SWE/Strahl processing is referenced to **this** angle.
4) Each full s/c spin is divided into 4096 "clicks" of the s/c spin-phase clock. A Basic Counting Index (BCI) is defined to be 42 clicks in this mode, providing the general construct for referring collected data back to a time-and-s/c-spin-phase-angle.

The "mode7" SWE/Strahl operation is ONLY different than mode6 in the handling of Strahl and VEIS data. It does NOT constitute a new science-mode in the sense of CDHF processing of KP data or in its effect on any other instrument. In fact, the only indicator of this mode's activity is a single (unused until now) byte in one of the housekeeping blocks (described in detail below). Otherwise, the new mode represents only a rearrangement within telemetry already allocated to SWE/Strahl and SWE/VEIS.

Acculmulation of mode7 data takes place over three (ALWAYS consecutive) spins, and a total energy-spectrum consisting of 15 energy-steps is generated during these three spins. There are usually gaps of one or more spins between spectra, but the spincount values at the beginning of each spectrum (the "spincount-begin" values) are given in the header of each spectrum in the LZ record (described in detail below). Azimuth-angle coverage is provided by the spinning of the s/c; each spin divided into 8 sectors, each energy being visited exactly once in each sector. Elevation-angle coverage is provided by the fixed angular spread of the 12 (pairwise-binned into 6) strahl detectors (all having the same azimuth orientation at any given time—elevation angles given in detail below).

In the first spin of a spectrum (spincount = <spincount-begin>+0) energy steps 0-4 are repeatedly visited in each of the 8 sectors. The first BCI (BCI = 0) of sector 0 of any spin comes exactly one BCI after the SWE DPU's delayed pseudo sun-pulse. Including this BCI, sector 0 subtends 12 BCIs (as do all sectors, but with different BCI values):

Sector 0

BCI	0	1	2	3	4	5	6	7	8	9	10	11
step	S	0	S	1	S	2	S	3	S	4	S	S

Where the 'S' symbol in the 'step' row represents the settling of HV power supplies, and 0-4 on this row represent acculmulation of counts at the 5 energy steps visited in this sector. The same pattern is exactly repeated in sectors 1-7 of this spin. In the 8 sectors of spin spincount = <spincount-begin>+1 the same pattern is seen, except that steps 5-9 replace 0-4 respectively; steps 10-14 replace 0-4 in the 8 sectors of spincount = <spincount-begin>+2. This completes the acculmulation of a full energy-spectrum.

6b. Detailed specifications.

Azimuth angles:
The interpretation of strahl data requires detailed angular information. Each energy-step of each sector has a different angular position at which counts are acculmulated. Basic angular information is provided as a s/c spin-phase angle, instrument position given in payload coordinates. As mentioned above, the s/c spin-axis is aligned with the –Z GSE axis, so that spin-phase/payload angles are defined opposite to GSE conventions (but +X-axis is in the same direction either way). Hence a 180-degree rotation about the x-axis transforms "payload" spin-phase angles into GSE azimuth angles.

The following table provides **degree** measurements at the **beginning** of each BCI in a full spin (assumed to be spincount = <spincount-begin>+0—make energy-step replacements described above for the two subsequent spins), with columns to be interpreted as follows ('*' indicates counts acculmulated this BCI):

BCI: Basic Counting Index (42 clicks) begun at these angles.
SECTOR: Integer value (0-7) giving sector number for this BCI.
STEP: Integer value (0-4) giving HV step for this BCI (first spin only).
STRAHL: S/c spin-phase *look-angle* of strahl detector (payload coords.).
FLIPPED: Strahl detector *look-angle* in GSE coords. (after rotation).
VELOCITY: Strahl *particle-velocity* angles in GSE (after 180^{o} phase-shift).

BCI	SECTOR	STEP	STRAHL	FLIPPED	VELOCITY
0	0	0	200.7	159.3	339.3
1	0	0	204.4*	155.6*	335.6*
2	0	1	208.1	151.9	331.9
3	0	1	211.8*	148.2*	328.2*
4	0	2	215.5	144.5	324.5
5	0	2	219.2*	140.8*	320.8*
6	0	3	222.9	137.1	317.1
7	0	3	226.6*	133.4*	313.4*
8	0	4	230.3	129.7	309.7
9	0	4	234.0*	126.0*	306.0*
10	0	5	237.6	122.4	302.4
11	0	5	241.3	118.7	298.7
12	1	0	245.0	115.0	295.0
13	1	0	248.7*	111.3*	291.3*
14	1	1	252.4	107.6	287.6
15	1	1	256.1*	103.9*	283.9*
16	1	2	259.8	100.2	280.2
17	1	2	263.5*	96.5*	276.5*
18	1	3	267.2	92.8	272.8
19	1	3	270.9*	89.1*	269.1*
20	1	4	274.6	85.4	265.4
21	1	4	278.2*	81.8*	261.8*
22	1	5	281.9	78.1	258.1
23	1	5	285.6	74.4	254.4
24	2	0	289.3	70.7	250.7
25	2	0	293.0*	67.0*	247.0*
26	2	1	296.7	63.3	243.3
27	2	1	300.4*	59.6*	239.6*
28	2	2	304.1	55.9	235.9
29	2	2	307.8*	52.2*	232.2*
30	2	3	311.5	48.5	228.5
31	2	3	315.2*	44.8*	224.8*
32	2	4	318.9	41.1	221.1
33	2	4	322.5*	37.5*	217.5*
34	2	5	326.2	33.8	213.8
35	2	5	329.9	30.1	210.1
36	3	0	333.6	26.4	206.4
37	3	0	337.3*	22.7*	202.7*
38	3	1	341.0	19.0	199.0
39	3	1	344.7*	15.3*	195.3*
40	3	2	348.4	11.6	191.6
41	3	2	352.1*	7.9*	187.9*
42	3	3	355.8	4.2	184.2
43	3	3	359.5*	0.5*	180.5*
44	3	4	3.2	356.8	176.8
45	3	4	6.8*	353.2*	173.2*
46	3	5	10.5	349.5	169.5
47	3	5	14.2	345.8	165.8
48	4	0	17.9	342.1	162.1
49	4	0	21.6*	338.4*	158.4*
50	4	1	25.3	334.7	154.7
51	4	1	29.0*	331.0*	151.0*
52	4	2	32.7	327.3	147.3
53	4	2	36.4*	323.6*	143.6*
54	4	3	40.1	319.9	139.9
55	4	3	43.8*	316.2*	136.2*
56	4	4	47.4	312.6	132.6
57	4	4	51.1*	308.9*	128.9*
58	4	5	54.8	305.2	125.2
59	4	5	58.5	301.5	121.5
60	5	0	62.2	297.8	117.8
61	5	0	65.9*	294.1*	114.1*
62	5	1	69.6	290.4	110.4
63	5	1	73.3*	286.7*	106.7*
64	5	2	77.0	283.0	103.0
65	5	2	80.7*	279.3*	99.3*
66	5	3	84.4	275.6	95.6
67	5	3	88.1*	271.9*	91.9*
68	5	4	91.7	268.3	88.3
69	5	4	95.4*	264.6*	84.6*
70	5	5	99.1	260.9	80.9
71	5	5	102.8	257.2	77.2
72	6	0	106.5	253.5	73.5
73	6	0	110.2*	249.8*	69.8*
74	6	1	113.9	246.1	66.1
75	6	1	117.6*	242.4*	62.4*
76	6	2	121.3	238.7	58.7
77	6	2	125.0*	235.0*	55.0*
78	6	3	128.7	231.3	51.3
79	6	3	132.4*	227.6*	47.6*
80	6	4	136.0	224.0	44.0
81	6	4	139.7*	220.3*	40.3*
82	6	5	143.4	216.6	36.6
83	6	5	147.1	212.9	32.9
84	7	0	150.8	209.2	29.2
85	7	0	154.5*	205.5*	25.5*
86	7	1	158.2	201.8	21.8
87	7	1	161.9*	198.1*	18.1*
88	7	2	165.6	194.4	14.4
89	7	2	169.3*	190.7*	10.7*
90	7	3	173.0	187.0	7.0
91	7	3	176.6*	183.4*	3.4*
92	7	4	180.3	179.7	359.7
93	7	4	184.0*	176.0*	356.0*
94	7	5	187.7	172.3	352.3
95	7	5	191.4	168.6	348.6
96	8	0	195.1	164.9	344.9
97	8	0	198.8	161.2	341.2

Elevation angles:

This list of GSE *particle-velocity direction* elevation angles (given in degrees above the eccliptic plane), for particles entering the 6 "pseudo detectors" that result from pairwise-binning the counts from the 12 actual detectors, is derived by pairwise-averaging the (known and fixed) values for the 12—resulting in 6 "center-angles":

```
-26.55     -17.10      -7.34       7.63      17.10      26.53
```

(Note: not in detector-order.)

Reading new-mode strahl LZ data records:

The file, swemode7.prt, from the 'swedatlib' directory contains a "map" of offsets into an LZ record array, allowing the count value for any detector, sector, energy-step and spectrum of the new mode strahl data to be correctly located in its LZ major-frame and stored for processing. The procedure, mode7map.pro, in the same directory reads this file and stores information about where in each major-frame to locate all housekeeping, Faraday cup and strahl data. The housekeeping (except for a previously-unused field, now storing a 'mode7 indicator') and Faraday cup data are unaffected, only the information read from the new-mode telemetry map is different from previous modes. The 'mode7 indicator' is a byte which takes on the value '0' (always has in the past) when a major-frame is not in "mode7", and takes on the value '7' when in that mode.

Spincounts, time-tags and null spectra:

As described above, each s/c spin has an associated spincount value, and each major-frame has one time-tagged spin. In general, the time-tags for each spectrum are defined by incrementing (or decrementing) the tagged time by the appropriate number of (calculated) spin-periods needed to account for the difference between the current spectrum's spincount-begin value and the time-tagged spincount value. There are two types of exceptions, which are accounted for in the code:

1) There was a rollover (from 255 to 0) in the spincount values.
2) The spincount-begin value (and all of the rest of the values in the current spectrum—including the second byte from the same spectrum-header) is 255. This indicates a "null spectrum" where no counts were acculmulated (due to *in-situ* time limits).

Compressed counts to phase densities:

To convert the log-compressed strahl level-zero counts into phase densities the definitions of the 'efficiency' and 'geometry' vectors from cts_f_strl.pro were revised to account for the pairwise binning of the detector counts:

```
efficiency = [0.75926, 0.75926, 0.75926, 0.82945, 0.82945, 0.82945]
geometry  = [(4.4349 + 5.4222), (6.1882 + 6.1182), (6.4422 + 6.5440),$
             (6.5149 + 6.2687), (5.9394 + 6.2334), (5.5779 + 4.5819)]
```

The change consisted of: taking efficiency values associated with the first-6 and last-6 detectors and associating them with the first-3 and last-3 of the 6 respective pseudo detectors; pairwise-summing (as above) the 12 geometric factors. Finally—in the conversion itself, again due to the pairwise binning, 1 is subtracted from the log-compressed LZ record values, then these values are uncompressed and converted to phase densities in the same way as with previous modes (but using the above values).

6c. WGGS software modifications.

Modifications to routines/sub-applications of the WGGS tool (located at <tool>):

<tool>/swelz/lzinput.pro	Calling mode7map, calling proc_rec to find mode7 science record.
<tool>/swelz/proc_rec.pro	Determining if in new science mode, calling mode7 to read a record.
<tool>/swelz/swedatlib/mode7map.pro	Reading telemetry map for new-mode records.
<tool>/swelz/mode7.pro	Reading a new-mode LZ record, unpacking/storing new-mode data.
<tool>/swelz/cts_f_strl.pro	Converting new-mode, pairwise-binned counts into phase densities.
<tool>/widgets/swe_levelzero.pro	Recognizing new-mode data, providing new-mode interface.
<tool>/swelz/strl_newmode.pro	Sel. new-mode rec. prelim. proc., calling strl_phth_newmode.
<tool>/swelz/lztimrec.pro	Makes time-to-record/spectrum (instead of record/spin) conversion.
<tool>/swelz/strl_phth_newmode.pro	Display current spectrum of new-mode strahl data.

6d. Use and function of SWE levelzero display with new mode.

See Appendix 3 for a detailed description of the use and function of the level-zero data interface widgets. This section provides a brief description of the differences in using the interface with new-mode data. There are several features which are "turned off" in the new-mode format, most of the remaining features behave as described in the appendix.

There are a few exceptions:

1) The 'Spin' button/field widget becomes the 'Spectrum' widget, but otherwise behaves the same. Allows the user to increment display by one spectrum.
2) The 'Plot-type' droplist has been replaced by a 'style' droplist:
   '**style 1**': The energies which make up a strahl spectrum are displayed in an "alternating" order which proceeds (in order of increasing energy) along each row before proceeding to the next. This display-style is useful because it displays the full strahl energy range in each column.
   '**style 2**': The energies are displayed in a "monotonic" order which proceeds (in order of increasing energy) down the left, then right, columns. Energy-dispersion effects are more easily seen in this style.

The new-mode strahl data display itself is to be interpreted in the following way. The azimuth and elevation *particle-velocity direction* angles described above provide the absissa and ordinate, resp., for each plot-panel (displaying phase-densities for counts of particles at the labelled energies). Each panel is overplotted with contours at the ¼-max and ½-max phase-density levels. The '+' and '-' symbols annotated on each plot-panel indicate the magnetic-field and anti-magnetic-field directions, resp. The vertical dotted black lines in each sector (denoted by blocks of constant phase-density color) of each plot-panel, indicate the angles at which count-acculmulation actually began for that particle-energy, in that sector. Finally, as a reference, the vertical solid white lines in each plot-panel mark the 0^o and 180^o (resp.) *particle-velocity direction* angles.

Appendix 1. How to start the WGGS tool and description of the startup procedure.

Installation of the WGGS tool.
The WGGS tool is packaged in the directory wggs00/ and its subdirectories. The latest version, where 00 designates version number, can be found as a tar file in the anonymous ftp site of the server machine leprjf:ftp/ftp/pub/exports/wggs00.tar. To install the tool, first copy wggs00.tar to the user machine and untar:

% *tar xvf wggs00.tar*

which creates the tool directory wggs00/ and its subdirectories.

Secondly copy the IDL startup procedure, wggs_startup.pro from the same leprjf ftp site to the user machine at the same directory level as wggs00/. The startup procedure includes the path to the most recent version of the WGGS tool software as well as other data paths and the setting of environment variables. The startup procedure wggs_startup.pro contains documentation with instructions on how to tailor it to the user's computer environment. The listing of the startup procedure is included in this appendix.

Thirdly, if this is a new installation, make sure that there is not a directory on the user machine named idlsav in the data path sav_dir , which can be found in a line near the beginning of wggs_startup.pro. A new idlsav directory will be created the first time the tool is used if a directory of that name does not already exist.

Running the WGGS tool.
The WGGS tool is now ready to run. The normal use of the WGGS tool begins with the start of an IDL session as follows:

% *idl wggs_startup*

where wggs_startup is the name of the startup procedure, wggs_startup.pro. The WGGS tool is started by typing at the IDL prompt:

IDL> *wanal*

which brings up the main *Survey Data Display*.

Editing the startup procedure.
The listing of the startup procedure with line numbers follows on the next pages. The documentation included in the listing should guide the user as to what needs to be changed or updated. The lines 1 – 44 contain *required* user settings, lines 8, 10, and 12 being the most important. The lines 45 – 148 contain *optional user settings,* the most important being the data paths to the SWE level zero data and the survey data. These data paths may be direct paths to specific data directories or to mount points on the user's machine.

Appendix 2. Use and Function of the Survey Data Display Widgets.

The following is the documentation to explain the use and function of all the widgets in the *Survey Data Display* which is available by clicking on the **HELP** button. The buttons, fields, droplists, and labels appear here in bold type, e..g., the **HELP** button, and to the right is a brief description of the action caused by the respective widget event, such as clicking on a button.

BUTTON/FIELD/DROPLIST	*ACTION*
SWE level zero	Starts/brings forward *SWE LZ Data Display*. Use this button rather than mouse button on window to bring forward *SWE LZ Data Display*!
ISEEf	Starts/brings forward ISEE f *DATA INTERFACE*. (ISEE moments MUST have already been read.)
Path	Displays the input (source) data paths for all of the various data types and permits changes to be made.
HELP	On-line documentation.
Quit	Normal exit.
Date/File	Toggle to File to select from a list of files. Toggle to Date to automatically search files.
yyyymmd	Enter date (yymmd) for file search by date; the date will also appear when file is manually selected.
Nr days	Select number of days for multiple day plot.
swe_strahlen	Use the droplists which display the two energies to be displayed when data type **swe_strahlen** is selected.

Button group **SELECT input data types, then READ** :
One or more data types (swe_moments etc) may be selected. The last selected data types are retained.
NOTE: When swe_moments are selected, swe_ionkp is automatically selected and overplotted on the electron plots.

READ	Click to read the data types last selected above. The data interval read is the number of days selected above beginning with the selected date in yyyymmdd. After the data is read,a list of available data variables appears from which to make plot selections.

(See **Select plot variables** button below.)

READ/PLOT sequence

A widget appears which permits data to be read and plotted on sequential days with a single button click. The data type will be the current data type selection, and the plot variables will be those stored in the selected plot variable buffer.
(see **Select plot variables** button below)

Data version

Displays data versions of data types for which multiple version exist. The default in all cases is **Latest**, but other versions may be selected.

Select plot variables

Widget *AVAILABLE DATA* appears. Select one or more data variables to plot. Button **Do plot** plots the data.

Short cuts: After making a plot variable selection, it may be saved by clicking on one of **Save X** buttons, where X=0,1,2,3. The saved selection is then plotted by the corresponding **Plot X** button. The **Save X** buffers are not reset with a new IDL session, but rather are kept.

Default time interval plotted: entire file.

Special cases: For certain data types, additional plot parameter choices can be made, For example, when plotting strahl peak flux,the available energies also appear in the *AVAILABLE DATA* widget.

Change plot parameters

Widget *CHANGE PRESET PLOT PARAMETERS* appears. Plot parameters such as y-axis range, i.e., Y min and Y max, yaxis labels, tick marks, etc can be altered from their default preset values for each panel individually. Changes made here are retained during the current IDL session. The "**Y-axis**" button described below toggles the Y-axis range between the preset and min-max of the plotted variables for all panels.

The vertical size of each panel relative to the other panels is displayed and can be changed. For example, a given panel can be made twice as large as the rest.

To select time intervals to plot:
The default time interval plotted is the entire file. To "zoom", i.e., to select a time subinterval to plot, click the left and middle mouse buttons at the begin and end times, respectively, of the desired interval. When the middle mouse button is clicked, a new widget pops up entitled, *SELECTED TIME INTERVAL*. These are the relevant buttons in the pop-up widget: Click on **Plot** to plot the new time interval. The new time interval becomes the current time interval and is retained until a different time interval is selected. Click on **Store interval and plot** to store any selected time interval to be kept for later recall even as the current interval changes.

Button group **Time interval**
The currently selected variables can be plotted for various time intervals:

Current The current time interval.

The current time selection may be replotted at any time. In particular, if program wanal is restarted in a given IDL session, data does not have to be reread, but rather the plot can be restored by clicking the **Current** button. NOTE: Going back and forth between windows may sometimes cause plot controls to become "unset" and the tool may appear unresponsive. Try clicking on **Current** or **Original** to reset.

Previous The time interval selected prior to the last (current) selection is plotted.The current time selection still in memory.

Original The input time selection is plotted and becomes the new current selection.

Stored The time interval saved in memory for later recall.

Array reduction To keep plot array sizes manageable, IDL library procedure congrid.pro reduces the array size using an interpolative method. Use of **congrid** is the default. The droplist povides the option to turn off array reduction. When using the IDLsave button (described below) to create a file of the plotted data, array reduction should be set to **off** to retain the full time resolution in the created data file.

Smooth Median smoothing, 3, 5 or 10 points (0 is no smoothing).

Y-axis Choices for the y axis scale are **Preset** (default) and **Minmax.** The Preset values can be changed using button **Change plot parameters**. The original default preset values can be reset by using button **Select plot variables** and

redoing the plot variable selection or using button **Change plot parameters** and clicking on **Restore**. These actions do not change the time interval.

Time axis The **Selected time interval** widget appears.

Hardcopy droplist:

Hrdcpy bw Makes black and white hardcopy of current plot.

Hrdcpy clr Makes color hardcopy.

Printer/file Pop-up widget displays and allows changes in names of printer and printfile.

Color scale droplist:

Color tbl IDL procedure xloadct.pro is used to display and/or modify the color table (stretching etc).

Restore clrs Current color table is restored and the top color (plot axes, etc) is set to white.

Application droplist:

WIND orbit Plots the orbit for the current day.

Local Appl Local user applications. Executes procedure local_appl.pro if it exists in directory specified by LOCALUSER environment variable in startup file.

IDLsave An IDL save file is made of the plotted data which may be retrieved by IDL restore (line plots only). It is adviseable to turn the array reduction FROM congrid TO off in order to retain full time resolution.
The saved data files may be accessed as follows:
".run idlsav_plot" to plot the data,
".run idlsave_to_ascii" to create an ascii file,
".run idlsave_to_ascii_cols" to create an ascii file in column format.

Appendix 3. Use and Function of the SWE Levelzero Data Interface Widgets.

The following is the documentation to explain the use and function of all the widgets in the *SWE LZ Data Display* which is available by clicking on the **HELP** button. The buttons, fields, droplists, and labels appear here in bold type, e..g., the **HELP** button, and to the right is a brief description of the action caused by the respective widget event, such as clicking on a button.

The top plot window contains one of survey plots from the parent widget.
Which of the survey plot variables that is plotted here can be selected using the first droplist in the second row of buttons above the plot panel.

The three lower windows are available for distribution function plots at selected times.

The top row of buttons:

BUTTON/FIELD/DROPLIST *ACTION*

Parent Returns to main or "parent" widget *Survey Data Display*. From *Survey Data Display*, click **SWE level zero**
to get back to this "child" widget.
NOTE: Use parent and child buttons to go back and forth between widget displays. Avoid using the windows mouse functions to bring windows forward.

HELP On-line documentation.

Quit Normal termination.

Dates Droplist containing all dates for survey data read in. Any date from this list may be selected and will be read when "Open LZ" is clicked.

Open LZ Opens SWE lz file, reads anciliary files,
orbit-attitude, 3sec magnetic field, sun glint mask,
VEIS background counts. Distribution function data can now be plotted directly using data from the opened levelzero file, as discussed below under "Ways to select time".

Veis data Brings up the SWE VEIS Counts Data display widget which has its own HELP button.

Strahl data Brings up the SWE Strahl Counts Data display widget which has its own HELP button.

Color adjustment droplist:

Xloadct A widget pops up which allows adjustment of color scale (stretching etc) or changing color table.

Restore colors Current color table restored which also sets the top color (plot axes, etc) to white.

Hardcopy droplist:

Hrdcpy bw Makes black and white hardcopy of current plot.

Hrdcpy clr Makes color hardcopy.

Applications droplist:

Orbit Window appears with orbit plot.

Display options Pop-up window appears providing various information about and control of display options. A HELP button is included.

Scan LZ file A new widget appears containing various instrument and data information from the telemetry record.

Save f Makes an ASCII file of perpendicular and parallel cuts and reduced F vs parallel velocity, as well as the measured f closest to parallel, anti-parallel, and perpendicular.

The second row of buttons:

BUTTON/FIELD/DROPLIST *ACTION*

Droplist of survey plot variables. Choose one to plot in upper panel.

mode The SWE/VEIS instrument mode is displayed: 1, 2, 4, or 6.

---------- ***Ways to select time***: ----------

There are several ways to select times for plotting distribution function data:

1. Click at desired time in the top panel (with left mouse button) and plot will appear in one of three bottom panels. Successive clicks on top panel will cause plots to cycle through the three bottom plot panels.
(A vertical line at the selected time will appear in the upper panel).

2. Click on any of three bottom panels and the plot at currently selected time will appear.

3. Click on Spin "+" or "-" button or click on Mfrm (major frame=7 spins) "+" or "-" button to increment the time index; the plot at the newly

selected time will appear. Successive clicks on "+" or "-" will cause plots to cycle through the three plot panels. The spin (mfrm) number will appear in the field to the right.

4. Click on the "auto" button to cause three successive plots to appear, one in each window.

5. Enter time explicity into "hhmmss" field.

Plot type droplist:

fcntrs Contours of f on perpendicular-parallel velocity grid with magnetic field direction along +vparallel.

f(en,pa) Color-coded pitch angle distribution on energy-pitch angle grid.

fcuts Parallel (solid line) and perpendicular (dashed line) cuts of f and measure data sampled closest to magnetic field (+/-) direction (triangles). Dotted line is one-count level.

redF Reduced distribution.

f fcuts Contours and cuts of f (default).

f F Contours of f and reduced f.

fsurface Perspective 3-D contour map of f.

triangles The triangulation mesh computed by triangulate.pro to help show the validity of the platewise interpolation used to do contouring.

fpolar Contours of f on perpendicular-parallel velocity grid with magnetic field direction along +vparallel.

vstps Truncate the upper range of energy steps included in plots of f by selecting a number less than 16.

pbin Select the value of the pitch angle bin used for the data in making the polar plots of f, i.e., contours, etc.

Appendix 4. How the Survey Data Display Works.

This section is an introduction to the inner workings of the tool. A working knowledge of the IDL language would be helpful though not essential in reading it. The reader whose only interest is in using the tool may skip this section. It is intended for those readers who may be involved in setting up the tool or wish to adapt it, i.e., to access and plot a new data type or to add a new application for an existing data type.

The following are the names of the experiment data types currently accessed by the *Survey Data Display*:

IDL> print, d.datype

swe_moments	SWE VEIS electron moments
swe_fpitch	SWE VEIS electron pitch angle distributions
mfi_mag3s	MFI 3s magnetic field data
swe_ionkp	SWE Faraday cup solar wind ion data
mfi_magkp	MFI key parameter magnetic field data
swe_strahl	SWE strahl sensor data
isee_moments	ISEE-1 VES electron moments and distributions
wav_tnr	WAV 1m TNR data
swe_redfcuts	SWE reduced velocity distributions
wav_hrtnr	WAV high resolution TNR data
swe_strahlen	SWE strahl data at selected energies
wind_orbit	WIND orbit data
swe_fparaperp	SWE 60° pitch angle averages
wav_nekp	WAV key parameter electron density
wav_nehr	WAV high resolution electron density

Data structure d.

The heart of the *Survey Data Display* functionality is the data structure *d.* It contains all that is necessary to read the selected input data, such as data paths, the input data itself, and all the parameters necessary for constructing and controlling the data display. The structure *d* is created automatically and is accessed by all parts of the program through the common block, *common shared,d*. The structure *d* with the tag names *NDVAR, DATYPE*, etc is described below using the IDL language command, *HELP,/STRUCTURE* . Explanatory notes are included to the right of only those tag names that are relevant to this introduction. Tag names of structure *d* which relate to the internal operation of the widget interface are not discussed.

IDL> help,d
D (SHARED) STRUCT = -> <Anonymous> Array[1]
IDL> help,d,/str

NDVAR	LONG	15	Number of input data types
DATYPE	STRING	Array[15]	Names of input data types
DIR	STRING	Array[15]	Data path for each data type

```
PATHENV        STRING    Array[15]                 Data path environment variables
FLTR           STRING    Array[15]                 Data filename extensions
FLNM           STRING    Array[15]                 Data filename for each data type
DATYPE_INPUT   INT       Array[15]
WILABL         STRING    Array[15]
PNLIST         STRUCT    -> <Anonymous> Array[1]
NDX            LONG      Array[2, 15]    Begin and end indices of current time interval.
NDX_ORIG       LONG      Array[2, 15]
NDX_LAST       LONG      Array[2, 15]
NDX_BUFF       LONG      Array[2, 15]
NDX_BUFF2      LONG      Array[2, 15]
NDX_STORED     LONG      Array[2, 15]
PNL            STRUCT    -> <Anonymous> Array[174]                 See below.
PNLSEL         INT       Array[174]
PNLSEL_LAST    INT       Array[174]
WDATYPE        LONG      Array[174, 15]
TIMSEL         STRING    'lz'
XSCROLL        INT       Array[15]
YSCROLL        INT       Array[15]
BTTN           INT       Array[15]
WITYPE         INT       Array[15]
REFSEC         DOUBLE          0.0000000          The reference time used for all plots.
MAXNUMBERDAYS  INT             4
DATYPE_MULTIDAY STRING   Array[8]
```

If for example, the data types, *swe_moments*, *swe_fpitch,* and *swe_strahl* were selected as input data, then the following tags referencing the input data would be concatenated to the structure *d*:

```
SWE_MDAT       STRUCT    -> <Anonymous> Array[12754]
SWE_PDAT       STRUCT    -> <Anonymous> Array[12749]
SWE_STRAHLDAT  STRUCT    -> <Anonymous> Array[12749]
```

Each of the 15 data types in the list, *d.datype*, has a corresponding list of variables available for plotting, and the variable lists for all data types are concatenated into a single list totaling 174 elements, each element being a plot variable name string. For each of the 174 plot variables, there is a set of plot control parameters, most of which correspond to standard keywords used in the IDL plot routines. The plot variable names, the corresponding data types, and plot control parameters are the tags of the structure, *d.pnl*, described below:

```
IDL> help,d.pnl
<Expression>   STRUCT    = -> <Anonymous> Array[174]
IDL> help,d.pnl,/str
  DTP          STRING    ''                        Data type of the plot variable, varname.
  VARNAME      STRING    ''                        Plot variable name.
```

In this document, the term *data type* will always refer to the data type name as given by *d.pnl.dtp* (or *d.datype*), and the term *plot variable* will always refer to the quantity to be plotted as given by *d.pnl.varname*. For example, a partial list of plot variables for the data type *swe_moments* is ‘N density’, ‘T temperature’, ‘U flow speed’, etc.

The remaining tags to *d.pnl* are plot control parameters:

```
 YPNLP          FLOAT          0.00000
 ZTITLE         STRING    ''
 LABL           STRING    ''
 RANGE          FLOAT     Array[2]
 TICKS          INT            2
 MINOR          INT            5
 TICKV          FLOAT     Array[30]
 TICKNAME       STRING    Array[30]
 SUBTITLE       STRING    ''
 TMLABL         STRING    ''
 TMRANGE        DOUBLE    Array[2]
 TMTICKS        INT            2
 TMINOR         INT            5
 FILL           FLOAT     -1.00000e+31
 TMTICKV        DOUBLE    Array[30]
 TMTICKNAME     STRING    Array[30]
 PLOTIO         INT            0
 PSYM           INT            0
 SYMSIZE        FLOAT          1.00000
 OPLOT          INT            0
 OPLOTVAR       STRING    ''
 OLINESTYLE     INT            0
 OCOLOR         INT          225
 PLTYPE         STRING    ''
 ENINDX         INT            0
 INDX           INT            0
 XORY           INT            0
 EV_VAL         INT            0
 STEP           FLOAT          0.00000
 LZRANGE        FLOAT     Array[2, 2]
 CHARTHICK      FLOAT          1.00000
 CHARSIZE       FLOAT          1.15000
 HORIZLIN       FLOAT     -1.00000e+31
```

Having outlined the essential parts of the structure, *d*, its use in the program will be discussed. The following table illustrates a typical selection of data variables to be plotted as a panel stack, beginning with the top panel:

Table 1.

Panel i	Data Type d.datype(ityp(i))	Type index ityp(i)	Data Variable d.pnl(ivar(i)).varname	Variable Index ivar(i)
0	swe_moments	0	heat flux	6
1	swe_fpitch	1	spin avg f(en,t)	45
2	swe_fpitch	1	94.3	55
3	swe_strahl	5	strahl energy spectrum	93

The data types and data variables are selected by the user from the widget interface using the names given in the second and fourth columns,respectively, of Table 1. The other columns in Table 1, i.e., the first, third, and fifth columns, are indices determined by the

program corresponding to the user selection and are used in structure *d* to reference the data, transparent to the user. The data type indices (third column) are

ityp = where(d.datype_input ne –1) = 0, 1, 5.

The *swe_strahl* data structure corrsponding to ityp(3)=5, for example, is referenced as

d.swe_strahldat(d.ndx(5,0): d.ndx(5,1)).*tag* ,

where d.ndx(5,0): d.ndx(5,1) is the range of indices of the *swe_strahl* data for the selected time interval, and the tag represents an input data variable, such as time or flux. The plot variable indices (fifth column) are

ivar = d.pnlsel(where(d.pnlsel ne –1)) = 6, 45, 55, 93.

The parameters for controlling the *strahl energy spectrum* plot corresponding to ivar(3)=93 are referenced as d.pnl(93).*tag* (unless overridden in the plot procedure itself), where the tag represents a parameter such as the y-axis range.

Survey data directory structure.

All of the procedures pertaining to a specific data type are located in a single subdirectory whose name is the same as the data type. The directory structure for the currently available data types is

wggs00 /survey/:

swe_moments /	swe_fpitch/	mfi_mag3s/
swe_ionkp/	mfi_magkp/	swe_strahl/
isee_moments/	wav_tnr/	swe_redfcuts/
wav_hrtnr/	swe_strahlen/	wind_orbit/
swe_fparaperp/	wav_nekp/	wav_nehr/

where wggs00/ is the top directory of the entire tool. Each data type subdirectory has a requisite set of procedures given by the following, where *exp_dtyp* represents one of the above data type names:

wggs00/survey/ *exp_dtyp*/:

*exp_dtyp*_list.pro	List of plot variables included in d.pnl.varname.
*exp_dtyp*_read.pro	Reads the input data.
*exp_dtyp*_timerange.pro	Returns begin and end times of the data.
*exp_dtyp*_datatime.pro	Returns data time relative to reference time.
*exp_dtyp*_struct.pro	Returns plot parameters for each plot variable listed in *exp_dtyp*_list.pro.
*exp_dtyp*_plt.pro	Plots the data corresponding to the plot variable selected in the panel whose position in the stacked plot panels is determined by the order of selection.
*exp_dtyp*var.pro	Called by *exp_dtyp*_plt.pro, returns the actual data for each plot variable selected for the current time interval.

The above procedures must be tailored to to each specific *exp_dtyp.* These are the

minimun requisite procedures but subdirectory wggs00/survey / *exp_dtyp* / may include other procedures or functions to be called by any of the above to meet a specific requirement. For example, the data type *swe_strahl* requires procedures for making both line plots and images, and therefore, swe_strahl_plt.pro calls another procedure swe_strahl_spectrum_img.pro, which is also located in subdirectory, wggs00/survey / swe_strahl. The requirements for each of the requisite set of procedures under each wggs00/survey/*exp_dtyp*/ is given in Appendix 5, which discusses in detail how to expand WGGS to include new data sets.

Survey data flow.

The following is the sequence of called procedures and widget actions necessary to select, read, and display a set of plot variables, represented by *var,* from a selected set of data types, represented by *exp_dtyp*. In the following, *Widget* and *Keyboard* refer to user actions via the widget interface and keyboard, respectively, and the fully qualified procedure name, *path/procedure.pro*, refers to the automatic execution of the named procedure by the program.

Action / called procedure	Result
1) Keyboard: wanal	Starts the tool.
wggs00/init/define_widgets.pro	Defines all widget interfaces.
wggs00/init/panelist.pro	Creates/initializes structure, *d*.
2) Widget: Enter begin date, nr. days	
3) Widget: Select data types, *exp_dtyp*	Stores data type selections, *exp_dtyp*.
4) Widget: Read	Initiates data read-in.
wggs00/init/panelist.pro	Structure *d* is re-initialized.
wggs00/survey/input.pro	Data type selections *exp_dtyp* are put into *d.datype_input.* Current data paths are searched for the selected data type files according to date.
*exp_dtyp*_read.pro	Data for data type *exp_dtyp* are read in and concatenated onto structure, *d.* Common reference time is established. Orbit and attitude data are read.
5) Widget: Select plot variables	
wggs00/widgets/select_pltvar.pro	Plot variables, *var*, are selected.
6) Widget: Do plot	Initiates the plot.
wggs00/survey/mstruct.pro	Plot parameters common to all panels stored in appropriate tags of *d.pnl*.

wggs00/survey/*exp_dtyp*/ *exp_dtyp*_timerange.pro	Set time axis scale.
wggs00/survey/*exp_dtyp*/ *exp_dtyp*_struct.pro	Set y-axis and other plot parameters for each plot variable of set, *var* and stored in d.pnl.
wggs00/survey/plt.pro	Set the plot window coordinates for each panel.
wggs00/survey/*exp_dtyp*/ *exp_dtyp*_plt	Plot data corresponding to each variable of set, *var*, in panel according to order of selection.

Appendix 5. Expanding WGGS to Include New Survey Data Sets.

The WGGS tool can be readily adapted to include new survey data sets. These are the steps to follow:

1. Select a descriptive name for the data type of the form *exp_dtyp,* where *exp* represents a satellite or project and *dtyp* represents a specific experiment or source of the data.
2. Select names for the variables to be plotted represented here as the set var={var1, var2,…..}. Note: The names of these variables *must* be unique among *all* datatype-variable-names. This is because sometimes (internal to WGGS) these names are used as the only identifier of a time-series, and non-uniqueness could cause problems.
3. A subdirectory named *exp_dtyp* must be created under the directory wggs00/survey. A template subdirectory with the requisite files exists which should be copied and given the name selected in step 1. The subdirectory and its files with a brief description is as follows:

wggs00/survey/ *exp_dtyp*/:

*exp_dtyp*_list.pro	List of plot variables *var*.
*exp_dtyp*_read.pro	Reads the input data.
*exp_dtyp*_timerange.pro	Returns begin and end times of the data.
*exp_dtyp*_datatime.pro	Returns data time relative to reference time.
*exp_dtyp*_struct.pro	Returns plot parameters for each plot variable listed in *exp_dtyp*_list.pro.
*exp_dtyp*_plt.pro	Plots the data corresponding to the selected plot variable.
*exp_dtyp*var.pro	Called by *exp_dtyp*_plt.pro, returns the actual data for each plot variable selected for the current time interval.

4. After naming the above directory with the name selected for new data type, each of the files may be readily modified by searching for the dummy data type name *exp_dtyp* wherever it occurs and substituting the selected data type name. Procedures

*exp_dtyp*_list.pro, *exp_dtyp*_struct.pro, and *exp_dtyp*var.pro will also require searching for the dummy variable names *var1,var2,...*and substituting the actual plot variable names. The procedure *exp_dtyp*_struct.pro contains plot axis and other plot appearance parameters and must be modified to meet the user's requirements. The procedure *exp_dtyp*_read.pro must also be specially modified to read the new data . The template *exp_dtyp*_read.pro contains all that is required and must be included, such as specific time formats, data index definition, and concatenation of structure *d.*

5. The directory wggs00/survey/ *exp_dtyp*/ also contains two additional procedures which are not part of the actual directory for the new data type, but are included as templates for the two remaining procedures to be modified. They are panelist_illustrative_version.pro and startup_file_ illustrative_version.pro. Follow the instructions in the documentation at the beginning of each file on how to modify. Then replace (or modify) the old wggs00/init/panelist.pro and your old startup file (located in the directory in which the IDL session is started) with the new versions.

6. Finally, be aware that—in some cases—there may be a need to (possibly with help from a SWE Data System developer) modify the following fileswhen adding new (or modifying old) data types: wggs00/survey/input.pro, wggs00/survey/get_flnm.pro and wggs00/survey/mstruct.pro. This requires advanced understanding of IDL.

7. This completes the installation of the new survey data type. All of the functionality of the tool is now available to the new data type.

Appendix 6. Relative gain balancing of VEIS detectors.

The six VEIS channeltrons have aged over time since the WIND launch with variable rates of degradation of detector response. The channeltron bias levels were raised periodically to counteract this natural aging process. In order to accurately compute the odd electron velocity moments such as the bulk flow velocity and heat flux vectors, it is necessary that the response of the six channeltrons be balanced relative to each other. To account for channeltron aging and changes in bias levels, the detectors were balanced on a regular basis, approximately once each five to ten days, and a set of six gain factors were determined. The set of six factors were normalized to one of the detectors, which appeared to be most constant over time. These periodically determined gain factors were used to compute by interpolation a table of gain factors, one set of six for each day, during the useful lifetime of the VEIS spectrometer, 1994 – 2002. This relative gain table is included within the tool and its application to the data is transparent to the user. The following is intended to document the gain balancing procedure and to serve as a guide should it be necessary to repeat the process.

The procedure for balancing the gains of the six VEIS detectors is outlined in the following steps. Graphical user interface names are given in italics, e.g., *Survey Data Display*, and widget buttons, fields, and droplists are in bold type, e..g., the widget button, **SWE level zero**.

1. Select a time period over which gain balancing is to be done, from 1-30 days, and plot the WIND plasma and magnetic field key parameters, Ni, Ui, B, θ_b, and φ_b in the *Survey Data Display* plot window.
2. Select a day containing an approximately one hour interval in which Ni > 5 and φ_b is approximately 90° or 270°, if possible.
3. Click on the widget button **SWE level zero** in the *Survey Data Display* which causes the *SWE LZ Data Display* interface to appear.
4. In the *SWE LZ Data Display*, select the chosen date from the droplist and click on **Open LZ**.
5. With the left mouse button, select a time causing a plot of $f(v_{\parallel}, v_{\perp})$ to appear.
6. Click **VEIS data** in the *SWE LZ Data Display* and the *SWE Veis Counts Data* interface will appear with the default plot, counts vs speed for each detector in sector 0. This is a display of raw counts for opposing pairs of detectors 0-5, 1-4, and 2-3. Sectors 0 through 5 can be displayed by incrementing **Sect** for the given spin and major frame. This plot is also created when **Cts_step** is clicked.
7. Click **Relative gain determination; Background** in *SWE Veis Counts Data* and the *Do counts average* widget interface will appear.
8. In the the *Do counts average* interface, select a detector, 0 through 5, to which the computed gains of each detector is to be normalized by using the droplist labeled **Normal detector.** Select the detector which has been most stable over time with high counts.
9. Select the energy for which the pitch angle distributions for each detector are to be computed in the gain balancing procedure by using the droplist labeled **Energy step (ev)**. Energy 29 eV is suggested.
10. Select which of the six detectors 0, 1, 2, 3, 4, and 5 are to be used in the gain balancing. If all six detectors were to have aproximately equal responses, than all six would be used. If one or two detectors were to have a severely diminished response compared to the rest, say down by a factor 10 or more, then those detectors should not be included in the gains determination. For example, if detectors 0 and 2 are not to be included, then select the set of detectors **1345** from the droplist labeled **Pitch fit: Det's**. Gains will be computed using detectors 1, 3, 4, and 5 and normalized to the detector selected in step 8. Detectors 0 and 2 will be assigned a gain of 0 in the gains table for the purpose of identification, but the gain factors actually used for detectors 0 and 2 will be unity.
11. Click on **Accumulate slctd spins (YES glint rmvd)** which will sum the raw counts for each detector (included in step10) over 30 major frames or 210 spins beginning at the current record and spin.
12. Click on **Pitch fit each detector, get rel gains.** A new set of six plots, one for each detector, will appear in the plot window. Each plot contains the sum of counts vs pitch angle and the parabolic fit for the given detector as well as the parabolic fit to the total counts of all detectors (only for detectors included in step 10) vs pitch angle. The ratio of the pitch angle fit using all (included) detectors to the pitch angle fit of each detector individually is defined as the gain of the given detector. The gains are then normalized to the gain of the detector selected in step 8 and is printed in the command window. These are the factors by which the raw counts are multiplied to correct for imbalance in the detector set, which is primarily due to differing rates of

aging of the channeltrons and changes in voltage bias levels of channeltrons that have been made at various times during the WIND mission to compensate for diminishing response.

13. If satisfied with the computed gains, then click on **Save relative gains** which appends the relative gains and date to the file wggs00/swelz/swecal/gains/gainsrev/add_to_lib.ascii.
14. Repeat steps 2 through 13 for other dates in the survey plot (step 1). Choosing dates 3 to 6 days apart is suggested.
15. The next step is to use the gains for selected dates saved in step 13 to compute gains for each day in the selected time period using a fitting procedure within wggs00/swelz/swecal/gains/gainsrev/getrelgains_tblgen_after_19971027.pro. Add the time period over which the fit is to be made by editing getrelgains_tblgen_after_19971027.pro (array date_range =), then run the procedure. A plot of the calculated input gains and the fitted gains will appear and a file of the fitted gains for each day will be created, both in ascii form and and as an IDL restore file. Add the time period (from the addition to the array date_range above) and the name of the IDL restore file to the appropriate else-if statement in wggs00/swelz/swecal/gains/gainsrev/getrelgains_tbl_flnm.pro. The ascii file provides a visual check of the daily gains table just created and the restore filename is returned by getrelgains_tbl_flnm.pro when referenced by date by wggs00/swelz/lzinput.pro. The restore file with the appropriate gains is read by lzinput.pro each time a level zero file for a new date is opened.
16. The final step is to check the daily gains just determined. Display again the survey data for the original time interval in the *Survey Data Display* plot window and click on **SWE level zero.** On the *SWE LZ Data Display*, click on **Open LZ** for any of the dates plotted. Select a time causing a distribution function to be plotted and then click on **Veis data** to bring up the *SWE Veis Counts Data*. Click on **f w/ new patch** which will display a fitted gaussian patch over the thermal core portion of the measured distribution function. The new gains are used in the patch and are displayed in the widget field labeled **Relative gain adjustment, Old**. The density, temperature, and flow velocity magnitude, elevation, and azimuthal angles of the fitted gaussian are displayed in the plot window. (The patch is Adolfo Vinas' standard 3D patch used in moments calulations and which uses data from all detectors and all sectors in a 3D gaussian fit. Certain detectors and sectors are not used in the fit depending on data quality and whether a particular detector or sector was included in the gain computation. Which detectors and sectors are used to compute patch is prescribed by the array of indices, swest.patch_include.) The criterion used for gains which balance the detectors reasonably well is that the flow velocity elevation angle should be between -30° and +30° of the ecliptic plane.

Appendix 7. Treatment of sun glint effects.

Soon after the WIND launch and onset of the operation of the SWE VEIS instrument, it became apparent that the measured electron spectra contained high count rates when certain detectors were either facing the Sun, or were facing a particular fixed direction relative to the Sun, and which were repeated with each spacecraft rotation. It was

concluded that the extraneously high counts were due to sunlight penetrating certain detectors viewing the Sun directly, and in the case of one particular detector, from sunlight penetrating via a glancing reflection into the detector. This so-called "sun glint" had the effect on the VEIS distributions of appearing to show a constant high flux of electrons from the direction of the Sun. The solar wind electron heat flux, for example, would always appear to come from the Sun instead of being magnetic field aligned. The solution to the problem was to identify and remove the effects of the sun glint.

Three methods were utilized. One was to put the VEIS instrument into a mode in which it would only measure the background spectra and not the ambient electrons. The measurements at *detector, energy sweep step,* and *sector* samples that were contaminated by sun glint stood out prominently against the normal background. This formed an initial identification of *sun-glint detector, energy sweep step,* and *sector* samples to be used in subtracting background from the measured electron spectra.

A second method of identification was to accumulate the differences in measured electron counts from opposing detectors for an extended period, usually one day, and plot the differences against sun phase angle of the measured sample. If there were no favored direction, it was assumed that the counts differences would average out to zero for the extended period. If the Sun were a favored direction then the differences would peak for measurements looking toward the Sun. The set of *sun-glint detector, energy sweep step,* and *sector* samples determined by this method were consistent with the set obtained by the first method.

A third method was used which was to visually inspect the spectral plots. Most of the *sun-glint detector, energy sweep step,* and *sector* samples from the first two methods were clearly identifiable, but not in every case.

A sun glint map using the above methods was determined for a particular period, say one week to one month, applied to the data and electron moments were computed. The operational criteria for success in eliminating or minimizing the sun-glint effects was that the solar wind bulk flow velocity vector should lie within +/- 20 degrees of the ecliptic and that the solar wind heat flux vector should track with the magnetic field direction when there is a significant heat flux magnitude. It was found that the sun glint map could be effectively fine-tuned by adding to or subtracting from the sun glint map by inspection of the spectral plots (method three above) and recomputing the moments velocity vector with the modified sun glint map. This method was applied during the early years of the WIND mission and a sun glint map was found to apply to nearly the whole mission. This indicates that the sun glint effects on the instrument were essentially constant over time and is consistent with the fact that the WIND attitude changed very little.

The application of the daily sun glint map is applied to the data transparent to the user. The *sun-glint detector, energy sweep step,* and *sector* samples are readily identified as highlighted points in the VEIS spectra vs electron speed which is the default plot in the *SWE Veis Counts Data* interface. Typically there are approximately 30 – 40 *sun-glint*

detector, energy sweep step, and *sector* samples which are eliminated entirely, which is only about 5% - 7% of all the data samples collected in one spacecraft rotation.

Appendix 8. Using strahl sensor observations of the Sun to recover WIND spin phase.

To date (December, 2001), there have been three high-flux solar proton events which disabled the Sun sensors on the Wind spacecraft. Normally the spacecraft X-axis is time-tagged by the spacecraft Sun sensor when the X-axis points to the Sun. When the Sun sensor becomes disabled , the spacecraft automatically generates a pseudo-sun pulse each 2.4 sec instead of the nominal 3s true spin period. However, the spin phase of the spacecraft X-axis is unknown at any of these 2.4s time tags. On-board processing keyed to the Sun pulse will therefore be out of phase, such as the spin phase sampled by the strahl sensor, which tracks with the on-board determined magnetic field. However, during each period of loss of the Sun pulse to date, the strahl sensor field of view frequently captured the Sun, providing the necessary spin phase information to compute spin period accurately. The procedure used for determining the true spin period during a no-sun pulse event is documented in procedure wggs00/swelz/nosunpuls_readlz.pro.

Appendix 9. Processed SWE Data File Coverage of Years 1995 – 2002.

The graphs on the following pages show the processed SWE electron data coverage during the years 1995 through 2002. There are three primary survey data types, swe_moments, swe_fpitch, and swe_strahl, for which daily files exist. Days for which daily survey files exist are represented in black, missing data in white. Missing data may be due to several factors such as, the instrument not being in a science mode, poor data quality, or, in the case of swe_moments, WIND not being in the solar wind. The storage location of these survey data files given in Chapter 4c and repeated below can be accessed publicly via anonymous ftp to leprjf:

swe_moments	leprjf:/data7/swe/moments	leprjf:ftp/pub/swe1/swe/moments
swe_fpitch	leprjf:/data9/swe/ptch	leprjf:ftp/pub/swe3/swe/ptch
swe_strahl	leprjf:/data8/swe/strl	leprjf:ftp/pub/swe2/swe/strl

There are three primary data coverage summaries for swe_moments and are differentiated by the file name extension:

1) The first swe_moments data coverage bar chart includes only files with extension *_sv13.mom,* which designate IDL restore files and version 13. These are considered to be the prime moments data set because the instrument was in mode 1, mode 4, or mode 6, and all data variables are considered reliable. This is the data set that has been archived in the NSSDC.

2) The second swe_moments data coverage bar chart adds instrument mode2, version 5 moments files with extension *_v05.mom* to the first summary of *_sv13.mom* files. Not all moments variables of the mode 2, version 5 moments files are reliable due to sun glint contamination. The electron temperature and anisotropy should be reliable, but the heat flux is not reliable and should be used with caution. The VEIS instrument was in mode 2 for parts of 1995 and 1996.

3) The third swe_moments data coverage bar chart includes all the IDL binary version 13 files with extension *_v13.mom* that were processed. The IDL restore files with extension *_sv13.mom* are a subset of the *_v13.mom* files. Most of the *_v13.mom* files were converted to IDL restore files after visual inspection, but a few files were not converted because of questionable quality.

13.2 SWE Reconfigured Strahl Notes

Wind/SWE "New mode" Electron Pitch-angle Analysis

Overview

Effectively, in this mode of the electron instrument, there are 13 energy-channels (electron speeds) making 48 observations (instrument counts for each particular velocity) over 8 sectors (~45° wide) and 6 elevations (~9° apart) at each energy. From these 624 observations (accumulated over 3 s/c spins, or ~9s) 13 pitch-angle distributions and one "spin-averaged" energy distribution are populated during every ~12s interval.

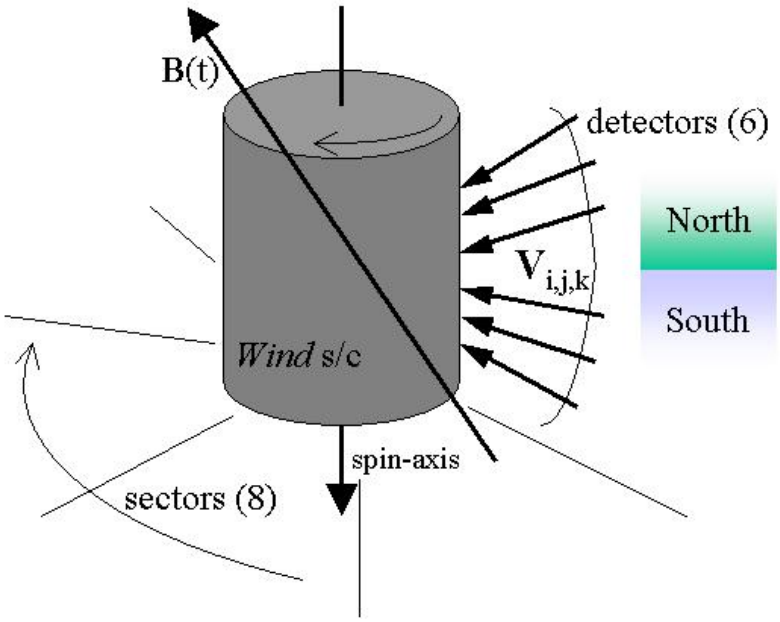

In the following discussion:

- The observed energies are represented as E_0, E_1, …, E_{12}. Where E_0, E_1, …, E_{10} are observed *once* in each sector; E_{11}, E_{12} are observed *twice*, then averaged. This achieves more statistically meaningful observations in energy-ranges where fewer counts are observed, and accounts for the mapping from the 15 energy-channels in the current operational mode to the 13 channels discussed here.
- i = 0, 1, …, 5 indexes *detector*.
- j = 0, 1, …, 7 indexes *sector*.
- k = 0, 1, …, 12 indexes *energy*.
- **B**, **V** vectors are given in GSE coordinates, with **B** being the temporally "nearest" 3s MFI observation to any given SWE observations of electron **V**.
- $\alpha_{i,j,k} = \cos^{-1}\{\mathbf{V}_{i,j,k} \bullet \mathbf{B}(t) / [|\mathbf{V}_{i,j,k}|\,|\mathbf{B}(t)|]\}$ gives the pitch-angle for each observation, with $c_{i,j,k}$ giving the corresponding count-value.

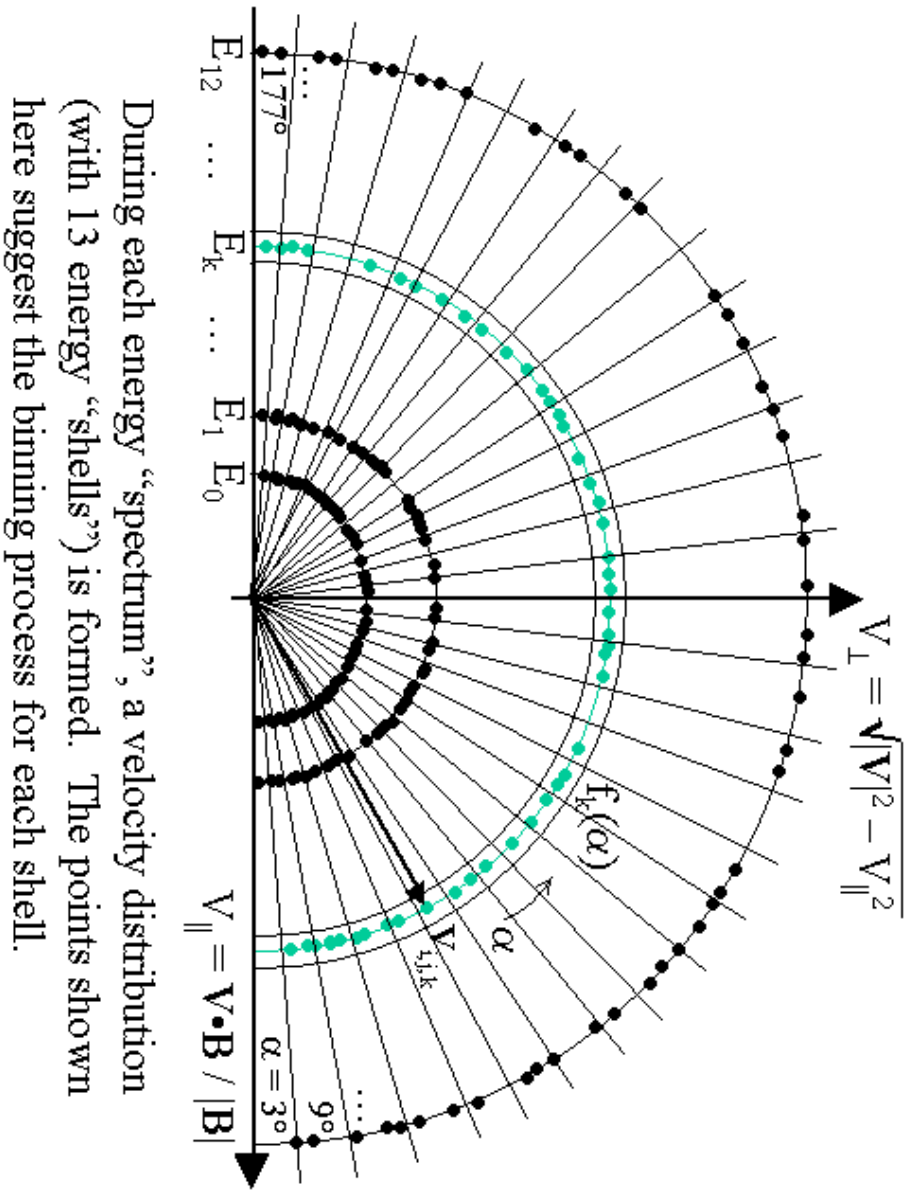

During each energy "spectrum", a velocity distribution (with 13 energy "shells") is formed. The points shown here suggest the binning process for each shell.

For E = E_k, the 30 pitch-angle bins (6° wide) of the k^{th} (of 13) pitch-angle distribution ($f_k(\alpha)$) are populated as follows…

Typically a conversion from counts to phase-space densities requires both energy and a "geometric factor" for each contributing detector. However, acknowledging that the following process unavoidably intermingles counts from different detectors, and that the geometric information from our instrument specifications gives a single conversion factor (call it cf_k) for each energy (E_k), averaged count-values are simply scaled by this factor to yield corresponding phase-space densities:

$$f_k(\alpha) = [\Sigma c_{i,j,k} / n]\ cf_k,\ \alpha = 3°, 9°, \ldots, 177°.$$

The summation is carried out over i,j s.t. $\alpha_{i,j,k}$ lies within 3° of the specified center-angle α (e.g. from 0° to 6° for α = 3°, 6°-12° for α = 9°, …, 174°-180° for α = 177°), and n is the number of detectors (observations) contributing counts to the sum.

One additional value is generated for each energy:

$$\langle f \rangle_k = [\Sigma c_{i,j,k} / N]\ cf_k$$

where the summation is carried out over *all* i,j and N is the number of detectors contributing counts to this "grand total" sum.

This completes the information needed to generate our <u>electron pitch-angle data product</u> for this mode (very similar to that of previous modes):

$f_0(\alpha)$, $f_1(\alpha)$, …, $f_{12}(\alpha)$ for α = 3°, 9°, …, 177° (30 6° bins) form the pitch-angle distributions, and [$\langle f \rangle_0$, $\langle f \rangle_1$, …, $\langle f \rangle_{12}$] forms the "spin-averaged" energy (speed) distribution, accumulated over each ~9s interval (available about every 12s).

For reference:

- The 6 GSE *particle-velocity direction* elevation angles used in our analysis are:
  -26.55°, -17.10°, -7.34°, 7.63°, 17.10°, and 26.53° (above the eccliptic).
- The 13 electron energies (E_k k = 0, 1, …, 12) are:
  19.34, 38.68, 58.03, 77.37, 96.71, 116.1, 193.4, 290.1, 425.5, 580.3, 773.7, 1006., and 1238. eV.
- The 13 corresponding electron speeds are:
  2.61, 3.69, 4.52, 5.22, 5.83, 6.39, 8.25, 10.1, 12.2, 14.3, 16.5, 18.8, and 20.9 x 10^8 cm/s.

Derived Products

From the electron pitch-angle distribution product described above, there are derived two additional data products: *the 'strahl' product* (useful both as a reduced summary of the pitch-angle product, and as an indication of whether the strahl phenomenon is being observed), and *the 'pitch-average' product* (another approach to reducing the pitch-angle product, this time by averaging over regimes of interest). Basic derivation and contents of these products is discussed below. Note that, as with the pitch-angle product, these products are very similar to those of previous modes.

<u>Strahl Product</u>: First, recall the 30 pitch-angle bins (6° wide) of the kth (of 13) pitch-angle distribution ($f_k(\alpha)$ for $E = E_k$) populated above…

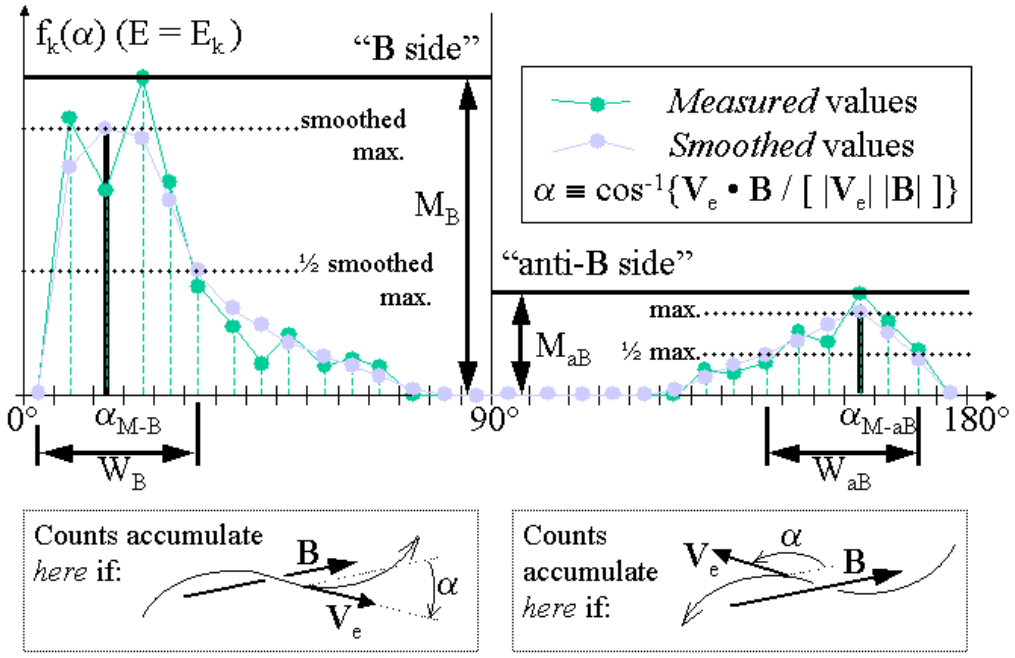

Next, a smoothing operation is applied to the "measured" values. Then we perform the following analysis on both the "**B** side" (the 15 bins associated with forward-streaming electrons) and the "anti-**B** side" (the other 15 bins associated with backward-streaming electrons). The maximum *measured* value is noted (call it M_B, and M_{aB}, respectively); giving a characteristic intensity for each side. After this, the maximum *smoothed* value is noted, as well as the corresponding half-maximum, and a search is conducted starting from this position. We seek the first bin, in each direction, whose value falls at or below the half-maximum value. We call the pitch-positions of the smoothed maxima α_{M-B}, and α_{M-aB}, respectively. The separation of the *half*-maximum bins we call W_B, and W_{aB}, respectively; as they give characteristic widths.

When the strahl phenomenon is being observed, these parameters describe the strahl "beams" being observed. In this case, M_* (* = B or aB) provides a measure (in units of phase-space density) of beam intensity, α_{M-*} provides a representative pitch-angle for each beam, and W_* provides a measure of (angular) beam-width. One typical use of this product (which is entirely consistent with previous modes of the electron instrument) is as an indicator of whether the strahl phenomenon is, in fact, being observed. When the phenomenon *is* being observed, we expect to see relatively intense beams with relatively small deviations from the 0° and 180° pitch-angle positions and relatively small widths. An investigator interested in this phenomenon could focus attention (on the underlying high-resolution data) only where these criteria were met. On

the other hand, this product is always useful as a reduced, summary representation of the pitch-distribution product; as it tends to capture (in a small amount of data) the sort of salient features apparent in our visualizations of the unreduced pitch product.

13 values (from pitch-angle distributions at each energy) of M_B, M_{aB}, $\alpha_{M\text{-}B}$, $\alpha_{M\text{-}aB}$, W_B and, W_{aB} (available about every 12s) form this data product.

<u>Pitch-average Product</u>: Derived, again, from the 30 pitch-angle bins (6° wide) of the k^{th} (of 13) pitch-angle distribution ($f_k(\alpha)$ for $E = E_k$) populated above…

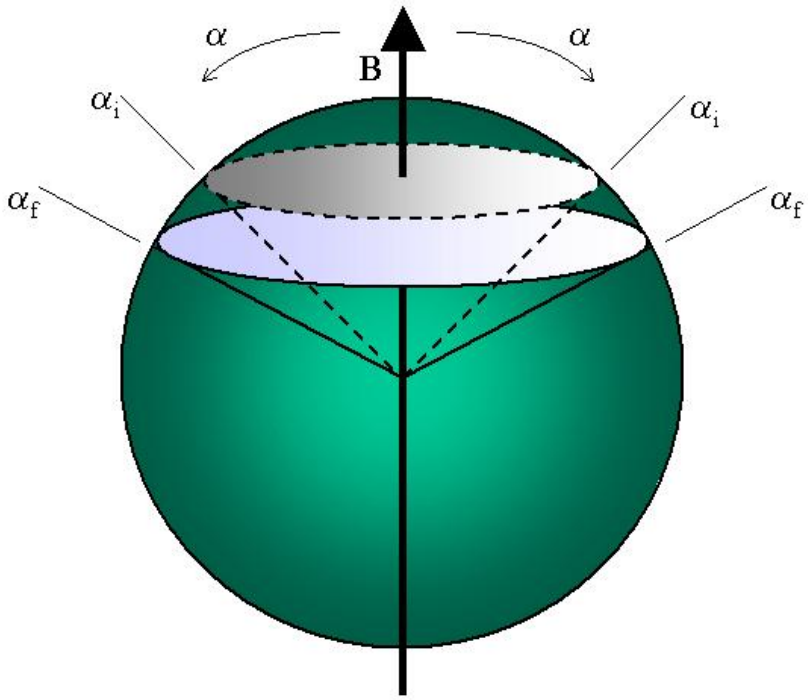

The figure for this section suggests the final approach for reducing our pitch-angle data: *averaging over regimes of interest on the **unit sphere***. This approach begins by identifying 28 annular "strips" (and two "polar caps") of solid angle by the relation $\alpha_i < \alpha < \alpha_f$, where the α_i and α_f values are the familiar pitch-angle bin boundaries from above. Next, we establish "weights" for our averaging process by calculating:

$$\Omega_m = {}_{\alpha i,m}\int^{\alpha f,m} [2\pi \sin\alpha]\, d\alpha = 2\pi\, [\cos\alpha_{i,m} - \cos\alpha_{f,m}]$$

for the m^{th} pitch-angle bin. Upon finally noting that the $0° < \alpha < 90°$, $60° < \alpha < 120°$, and $90° < \alpha < 180°$ regions all have solid angle 2π str—the entire sphere having solid angle 4π str; we may proceed with averaging. The results (k^{th} pitch-distribution) are:

$$f_{para,k} = 1/2\pi\, \Sigma_{m=0,14}\, [f_k(\alpha_m)\, \Omega_m],$$ ("parallel" bins, where $0° < \alpha < 90°$)

$$f_{perp,k} = 1/2\pi\, \Sigma_{m=10,19}\, [f_k(\alpha_m)\, \Omega_m],$$ ("perpendicular" bins, where $60° < \alpha < 120°$)

$f_{anti,k} = 1/2\pi \Sigma_{m=15,29} [f_k(\alpha_m) \Omega_m]$, ("anti-parallel" bins, where $90° < \alpha < 180°$)

$f_{omni,k} = 1/4\pi \Sigma_{m=0,29} [f_k(\alpha_m) \Omega_m]$, (*all* bins, where $0° < \alpha < 180°$)

13 values of $f_{para,k}$ ($f_{para,0}$, $f_{para,1}$, …, $f_{para,12}$), along with the corresponding 13 values of $f_{perp,k}$, $f_{anti,k}$, and $f_{omni,k}$ (available about every 12s) form this data product.

Data-product Files for this Mode

Each data-product described above is stored as both a "flat binary" file and a CDF file for each day of processed data. For reference, a typical day yields 6000-7000 energy "spectra" (about 1 every 12s, with data accumulated over 9s; accounting for "null spectra", data gaps, etc.). Each non-null spectrum yields the set of values described above. Noting that the naming conventions are mostly historical in nature (with the exceptions of 'h' for "high resolution" and 'm' for "modified", as in derived, in the CDF files), the files for each *yyyymmdd* date are named:

Product	Flat-binary filename	ISTP-compliant CDF filename
***Pitch*-angle distributions**	`yyyymmdd_v06.pit`	`wi_h3_swe_yyyymmdd_v01.cdf`
Pitch-distrib. *averages*	`yyyymmdd_v06.pitavg`	`wi_m0_swe_yyyymmdd_v01.cdf`
***Strahl* beam-descriptions**	`yyyymmdd_v08.str`	`wi_m1_swe_yyyymmdd_v01.cdf`

Notes: The first date of processed new-mode data is ***yyyymmdd*=20020816**. While accessing the data from our flat-binary files requires the specialized software used internally by the SWE electron science team, the CDF files are self-describing and a variety of software tools exist for accessing their data.

14 *Wind* SWE Ions

This section will include notes from *Kasper* [2002] in conjunction with the SWE ion software [*Wilson III et al.*, 2021c]. Additional calibration and accuracy information can be found in *Kasper et al.* [2006].

14.1 SWE Faraday Cup Notes

Chapter 2

Bi-Maxwellian Analysis of Wind/SWE Ion Spectra

ABSTRACT: *A description of the Faraday Cup ion instruments on the Wind spacecraft. Extension of existing analysis techniques to measure the bi-Maxwellian nature of ion species. Evaluation of the analysis, comparison with other methods, instruments, and spacecraft. A brief survey of the typical properties of solar wind protons.*

2.1 Introduction

This chapter presents my analysis of data taken by the Faraday Cup (FC) instruments which make up the ion portion of the Solar Wind Experiment (SWE) on the Wind spacecraft [Ogilvie et al., 1995]. The data produced as a result of this analysis are the basis for the research detailed in subsequent chapters of this thesis.

The goal of SWE/FC is to characterize the bulk properties of the major ions in the solar wind, namely $^{+}$H and $^{+2}$He, but also $^{+}$He in the rare situations in which it is seen. The Faraday Cups probe the three-dimensional distribution of proton and alpha particles in velocity space $f_p(\vec{v})$ and $f_\alpha(\vec{v})$ through measurements of the reduced distribution function (1.65). Most scientific investigations do not require this detailed information about the ion properties. As shown in Section 1.2.6 and Section 1.2.7, to first order we can describe the solar wind in as a fluid,with temperature T, velocity $\vec{U}$, and density n as a function of location and time. In theory calculating these contracted properties of the distribution function follows the integrals listed in Section 1.2.6. In practice the features of the instrument must be taken into account in order to produce accurate values of these "key parameters". In this chapter the proton spectra are analyzed both through a detailed comparison of observations and a model response function, which will be referred to as the *non-linear* analysis method, and through a simplified moment routine, the *moment* analysis procedure, based on the derivations in Section 1.2.6.

The primary data products which the Wind/SWE Faraday Cups produce are the velocity, thermal speed, and density of the protons, along with the relative abundance ratio of alpha particles to the protons. John Steinberg, currently at the Los Alamos

National Laboratory, supervised the original key parameter analysis which produced the proton velocity $\vec{V}_p$, thermal speed w_p and density n_p, and started the analysis of helium [Steinberg et al., 1996]. The full alpha particle analysis was done by Matthias Aellig, producing the alpha velocity, $\vec{V}_\alpha$, thermal speed, w_α, and number density n_α [Aellig et al., 2001b]. I have extended our ability to characterize the ion spectra by deriving an analytical expression for the response of a Faraday Cup to the convected, field-aligned, bi-Maxwellian velocity distribution function described in Section 1.2.5. Instead of the single thermal speed w_p the parallel ($w_{\|p}$) and perpendicular ($w_{\perp p}$) thermal speeds are measured. This chapter describes this analysis of the Wind Faraday Cup proton spectra. In addition to the new response function I have introduced a new method for determining the effective collecting area of the instrument, carried out the first detailed analysis of the accuracy with which the Faraday Cup can quantify the solar wind ions, and compared the results of the non-linear and moment analysis techniques.

There are several reasons why we would like to measure anisotropies in the plasma species seen by the WIND Faraday Cup:

- Based upon the χ^2 merit function defined and discussed in Section 2.4.2, the bi-Maxwellian velocity distribution function is a more accurate description of ion species seen in the solar wind than a single isotropic Maxwellian VDF. From the simple point of view of conducting the best analysis of existing data as possible we should make the extension to a two-temperature model.

- Plasma micro-instabilities should place limits on the maximum temperature anisotropies allowed in the solar wind. Knowledge of these instabilities is of interest to the general plasma community.

- The existence of anisotropies in the ion distributions may significantly alter the results of certain analysis methods, for example in the study of collisionless magnetohydrodynamic shocks.

- Recent results with data from the SOHO spacecraft [Antonucci et al., 2000; Cranmer, 1999] suggest that extreme ion anisotropies exist in the solar corona. Anisotropies observed in the solar wind may contain information about this process and are therefore useful in the study of the corona and origin of the solar wind.

Section 2.2 describes how the Faraday Cup works and then details the derivations of FC response functions for a given velocity distribution function. The non-linear analysis algorithm is outlined in Section 2.3. In Section 2.4 the uncertainties in each of the derived parameters are explored.

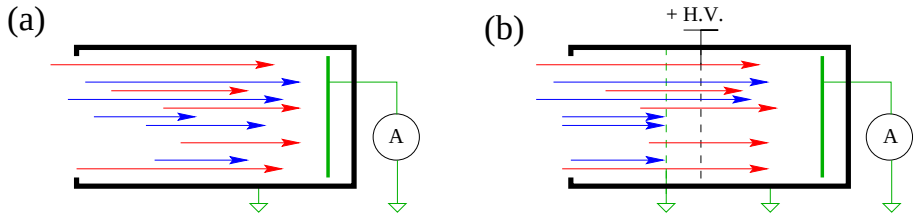

Figure 2-1: A simple cartoon showing how a Faraday Cup measures charged particle fluxes. In (a) particles of various energies (energy $\propto$ length of arrow) and different charges (red,blue) are allowed to flow through an opening into a grounded metal container. An insulated metal plate at the back of the cup collects the particles and the total current is measured as these particles flow through the wire (green) to ground. In (b) two metal grids have been inserted into the cup. The outer grid is grounded and a voltage is applied to the inner grid to repel particles of the desired charge.

2.2 Faraday Cup Measurements of Ion Distribution Functions

The operating principles of a Faraday Cup are straightforward. In fact the FC is one of the few instruments for which analytic expressions may be derived for the response to a given ion distribution. Access to an analytic expression is a tremendous advantage because it allows us to compare a model distribution function with the observations and to vary the parameters of that model to produce the best agreement with the observations. As a byproduct of that analysis, we also get estimates of the uncertainty in each parameter. One of the themes of this thesis is that these uncertainties may be propagated through to any derived quantity we wish to explore, which then allows us to express a rigorous value for the statistical significance of any result.

The operational design of a Faraday Cup is outlined in Section 2.2.1, followed in Section 2.2.2 by a description of a single ion spectrum measured by the two Faraday Cup (FC) instruments on Wind. In Section 2.2.3 the response of a FC to an isotropic Maxwellian distribution function is derived. In Section 2.2.4 that response is extended to a bi-Maxwellian VDF. As a second method for analyzing FC ion spectra the moment analysis procedure is described in Section 2.2.6, and an algorithm for determining temperature anisotropies with moments is detailed in Section 2.2.7. A new method for calculating the correct effective collecting area of the FC due to the transparency of the grids is presented in Section 2.2.5.

2.2.1 Operational Design of the Wind/SWE Faraday Cups

The basic principle of operation of a Faraday Cup ion instrument is to measure the current produced by the flux of particles which pass through the instrument and impact one or more electrically insulated collector plates. This processes is indi-

cated schematically in Figure 2-1. In the left image particles of positive and negative charges, q_+, q_- (red and blue arrows) and varying speeds $v_\parallel$ parallel to the instrument symmetry axis (proportional to the lengths of the arrows) pass through an entrance with area A and impinge upon a collector plate which is insulated from the instrument. Excess charge does not build up on the collector because it is grounded through the green wire. As current flows through the wire it is measured by an ammeter. But what is the relationship between the measured current and the VDF? If the VDF of the particles are uniform across the entrance and their average speeds and densities are $U_{\parallel+}, U_{\parallel-}$ and $\rho_{\parallel+}, \rho_{\parallel-}$, then the measured current is,

$$I_{\text{meas}} = q_+\rho_+U_{\parallel+} + q_+\rho_+U_{\parallel+}. \tag{2.1}$$

The problem with this configuration is that the properties of the positive and negative particles are intertwined. Indeed, if they had the same average speeds and the plasma were neutral overall then no current would be measured. An improvement to the design is shown in the second image of Figure 2-1, in which two wire grids have been inserted within the instrument, between the entrance and the collector plate. The outer grid is grounded and a positive high voltage $V_{\text{H.V.}}$ is applied to the inner grid relative to the instrument. This has the effect of shielding the collector plate from positively charged particles with insufficient energy to penetrate the region between the grids. A particle of mass m and charge q is reflected unless

$$\frac{\frac{1}{2}mv_\parallel^2}{q} \geq V_{\text{H.V.}}, \tag{2.2}$$

which now allows the FC to probe the distribution of particles $f(v_\parallel)$ as a function of their speed normal to the grids by varying $V_{\text{H.V.}}$ and recording I_{meas}. There are still several aspects which need improvement. For example, photoelectrons produced by ultraviolet rays from the sun illuminating the collector plates or secondary electrons produced when a particle strikes the collector surface and subsequently escape could generate additional currents which may overwhelm the real signal. Additionally in this example the VDF of the particles which have sufficient energy to pass the high voltage grid has been altered. Still, this does illuminate the the basic operating principles of a Faraday Cup. Since (2.2) does not involve the phase space density's dependence upon speeds $\vec{v}_\perp$ perpendicular to the cup axis, the FC measures a quantity related to the reduced distribution function (1.65), as described in Section 1.2.6. The three-dimensional characteristics of the VDF are then resolved by placing the instrument on a rotating spacecraft. The first observations of ion fluxes in space were performed using such a Faraday Cup, with a large, fixed negative voltage to prevent the entrance of electrons into the detector [Gringauz et al., 1960]. The fixed voltage design is still used today [Němeček et al., 1997; Santolík et al., 1997], mainly due to its simplicity and ability to rapidly characterize the ions through single measurements of the flux, resulting in measurements with a high cadence [Unti et al., 1973], but at the loss of resolving the VDF.

Faraday Cups have been a workhorse for space plasma measurements for the du-

ration of *in-situ* space exploration [Vasylinuas, 1971; Gloeckler, 1990]. Over the last four decades the MIT space plasma group has developed and extended the capabilities of these instruments for exploring the heliosphere [Bridge et al., 1977; Gazis et al., 1989], by reducing their mass and power requirements, [Lazarus et al., 1993], increasing their cadence [Aellig et al., 2001a], and extracting additional information from existing observations [Richardson, 1986; Kasper et al., 2001a,b].

Many improvements may be made to the basic design, and the Faraday Cups flown on the Wind spacecraft reflect this. The design characteristics of the two Faraday Cups of the Solar Wind Experiment (SWE) on the Wind satellite are shown in Figure 2-2 There are a total of nine grids in the Wind Faraday Cups, each serving a special purpose. Instead of the pair of grounded and high voltage grids in Figure 2-1, a modulator assembly contains a high voltage grid surrounded by two ground grids. As a result, any particle which manages to pass the high voltage grid is re-accelerated to its original velocity by the time it leaves the assembly, eliminating any distortion of the original VDF. A high-voltage power supply within the instrument applies a square-wave voltage waveform to the grid at the center of the modulator. The square-wave oscillates between two high voltages, V_1 and V_2 at 200Hz, with $(V_2 - V_1)/V_1 \sim 10\%$. As shown in the figure there are three categories of particles for a given set of (V_1, V_2): those that always reach the collector plates, those that never reach the collector plates, and those particles with parallel speeds $V_1/q \leq 1/2mv_{||}^2 \leq V_2$ which only reach the collector plates 1/2 of the time and produce a current which is modulated at 200 Hz. The exact details of the conversion of this alternating current into a measurement which is sent back down to Earth are detailed elsewhere [Ogilvie et al., 1995], but the key is that only the modulated current is recorded. This eliminates the effects of photoelectrons, solar wind electrons, and any other background signals. By stepping through increasing voltages the VDF of ions may be scanned. Two outer ground grids isolate the rest of the spacecraft from electromagnetic interference generated by the oscillating electric fields, and three inner ground grids prevent the modulator from inducing stray currents on the collector plates. A final grid, the suppressor grid, is mounted right above the collector plates and is maintained at -100 volts, a sufficient amount to drive any secondary electrons back into the collector plates.

Another feature of the Wind Faraday Cups is the combination of the limiting aperture located immediately underneath the modulating assembly, and the fact that the collecting surface at the back of the instrument has been divided into two equal semi-circular plates. There is a small but treatable abberation of particles as they travel through the modulator: since the electric field is perpendicular to the grids, each particle maintains its velocity component parallel to the grids. Therefore as it is slowed down and subsequently reaccelerated in the modulator it continues to travel in the plane of the collectors. The net result is a translation of the beam of particles which is a function of their energy (in an analytic treatment it ranges from the geometrical projection at high energies to exactly twice that in the case that the particles just make it through the modulator). The limiting aperture removes this problem over a large range of angles because up to approximately 45° the aperture is evenly illuminated. Thus a clean circular beam is projected onto the collector plates.

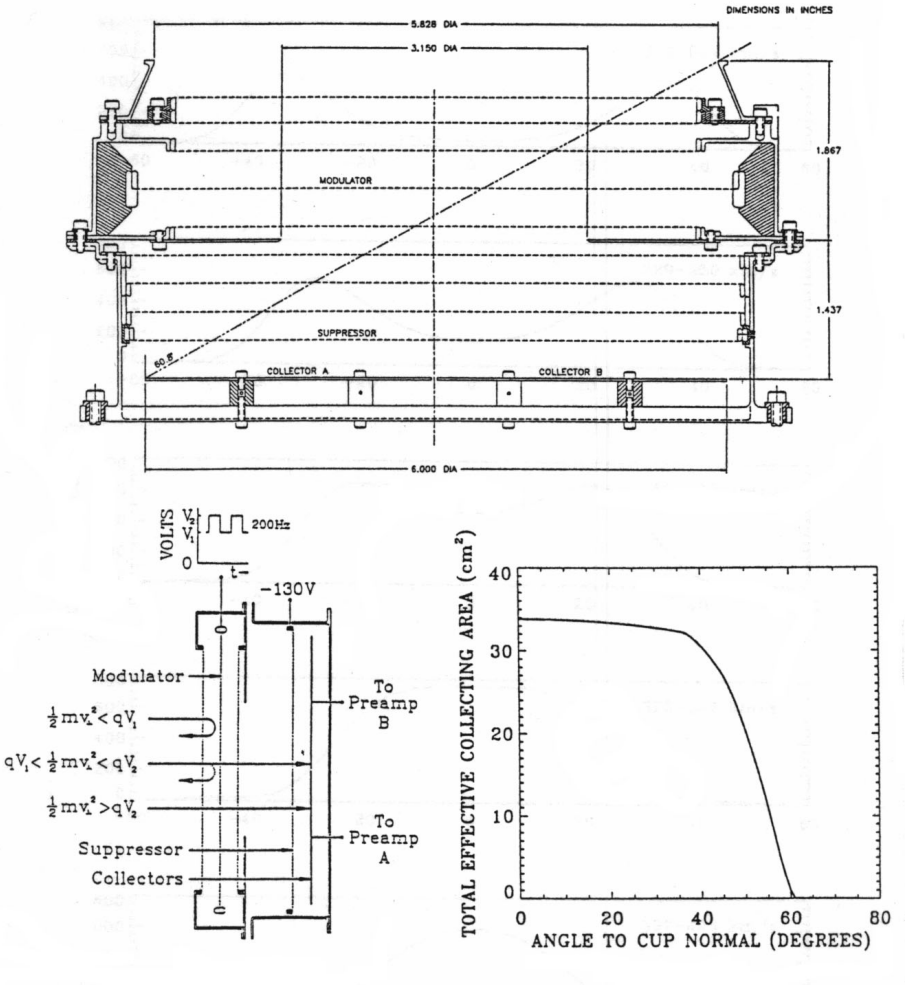

Figure 2-2: An overview of the properties of the Faraday Cups on the Wind spacecraft adapted from [Ogilvie et al., 1995]. *Top:* A cross-section of the instrument along its symmetry axis, showing the entrance aperture, modulator assembly, limiting aperture, suppressor grid, and collector plates. *Bottom Left:* A sketch of the operating principle of the modulator assembly with the three categories of particles: those that always do or do not make it past the high voltage grid, and those which only pass through at one energy and produce a current which is modulated at 200 Hz. *Bottom Right:* The effective collecting area as a function of angle of incidence, this figure includes geometrical effects and the transparency of the wire grids.

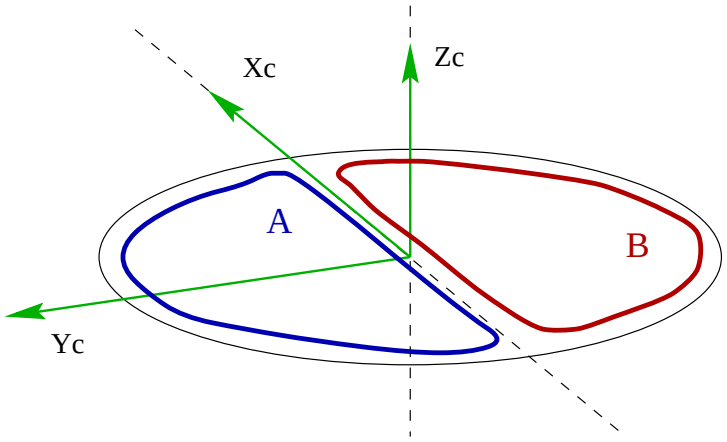

Figure 2-3: Illustration of the Faraday Cup coordinate system for the Wind instruments. The two collector plates, A and B, lie in the $\hat{x}_c - \hat{y}_c$ plane, with $\hat{x}_c$ directed along the split between the plates. The $\hat{z}_c$ axis is normal to the collector plates. In subsequent discussion the "cup orientation" $\hat{n}$ is the direction of $\hat{z}_c$ in the GSE coordinate system.

Since the plates are split, it is then a simple matter to determine the flow angle of the incoming particles based on the relative currents seen by each plate. This allows each cup to individually determine the three dimensional properties of the solar wind ions in the event that one instrument fails. For the purposes of this thesis we will treat each FC as having a single collector plate and simply sum the two currents.

The plot in Figure 2-2 is of the effective collecting area of the instrument as a function of the angle of incidence. There are three factors which determine this. First the size of the limiting aperture, which is about 33 cm^2. Second there is the transparency of the grids, which decreases very slowly from 0° to 40° but then falls off rapidly to zero. The transparency is determined by the thickness of the wires used in the grids and the average separation between wires. It can be calculated analytically and compared with observations in a calibration beam on Earth. Finally at extreme angles, greater than about 45°, the limiting aperture is no longer completely illuminated and the response becomes much more difficult to describe analytically. Numerical simulations have however yielded corrections to the effective collecting area which have been folded into the curve shown in Figure 2-2.

2.2.2 Description of a Single Wind/SWE Faraday Cup Spectrum

Wind rotates once every three seconds, so the following derivations of the response of a Faraday Cup to ion distributions will require transformations between the Geocentric Solar Ecliptic (GSE) coordinate system (described in Section 1.3), and the frame of the instrument. A sketch of the Faraday Cup coordinate system used in all of these

derivations is shown in Figure 2-3. A transformation matrix that converts a vector in GSE components $\vec{V}^G$ to the frame normal to a Faraday cup on Wind, $\vec{V}^C$, is shown below. Call the tilt angle of each cup out of the ecliptic θ, and the azimuthal angle in the ecliptic ϕ. Define ϕ as zero along $\hat{x}_{\rm GSE}$ and increasing towards $\hat{y}_{\rm GSE}$. In component form a vector transformed into the cup frame becomes

$$\begin{aligned} V_x^C &= V_x^G \sin\phi + V_y^G \cos\phi \\ V_y^C &= V_x^G \cos\phi \sin\theta - V_y^G \sin\phi \sin\theta + V_z^G \cos\theta \\ V_z^C &= V_x^G \cos\phi \cos\theta - V_y^G \sin\phi \cos\theta - V_z^G \sin\theta \end{aligned} \tag{2.3}$$

The positions of the instruments which comprise the Solar Wind Experiment, including the two Faraday Cups, on the Wind spacecraft are shown in Figure 2-4. The spin-axis of the spacecraft, labeled "Z" in the figure, is perpendicular to the ecliptic plane of the solar system. The Faraday Cups are located 180° apart and look ±15° out of the spacecraft equatorial plane, with FC1 looking slightly northward and FC2 southward. The line dividing the split collector plates also lies in the ecliptic plane, so the relative current on each plate is related to the flow angle of the solar wind out of that plane, or the "North-South" flow angle. This was done so that a single cup could extract the three dimensional solar wind parameters in the event of a failure.

Each instrument must know the azimuthal orientation of the spacecraft to a high degree of accuracy. The exact period is therefore measured on board by a sun-pulse sensor. The sensor is essentially a photodiode with a narrow field of view mounted on the side of the spacecraft, and each time that side of Wind faces the Sun it generates a pulse. A circuit tracks the average spin rate over several rotations and divides each rotation into 1000 sub-intervals. Small variations in the temperature of the spacecraft change its moment of inertia and thus alter the exact spin period.

A single ion spectrum consists of a set of measurements by the two cups of the reduced distribution function along a series of angles and over consecutive energy windows. Figure 2-5 is a diagram of the measurement sequence. A single spectrum is taken as follows: When the cups are instructed by the SWE Digital Processing Unit (DPU) to begin a spectral observation they wait until a signal is received by the Sun-sensor and then start by performing an internal calibration run for one spacecraft rotation. When the calibration is complete the high voltage power supplies on each cup are enabled and begin modulating between the first pair of voltages. Based on the timing signals from the Sun-pulse sensor the SWE DPU commands each of the two Faraday cups to perform measurements of the current at the single energy window along 20 angles. These angles may be modified through commands from the ground at any time, but they have been kept in the same location since launch: 18 angles spaced evenly at $\sim 3.5°$ intervals in ϕ and two angles directed anti-Sunward, each 35° on either side of the $-\hat{x}_{\rm GSE}$ axis. Upon completion of the spin each modulator is commanded to the next higher voltage pair, and this process continues until the highest energy window is processed.

The FC high voltage power supplies produce a square-wave waveform oscillating

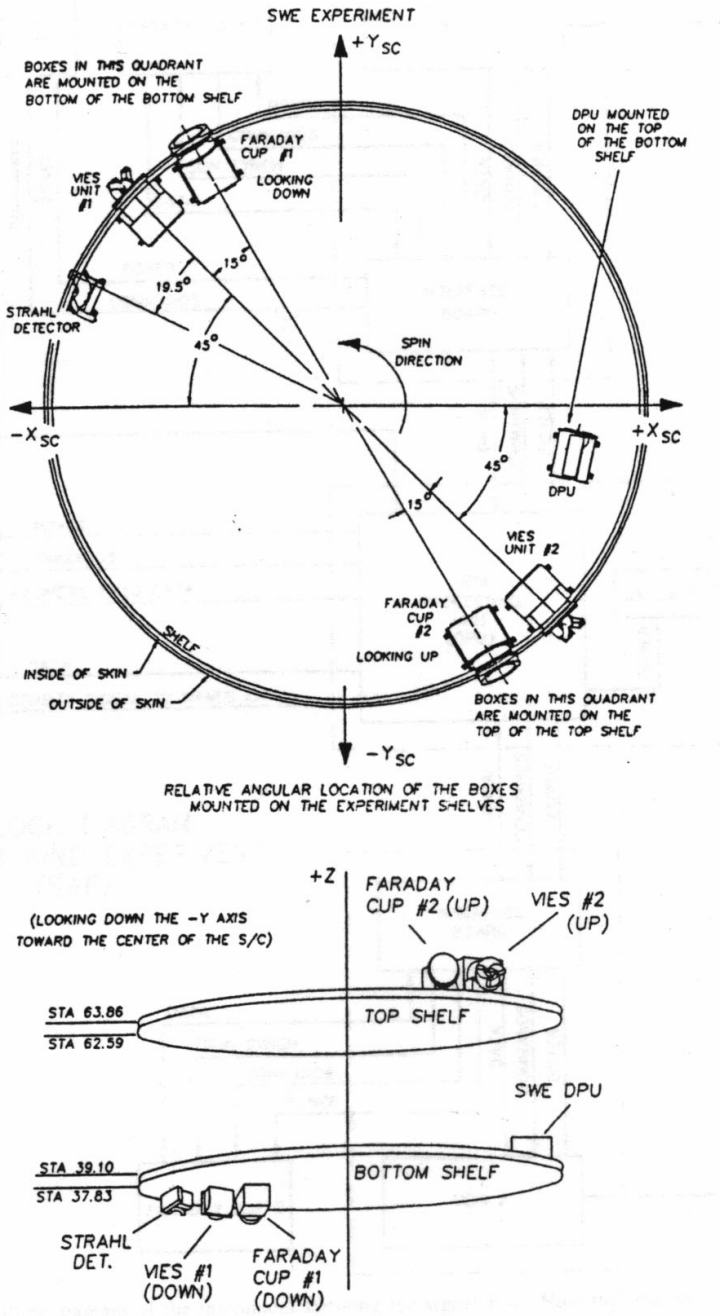

Figure 2-4: Configuration of the SWE instruments on the Wind spacecraft, adapted from [Ogilvie et al., 1995]. The two Faraday Cup ion instruments are mounted ±15° out of the ecliptic plane, with the upper cup looking slightly northward, and the lower cup downward. Also shown are the Vector Ion-Electron Spectrometers (VEIS), the field-aligned electron Strahl detector, and the SWE DPU.

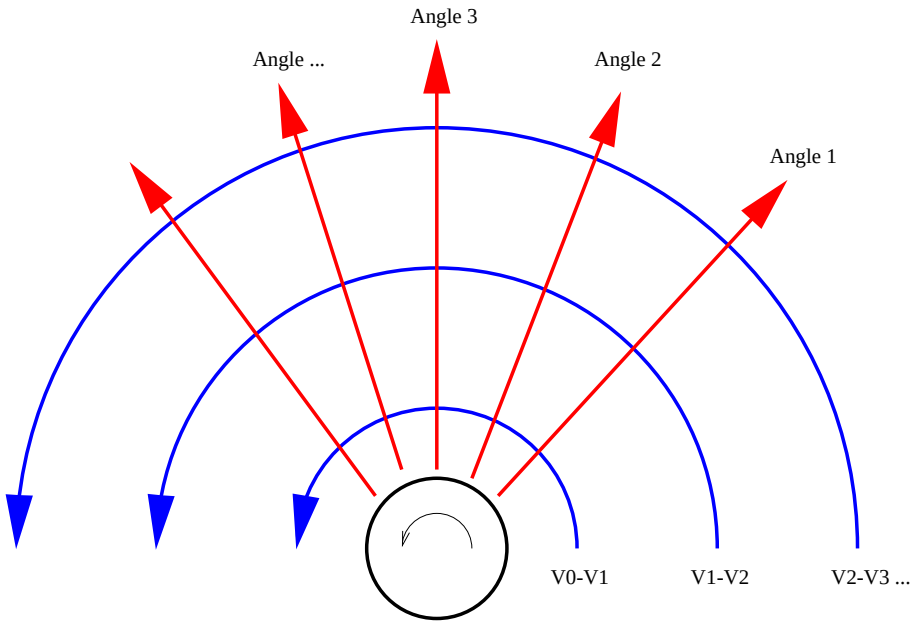

Figure 2-5: Diagram indicating the measurement of a single ion spectrum. In each single rotation the FC measures along each of the angles indicated by red arrows at a single energy window indicated by the blue arrows.

between two voltages selected from a list $\{V_i\}$ of 64 voltages logarithmically spaced from 200 V to 8 KV, with $\Delta V_i/V_i = (V_{i+1} - V_i)/V_i$ a constant 10%. A pair of voltages defines an energy window. There are four modes that the instruments are run in, based on the width and number of energy windows in a spectrum. Single energy windows are bounded by the voltage pair (V_i, V_{i+1}), double energy windows are twice as large, with voltages (V_i, V_{i+2}). The instrument may either conduct a full scan, stepping from the lowest to the highest energy windows, or it may "peak-track", by only observing a subset of windows which bracket the window from the previous observation which returned the highest current. In general the Wind cups operate either in full-scan with double width energy windows or peak-track with single energy windows. The net result is that there are almost always 30 total energy windows in each spectrum.

A FC spectrum thus consists of 2400 measured currents $I_{\rm meas}$ as a function of the orientation of the instrument (θ, ϕ) and the location of the energy window $(V, \Delta V)$,

$$2 \text{ instruments} \times 2 \text{ collectors} \times 20 \text{ angles} \times 30 \text{ windows} = 2400 \qquad (2.4)$$

For this study the currents from the two collector plates in each cup are summed together, so there are 1200 measurements in a spectrum. The goal is to extract accurate and precise ion parameters from this set of currents. In the following two sections I derive the expected currents from two model ion distribution functions,

the Maxwellian and the bi-Maxwellian VDF. Once we have a relation for the model current I_{model} as a function of the model parameters and the instrument variables,

$$I_{\text{model}}[\theta, \phi, V_\circ, \Delta V; f_{\text{model}}(\vec{v})], \tag{2.5}$$

we can determine the parameters which produce the best fit to the observations. Section 2.2.6 describes an approximate method for extracting the same parameters for protons by calculating the moments of the observed currents.

2.2.3 Response to an Isotropic Maxwellian Ion Distribution

First consider the current incident on a collector plate with area A in response to an isotropic, convected Maxwellian plasma with charge q, number density n, bulk velocity $\vec{U}$ and thermal width w. The collecting area A is a function of the size of the limiting aperture, but it additionally reflects the transparency due to the wires of the grids, so it is a function of the angle of incidence. During a single measurement, the FC high voltage modulator alternates rapidly between two voltages. These two voltages correspond to the minimum speeds, $V_\circ$ and $V_\circ + \Delta V_\circ$, that a particle must have *normal to the grids* to pass through the modulator and impact the collector plates. The instrument returns the difference in currents observed when the grids are set to $V_\circ$ and $V_\circ + \Delta V$. We can do the same by integrating over the region of velocity space which contributes to that final signal.

The differential amount of current dI produced by a small element of plasma with velocity $\vec{v}$ in the frame of the FC (and speed $v_z = \vec{v} \cdot \hat{z}_{\text{c}}$ normal to the cup) is given by

$$dI = A(\vec{v}/v) q v_z f(\vec{v}) d^3\vec{v}, \tag{2.6}$$

which is a more general form of the current seen by the simple FC (2.1).

Inserting the isotropic Maxwellian distribution (1.54), the total current produced is obtained by integrating over the entire window,

$$I_{\text{iso}} = \frac{Anq}{\pi^{3/2} w^3} \iiint_{\text{window}} v_z e^{-\frac{(\vec{v}-\vec{U})^2}{w^2}} d^3\vec{v}. \tag{2.7}$$

Now we have to make two assumptions in order to get an analytical result. These are both justified because the typical ratio of the bulk speed of the ions in the frame of the Faraday Cup to the thermal width of the distribution in the solar wind is $U/w \sim 10 - 20$, so the ions appear from a $2^\circ - 6^\circ$ region of the sky. The validity of this assumption is demonstrated in Figure 2-19 of Section 2.5 using the results of the analysis.

- The effective area of the instrument does not have to be folded into the integration. Instead it can be pulled out of the integral and estimated by using the angle from which the bulk of the particles contributing to the current measured in this energy window were incident. The proper subsequent calculation of the effective area is discussed in Section 2.2.5.

- When examining the current produced by a region in phase space bounded in the cup frame by $V_z : [V_\circ, V_\circ + \Delta V_\circ]$, particles in phase space with all possible velocities perpendicular to the instrument symmetry axis contribute. In reality there is a maximum possible angle of incidence into the FC, above which incoming particles are blocked. We assume here that the FC measures the current produced by an entire plane of thickness $\Delta V_\circ$ in phase space.

Moving to the rest frame of the plasma by subtracting the bulk motion $\vec{U}$ of the ions,

$$\vec{W} \equiv \vec{v} - \vec{U} \rightarrow d^3\vec{W} = d^3\vec{v}, \tag{2.8}$$

simplifying the exponential term in (2.7). With the integrals in the $\hat{x}_c - \hat{y}_c$ frame running from $[-\infty, \infty]$ the integral takes the form,

$$\frac{Anq}{\pi^{3/2}w^3} \int_{V_\circ - U_z}^{V_\circ + \Delta V_\circ - U_z} \int_{-\infty}^{\infty} \int_{-\infty}^{\infty} (W_z + U_z) e^{-(W_x^2 + W_y^2 + W_z^2)/w^2} d^3\vec{W}. \tag{2.9}$$

The exponential may be broken into three parts, and the two integrations in W_x and W_y carried out separately,

$$\frac{Anq}{\pi^{3/2}w^3} \int_{V_\circ - U_z}^{V_\circ + \Delta V_\circ - U_z} (W_z + U_z) e^{-(W_z^2/w^2)} dW_z \left[\int_{-\infty}^{\infty} e^{-(W_{x,y}^2/w^2)} dW_{x,y} \right]. \tag{2.10}$$

Using the standard relation for the full integral over a Gaussian distribution,

$$\int_{-\infty}^{\infty} e^{-(x^2/\alpha^2)} dx = \alpha\sqrt{\pi}, \tag{2.11}$$

only the integration over W_z remains,

$$\frac{Anq}{\sqrt{\pi}w} \int_{V_\circ - U_z}^{V_\circ + \Delta V_\circ - U_z} (W_z + U_z) e^{-(W_z^2/w^2)} dW_z. \tag{2.12}$$

This can be separated into two parts by breaking up the $V_\circ - U_z$ sum and writing two integrals,

$$\frac{Anq}{\sqrt{\pi}w} \left[\int_{V_\circ - U_z}^{V_\circ + \Delta V_\circ - U_z} W_z e^{-(W_z^2/w^2)} dW_z + U_z \int_{V_\circ - U_z}^{V_\circ + \Delta V_\circ - U_z} e^{-(W_z^2/w^2)} dW_z \right]. \tag{2.13}$$

The integral on the left has an analytical solution because of the additional factor of W_z proceeding the exponential. The right integral does not, but its value may be expressed using the definition of the error function *erf*, [Abramowitz and Stegun, 1972, §6],

$$\mathrm{erf}(x) \equiv \frac{2}{\sqrt{\pi}} \int_0^x e^{-t^2} dt = 1 - \frac{2}{\sqrt{\pi}} \int_x^{\infty} e^{-t^2} dt. \tag{2.14}$$

The solution is,

$$\frac{Anq}{\sqrt{\pi}w}\left[-\frac{w^2}{2}e^{-W_z^2/w^2}\Big|_{V_o-U_z}^{V_o+\Delta V_o-U_z}+U_z\frac{\sqrt{\pi}}{2}\mathrm{erf}\Big|_{(V_o-U_z)/w}^{(V_o+\Delta V_o-U_z)/w}\right]. \tag{2.15}$$

After simplification we have the model current I_{iso} a Faraday Cup would observe due to the presence of a convected, supersonic, isotropic Maxwellian particle VDF,

$$\begin{aligned} I_{\mathrm{iso}} = \frac{ANq}{2}\Bigg[&\frac{w}{\sqrt{\pi}}\left(e^{-(V_o-U_z)^2/w^2}-e^{-(V_o+\Delta V_o-U_z)^2/w^2}\right)\\ &+U_z\left(\mathrm{erf}\frac{V_o+\Delta V_o-U_z}{w}-\mathrm{erf}\frac{V_o-U_z}{w}\right)\Bigg] \end{aligned} \tag{2.16}$$

This formula has been used historically for fitting Faraday Cup ion spectra. The response functions derived here and in the following section are valid for any supersonic VDF ($|\vec{U}|/w \gg 1$), and they are used in Chapter 4 to characterize alpha particles. The response is a function of the charge q of the species in question, and it is worth noting that an equal flux of $^{+2}$He produces twice the current of protons. This response is also a function of the mass of the particles, because the relationship between the modulator voltages and the speeds corresponding to either limit of the window are functions of the charge to mass ratio of the species, as can be seen in (2.2). Thus observations of alphas and protons, which travel at approximately the same velocity in the solar wind, appear at different voltages in FC spectra (see example (b) in Figure 2-6).

2.2.4 Response to a Bi-Maxwellian Ion Distribution

Figure 2-6 has four examples of possible solar wind ion spectra. They are presented in the raw form in which observations by the Faraday Cups are returned to Earth: the observed current in a given energy window as a function of the energy per ion charge at which the instrument was scanning. Panel (a) is a typical spectra seen in the solar wind, with protons and alpha particles moving with approximately the same speed. The alphas appear at a higher voltage due to their larger mass per charge. The black histogram is the measured current and the blue and red curves are the model responses for protons and alphas respectively which best fit the observations.

Panel (b) of Figure 2-6 shows two measurements of the same ion distribution, but at two angles with respect to the ambient magnetic field. As we shall see this is indicative of a bi-Maxwellian distribution. This chapter details my extension of the analysis of Wind FC ion spectra by fitting the data with a model for the instrument response to convected, bi-Maxwellian velocity distribution functions (1.58) described in Section 1.2.5.

There are other departures from Maxwellian VDFs seen solar wind which will not be examined in this thesis. In Panel (c) the measured currents produced by protons are shown along two angles with respect to the magnetic field, with the black curve

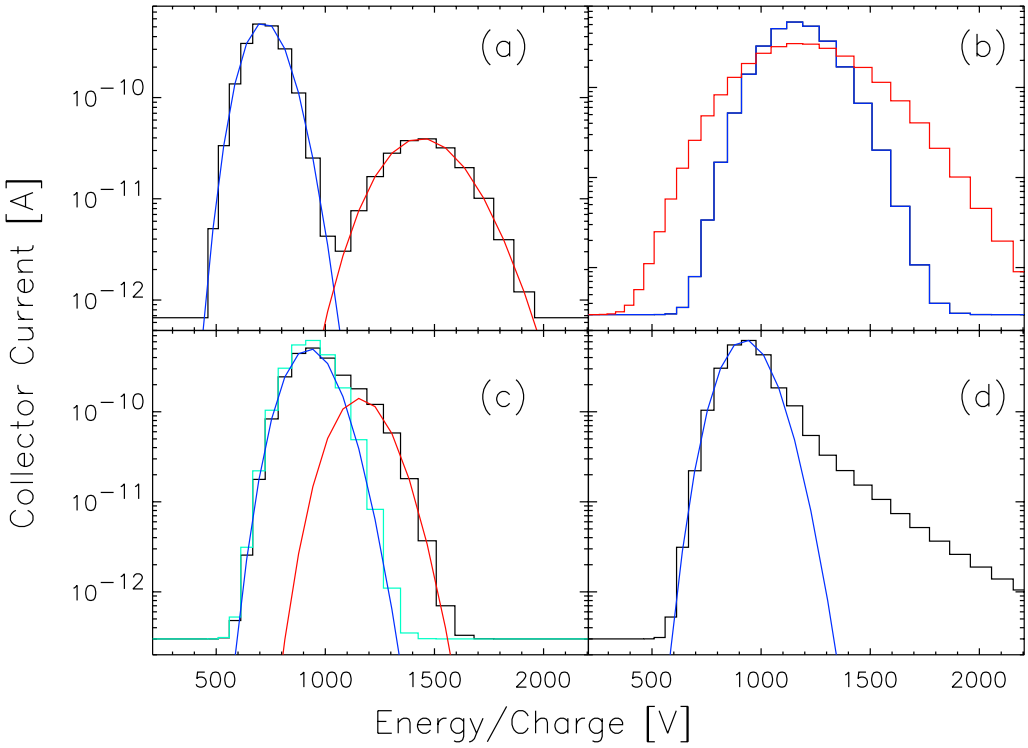

Figure 2-6: A series of examples of ion distributions as a function of energy in the solar wind. Shown are the raw currents recorded by a Faraday Cup on Wind as a function of the center voltage E/q of the window. (a) Maxwellian protons and alpha particles with approximately the same speed. The black histogram is the measured current, while the red and blue curves are the calculated currents using the derived instrument response function and the best-fit parameters; (b) A proton distribution function viewed at two angles relative to the ambient magnetic field. The red curve is from a measurement nearly along the magnetic field, while the blue curve was nearly perpendicular to the fiele. This demonstrates a remarkable temperature anisotropy with $T_{\|p} > T_{\perp p}$; (c) Double double streaming: two separate, differentially streaming Maxwellian proton distributions. The red and blue curves are the predicted currents due to each of the proton distributions, and the green curve is the sum; (d) Protons with a non-Maxwellian high energy tail, which is not fit well by the model response function.

corresponding to measurements made along the field direction. It can be seen that in this case the proton distribution is actually composed of two, separate, possibly bi-Maxwellian distributions. This phenomenum is called double-streaming, and it is being investigated by Dorian Clack [Clack et al., 2001, 2002]. For example, panel (d) demonstrates the directed heat flux $\vec{Q}$ described in Section 1.2.6.

We are now ready to derive the Faraday Cup response to a convected, field-aligned, bi-Maxwellian VDF. In addition to density and bulk velocity, there are now two thermal speeds, $w_\perp$ and $w_\parallel$, perpendicular and parallel to an ambient magnetic field $\vec{B}_\circ$. The starting point is again an integration over the accessible energy window, but with a bi-Maxwellian distribution (1.58),

$$I_{\text{ani}} = \frac{Anq}{\pi^{3/2}w^3} \iiint_{\text{window}} v_z e^{-\left(\frac{v_\perp^2}{w_\perp^2}+\frac{v_\parallel^2}{w_\parallel^2}\right)} d^3\vec{v}, \tag{2.17}$$

where the collecting area has already been pulled out of the integral. In addition to the thermal speeds we must take into account the alignment of the magnetic field. The magnetic field must be transformed into the frame of the cup for each measurement through (2.3). With the unit vector $\hat{b} = \vec{B}_\circ/B_\circ$ defining the orientation of the magnetic field seen by the cup, the integral has been simplified by the substitution

$$\vec{v}_\parallel \equiv (\vec{v}-\vec{U})\cdot\hat{b}, \qquad \vec{v}_\perp \equiv (\vec{v}-\vec{U}) - [(\vec{v}-\vec{U})\cdot\hat{b}]\hat{b} \tag{2.18}$$

The two velocities $\vec{v}_\perp$ and $\vec{v}_\parallel$ are the components of velocity in phase space in the rest frame of the plasma perpendicular and parallel to the magnetic field. The dependence on $\hat{b}$ will complicate the integration, but it is still manageable. With $\hat{b}$ in the frame of the cup we expand $\vec{v}_\perp$ and $\vec{v}_\parallel$, using the same definition of $\vec{W}$ from the previous section,

$$\begin{aligned} \vec{v}_\parallel &= W_x b_x \hat{x} + W_y b_y \hat{y} + W_z b_z \hat{z} \\ v_\parallel^2 &= W_x^2 b_x^2 + W_y^2 b_y^2 + W_z^2 b_z^2 \end{aligned} \tag{2.19}$$

and,

$$\begin{aligned} \vec{v}_\perp = &[W_x - b_x(W_x b_x + W_y b_y + W_z b_z)]\,\hat{x} \\ &+ [W_y - b_y(W_x b_x + W_y b_y + W_z b_z)]\,\hat{y} \\ &+ [W_z - b_z(W_x b_x + W_y b_y + W_z b_z)]\,\hat{z}. \end{aligned} \tag{2.20}$$

The magnitude of $\vec{V}_\perp$ is

$$\begin{aligned} \vec{v}_\perp \cdot \vec{v}_\perp = &(1-b_x^2)W_x^2 + (1-b_y^2)W_y^2 + (1-b_z^2)W_z^2 \\ &- 2b_x b_y W_x W_y - 2b_x b_z W_x W_z - 2b_y b_z W_y W_z. \end{aligned} \tag{2.21}$$

The additional assumption of this expansion is that $\hat{b}$, in addition to the ion VDF, does not vary over the course of the measurement. Substituting these expressions for

$v_\perp^2$ and $v_\parallel^2$ back into (2.17), the integral takes the slightly longer form,

$$\begin{aligned} I =& \frac{Anq}{\pi^{3/2} w_\perp^2 w_\parallel} \int_{V_\circ - U_z}^{V_\circ + \Delta V_\circ - U_z} dW_z \int_{-\infty}^{\infty} dW_x \int_{-\infty}^{\infty} dW_y (W_z + U_z) \cdot \\ & \mathrm{Exp}\Bigg(- \Big[(1-b_x^2) W_x^2 + (1-b_y^2) W_y^2 + (1-b_z^2) W_z^2 \\ & - 2 b_x b_y W_x W_y - 2 b_x b_z W_x W_z - 2 b_y b_z W_y W_z \Big] / w_\perp^2 \\ & - \Big[b_x^2 W_x^2 + b_y^2 W_y^2 + b_z^2 W_z^2 + 2 b_x b_y W_x W_y + 2 b_x b_z W_x W_z \\ & + 2 b_y b_z W_y W_z \Big] / w_\parallel^2 \Bigg). \end{aligned} \tag{2.22}$$

While the term in the exponential has a more complex form than the isotropic Maxwellian case, the integration is still straightforward. The final result for the current I_{ani} due to a supersonic convected bi-Maxwellian VDF is,

$$\begin{aligned} I_{\mathrm{ani}} =& \frac{Anq}{2} \Bigg[\frac{\tilde{w}}{\sqrt{\pi}} \left(e^{-(V_\circ - U_z)^2/\tilde{w}^2} - e^{-(V_\circ + \Delta V_\circ - U_z)^2/\tilde{w}^2} \right) \\ & + U_z \left(\mathrm{erf} \frac{V_\circ + \Delta V_\circ - U_z}{\tilde{w}} - \mathrm{erf} \frac{V_\circ - U_z}{\tilde{w}} \right) \Bigg], \end{aligned} \tag{2.23}$$

where now there is an effective thermal speed $\tilde{w}$ which is a function of the orientation of the magnetic field with respect to the cup,

$$\tilde{w} \equiv \sqrt{b_z^2 w_\parallel^2 + (b_x^2 + b_y^2) w_\perp^2} = \sqrt{b_z^2 w_\parallel^2 + (1 - b_z^2) w_\perp^2} \tag{2.24}$$

By virtue of the fact that the Faraday Cup measures the reduced distribution function, a bi-Maxwellian VDF looks exactly like an isotropic Maxwellian, with an effective thermal speed determined through a simple projection. Note that $\tilde{w}$ only depends on the projection of the field parallel and perpendicular to the cup, and not on the specifics of the field orientation in the cup's $\hat{x}_c - \hat{y}_c$ plane. This result is due to our approximation of the cup as having infinite response in velocity space perpendicular to the collector plates and because we are summing the currents measured by the individual plates in each cup.

We can make a few checks to verify that (2.23) holds under simplifying circumstances.

- **Magnetic field points straight into the Faraday cup**

  In this case b_x and b_y are both zero, and the effective thermal speed reduces to $\tilde{w} = w_\parallel$, as expected.

- **Magnetic field is aligned parallel to the collectors**

If $b_x^2 + b_y^2 = 1$, then there is no b_z component and $\tilde{w}$ reduces to $w_\perp$.

- **There is no anisotropy**

  We have $w_\perp = w_\parallel = w$. Therefore

$$\tilde{w} = \sqrt{b_z^2 w^2 + (b_x^2 + b_y^2) w^2} = w\sqrt{b_x^2 + b_y^2 + b_z^2} = w \tag{2.25}$$

2.2.5 Choice of Effective Collecting Area for bi-Maxwellian Distribution

In the derivations of the Faraday Cup response functions to isotropic and anisotropic Maxwellian distribution functions the effective area A was pulled out of the integral over the energy window. This approximation is justified because A is a slowly varying function of the angle of incidence and because the phase space density is sharply peaked at a single point in the energy window. The VDF will indeed be peaked, both because we are dealing with Gaussian quantities and because the Mach number of the solar wind is very high.

The variation of the effective collecting area as a function of the angle of incidence has been both derived analytically and determined through numerical simulations. The two dominant effects are the varying transparency of the wires which comprise the various grids in the cup, and blocking of the limiting aperture under extreme angles of incidence. Therefore for the purposes of this section $A(\theta)$ is taken as a given, where θ is the the angle of the incident particles relative to the cup normal. Increasingly sophisticated methods for calculating θ are now presented, starting with the original key parameter analysis, the algorithm used for the isotropic alpha-proton analysis [Aellig et al., 2001b], and ending with a new derivation for an anisotropic VDF.

The original key parameter algorithm used a fixed value for A corresponding to its maximum value of 33.8 cm^2 at normal incidence ($\theta = 0$). The non-linear code developed by Aellig for the isotropic analysis of the protons and alphas used the angle between the cup orientation $\hat{n}$ and the bulk flow $\vec{U}$ (for this section $\vec{U}$ is in the frame of the FC),

$$\theta = \cos^{-1} \frac{U_z}{|\vec{U}|}. \tag{2.26}$$

Consider the two example proton velocity distribution functions (a) and (b) shown in Figure 2-7 in the rest frame of a Faraday Cup. $V_\perp$ is the speed perpendicular to the cup normal, and $V_\parallel$ is the speed along the normal axis. The shaded ellipses represent the phase space density of the protons, with the rainbow coloring indicating six thermal widths from the peak. Both VDF have the same bulk velocity $\vec{U}$ and density n, but in (a) the distribution is isotropic with $w = 30$ km/s, while in (b) it is anisotropic, with thermal speeds $w_\perp = 30$ km/s and $w_\parallel = 60$ km/s aligned with the field orientation indicated by the black arrow. The solid blue lines indicate the 45° angle of of incidence to the FC at which the effective area begins to drop

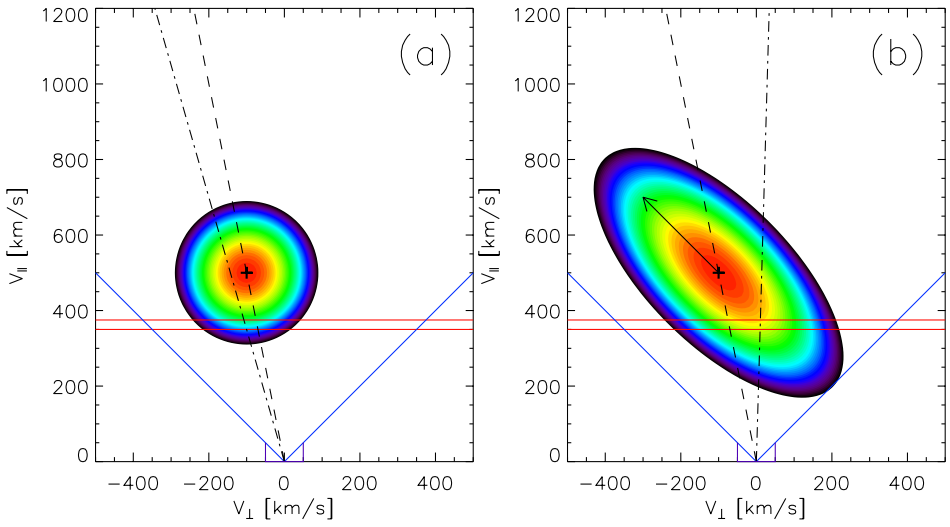

Figure 2-7: Two example distributions in velocity space. *Left:* An isotropic velocity distribution function with a single thermal speed of 30 km/s. *Right:* An anisotropic VDF with $w_\perp = 30$ km/s and $w_\parallel = 60$ km/s, and magnetic field orientation indicated by the black arrow. In both images the cross identifies the maximum density of the VDF, the solid red lines indicate the selected velocity window, the blue lines are the nominal field of view of the instrument, the dashed line connects the origin to the point in the VDF with maximum density, and the dotted-dashed line connects the origin to the point in the energy window with the highest density. It is clear from this example that for an anisotropic distribution we need a better way of determining the angle of incidence than the historical technique.

rapidly, and the two solid red lines mark the upper and lower boundaries of the energy window which we shall now consider. It is clear that for this example the supersonic distributions fit entirely within the region of the energy window seen by the cup. The crosses indicate the location of the bulk velocity of the plasma in each panel, and the dashed lines show the angle determined by (2.26). The dotted-dashed lines are the line from the origin to the actual location of the point in the energy window which contributes the must to the total flux in this measurement.

In the case of the isotropic VDF in Figure 2-7, the difference between the two angles is due to the fact the maximum current in the window does not necessarily come from the same angle as the bulk flow. So the first correction, which works at least for isotropic distributions, is to use the speed $V_\circ$ of the window instead of the

component of the bulk speed normal to the cup, U_z,

$$\theta = \cos^{-1}\frac{V_\circ}{|\vec{U}|}. \tag{2.27}$$

In the case of the anisotropic distribution in (b) however, even (2.27) produces the wrong angle. In fact, both (2.26) and (2.27) may be off by a great deal in the case of large temperature anisotropies. The solution is to derive the location of the point in phase space $(V_x^{\max}, V_y^{\max}, V_z^{\max})$ for a bi-Maxwellian distribution function with the maximum density in a specified velocity window. Under the assumption that $\Delta V_\circ/V_\circ \ll 1$, $V_z^{\max} \simeq V_\circ$, so the problem is now two-dimensional. Start with a differential form of the original anisotropic response equation (2.17),

$$\frac{dI}{d^3\vec{v}'} = \frac{ANq}{\phi^{3/2} w_\perp^2 w_\parallel}(\vec{v}'\cdot\hat{n})e^{-\left(v_\perp^2/w_\perp^2 + v_\parallel^2/w_\parallel^2\right)}, \tag{2.28}$$

where through (2.18) $v_\perp$ and $v_\parallel$ are functions of $\hat{b}$ and $\vec{U}$. Since variations normal to the cup are being neglected, $\vec{v}'\cdot\hat{n}$ is a constant. The collecting area A varies slowly over the range in angles we are considering (in the analysis of a single ion spectrum we will discard point at large angles of incidence). So defining R as the natural logarithm of (2.28) and discarding the area term and any constants,

$$R \equiv -\ln\frac{dI}{d^3\vec{v}'} \propto \frac{v_\perp^2}{w_\perp^2} + \frac{v_\parallel^2}{w_\parallel^2}. \tag{2.29}$$

Now it is just a matter of finding the $(V_x^{\max}, V_y^{\max})$ which maximizes R for a given $\vec{U}$, $\hat{b}$, $w_\perp$, and $w_\parallel$. This is done by differentiating R with respect to V_x and V_y and identifying the point $(V_x^{\max}, V_y^{\max})$ where it vanishes. After some algebra,

$$\begin{aligned} v_x^{\max} &= U_x - \frac{b_x b_z (v_z - U_z)(w_\perp - w_\parallel)(w_\perp + w_\parallel)}{b_z^2 w_\parallel^2 + (1-b_z^2) w_\perp^2} \\ v_y^{\max} &= U_y - \frac{b_y b_z (v_z - U_z)(w_\perp - w_\parallel)(w_\perp + w_\parallel)}{b_z^2 w_\parallel^2 + (1-b_z^2) w_\perp^2}, \end{aligned} \tag{2.30}$$

and the angle of incidence used for the analysis of anisotropic distributions is

$$\theta = \cos^{-1}\frac{V_\circ}{\sqrt{(V_x^{\max})^2 + (V_y^{\max})^2}}. \tag{2.31}$$

2.2.6 Moments of Faraday Cup Spectra

In Section 2.2.3 and Section 2.2.4 we explicitly derived the response of a FC instrument to convected supersonic Maxwellian and bi-Maxwellian ion velocity distributions. Section 2.3 discusses the *non-linear* analysis technique, in which these models are compared with observations to produce a set of ion parameters which give the

best fit to the data. The current section presents a routine for estimating the bulk properties in the solar wind by following the methods described in Section 1.2.6 for collapsing the details of the VDF. This is called the *moment* analysis technique. There are several good reasons to pursue the moment analysis as well as the non-linear method: It is a good consistency check on both methods, and the moments provide an easy visualization of the FC observations of the anisotropies. Additionally, moments are a common method used by investigators to characterize the properties of ions and electrons in the solar wind. As will be seen, the non-linear technique is far more robust and provides much more information about the VDF. Generally the moments are used because of their simplicity, but also because it is not possible in general to produce the same analytic expressions developed in the previous sections for all instrument types. Since there has been a great deal of discussion of differences in solar wind parameters reported by different investigations, which generally involve non-linear analysis of Faraday Cup data and moment analysis of another class of ion instruments, electrostatic analyzers, it is important to apply both methods to the same dataset. In Section 2.4.4 the two techniques are compared and the sources of discrepancies are identified.

The current seen by a FC oriented in the direction $\hat{n}(\theta, \phi)$ and scanning in the window $(V_\circ, V_\circ + \Delta V)$ is the integration over (2.6),

$$dI = A(\vec{v}/v)qv_z f(\vec{v})d^3\vec{v}. \tag{2.32}$$

The FC measures the reduced distribution function (1.65), so with $\bar{A}$ representing the appropriate value for $A(\vec{v}/v)$, which will be determined once we know the bulk velocity of the protons, we write the differential current

$$dI = \bar{A}qv_z f(v_z)dv_z \tag{2.33}$$

as a one-dimensional problem. The most significant approximation of the moment analysis technique is that $f(v_z)$ does not vary much over the width of the speed window ΔV, so we may approximately write the total current ΔI as

$$\Delta I \simeq \bar{A}qv_z f(v_z)\Delta V. \tag{2.34}$$

The phase space density f_i of the reduced distribution function along $\hat{n}$ for the i^{th} window at $(V_i, \Delta V_i)$ is then approximately

$$f_i = \frac{\Delta I_i}{\bar{A}qV_i\Delta V_i}. \tag{2.35}$$

There are several problems with this treatment. First, $f(v_z)$ is a rapidly varying function of v_z, so the approximate integral will be in error. By simply normalizing the current by ΔV_i we have not weighted each part of the energy window correctly. Additionally, we have assumed that all particles move with speed V_i in determining f_i and we know that $\Delta V_i/V_i \simeq 10\%$. Expecting errors on the order of several percent, we can still proceed to calculate proton parameters. Assuming that the entire VDF

is in the energy range swept out by the FC in this spectrum, the apparent proton number density along this angle $n(\hat{n})$ is just the sum of f_i over all measurements in this direction,

$$n(\hat{n}) = \sum_i \frac{\Delta I_i}{\bar{A} q V_i \Delta V_i}. \tag{2.36}$$

In a similar manner to (1.62), the average speed of the distribution viewed in this direction, $U(\hat{n})$, is

$$U(\hat{n}) = \frac{1}{n(\hat{n})} \sum_i f_i V_i. \tag{2.37}$$

Following (1.63) and the fact that in the previous section it was shown that even the bi-Maxwellian distribution will appear isotropic when viewed in a single arbitrary direction, we write the effective thermal speed $w(\hat{n})$,

$$w(\hat{n}) = \sqrt{2} \left(\frac{\sum_i f_i (V_i - U(\hat{n}))^2}{n(\hat{n})} \right)^{1/2}. \tag{2.38}$$

Typically the moments may be calculated along 20 to 30 of the angles in a spectrum, so there are many measurements of the projection $U(\hat{n}) = \vec{U} \cdot \hat{n}$ of the bulk velocity vector $\vec{U}$ into the cup frame. The projection effect is linear, so we have an over-determined set of equations which can be inverted to determine the bulk velocity. The Singular Value Decomposition (SVD) method is used to determine $\vec{U}$ [Press et al., 1999, §2.6].

Finally, the value of $\vec{U}$ is used to renormalize the apparent density $n(\hat{n})$ by taking into account the change of the effective area with angle of incidence, $\theta = \cos^{-1} \vec{U} \cdot \hat{n} / U$, and produce a corrected proton number density, n_c,

$$n_c(\hat{n}) = \frac{A(\theta)}{\bar{A}} n(\hat{n}). \tag{2.39}$$

It is worth mentioning that the moment determinations were not dependent on the actual number density along a given angle as long as A is not a noticeable function of the speed of the energy window.

In the standard moment analysis the proton density and thermal speeds are given by the average values of $n_c(\hat{n})$ and $w(\hat{n})$ over all angles, and the deviation of these quantities is an estimate of their uncertainty. The following section outlines the method for determining the temperature anisotropy from $w(\hat{n})$.

2.2.7 Temperature Anisotropy with Moments

It was shown that observations of a bi-Maxwellian VDF by a Faraday Cup appear isotropic along a given angle (2.23). The simple form of the projected effective thermal speed $\tilde{w}$ in (2.24) suggests that the thermal speeds $w(\hat{n})$ calculated by the moment

analysis may be used to determine the parallel and perpendicular thermal speeds.

The Sunward-facing component of a spectrum contains scans through the proton VDF at 36 (2 cups × 18 angles) angles relative to the magnetic field. Starting with $w(\hat{n})$ and the average background magnetic field $\vec{B}_\circ$, we fit

$$\tilde{w}(\hat{n}) = \sqrt{(\hat{b}\cdot\hat{n})^2 w_\parallel^2 + (1-(\hat{b}\cdot\hat{n})^2) w_\perp^2} \tag{2.40}$$

to the observations with $w_\perp$ and $w_\parallel$ as free parameters.

If the moment and non-linear results agree this will be a good demonstration of the robustness of the ability of a FC to measure anisotropies. There are two cases that could create a disagreement between the results, but this difference could be useful in highlighting intervals in the solar wind which merit further study. In certain cases, especially in the high speed coronal solar wind, the proton VDF generally takes the form of two separate bi-Maxwellian distributions, with a differential flow speed aligned with the magnetic field. Sometimes the solar wind ions possess an appreciable heat flux, which is also directed along the magnetic field. In both of these cases one would expect the moment parallel thermal speed, $w_{\parallel\mathrm{mom}}$ to be greater than the non-linear parallel thermal speed, $w_{\parallel\mathrm{nl}}$.

2.3 Outline of Analysis Procedure

This section is an outline of how the methods developed in Section 2.2 are applied to the ion spectra. In Chapter 4 this routine is extended to include the analysis of alpha particles. The procedure has also been modified to characterize the nature of double streaming protons in the solar wind [Clack et al., 2002].

2.3.1 Preparation of a Single Ion Spectrum

The spacecraft spin rate and the number of energy windows in the spectrum are used to calculate the duration of the observation, which on average is 92 seconds. The set of three-second vector magnetic field measurements provided by the MFI investigation which were made during this observation period are collected and the average ambient magnetic field $\vec{B}_\circ$ is calculated,

$$\vec{B}_\circ \equiv \frac{\sum_i^N \vec{B}_i}{N}, \tag{2.41}$$

along with the deviation of the magnitude of the three-second field measurements, ΔB, and the angular fluctuation of the direction of the field, $\Delta\theta_B$ over the course of the ion spectrum,

$$\Delta\theta_B \equiv \text{Std. Dev}\left(\cos^{-1}\frac{\vec{B}_i\cdot\hat{b}}{|\vec{B}_i|}\right). \tag{2.42}$$

The direction of the field normal, $\hat{b}$, is then calculated in the frame of each of the ~ 1200 individual measurements in the spectrum through the transformation matrix (2.3), under the assumption that the direction does not change much over the duration of the observation. The validity of this assumption is assessed in Section 2.4.4.

2.3.2 Moment Analysis of the Proton Distribution

The moments described in Section 2.2.6 are calculated using data selected from each angle in the spectrum. The data selection proceeds as follows independently for each angle. The speed window V with the largest current $I_{\max}$ (and corresponding flux $f_{\max}$) is identified. All measurements with speeds within $V/2$ of V, fluxes greater than 1% of $f_{\max}$, and currents greater than $1 \cdot 10^{-12}$ A (compare to the instrumental background current $\sim 2 \cdot 10^{-13}$ A) are selected. The moments are then calculated along every angle that has at least three selected measurements, yielding $w(\hat{n})$, $n(\hat{n})$, and $U(\hat{n})$. Application of the SVD algorithm to the $U(\hat{n})$ produces the bulk velocity $\vec{U}$, which is then used to correct the number densities with a better estimate of the effective area. Since the anisotropy of the protons is not known we cannot use (2.31). The moments are calculated over the entire distribution function, so (2.27) is also not well defined. The best that can be done is to use the bulk velocity and (2.26).

Figure 2-8 is a plot of $n(\hat{n})$ as a function of the angle between $\hat{n}$ and the bulk velocity $\vec{U}$ using the moments of a spectrum observed by Wind in the solar wind at 2032 UT on November 3, 1998. The number densities determined by each cup are shown, after the correction to the effective area to reflect the flow angle relative to the cup, with diamonds for FC1 and crosses for FC2. Note the large drop in the calculated number density for angles greater than about 35°. The drop is due to several effects including the rapid change in the effective area which begins near this angle of incidence and the possibility that a portion of the proton VDF is no longer in the field of view of the FC. The median value of the 20 largest densities is calculated, and all measurements of $n(\hat{n})$ within 5% of that value measured at angles less than 40° from the bulk flow of the plasma are selected for subsequent analysis. The selected points in the spectrum displayed in the figure are shown with solid symbols, while the grey symbols indicate density measurements discarded as suspicious. The moment number density is the average of the selected values.

The top panel of Figure 2-9 shows the moment determination of the proton thermal speed $w(\hat{n})$ as a function of the angle between the cup orientation $\hat{n}$ and the average direction of the magnetic field $\hat{b}$ for the same spectrum. The points which are shown as grey symbols correspond to the same points from the previous figure which were discarded as having suspicious number densities. Note the remarkably linear dependence of $w(\hat{n})^2$ on $\hat{b} \cdot \hat{b}$, in agreement with the prediction of (2.24). The over-plotted line is the result of a robust straight-line fit [Press et al., 1999, §15.7] of (2.24) to the observations. The values of $w_\perp$ and $w_\parallel$ which produced the best fit to the observations are listed in the plot, along with the percent error of the fit (The percent error is the best estimate of the quality of the fit possible because we do not know the uncertainties of each moment determination of the thermal speed). For this spectrum $w_\parallel > w_\perp$. The bottom panel of Figure 2-9 is an example of a proton

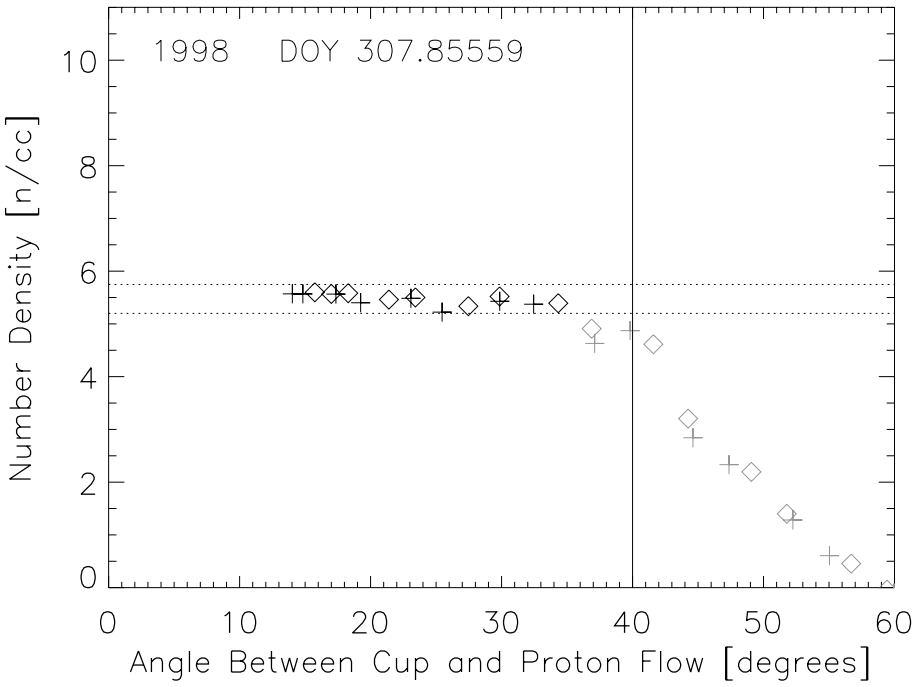

Figure 2-8: An example of the selection of FC angles $\hat{n}$ for a single spectrum to be used for moment determination of density and thermal anisotropy. The number densities determined by each cup are shown, with diamonds for FC1 and crosses for FC2. All points indicated by grayed symbols are discarded from the subsequent analysis because they have a flow angle of greater than 40° from the cup normal or erroneous densities.

spectrum with $w_{\|} > w_{\perp}$.

The optimum limits for data selection and the fitting routine for the anisotropy analysis of the moment data were developed by an undergraduate in the group, James Tanabe [Tanabe et al., 2001], in parallel with my development of the non-linear analysis. Once we had generated plots of $w(\hat{n})^2$ vs $\hat{b} \cdot \hat{b}$ it was clear that the Faraday Cup can indeed make robust measurements of the proton temperature anisotropy.

2.3.3 Initial Guess

An initial guess for the parameters of the proton distribution is needed for the selection of data and as input to the fitting routine. The free parameters are $U_x, U_y, U_z, w_{\perp}, w_{\|}$, and n_p. If the moment analysis succeeded and produced "reasonable" proton parameters then it is used as the initial guess. A reasonable set of parameters is defined as being supersonic ($U/w_{\perp} > 1, U/w_{\|} > 1$), with realistic velocity $U_x < 0$, $200 \leq U \leq 1200$, and density $0.01 \leq n_p \leq 300$.

If the moment analysis was not successful, or the moment parameters are judged to be questionable, then the initial guess is formed directly from the raw currents. It is assumed that the flow is radial, so U_y and U_z are both zero. The bulk speed U is estimated as the speed of the window with the highest current, and $U_x = -U$. A mach number of 10 is assumed, so both $w_{\perp}$ and $w_{\|}$ are set to $U/10$. A fixed number density of 10 protons cm^{-3} is used because the fitting procedure is the least sensitive to the initial guess of the density.

2.3.4 Selection of Proton Data

Individual measurements from the two cups are selected for comparison with the bi-Maxwellian model based upon the initial guess proton parameters. It is important that only currents due to the protons are included in this set, as the inclusion of currents due to effects not accounted for in the model will contaminate the results of the fit. From experience, contamination will effect the bulk velocities least, followed by the number density. The thermal widths are the most sensitive to the inclusion of observations which are inconsistent with the model. Measurement selection is dictated by the four parameters `ANGLEMAX`, `THERMALMAX`, `CURRMIN`, and `PEAKFRAC`, which are now described and justified. The final values of the parameters were determined in a procedure described in Section 2.4.1 and their values are listed in Table 2.1

There are two contamination sources, physical and model/instrumental. Physical factors include the presence of alpha particles, a second proton distribution, or a non-negligable proton heat flux. To avoid substantial contamination from alpha particles the parameter `THERMALMAX` is the maximum number of thermal widths above and below the projected proton speed along each angle in which the selected data must fall. The effective thermal speed is calculated along each angle based on the magnetic field orientation and the current values of the parallel and perpendicular thermal speeds. The effect of non-Maxwellian characteristics like heat flux are limited in part by only taking measurements with currents greater than `PEAKFRAC` times the maximum current in the spectrum.

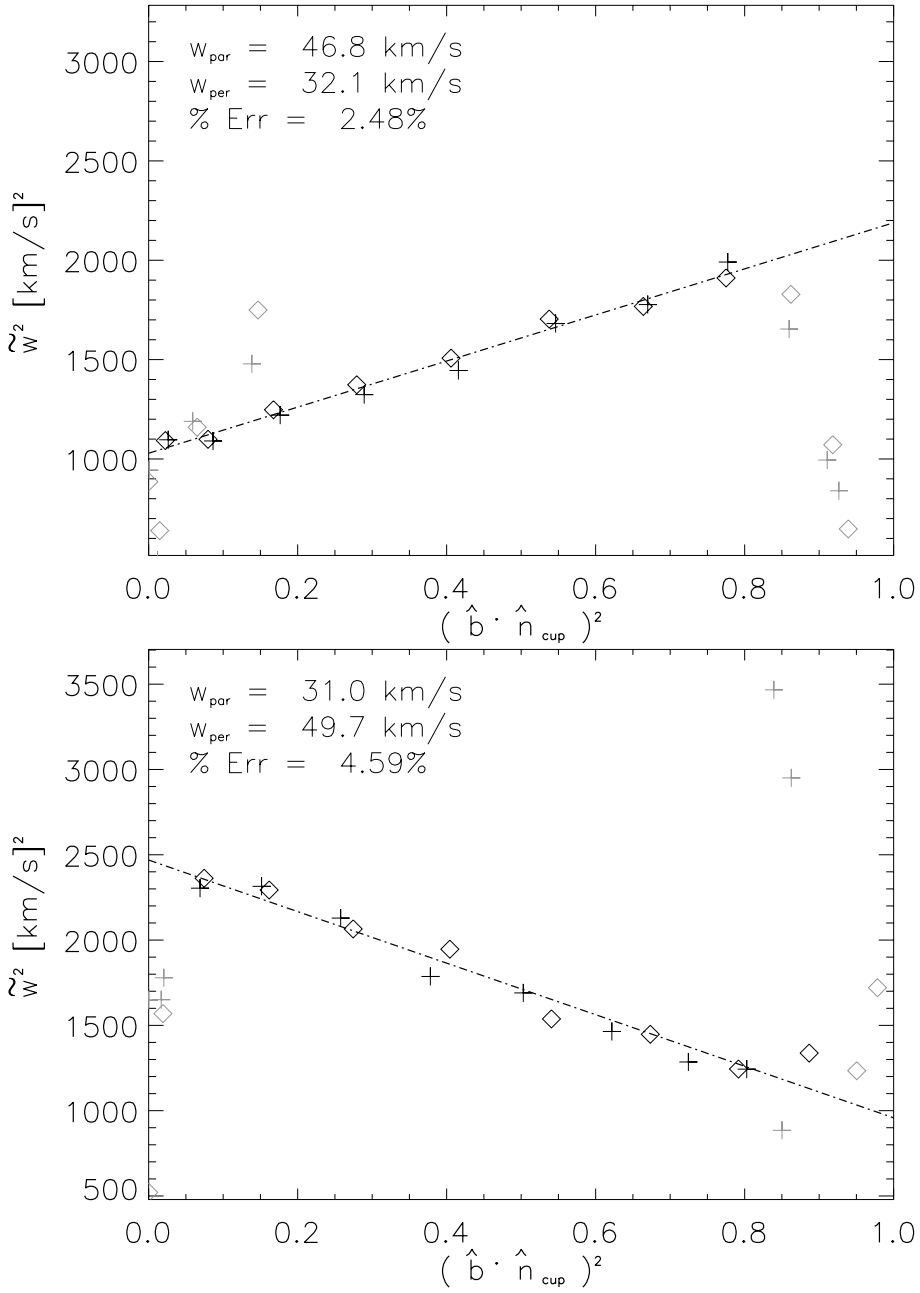

Figure 2-9: Scatter plot of observed thermal speed $w(\hat{n})$ as a function of FC direction relative to the field orientation $\hat{n}$. Grey symbols indicate points discarded due to suspicious densities. The lines are the best fit of (2.24) to the selected observations. The data in the top panel are for the same spectrum shown in Figure 2-8 and have $w_{\|} > w_{\perp}$, whereas in the bottom panel $w_{\|} > w_{\perp}$.

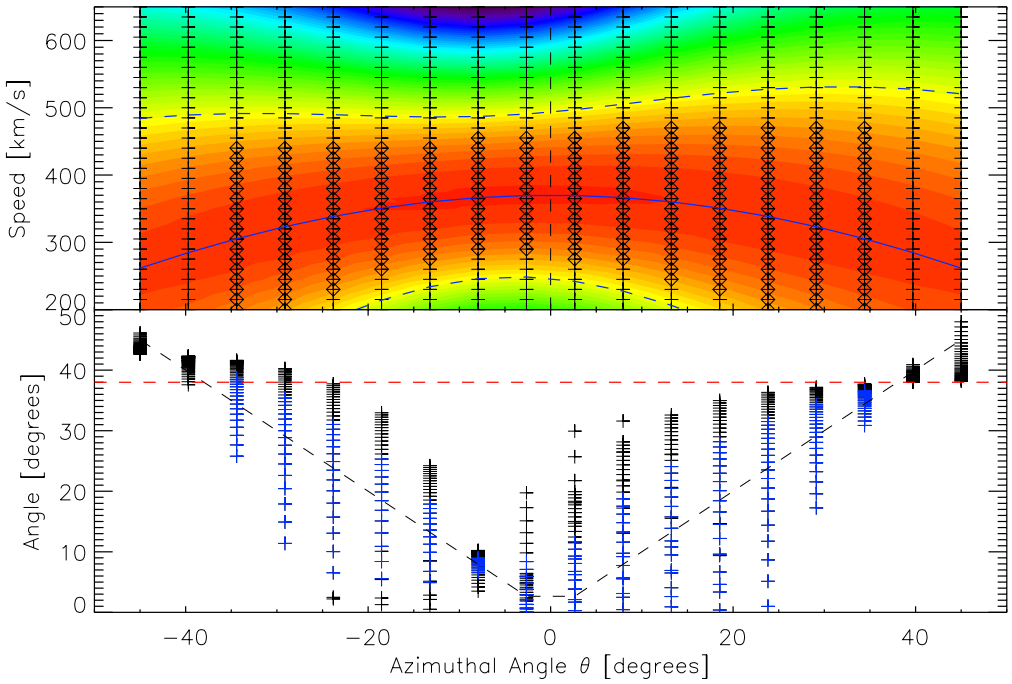

Figure 2-10: Selecting measurements of anisotropic proton distribution for fitting to bi-Maxwellian model. *Top panel:* Color shading indicates logarithmic distribution of observed current as a function of speed window and azimuthal angle; crosses are locations of measurements and diamonds are the selected points; solid line is projection of bulk velocity along each angle and dashed lines mark three thermal widths above and below this projection. *Bottom panel:* Crosses indicates the angle of incidence of the maximum flow for each measurement; Dashed horizontal line (red) is the maximum angle `ANGLEMAX` for selection; Dashed curve is the angle between the cup and the bulk flow; colored (blue) crosses are selected data.

Model/instrumental effects are due to properties of the Faraday Cups which are either not included in the derived models or limit the observations. Due to thermal fluctuations in the amplification electronics there is a background current of approximately $2 \cdot 10^{-13}$ A that the proton flux must exceed to be detected. In addition, an intermittent increase in the background current along a single angle has been observed in the past. It is small compared to ion signatures and has the same value at each energy window along the single angle. The particular angle effected is also seen to change with time, leading us to believe that sunlight is glinting off an object on the spacecraft. Both of these effects are avoided by setting a minimum current `CURRMIN` which observations must exceed.

The final issue is due to the effects of ions at large angles of incidence to the cup. Several of the derivations fail for large angles of incidence: The initial assumptions listed in Section 2.2.3 for deriving the response functions required that the protons were supersonic and entirely in the field-of-view of the cup, thus allowing us to extend the integration in velocity space to an infinite slab; The derivation in Section 2.2.5 of the appropriate effective area was based on the assumption that the protons which contribute most to the measured current flow from an angle where the effective area varies slowly. In addition, at large angles the beam of particles which pass through the limiting aperture and illuminate the collecting plates may in part miss the collectors. As the modulator voltages alternates between the two edges of the window, the beam will partly walk on and off the collectors. This creates an artificial signal which is modulated at 200 Hz and is included in the final measured current. This feature is most often seen at very low voltages and large angles. Data which may experience any of these problems are discarded by setting a maximum angle `ANGLEMAX` to the cup normal. This limit is applied both to the angle between the cup normal and the bulk velocity and to the angle determined by (2.31) for the optimum effective area.

The main aspects of the point selection algorithm are illiustrated in Figure 2-10 for a model proton spectrum. The proton VDF is bi-Maxwellian, flowing radially at -350 km/s with $\hat{b}$ in the ecliptic, -7° from the Sun-Earth line and $w_\perp = 2w_{||}$. The color shading is the logarithm of the observed current as a function of speed window and the azimuth angle of the cup. The crosses mark the location of every measurement in this spectrum and the diamonds are the selected observations. The solid blue line is the projection of the proton bulk speed as a function of the azimuth angle. The two dashed blue lines indicate the upper and lower speed limits with `THERMALMAX` set to 3. Note the variation in these bounds as a function of angle due to the varying effective thermal speed. The bottom panel shows the angle to the maximum flux as determined by (2.31) for each measurement as crosses. The dashed black curve is the angle between the cup and the bulk flow of the protons. The horizontal red dashed line is `ANGLEMAX`, which has been set to 38°. Selected points are colored blue.

A minimum of forty measurements of the proton distribution are required for the analysis to proceed on a given spectrum. Typically at least 200 points were selected.

2.3.5 Non-Linear Fit of Model to Observations

With the magnetic field orientation specified by the MFI field observations, there are six free parameters in the bi-Maxwellian proton model: $\vec{U}, w_\perp, w_\parallel$, and n. Define a χ^2 merit function,

$$\chi^2 = \sum_{i=1}^{N} \left[\frac{I_i^{\text{meas}} - I_i^{\text{mod}}}{\sigma_i} \right]^2 , \tag{2.43}$$

where for each measurement i of the total N observations there is an observed current I_i^{meas}, the current predicted by the model, I_i^{mod}, and the uncertainty σ_i of that measurement. The best-fit values of the parameters are determined by minimizing χ^2. We employ the Levenberg-Marquardt non-linear least-squares method, which is a combination of the inverse-Hessian and steepest descent methods [Press et al., 1999, §15.5]. In addition to the best-fit parameters and the final minimum value of χ^2, a covariance matrix is calculated and inverted to yield one-σ estimates of the uncertainty of each parameter. The final value of χ^2, combined with the number of measurements used in the fit, will indicate how well the bi-Maxwellian model describes solar wind protons.

If the Faraday Cup counted individual particles then the uncertainties σ_i in (2.43) would simply be proportional to the square root of the total number of particles detected. The uncertainty in the currents measured by the a FC is actually limited by the digitization of the observed currents are they are telemetered back to Earth. For the Wind cups the resolution of the telemetered currents is 1%. The weighting factor is set to the larger of one percent of the measured current or the thermal background current,

$$\sigma_i = \left(0.01 \cdot I_i^{\text{meas}} > 4 \cdot 10^{-13}\right)^{-1} . \tag{2.44}$$

Note that the uncertainty of a Faraday Cup current measurement of N particles is not proportional to $\sqrt{N}$, but instead is fixed at $0.01 \cdot N$. It is not a great loss that the uncertainty due to the digitization is larger than simple $\sqrt{N}$ statistics because the approximations we have used in deriving the instrument response introduce errors less than but near that same level.

2.4 Results: Proton Parameters, Uncertainty Propagation and Analysis

The original analysis code written to analyze Wind FC spectra was extended to incorporate the methods described in the previous section. The procedure is completely automated and processes a single day at a time, saving the results in a binary file. For each measurement the time, spacecraft location, magnetic field averages and fluctuations, results from the moment analysis, initial guess, best-fit parameters and their uncertainties, number of measurements selected for fitting, and the minimum value

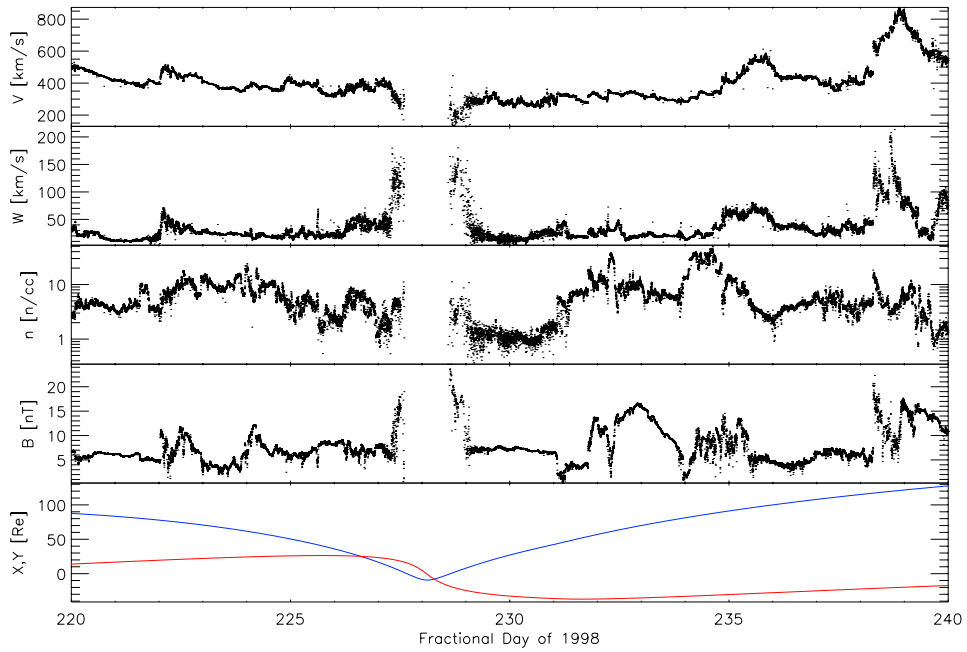

Figure 2-11: Selection of an interval in 1998 for the optimization of the analysis code. Shown from top to bottom are the bulk speed, thermal speed, number density, magnetic field, and location of the spacecraft ($x_{\rm gse}$ blue; $y_{\rm gse}$ red).

of χ^2 are recorded.

On average it takes ten minutes to analyze one day of observations, so our computer system can process the entire mission in approximately one week. Section 2.4.1 demonstrates how the small computing time allows us to optimize the data selection parameters which were described in Section 2.3.4.

The overall convergence of the non-linear analysis and the distribution of values of χ^2 are reviewed in Section 2.4.2. In the subsequent sections the uncertainties of the proton parameters are calculated, and any interesting dependencies are explored.

2.4.1 Optimizing the Analysis

In order to determine the best values for the two analysis parameters `THERMALMAX` and `ANGLEMAX` an interval of obeservations which cover a broad range of interplanetary conditions was selected and processed repeatedly. The "optimum" values of `THERMALMAX` and `ANGLEMAX` produce the best overall minimum average $\chi^2/d.o.f.$ and anisotropic thermal speed uncertainties, $\sigma_{w_\perp}$ and $\sigma_{w_\parallel}$.

Twenty days in 1998, from August 8 through August 28, containing 18,200 spectra, were selected for this procedure. A summary of the bulk speed, average thermal

Parameter	Value	Description
ANGLEMAX	28°	The maximum angle the bulk flow vector and the point in phase space making the greatest contribution to the current in this window may make
THERMALMAX	$3 \times \tilde{w}(\hat{b})$	Number of thermal widths from the peak using projected effective thermal speed at this angle
CURRMIN	1×10^{-12}[A]	Minimum current
PEAKFRAC	5×10^{-3}	Currents must be greater than this fraction of the peak current seen in the entire spectrum
ANGLEMOM	28°	Maximum angle from peak for moment analysis

Table 2.1: The final values of the free parameters used for the anisotropic analysis of protons.

speed, number density, magnetic field strength, and spacecraft location during this period is shown in Figure 2-11. The period was selected because it contained high and low speed solar wind, an encounter with the Earth's bow shock, and several notable interplanetary shocks, especially the August 28 event.

The entire period of selected observations was processed four hundred times, using twenty values of THERMALMAX spaced evenly between 1.0 and 3.4, and twenty values of ANGLEMAX ranging from 10° to 50°. The median values for $\chi^2/d.o.f.$, $\sigma_{w\perp}$, and $\sigma_{w\parallel}$ were calculated. The dependence of $\chi^2/d.o.f.$ and $\sigma_{w\parallel}$ on the choice of THERMALMAX and ANGLEMAX are shown as contour plots in Figure 2-12. For ANGLEMAX less than 18° the model fit the selected observations very well, but the resulting parameters were erratic, suggesting that there was insufficient data to constrain the model successfully. Focusing on the contour of $\chi^2/d.o.f.$, there are two clear trends. First the median value of $\chi^2/d.o.f.$ is a sharply decreasing function of THERMALMAX until approximately 2.5 thermal widths of data are selected. Second, $\chi^2/d.o.f.$ reaches its minimum value for ANGLEMAX greater than about 25°, and decreases slowly afterwards. Examination of several individual events suggested that this slow decrease in $\chi^2/d.o.f.$ was just due to adding more measurements which did not require the model to change a great deal. Recall that the model has 6 free parameters, while as ANGLEMAX increases in this range, the number of observations selected increases from $\sim$ 150 to upwards of $\sim$ 250 measurements. For the uncertainty in the thermal speed the best results came with ANGLEMAX greater than 25° and THERMALMAX greater than 2. The same results were seen in the median uncertainty in the perpendicular thermal speed. The slower variation of the results with THERMALMAX greater than 2.5 appears to be due to setting PEAKFRAC to 0.01, resulting in a limit to the number of measurements selected with inxreasing THERMALMAX.

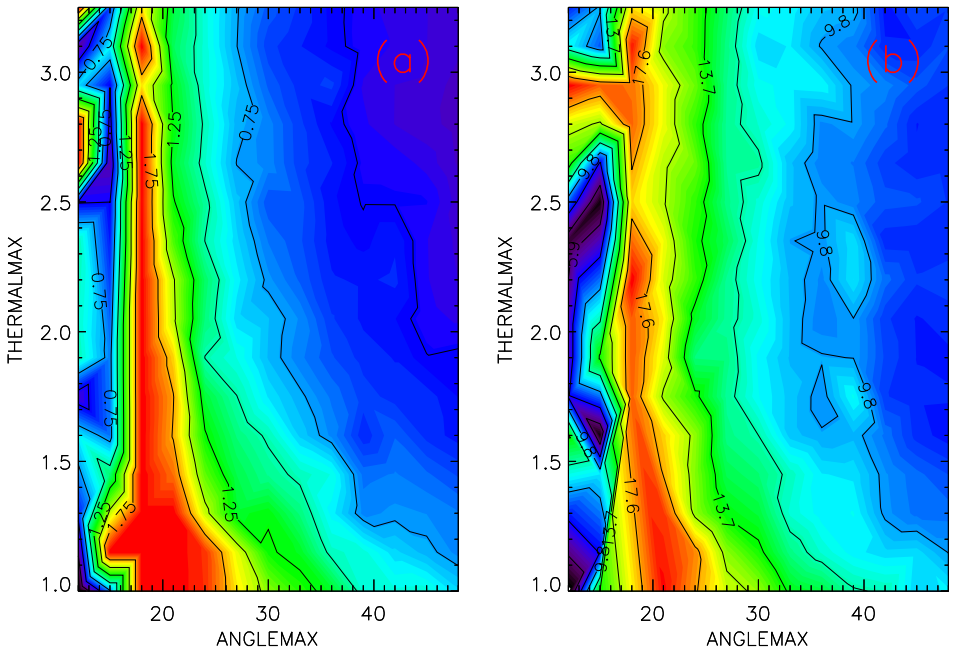

Figure 2-12: Two samples of the optimization procedure for selecting the values of `ANGLEMAX` and `THERMALMAX` which result in the best overall analysis. Panel (a) is the median value of χ^2/d.o.f. and panel (b) is the median value of the percent uncertainty of the parallel thermal speed for each run over the 18,200 spectra contained in the selected interval.

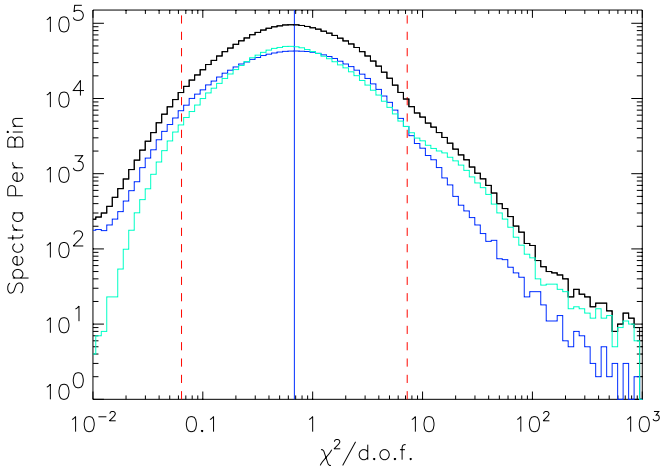

Figure 2-13: Distribution of the final value of χ^2/d.o.f. for all spectra analyzed (black), slow solar wind $v < 400$ km/s (green), fast solar wind $v > 400$ km/s (blue). The average value of χ^2/d.o.f. over all spectra was 0.68 (blue vertical line). The distribution of spectra is approximately log-normal, and 99.9% of the spectra, had final values of χ^2/d.o.f. between 0.07 and 7.3 (red lines). It has approximately the same distribution

2.4.2 Overall Summary: Convergence, $\chi^2/d.o.f.$

To date the Faraday Cups have recorded 2,208,024 measurements, and this analysis produced a converging fit to 99.9957% of these spectra. The 95 spectra which were not fit all had measurements which were suggestive of some form of telemetry error, generally either one or more isolated currents at the maximum value of 10^{-8} A measurable by the cups or empty observations containing no data. This is not to imply that the remaining fits were perfect, there are plenty of factors which come to mind that could cause trouble, such as low Mach numbers or large magnetic fluctuations. In the following sections we will examine the uncertainties in the derived parameters, but here we look at the values of $\chi^2/d.o.f.$ as indicative of how well the bi-Maxwellian model describes solar wind proton velocity distributions.

The value of χ^2 may be used to identify how well the model describes the observations. For a system with ν degrees of freedom the probability of measuring a value of up to χ^2 is given by [Abramowitz and Stegun, 1972, §6.5],

$$P(\chi^2|\nu) = \frac{1}{2^{\frac{1}{2}\nu}\Gamma\left(\frac{\nu}{2}\right)} \int_0^{\chi^2} t^{\frac{1}{2}\nu-1} e^{-t/2} dt. \tag{2.45}$$

There are six parameters in the model, and if a total of N measurements were selected for fitting then there are $\nu = N - 6$ degrees of freedom in the fit. The distribution of

the χ^2/ν for all solar wind observations and separatly for the slow and fast solar wind are shown in Figure 2-13. The average value of χ^2/ν is slightly less than unity, and 99.9% of the observations had values of $\chi^2/\nu \leq 7.3$ To evaluate what this distribution tells us about the quality of the fits, (2.45) was evaluated individually for each spectrum. If the model described the data perfectly, then 50% of the time $P(\chi^2|\nu)$ would be greater than 0.5 and 50% of the time it would be less than 0.5. The result of the calculation was 59% of the observations had $P(\chi^2|\nu) < 0.5$, 41% had $P(\chi^2|\nu) > 0.5$, which is close to the ideal values. It is expected that more of the spectra produced smaller values of χ^2/ν because of the nature of the uncertainty in the current being driven by the quantization of the signal and not the actual (and smaller) error due to counting statistics. It should be noted that the values of χ^2/ν recorded are an indication of how well the bi-Maxwellian model described the selected observations and not of how well or how completely the solar wind consists of anisotropic protons.

2.4.3 Bulk Speed, Velocity Components, and Flow Angles

Once the best-fit values of the solar wind parameters have been determined, the bulk velocity of the protons in the spacecraft frame is corrected for the 30 km/s aberration produced by the orbital velocity of the spacecraft and Earth around the Sun. Since the $\hat{y}_{\rm GSE}$ axis is anti-parallel to the direction of Earth's motion, this is done by subtracting 30 km/s from the $\hat{y}_{\rm GSE}$ component. I then took the individual uncertainties in the components of the velocity and calculated the propagated uncertainty in the bulk speed of the protons,

$$\sigma_U^2 = \Sigma_{i=x,y,z}\sigma_{U_i}^2\left(\frac{\partial U}{\partial U_i}\right)^2 = \frac{\sigma_{U_x}^2 U_x^2 + \sigma_{U_y}^2 U_y^2 + \sigma_{U_y}^2 U_y^2}{U^2}. \tag{2.46}$$

We also use the components of the velocity to calculate the flow angles of the solar wind, traditionally defined at MIT as the direction *from which* the plasma is flowing. We calculate the East-West flow angle in the ecliptic plane,

$$\theta_{\rm EW} = \tan^{-1}\frac{U_y}{U_x}, \tag{2.47}$$

and its uncertainty,

$$\sigma_{\rm EW}^2 = \Sigma_{i=x,y}\sigma_{U_i}^2\left(\frac{\partial \theta_{\rm EW}}{\partial U_i}\right)^2 = \frac{U_x^2\sigma_{U_x}^2 + U_y^2\sigma_{U_y}^2}{(U_x^2+U_y^2)^2}, \tag{2.48}$$

and the North-South flow angle out of the plane of the ecliptic,

$$\theta_{\rm NS} = \tan^{-1}\frac{U_z}{\sqrt{U_x^2+U_y^2}}, \tag{2.49}$$

and its uncertainty,

$$\sigma^2_{\rm NS} = \Sigma_{i=x,y,z}\sigma^2_{U_i}\left(\frac{\partial\theta_{\rm NS}}{\partial U_i}\right)^2 = \frac{(U_x^2+U_y^2)^2\sigma^2_{U_z} + (U_x^2\sigma^2_{U_x} + U_y^2\sigma^2_{U_y})U_z^2}{(U_x^2+U_y^2)U^4} \tag{2.50}$$

2.4.4 Thermal Speeds

There are two possible issues that would prevent an accurate determination of $w_\perp$ and $w_\parallel$ which should be examined in detail: (1) if there is a large angular fluctuation of the magnetic field direction during the 92-second plasma spectrum I would expect any anisotropies in the thermal speed to "wash out"; (2) certain orientations of the magnetic field, even if it is steady, could make it difficult to determine one or both of the thermal speeds.

To address fluctuations, I looked at the ratio of the thermal speeds under two cases: spectra recorded with a large fluctuation of the magnitude of the field but little change in the direction of the field, and the opposite, cases where the magnitude of the field did not change much, but there was a large angular fluctuation. The results are shown in Figure 2-14. It is clear that while changes in the magnitude of the field do not appear to change the distribution of thermal speed ratios, there is a dramatic drop in anisotropy when the angular fluctuation of the magnetic field exceeds x degrees. For subsequent analysis of temperature anisotropies therefore I will restrict myself to cases where the angular fluctuation is less than 20° (this choice leaves 96% of the total spectra). It is worth asking if a plasma undergoing significant angular fluctuation of the magnetic field orientation over the course of the 92-second recording time of a Faraday Cup spectra actually becomes isotropic. One expects high frequency oscillations on the order of the ion cyclotron frequency to efficiently couple to the ion distribution function, so that under the influence of fluctuations on the order of minutes one would expect the field to remain frozen in to the plasma, and for little mixing of the thermal speeds to occur. A future investigation might pursue fitting the wind observations with $\tilde{w}(\hat{b}(t))$, using the fastest possible magnetic field data, preferably the 40 millisecond measurements, and checking to see if that produces a better fit. A detailed study of the quality of the fit as a function of the frequency of the fluctuations might provide insight into the exact mechanisms by which the electromagnetic fluctuations are coupling to the particle distributions.

To explore the uncertainties in the thermal speeds, plots of the median uncertainty of $w_\perp$ and $w_\parallel$ as a function of magnetic field latitude, θ_B,

$$\theta_B \equiv \tan^{-1}\frac{B_z}{\sqrt{B_x^2+B_y^2}}, \tag{2.51}$$

and magnetic longitude,

$$\phi_B \equiv \tan^{-1}\frac{B_y}{B_x}, \tag{2.52}$$

were generated for each parameter. The magnetic field typically lies in the plane of

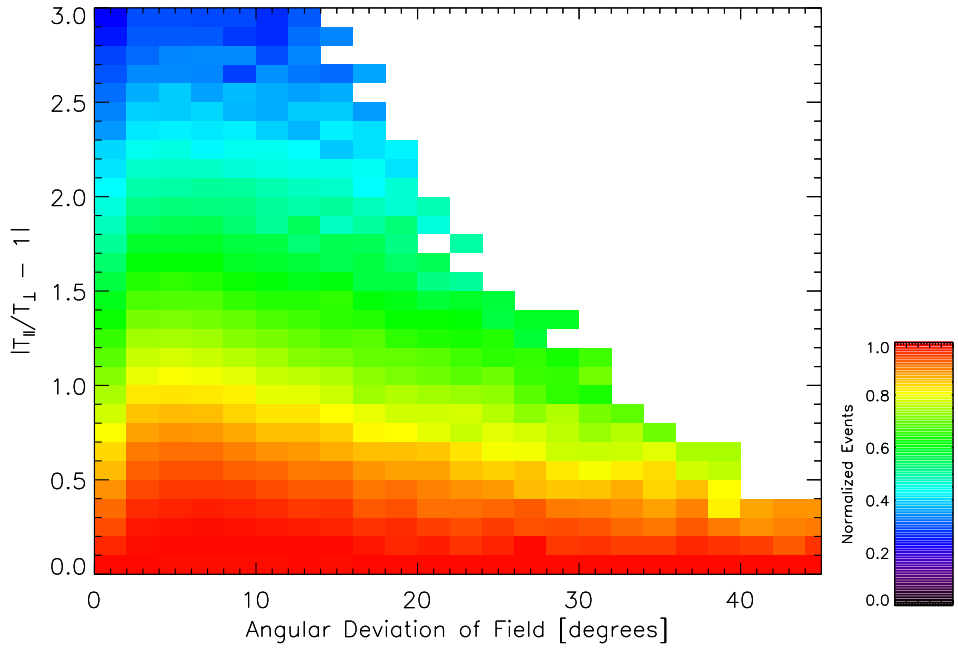

Figure 2-14: Testing the effect of angular field fluctuations during recording of ion spectrum. This is a plot of the temperature anisotropy as a function of the angular deviation of the field, as defined by equation (2.42).

the eccliptic along the Parker spiral angle of about 45°. Therefore the (θ_B, ϕ_B) plane is not evenly covered by the observations.

A summary of the agreement between the moments and the non-linear analysis was presented by Tanabe et al. [2001]. In general the two techniques produced results which agreed to within 30%. The largest differences occurred near interplanetary shocks and in very high speed solar wind.

To determine if the average disagreements between moment and non-linear analysis techniques are instrumental or physical the observed discrepancy is compared to Monte-Carlo simulations of solar wind ion spectra. For each given value of $w_{||}$, 50000 solar wind parameters were generated randomly and the Faraday Cup response was determined using the non-linear bi-Maxwellian response function. This response was then fed into the anisotropic moment analysis code and the results were compared. The diamonds are the observed differences from Figure 2.4.4, the blue lines are the result of the first simulation (thick line is average value of ratio, thin lines mark on standard deviation from mean). Result are reproduced well for $w_{||} \geq 90$ but the simulation does not predict the large errors at smaller values of $w_{||}$. The simulation was improved by including a distribution of alpha particles, resulting in the red curves, which provide a much better agreement with observations. It seems clear that on average the $\sim 20\%$ differences between thermal speeds determined by moment and non-linear analysis techniques are due to a breakdown of the moment method, through contamination by alpha particles and loss of part of the distribution in the case of hot spectra.

For the thermal speeds we would also like to produce an equivalent thermal speed. Starting with the idea of forming a single pressure from an isotropic pressure tensor $\mathbf{P}$ by taking the trace,

$$P_{\rm iso} \equiv {\rm Trace}(\mathbf{P})/3, \tag{2.53}$$

then there is an equivalent relation for the temperatures,

$$T_{\rm iso} \equiv {\rm Trace}(\mathbf{T})/3 = 2T_{\perp} + T_{||}, \tag{2.54}$$

where we have assumed we are dealing with a gyrotropic bi-Maxwellian distribution function. Since $T_{\perp} = \frac{1}{2} m_p w_{\perp}^2, T_{||} = \frac{1}{2} m_p w_{||}^2$, we can then write down a relation for the isotropic thermal speed $w_{\rm iso}$,

$$w_{\rm iso} \equiv \sqrt{(2w_{\perp}^2 + w_{||}^2)/3}, \tag{2.55}$$

and its associated propagated uncertainty,

$$\sigma_{w_{\rm iso}}^2 = \frac{w_{||}^2 \sigma_{w_{||}}^2 + 4w_{\perp}^2 \sigma_{w_{\perp}}^2}{3w_{||}^2 + 6w_{\perp}^2}. \tag{2.56}$$

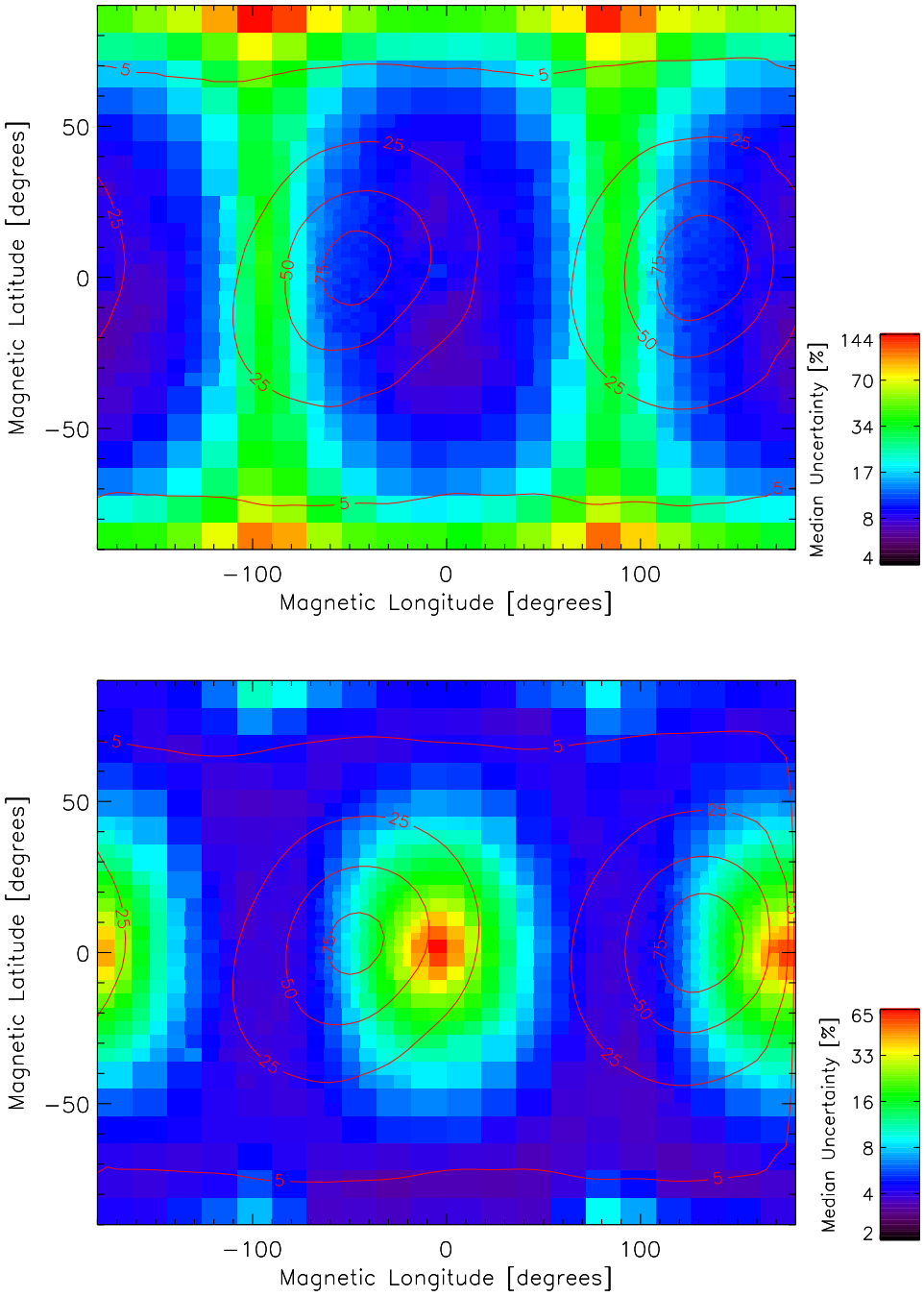

Figure 2-15: Dependence of the uncertainty in parallel (upper panel) and perpendicular (lower panel) proton thermal speeds as a function of magnetic latitude and longitude. Color shading indicates median uncertainty as indicated by color bars on left. Red curves indicate 5,25,50,75% measurement contours. See text for details.

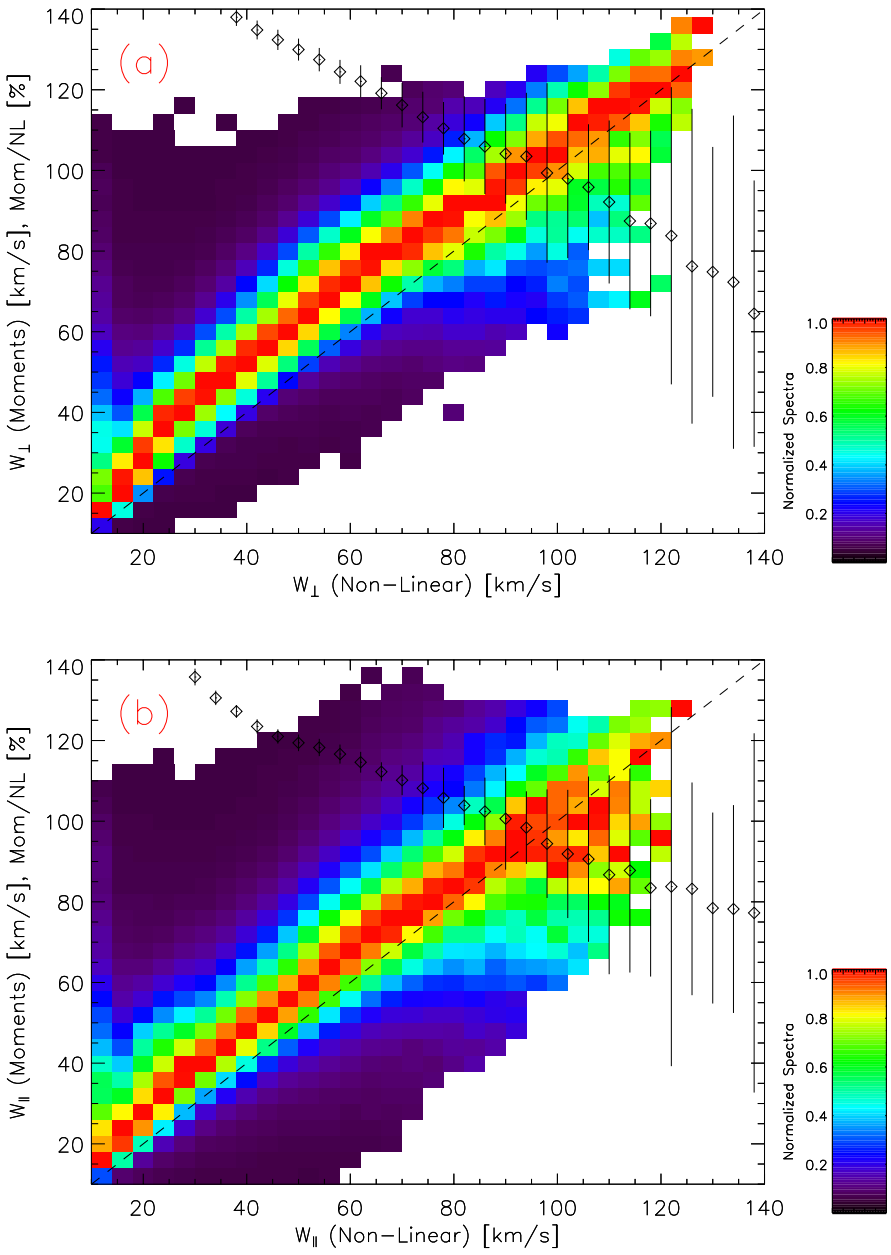

Figure 2-16: Comparison of the thermal speeds as determined by the non-linear and moment analysis techniques. Colored bins indicate the number of spectra in a two-dimensional histogram. Each column has been normalized to unity. Dashed line indicates equality between methods; diamonds are the average ratio between the methods (in percent) as a function of the non-linear value, with error bars indicating the deviation of the ratio in each bin.

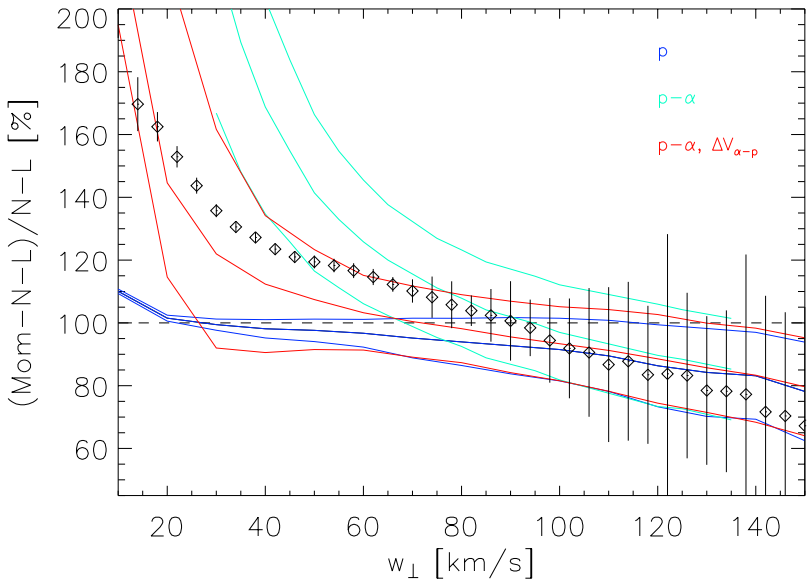

Figure 2-17: Comparison of moment and non-linear anisotropies with the predictions of numerical Monte-Carlo simulations.

2.4.5 Number Density

The average uncertainty in the proton number density over all spectra was $x \pm y\%$, with a median value of $x\%$. The two parameters this uncertainty is most dependent on are the bulk speed of the protons, U_p, and the thermal width of the proton distribution, where for simplicity here I will overlook any temperature anisotropies by using the single isotropic thermal speed, w_{iso} defined by (2.55).

To get a good idea of the percent uncertainty in the number density,

$$100\% \times \frac{\sigma_{n_p}}{n_p}, \tag{2.57}$$

due to the instrument response as a function of U_p and w_{iso}, we generated the plot shown in Figure 2-18.

It is most dependent on the thermal speed and the bulk speed, so I generated a two-dimensional plot of the average percent uncertainty of the number density as a function of the proton bulk speed and the isotropic thermal speed (2.55). I initially divided the plot into 20 intervals spaced logarithmically in number density and linearly spaced in thermal speed. Then I looked at each interval and if there were more than 50 points in that bin I subdivided the bin into quarters. This procedure results in a two-dimensional visualization of the dependence of the thermal speed, with higher resolution in areas with more data.

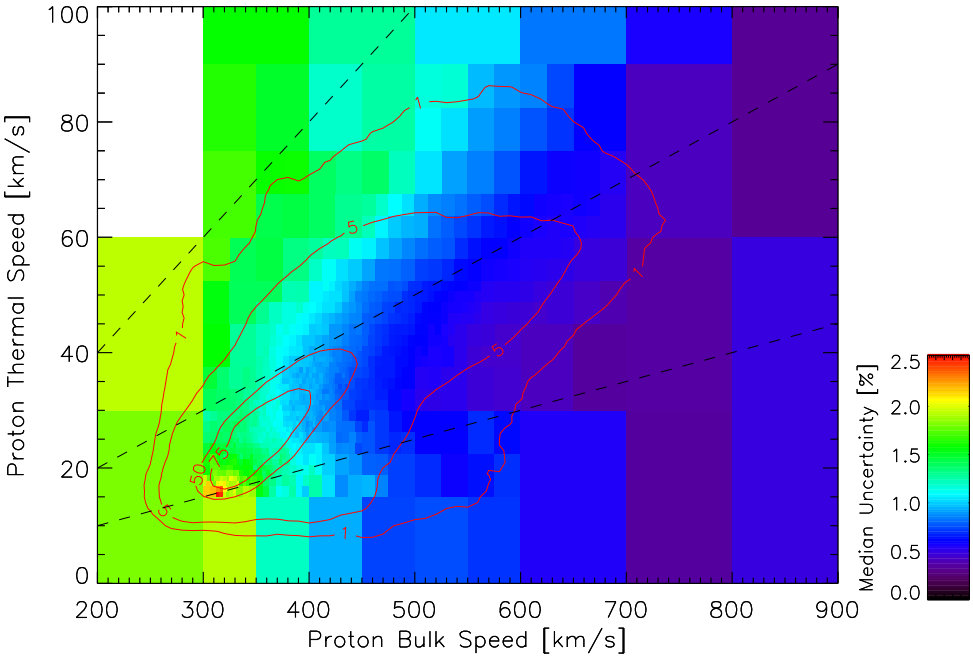

Figure 2-18: The median uncertainty in proton number density as a function of the bulk speed the the calculated isotropic thermal speed. Each bin contains at least $1,000$ spectra; and, where the density of measurements permitted, the resolution of the bins has been increased. The four red contours mark the boundaries at which the density of measurements has fallen to $1, 5, 50$, and 75% of the maximum value. Dashed black lines indicate thermal to bulk speed ratios of 5, 10, and 20.

Parameter	Units	Mean	Median	Stdev	Mean %	Median %
$\|U\|$	km/s	13.5	10.1	10.8	3.1	2.6
U_x	km/s	13.6	10.1	10.9	3.1	2.7
U_y	km/s	1.8	1.0	2.9	12.2	10.5
U_z	km/s	1.7	0.9	2.5	10.7	9.2
θ_{EW}	degree	0.03	0.03	0.02	N/A	N/A
θ_{NS}	degree	0.04	0.03	0.01	N/A	N/A
$w_{\perp}$	km/s	2.6	1.3	4.0	7.7	4.9
$w_{\parallel}$	km/s	6.0	3.3	7.8	15.5	10.7
n_p	cm^{-3}	0.2	0.1	0.4	1.4	1.2

Table 2.2: Uncertainties in each of the derived parameters from the best-fit to individual solar wind spectra.

2.5 Summary

The response of the Faraday Cup instruments on Wind to a convected, bi-Maxwellian distribution of ions has been derived and applied to the observations for the first time. Faraday Cups are the only thermal plasma instruments for which analytical response functions have been derived. Therefore while other investigations in the past have determined ion plasma parameters including temperature anisotropies, this is the first analysis which produced uncertainty estimates for each of the derived parameters along with the $\chi^2/d.o.f.$ estimate of the quality of the fit. Indeed the dataset submitted to the NSSDC, which includes these uncertainties for each spectrum, is the first of its kind. It has been shown that the typical uncertainties of the proton solar wind parameters determined by the FC instruments are all on the order of a few percent, that the average $\chi^2/d.o.f.$ near unity implies that bi-Maxwellian distributions are a good description of the solar wind ions at 1 A.U., and that differences between the moment and non-linear analysis techniques are predominantly due to failures in the approximations which go into the moments.

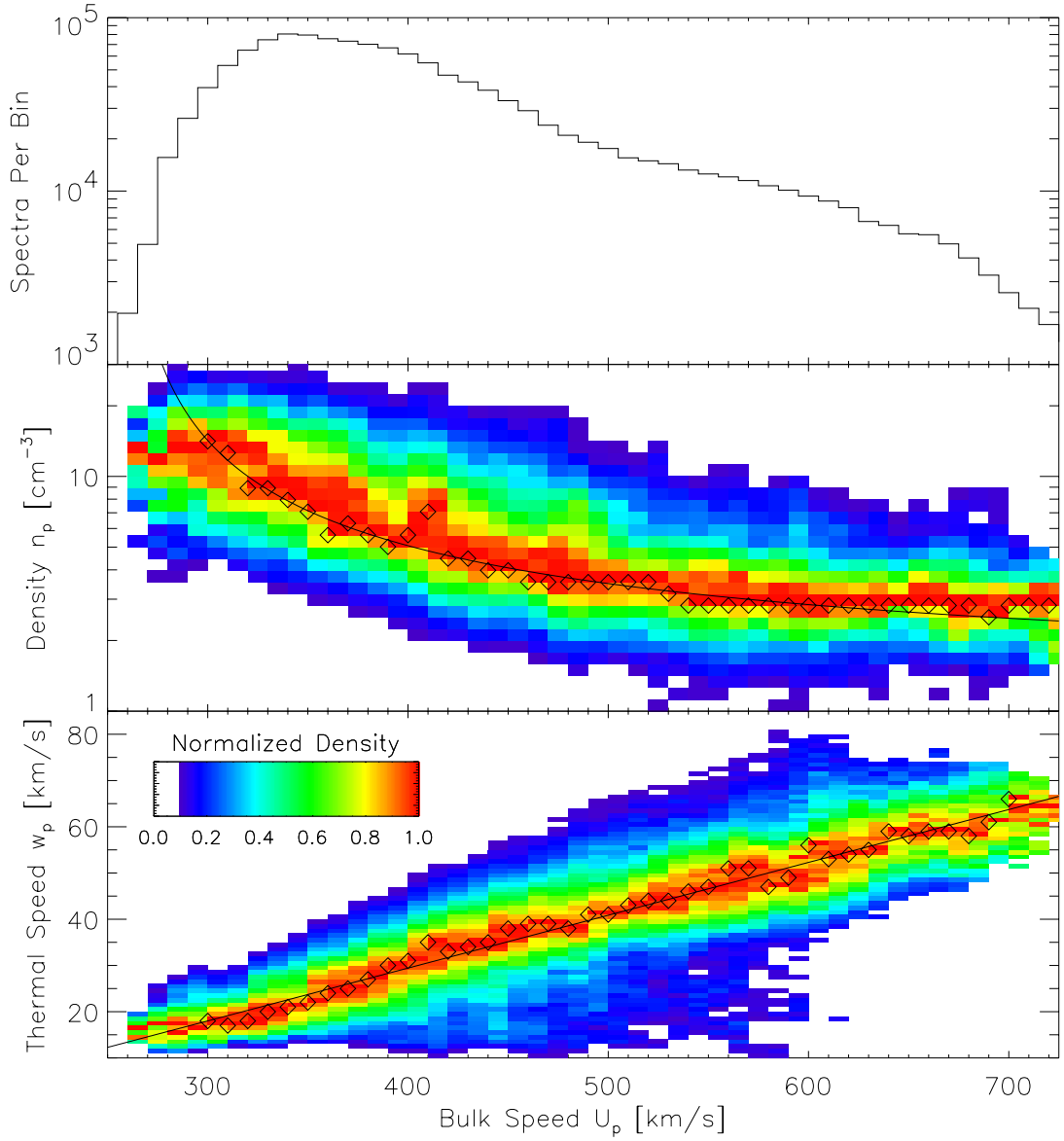

Figure 2-19: Survey of proton parameters in the solar wind at 1 AU as seen by the Wind Faraday Cup instruments. *Upper panel:* The distribution of proton number densities n_p as a function of bulk speeds U_p, showing that on average the particle flux $n_p U_p$ is conserved. *Lower panel:* Single proton temperature $T_p = (2T_{p\perp} + T_{p\|})/3$ as a function of bulk speed, showing that on average the solar wind has a mach number $U_p/w_p \sim 10$.

Chapter 4

Extension of Analysis to Helium

ABSTRACT: *The bi-Maxwellian analysis techniques developed in Chapter 2 to characterize Faraday Cup observations of protons are extended to alpha particles. The success of this procedure is reported, and the results are used to compare Faraday Cup densities with WAVES/TNR observations of the electron plasma frequency.*

4.1 Ion Composition of the Solar Wind

Protons are not the only constituent of the ion component of the solar wind. Fully ionized helium or alpha particles generally account for $1\% - 5\%$, and sometimes as much as 10%, of the ions by number density. Minor ions such as oxygen and iron make up an additional 1%. The properties of these additional ion species contain a great deal of information which is useful for a variety of applications. Broadly speaking the details of the additional ion species are interesting because they effect the dynamics of the interplanetary medium, reflect the origin and acceleration mechanisms of the solar wind, and exhibit the effects of a range of kinetic plasma micro-instabilities.

The Faraday Cup (FC) ion instruments on the Wind spacecraft were introduced in Chapter 2, along with the derivation and application of the convected, field-aligned, bi-Maxwellian velocity distribution function (VDF). As a result of that analysis a best-fit to each ion spectrum yielded a set of proton parameters $\vec{U}_p, T_{\perp p}, T_{\parallel p}, n_p$, their uncertainties, and the χ^2/ν parameter. This chapter describes the extension of that analysis to produce, when possible, the same set of bulk parameters for the alpha particles, $\vec{U}_\alpha, T_{\perp\alpha}, T_{\parallel\alpha}, n_\alpha$. Scientific applications of the alpha measurements are considered in the following chapter.

The additional procedures created to analyze the helium in addition to the protons are described in Section 4.2. Section 4.3 details the results of this analysis, including the success rates. In Section 4.4 the proton and alpha number densities are used in conjunction with the WAVES experiment on Wind to conduct a study of the absolute calibration of the Wind Faraday Cups. In order to continue treating the solar wind as a fluid in the presence of multiple ion species a single fluid description must be developed, and this is done in Section 4.5. A brief summary following in Section 4.6.

4.2 Extension of the Existing Analysis Code

The analysis code was extended to include fitting of the alpha measurements using the methods developed by Aellig as a starting point [Aellig et al., 2001b]. Since the alphas often partially overlap with the protons it was decided that the moment analysis was too susceptible to contamination by hydrogen, so only the non-linear analysis is applied to the helium component of the measurements. No additional work is needed to produce the alpha particle response function. The derivation of the convected bi-Maxwellian response in Section 2.2.4 is used for the alphas, just with the substitution of with charge $2q$ and mass $4m_p$.

The additional program starts after the existing code has successfully produced a converging fit to the proton VDF. If the proton fit was successful then the spectrum is assigned a fit status of 11, if it failed then the fit status is 0 and the code proceeds with the next spectrum. An initial guess is made that the alpha particles have the same parameters as the protons, except with $n_\alpha/n_p = 5\%$, which is a typical value in the solar wind. An extension of the data selection algorithm described in Section 2.3.4 then identifies measurements in the spectrum which are expected to correspond to either protons or alphas. At least 10 points from each cup corresponding to alphas must be selected for the analysis to proceed. The selected data, typically 300-400 measurements, are then subjected to a simultaneous fit with twelve free parameters, $\vec{U}_p, w_{\perp p}, w_{\parallel p}, n_p, \vec{U}_\alpha, w_{\perp\alpha}, w_{\parallel\alpha}$, and n_α.

An single isotropic thermal speed for each species is then calculated, $w_j^2 = (2w_{\perp j}^2 + w_{\parallel j}^2)/3$. In Section 5.3 it will be shown that in general $T_\alpha = T_p$ or $T_\alpha = 4T_\perp$. This is because ion species in the solar wind are generally either in thermal equilibrium, in which case $w_\alpha = w_p/2$, or have equal thermal speeds. If $w_\alpha/w_p \leq 0.75$ then the spectrum is assigned a fit status of 8. No further action is taken but the spectrum is flagged for future investigation as a period where the alphas are cold. If $w_\alpha/w_p \geq 2.2$ then there is the possibility that the alpha and proton distributions overlap and as a result the alpha temperature is too high. In this case fit status is 9 and the analysis will re-perform the alpha fit after subtracting the best fit to the proton distribution.

If $U_\alpha/U_p \geq 1.1$ then the spectrum is assigned a fit status of 7. No further action is taken but the measurements might be useful in studies of intervals with fast alpha particles. If $U_\alpha/U_p \leq 0.97$ or $n_\alpha/n_p \geq 20\%$ then there is the danger that a double streaming proton distribution has been accidently fit as the alpha distribution. In this case the proton fit is subtracted and the alpha distribution is fit to the remaining data.

If after subtraction of the proton data the alpha parameters seem reasonable then the spectrum is assigned a fit status of 5. If after subtraction the parameters are still suspicious then the final fit status is 4 if the alphas are too cold, 3 if they seem too hot, and 2 if they appear too slow. If there are multiple problems with a spectrum it is assigned a fit status of zero.

The final results are the same as described in Section 2.4, just with the addition of the alpha parameters and the fit status. For each spectrum the best-fit parameters, $\vec{U}_p, w_{\perp p}, w_{\parallel p}, n_p, \vec{U}_\alpha, w_{\perp\alpha}, w_{\parallel\alpha}$, and n_α, estimates of their one-sigma uncertainties, the number of measurements selected in each cup, the final value of χ^2/ν, and an array

Fit Status	All	Solar wind	Fast SW $V_p > 400$	Slow SW $V_p < 400$	MSH
0	1.71	1.35	1.42	1.30	14.02
1	16.46	16.06	16.34	15.67	31.41
2	12.66	12.70	15.31	10.08	11.40
3	10.92	11.15	15.37	6.89	2.81
4	0.01	0.01	0.01	0.03	0.00
5	2.43	2.49	2.18	2.82	0.63
6	1.36	1.37	1.40	1.36	0.92
7	3.00	2.58	4.64	0.49	14.76
8	0.08	0.08	0.03	0.14	0.00
9	0.99	1.01	0.44	1.60	0.45
10	48.41	49.45	40.98	58.06	16.45
11	1.92	1.68	1.87	1.47	7.08
Total spectra	2,351,008	2,257,338	1,135,940	1,120,949	57,344

Table 4.1: The success rate of the alpha-proton analysis procedure in various regions in space as a function of the final status of the fit.

of diagnostic parameters are saved to file.

4.3 Results of the Analysis

As of summer 2002 the bi-Maxwellian alpha-proton analysis procedure has been run on more than 2.3 million Faraday Cup spectra. The success of the analysis is illuminated by the statistics in Table 4.1, which break down the percentage of ion spectra as a function of final fit status. The percentage distribution is broken down into several regimes in the solar wind, including all observations, all solar wind observations, and intervals in the fast solar wind ($U_p \geq 400$ km/s), slow solar wind ($U_p \leq 400$ km/s), and magnetosheath intervals. In general there was insufficient data to characterize the alpha distribution 1.9% of the time, based on the number of spectra with a fit status of 11. This was a much larger problem in the magnetosheath, where it occurred 7% of the time. The greatest obstacle to characterizing the alpha particles with a Faraday Cup spectrum is when the proton temperature is especially high, and this is a frequent occurrence in the magnetosheath.

A perfect fit status of 10 occurred 58% of the time in the slow solar wind, and 40% of the time in the fast wind. This can be attributed to three factors. First, as will be discussed in the following chapter, more collisions have occurred in slow solar wind as it propagates from the corona, due to the higher densities and slower travel speeds. As a result the alpha and proton velocities and temperatures tend to be in better agreement as the wind has settled into a more classical definition of equilibrium. Additionally, double streaming protons are a very common feature of the

Parameter	Units	Mean	Median	Stdev	Mean %	Median %
$\|U\|$	km/s	57.7	44.7	43.7	14.1	11.9
U_x	km/s	57.8	44.8	43.8	14.2	11.9
U_y	km/s	6.0	3.7	7.5	45.6	42.3
U_z	km/s	5.4	3.3	6.5	42.2	38.3
θ_{EW}	degree	0.18	0.13	0.33	N/A	N/A
θ_{NS}	degree	0.24	0.01	0.17	N/A	N/A
$w_{\perp}$	km/s	10.2	5.7	11.4	32.7	27.1
$w_{\parallel}$	km/s	13.9	8.9	13.8	45.9	43.1
n_{α}	cm^{-3}	$4 \cdot 10^{-4}$	$2 \cdot 10^{-4}$	0.003	0.12	0.11

Table 4.2: Uncertainties in each of the derived alpha parameters from the best-fit to individual solar wind spectra. Compare with same table for proton parameters in Table 2.2.

high speed solar wind [Clack et al., 2002]. Finally, at high speeds the alpha particle VDF is sometimes not completely observed by the Faraday Cups in their standard speed windows. As a result the fits to the alpha particles at very high speeds do not succeed as often.

4.4 Absolute Calibration of Number Densities

The analysis of Wind Faraday Cup ion spectra in Chapters 2 and 4 have established the accuracy with which we can measure proton and alpha particle number densities in the solar wind. The survey in Section 2.4.5 demonstrated how the one-sigma estimates of the uncertainties from the non-linear fits yielded averages values of $\sigma_{np}/n_p \sim 0.5\%$ and $\sigma_{n\alpha}/n_{\alpha} \sim 1\%$ over a broad range of solar wind conditions. This is the accuracy with which the convected bi-Maxwellian response function derived in Section 2.2 and applied to the observations can determine the number densities. In this section we will examine the the *precision*, or absolute uncertainty, of these measurements.

Traditional tests of the precision of bulk solar wind parameters involve the comparison of observations by different instruments on the same spacecraft, of observations from multiple spacecraft. Of course this comparison introduces additional uncertainties. Each instrument has its own sensitivities, and each investigator has a preferred analysis methodology which can result in systematic discrepancies. Recall the comparison in Section 2.4.4 of proton thermal speeds using data from the *same* Faraday Cup but with the application of the moment and non-linear techniques. Additionally factors such as differing measurement cadences must also be taken into account. Multi-spacecraft comparisons suffer from the spacecraft separation and the intrinsic temporal and spatial variation of the solar wind. It has been known for some time that there are correlation lengthscales in the interplanetary medium which are in general are also of the order of typical spacecraft separations [Jurac and Richardson, 2001].

Additionally, recent studies have shown that the boundaries between structures in the solar wind, while often planar on the length-scale of spacecraft separations, are in general not radial [Weimer et al., 2002]. Thus it is not a simple procedure to propagate observations from one spacecraft to another.

This study makes uses another instrument on the same spacecraft which measures the total electron number density in a completely independent manor. The Thermal Noise Receiver (TNR) instrument in the WAVES experiment measures the power of electromagnetic fluctuations at a very high cadence of 0.2-4.5 seconds in the frequency range from $4-300$ KHz [Bougeret et al., 1995]. It was shown in Section 1.2.8 that the solar wind plasma fluctuates at the electron plasma frequency $\omega_{p,e}$, a quantity which is only a function of the total electron number density (1.92) and which varies from $50-300$ KHz in typical solar wind conditions. Generally a single TNR power spectrum may be used to determine the electron number density using a neural network which identifies the peak of the plasma frequency line.

The goal of this section therefore is to compare a predicted value for the electron number density n_e based on the observed proton n_p and alpha n_α number densities and compare with the TNR measurements. Since hydrogen and helium are fully ionized in the solar wind the total electron number density due to protons and alphas is $n_p + 2n_\alpha$. In order to do this correctly however we need to take into account the contribution of other ion species in the solar wind. Recall that $\sim 1\%$ of the solar wind by number density is composed of minor ions like oxygen and iron. While these minor ions are rare the typical charge states observed are $^{+7}$O and $^{+10}$Fe, so a small abundance can result in a significant contribution to n_e. As was shown in Section 1.2.7, on the time scale of a FC measurement of the ion VDF there are no electric fields other than that due to the convection of the plasma and the solar wind is neutral. The requirement of charge neutrality may be written,

$$|q_e| n_e = \sum_j q_j n_j, \tag{4.1}$$

where q_j is the average charge state of the j^{th} species which has a number density n_j. If n_e is the total electron number density measured by TNR, and all of the measurements were exact, then the fraction F_m of n_e due to minor ions is,

$$F_m \equiv \frac{1}{n_e}(n_e - n_p - 2n_\alpha) = 1 - \frac{n_p}{n_e} - 2\frac{n_\alpha}{n_e}. \tag{4.2}$$

In reality each of the measurements which go into (4.2) have an uncertainty which we will label σ_p, σ_α, and σ_e. The propagated uncertainty in F_m, or σ_m, is then,

$$\sigma_m^2 = (n_p + 2n_\alpha)^2 \frac{\sigma_e^2}{n_e^2} + \frac{\sigma_p^2}{n_e^2} + \frac{\sigma_\alpha^2}{n_e^2}. \tag{4.3}$$

In this study we will look at the average value of F_m and its variation ΔF_m as a function of the proton speed and the year of the mission. This is because many properties of the minor ions have been demonstrated to be speed and solar cycle

Component	Relative Abundance	Electrons	Similar Species	Total Electrons
Hydrogen	10^3	10^3	1	10^3
Helium	50	$2 \cdot 50$	1	100
Oxygen	1	$7 \cdot 1$	3	28
Iron	0.1	$10 \cdot 0.1$	6	7

Table 4.3: Estimating the contribution of minor ion species to the total electron content. With the numbers listed here $F_m \simeq 3.1\%$.

dependent. If the absolute calibrations of both the FC and TNR instruments are correct then F_m should agree with the results of other studies. Additionally, if all of the instrumental effects are correctly captured in σ_p, σ_α, and σ_e, then the quantity $(\Delta F_m^2 - \sigma_e^2)^{1/2}$ is indicative of the natural variation of the minor ion component. It is a convolution of the variation in minor ion abundance and charge state distribution.

A comparison of SWE/FC and WAVES/TNR observations, limited to six days in 1996, was reported previously [Maksimovic et al., 1998, Figure 2]. In that study there was a general disagreement on the order of $F_m \sim 1\%$ and a spread of approximately 5%. There are several compelling reasons to pursue this comparison in more detail. Significantly, the analysis of the TNR data have subsequently been refined due to a better understanding of the antennae and the TNR frequency bins. This has increased the observed values of F_m, but we hope to explain this by factoring in the effect of the minor ions. In addition, six days is insufficient to probe possible dependencies on solar wind conditions, such as the bulk speed. Finally, with our new knowledge of σ_p and σ_α from the non-linear analysis we can separate the contributions of the protons, alphas, and minor ions to the observed 5% spread in F_m.

In preparation for this study we can estimate F_m. Table 4.3 lists values which are used in the following simple calculation [T. Zurbuchen, private communication]. The second column lists the relative abundances of each element, normalized to oxygen. Assuming that the hydrogen and helium are fully ionized, that oxygen and 3 more species like it are in a +7 charge state, and that iron and 6 species like it are in charge state +10, then

$$F_m \simeq 3.1\%. \tag{4.4}$$

Of course this is an approximation: There are other ions, and the charge states and relative abundances are highly variable. Predictions of $F_m \sim 5\%$ were also discussed, and so the expected range in F_m is between $3\% - 5\%$.

4.4.1 Preparation of Measurements

This study uses all solar wind observations in the interval 1995-2000. Since the end goal is to produce as clear and confident a value for F_m as possible, any measurements

which seem at all suspicious are discarded. For the alpha particle analysis only spectra with a perfect final fit status of 10 (Section 4.2) are selected.

An infrequent issue with the high voltage power supply on FC1, the southward facing cup on Wind had to be addressed. On several occasions, especially early in the mission and during a 10-day interval in 1996, an error with the selection of energy windows for FC1 lead to incorrect density measurements. The standard key-parameter analysis code is designed to switch to a single-cup mode in the event of poor data quality from a single cup. Since the bi-Maxwellian analysis requires observations at as many angles relative to the ambient magnetic field as possible, it was decided that we would not conduct an anisotropy analysis during those intervals. To identify questionable spectra we ran the moment analysis code separately on the observations from each cup individually for each spectra and then compared the two determinations of the proton number density from each cup, n_{p1} and n_{p2}. The top panel of Figure 4-1 is a series of histograms of the density ratio n_{p1}/n_{p2} for each year from 1995-2000. The core of each histogram is a Gaussian with an average width of 2% and centers ranged between 99.1% and 100.2%. Statistically then the proton number densities in general determined independently by the two Faraday Cups using the moment analysis technique differ by 2%. The $\pm 0.5\%$ range in the centers suggests that there is no bias in densities between the two cups. The result of the extended anomalous period in 1996 is clear in the top middle histogram in the form of the bulge on the n_{p1}/n_{p2} side. To be safe we will discard all measurements which do not satisfy $0.9 \leq n_{p1}/n_{p2} \leq 1.1$, or 0.18% of the total dataset.

The typical duration of a single SWE/FC ion spectrum is 92 seconds. The WAVES/TNR neural network data which were made available for this study are produced at a rate of at least one every 6 seconds. For the purposes of this study the TNR data were matched up to each FC spectrum and the average n_e, median, standard deviation Δn_e, and number of TNR measurements N were recorded. The quoted uncertainty in an individual TNR neural network electron density measurement is $2\% - 3\%$. Since there were generally at least 10 TNR measurements per FC spectrum, the uncertainty in the mean of the TNR measurements of n_e, or $\sigma_e = \Delta n_e/\sqrt{N-1}$, is used for the uncertainty in n_e. Only FC spectra with $N \geq 10$ were selected for this study.

The bottom panel in Figure 4-1 is a histogram of the distribution the uncertainties with which each component of (4.3) contributes to the overall uncertainty in F_m. In addition, the distribution of F_m itself is also plotted. It is clear that the uncertainty in n_α does not strongly effect the calculation of F_m. The uncertainty in the proton number density is the next most significant factor, and the value for n_e measured by TNR has the largest average uncertainty. The average values of the uncertainties are $\sigma_p = 1.0\%$, $\sigma_\alpha = 0.004\%$, $\sigma_e = 3.1\%$, and $\sigma_m = 3.5\%$, which should be compared to the average value for F_m of $\sim 6\%$.

For values of $F_m \leq 20$ the uncertainty in F_m is less than the average value of F_m itself, as is suggested by this figure and verified by plotting the ratio of σ_m/F_m for $F_m \neq 0$. It is telling that the portion of the histogram with values of $F_m \geq 30\%$ overlaps exactly with the upper tail of the histogram of the total uncertainty in σ_m (and the distribution of σ_e, which dominates σ_m in this interval). The implication,

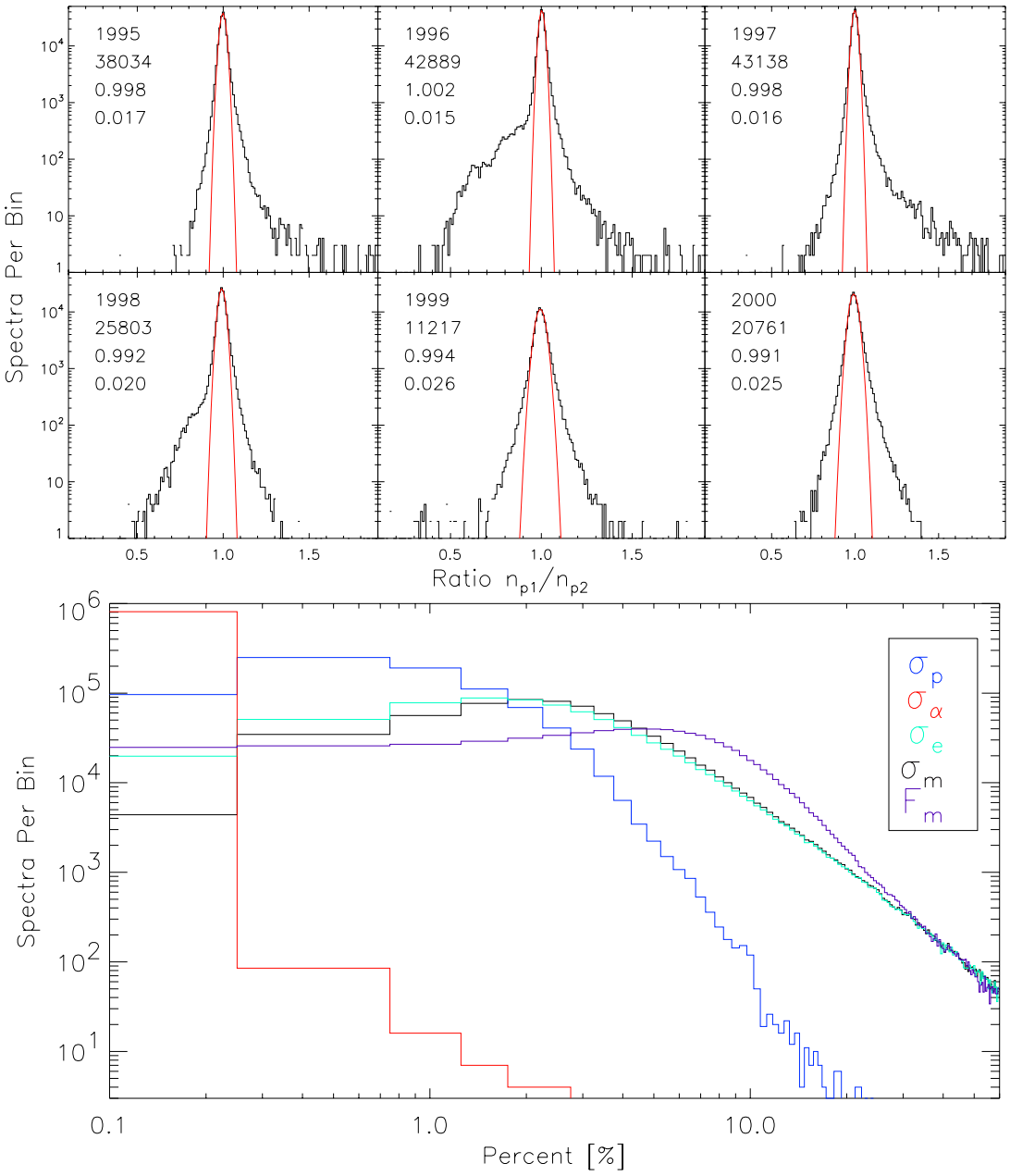

Figure 4-1: Predicted fraction F_m of the total electron number density due to minor ions as a function of proton bulk speed and year.

which was verified through a scatter plot to associate the points, is that the large departures of F_m from zero, which are rarely seen, are due to periods in the solar wind when the variation of the TNR electron number density was very large. The two in fact correspond exactly. The consequences of this are that very large values of F_m may be attributed to intervals with large fluctuations and a large resulting statistical uncertainty in F_m, and not due to periods when one instrument or the other is not functioning ideally. The other conclusion is that the variation of F_m is dominated by the fluctuation of the electron measurements from TNR, which are on the order of 3.1%. A spread in F_m on the order of 3.5% therefore would only reflect the variation of the electron number density measurements, and not any intrinsic error in the proton, alpha, or electron number densities.

We are not interested in comparing the instruments over the entire range of interplanetary conditions. Since the focus is on quite periods where the values measured are more trustworthy the study is further restricted to spectra with $\sigma_p \leq 5\%$, $\sigma_\alpha \leq 1\%$, and $\sigma_e \leq 10\%$. A total of 713, 742 spectra, or 78% of the total dataset passed all of the cuts described in this section and were used for the study of F_m.

4.4.2 Survey Over Mission

The median value of F_m over the entire selected dataset was 5.86%, with an average value of 6.36% and a standard deviation of 5.1%. The standard deviation is in agreement with the observations of [Maksimovic et al., 1998], although F_m is 4% larger than was reported in that same study. This can be attributed in part to the refined analysis of the TNR data since that study and to the fact that on average the proton number densities derived from the bi-Maxwellian analysis are about 1% smaller than the key-parameter number densities which were used in that study. We believe that the 1% shift in the FC number denies is due to the use of new effective area and response functions, as derived in Chapter 2.

The average value of F_m is slightly larger than the median value because there is an excess of observations on the $F_m \geq 5\%$ side. In fact the distribution of the entire set of measurements does not appear to be exactly Maxwellian. We interpreted this as evidence that the overall histogram reflected the variation of F_m over a set of variables. Two factors which we believed could influence F_m are the bulk speed of the solar wind and the period in the solar cycle. Studies of minor ion charge states have demonstrated that statistically speaking the freeze-in temperature of the minor ions is cooler at higher solar wind speeds, and therefore less ionized. Additionally, the abundance of species other than protons reflects in part evolution of the corona material at the origin of the solar wind. Studies have shown that the helium abundance is an increasing function of speed. If the same process occurred with the other minor ions then it might be expected that the minor ion abundance at high speeds would be larger. The actual effect of these two competing processes on the F_m as a function of U_p is not clear, but we must take that possibility into account. Additionally the helium abundance has been demonstrated to vary over the course of the solar cycle. Therefore we decided to look at the distribution of F_m as a function of year from 1995-2000 and bulk proton speed.

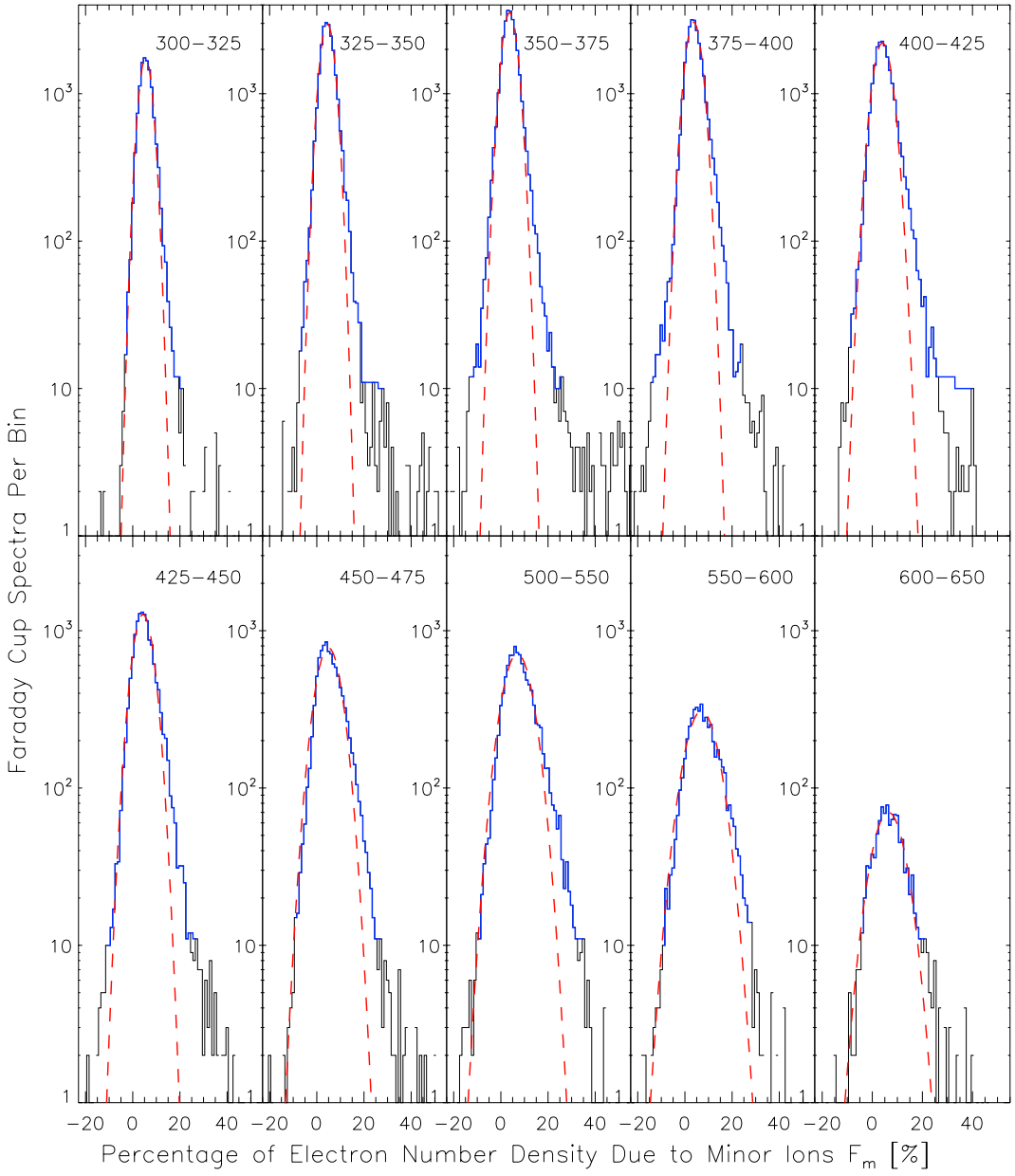

Figure 4-2: Histograms of F_m in six speed windows using selected data in 1995. Black histogram is the number of spectra observed per 0.5% bin in F_m, blue line is portion of the histogram selected for fit with Gaussian, and red is the best-fit Gaussian distribution. Note that the width increases with speed and that observations with $F_m < 0$ are in agreement with tail of Gaussian.

For each year the selected observations were divided into ten intervals in speed ranging from 300 to 650 km/s. The first seven windows are 25 km/s wide. Since the number of measurements decreases with speed, the final three windows are 50 km/s wide to improve the statistics of the high speed intervals. The ten histograms of F_m as a function of speed window for 1995 are shown in Figure 4-3. In each histogram all intervals with more than 10 spectra were selected and fitted with a Gaussian probability distribution. The blue curves indicate the bins which were selected for fitting and the dashed red lines are the best-fit Gaussians.

Overall the Gaussians fit the observed distributions well. Several trends are worthy of comment. First note that in most cases the portion of each histogram with values of $F_m < 0$, an unphysical result, may be accounted for by the natural width ΔF_m of the distributions. In other words if the ΔF_m in part represent the overall uncertainty of F_m then it is natural for this amount of observations to have $F_m < 0$. Of course ΔF_m is additionally due to the natural variation of the contribution to n_e from minor ions, and that variation can be estimated. Note as well that the ΔF_m increase as a function of speed. Additionally, there appears to be a bias, or tail in many of the distributions at high values of F_m, suggesting that there are some intervals where F_m is enhanced beyond the simple Gaussian variation observed. Helium enhancements are often observed in the material associated with coronal mass ejections, for example, and the same rare effect may account for this tail, which is still small compared with the overall distribution.

The determination of the average value of F_m as a function of speed and year, and the estimate of the natural variation of the minor ion component, are detailed in Figure 4-3. In the upper panel colored solid lines indicate the width ΔF_m of the best-fit Gaussian distributions to the observations as a function of speed for each year. The colored years printed at the top of the plot correspond to each of these curves. In general ΔF_m increased linearly from about 1.5% to 3% as the speed ranged from 300-650 km/s. There is a suggestion of a time dependent increase in the width of the distributions in the speed range 375-475 km/s with solar cycle. The connected diamonds plotted in this panel are the average uncertainties of the proton, electron, and alpha particle contributions to n_e in each speed interval. It is clear that the total uncertainty σ_m in F_m derived from these individual uncertainties through (4.3) is dominated by the variation in the TNR electron measurements over each FC spectrum, and that σ_m is a decreasing function of U_p. According the the discussion in the previous section, we interpret $(\Delta F_m^2 - \sigma_m^2)^{1/2}$ as the natural variation of F_m due to the variation of the abundance and charge state of the minor ions in the solar wind.

In the final panel of Figure 4-3 the center of the F_m distribution is plotted as a function of speed for each of the years from 1995-2000. Measurements in the same speed window have been offset by several km/s to avoid confusion. The horizontal error bars are the widths of the bins and the vertical error bars are the natural variations of F_m derived from the date in the upper panel. The two dashes lines indicate the two estimates of F_m in the introduction. There are variations in F_m with speed which should be compared with more detailed predictions. Additionally there appears to be a two-state distribution in the interval $U_p \leq 425$ km/s, with

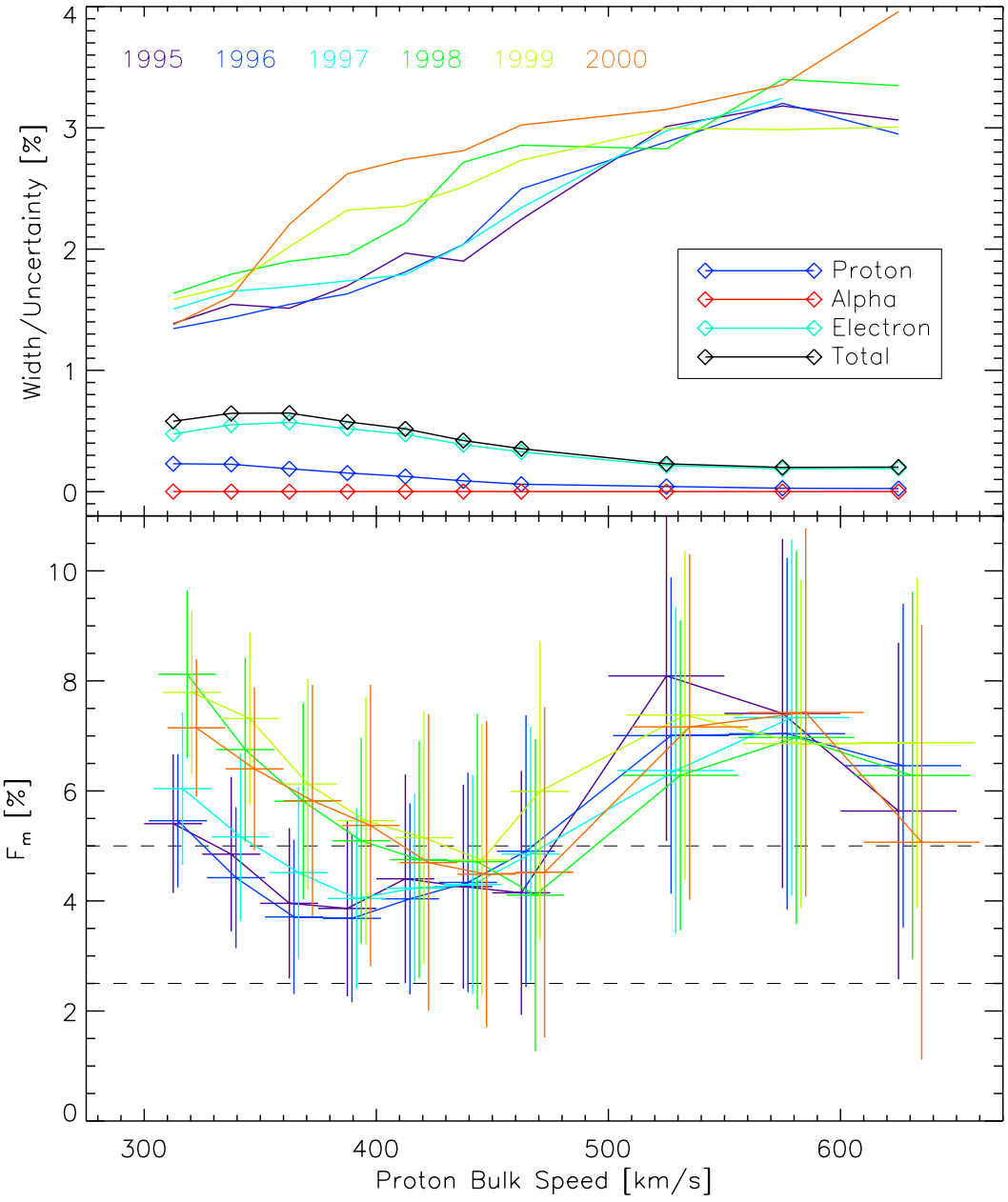

Figure 4-3: Predicted fraction F_m of the total electron number density due to minor ions as a function of proton bulk speed and year. *Upper panel:* Solid lines are the widths of the Gaussian fits to the distribution of F_m in each speed/year interval, connected diamonds are the corresponding average uncertainties in F_p, F_α, and F_e. *Lower panel:* Center of F_m distributions and natural widths as a function of speed and year. Dashed lines indicate estimates of the expected contribution of minor ions to the total electron number density.

all observations in 1995-1997 and in 1998-2000 falling into two distinct intervals. This could be a signature of the type of speed and solar cycle modulation which has been seen in the past with helium observations. For $U_p \geq 500$ km/s F_m is consistently greater then the predicted values. This could be a reflection of the enhanced abundance of minor ions in high speed solar wind. But it might also reflect the fact that high speed solar wind often contains two proton distributions, and that this second proton distribution is not reflected in this analysis. A followup to this investigation should include the double streaming analysis currently being conducted by Dorian Clack.

In summary, the estimates of F_m, the TNR electron measurements, and the SWE/FC proton and alpha number densities agree to within a few percent. The widths of the F_m distributions are consistent with the derived uncertainties in the proton and alpha number densities being less that 1%. Furthermore the agreement between F_m and theory is consistent with the Wind Faraday Cups having correct and stable density calibrations within approximately 2% of the absolute values.

4.5 A Single Effective Ion Species

If a single fluid description of the solar wind is desired then it is necessary to merge the proton and alpha data to create an effective ion species. In Chapter 6 this single effective ion species will be used in the characterization of shocks through conservation of the MHD equations. The value of a single species for a treatment of kinetic processes is questionable, as this aspect is explored in Section 5.4. This section presents a derivation of the single fluid properties based on the method of reducing ion and electron data for the single fluid MHD problem outlined in Section 1.2.7. A valuable asset of the proton and alpha parameters derived from the Faraday Cup data are the one-sigma uncertainties which are produced during the non-linear fits. The goal of this section is therefore to derive the single ion parameters but in addition to propagate the uncertainties from the alpha and proton analysis.

The reduced ion species will have the same mass as the protons, so the number density n_i is just the total of the number of protons and neutrons,

$$n_i \equiv n_p + 4n_\alpha \tag{4.5}$$

with an accompanying uncertainty σ_{n_i} given by,

$$\sigma_{n_i}^2 = \sigma_{n_p}^2 + 16\sigma_{n_\alpha}^2. \tag{4.6}$$

For the bulk velocity use the velocity $\vec{U}_i$ of the center of mass of the two ion species by weighting the individual proton $\vec{U}_p$ and alpha $\vec{U}_\alpha$ velocities by their mass densities,

$$\vec{U}_i \equiv \frac{n_p\vec{U}_p + 4n_\alpha\vec{U}_\alpha}{n_p + 4n_\alpha}. \tag{4.7}$$

The uncertainty in $\vec{U}_i$ is a function of both species number densities and velocities. The uncertainty of the j^{th} component of the velocity, $U_{i,j}$, is given by,

$$\begin{aligned}\sigma^2_{U_{i,j}} =& \frac{1}{(n_p + 4n_\alpha)^4}(256n_\alpha^4\sigma^2_{U_{\alpha j}} + 128n_\alpha^3 n_p\sigma^2_{U_{\alpha j}} + 8n_\alpha n_p^3\sigma^2_{U_{pj}} + n_p^2(n_p^2\sigma^2_{U_{pj}} \\ &+ 16\sigma^2_{n_\alpha}(U_{\alpha j} - U_{pj})^2) + 16n_\alpha^2(n_p^2(\sigma^2_{U_{\alpha j}} + \sigma^2_{U_{pj}}) + \sigma^2_{n_p}(U_{\alpha j} - U_{pj})^2))\end{aligned} \tag{4.8}$$

To determine the average thermal speed of the ions, w_i, I started with the individual pressures of the individual ion species,

$$P_p = n_p k_B T_p = \frac{1}{2} n_p m_p w_p^2, \qquad P_\alpha = n_\alpha k_B T_\alpha = \frac{1}{2} n_\alpha m_\alpha w_\alpha^2, \tag{4.9}$$

combined them and then set them equal to the pressure which would be produced by the single ion,

$$\begin{aligned}P_i = P_{\text{tot}} &= P_p + P_\alpha = \frac{1}{2} m_p(n_p w_p^2 + n_\alpha m_\alpha w_\alpha^2) \\ &= \frac{1}{2} m_p(n_p w_p^2 + 4n_\alpha w_\alpha^2) \\ &= \frac{1}{2} m_i w_i^2\end{aligned} \tag{4.10}$$

again using the fact that that the ion has mass m_p we can solve for the thermal speed,

$$w_i^2 \equiv \frac{n_p w_p^2 + 4n_\alpha w_\alpha^2}{n_p + 4n_\alpha}, \tag{4.11}$$

and its associated uncertainty,

$$\begin{aligned}\sigma^2_{w_i} =& \Big(16n_\alpha^2(4n_\alpha + n_p)^2\sigma^2_{w_\alpha} w_\alpha^2 + 4(n_p^2\sigma^2_{n_\alpha} + n_\alpha^2\sigma^2_{n_p})w_\alpha^4 + (n_p^2(4n_\alpha + n_p)^2\sigma^2_{w_p} \\ &- 8(n_p^2\sigma^2_{n_\alpha} + n_\alpha^2\sigma^2_{n_p})w_\alpha^2)w_p^2 + 4(n_p^2\sigma^2_{n_\alpha} \\ &+ n_\alpha^2\sigma^2_{n_p})w_p^4\Big)\Big[(4n_\alpha + n_p)^3(4n_\alpha w_\alpha^2 + n_p w_p^2)\Big]^{-1}.\end{aligned} \tag{4.12}$$

The dominant effect of the helium is to increase the particle mass density. The largest effects now neglected are the mass density of minor ions in the solar wind and the temperature of the electrons, which may contribute to the overall pressure. Since electrons have approximately the same temperatures as the ions in the solar wind, they generally have bulk velocities much less than their thermal widths and as a result do not contribute to the effective velocity, but can at times dominate the total pressure.

4.6 Summary

The analysis of the SWE/FC ion spectra has been extended to include the determination when possible of alpha parameters using the techniques developed by [Aellig et al., 2001b], but with a bi-Maxwellian distribution VDF for the alpha particles as well as the protons.

It has been shown that the the absolute precision of the FC number densities is off by less than a couple percent from the true values, and that the uncertainty in the densities is indeed on the order of a single percent.

In the following chapters the relative kinetic properties of protons and alphas in the solar wind are compared and their limits are explored. The usefulness of the single ion species derived in the previous section will be examined in terms of collisionless shocks and kinetic instabilities.

Bibliography

M. Abramowitz and I. A. Stegun. *Handbook of Mathematical Functions*. Dover Publications, New York, ninth edition, 1972.

M. R. Aellig, A. J. Lazarus, J. C. Kasper, and K. W. Ogilvie. Rapid Measurements of Solar Wind Ions with the Triana PlasMag Faraday Cup. *apss*, 277:305–307, 2001a.

M. R. Aellig, A. J. Lazarus, and J. T. Steinberg. The Solar Wind Helium Abundance: Variation with Wind Speed and the Solar Cycle. *Geophysical Research Letters*, 28: 2767, July 2001b.

H. Alfvén. On the Existence of Electromagnetic-Hydrodynamic Waves. *Arkiv for Astronomi*, 29:1–7, 1943.

B. J. Anderson, S. A. Fuselier, S. P. Gary, and R. E. Denton. Magnetic spectral signatures in the Earth's magnetosheath and plasma depletion layer. *Journal of Geophysical Research*, 99:5877–5891, 1994.

E. Antonucci, S. Giordano, and M. A. Dodero. Hydrogen and Oxygen Temperatures in Coronal Holes. *Advances in Space Research*, 25:1923–1926, 2000.

J. A. Araneda, A. F. Vinas, and H. F. Astudillo. Proton core temperature effects on the relative drift and anisotropy evolution of the ion beam instability in the fast solar wind. *Journal of Geophysical Research, In Press*, page 1, 2002.

W. I. Axford. The Interaction between the Solar Wind and the Earth's Magnetosphere. *Journal of Geophysical Research*, 67:3791, September 1962.

A. Barnes. Collisionless damping of hydromagnetic waves. *Phys. Fluids*, 9:1483, 1966.

J. W. Belcher and R. Burchsted. Energy densities of Alfven waves between 0.7 and 1.6 AU. *Journal of Geophysical Research*, 79:4765–4768, November 1974.

D. B. Berdichevsky, R. P. Lepping, A. Szabo, and A. J. Lazarus. Estimation of interplanetary shock-normals using multispacecraft observations: Cases of shocks within minutes of magnetohydrodynamic discontinuities. In *American Geophysical Union, Spring Meeting 2001, abstract #SH42B-10*, page 42, May 2001.

L. Biermann. Kometenschweife und solare Korpuskularstrahlung. *Zeitschrift Astrophysics*, 29:274, 1951.

L. Biermann. Solar corpuscular radiation and the interplanetary gas. *The Observatory*, 77:109–110, June 1957.

N. N. Bogoliubov. In J. de Boer and G. E. Uhlenbeck, editors, *Studies in Statistical Mechanics*, volume 1. North-Holland, Amsterdam, 1962.

A. Bonanno, H. Schlattl, and L. Paternò. The age of the Sun and the relativistic corrections in the EOS. *Astronomy and Astrophysics*, 390:1115–1118, August 2002.

J.-L. Bougeret, M. L. Kaiser, P. J. Kellogg, R. Manning, K. Goetz, S. J. Monson, N. Monge, L. Friel, C. A. Meetre, C. Perche, L. Sitruk, and S. Hoang. Waves: The Radio and Plasma Wave Investigation on the Wind Spacecraft. *Space Science Reviews*, 71:231–263, February 1995.

H. S. Bridge. Solar cycle manifestations in the interplanetary medium. In *Proceedings of the International Symposium on Solar-Terrestrial Physics*, volume 1, pages 47–62, June 1976.

H. S. Bridge, J. W. Belcher, R. J. Butler, A. J. Lazarus, A. M. Mavretic, J. D. Sullivan, G. L. Siscoe, and V. M. Vasyliunas. The plasma experiment on the 1977 Voyager mission. *Space Science Reviews*, 21:259–287, December 1977.

M. Bzowski, H. J. Fahr, and D. Ruciński. Ionization-induced Heat Flow in Heliospheric Hydrogen: Virtues and Flaws of Hydrodynamic Treatments. *Astrophysical Journal*, 544:496–507, November 2000.

I. H. Cairns, D. H. Fairfield, R. R. Anderson, K. I. Paularena, and A. J. Lazarus. Reply. *Journal of Geophysical Research*, 101:7679–7684, April 1996.

S. Chandrasekhar. *Princliples of Stellar Dynamics*. University of Chicago Press, Chicago, 1942.

S. Chandrasekhar. Dynamical friction. i. general considerations: the coefficient of dynamical friction. *Astrophysical Journal*, pages 255–262, 1943.

S. Chandrasekhar, A. N. Kaufman, and K. M. Watson. The stability of the pinch. *Proc. Roy. Cos. London., Ser. A*, 245:435, 1958.

J. K. Chao, L. H. Lyu, B. H. Wu, A. J. Lazarus, T. S. Chang, and R. P. Lepping. Observations of an intermediate shock in interplanetary space. *Journal of Geophysical Research*, 98:17443–17450, October 1993.

G. F. Chew, M. L. Goldberger, and F. E. Low. The boltzmann equation and the one-fluid hydromagnetic equations in the absence of particle collisions. pages 112–118, 1965.

D. Clack, A. Lazarus, J. Kasper, and M. Kaiser. Wind SWE observations of proton double streaming and correlations with wave activity. In *American Geophysical Union, Fall Meeting 2001, abstract #SH21A-0734*, page A734, December 2001.

D. Clack, A. J. Lazarus, and J. C. Kasper. A Statistical Study of Proton Double Streaming Observed by Wind/SWE. In *American Geophysical Union, Spring Meeting 2002, abstract #SH21C-07*, page C7, May 2002.

S. R. Cranmer. New Insights into Solar Coronal Plasma Kinetics from UVCS/SOHO. *American Astronomical Society Meeting*, 31:871, May 1999.

N. U. Crooker, T. E. Eastman, and G. S. Stiles. Observations of plasma depletion in the magnetosheath at the dayside magnetopause. *Journal of Geophysical Research*, 84:869–874, March 1979.

P. B. Dusenbery and J. V. Hollweg. Ion-cyclotron heating and acceleration of solar wind minor ions. *Journal of Geophysical Research*, 86:153–164, January 1981.

W. A. Dziembowski, G. Fiorentini, B. Ricci, and R. Sienkiewicz. Helioseismology and the solar age. *Astronomy and Astrophysics*, 343:990–996, March 1999.

A. Eviatar and M. Schultz. Ion-temperature anisotropies and the structure of the solar wind. *Planet. Spa. Sci.*, 18:321, 1970.

T. E. Faber. *Fluid Dynamics for Physicists*, pages 37–40. Cambridge University Press, Cambridge, 1995.

R. P. Feynman. *Statistical Mechanics: A Set of Lectures*, pages 2–5. Addison Wesley, Reading, 1972.

S. P. Gary. *Theory of Space Plasma Microinstabilities*. Cambridge University Press, Cambridge, 1993.

S. P. Gary, B. E. Goldstein, and J. T. Steinberg. Helium ion acceleration and heating by Alfvén/cyclotron fluctuations in the solar wind. *Journal of Geophysical Research*, 106:24955–24964, November 2001.

S. P. Gary, H. Li, S. O'Rourke, and D. Winske. Proton resonant firehose instability: Temperature anisotropy and fluctuating field constraints. *Journal of Geophysical Research*, 103:14567–14574, 1998.

S. P. Gary, M. E. McKean, D. Winske, B. J. Anderson, R. E. Denton, and S. A. Fuselier. The proton cyclotron instability and the anisotropy/B inverse correlation. *Journal of Geophysical Research*, 99:5903–5914, 1994.

S. P. Gary, J. Wang, D. Winske, and S. A. Fuselier. Proton temperature anisotropy upper bound. *Journal of Geophysical Research*, 102:27159–27170, 1997.

P. R. Gazis, J. D. Mihalov, A. Barnes, A. J. Lazarus, and E. J. Smith. Pioneer and Voyager observations of the solar wind at large heliocentric distances and latitudes. *Geophysical Research Letters*, 16:223–226, March 1989.

G. B. Gelfreikh, V. I. Makarov, A. G. Tlatov, A. Riehokainen, and K. Shibasaki. A study of development of global solar activity in the 23rd solar cycle based on radio observations with the Nobeyama radio heliograph. II. Dynamics of the differential rotation of the Sun. *Astronomy and Astrophysics*, 389:624–628, July 2002.

G. Gloeckler. Ion composition measurement techniques for space plasmas. *Review of Scientific Instruments*, 61:3613–3620, November 1990.

H. Goldstein. *Classical Mechanics*. Addison-Wesley, Reading, second edition, 1980.

R. J. Goldston and P. H. Rutherford. *Introduction to Plasma Physics*. Institute of Plasma Physics, Philadelphia, 1997.

L. G. Golub and J. M. Pasachoff. *The Solar Corona*, pages 22–71. Cambridge University Press, Cambridge, 1997.

K. I. Gringauz, V. V. Bezrukikh, V. D. Ozerov, and R. E. Rybchinskii. *Dokl. Akad. Nauk. SSSR*, 131:1301, 1960.

C. J. Hanson and S. D Kawaler. *Stellar Interiors: physical principles, structure, and evolution*, pages 261–311. Springer-Verlag, New York, 1994.

S. Hayakawa. *Cosmic Ray Physics: Nuclear and Astrophysical Aspects*, pages 688–704. John Wiley and Sons, 1969.

C. Hoffmeister. Physikalische Untersuchungen an Kometen. II. Die Bewegungen der Schweifmaterie und die Repulsivkraft der Sonne beim Kometen 1942 g. *Zeitschrift Astrophysics*, 23:1–18, 1944.

J. V. Hollweg. Heating and acceleration of the solar wind in coronal holes: cyclotron resonances. *Advances in Space Research*, 30:469–469, 2002.

K. Huang. *Statistical Machanics*, chapter 3-5. John Wiley and Sons, 1963.

D. E. Huddleston, A. D. Johnstone, A. J. Coates, and F. M. Neubauer. Quasi-linear pitch angle and energy diffusion of pickup ions near Comet Halley. *Journal of Geophysical Research*, 96:21329, December 1991.

P. A. Isenberg. Resonant acceleration and heating of solar wind ions Anisotropy and dispersion. *Journal of Geophysical Research*, 89:6613–6622, August 1984.

P. A. Isenberg. Energy Diffusion of Pickup Ions Upstream of Comets (JGR 92 (A8) 1987). In *Comet Encounters*, page 32, 1998.

J. D. Jackson. *Classical Electrodynamics*. John Wiley and Sons, third edition, 1999.

S. Jurac, J. C. Kasper, J. D. Richardson, and A. J. Lazarus. On the Geoeffectiveness of Interplanetary Shocks. In *American Geophysical Union, Spring Meeting 2001, abstract #SH62A-10*, page 62, May 2001a.

S. Jurac, J. C. Kasper, J. D. Richardson, and A. J. Lazarus. The geoeffective scale sizes of solar wind events. In *American Geophysical Union, Fall Meeting 2001, abstract #SH31A-0705*, page A705, December 2001b.

S. Jurac and J. D. Richardson. The dependence of plasma and magnetic field correlations in the solar wind on geomagnetic activity. *Journal of Geophysical Research*, 106:29195–29206, December 2001.

J. C. Kasper, D. Clack, A. J. Lazarus, and A. Szabo. High Time Resolution Plasma Measurements with WIND. In *American Geophysical Union, Spring Meeting 2001, abstract #SH42B-08*, page 42, May 2001a.

J. C. Kasper, A. J. Lazarus, D. Clack, and S. Jurac. Wind/SWE Observations of the Role of Instabilities in CME Ejecta. In *American Geophysical Union, Spring Meeting 2002, abstract #SH21A-08*, page A8, May 2002a.

J. C. Kasper, A. J. Lazarus, S. Gary, and A. Szabo. A Statistical Study of Proton Temperature Anisotropies Measured by Wind/SWE. In *American Geophysical Union, Fall Meeting 2001, abstract #SH21A-0733*, page A733, December 2001b.

J. C. Kasper, A. J. Lazarus, and S. P. Gary. Wind/SWE observations of firehose constraint on solar wind proton temperature anisotropy. *Geophysical Research Letters, in press*, 2002b.

J. C. Kasper, A. J. Lazarus, S. P. Gary, and A. Szabo. Solar Wind Temperature Anisotropies. In *Solar Wind 10 Conference*, July 2002c.

J. C. Kasper, A. J. Lazarus, and P. Seeluangsawat. Wind/SWE Plasma Observations of Kinetic-Scale Magnetic Holes. In *American Geophysical Union, Spring Meeting 2002, abstract #SH21C-06*, page C6, May 2002d.

P. J. Kellogg. Flow of Plasma around the Earth. *Journal of Geophysical Research*, 67:3805, September 1962.

C. F. Kennel and H. E. Petscheck. Limit on stably trapped particle fluxes. *Journal of Geophysical Research*, 71:1–28, 1966.

L. W. Klein, K. W. Ogilvie, and L. F. Burlaga. Coulomb collisions in the solar wind. *Journal of Geophysical Research*, 90:7389–7395, August 1985.

L. D. Landau and E. M. Lifshitz. *Course of Theoretical Physics: Physical Kinetics*, volume 10. Pergamon Press, Elmsford, New York, second edition, 1981.

G. Lapenta and J. U. Brackbill. Contact discontinuities in collisionless plasmas: A comparison of hybrid and kinetic simulations. *Geophysical Research Letters*, 23: 1713, 1996.

A. J. Lazarus, J. T. Steinberg, and R. L. McNutt. A low-mass faraday cup experiment for the solar wind. *Unknown*, 93:27078, 1993.

R. P. Lepping, D. B. Berdichevsky, L. F. Burlaga, A. J. Lazarus, J. Kasper, M. D. Desch, C.-C. Wu, D. V. Reames, H. J. Singer, C. W. Smith, and K. L. Ackerson. The Bastille day Magnetic Clouds and Upstream Shocks: Near-Earth Interplanetary Observations. *Solar Physics*, 204:285–303, December 2001.

R. P. Lepping, L. F. Burlaga, A. Szabo, K. W. Ogilvie, W. H. Mish, D. Vassiliadis, A. J. Lazarus, J. T. Steinberg, C. J. Farrugia, L. Janoo, and F. Mariani. The Wind magnetic cloud and events of October 18-20, 1995: Interplanetary properties and as triggers for geomagnetic activity. *Journal of Geophysical Research*, 102: 14049–14064, July 1997.

R. P. Lepping, A. Szabo, K. W. Ogilvie, R. J. Fitzenreiter, A. J. Lazarus, and J. T. Steinberg. Magnetic cloud-bow shock interaction: WIND and IMP 8 observations. *Geophysical Research Letters*, 23:1195, 1996.

R.-F. Lottermoser, M. Scholer, and A. P. Matthews. Ion kinetic effects in magnetic reconnection: Hybrid simulations. *Journal of Geophysical Research*, 103:4547–4560, March 1998.

M. Maksimovic, J.-L. Bougeret, C. Perche, J. T. Steinberg, A. J. Lazarus, A. F. Viñas, and R. J. Fitzenreiter. Solar wind density intercomparisons on the Wind spacecraft using WAVES and SWE experiments. *Geophysical Research Letters*, 25: 1265, April 1998.

E. Marsch, R. Schwenn, H. Rosenbauer, K.-H. Muehlhaeuser, W. Pilipp, and F. M. Neubauer. Solar wind protons - Three-dimensional velocity distributions and derived plasma parameters measured between 0.3 and 1 AU. *Journal of Geophysical Research*, 87:52–72, January 1982.

D. C. Montgomery and D. A. Tidman. *Plasma Kinetic Theory*. Mc Graw - Hill, New York, 1964.

J. T. Nolte, A. S. Krieger, A. F. Timothy, R. E. Gold, E. C. Roelof, G. Vaiana, A. J. Lazarus, J. D. Sullivan, and P. S. McIntosh. Coronal Holes as Sources of Solar Wind. *Solar Physics*, 46:303–322, 1976.

Z. Němeček, J. Šafránková, O. Santolík, K. Kudela, and E. T. Sarris. Energetic particles in the vicinity of the dawn magnetopause. *Advances in Space Research*, 20:851–856, September 1997.

K. W. Ogilvie, D. J. Chornay, R. J. Fritzenreiter, F. Hunsaker, J. Keller, J. Lobell, G. Miller, J. D. Scudder, E. C. Sittler, R. B. Torbert, D. Bodet, G. Needell, A. J. Lazarus, J. T. Steinberg, J. H. Tappan, A. Mavretic, and E. Gergin. SWE, A Comprehensive Plasma Instrument for the Wind Spacecraft. *Space Science Reviews*, 71:55–77, February 1995.

K. W. Ogilvie, J. T. Steinberg, R. J. Fitzenreiter, C. J. Owen, A. J. Lazarus, W. J. Farrell, and R. B. Torbert. Observations of the lunar plasma wake from the WIND spacecraft on December 27, 1994. *Geophysical Research Letters*, 23:1255, 1996.

E. Parker. Extension of the Solar Corona into Interplanetary Space. *Journal of Geophysical Research*, 64:1675, November 1959.

E. N. Parker. Dynamical Instability in an Anisotropic Ionized Gas of Low Density. *Physical Review*, 109:1874–1876, March 1958a.

E. N. Parker. Suprathermal Particle Generation in the Solar Corona. *Astrophysical Journal*, 128:677, November 1958b.

E. N. Parker. The Hydrodynamic Theory of Solar Corpuscular Radiation and Stellar Winds. *Astrophysical Journal*, 132:821, November 1960a.

E. N. Parker. The Hydrodynamic Treatment of the Expanding Solar Corona. *Astrophysical Journal*, 132:175, July 1960b.

G. K. Parks. *Physics of Space Plasmas: An Introduction*. Addison-Wesley, 1991.

G. Paschmann, A. N. Fazakerly, and S. J. Schwartz. Moments of plasma velocity functions. In G. Paschmann and P. W. Daley, editors, *Analysis Methods for Multi-Spacecraft Data*. ESA Publications Division, Noordwijk, 1998.

R. K. Pathria. *Statistical Mechanics*, pages 43–55. Reed Elsevier, New Delhi, India, second edition, 1972.

K. I. Paularena and A. J. Lazarus. Comment on 'Intercalibration of solar wind instruments during the International Magnetospheric Study' by S. M. Petrinec and C. T. Russell. *Journal of Geophysical Research*, 99:14777, August 1994.

K. I. Paularena, G. N. Zastenker, A. J. Lazarus, and P. A. Dalin. Solar wind plasma correlations between IMP 8, INTERBALL-1, and WIND. *Journal of Geophysical Research*, 103:14601–14618, July 1998.

R. P. Pfaff, J. E. Borovsky, and D. T. Young, editors. *Measurement Techniques in Space Plasmas: Fields*, volume 1 of *Geophysical Monograph 103*. American Geophysical Union, Washington, D. C., 1998a.

R. P. Pfaff, J. E. Borovsky, and D. T. Young, editors. *Measurement Techniques in Space Plasmas: Particles*, volume 2 of *Geophysical Monograph 103*. American Geophysical Union, Washington, D. C., 1998b.

T.-D. Phan, G. Paschmann, W. Baumjohann, N. Sckopke, and H. Luehr. The magnetosheath region adjacent to the dayside magnetopause: AMPTE/IRM observations. *Journal of Geophysical Research*, 99:121–141, 1994.

W. H. Press, S. A. Teukolsky, W. T. Vetterling, and B. P. Flannery. *Numerical Recipes in C: The Art of Scientific Computing*. Cambridge Univerisy Press, Cambridge, second edition, 1999.

A. Raichoudhuri. *The Physics of Fluids and Plasmas: An Introduction for Astrophysicists*. Cambridge University Press, Cambridge, first edition, 1998.

F. Reif. *Fundamentals of Statistical and Thermal Physics*. McGraw Hill, 1965.

I. G. Richardson and H. V. Cane. Signatures of shock drivers in the solar wind and their dependence on the solar source location. *Journal of Geophysical Research*, 98: 15295, September 1993.

J. D. Richardson. Thermal ions at Saturn - Plasma parameters and implications. *Journal of Geophysical Research*, 91:1381–1389, February 1986.

J. D. Richardson, J. C. Kasper, A. J. Lazarus, K. I. Paularena, and A. Wallace. Solar Cycle Variation of Shocks in the Heliosphere. In *American Geophysical Union, Fall Meeting 2001, abstract #SH21B-01*, page B1, December 2001.

P. Riley, Z. Mikic, J. A. Linker, R. Lionello, and A. J. Lazarus. The Large-Scale Variability of Solar Wind Streams. In *American Geophysical Union, Fall Meeting 2001, abstract #SH32A-0729*, page A729, December 2001.

D. E. Robbins, A. J. Hundhausen, and S. J. Bame. Helium in the solar wind. *Journal of Geophysical Research*, 75:1178–1187, March 1970.

B. Rossi and S. Olbert. *Introduction to the Physics of Space*. McGraw-Hill, New York, 1970.

O. Santolík, J. Šafránková, Z. Němeček, J.-A. Sauvaud, A. Fedorov, and G. Zastenker. Two-point measurement of hot plasma structures in the magnetotail lobes. *Advances in Space Research*, 20:993–997, September 1997.

M. Schwarzschild. *Structure and Evolution of the Stars*, pages 30–95. Dover Publications, New York, 1965.

L. Spitzer. *Physics of Fully Ionized Gasses*. Interscience Publishers, New York, 1956.

J. T. Steinberg, W. C. Feldman, R. M. Skoug, J. C. Kasper, A. J. Lazarus, and L. Alaoui. Characteristics of the Distant Magnetosheath: Wind Measurements at 45 to 80 Earth Radii. In *American Geophysical Union, Spring Meeting 2001, abstract #SM42D-12*, page 42, May 2001.

J. T. Steinberg, A. J. Lazarus, J. T. Ogilvie, R. Lepping, J. Byrnes, D. Chornay, J. Keller, R. B. Torbert, D. Bodet, and G. J. Needell. WIND measurements of proton and alpha particle flow and number density. In *Solar Wind 8 Conference*, page 36, June 1995.

J. T. Steinberg, A. J. Lazarus, K. W. Ogilvie, R. Lepping, and J. Byrnes. Differential flow between solar wind protons and alpha particles: First WIND observations. *Geophysical Research Letters*, 23:1183, 1996.

T. H. Stix. *Waves in Plasmas*. Springer-Verlag, New York, 1992.

A. Szabo. An improved solution to the 'Rankine-Hugoniot' problem. *Journal of Geophysical Research*, 99:14737, August 1994.

M. Tátrallyay, M. I. Verigin, K. Szegő, T. I. Gombosi, K. C. Hansen, K. Schwingenschuh, M. Delva, I. Apáthy, A. P. Remizov, and T. Szemerey. On the Distribution of Pickup Ions as Observed by the Vega Spacecraft at Comet Halley. *Advances in Space Research*, 26:1565–1568, 2000.

J. T. Tanabe, J. C. Kasper, and A. J. Lazarus. Proton and Alpha Particle Temperature Anisotropies in the Solar Wind with the WIND/SWE Faraday Cup. In *American Geophysical Union, Spring Meeting 2001, abstract #SH31A-11*, page 31, May 2001.

R. M. Thorne and B. T. Tsurutani. The generation mechanism for magnetosheath lion roars. *Nature*, 293:384–386, October 1981.

B. T. Tsurutani, E. J. Smith, R. R. Anderson, K. W. Ogilvie, J. D. Scudder, D. N. Baker, and S. J. Bame. Lion roars and nonoscillatory drift mirror waves in the magnetosheath. *Journal of Geophysical Research*, 87:6060–6072, August 1982.

T. W. J. Unti, M. Neugebauer, and B. E. Goldstein. Direct Measurements of Solar-Wind Fluctuations Between 0.0048 and 13.3 HZ. *Astrophysical Journal*, 180:591–598, March 1973.

V. M. Vasylinuas. 12. Deep Space Plasma Measurements. In *Methods of Experimental Physics*, volume 98, pages 49–88, New York, 1971. Academic Press.

A. F. Vinas and J. D. Scudder. Fast and optimal solution to the 'Rankine-Hugoniot problem'. *Journal of Geophysical Research*, 91:39–58, January 1986.

D. R. Weimer, D. Ober, N. C. Maynard, W. J. Burke, M. R. Collier, D. J. McComas, and C. W. Smith. Variable time delays in the propagation of the interplanetary megnetic field. *Journal of Geophysical Research*, 107, 2002.

D. Winske and N. Omidi. *Computer Space Plasma Physics: Simulation Techniques and Software*, chapter Methods and applications, page 103. Terra Sci., Tokyo, 1997.

P. H. Yoon. Electromagnetic fire-hose instability in a fully relativistic bi-Maxwellian plasma. *Physics of Fluids B*, 2:842–844, April 1990.

15 *Wind* MFI

The *Wind* MFI [*Lepping et al.*, 1995] calibration process are described in *Farrell et al.* [1995], *Kepko et al.* [1996], and *Leinweber et al.* [2008], available at the *Wind* Project webpage. Additional information involved in the removal of spin tone higher harmonics can be found in *Koval and Szabo* [2013].

The MFI calibration software can be found in the *Wind* lz decommutation softare *Wilson III et al.* [2021c] and is thus not further discussed.

16 *Wind* WAVES

The WAVES TDS and Radio detectors are fully described in the WAVES instrument paper [*Bougeret et al.*, 1995]. Further, the calibration software can be found in the *Wind* lz decommutation softare *Wilson III et al.* [2021c] and is thus not further discussed. The calibration of the search coil magnetometer (SCM), however, will be discussed using notes from *Hospodarsky* [1992]. Further discussion can also be found in *Hospodarsky* [2016].

16.1 WAVES SCM Notes

CHAPTER II. BASIC PRINCIPLES

The basic operating principle of a search coil magnetometer is Faraday's law of magnetic induction. This law states that a loop of wire with a time-varying magnetic field passing through it will have a time-varying voltage induced across it that is proportional to the time rate of change of the magnetic field. This law can be written as

$$V = -C\frac{d}{dt}[\vec{B}\cdot\hat{n}] \qquad (1)$$

where C is a constant that depends on the area of the loop and on the properties of the core material, $\vec{B}$ is the magnetic field vector, and $\hat{n}$ is a unit vector along the axis of the coil. Expanding the derivative, taking into account the possible motion of the coil and considering both temporal and spatial variations of the field, it can be shown that

$$V = -C[\vec{B}\cdot\frac{d\hat{n}}{dt} + \hat{n}\cdot\frac{d\vec{B}}{dt} + \vec{u}\cdot\nabla[\vec{B}\cdot\hat{n}]] \quad . \qquad (2)$$

The first term represents the voltage induced by the angular motion of the coil. The second term represents the voltage induced by explicit time variations of the magnetic field. This term is the one we are most interested in, as it represents the magnetic component of electromagnetic waves. The third term represents the voltage induced by convective motions of the coil with velocity $\vec{u}$ relative to the magnetic field $\vec{B}$. This

third term includes the voltage induced by the search coil moving through a magnetic field gradient. In most space environments, the first and third terms are negligible or can be filtered out, and the second term dominates.

The induced voltage for a search coil magnetometer that has a solenoidal coil of N turns of wire enclosing a ferromagnetic core can be written

$$V = -NA\mu_e\left(\frac{dB}{dt}\right) \quad , \tag{3}$$

where A is the cross-sectional area of the core, μ_e is the effective permeability of the core, and (dB/dt) is the time variation of the magnetic field component parallel to the coil axis. If the variation of the magnetic field is sinusoidal, this equation reduces to

$$V = -2\pi NA\mu_e f B_o \times 10^{-7} \mu V \tag{4}$$

where B_o is the amplitude of the magnetic signal in nT, A is in cm^2, and f is the frequency of the time variation. This expression can be simplified, and is usually written

$$V = -KfB_o \ \mu V \tag{5}$$

where K is defined as the coil constant of the search coil and is given by

$$K = 2\pi NA\mu_e \times 10^{-7} \ \frac{\mu V}{nT\ Hz} \quad . \tag{6}$$

The above analysis assumed that a search coil magnetometer is a pure inductor, but search coil magnetometers also have a resistance, due to the resistance of the wire,

and a capacitance, due to the self capacitance between the turns in the coil. These additional properties can be modeled using the equivalent circuit shown in Figure 3. The voltage induced by a time varying magnetic field is represented by a voltage source in series with an inductor, labeled L. The resistance of the wire, modeled by the resistor labeled R_1, is in series with the inductor. The resistor R_1 also accounts for any losses due to eddy currents, hysteresis, skin effects, and proximity to nearby conductors. In most cases, these losses are much smaller than the loss due to the resistance of the wire, and these losses can be neglected. The self capacitance, modeled by the capacitor labeled C, is parallel to L and R_1. The self capacitance is due to a potential difference between adjacent turns and layers of the coil. The resistor labeled R_D is called the damping resistor. This resistor controls the sharpness of the resonant peak, and accounts for the input impedance of the preamplifier. An analysis of the circuit shows that Equation 5 is modified to

$$V = \frac{-KfB_o}{\sqrt{(1+\frac{R_1}{R_D}-\omega^2LC)^2+(\frac{\omega L}{R_D}+\omega CR_1)^2}} \quad \mu V \tag{7}$$

where $\omega = 2\pi f$. For typical values of L, C, R_1, and R_D, the denominator is ≈ 1, for ω below $\omega_r = 1/\sqrt{LC}$, where $f_r = \omega_r/2\pi$ is called the resonant frequency. The resonant frequency is the frequency which produces the largest induced voltage. For frequencies near ω_r, the denominator may be much less than 1, depending on the exact values of L, C, R_1, and R_D. For frequencies well above the resonant frequency, Equation 7 is

no longer valid, as secondary capacitances and other effects start to become important. These higher order effects are difficult to model, and may change a great deal with temperature, and over time. Because of these second order effects, search coil magnetometers are usually designed with resonant frequencies above the frequency range they are expected to measure.

Another important characteristic of the equivalent circuit is its impedance. The real part of the impedance determines the thermal noise (also called Johnson noise) voltage produced by the search coil. The noise voltage must be small to allow the measurement of weak magnetic fields. The real part of the impedance of the circuit in Figure 3 is

$$Z_r = \frac{R_1(1+\frac{R_1}{R_D}-\omega^2 LC)+\omega L(\frac{\omega L}{R_D}+\omega C R_1)}{(1+\frac{R_1}{R_D}-\omega^2 LC)^2+(\frac{\omega L}{R_D}+\omega C R_1)^2} \; ohms \quad . \qquad (8)$$

An analysis of this equation shows that the real part of the impedance ranges from $\approx R_1$ ohms at low frequencies, to $\approx R_D$ ohms near the resonant frequency. The Johnson noise voltage of a search coil over a frequency bandwidth Δf, is given by Robinson [1974] as

$$\frac{V_{Johnson}}{\sqrt{\Delta f}} = \sqrt{4k_B T Z_r} \quad \frac{Volts}{\sqrt{Hz}} \tag{9}$$

where k_B is Boltzmann constant, T is the temperature in degrees Kelvin, and Z_r is the real part of the impedance defined in Equation 8. The Johnson noise will be discussed in more detail later.

The noise voltage is needed to determine one of the most important characteristics of a search coil, its noise level. The noise level is defined as the magnetic signal strength that induces a voltage equal to the noise voltage. Setting the noise level, Equation 9, equal to the output voltage, Equation 7, and solving for the magnetic signal, we find

$$\frac{B_N}{\sqrt{\Delta f}} = \frac{\sqrt{4k_B T(R_1 + \frac{R_1^2}{R_D} + \frac{\omega^2 L^2}{R_D})}}{Kf} \quad \frac{nT}{\sqrt{Hz}} \tag{10}$$

The noise level is usually squared,

$$\frac{B_N^2}{\Delta f} = \frac{4k_B T}{K^2 f^2}(R_1 + \frac{R_1^2}{R_D} + \frac{\omega^2 L^2}{R_D}) \quad \frac{nT^2}{Hz} \tag{11}$$

which has units of magnetic field spectral density. The noise level determines the minimum magnetic signal a search coil magnetometer can measure over a given frequency bandwidth. Analyzing Equation 11 for typical values of L, C, R_1, and R_D, $R_1 \ll R_D$, $R_1^2/R_D \ll R_1$, and $L^2/R_D \ll R_1$, we find

$$\frac{B_N^2}{\Delta f} \simeq \frac{4k_BT}{(NA\mu_e \times 10^{-7})^2} \left(\frac{R_1}{\omega^2} + \frac{L^2}{R_D}\right) \frac{nT^2}{Hz} \quad . \tag{12}$$

At low frequencies R_1/ω^2 determines the noise level, but at higher frequencies L^2/R_D sets a lower limit. This equation does not include the noise voltage of the preamplifier. Including the preamplifier noise voltage in Equation 11, the noise level becomes

$$\frac{B_N^2}{\Delta f} = \frac{4k_BT\left(R_1 + \frac{R_1^2}{R_D} + \frac{\omega^2L^2}{R_D}\right)}{(Kf)^2} + \frac{(n_{amp}^2/\Delta f)}{(Kf)^2}\left[\left(1 + \frac{R_1}{R_D} - \omega^2LC\right)^2 + \left(\frac{\omega L}{R_D} + \omega CR_1\right)^2\right] \frac{nT^2}{Hz} \tag{13}$$

where $n_{amp}^2/\Delta f$ is the noise spectral density of the preamplifier. Analyzing Equation 13 for typical values of L, C, R_1, and R_D, we find

$$\frac{B_N^2}{\Delta f} \simeq \frac{4k_BT}{(NA\mu_e \times 10^{-7})^2}\left(\frac{R_1}{\omega^2} + \frac{L^2}{R_D}\right) + \frac{(n_{amp}^2/\Delta f)}{(NA\mu_e \times 10^{-7})^2}\left(\frac{1}{\omega^2}\right) \frac{nT^2}{Hz} \quad . \tag{14}$$

This equation shows that the noise of the preamplifier can play an important role in the noise level of a search coil magnetometer, especially at low frequencies. A good search coil magnetometer design uses the optimum combination of the above variables to obtain the lowest noise level possible in the frequency range of interest.

CHAPTER III. DESIGN CONSIDERATIONS

Effective Permeability

The effective permeability of the core is needed to determine the sensitivity of the search coil from Equation 4. Magnetic materials are rated according to their permeability, μ_i, where permeability is defined as the ratio of the magnetic flux density in the material to the ambient magnetic field density in the absence of the material. For the analysis of a laminated bar or rod, the more significant parameter is the effective permeability, μ_e. The effective permeability of long rods constructed of high permeability materials is less than the closed-loop permeability by which ferromagnetic materials are rated [Bozorth and Chapin, 1942]. The effective permeability is determined by the length to diameter, ℓ/d, ratio of the rod. Hayashi [1988] gives for $\mu_i \gg 1$, and $\ell \gg$ d

$$\mu_e = \frac{1}{D_B(1 - \frac{1}{\mu_i}) + \frac{1}{\mu_i}} \qquad (15)$$

where μ_i is the closed-loop permeability of the material and D_B is the demagnetizing factor determined from

$$D_B = \frac{\ell n(\frac{3}{2}\frac{\ell}{d}) - 1}{(\frac{\ell}{d})^2} \quad . \tag{16}$$

It should be noted that both μ_i and μ_e are dimensionless constants. This equation gives the theoretical value of μ_e at the center of the rod, but the effective permeability is known to decrease near the ends of the rods [Bozorth and Chapin, 1942]. Hill [1962] gives μ_e as a function of distance from the center of the rod

$$\mu_e = \mu_1(1 - F\frac{x^2}{\ell^2}) \tag{17}$$

where μ_1 is the effective permeability at the mid-point of the core determined from Equation 15, x is the distance from the center of the core, ℓ is the length of the core, and F is a dimensionless constant that specifies the permeability near the end of the core. Hill states that F=3.6.

The effective permeability in Equation 4 is defined as the effective permeability at the position of the turns of wire. Equation 17 shows that the largest effective permeability is achieved for coils located near the center of the core. Equation 15 also shows that a larger ℓ/d ratio produces a larger μ_e. However, the effective permeability for large ℓ/d ratios ($\gtrsim$ 100) is sensitive to temperature changes and mechanical stresses. Also, there are size and weight limits for search coil magnetometers designed for space applications which restrict the ℓ/d ratio.

Resistance of the Wire

Underhill [1910] gives for the resistance of the wire of a search coil with a square bobbin

$$R = 4(a + 0.7854T)N\rho \text{ ohms} \tag{18}$$

where a is the width of the bobbin, T is the depth of the windings, ρ is the resistance per unit length, and N is the number of turns. The type of wire and the diameter of the wire determine ρ. For a given number of turns, the depth of the windings, T, will also depend on the diameter of the wire. From Equations 12 and 14, we can see that the resistance of the wire should be kept as small as possible in order to minimize the noise level of the search coil. This minimization is accomplished by choosing the largest diameter wire that will fit on the bobbin for a given number of turns.

Inductance

The inductance of a solenoid on a high permeability core can be estimated from the following formula [Parady, 1974]

$$L = \frac{\mu_0 \mu_e N^2 A}{\ell} \tag{19}$$

where μ_0 is the permeability constant, μ_e is the effective permeability of the core, A is the cross-sectional area of the core in square meters, N is the number of turns, and ℓ is the length of the core in meters. It should be noted that the inductance varies with the square of the number of turns and is proportional to μ_e. As the resonant frequency

is proportional to the inverse of the square root of the inductance, the resonant frequency is proportional to the inverse of the number of turns and also to the inverse of the square root of μ_e. This relationship leads to a trade off as more turns leads to a better sensitivity, but decreases the bandwidth of the search coil.

Capacitance

The capacitance of a solenoid is difficult to model, as the method of winding the solenoid has a large effect on the final capacitance. Also, capacitance from the wires connecting the bobbin to the preamplifier, or in the preamplifier itself can also play a large role. An estimate for the capacitance of one section of a multi-section coil is given by Hill [1962]

$$C = \frac{0.00381\,\pi\, r_1\, \epsilon_r\, W}{(K_1 - 1) d\, \lambda} \quad pF \qquad (20)$$

where r_1 is the mean radius of the coil, W is the width of the coil, ϵ_r is the average dielectric constant of the insulation on the wire, K_1 is the ratio of the distance between the center of two adjacent wires and the diameter of the wire, d is the diameter of the wire, and λ is the number of layers of wire.

Equation 7 shows that for a large resonant frequency, it is desirable for the capacitance to be as small as possible. One way to accomplish a lower capacitance is to split the coil into sections. If a coil that originally had a capacitance C, is split into n sections, each section would have a capacitance C/n. These sections are connected in series, which gives a new capacitance of C/n^2 for the whole search coil. There is

also a capacitance between the sections, which when taken into account, gives a total capacitance of

$$C_{tot} = \frac{C}{n^2} + \frac{C_1}{(n-1)} \tag{21}$$

where C_1 is the capacitance between adjacent sections. As we want C_{tot} to be smaller than the original capacitance, C_1 should be kept small. This reduction in the capacitance is accomplished by having a space between the sections. There is a limit to the effectiveness of splitting the coils. If n is small, C_{tot} varies inversely to n^2, but as n becomes large, the $C_1/(n-1)$ term starts to dominate. Another limitation is that the resistance of the wire increases as the number of sections are increased, which raises the noise level of the searce coil as seen from Equation 11. There is also a size limit on a search coil to be flown in space, which limits both the number of sections, and the space between each section.

Damping Resistor

The damping resistor plays an important role in the sensitivity and noise level of the search coil as shown in Equations 7 and 13. The damping resistor can be an actual resistor placed in parallel with the coils, the input impedance of the preamplifier, or a combination of the two.

Noise and Noise Sources

The ability for search coil magnetometers to measure weak signals is determined by the amount of noise present. Noise is the unwanted signal that obscure the desired

signal. There are various types and sources of noise. Some of the most important ones are: the Johnson noise due to the resistance of the coil, noise in the amplifier, and interference from outside sources. Johnson noise, also known as Nyquist noise or thermal noise, is the noise found in any material with a resistance. It is caused by the random motion of the free electrons in the material. This random motion produces small instantaneous potential differences between the ends of the material. Since the noise voltage is random, it has a flat frequency spectrum, and is often called "white noise." For resistors, it is usually written as

$$V_{Johnson} = \sqrt{4k_B T\, R\, \Delta f} \qquad Volts \tag{22}$$

where T is the temperature in degrees Kelvin, k_B is Boltzmann's constant, R is the resistance, and Δf is the frequency bandwidth. It is important to notice that Johnson noise depends on the square-root of the temperature. In a complex circuit the resistance R must be replaced with the real impedance Z_r of the circuit [Robinson, 1974]. This substitution gives the Johnson noise as shown in Equation 9.

The other type of noise found in a search coil magnetometer is noise from the preamplifier. This noise is usually made up of three main components, 1/f, or flicker noise, shot noise, and Johnson noise. The 1/f noise usually dominates at low frequencies, while shot and Johnson noise dominates at higher frequencies.

The 1/f noise is given its name due to the fact that it has a spectrum proportional to the inverse of the frequency. The magnitude of this noise varies markedly with the material, and also the construction of the component can have a large effect on the

noise magnitude. Resistors can exhibit this noise, along with transistors, FETs, diodes and vacuum tubes. The 1/f noise is also found in many non-electronic systems. The flow of sand in an hour glass, the flow of traffic on an expressway, and the loudness of classical music versus time all show a 1/f spectrum [Horowitz and Hill, 1980]. This dependance on the material and construction technique makes it difficult to estimate its magnitude before an actual amplifier is built.

Shot noise is due to the current not being a continuous flow, but actually made up of discrete electrical charges. This discreteness results in statistical fluctuations of the current. Horowitz and Hill [1980] gives

$$I_{shot} = \sqrt{2\ q\ I_{dc}\ \Delta f} \tag{23}$$

where q is the electric charge, I_{dc} is the dc current, and Δf is the bandwidth. For large currents, the noise current is usually a very small fraction of the original current, but for small currents, the fluctuations can become a significant fraction of the original current. Shot noise is found in solid state devices, such as transistors and diodes, where electrons randomly cross a pn junction. This effect is analogous to the noise of raindrops hitting a tin roof, which is where it gets its name. It has a flat frequency response like Johnson noise, and in a circuit, it may be difficult to distinguish which of the two is the major noise source at the output.

The total noise voltage of a search coil magnetometer with no outside signals present, is given by

$$n_{total} = \sqrt{(n_{coil}G)^2 + (n_{amp})^2} \quad (24)$$

where n_{coil} is the noise voltage due to the coil from Equation 9, G is the gain of the amplifier, and n_{amp} is the noise voltage due to the amplifier.

The other type of noise important in search coil magnetometers flown on spacecraft is interference. This noise includes interference during testing and calibration, and interference from other instruments on the spacecraft while operating in space.

The interference most often encountered in the lab with a search coil magnetometer is 60 Hz interference from the power lines. Other sources of interference are from computer monitors, usually in the tens of kHz range, and signals from radio stations, 800 kHz and above. This interference must be reduced or removed to get a good calibration of the instrument. The actual noise voltage of the search coil magnetometer can only be found if this interference is removed. This problem is discussed in more detail in the calibration section.

Electrical interference from the spacecraft also increases the noise level, as it obscures the natural signals the instrument is trying to measure. Figure 4 shows an example of interference from the Galileo spacecraft. A complex spectrum of interference can be observed between 100 Hz and 1000 Hz. This interference makes it difficult to measure any natural signals in this frequency range. Various steps can and should be taken to reduce magnetic interference. Magnetometers should be deployed as far from the spacecraft body as possible. Most interference fields are

dipole in nature. Dipole magnetic fields vary as $1/r^3$, where r is the distance between the noise source and the sensor. If r is large, then the interference will be reduced, hopefully below the noise level of the search coil. For this reason, search coil magnetometers are often mounted on the end of a boom, far from the spacecraft electrical systems. Current carrying wires should be twisted pairs, and large current loops in the spacecraft harness design should be avoided. Any current loops that are necessary should be made as small as possible to minimize the magnetic moment, AI. Power converters should operate at the highest possible frequency, preferably above the frequency range of the sensor. Shielding can reduce magnetic interference, but due to weight considerations, shielding can only be applied to small components. At spacecraft testing and calibration, each instrument should be tested individually with the magnetometers to examine its possibility for generating interference.

CHAPTER IV. POLAR AND WIND SEARCH COILS

The Polar and Wind search coils are the first search coils built at The University of Iowa to use preamplifiers constructed with surface mount technology. The new preamplifiers improve the sensitivity and noise level of the search coil magnetometers over earlier University of Iowa search coil designs. Figure 5 shows an outline drawing of the search coils. The main components are the housing that contains and protects the electronics, a high permeability core, two bobbins containing thousands of turns of wire each, and a preamplifier located in the center section of the housing. Each component will be discussed in more detail below.

Housings

The housing of the Polar and Wind search coils are shown in Figure 6. They are constructed of Vespel and were coated at Goddard Space Flight Center with vacuum deposited aluminum and silver conductive paint to provide a electrostatic shield, and then painted with black paint to provide the proper thermal properties.

Core and Bobbins

The core of the Polar and Wind search coils was purchased from the Arnold Engineering Company and consists of a 4 mil supermalloy laminated bar with dimensions of 3/16 x 3/16 x 15.5 inches. It has an initial permeability, μ_i, of 60,000 at 100 Hz. The ℓ/d ratio of 82.7 and μ_i = 60,000 gives an effective permeability at

the center of the rod of 1738 (see Equation 15). For the Polar and Wind search coils, the bobbins are positioned 1.275 inches from the center of the core as shown in Figure 7. The bobbins were machined from Delrin and are shown in Figure 8. There are eight sections containing the wire, seven of which contain the primary windings, and one that contains a calibration winding as shown in Figure 9. The Polar search coils contains 1430 turns of #40 AWG wire per section for the primary winding, for a total of 10,010 turns per bobbin. The Wind search coils contains 5715 turns of #44 AWG wire per section for a total of 40,005 turns per bobbin. Both the Polar and Wind search coils contain a calibration winding of 1000 turns of #40 AWG wire in the eighth section.

The variation of μ_e over the length of the core coupled with the location of the bobbins on the core causes a reduction in the effective permeability determined above. This correction factor of the effective permeability was determined by finding μ_e for the center of each section of primary winding from Equation 17. The average of the correction factors of the seven sections was determined and this average was multiplied by the value 1738 determined from Equation 15 for the center of the core. The average correction factor was found to be 0.876, which gives a corrected effective permeability of 1522.

The effects of the position of the bobbins on the core was examined with the Polar engineering model search coil. The effective permeability was determined from Equation 17 for each position of the bobbins on the core. Figure 10 shows the

variation of output voltage of one side of the preamplifier with the effective permeability As can be seen, the curve is approximately a straight line, as expected from the linear relation of output voltage to μ_e from Equation 4. Figure 11 shows the variation of the inductance of the two bobbins with the effective permeability. These curves are also approximately straight lines, as expected from the linear relation of L and μ_e from Equation 19. These small deviations from a straight line are probably due to Equation 17 losing some accuracy near the ends of the core. The difference in the inductance between the two bobbins is probably due to the bobbins having a different number of turns. This hypothesis is supported by the fact that the resistance of bobbin 1 is 1136 ohms and bobbin 2 is 1260 ohms.

The effective permeability at the center of the core was calculated from these induction measurements by rewriting Equation 19 as

$$\mu_e = \frac{L\,\ell}{f\,A\,N^2\mu_0} \tag{25}$$

where ℓ is the length of the core in meters, L is the measured inductance in Henrys, N the number of turns (assumed to be 10,010), A is the area of the core in square meters, μ_0 is the permeability constant, and f is the correction factor of μ_e for the position of the bobbin on the core. This equation gives $\mu_e = 2375$ for bobbin 1, and $\mu_e = 2760$ for bobbin 2. These values are much larger than the value of 1738 obtained from Equation 15. This discrepancy will be discussed in the next section.

Resistance, Inductance, and Capacitance

The resistance, inductance, and capacitance of the Polar and Wind search coils were measured on a HP 4192A LF Impedance Analyzer. The results and the theoretical predictions from Equations 18, 19, and 20 are shown in Table 1. As can be seen, the theoretical and measured values do not agree. This discrepancy in the capacitance is not unexpected due to the previously mentioned difficulties of modeling the self capacitance of a multilayered coils. There are also capacitance effects present from the leads coming off the bobbins which were not considered in Equation 20. It was observed that moving the leads could cause a small ($<10\%$) change in the measured capacitance. The measured inductance was found to be $\approx 35\%$ larger than the predicted value. The Japanese Geotail search coil's inductance [Hayashi, 1988], was also compared to the theoretical value predicted from Equation 19, and was also found to be $\approx 35\%$ too large. The difference between the theoretical and the experimental value may be due to the length term, ℓ in the denominator of Equation 19. Pasahow [1985] states that ℓ is the magnetic path length of the core. Since the permeability of the core decreases near the ends, it would be reasonable to assume that the magnetic path length is smaller than the actual core length.

The theoretical and measured resistances of the Polar and Wind search coils agree reasonably well. The small difference is probably due to difficulties in determining the depth of the windings and the exact width of the bobbin which are needed in Equation 18 to determine the theoretical resistance.

Preamplifiers

The Polar and Wind search coil preamplifiers are a new design. They were the first search coil preamplifiers to be built using surface mount technology at the University of Iowa. A circuit built using surface mount technology occupies less volume than the same circuit built using the old cordwood mounting technique. This reduction in size allowed the new, more advance preamplifier to be built, without increasing the size or weight of the search coils. Figure 12 shows a schematic of the Polar search coil preamplifier. The amplifier design is the same for the Polar and Wind search coils except for the resistors R2 and R26. These resistors control the value of the input impedance of the amplifier, which determines the damping resistance. Figure 13 shows a simplified block diagram of the amplifier. For a differential signal across the inputs, the amplifier acts like two separate amplifiers as shown in Figure 14.

The separation into two amplifiers allows the coils to be isolated from each other, which for a fixed resonance frequency permits the number of turns on each bobbin to be doubled. This doubling of the number of turns increases the sensitivity of the search coil by a factor of two, but keeps the same frequency bandwidth as a single coil with half as many turns.

The net effect is a $\sqrt{2}$ improvement in the signal-to-noise ratio. To see this improvement, note that the noise voltage out of each side of the preamplifier adds as

$$n_{amp} = \sqrt{V_n^2 + V_n^2} = \sqrt{2}\,V_n \qquad \frac{Volts}{\sqrt{Hz}} \tag{26}$$

where V_n is the noise voltage of one side of the preamplifier. This equation assumes tha the noise is the same on both outputs. The noise level improvement due to the nev amplifier can be determined from

$$\frac{B_N}{\sqrt{\Delta f}} = \frac{\sqrt{2}\ V_n}{2V_{out}} = \frac{V_n}{\sqrt{2}\ V_{out}} \frac{nT}{\sqrt{Hz}} \tag{27}$$

where V_{out} is the voltage out of each side of the preamplifier. This amplifier desig gives a $\sqrt{2}$ improvement of the noise level with the same bandwidth compared to search coil with the old preamplifiers. In theory, one could continue this process with preamplifiers, which would give you a $\sqrt{n}$ improvement. Of course, there is a limit t the size, weight, and power that can be allocated to a search coil that is to be flown o a spacecraft which would limit n.

The gain of the amplifier can be found from Figure 14 to be

$$G = \frac{A(11{,}999)}{499A + (11{,}999)} \tag{28}$$

where A is the open loop gain. The open loop gain of the Wind search coil amplifier were measured and found to be $\approx$70, which gives a gain $\approx$18. This value of the gai agrees very well with measured sensitivities of the Wind search coils.

Polar Search Coils

The Polar search coils have 10,010 turns of #40 AWG wire on each bobbin, fo a total of 20,020 turns. The coil constant, K, from Equation 6 is approximately 3.9 μV/(nT Hz). Taking into account a preamplifier gain of 18, we have a total sensitivity

resistance of the wire is approximately 1250 ohms, which gives a noise voltage of 4.5 nV/$\sqrt{\text{Hz}}$ at 300° K. The new preamplifier design increased the sensitivity by a factor of two compared to the ISEE 1 and 2 search coils, which had coil plus amplifier sensitivity of $\approx$35 μV/(nT Hz), and a resonant frequency of 10,000 Hz [Gurnett et al., 1978]. The transfer function of the Polar prototype search coil and the theoretical prediction from Equation 7 are shown in Figure 15. The values used to determine the theoretical curve were

$$\begin{aligned} R_1 &= 1250\ \Omega \\ R_D &= 2.25\ M\ \Omega \\ L &= 17\ H \\ C &= 10.3\ pF \\ N &= 20{,}020 \\ \mu_e &= 1522 \\ G &= 18 \end{aligned} \qquad (29)$$

The noise level of the Polar prototype search coil was measured in the lab by the μ-metal shield method. Figure 16 compares the Polar measured noise level with the ISEE 1 and 2 noise levels [Gurnett and Anderson, 1978]. As can be seen, above 800 Hz the Polar noise level is approximately $\sqrt{2}$ times lower than the ISEE noise levels as expected from the new amplifier design. Below 800 Hz, the higher noise level of the Polar search coil is probably caused by interference signals, mostly 60 Hz, and its

harmonics. A noise voltage calibration will be done with the flight units at a low noise site to determine the actual noise level at these lower frequencies. The flight Polar search coils are currently being constructed, with completion scheduled for June, 1992.

Wind Search Coils

The Wind search coils are similar to the Polar search coils but are optimized for lower frequencies. They consists of 40,005 turns of #44 AWG wire on each bobbin for a total of 80,010 turns. The resistance of the wire on each bobbin is approximately 12,850 ohms. This resistance gives a noise voltage of 14.6 nV/$\sqrt{\text{Hz}}$ at 300° K. The coil constant from Equation 6 is approximately 16.0 μV/(nT Hz). The total coil constant taking into account an amplifier gain of 18 is approximately 288 μV/(nT Hz). The resonant frequency is $\approx$1600 Hz. This resonant frequency is much lower than predicted by Equation 7 for the measure capacitance and inductance of the bobbins (see Table 1). The deviation from the theoretical value is due to a stray capacitive coupling on the flight preamplifier boards. Figure 17 shows the transfer function of the Wind spare search coil and the theoretical curve from Equation 7 with an added capacitance to correct for the stray capacitance. The values used for the theoretical calculation were

$$
\begin{aligned}
R_1 &= 12{,}850 && \Omega \\
R_D &= 4.535 && M\,\Omega \\
L &= 280 && H \\
C &= 34.26 && pF \\
N &= 80{,}010 \\
\mu_e &= 1522 \\
G &= 17.74
\end{aligned}
\qquad (30)
$$

Figure 18 compares the noise level of the Wind spare search coil measured at a low noise field site and the ISEE 3 search coil inflight noise levels [Gurnett and Anderson, 1978]. These two search coils have the same number of total turns, 80,010, so their noise levels should be similar. The Wind search coils have a higher resonant frequency which gives them a lower noise level at higher frequencies.

The Wind flight search coils have been constructed, tested, calibrated, and delivered to the University of Minnesota for integration with their plasma wave instrument. Figure 19 shows a photograph of the Wind B_z search coil magnetometer.

CHAPTER V. CALIBRATION

The sensitivity of the Polar and Wind search coil magnetometers are calibrated by two different methods. They both involved applying a sinusoidal magnetic field of a known frequency, phase, and magnitude, and measuring the search coil's output frequency, phase, and voltage. The first method employs a transmitting loop to produce the applied magnetic field. The second method employs a shielded solenoid to produce the applied magnetic field. Sixty Hertz interference from power lines, and other low frequency emissions, primarily from computers, are easily detected by the search coil magnetometers, and can often saturate the preamplifier. This interference must be reduced or eliminated to obtain accurate calibrations.

The transmitting loop method involves driving a triangular transmitting loop with a known current and frequency at a known distance from the search coil. The magnetic field produced by the loop at the search coil location can be calculated exactly since the current and the geometry and are known. Figure 20 shows a typical setup of this method. The search coil is placed at a distance L from the center of a triangular transmitting loop, and a height h from the bottom of the loop as shown. The axis of the search coil is perpendicular to the plane of the transmitting loop. The voltage across the eight ohm resistor is measured to determine the current, I, in the transmitting loop. The

magnetic field produced by the transmitting loop at the search coil is determined from this current for a given L, d, and h from

$$|\vec{B}| = \frac{N\mu_o I}{4\pi}\left[\frac{1}{r_1}(\cos\alpha_1 - \cos B_1) - \frac{1}{r_2}(\cos\alpha_2 - \cos B_2) + \frac{1}{r_3}(\cos\alpha_3 - \cos B_3)\right] \quad Tesla \tag{31}$$

where

$$r_1 = h$$

$$r_2 = D_3 \sin\alpha_2$$

$$r_3 = D_3 \sin B_3$$

$$\alpha_1 = \cos^{-1}\left(\frac{L + \frac{d}{2}}{D_1}\right)$$

$$\alpha_2 = 1.0472 - \cos^{-1}\left(\frac{L}{D_3}\right)$$

$$\alpha_3 = 1.0472 - \alpha_1$$

$$B_1 = \cos^{-1}\left(\frac{L - \frac{d}{2}}{D_2}\right)$$

$$B_2 = 1.0472 + B_1$$

$$B_3 = 2.094395 - \alpha_2$$

$$D_1 = [(L + \frac{d}{2})^2 + h^2]^{1/2}$$

$$D_2 = [(L - \frac{d}{2})^2 + h^2]^{1/2}$$

$$D_3 = [(0.866\ d - h)^2 + L^2]^{1/2}$$

and N is the number of turns of the transmitting loop. Substituting I=V/R, R=8 ohms, N=8 turns, and V equal to the voltage measured across the resistor, we find

$$|\vec{B}| = \frac{N\ V}{R} \times 10^{-7}\ C(L,\ d,\ h) = V \times 10^{-7}\ C(L,\ d,\ h)\ \ Tesla \qquad (32)$$

where C(L,d,h) is the term from Equation 31 that depends on L, d, and h.

The transmitting loop method must be performed away from low frequency interference sources, such as 60 Hz interference from power lines, and also away from magnetic materials, such as steel beams or metal lab benches. Magnetic materials distort the applied field, causing an error in the calibration. This distortion can be observed in Figure 21, which shows the measured coil constant, K, of the Wind spare search coil using the transmitting loop method in the lab. The curves are for distances of L=5 feet and L=8 feet. If there was no distortion present, the two curves would be identical, as was observed when the test was repeated at a low noise field site. It is believed that the steel beams in the floor and ceiling caused the distortion. No magnetic shield room exists at the University of Iowa so the transmitting loop calibration must be performed

at a field site if an accurate calibration is required. This method gives a very accurat magnitude and phase calibration. The main drawback with the method is that accurat calibrations cannot be obtained in the lab. Weather limits when field calibration may b attempted, as rain and snow may damage the test equipment and the search coils Cleanliness and static protection are also difficult to control in the field.

The shielded solenoid method involves placing the search coil in the center of long solenoid. A known current is applied to the solenoid, which produces the magneti field. The solenoid consist of ten turns of wire with a radius of 13 cm. Each turn i separated by 6.7 cm, with a total length of the solenoid of 60.3 cm. The equivalen circuit of the solenoid is shown in Figure 22. The magnetic field produced at the cente of the solenoid by each individual coil can be determined from the following formula:

$$B(z) = \frac{\mu_0 I}{2}\left(\frac{r^2}{(z^2 + r^2)^{3/2}}\right) \quad Tesla \tag{33}$$

where r is the radius of the coil, I is the current in each turn, and z is the distance from the coil to center of the solenoid. Summing over all ten turns of the solenoid, and substituting I=V/R, we find for the center of the solenoid

$$B = \frac{\mu_0 V}{2(5000)}(28.02) = 3.52\times10^{-9}\ V \quad Tesla \tag{34}$$

where V is the voltage measured across the 50 ohm resistor.

To reduce the interference signals, the solenoid is enclosed in a μ-metal shield. The magnetic shielding allows calibration measurements to be performed in the lab. The

current μ-metal shield reduces the interference signals by over 60 dB. However this shielding approach has certain problems. First, in some cases the μ-metal shield does not reduce the interference signals to levels low enough to allow a good calibration. Second, the μ-metal shield changes the field characteristics of the solenoid. If the perturbation is large enough, the errors in the calibration can be excessive. Figure 23 show a comparison of the transfer function of the Wind spare search coil obtained at a low noise field site by the transmitting loop method at two distances verses the solenoid in the μ-metal shield method measured in the lab. As can be seen, the perturbation in the applied magnetic field is small, confirming that the shielded solenoid provides a good calibration technique for determining the sensitivity of the search coils.

The noise voltage of the search coil must also be measured and calibrated to determine the noise level of the search coil. This calibration is usually done in the μ-metal shield with no calibration signal present. As the μ-metal does not eliminate all the 60 Hz interference found in the lab, best results are obtained at a low noise field site. The search coil is placed in the μ-metal shield and powered by a set of batteries. The noise voltage of the search coil is then measured by a spectrum analyzer. Figure 24 shows the setup for such a noise level calibration.

The noise voltage of the Wind search coils was measured both in the lab and at a low noise field site using the solenoid in the μ-metal shield. The resulting noise levels are shown in Figure 25. As can be seen, the noise level at low frequencies is much lower when measured at a low noise field site. At higher frequencies, the noise levels are very similar.

CHAPTER VI. FUTURE WORK

Various possible design changes which may have improved the search coi magnetometers were discovered during this project, but due to time constraints ir building the search coils, were not examined in detail, or implemented. These desigr changes should be examined before future search coils are built, and if improvements are found to exists, the changes should be implemented.

The first design change that should be implemented is to place the bobbins at the center of the core. This placement will increase the sensitivity by over 10% compared to the Polar and Wind search coils. The placement in the center of core will require the housing to be redesigned to allow a compartment for the preamplifier.

A second possible design change would be to redesign the preamplifier, specifically to lower its noise voltage. The preferred approach would be to use prefabricated chip amplifiers, whose small size would allow the coil to be split into more sections. This splitting would lower the noise level by $\sqrt{n}$ as shown in Equation 27 where n is the number of separate coils. One difficulty with prefabricated chip amplifiers is their high cost, much higher than the current preamplifiers.

Another possible design change would be to adopt a negative feedback system, as shown in Figure 26 [Hayashi, 1988]. This type of system has been flown on the Galileo spacecraft, and is to be flown on the Geotail spacecraft. The use of a feedback

winding on the core flattens the transfer function, allowing one to make the damping resistance infinite. Looking at Equation 11 for the noise level, we see that as R_f increase, the noise level decreases. Although this approach should reduce the noise level, we note that the noise levels of the Galileo and Geotail search coil magnetometers do not show a marked improvement over the Polar and Wind search coils. Future work should be done to determine if a feedback winding would improve the noise level of the present search coil magnetometer design.

One last possible design change would be to lower the temperature or use superconducting wire for the coil. This change would lower the noise level in Equation 11 since R_1 would be reduced. There would still be the noise due to the amplifier as shown in Equation 13, so the overall improvement would depend on the amplifier noise. There is also the added complication of providing a low temperature, particularly if the wire was maintained in a superconducting state.

CHAPTER VII. CONCLUSION

The Polar and Wind search coil magnetometers provide improvement over the earlier University of Iowa search coil designs. The higher sensitivity, and lower noise levels of the Polar and Wind search coils will allow weaker magnetic signals to be measured. They will provide new data for understanding the plasmas in our solar system, and for investigating the interaction of low frequency electromagnetic waves with plasmas.

REFERENCES

Bozorth, R. M., and D. M. Chapin, Demagnetizing Factors of Rods, J. Applied Phys., 13, 320, 1942.

Gurnett, D. A., and R. R. Anderson, et al., ISEE 1, ISEE 2, and ISEE 3 Plasma Wave Investigation Calibration Records, The University of Iowa, Iowa City, Iowa, 1978.

Gurnett, D. A., F. L. Scarf, R. W. Fredricks, and E. J. Smith, The ISEE-1 and ISEE-2 Plasma Wave Investigation, IEEE Trans. Geo. Elect., GE-16, 253, 1978.

Hayashi, K., Improvement of the Tri-Axial Search Coils Onboard Geotail Satellite and Electromagnetic Interference (EMI) Problem on the Satellite, Thesis, Kanazawa University, 1988.

Hill, L. K., Micropulsation Sensors with Laminated MUMETAL Cores, Thesis, The University of Texas, 1962.

Horowitz, P., and W. Hill, The Art of Electronics, Cambridge University Press, Cambridge, 1980.

Parady, B., Measurement of Low Frequency Magnetic Fluctuations in the Magnetosphere, Thesis, University of Minnesota, 1974.

Pasahow, E., Electronics Ready Reference Manual, McGraw-Hill Book Company, New York, 1985.

Robinson, F., N. H., Noise and Fluctuations in Electronic Devices and Circuits, Oxford University Press, London, 1974.

Underhill, C. R., Solenoids Electromagnets and Electromagnetic Windings, D. Van Nostrand Company, New York, 1910.

Table 1. Comparison of Theoretical and Measured Values for the Polar and Wind Search Coil

	Polar		Wind	
	Theory	Measured	Theory	Measured
Inductance (H)	11	17	176	280
Capacitance (pF)	4.5	13.8	1.22	11.3
Resistance (ohms)	1170	1250	12,967	12,800

Figure 1. A sketch of the basic configuration of a search coil magnetometer.

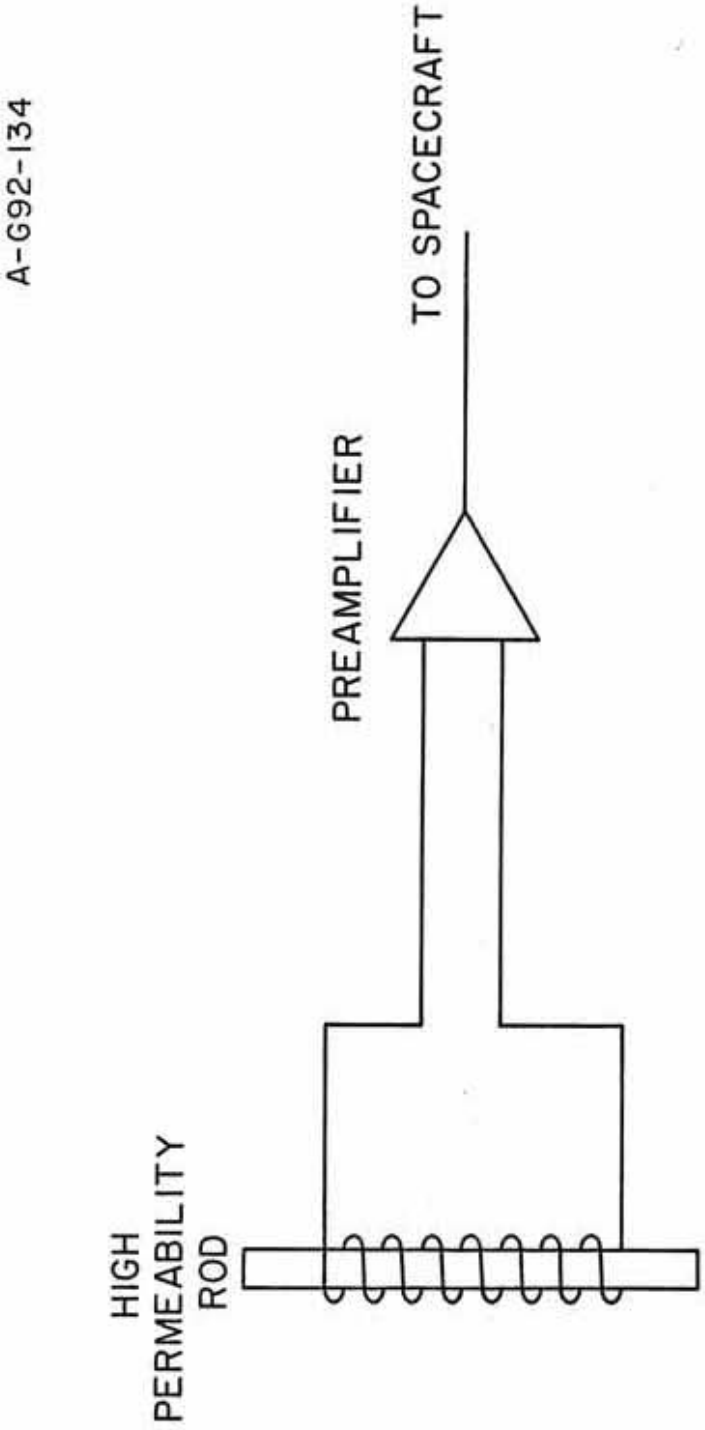
A-692-134
TO SPACECRAFT
PREAMPLIFIER
HIGH PERMEABILITY ROD

Figure 2. A sketch of several space plasma phenomena, and their typical magnetic field amplitudes and frequencies. The curved line is the noise level of the ISEE 1 and 2 search coils which were constructed at the University of Iowa and launched in 1977.

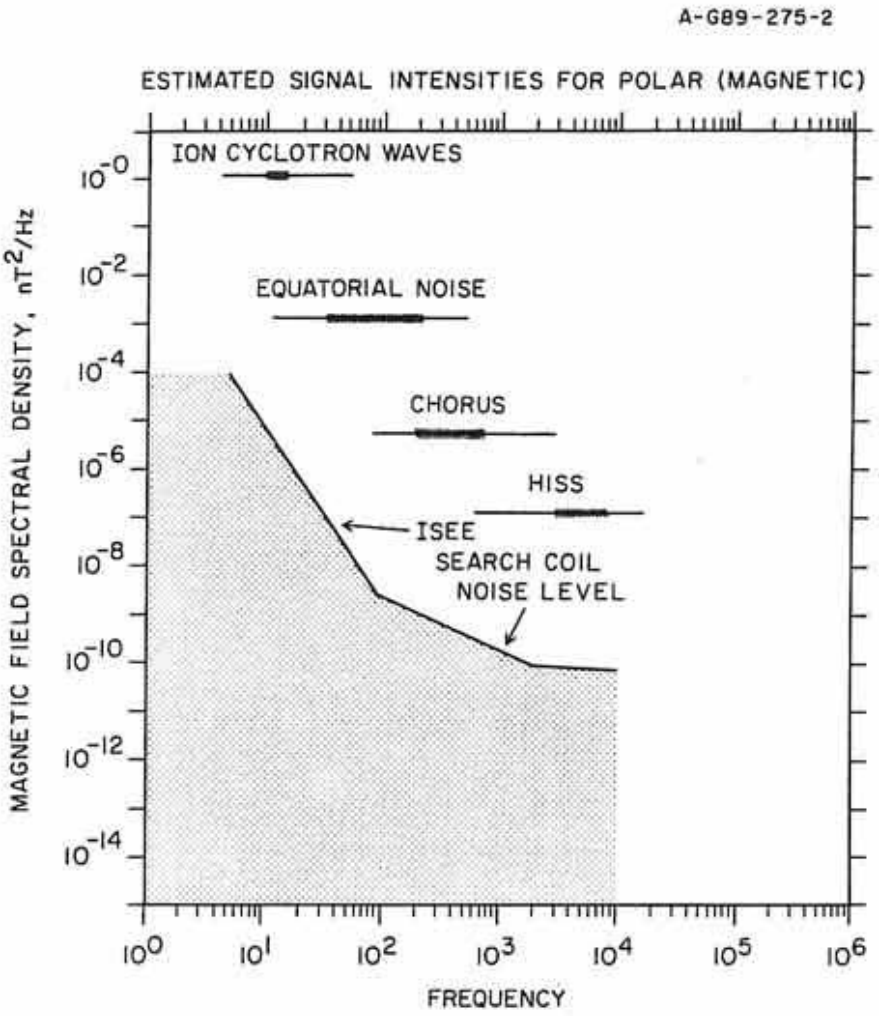
A-G89-275-2
ESTIMATED SIGNAL INTENSITIES FOR POLAR (MAGNETIC)
ION CYCLOTRON WAVES
EQUATORIAL NOISE
CHORUS
HISS
ISEE
SEARCH COIL
NOISE LEVEL
MAGNETIC FIELD SPECTRAL DENSITY, nT²/Hz
10⁻⁰
10⁻²
10⁻⁴
10⁻⁶
10⁻⁸
10⁻¹⁰
10⁻¹²
10⁻¹⁴
10⁰
10¹
10²
10³
10⁴
10⁵
10⁶
FREQUENCY

Figure 3. The equivalent circuit of the search coil magnetometer.

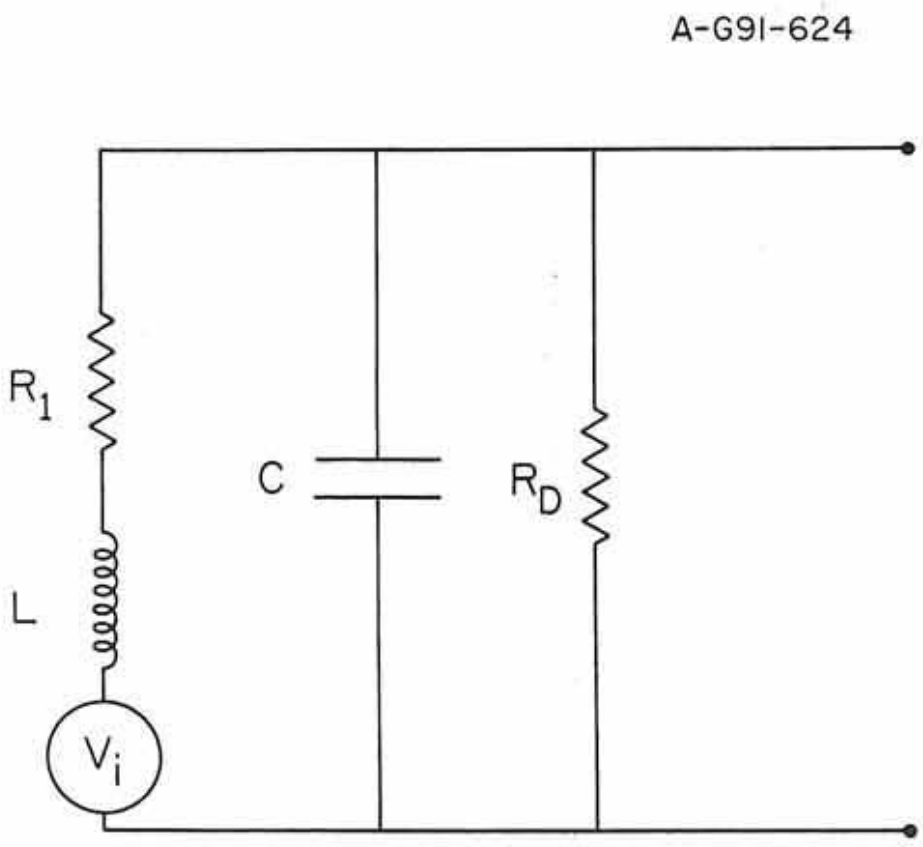
A-G91-624
R1
L
C
RD
Vi

Figure 4. A spectrogram showing spacecraft-generated interference measured by the Galileo search coil magnetometer. A complex spectrum of interference is observed from below 100 Hz to about 1000 Hz.

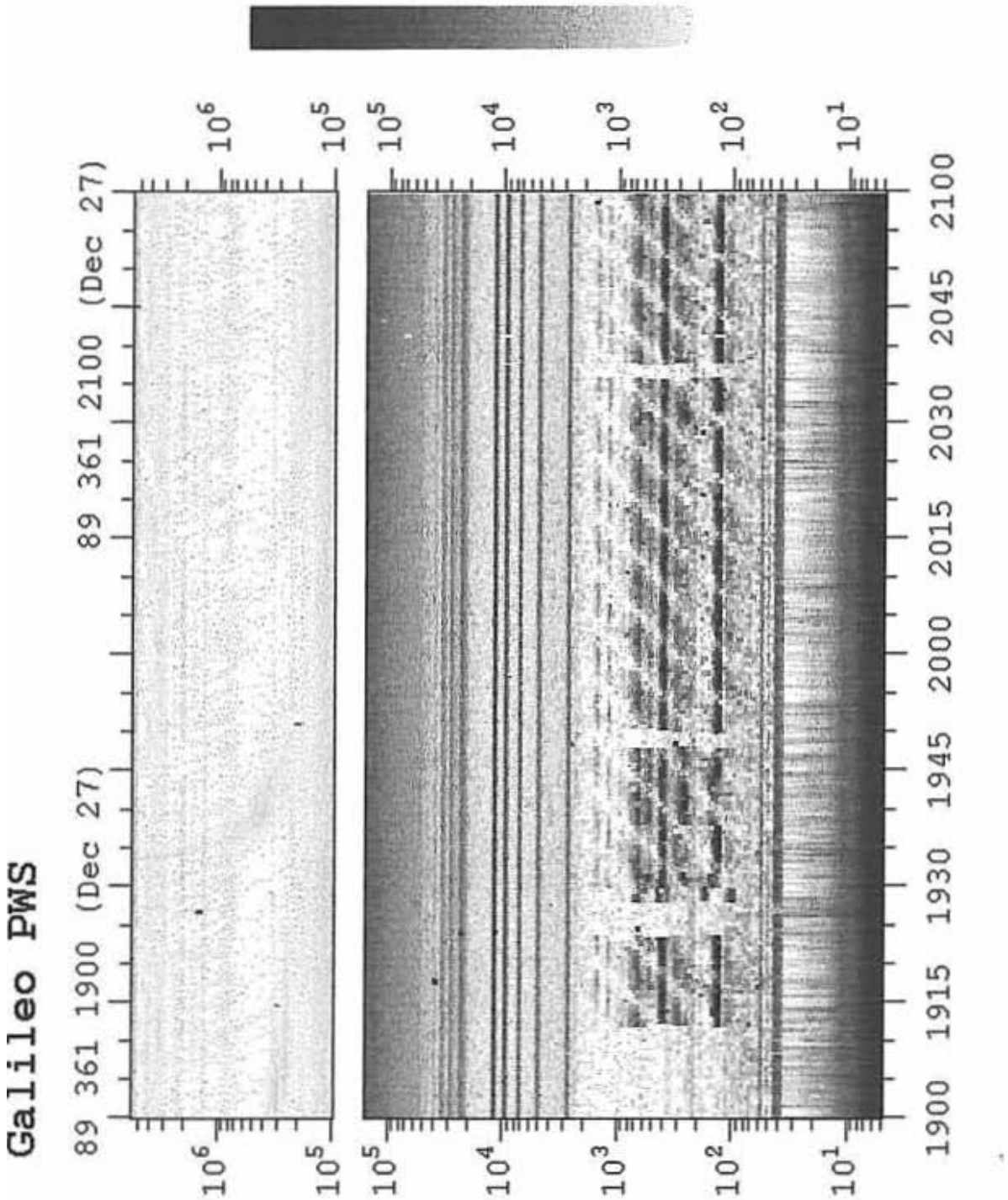
Galileo PWS
89 361 1900 (Dec 27)
89 361 2100 (Dec 27)
1900 1915 1930 1945 2000 2015 2030 2045 2100
10^6
10^5
10^4
10^3
10^2
10^1

Figure 5. A sketch of the Polar and Wind search coil magnetometer showing the main components.

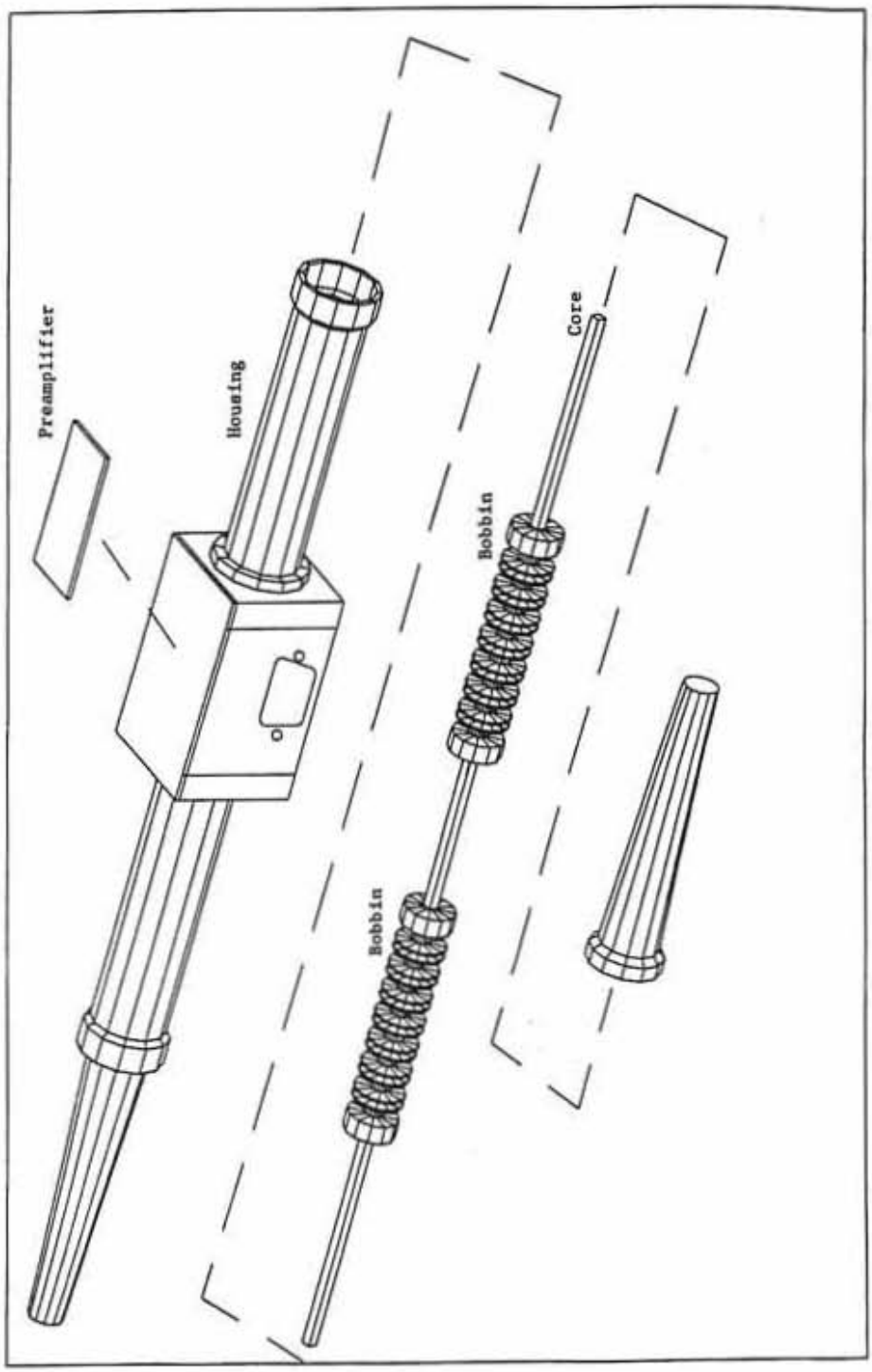
Preamplifier
Housing
Core
Bobbin
Bobbin

Figure 6. The Polar and Wind search coil magnetometer housings. The dimensions are given in inches.

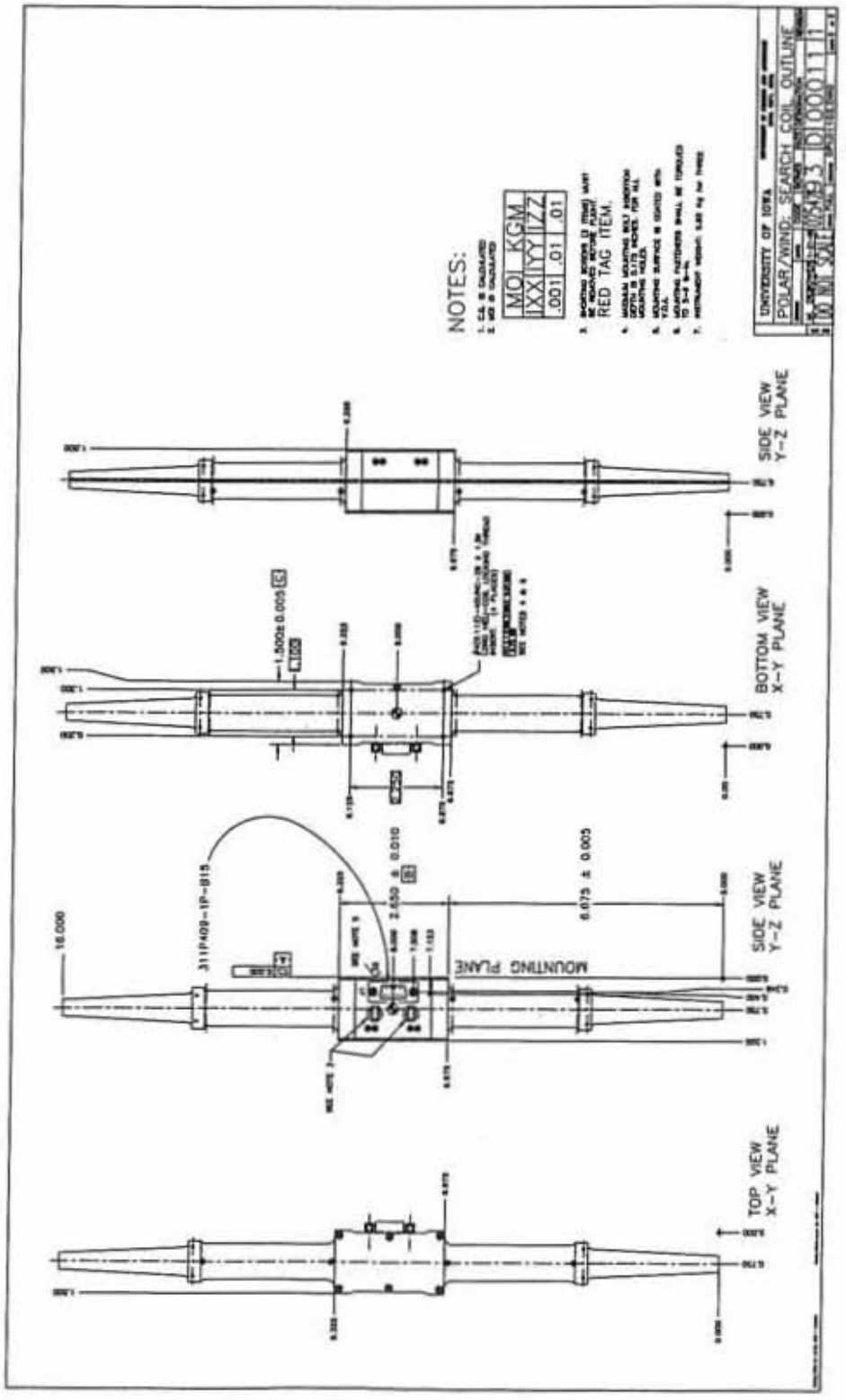
NOTES:
MOI KGM
IXX IYY IZZ
.001 .01 .01
RED TAG ITEM.
UNIVERSITY OF IOWA
POLAR/WIND: SEARCH COIL OUTLINE
SIDE VIEW Y-Z PLANE
BOTTOM VIEW X-Y PLANE
SIDE VIEW Y-Z PLANE
MOUNTING PLANE
TOP VIEW X-Y PLANE

Figure 7. A sketch showing the location of the bobbins on the core. The dimensions are given in inches.

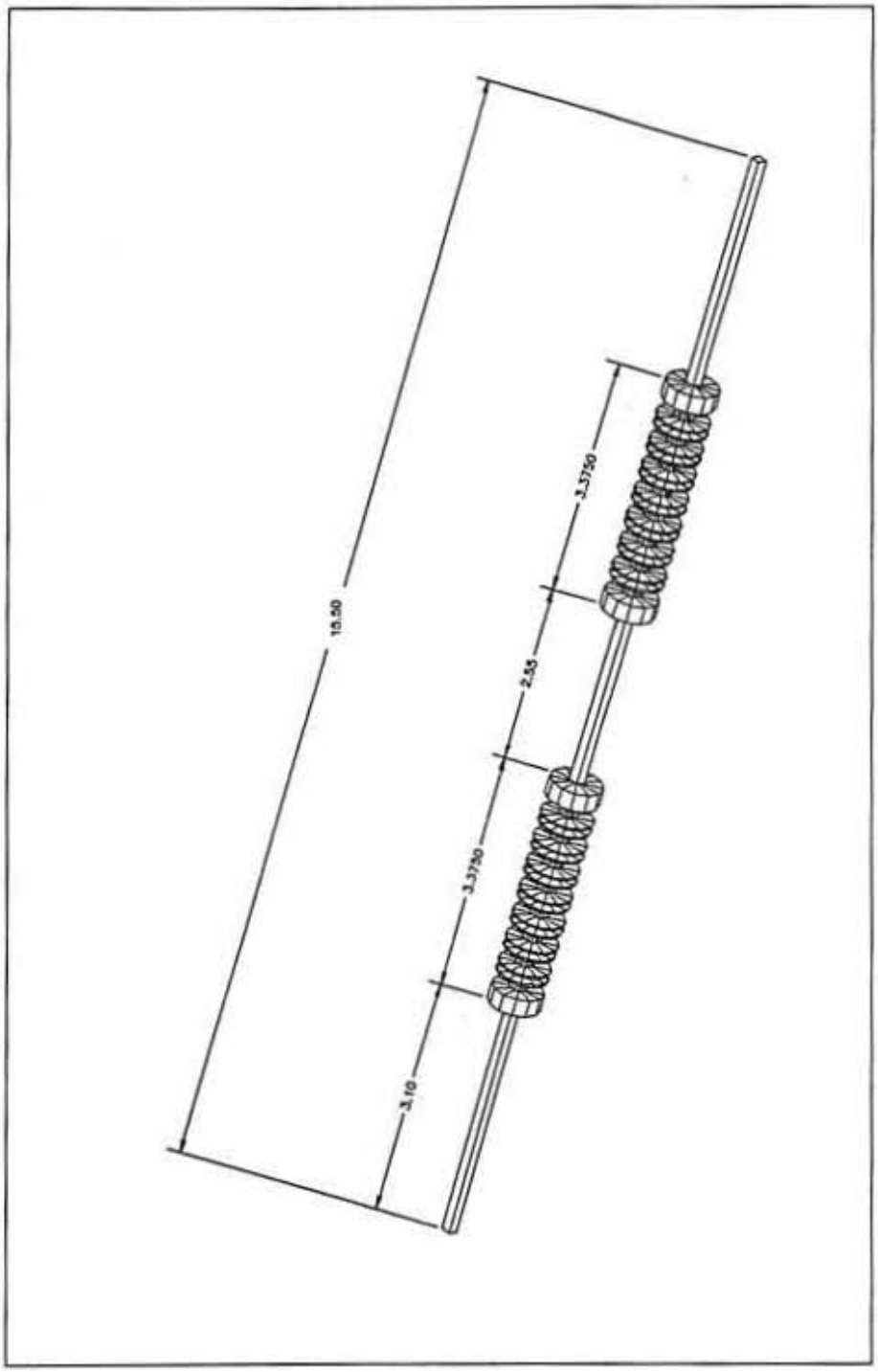
15.50
3.3750
2.55
3.3750
3.10

Figure 8. A sketch of the Polar and Wind search coil bobbins. Dimensions are given in inches.

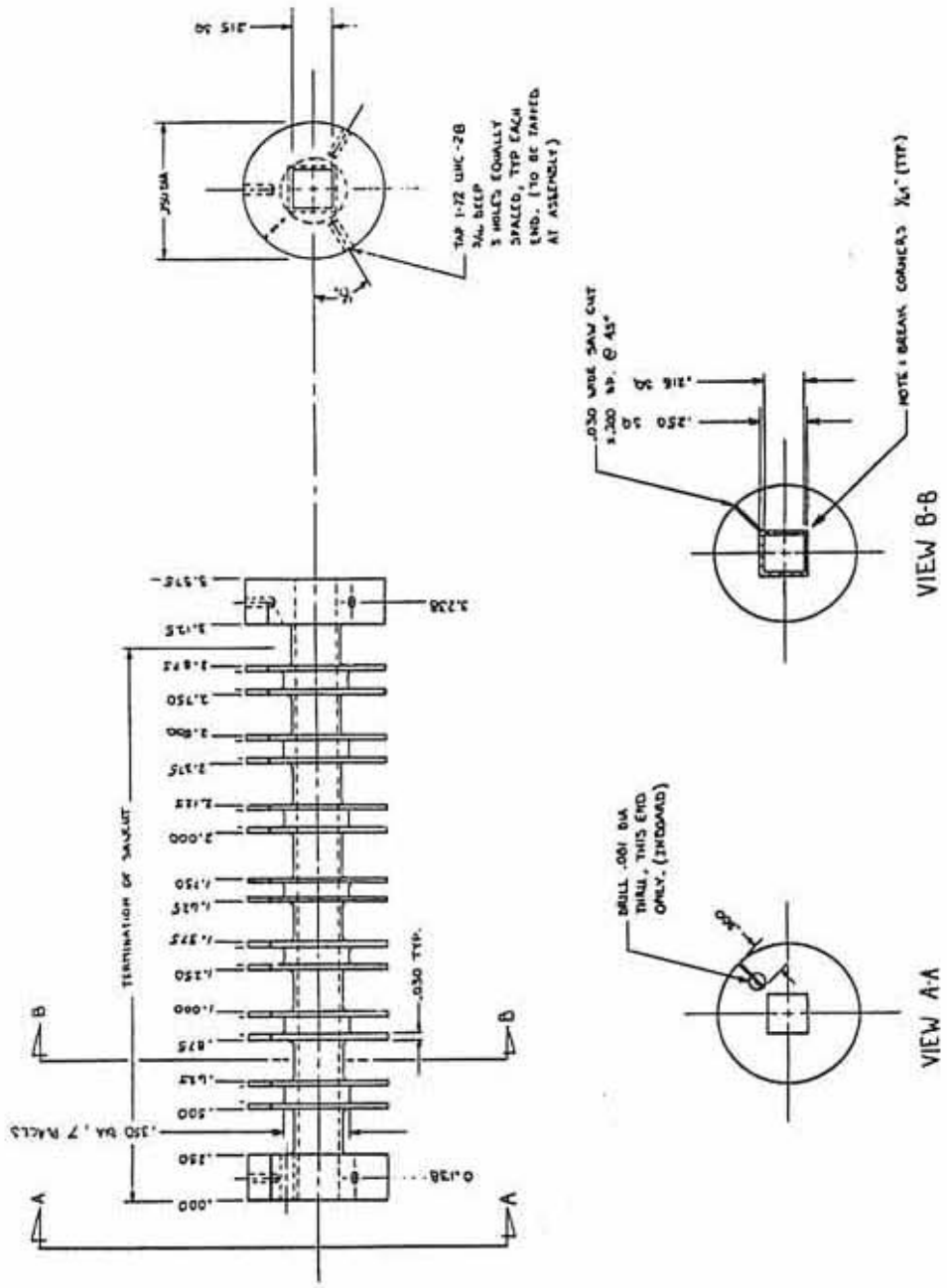
VIEW B-B
VIEW A-A
TERMINATION OF SHIELDS
.030 TYP.
.350 DIA. 7 PLCS.
0.138
A
B

Figure 9. A sketch of the Polar and Wind search coil bobbins. The primary windings are located in sections 1 through 7. The calibration winding is located in section 8.

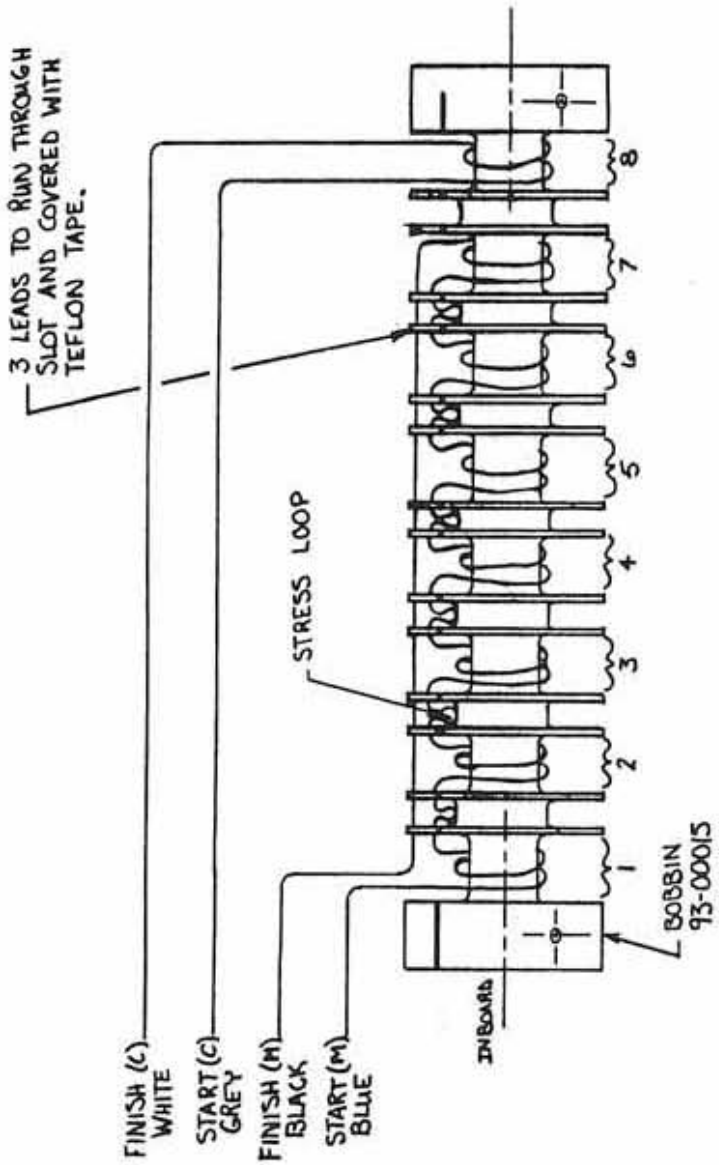
3 LEADS TO RUN THROUGH SLOT AND COVERED WITH TEFLON TAPE.
STRESS LOOP
1
2
3
4
5
6
7
8
BOBBIN 93-00015
INBOARD
FINISH (C) WHITE
START (C) GREY
FINISH (M) BLACK
START (M) BLUE

Figure 10. The relationship of the effective permeability determined from the position of the bobbins on the core to the output voltage of the preamplifier as measured on the Polar engineering model search coil.

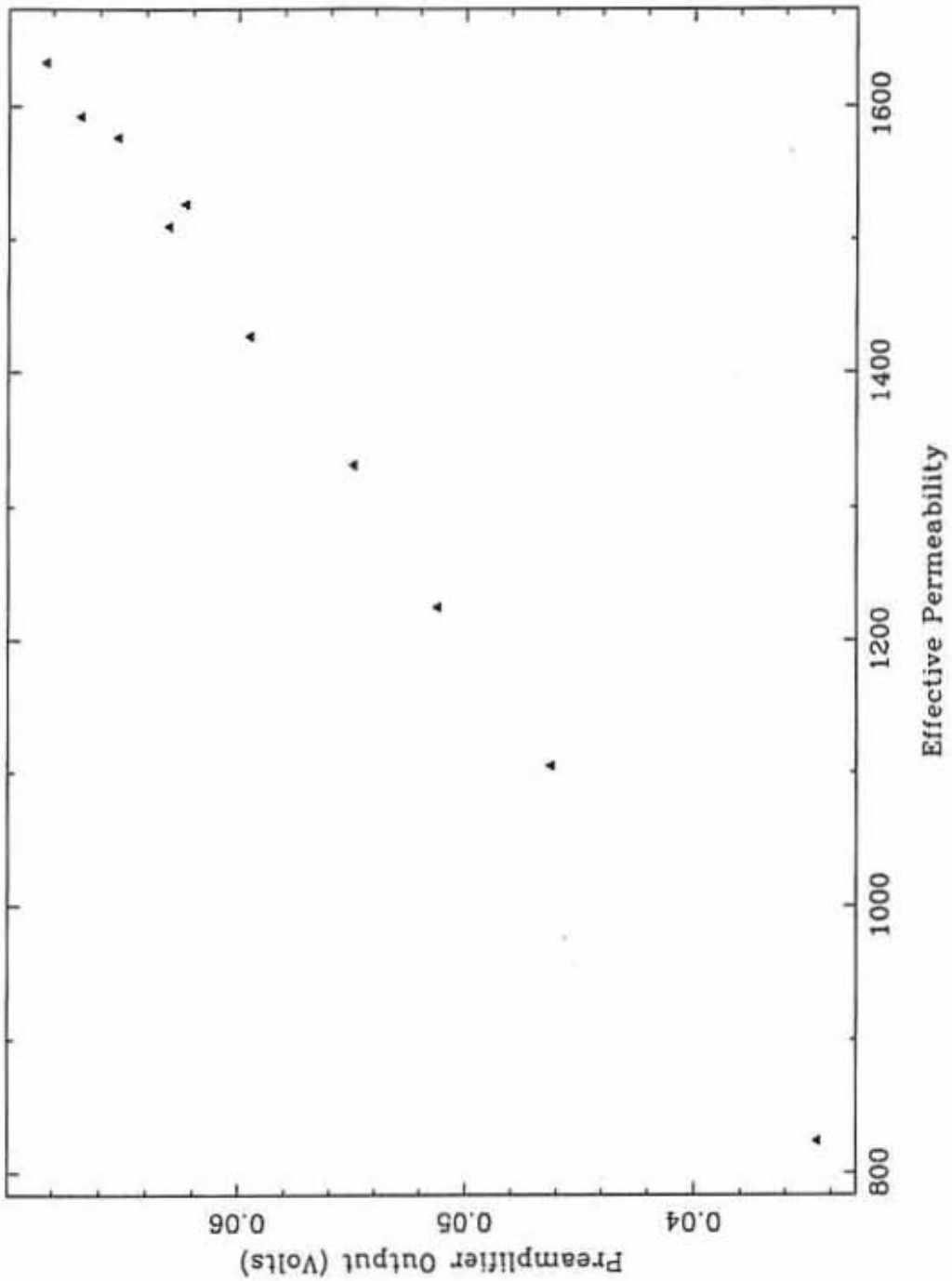
Effective Permeability
800
1000
1200
1400
1600
0.04
0.05
0.06
Preamplifier Output (Volts)

Figure 11. The relationship of the effective permeability determined from the positior of the bobbins on the core to the inductance of the coils as measured or the Polar engineering model search coil. The inductance of bobbin 1 is represented by the circles and bobbin 2 by the squares.

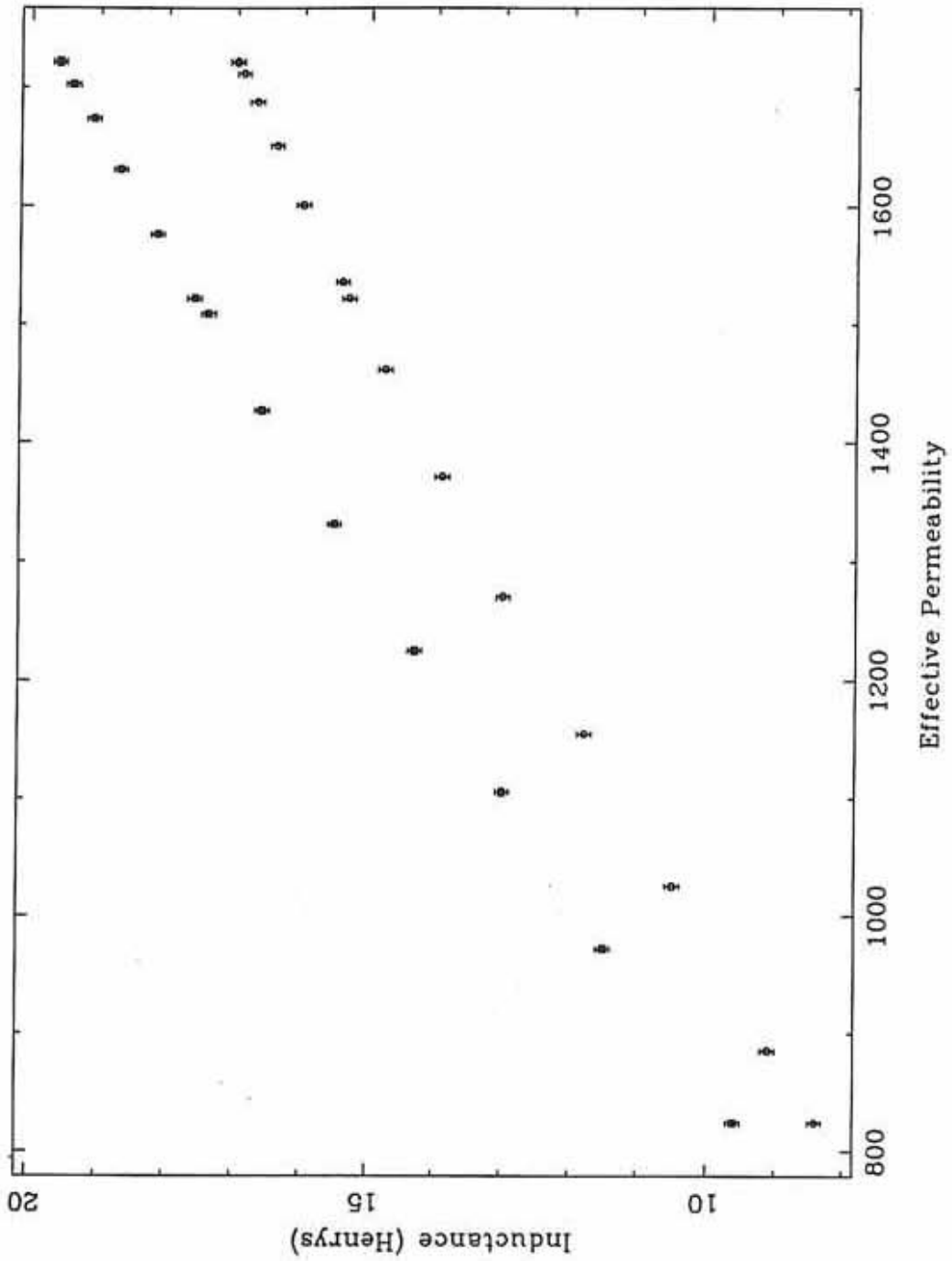
Inductance (Henrys)
20
15
10
Effective Permeability
1600
1400
1200
1000
800

Figure 12. A schematic of the Polar search coil preamplifier. The Wind search coil preamplifier is identical except for resistors R2 and R26, which have a value of 1 M ohm.

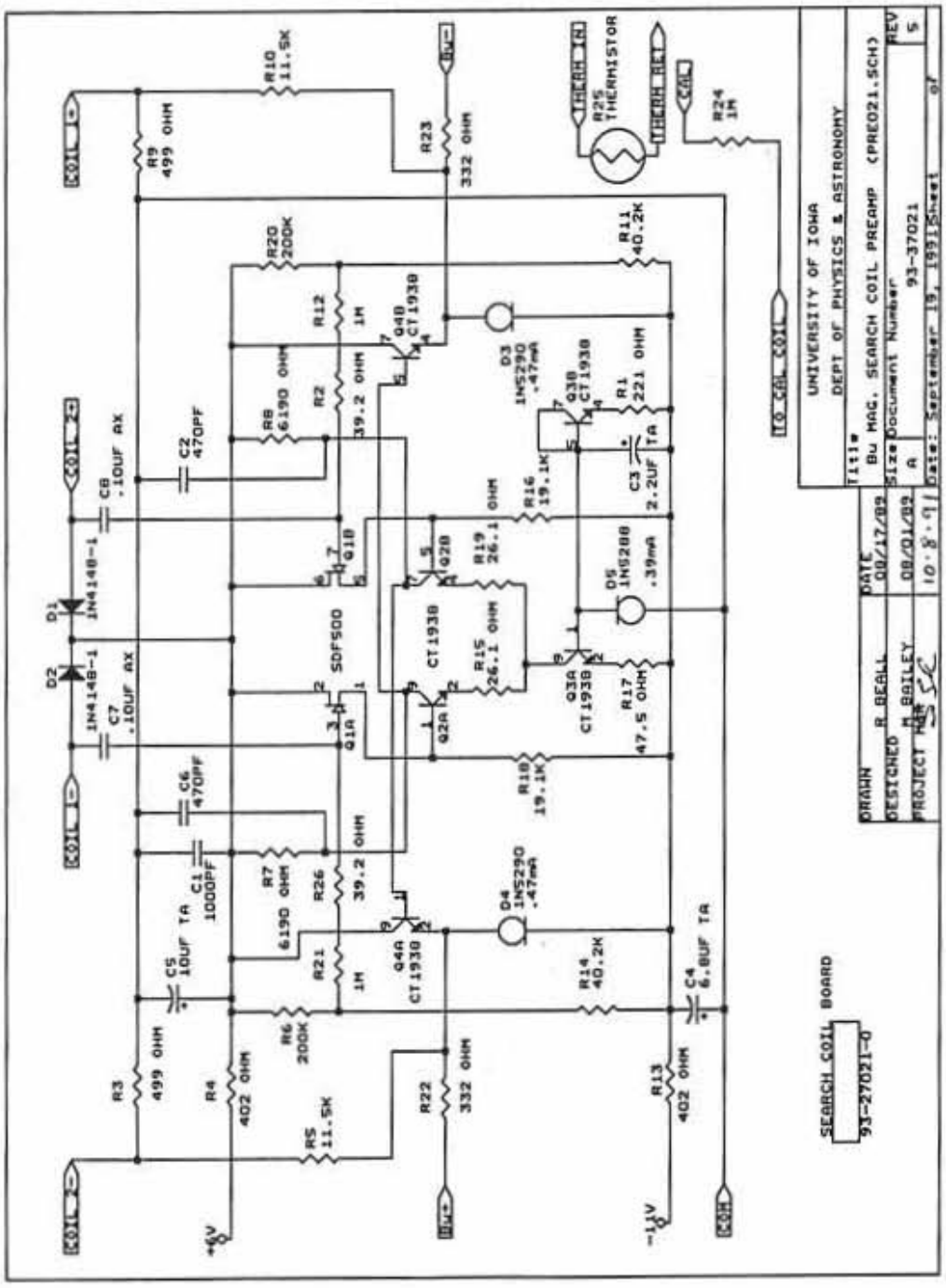
UNIVERSITY OF IOWA
DEPT OF PHYSICS & ASTRONOMY
Title: BW MAG. SEARCH COIL PREAMP (PRE021.SCH)
Size: A
Document Number: 93-37021
REV: S
Date: September 19, 1991 Sheet of
DRAWN R BEALL 08/17/93
DESIGNED M BAILEY 08/01/92
PROJECT MGR
SEARCH COIL BOARD
93-37021-0
TO CAL COIL
THERM IN
THERM RET
CAL
R25 THERMISTOR
R24 1M
R23 332 OHM
R10 11.5K
R9 499 OHM
R20 200K
R11 40.2K
R12 1M
R8 6190 OHM
R2 39.2 OHM
Q4B CT1938
D3 IN5290 .47mA
Q3B CT1938
R1 221 OHM
C2 470PF
C8 .10UF AX
C3 2.2UF TA
R16 19.1K
Q1B
Q2B
R19 26.1 OHM
D5 IN5288 .39mA
D1 IN4148-1
D2 IN4148-1
C7 .10UF AX
SDF500
CT1938
R15 26.1 OHM
Q3A CT1938
R17 47.5 OHM
Q1A
Q2A
C6 470PF
R18 19.1K
C1 1000PF
R7 6190 OHM
R26 39.2 OHM
D4 IN5290 .47mA
C5 10UF TA
R21 1M
Q4A CT1938
R14 40.2K
C4 6.8UF TA
R6 200K
R3 499 OHM
R4 402 OHM
R5 11.5K
R22 332 OHM
R13 402 OHM
+6V
-11V
COM

Figure 13. A block diagram of the Polar and Wind search coil preamplifier.

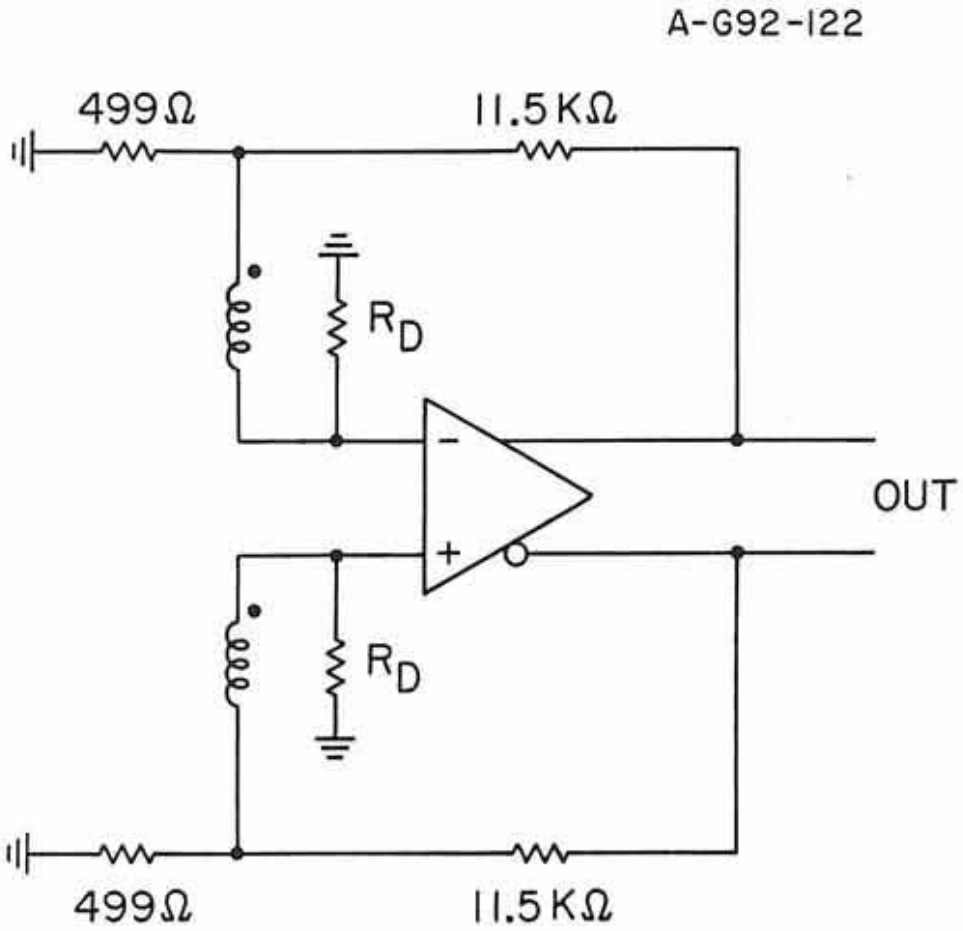
A-G92-122
499Ω
11.5KΩ
R_D
OUT
R_D
499Ω
11.5KΩ

Figure 14. A block diagram of the Polar and Wind search coil preamplifier when a differential signal is applied at the inputs.

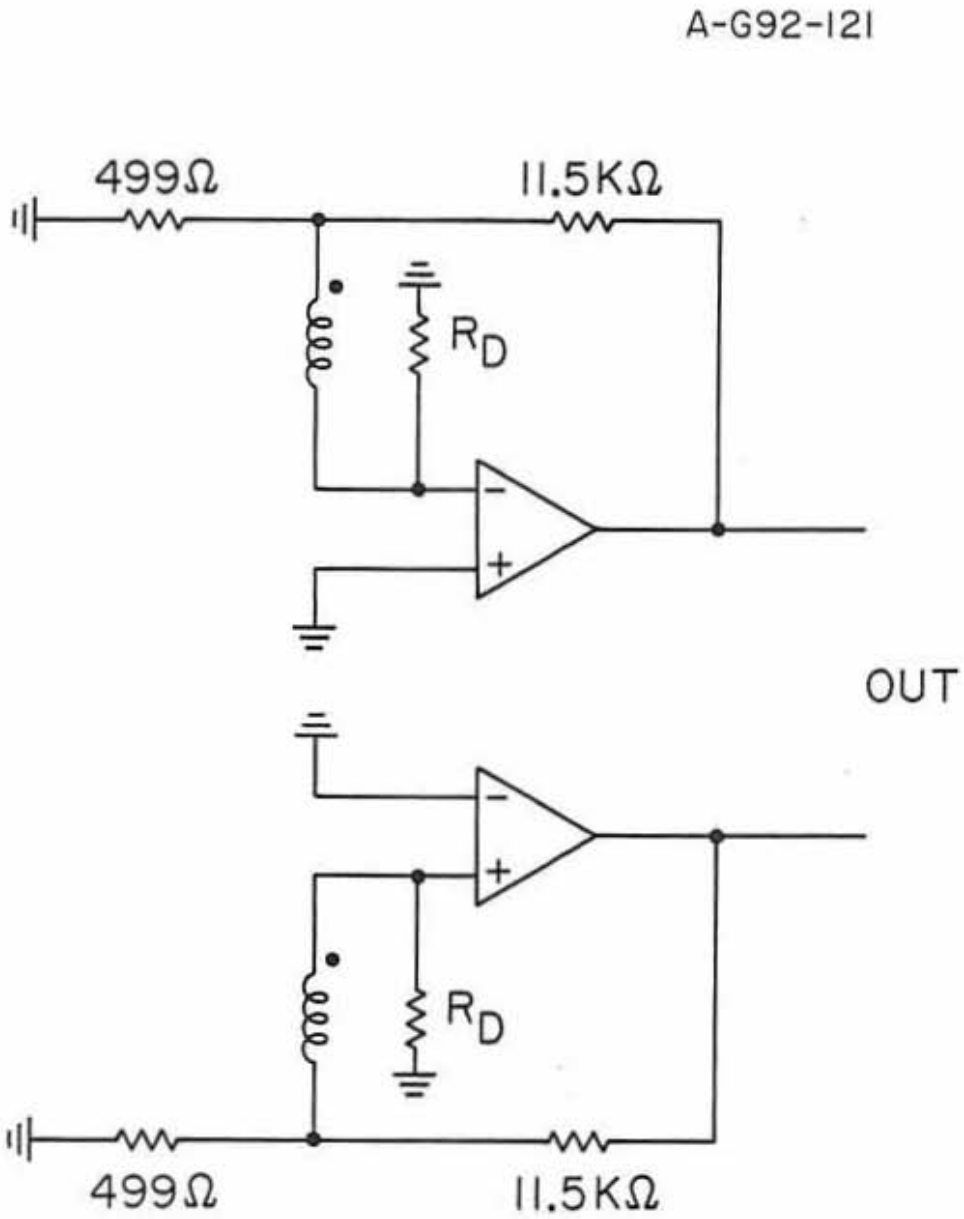
A-G92-121
499Ω
11.5KΩ
R_D
OUT
R_D
499Ω
11.5KΩ

Figure 15. The transfer function of the Polar prototype model search coil (circles) compared to the theoretical prediction (solid line) from Equation 7.

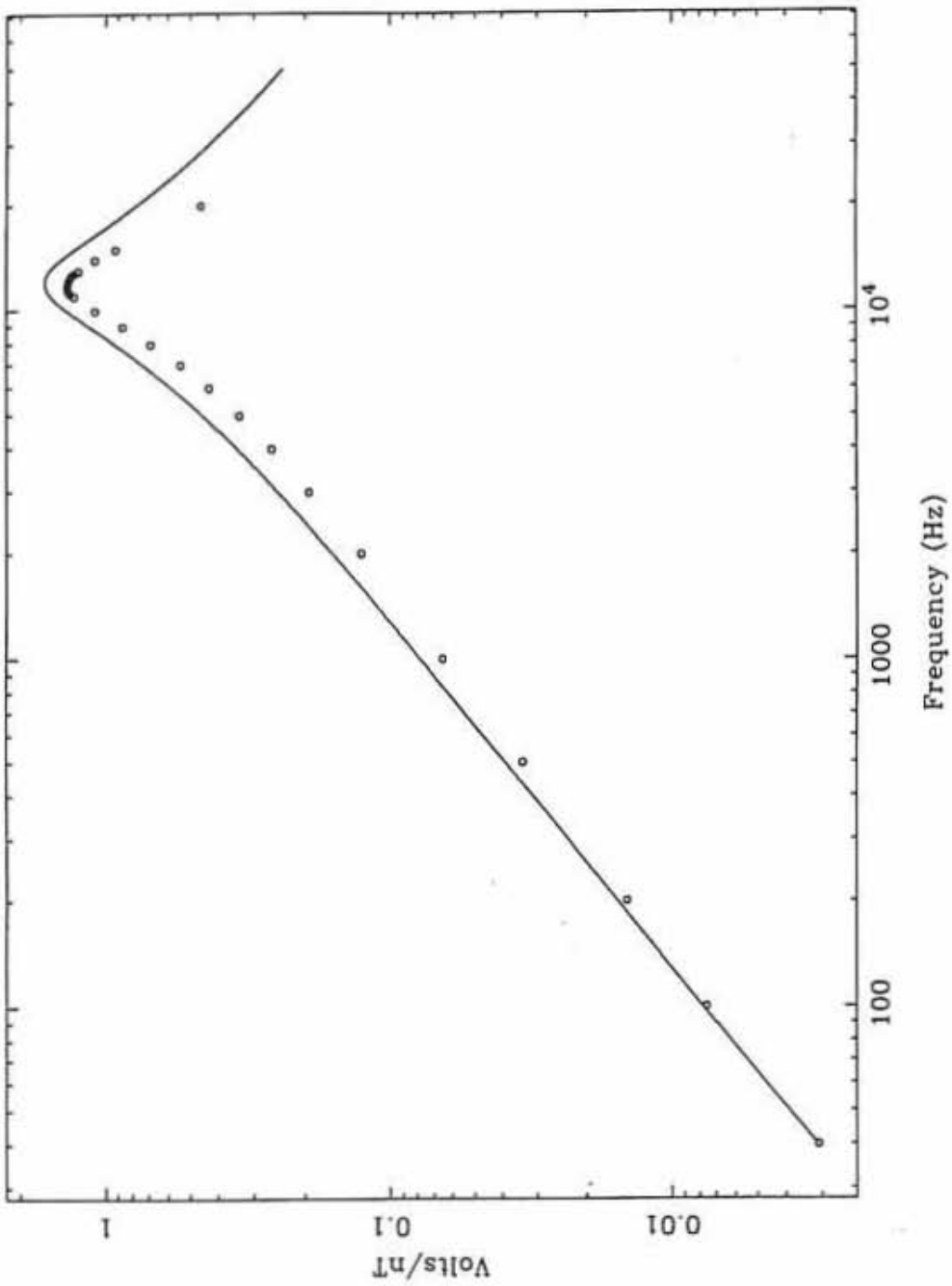
Volts/nT
0.01
0.1
1
Frequency (Hz)
100
1000
10^4

Figure 16. A comparison of the Polar prototype model search coil noise leve (squares) with the ISEE 1 and 2 search coil noise levels (solid lines).

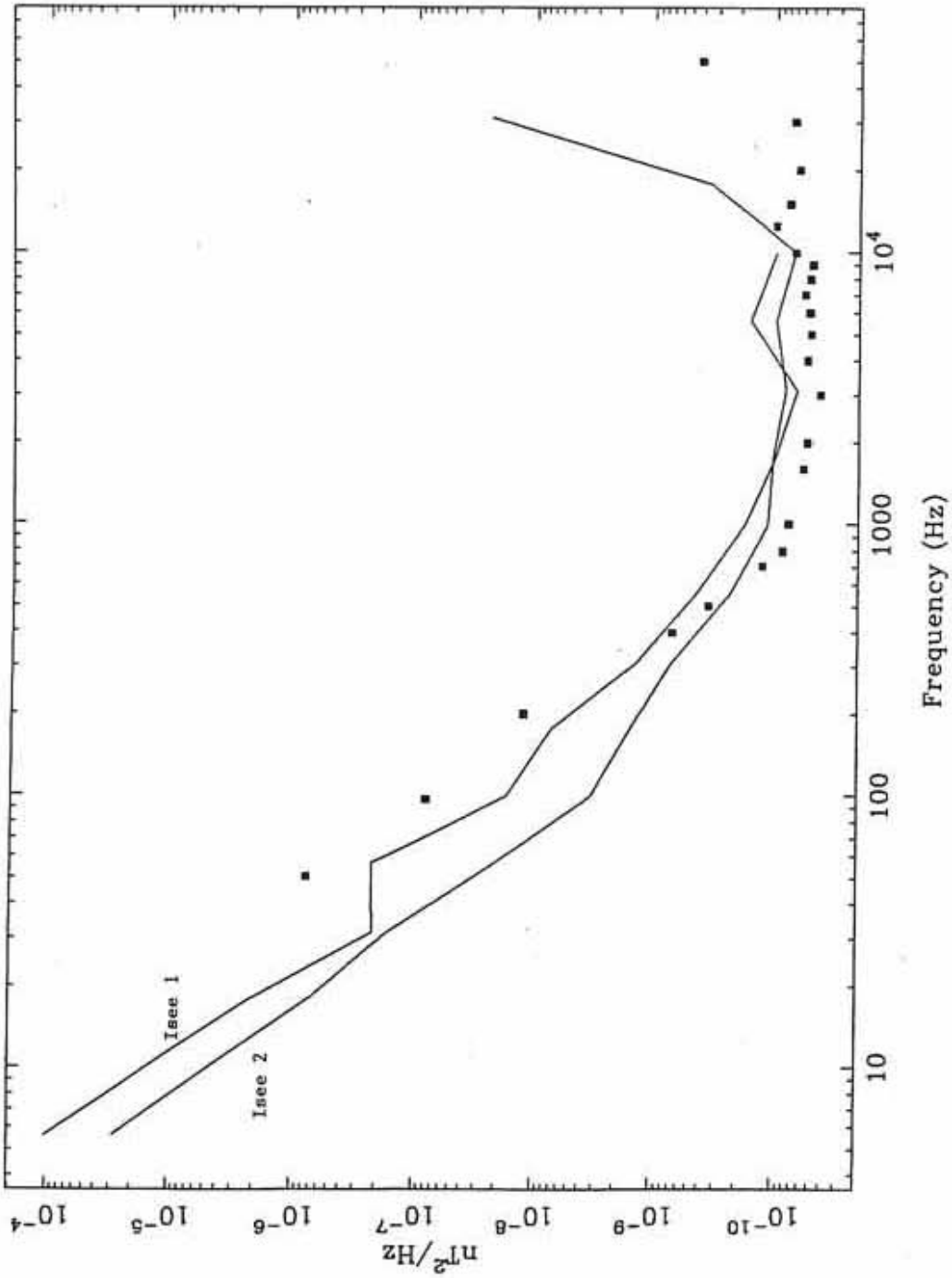
Isee 1
Isee 2
nT²/Hz
10⁻⁴
10⁻⁵
10⁻⁶
10⁻⁷
10⁻⁸
10⁻⁹
10⁻¹⁰
10
100
1000
10⁴
Frequency (Hz)

Figure 17. The transfer function of the Wind spare search coil (circles) compared tc the theoretical prediction (solid line) from Equation 7.

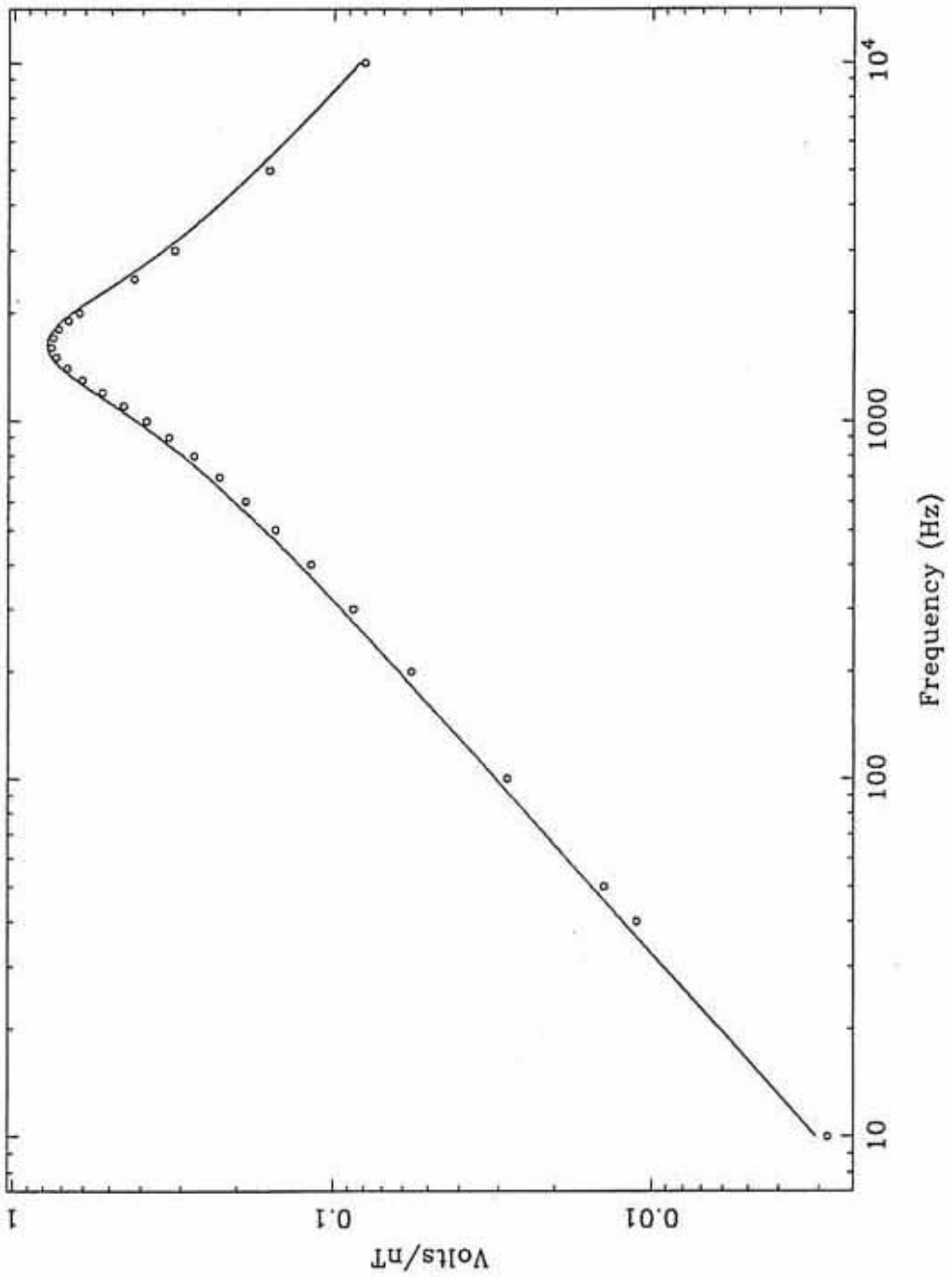
Volts/nT
0.01
0.1
1
10
100
1000
10^4
Frequency (Hz)

Figure 18. A comparison of the Wind spare search coil noise level (squares) with the ISEE 3 search coil noise levels (solid line).

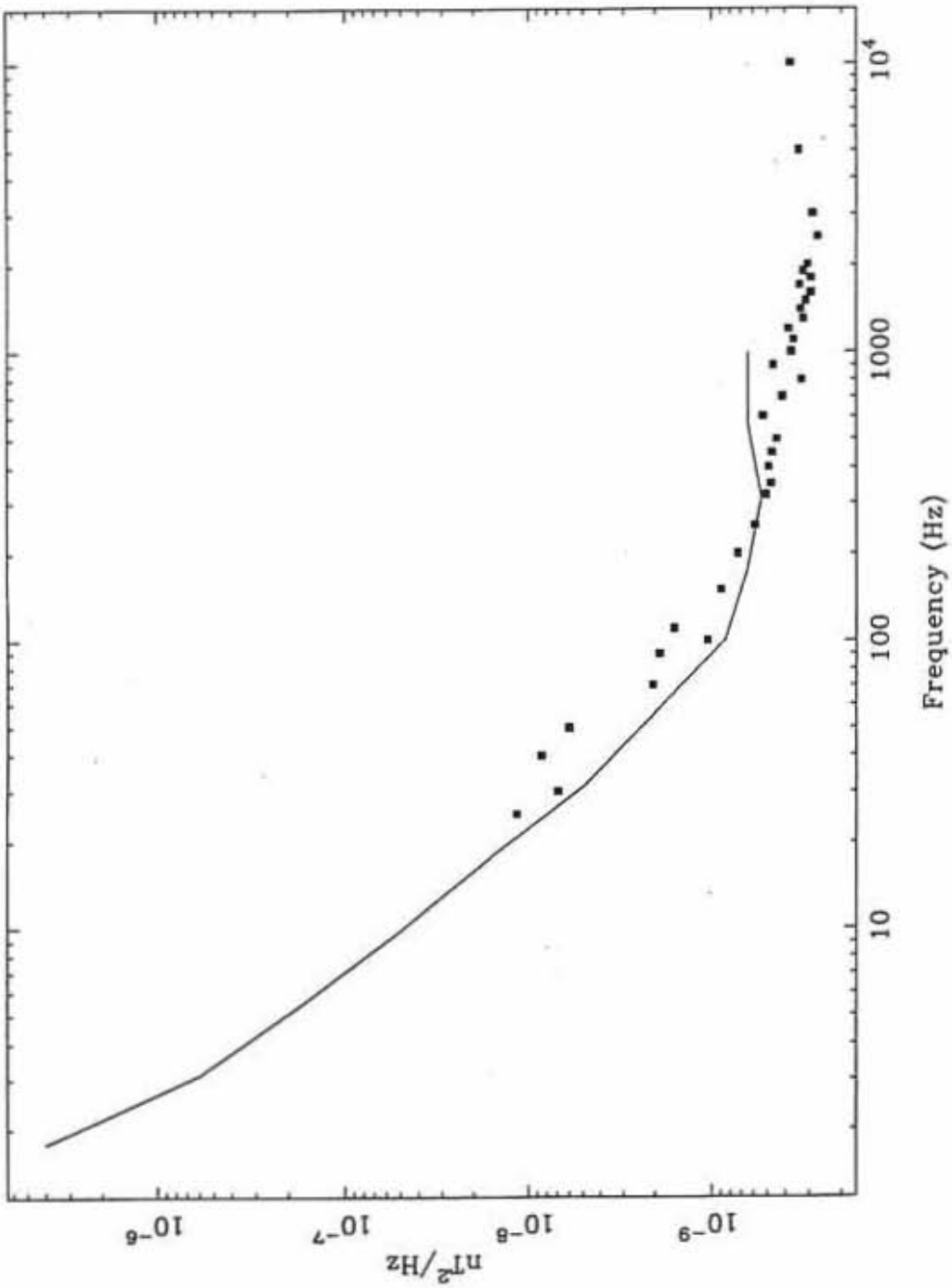
Frequency (Hz)
10
100
1000
10^4
10^{-9}
10^{-8}
10^{-7}
10^{-6}
nT^2/Hz

Figure 19. A photograph of the Wind B_z search coil magnetometer.

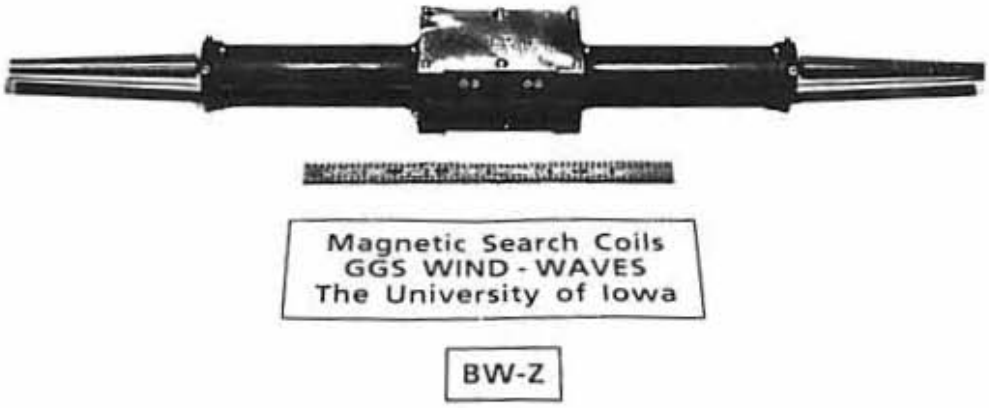
Magnetic Search Coils
GGS WIND - WAVES
The University of Iowa
BW-Z

Figure 20. A sketch of a typical setup of the transmitting loop calibration method.

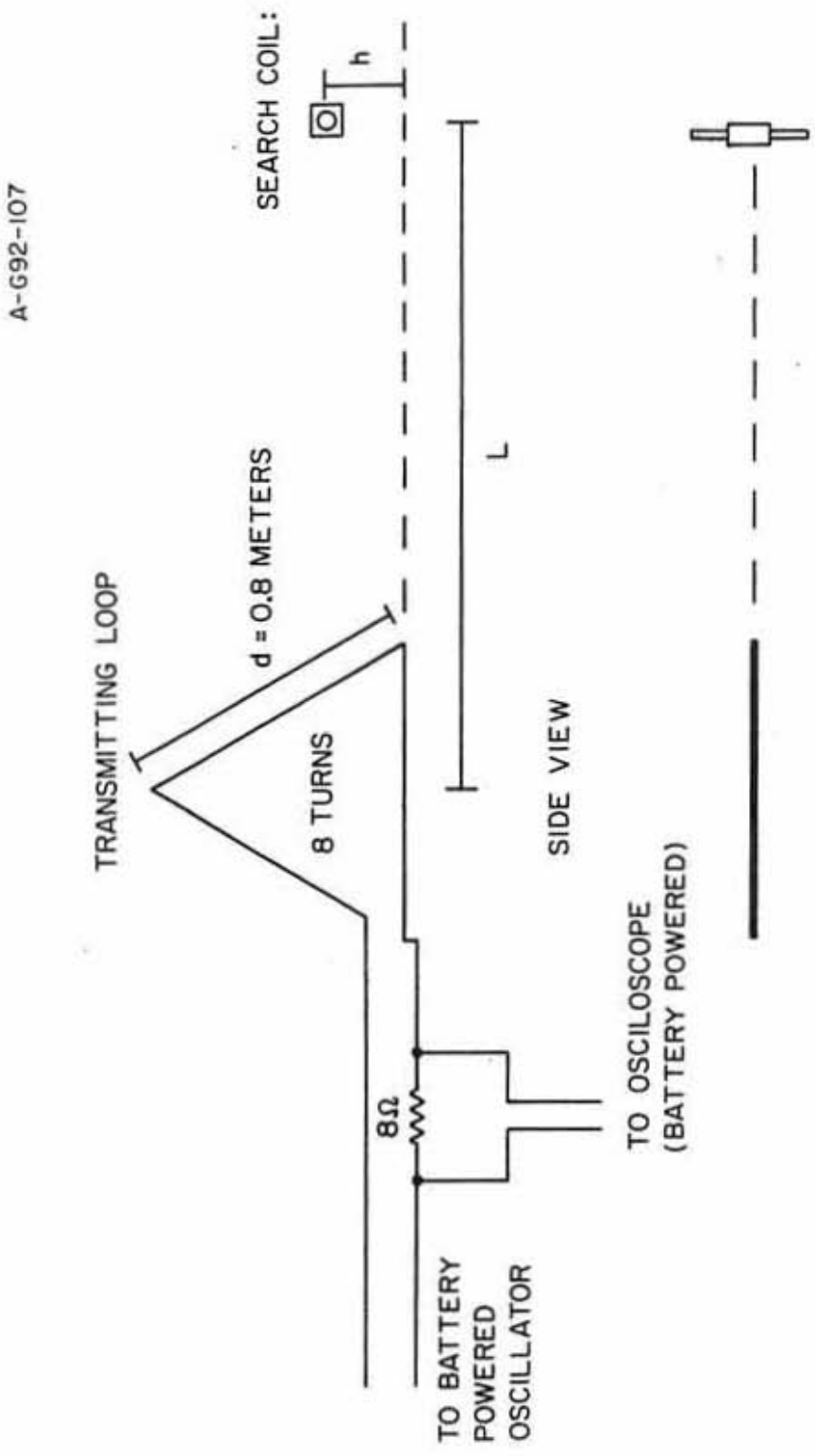
A-G92-107
SEARCH COIL:
h
TRANSMITTING LOOP
d = 0.8 METERS
8 TURNS
L
SIDE VIEW
TOP VIEW
8Ω
TO BATTERY POWERED OSCILLATOR
TO OSCILOSCOPE (BATTERY POWERED)

Figure 21. A comparison of the coil constant determined by the transmitting loop method in the lab at L = 5 feet (squares) and L = 8 feet (circles). The difference of the curves is probably due to the steel beams in the floor and ceiling distorting the calibration signal.

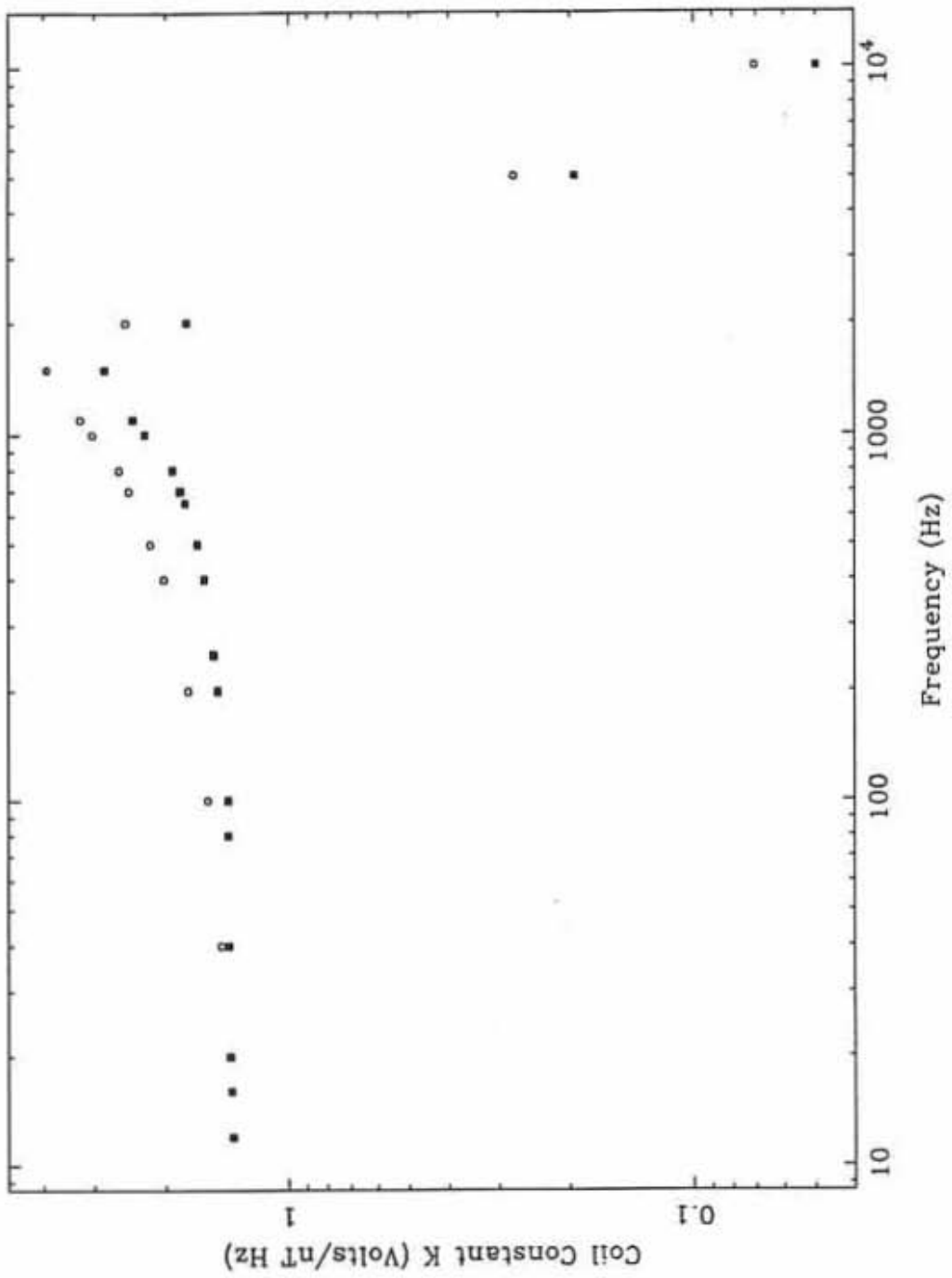
Coil Constant K (Volts/nT Hz)
0.1
1
10
100
1000
10^4
Frequency (Hz)

Figure 22. The equivalent circuit of the solenoid used to calibrate the search coi magnetometers.

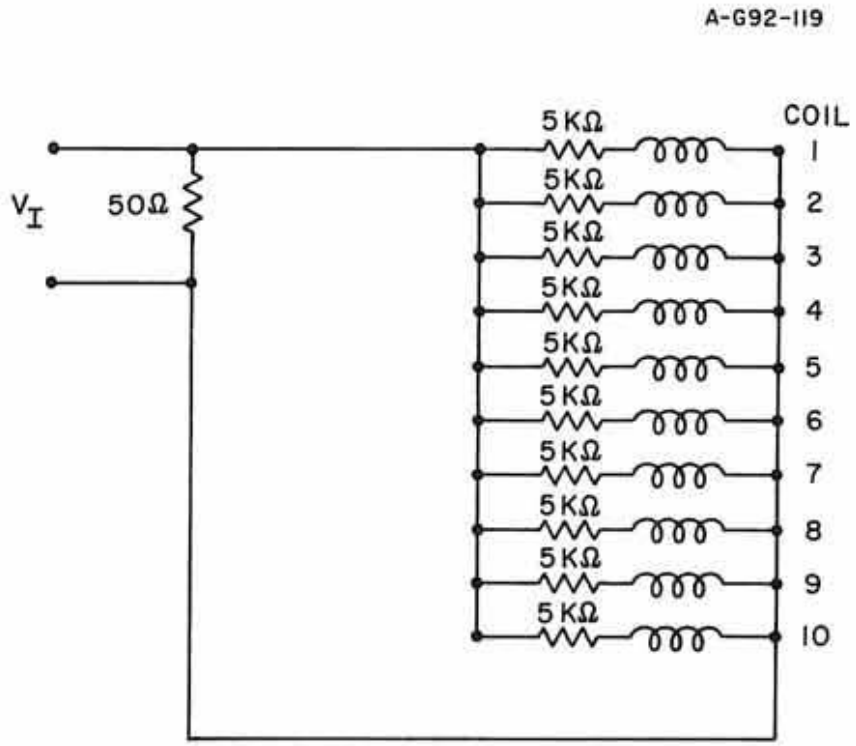
A-G92-119
V_I
50Ω
5KΩ
COIL
1
2
3
4
5
6
7
8
9
10

Figure 23. A comparison of the transfer function of the Wind spare search coil magnetometer determined by the solenoid in the μ-metal shield and the transmitting loop method at L = 5 feet and L = 8 feet. The circles are the μ-metal shield method. The triangles are the transmitting loop method at L = 5 feet, and the squares are L = 8 feet.

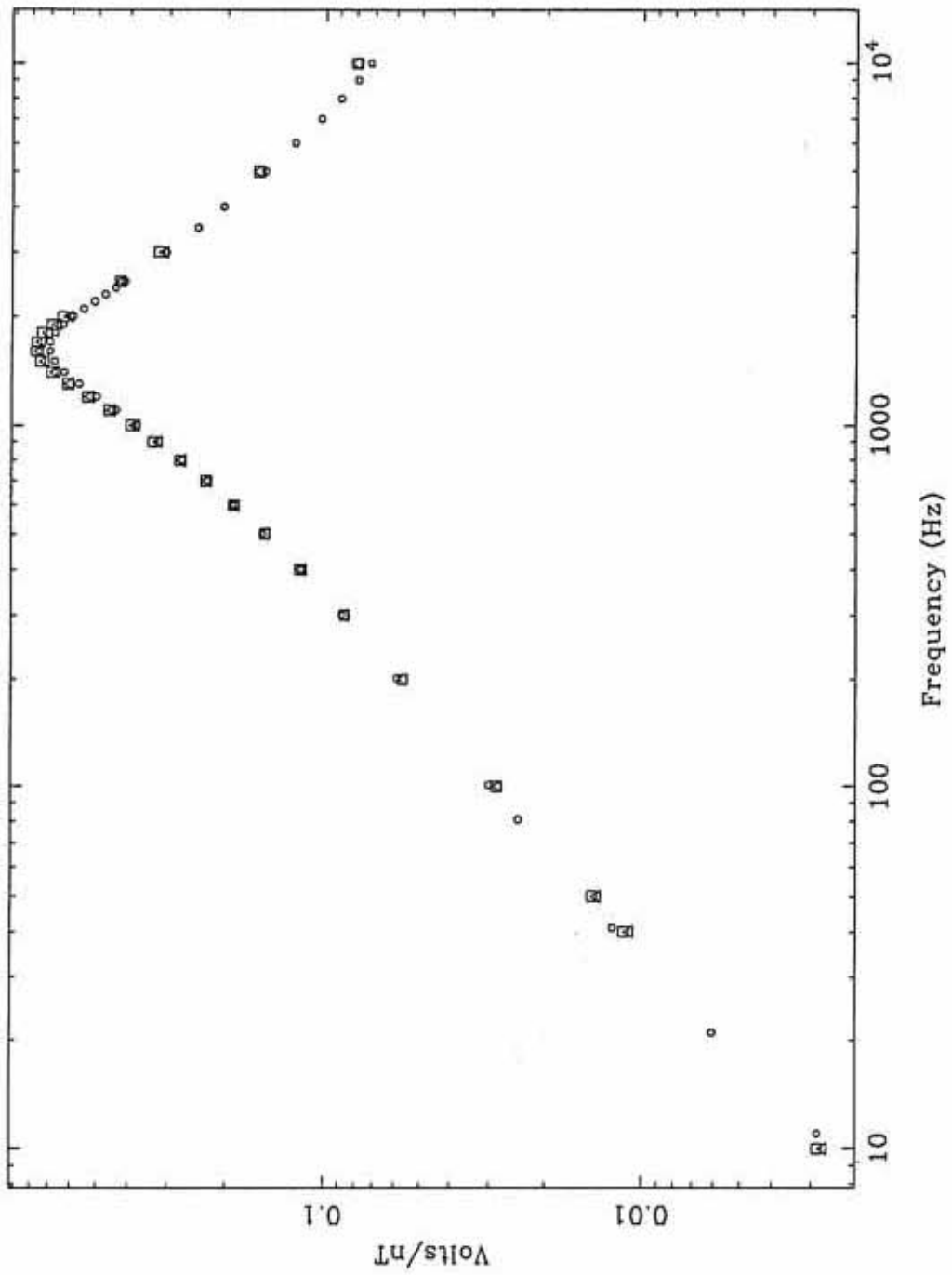
Volts/nT
0.01
0.1
10
100
1000
10^4
Frequency (Hz)

Figure 24. A sketch of the setup for the noise voltage calibration. The search coil magnetometer is placed in a μ-metal shield and powered by batteries. The noise voltage is measured by a spectrum analyzer.

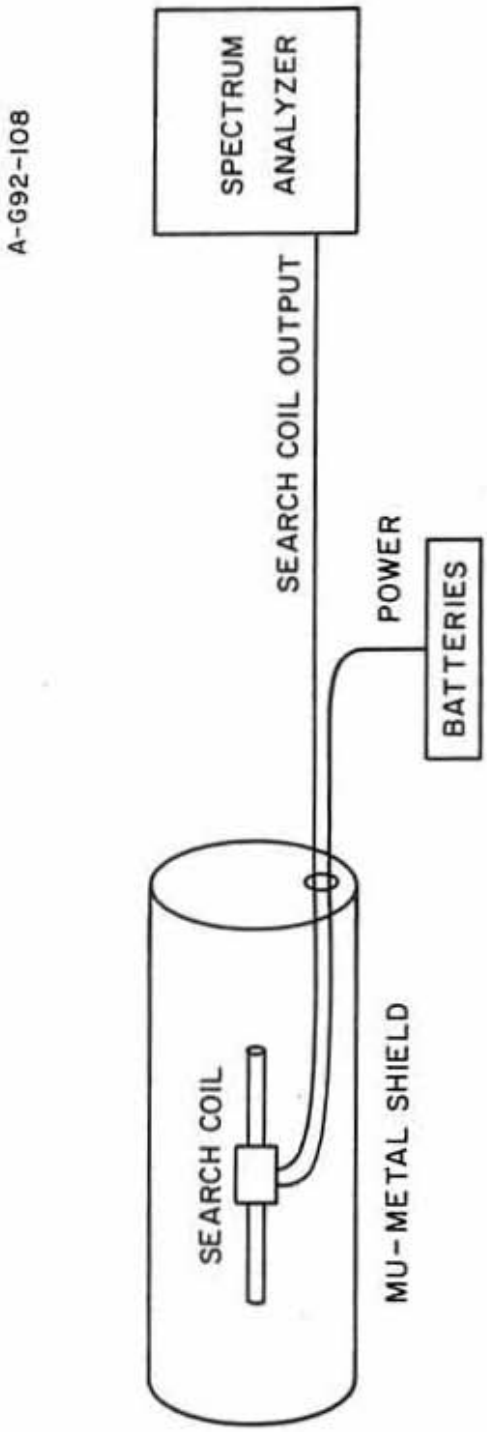
A-G92-108
SPECTRUM ANALYZER
SEARCH COIL OUTPUT
POWER
BATTERIES
SEARCH COIL
MU-METAL SHIELD

Figure 25. A comparison of the Wind search coil noise level determined in the lab (circles) and at a low noise field site (squares).

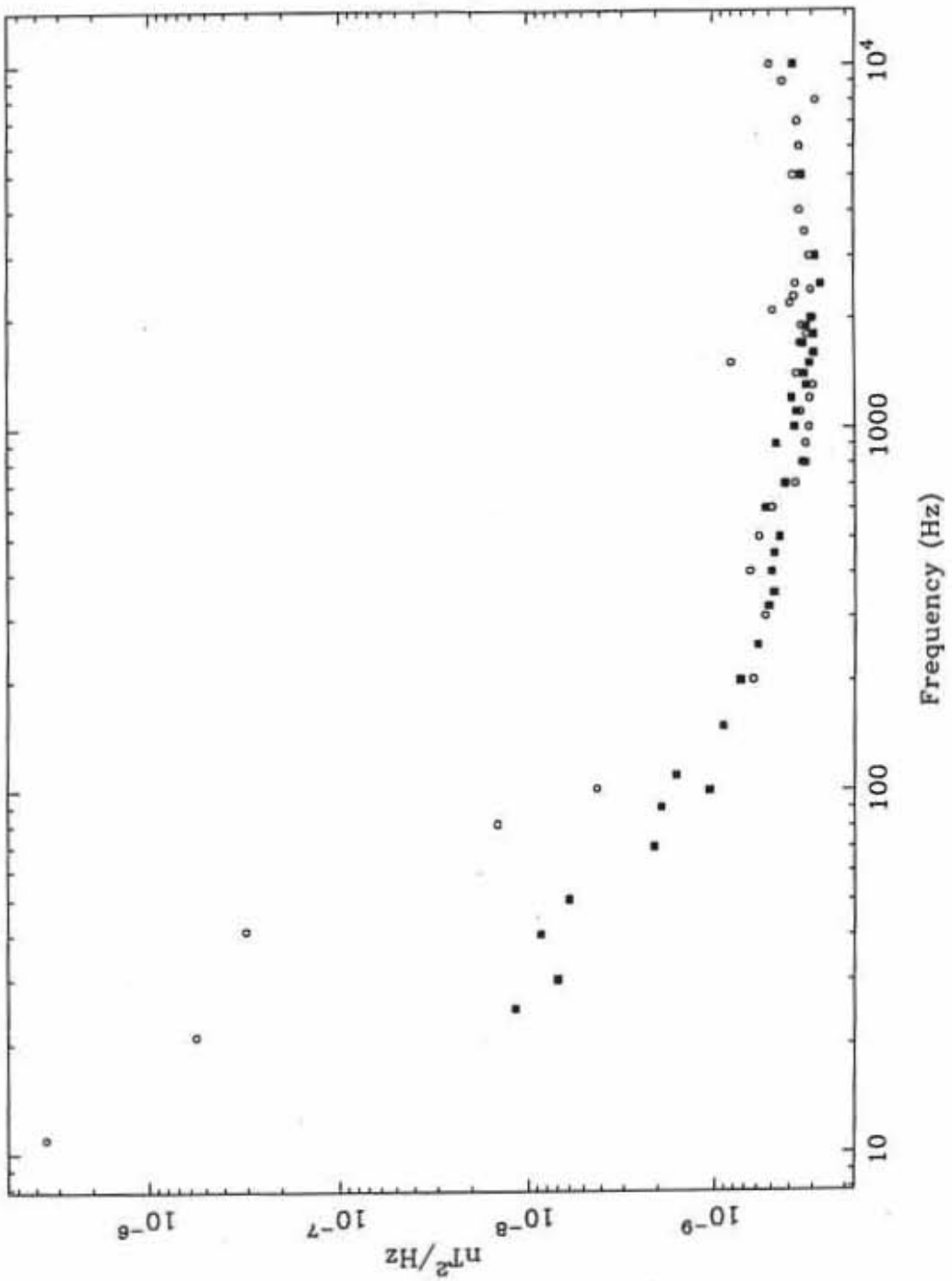
Frequency (Hz)
10
100
1000
10^4
nT^2/Hz
10^{-9}
10^{-8}
10^{-7}
10^{-6}

17 *Wind* 3DP LZ Software

This section will discuss the *Wind* 3DP LZ software libraries [*Wilson III*, 2021] written and maintained by the project scientist, Lynn B. Wilson III. The software began as a 3DP-specific code, based upon the original University of California Berkeley SSL code written mostly by Davin Larson. The software now includes general routines that can be (and have been) used on other missions such as THEMIS, MMS, STEREO, *Venus Express*, *Galileo*, and *Parker Solar Probe*. The library provides detailed crib sheets and example usages from crib sheets actually used in several publications by the project scientist. The software can be used as a standalone library or in conjunction with the SPEDAS libraries [*Angelopoulos et al.*, 2019]. Below we describe some of the basic information necessary to get started and provide some examples and details necessary to understand the code. For brevity, I will refer to this software library as the ***UMN Modified* Wind*/3DP*** IDL library or package or code.

17.1 Getting Started: IDL Initialization

Note that the following is specific to Unix-based machines and will not provide details for equivalents for Windows-based machines[39]. The first thing that needs to be done is to initialize the paths for the Interactive Data Language (IDL) software. If your machine still uses a bash shell script then the following should be placed in your .bash_profile or .bashrc:

```
########## IDL setup #############
##  Let IDL's bash script define default IDL paths
source /Applications/harris/idl/bin/idl_setup.bash
##  Add current working directory path and any subdirectory paths
##    onto IDL's default paths
unset IDL_PATH
if [ ${IDL_DIR:-0} != 0 ] ; then
  export IDL_PATH ; IDL_PATH=$IDL_DIR
  ##  Make sure to recursively search subdirectories
  IDL_PATH=${IDL_PATH}:$(find $IDL_DIR -type d | tr '\n' ':' | sed 's/:$//')
  ##  Add my directories
  IDL_PATH=$IDL_PATH:+.:+$HOME/Desktop/idllibs
else
  export IDL_PATH ; IDL_PATH=:+.:+/Applications/harris/idl/lib:+$HOME/Desktop/idllibs
fi
```

The following is an example of how to use a bash script to initialize IDL specific to the SPEDAS software:

```
################################################################################
# Set up SPEDAS, THEMIS
function spedas {
   # We have to unset the IDL_PATH to avoid TPLOT conflicts... kludgy.
   # If you have personal IDL routines that you normally include (as long as
   # they don't include any TPLOT routines!), you may add them to the IDL_PATH
   # after we clobber it below.
   unset IDL_PATH
   #  Define the SPEDAS path
   export SPEDAS_LBW=$HOME/Desktop/Old_or_External_IDL/SPEDAS/spedas_1_00
   #  Define the ITT IDL path
   IDL_LOC='/Applications/harris/idl/'
   source ${IDL_LOC}/bin/idl_setup.bash
```

[39] Because I, Lynn B. Wilson III, do not know how to adapt this to a Windows-based machine. Further, **there are currently no shared object libraries – pre-compiled executables necessary to read the 3DP lz files – for a Windows OS.**

```
   source $SPEDAS_LBW/idl/projects/themis/setup_themis_bash
   idl
   ##  Reset bash on exit
   source $HOME/.bash_profile
}
```

Similarly, if the user wishes to use a bash function to initiate the ***UMN Modified* Wind/*3DP*** code, then they would put the following in their .bash_profile:

```
################################################################################
# Set up Wind/3DP
function uidl64 {
   # We have to unset the IDL_PATH to avoid TPLOT conflicts... kludgy.
   # If you have personal IDL routines that you normally include (as long as
   # they don't include any TPLOT routines!), you may add them to the IDL_PATH
   # after we clobber it below.
   unset IDL_PATH
   source $HOME/.bashrc
   source $HOME/Desktop/swidl-0.1/wind_3dp_pros/umn3dp_start_64
   source $HOME/.bashrc
}
```

If you use a Mac with OS X 10.15 or later, then you may have migrated to zshell (or zsh). In which case you would want to put the same path-setting **IF...THEN...ELSE** bash statement seen above in your .zshenv file. The initialization of the SPEDAS software will change slightly to the following and should be placed in your .zshrc:

```
################################################################################
# Set up SPEDAS, THEMIS
function spedas {
   # We have to unset the IDL_PATH to avoid TPLOT conflicts... kludgy.
   # If you have personal IDL routines that you normally include (as long as
   # they don't include any TPLOT routines!), you may add them to the IDL_PATH
   # after we clobber it below.
   unset IDL_PATH
   source ${SIDL_LOC}/bin/idl_setup.bash
   emulate -L sh
   source $SPEDAS_LBW/idl/projects/themis/setup_themis_bash
   idl
   source $HOME/.zshrc
}
```

The initialization function for the ***UMN Modified* Wind/*3DP*** code would also go in the .zshrc file but instead of sourcing the *umn3dp_start_64* bash script, you would source the *umn3dp_start_64_z* zsh script (both are included with the ***UMN Modified* Wind/*3DP*** code).
Note that all file path declarations shown above (and herein) should be changed accordingly on each user's machine as they are likely different than my own. These are only shown as figurative examples.

17.2 Getting Started: IDL Paths

The ***UMN Modified* Wind/*3DP*** code can be downloaded from:
https://github.com/lynnbwilsoniii/wind_3dp_pros.
The main folder/directory will have the name **wind_3dp_pros** and this should not be changed. Place the folder with all the subfolders/subdirectories in a desired location[40], e.g., the directory from which you will run IDL. Some details and notes on how to get started can also be found at:
https://github.com/lynnbwilsoniii/wind_3dp_pros/wiki/Software-Documentation.
The 3DP lz files should all be located in the following directories:
~/wind_3dp_pros/wind_data_dir/data1/wind/3dp/lz/????
where **????** is the four digit year. In this same directory, one needs a look up file called **wi_lz_3dp_files** which contains the locations of all the level zero files. This should be included with the software download (if one downloads the whole package). Each 3DP lz file will have a version number, most of which are **v01**, however the number can vary up to **v08**. The file included with the download should have the correct version number associated with each date up through the end of 2019. If the version number differs from that in the **wi_lz_3dp_files** file, the software will not load the data and the user need only change the text in the **wi_lz_3dp_files** file to match the file version number. The format for each file name in the **wi_lz_3dp_files** file should be, using April 1, 1995, as an example:

1995-04-01/00:00:00 1995-04-02/00:00:00 /data1/wind/3dp/lz/1995/wi_lz_3dp_19950401_v01.dat.

So long as the IDL paths are initialized properly using either one of the bash/zsh functions shown above or directly sourcing the ***setup_wind3dp_bash*** file prior to starting IDL or entering the following on the command line immediately after starting IDL[41]:

```
IDL> @./wind_3dp_pros/start_umn_3dp.pro
```

To check if the IDL paths are correctly set, try compiling a routine. For instance, typing the following should generate no errors if the above is done correctly:

```
UMN> .compile get_3dp_structs.pro
```

If errors occur, or the routine cannot be found, then you did not start IDL from the same directory where **~/wind_3dp_pros** is located or there is an issue with your IDL paths. Make sure you followed these instructions and try again. Note that ***start_umn_3dp.pro*** has been modified numerous times to attempt to account for all possible variations in the IDL path identification based upon IDL version back to pre-5.0. It is not perfect, but it will work for most cases and should provide the user with a simple way to avoid setting the paths manually.

[40] If you intend to use SPEDAS, place the **wind_3dp_pros** in a location separate from the SPEDAS IDL folder.
[41] Note that in IDL, the period immediately after the symbol implies "current working directory." That is, it will prepend the file path to the current location from which you started IDL in the terminal (or the starting directory defined by the user in the IDL GUI). So before starting IDL, if the user types **ls -l** into the command line and does not see **wind_3dp_pros** listed as a directory, then the following call to ***start_umn_3dp.pro*** will not work.

17.3 Getting Started: Data

The first thing the user will want to do is grab some 3DP lz files. The user can accomplish this by calling the ***get_http_3dp_lz_files.pro*** routine. Read the **man page**[42] for usage examples and syntax. If called correctly, the routine will grab files from the 3DP website and put them on your machine int he proper directory at:

~/wind_3dp_pros/wind_data_dir/data1/wind/3dp/lz/????

The next required data product is the fluxgate magnetometer (MFI) [*Lepping et al.*, 1995] data, which can be taken the SPDF CDAWeb webpages[43]. Unfortunately, I have not had time to write a routine that will do this for the user. If on a Unix- or Linux-based machine, however, the user can use the built-in **curl** function. As an example, one can grab all the WAVES TNR [*Bougeret et al.*, 1995] for 2019 using the following command:

```
curl --ftp-ssl -k ftp://spdf.gsfc.nasa.gov/pub/data/wind/waves/tnr_ascii_compressed/2019/
wind_waves_tnra_201901{day}.tnr.Z --output "$HOME/Desktop/temp/201901#1.tnr.Z"
```

This will output the files to a temporary folder called **temp** on the users **Desktop** (it will NOT create this folder, so make sure it exists prior to calling). The user need only change **waves/tnr_ascii_compressed/...** to **mfi/mfi_h0/...** to get the H0 MFI data files. One can also use the **wget** function, part of the *Homebrew* Unix/Linux distribution. An example would be as follows:

```
wget --no-verbose --no-parent --recursive --level=1 --no-directories -e robots=off -A
"wi_lz_3dp_200301*.dat"  http://sprg.ssl.berkeley.edu/wind3dp/data/wi/3dp/lz/2003/
```

This will grab all *Wind* 3DP lz files for March 2003 and store them in the current working directory (i.e., the location returned when you enter **pwd** into Unix on the command line). The user can either manually transfer them to the proper directory described above for the *Wind* 3DP lz files. The final location of the MFI files must be:
~/wind_3dp_pros/wind_data_dir/MFI_CDF/.
If the user wishes to grab the high resolution MFI data as well, then change **mfi/mfi_h0/...** to **mfi/mfi_h2/...** and the final file location to:
~/wind_3dp_pros/wind_data_dir/HTR_MFI_CDF/.
Wind orbit information can be obtained from the following website:
https://sscweb.gsfc.nasa.gov/cgi-bin/sscweb/Locator.cgi.

The data should be placed in the following directory:
~/wind_3dp_pros/wind_data_dir/Wind_Orbit_Data/

which is already defined in the software download. The format used by the routine **read_wind_orbit.pro** is obtained through the following steps:

1. Select the *Wind* spacecraft from the list
2. Enter a start and end time [*e.g.* Start Time: 1996/01/01 00:00:00, End Time: 1996/01/02

[42](man page ≡ Manual Page) I'll refer to these periodically throughout this tutorial. It's a header in each program that documents the code and explains to the user how to use the code and other miscellaneous things.
[43]e.g., https://cdaweb.gsfc.nasa.gov/pub/

00:00:00] and make sure it encompasses only one day, nothing less and nothing more.
3. Click on **Output Options** button
4. Select the following: XYZ-GSE, XYZ-GSM, LAT/LON-GSE, LAT/LON-GSM, Dipole L Value (under **Additional Options**), and Dipole Inv Lat (under **Additional Options**)
5. Click on **Output Units/Formatting** button
6. Select the following: yy/mm/dd (under **Date**), hh:mm:ss (under **Time**), and km-Kilometers with 3 decimal places (under **Distance**)
7. Click on **Submit query and wait for output** button .

The header of the file should have 14 lines of information before any lines of data. If this basic format is kept, then the routine **read_wind_orbit.pro** will be able to read these ASCII files given either a date of interest or a time range (which may encompass several dates). The typical header file format can be found in one of the example files provided in the distribution.

17.4 Getting Started: TPLOT

Much of the ***UMN Modified* Wind/*3DP*** library is based upon some software written largely by Davin Larson and others at Berkeley SSL called TPLOT. TPLOT is a conglomeration of routines that were an attempt to make plotting and changing plots faster in IDL. However, let's start with some basic information/background about TPLOT.

To load data into TPLOT, one creates a generalized data structure with the following tags:

- **X** : (Required) {N}-Element array [double] of time stamps in units of Unix time[44] to act as the independent variable. Note that the time stamps need not be Unix times per se, but the software will assume any double-precision numbers in this tag to be so.
- **Y** : (Required) {N[,E,A]}-Element array [float or double] of dependent variable data, where each N_j in **Y** corresponds to each N_j in **X**. For vectors (e.g., magnetic fields), then $E = 3$, $A = 0$.
- **V** : (Optional) {[N,]E}-Element array [float or double] of a second dependent variable. If included, then the values in **Y** will often be shown using a color-scale and the data in **V** will be on the vertical plot axis (e.g., wavelet transform data, where each element of **V** corresponds to a frequency).
- **SPEC** : (Optional) Scalar [numeric] defining whether the data should be shown as a stacked line plot [Default = FALSE] or a spectrogram [= TRUE].
- In the most complicated form, there are two additional tags but when these are defined, then **V** is not. This almost always corresponds to data that contains both energy and pitch-angle bins. Note that if **V1** and **V2** are set, then **Y** must be a three-dimensinal array with the correct {N,E,A} number of elements. So in the case of particle spectra, we have:
  - **V1** : (Optional) {N,E}-Element array [float or double] of energy bin values
  - **V2** : (Optional) {N,A}-Element array [float or double] of pitch-angle bin values

Once this structure is created, say in the following way:

```
UMN> struc = {X:unix,Y:data,V:freqs}
```

then the user can send this data to TPLOT using the following:

```
UMN> store_data,'TPLOT_Handle_1',DATA=struc
```

where 'TPLOT_Handle_1' is a unique string that will identify the data stored in the *struc* structure. Once in TPLOT, the user can refer to this data either by its string handle or an integer number defined by the order in which the data was loaded into TPLOT relative to other data. The user can then plot the data, add options to the format of the output plots, manipulate the data, etc. all from the command line. Before moving on, assume we sent in two other sets of data and called them 'TPLOT_Handle_2' and 'TPLOT_Handle_3'.

To see whether data was loaded into TPLOT, type the following:

```
UMN> tplot_names
```

where you should at least see the following output:

```
   1 TPLOT_Handle_1
```

[44] seconds elapsed since 00:00:00 UTC on January 1, 1970

```
2 TPLOT_Handle_2
3 TPLOT_Handle_3
```

Note that the string you choose (hopefully not 'TPLOT_Handle_1') can be changed and is not restricted to explicitly follow any of the names seen in this tutorial. You are free to define the names as you please. If you see names that are not exactly the same as those shown herein, do not worry. The TPLOT handle is just a unique name one uses to distinguish one set of data from another. So long as you are consistent, you are free to name things as you wish[45].

The user can alter the plotting options (e.g., line color, YRANGE, etc.) for each TPLOT handle using the ***options.pro*** routine. The syntax is as follows:

```
UMN> options,[TPLOT handle to be altered],[PLOT keyword],[value],DEFAULT=[FALSE|TRUE]
```

where *[TPLOT handle to be altered]* is the string or integer TPLOT handle of the variable for which you wish to alter plotting options, *[PLOT keyword]* is a string of nearly any keyword accepted by the IDL built-in routine ***PLOT.PRO***[46], *[value]* is the input appropriate for the associated keyword, and the *DEFAULT* setting determines whether the plotting option is a default (TRUE) or not (FALSE) option for this variable[47].

Note that the user can call ***options.pro*** in a slightly different manner given by:

```
UMN> options,[TPLOT handle to be altered],[PLOT keyword]=[value],DEFAULT=[FALSE|TRUE]
```

where *[PLOT keyword]* is no longer a string but just the characters for the appropriate keyword. For instance, the following two lines would produce identical results:

```
UMN> options,'TPLOT_Handle_1','YRANGE',[0,1],/DEFAULT
UMN> options,'TPLOT_Handle_1',YRANGE=[0,1],/DEFAULT
```

To plot data in TPLOT is very easy, just type one of the following:

```
UMN> tplot,[1]
```

or...

```
UMN> tplot,'TPLOT_Handle_1'
```

Both commands should have the same effect (assuming 'TPLOT_Handle_1' is associated with the integer 1). If you want to plot multiple things in one window, then just combine into an array as

[45] I repeat, do NOT blindly follow the commands in this tutorial. Some are meant as general references and others are just specific examples.

[46] Typical strings used include 'YTITLE', 'YLOG', 'YRANGE', 'YSTYLE', 'YMINOR', 'YTICKNAME', 'YTICKV', 'YTICKS', etc. Usually one only sets the Y-Axis labels/titles since the X-axis is defaulted to times (shown as UT times when plotted).

[47] Note that the user could have set these options when originally defining the TPLOT handle by using the keywords *DLIMITS* and/or *LIMITS*, when calling ***store_data.pro***, for default and regular plotting options, respectively. The inputs should be structures with tag names matching the keywords accepted by routines like ***PLOT.PRO***.

follows:

```
UMN> tplot,[1,2,3]
```

or...

```
UMN> tplot,['TPLOT_Handle_1','TPLOT_Handle_2','TPLOT_Handle_3']
```

The user can also pass specific time ranges to ***tplot.pro*** using the *TRANGE* keyword, which accepts a [2]-element array of Unix times corresponding to the start and end time of the time range you wish to view.
If you wish to retrieve the data from TPLOT, you need only use ***get_data.pro***. The syntax is as follows:

```
UMN> get_data,[TPLOT handle to get],DATA=struc,DLIMITS=dlim,LIMITS=lim
```

where *[TPLOT handle to get]* is the string or integer TPLOT handle of the variable to return, *struc* will be an IDL structure of similar format to the one described above when creating a TPLOT variable, and *dlim* and *lim* will be IDL structures containing default and regular plotting options, respectively, set by the user[48].

The advantage to using TPLOT is that you can add plotting options, plot the data, and then change the time range very quickly (e.g., using ***tlimit.pro***) without re-entering a great deal of commands. TPLOT has a great deal of versatility and options, which makes it both highly information dense and highly useful. The user is invited to view and try the example crib sheets located in:
~/wind_3dp_pros/wind_3dp_cribs/
or those in:
~/wind_3dp_pros/publication_crib_sheets/.
Note, however, that the user is expected to take care to alter file paths and commands accordingly for their own system. The crib sheets are meant to be examples for how to call certain routines, not verbatim examples to be used without some manipulation.

[48] If no options were set, then both *dlim* and *lim* will be equal to 0.

17.5 Loading lz Data

Assuming the user managed to source all of the environment variables correctly, have level zero (lz) data in the proper location, and have *Wind*/MFI CDF files, then one can get started.

Now that 3DP can locate the data, we can load some into IDL. The following lines will illustrate how to do this using the original (and updated) versions of the ***UMN Modified* Wind/*3DP*** code:

```
UMN> date     = '040196' ;; -> i.e., 1996-04-01
UMN> duration = 46 ;; -> 46 hours of data to load
UMN> tra      = ['1996-04-01/00:00:00','1996-04-02/22:00:00']
UMN> trange   = time_double(tra)
UMN> memsize  = 150.
UMN> load_3dp_data,'96-04-01/00:00:00',duration,QUALITY=2,MEMSIZE=150.
```

where **load_3dp_data.pro** will load both the level zero binary file data into IDL and the magnetic field data for the dates of interest into TPLOT. We still have to retrieve specific data within these lz files, but now the file information is ready to be distilled.

Now that we have loaded the data (assuming the program didn't break or didn't find any data), let's get some particle data. In the original version of the 3DP software library, this next step could be a rather arduous and painful task. Depending on whether you were curious about the ESAs or the SST data, one might end up typing tens to dozens of lines on the command prompt to get all the particle structures desired within a given time range. The software written by *Wilson III* [2021] has reduced that to only one line of code, for instance, to grab all the EESA Low data in a given time range defined by the keyword *TRANGE*:

```
UMN> dat = get_3dp_structs('el',TRANGE=trange)
```

where *dat* is a data structure with tags containing an {N,2}-element time array (Unix Times) and an array of 3DP data structures, consistent with what you would get from a FOR loop repeatedly calling **get_??.pro**[49].

The program, **get_3dp_structs.pro**, eliminates any non-valid structure (i.e., dat.VALID=0) before returning them to the user, thus all the structures should be good. The *DATA* structure tag will contain all structures in your defined time range, or all the structures available from the amount of data you originally loaded. Originally, the ***get_??.pro*** occasionally returned structures or non-structures which would result in a *Conflicting Data Structures* error in IDL when trying to concatinate structure arrays. I even managed to get around the PESA High mapcodes which cause ***get_ph.pro*** and ***get_phb.pro*** to return structures with different values for the structure tag *NBINS*, depending on the data mode. Regardless, now we have data, so let's see what we can do with it.

To start with, let's add the magnetic field to our data structures. This will allow us to create pitch-angle distributions later. Now assuming you have loaded the MFI data correctly, then do the following:

```
UMN> ael = dat.DATA
UMN> add_magf2,ael,'wi_B3(GSE)'
```

where ***add_magf2.pro*** is an adapted version of ***add_magf.pro*** but vectorized (thus much faster

[49] ?? = 'el','elb','ehb','sf','ph','plb', etc.

when the number of structures in *ael* becomes large). The magnetic field data is now in every structure that has its time range within the time range of loaded MFI data.

Note that all of the above is now contained within a single routine called ***general_load_and_save_wind_3dp_data.pro***. See detailed documentation in example crib sheets and at:
https://github.com/lynnbwilsoniii/wind_3dp_pros/wiki/Software-Documentation. Note this general loading routine will also load SWE velocity moments, onboard 3DP velocity moments, *Wind* orbit data, and the 3D VDFs for each of the 3DP detectors, if the user so chooses.

17.6 3DP VDF Data Structures

Suppose we take one of the VDF data structures found from the routine **get_3dp_structs.pro** discussed in the previous section and examined it. We can type the following:

```
UMN> HELP, ael, /STRUCTURE
```

to get a list of structure tags defined as follows[50] (not necessarily in this exact order):

- **PROJECT_NAME** ≡ scalar [string] 'Wind 3D Plasma'
- **DATA_NAME** ≡ scalar [string] 'SST Foil' or 'SST Open' or 'Eesa High' or 'Eesa Low' or 'Pesa High' or 'Pesa Low'[51]
- **UNITS_NAME** ≡ scalar [string] 'Counts' or 'df' or 'flux' or 'eflux' or 'rate' or 'crate'
- **UNITS_PROCEDURE** ≡ scalar [string] 'convert_so_units' or 'convert_sf_units' or 'convert_ph_units' or 'convert_esa_units'[52]
- **TIME** ≡ scalar [double] Unix time associated with start of data sample (seconds since January 1, 1970)[53].
- **END_TIME** ≡ scalar [double] Unix time associated with end of data sample
- **TRANGE** ≡ [2]-Element [double] indicating the start and end time of the VDF, i.e., [**TIME**, **END_TIME**] (s)
- **INTEG_T** ≡ scalar [double] integration time (s) [= **END_TIME** - **TIME**]
- **DELTA_T** ≡ scalar [double] a tag that may be a remnant from a previous mission, e.g., FAST[54]
- **MASS** ≡ scalar [double] particle mass [(eV/c)^2 with c in km/s] (e.g., for EL or EH, mass = 5.6856591×10^{-6})
- **GEOMFACTOR** ≡ scalar [double] total geometry factor (E cm^2-sr) reported in original instrument paper [*Lin et al.*, 1995] determined from simulations and physical geometry of the detector
- **INDEX** ≡ scalar [long] integer tag associated with structure indexing number
- **N_SAMPLES** ≡ scalar [long] defining the number of 3DP VDFs included in this IDL structure (can vary if one desires data for long time periods)
- **SHIFT** ≡ scalar [byte] defining the byte shift of some parameter (not immediately obvious that this matters at all for anything after data is pulled from the lz files)
- **VALID** ≡ scalar [integer] value of 1 or 0 depending on whether the structure has useful data or not, respectively
- **SPIN** ≡ scalar [long] defining the spacecraft spin number
- **NBINS** ≡ scalar [integer] value defining the number of solid-angle bins
- **NENERGY** ≡ scalar [integer] value defining the number of energy bins
- **DACCODES** ≡ [8,**NENERGY**]-Element [integer] array for digital to analog converter (DAC)

[50] Note that the below will be more generalized than the specific example of looking at just an EESA Low VDF IDL structure.

[51] Note that each of these can be appended with ' Burst' if in burst mode.

[52] Note that PH structures incorrectly mark this value as 'convert_esa_units' instead of 'convert_ph_units'. The ***UMN Modified* Wind/*3DP*** software corrects this in the **get_3dp_structs.pro** routine.

[53] Note that all spacecraft times are in UTC, so this double-precision number is not a true Unix time but already contains leap seconds. However, the conversion between a string of the form 'YYYY-MM-DD/hh:mm:ss' and this double-precision time format will not care and will work correctly, i.e., the output string will be the correct UTC time stamp.

[54] This tag and **INTEG_T** are different in, for instance, the THEMIS ESA data structures. There the **INTEG_T** corresponds to the average time needed for the 1024 counter readouts per spin (s) [= (**END_TIME** - **TIME**)/1024] while **DELTA_T** is just the total duration of IDL structure [= **END_TIME** - **TIME**].

information[55]

- **VOLTS** ≡ [8,**NENERGY**]-Element [float] array of voltage for DAC (not something user usually needs to worry about). Note that the dimensions will be the same as **DACCODES** for the various detectors.
- **DATA** ≡ [**NENERGY**,**NBINS**]-element [float] array of data points (units defined by **UNITS_NAME**)
- **DDATA** ≡ [**NENERGY**,**NBINS**]-element [float] array of uncertainty in data[56]
- **ENERGY** ≡ [**NENERGY**,**NBINS**]-element [float] array of energy bin mid-point values [eV]
- **DENERGY** ≡ [**NENERGY**,**NBINS**]-element [float] array defining the energy range [eV] of each value of **ENERGY**
- **PHI** ≡ [**NENERGY**,**NBINS**]-element [float] array of azimuthal mid-point GSE angle [deg] for each data point at each energy (i.e., +180° is roughly in the sun direction)
- **DPHI** ≡ [**NENERGY**,**NBINS**]-element [float] array defining the angular range(uncertainty) [deg] for each value of **PHI**
- **THETA** ≡ [**NENERGY**,**NBINS**]-element [float] array defining the mid-point GSE poloidal angle[57] [deg] for each bin
- **DTHETA** ≡ [**NENERGY**,**NBINS**]-element [float] array defining the angular range(uncertainty)[58] [deg] for each value of **THETA**
- **BINS** ≡ [NENERGY,NBINS]-element [byte] array of values that define whether data is good (and should be used) for any particular energy-angle bin (i.e., 1 = good, 0 = bad)
- **DT** ≡ [**NENERGY**,**NBINS**]-element [float] array of anode accumulation times [s] of any given energy-angle bin
- **GF** ≡ [**NENERGY**,**NBINS**]-element [float] array defining the relative geometric factor per energy-angle bin. In unit conversion routines, the geometric factor used is defined as the product of **GF** and **GEOMFACTOR**. In practice, **GF** is supposed to account for MCP and anode degredation over time so therefore should be updated with look-up calibration tables for time-specific intervals.
- **BKGRATE** ≡ [**NENERGY**,**NBINS**]-element [float] array of background values (similar to **DDATA**, the user is required to determine these values)
- **DEADTIME** ≡ [**NENERGY**,**NBINS**]-element [float] array of times where detectors were not taking data (see definition in Section 2.1.2)
- **DVOLUME** ≡ [**NENERGY**,**NBINS**]-element [float] array defining the differential volume for each energy-angle bin
- **DOMEGA** ≡ [**NBINS**]-element [float] array of solid angles [steradians] covered for each energy-angle bin
- **MAGF** ≡ [3]-Element [float] array defining the average magnetic field vector [nT, GSE] for the duration of the distribution
- **VSW** ≡ [3]-Element [float] array defining the average bulk flow velocity [km/s, GSE] for the duration of the distribution
- **SC_POT** ≡ scalar [float] defining the estimate of the average spacecraft potential [eV] for the duration of the distribution

There are other tags specific to some of the other detectors but for nearly all intents and

[55]The size of this array is always [8,15]-elements for EESA Low and High, [4,14]-elements for PESA Low (Burst and Survey), and [120]-elements for all PESA High VDFs. This tag is replaced by a **DETECTOR** tag for the SST VDFs that always contains [48]-elements for both Open and Foil.

[56]User typically needs to supply this and a good method is to define it as the square-root of the values in **DATA** when in units of counts.

[57]$-90° \leq \theta \leq +90°$, where 0° is roughly in the spin plane

[58]this is limited primarily by the anodes being used in a particular mode

purposes, the user will not know about or care about them and they will be handled internally by the software.

17.7 Plotting 3DP VDFs

The ***UMN Modified* Wind/*3DP*** software [*Wilson III*, 2021] provides several crib sheets (meant to be entered line-by-line by hand) illustrating generic ways to use many of the routines to load 3DP data and then plot it. The crib sheets can be found in the
~/wind_3dp_pros/wind_3dp_cribs/
folder of the ***UMN Modified* Wind/*3DP*** software download. There are additional examples found in the
~/wind_3dp_pros/publication_crib_sheets/
folder as well. Again, note that these crib sheets are not meant to be used literally or verbatim but only meant as generic guides to help the user get familiar with the software. Further, all of the routines written by Lynn B. Wilson III have detailed Man. pages describing the purpose and inputs/keywords necessary to make the routines work.

The ***UMN Modified* Wind/*3DP*** software has been used in multiple refereed publications [e.g., *Liu et al.*, 2021; *Turner et al.*, 2018; *Wilson III et al.*, 2010, 2011, 2012, 2013a,b, 2014a,b, 2016, 2017, 2018, 2019a,b, 2020, 2021a,b, 2023a,b] and some of it has been adapted/transferred to the SPEDAS softare libraries [*Angelopoulos et al.*, 2019].

Definitions and Notation

This appendix lists the symbols/notation used throughout.

fundamental and/or astronomical parameters

- $\varepsilon_o = 8.854187817 \text{ x } 10^{-12}\ F\ m^{-1} \equiv$ permittivity of free space
- $\mu_o = 4\pi \text{ x } 10^{-7}\ H\ m^{-1} \equiv$ permeability of free space
- $c = 2.99792458 \text{ x } 10^{5}\ km\ s^{-1} \equiv$ speed of light in vacuum $= (\varepsilon_o\ \mu_o)^{-1/2}$
- $k_B = 1.38064852 \text{ x } 10^{-23}\ J\ K^{-1} \equiv$ the Boltzmann constant
- $e = 1.6021766208 \text{ x } 10^{-19}\ C \equiv$ the fundamental charge
- $1\ amu = 1.66053904 \text{ x } 10^{-27}\ kg \equiv$ atomic mass unit
- $m_e = 9.10938356 \text{ x } 10^{-31}\ kg \equiv$ electron rest mass
- $m_p = 1.672621898 \text{ x } 10^{-27}\ kg \equiv$ proton rest mass
- $N_A = 6.02214076 \text{ x } 10^{23}\ mol^{-1} \equiv$ Avagadro's constant
- $R_E = 6.3781366 \text{ x } 10^{3}\ km \equiv$ mean equatorial radius of Earth
- $R_L = 1.7374 \text{ x } 10^{3}\ km \equiv$ mean equatorial radius of Earth's moon
- $R_s = 6.957 \text{ x } 10^{5}\ km \equiv$ mean solar radius
- $1\ AU = 1.495978707 \text{ x } 10^{8}\ km \equiv$ astronomical unit
- $1\ eV = 1.6021766208 \text{ x } 10^{-19}\ J \equiv$ conversion between electron volts and joules
- $1\ eV = 1.1604522 \text{ x } 10^{4}\ K \equiv$ conversion between electron volts and Kelvin

plasma parameters

- $\mathbf{B}_o \equiv$ quasi-static magnetic field vector $[nT]$ with magnitude B_o
- $n_s \equiv$ the number density $[cm^{-3}]$ of species s
- $m_s \equiv$ the mass $[kg]$ of species s
- $Z_s \equiv$ the charge state of species s
- $q_s = Z_s\ e \equiv$ the charge $[C]$ of species s
- $\rho_m = \sum_s m_s n_s \equiv$ total mass density $[kgcm^{-3}]$
- $\gamma_s \equiv$ polytropic index or ratio of specific heats $[N/A]$ of species s
- $T_{s,j} \equiv$ the scalar temperature $[eV]$ of the jth component of species s, j = $\parallel$, $\perp$, or tot where $\parallel(\perp)$ is parallel(perpendicular) with respect to $\mathbf{B}_o$ (see Equation 29a)
- $P_{s,j} = n_s\ k_B\ T_{s,j} \equiv$ the partial thermal pressure $[eV\ cm^{-3}]$ of the jth component of species s
- $P_{t,j} = \sum_s\ P_{s,j} \equiv$ the total pressure $[eV\ cm^{-3}]$ of the jth component, summed over all species
- $V_{Ts,j} \equiv$ the most probable thermal speed $[km\ s^{-1}]$ of a one-dimensional velocity distribution (see Equation 29b)
- $w_{Ts,j} = V_{Ts,j}/\sqrt{2} \equiv$ the rms thermal speed $[km\ s^{-1}]$ of a one-dimensional velocity distribution
- $\Omega_{cs} = 2\ \pi f_{cs} \equiv$ the angular cyclotron frequency $[rad\ s^{-1}]$ (see Equation 29c)
- $\omega_{ps} = 2\ \pi f_{ps} \equiv$ the angular plasma frequency $[rad\ s^{-1}]$ (see Equation 29d)
- $\Omega_{lh} = 2\ \pi\sqrt{f_{ce}\ f_{ci}} \equiv$ the angular lower hybrid resonance frequency $[rad\ s^{-1}]$
- $\Omega_{uh} = 2\ \pi\sqrt{{f_{ce}}^2 + {f_{pe}}^2} \equiv$ the angular upper hybrid resonance frequency $[rad\ s^{-1}]$
- $\lambda_{De} \equiv$ the electron Debye length $[m]$ (see Equation 29e)
- $\rho_{cs} \equiv$ the thermal gyroradius $[km]$ (see Equation 29f)
- $\lambda_s \equiv$ the inertial length $[km]$ (see Equation 29g)
- $\beta_{s,j} \equiv$ the plasma beta [N/A] of the jth component of species s (see Equation 29h)
- $V_A \equiv$ the Alfvén speed $[km\ s^{-1}]$ (see Equation 29i)
- $C_s \equiv$ the sound or ion-acoustic sound speed $[km\ s^{-1}]$ (see Equation 29j)
- $V_f \equiv$ the fast mode speed $[km\ s^{-1}]$ (see Equation 29l)

where multiple parameters are given in the following equations:

$$T_{s,tot} = \frac{1}{3}\left(T_{s,\parallel} + 2\ T_{s,\perp}\right) \tag{29a}$$

$$V_{Ts,j} = \sqrt{\frac{2\ k_B\ T_{s,j}}{m_s}} \tag{29b}$$

$$\Omega_{cs} = \frac{q_s\ B_o}{m_s} \tag{29c}$$

$$\omega_{ps} = \sqrt{\frac{n_s\ {q_s}^2}{\varepsilon_o\ m_s}} \tag{29d}$$

$$\lambda_{De} = \frac{V_{Te,tot}}{\sqrt{2}\ \omega_{pe}} = \sqrt{\frac{\varepsilon_o\ k_B\ T_{e,tot}}{n_e\ e^2}} \tag{29e}$$

$$\rho_{cs} = \frac{V_{Ts,tot}}{\Omega_{cs}} \tag{29f}$$

$$\lambda_s = \frac{c}{\omega_{ps}} \tag{29g}$$

$$\beta_{s,j} = \frac{2\mu_o n_s k_B T_{s,j}}{{B_o}^2} \tag{29h}$$

$$V_A = \frac{B_o}{\sqrt{\mu_o n_i M_i}} \tag{29i}$$

$${C_s}^2 = \frac{\partial P}{\partial \rho_m} = \frac{\sum_s \gamma_s P_s}{\rho_m} \tag{29j}$$

$$2{V_f}^2 = \left({C_s}^2 + {V_A}^2\right) \tag{29k}$$

$$+ \sqrt{({C_s}^2 - {V_A}^2)^2 + 4{C_s}^2{V_A}^2 \sin^2\theta_{Bn}} \tag{29l}$$

Acronyms and Initialisms

3D . . . . . three-dimensional

3DP . . . . . Three-Dimensional Plasma and Energetic Particle Investigation (*Wind*/3DP)

ACE . . . . . Advanced Composition Explorer

ADC . . . . . Analog-to-Digital-Converter

APE . . . . . Alpha-Proton-Electron telescope (part of *Wind* EPACT/ELITE)

ARTEMIS . . . . . Acceleration, Reconnection, Turbulence and Electrodynamics of the Moon's Interaction with the Sun

AU . . . . . Astronomical Unit

CAP . . . . . Command and Attitude Processor

CCMC . . . . . Coordinated Community Modeling Center

CDAWeb . . . . . Coordinated Data Analysis Web

CDF . . . . . Common Data Format

CMAD . . . . . Calibration and Measurement Algorithms Document

CME . . . . . Coronal Mass Ejection

DSN . . . . . Deep Space Network

DTR . . . . . Digital Tape Recorder

EESA . . . . . Electron Electrostatic Analyzer (*Wind*/3DP)

ELITE . . . . . Electron-Isotope Telescope system (*Wind*/EPACT)

EPACT . . . . . Energetic Particles: Acceleration, Composition, and Transport (APE-ELITE-IT-LEMT package on *Wind*)

ESA . . . . . ElectroStatic Analyzer

ESA (agency) . . . . . European Space Agency

FC . . . . . Faraday Cup (e.g., *Wind*/SWE)

FOT . . . . . Flight Operations Team

FOV . . . . . Field-of-View

FTE . . . . . Full Time Equivalent

FTP	File Transfer Protocol
FWFM	Full Width Fiftieth Maximum $\simeq$ 2.38 FWHM
FWHM	Full Width Half Maximum
GCN	Gamma-ray Coordinates Network
GeV	Giga-electron volt
GF	Giant Flare
GGS	Global Geospace Science
GLE	Ground-Level Events
GRB	Gamma Ray Burst
GSFC	Goddard Space Flight Center
GUI	Graphical User Interface
HDP	Heliophysics Data Portal
HET	High-Energy Telescope
HETE-2	High Energy Transient Explorer-2
HGO	Heliophysics Great Observatory
HK	House Keeping
HSO	Heliophysics System Observatory
HTR	High Time Resolution
ICME	Interplanetary Coronal Mass Ejection
IMF	Interplanetary Magnetic Field
INTEGRAL	INTErnational Gamma-Ray Astrophysics Laboratory
IP	Interplanetary
IPD	Interplanetary Dust
IPM	Interplanetary Medium
IPN	Interplanetary GRB Network
ISD	Interstellar Dust
ISS	International Space Station
ISTP	International Solar-Terrestrial Physics
IT (detector)	Isotope Telescope (part of *Wind* EPACT/ELITE)

ITOS	Integrated Test and Operations System
keV	kilo-electron volt
KONUS	Gamma-Ray Spectrometer (*Wind*/KONUS)
KP	Key Parameter
LEMT	Low Energy Matrix Telescopes (*Wind*/EPACT)
LET	Low Energy Telescope
LWS	Living With a Star
LZ	Level Zero
LZP	Level Zero Processing
MAG	Magnetic Field Experiment
MASS	high-resolution MASS spectrometer (*Wind*/SMS)
MCP	MicroChannel Plate
MeV	Mega-electron volt
MFI	Magnetic Field Investigation (*Wind*/MFI)
MMOC	Multi-Mission Operations Center
NASA	National Aeronautics and Space Administration
NRT	Near-Real-Time telemetry stream
OMNI	dataset on CDAWeb
PDMP	Project Data Management Plan
PESA	Ion (Proton) ESA (*Wind*/3DP)
PHA	Pulse Height Analyzed
POC	Point of Contact
PWG	Polar-Wind-Geotail ground system
RAD1	radio receiver band 1
RAD2	radio receiver band 2
SC	Solar Cycle
SCT	Stored Command Table

SEP . . . . . Solar Energetic Particle

SEPT . . . . . Solar Electron and Proton Telescope

SEU . . . . . Single Event Upset

SEZ . . . . . Solar Exclusion Zone

SGR . . . . . Soft Gamma Repeater

SIS . . . . . Solar Isotope Spectrometer

SIT . . . . . Suprathermal Ion Telescope

SMS . . . . . Solar Wind and Suprathermal Ion Composition Experiment (SWICS-MASS-STICS package on *Wind*)

SPASE . . . . . Space Physics Archive Search and Extract

SPDF . . . . . Space Physics Data Facility

SPEDAS . . . . . Space Physics Environment Data Analysis System

sps . . . . . samples per second

SSD . . . . . Solid State Detector

SST . . . . . Solid-State (semi-conductor detector) Telescope (*Wind*/3DP)

STE . . . . . SupraThermal Electron instrument

STEP . . . . . SupraThermal Energetic Particle Telescope (*Wind*/EPACT)

STEREO . . . . . Solar-Terrestrial Relations Observatory

STICS . . . . . SupraThermal Ion Composition Spectrometer (*Wind*/SMS)

STP . . . . . Solar Terrestrial Probe

Strahl . . . . . electron strahl sensor of *Wind*/SWE

SWE . . . . . Solar Wind Experiment (*Wind*/SWE)

SWEA . . . . . Solar Wind Electron Analyzer

SWEPAM . . . . . Solar Wind Electron Proton Alpha Monitor (ACE)

SWICS . . . . . Solar Wind Ion Composition Spectrometer (*Wind*/SMS)

SWIMS . . . . . Solar Wind Ion Mass Spectrometer

TDS . . . . . Time Domain Sampler (*Wind*/WAVES)

TDSF . . . . . TDS Fast Receiver (*Wind*/WAVES)

TDSS . . . . . TDS Slow Receiver (*Wind*/WAVES)

TGRS . . . . . Transient Gamma-Ray Spectrometer (*Wind*/TGRS)

THEMIS . . . . . Time History of Events and Macroscale Interactions during Substorms

TNR . . . . . Thermal Noise Receiver (e.g., part of *Wind*/WAVES)

TOF . . . . . Time-Of-Flight

TUA . . . . . Tape Unit A

TUB . . . . . Tape Unit B

ULEIS . . . . . Ultra Low Energy Isotope Spectrometer

UV . . . . . Ultra Violet [light]

VAX . . . . . Virtual Address eXtension

VDF . . . . . Velocity Distribution Function

VEIS . . . . . Vector Ion-Electron Spectrometers (*Wind*/SWE)

VHO . . . . . Virtual Heliophysics Observatory

VMS . . . . . Virtual Memory System

WYE . . . . . Work Year Equivalent

References

Acuña, M. H., K. W. Ogilvie, D. N. Baker, S. A. Curtis, D. H. Fairfield, and W. H. Mish (1995), The Global Geospace Science Program and Its Investigations, *Space Sci. Rev.*, **71**(1), 5–21, 10.1007/BF00751323.

Angelopoulos, V., P. Cruce, A. Drozdov, E. W. Grimes, N. Hatzigeorgiu, D. A. King, D. Larson, J. W. Lewis, J. M. McTiernan, D. A. Roberts, C. L. Russell, T. Hori, Y. Kasahara, A. Kumamoto, A. Matsuoka, Y. Miyashita, Y. Miyoshi, I. Shinohara, M. Teramoto, J. B. Faden, A. J. Halford, M. McCarthy, R. M. Millan, J. G. Sample, D. M. Smith, L. A. Woodger, A. Masson, A. A. Narock, K. Asamura, T. F. Chang, C.-Y. Chiang, Y. Kazama, K. Keika, S. Matsuda, T. Segawa, K. Seki, M. Shoji, S. W. Y. Tam, N. Umemura, B.-J. Wang, S.-Y. Wang, R. Redmon, J. V. Rodriguez, H. J. Singer, J. Vandegriff, S. Abe, M. Nose, A. Shinbori, Y.-M. Tanaka, S. UeNo, L. Andersson, P. Dunn, C. Fowler, J. S. Halekas, T. Hara, Y. Harada, C. O. Lee, R. Lillis, D. L. Mitchell, M. R. Argall, K. Bromund, J. L. Burch, I. J. Cohen, M. Galloy, B. Giles, A. N. Jaynes, O. Le Contel, M. Oka, T. D. Phan, B. M. Walsh, J. Westlake, F. D. Wilder, S. D. Bale, R. Livi, M. Pulupa, P. Whittlesey, A. DeWolfe, B. Harter, E. Lucas, U. Auster, J. W. Bonnell, C. M. Cully, E. Donovan, R. E. Ergun, H. U. Frey, B. Jackel, A. Keiling, H. Korth, J. P. McFadden, Y. Nishimura, F. Plaschke, P. Robert, D. L. Turner, J. M. Weygand, R. M. Candey, R. C. Johnson, T. Kovalick, M. H. Liu, R. E. McGuire, A. Breneman, K. Kersten, and P. Schroeder (2019), The Space Physics Environment Data Analysis System (SPEDAS), *Space Sci. Rev.*, **215**, 9, 10.1007/s11214-018-0576-4.

Aptekar, R. L., D. D. Frederiks, S. V. Golenetskii, V. N. Ilynskii, E. P. Mazets, V. N. Panov, Z. J. Sokolova, M. M. Terekhov, L. O. Sheshin, T. L. Cline, and D. E. Stilwell (1995), Konus-W Gamma-Ray Burst Experiment for the GGS Wind Spacecraft, *Space Sci. Rev.*, **71**, 265–272, 10.1007/BF00751332.

Bordoni, F. (1971), Channel electron multiplier efficiency for 10-1000 eV electrons, *Nucl. Inst. & Meth.*, **97**, 405, 10.1016/0029-554X(71)90300-4.

Bougeret, J.-L., M. L. Kaiser, P. J. Kellogg, R. Manning, K. Goetz, S. J. Monson, N. Monge, L. Friel, C. A. Meetre, C. Perche, L. Sitruk, and S. Hoang (1995), Waves: The Radio and Plasma Wave Investigation on the Wind Spacecraft, *Space Sci. Rev.*, **71**, 231–263, 10.1007/BF00751331.

Chotoo, K. (1998), Measurements of H(+), He(2+), and He(+), in Corotating Interaction Regions at 1 AU, Ph.D. thesis, University of Maryland College Park.

Chotoo, K., M. R. Collier, A. B. Galvin, D. C. Hamilton, and G. Gloeckler (1998), Extended solar wind helium distribution functions in high-speed streams, *J. Geophys. Res.*, **1031**, 17,441–17,446, 10.1029/98JA01173.

Domingo, V., B. Fleck, and A. I. Poland (1995), The SOHO Mission: an Overview, *Solar Phys.*, **162**(1-2), 1–37, 10.1007/BF00733425.

Escoubet, C. P., R. Schmidt, and M. L. Goldstein (1997), Cluster - Science and Mission Overview, *Space Sci. Rev.*, **79**, 11–32, 10.1023/A:1004923124586.

Farrell, W. M., R. F. Thompson, R. P. Lepping, and J. B. Byrnes (1995), A method of calibrating magnetometers on a spinning spacecraft, *IEEE Trans. Mag.*, **31**, 966–972, 10.1109/20.364770.

Feldman, W. C., J. R. Asbridge, S. J. Bame, M. D. Montgomery, and S. P. Gary (1975), Solar wind electrons, *J. Geophys. Res.*, **80**, 4181–4196, 10.1029/JA080i031p04181.

Feldman, W. C., J. R. Asbridge, S. J. Bame, and J. T. Gosling (1978), Long-term variations of selected solar wind properties - IMP 6, 7, and 8 results, *J. Geophys. Res.*, **83**, 2177–2189, 10.1029/JA083iA05p02177.

Filwett, R. J., M. I. Desai, M. A. Dayeh, and T. W. Broiles (2017), Source Population and Acceleration Location of Suprathermal Heavy Ions in Corotating Interaction Regions, *Astrophys. J.*, **838**(1), 23,

10.3847/1538-4357/aa5ca9.

Filwett, R. J., M. I. Desai, R. W. Ebert, and M. A. Dayeh (2019), Spectral Properties and Abundances of Suprathermal Heavy Ions in Compression Regions near 1 au, *Astrophys. J.*, **876**(1), 88, 10.3847/1538-4357/ab12cf.

Franz, J. R., P. M. Kintner, and J. S. Pickett (1998), POLAR observations of coherent electric field structures, *Geophys. Res. Lett.*, **25**, 1277–1280, 10.1029/98GL50870.

Fränz, M., and D. Harper (2002), Heliospheric coordinate systems, *Planet. Space Sci.*, **50**, 217–233.

Fraser, G. W. (1983), The electron detection efficiency of microchannel plates, *Nucl. Inst. & Meth. Phys. Res.*, **206**(3), 445–449, 10.1016/0167-5087(83)90381-2.

Fraser, G. W. (2002), The ion detection efficiency of microchannel plates (MCPs), *Int. J. Mass Spectrom.*, **215**, 13–30, 10.1016/S1387-3806(01)00553-X.

Fraser, G. W., M. T. Pain, J. E. Lees, and J. F. Pearson (1991), The operation of microchannel plates at high count rates, *Nucl. Inst. & Meth. Phys. Res. A*, **306**(1), 247–260, 10.1016/0168-9002(91)90329-O.

Fraser, G. W., M. T. Pain, and J. E. Lees (1993), Microchannel plate operation at high count rates: further studies, *Nucl. Inst. & Meth. Phys. Res. A*, **327**(2), 328–336, 10.1016/0168-9002(93)90698-H.

Frederiks, D., D. Svinkin, A. Tsvetkova, R. Aptekar, S. Golenetskii, A. Kozlova, A. Lysenko, and M. Ulanov (2019), GRB observations with Konus-WIND experiment, *Mem. Soc. Astron. Ital.*, **90**(1–2), arXiv:1907.00402.

Gershman, D. J., U. Gliese, J. C. Dorelli, L. A. Avanov, A. C. Barrie, D. J. Chornay, E. A. MacDonald, M. P. Holland, B. L. Giles, and C. J. Pollock (2016), The parameterization of microchannel-plate-based detection systems, *J. Geophys. Res.*, **121**(10), 10,005–10,018, 10.1002/2016JA022563.

Gloeckler, G., H. Balsiger, A. Bürgi, P. Bochsler, L. A. Fisk, A. B. Galvin, J. Geiss, F. Gliem, D. C. Hamilton, T. E. Holzer, D. Hovestadt, F. M. Ipavich, E. Kirsch, R. A. Lundgren, K. W. Ogilvie, R. B. Sheldon, and B. Wilken (1995), The Solar Wind and Suprathermal Ion Composition Investigation on the Wind Spacecraft, *Space Sci. Rev.*, **71**, 79–124, 10.1007/BF00751327.

Goruganthu, R. R., and W. G. Wilson (1984), Relative electron detection efficiency of microchannel plates from 0-3 keV, *Rev. Sci. Inst.*, **55**, 2030–2033, 10.1063/1.1137709.

Gruesbeck, J. R. (2013), Exploring the Origin of Coronal Mass Ejection Plasma from In Situ Observations of Ionic Charge State Composition, Ph.D. thesis, University of Michigan, Ann Arbor, advisor: Susan T. Lepri.

Hamilton, D. C., G. Gloeckler, F. M. Ipavich, R. A. Lundgren, and R. B. Sheldon (1990), New high-resolution electrostatic ion mass analyzer using time of flight, *Rev. Sci. Inst.*, **61**(10), 3104–3106, 10.1063/1.1141695.

Harten, R., and K. Clark (1995), The Design Features of the GGS Wind and Polar Spacecraft, *Space Sci. Rev.*, **71**, 23–40, 10.1007/BF00751324.

Ho, G. (1998), Helium-3 Enhancements and Unusual Ion Charge State Composition in Coronal Mass Ejections, Ph.D. thesis, University of Maryland College Park.

Hospodarsky, G. B. (1992), Search coil magnetometers for the ISTP *Polar* and *Wind* spacecraft, Master's thesis, University of Iowa, advisor: Donald A. Gurnett.

Hospodarsky, G. B. (2016), Spaced-based search coil magnetometers, *J. Geophys. Res.*, **121**(12), 12,068–12,079, 10.1002/2016JA022565.

Ipavich, F. M., R. A. Lundgren, B. A. Lambird, and G. Gloeckler (1978), Measurements of pulse-height defect in Au–Si detectors for H, He, C, N, O, Ne, Ar, Kr from ≈2 to ≈ 400 keV/nucleon, *Nucl. Inst. & Meth.*, **154**(2), 291–294, 10.1016/0029-554X(78)90412-3.

Jackson, J. D. (1998), *Classical Electrodynamics, 3rd Edition*, John Wiley & Sons, Inc., New York, NY.

Janni, J. F. (1982a), Proton Range-Energy Tables, 1 keV-10 GeV, Energy Loss, Range, Path Length, Time-of-Flight, Straggling, Multiple Scattering, and Nuclear Interaction Probability. Part I. For 63 Compounds, *Atomic Data and Nuclear Data Tables*, **27**, 147, 10.1016/0092-640X(82)90004-3.

Janni, J. F. (1982b), Proton Range-Energy Tables, 1 keV-10 GeV, Energy Loss, Range, Path Length, Time-of-Flight, Straggling, Multiple Scattering, and Nuclear Interaction Probability. Part II. For 92 Elements, *Atomic Data and Nuclear Data Tables*, **27**, 341, 10.1016/0092-640X(82)90005-5.

Kanaya, K., and H. Kawakatsu (1972), Secondary electron emission due to primary and backscattered electrons, *J. Phys. D Appl. Phys.*, **5**(9), 1727–1742, 10.1088/0022-3727/5/9/330.

Kasper, J. C. (2002), Solar wind plasma: Kinetic properties and micro-instabilities, Ph.D. thesis, MASSACHUSETTS INSTITUTE OF TECHNOLOGY, advisor: Alan J. Lazarus.

Kasper, J. C., A. J. Lazarus, J. T. Steinberg, K. W. Ogilvie, and A. Szabo (2006), Physics-based tests to identify the accuracy of solar wind ion measurements: A case study with the Wind Faraday Cups, *J. Geophys. Res.*, **111**, 3105, 10.1029/2005JA011442.

Kepko, E. L., K. K. Khurana, M. G. Kivelson, R. C. Elphic, and C. T. Russell (1996), Accurate determination of magnetic field gradients from four point vector measurements. I. Use of natural constraints on vector data obtained from a single spinning spacecraft, *Trans. Mag.*, **32**(2), 377–385, 10.1109/20.486522.

Kleinknecht, K. (1998), *Detectors for particle radiation*, Cambridge University Press, The Edinburgh Building, Cambridge CB2 2RU, UK.

Knoll, G. F. (2000), *Radiation detection and measurement*, John Wiley & Sons, Inc., 111 River Street, Hoboken, NJ 07030-5774.

Koval, A., and A. Szabo (2013), Magnetic field turbulence spectra observed by the Wind spacecraft, in *American Institute of Physics Conference Series*, *American Institute of Physics Conference Series*, vol. 1539, edited by G. P. Zank, J. Borovsky, R. Bruno, J. Cirtain, S. Cranmer, H. Elliott, J. Giacalone, W. Gonzalez, G. Li, E. Marsch, E. Moebius, N. Pogorelov, J. Spann, and O. Verkhoglyadova, pp. 211–214, 10.1063/1.4811025.

Ladislas Wiza, J. (1979), Microchannel plate detectors, *Nucl. Inst. & Meth.*, **162**, 587–601, 10.1016/0029-554X(79)90734-1.

Lavraud, B., and D. E. Larson (2016), Correcting moments of in situ particle distribution functions for spacecraft electrostatic charging, *J. Geophys. Res.*, **121**, 8462–8474, 10.1002/2016JA022591.

Leinweber, H. K., C. T. Russell, K. Torkar, T. L. Zhang, and V. Angelopoulos (2008), An advanced approach to finding magnetometer zero levels in the interplanetary magnetic field, *Measurement Sci. Tech.*, **19**(5), 055104, 10.1088/0957-0233/19/5/055104.

Lepping, R. P., M. H. Acũna, L. F. Burlaga, W. M. Farrell, J. A. Slavin, K. H. Schatten, F. Mariani, N. F. Ness, F. M. Neubauer, Y. C. Whang, J. B. Byrnes, R. S. Kennon, P. V. Panetta, J. Scheifele, and E. M. Worley (1995), The Wind Magnetic Field Investigation, *Space Sci. Rev.*, **71**, 207–229, 10.1007/BF00751330.

Liavas, A. P., and P. A. Regalia (1998), Numerical stability issues of the conventional recursive

least squares algorithm, *Proc. IEEE Intl. Conf. Acoust. Speech Signal Processing*, **3**, 1409–1412, 10.1109/ICASSP.1998.681711.

Lin, R. P., K. A. Anderson, S. Ashford, C. Carlson, D. Curtis, R. Ergun, D. Larson, J. McFadden, M. McCarthy, G. K. Parks, H. Rème, J. M. Bosqued, J. Coutelier, F. Cotin, C. D'Uston, K.-P. Wenzel, T. R. Sanderson, J. Henrion, J. C. Ronnet, and G. Paschmann (1995), A Three-Dimensional Plasma and Energetic Particle Investigation for the Wind Spacecraft, *Space Sci. Rev.*, **71**, 125–153, 10.1007/BF00751328.

Liu, T. Z., Y. Hao, L. B. Wilson III, D. L. Turner, and H. Zhang (2021), Magnetospheric Multiscale observations of Earth's oblique bow shock reformation by foreshock ultra-low frequency waves, *Geophys. Res. Lett.*, **48**(2), e2020GL091,184, 10.1029/2020GL091184.

Lutz, G. (1999), *Semiconductor Radiation Detectors*, Springer-Verlag, Berlin, Heidelberg, 10.1007/978-3-540-71679-2.

Mackenzie, J. D. (1977), Mcp glass analysis studies, final Technical Report.

Maksimovic, M., V. Pierrard, and P. Riley (1997), Ulysses electron distributions fitted with Kappa functions, *Geophys. Res. Lett.*, **24**, 1151–1154, 10.1029/97GL00992.

Maksimovic, M., I. Zouganelis, J.-Y. Chaufray, K. Issautier, E. E. Scime, J. E. Littleton, E. Marsch, D. J. McComas, C. Salem, R. P. Lin, and H. Elliott (2005), Radial evolution of the electron distribution functions in the fast solar wind between 0.3 and 1.5 AU, *J. Geophys. Res.*, **110**, A09104, 10.1029/2005JA011119.

Malaspina, D. M., and L. B. Wilson III (2016), A database of interplanetary and interstellar dust detected by the Wind spacecraft, *J. Geophys. Res.*, **121**, 9369–9377, 10.1002/2016JA023209.

Malaspina, D. M., M. Horanyi, A. Zaslavsky, K. Goetz, L. B. Wilson III, and K. Kersten (2014), Interplanetary and interstellar dust observed by the Wind/WAVES electric field instrument, *Geophys. Res. Lett.*, **41**, 266–272, 10.1002/2013GL058786.

Markwardt, C. B. (2009), Non-linear Least-squares Fitting in IDL with MPFIT, in *Astronomical Data Analysis Software and Systems XVIII*, *Astronomical Society of the Pacific Conference Series*, vol. 411, edited by D. A. Bohlender, D. Durand, and P. Dowler, p. 251.

Meeks, C., and P. B. Siegel (2008), Dead time correction via the time series, *Amer. J. Phys.*, **76**, 589–590, 10.1119/1.2870432.

Meier, R., and P. Eberhardt (1993), Velocity and ion species dependence of the gain of microchannel plates, *Int. J. Mass Spectrom. Ion Proc.*, **123**(1), 19–27, 10.1016/0168-1176(93)87050-3.

Meyer-Vernet, N., and C. Perche (1989), Tool kit for antennae and thermal noise near the plasma frequency, *J. Geophys. Res.*, **94**, 2405–2415, 10.1029/JA094iA03p02405.

Moré, J. J. (1978), The Levenberg-Marquardt algorithm: Implementation and theory, in *Numerical Analysis*, *Lecture Notes in Mathematics*, vol. 630, edited by G. A. Watson, pp. 105–116, Springer Berlin Heidelberg, 10.1007/BFb0067700, proceedings of the Biennial Conference Held at Dundee, June 28–July 1, 1977.

Nishida, A. (1994), The Geotail mission, *Geophys. Res. Lett.*, **21**(25), 2871–2873, 10.1029/94GL01223.

Ogilvie, K. W., and M. D. Desch (1997), The wind spacecraft and its early scientific results, *Adv. Space Res.*, **20**, 559–568, 10.1016/S0273-1177(97)00439-0.

Ogilvie, K. W., D. J. Chornay, R. J. Fritzenreiter, F. Hunsaker, J. Keller, J. Lobell, G. Miller, J. D. Scudder, E. C. Sittler, Jr., R. B. Torbert, D. Bodet, G. Needell, A. J. Lazarus, J. T. Steinberg, J. H. Tappan, A. Mavretic, and E. Gergin (1995), SWE, A Comprehensive Plasma Instrument for the Wind

Spacecraft, *Space Sci. Rev.*, **71**, 55–77, 10.1007/BF00751326.

Owens, A., R. Baker, T. L. Cline, N. Gehrels, J. Jermakian, T. Nolan, R. Ramaty, G. Smith, D. E. Stilwell, and B. J. Teegarden (1991), The transient gamma-ray spectrometer, *IEEE Trans. Nucl. Sci.*, **38**, 559–567, 10.1109/23.289357.

Owens, A., R. Baker, T. L. Cline, N. Gehrels, J. Jermakian, T. Nolan, R. Ramaty, H. Seifert, D. A. Shephard, G. Smith, D. E. Stilwell, B. J. Teegarden, C. P. Cork, D. A. Landis, P. N. Luke, N. W. Madden, D. Malone, R. H. Pehl, H. Yaver, K. Hurley, S. Mathias, and A. H. Post, Jr. (1995), A High-Resolution GE Spectrometer for Gamma-Ray Burst Astronomy, *Space Sci. Rev.*, **71**, 273–296, 10.1007/BF00751333.

Paschmann, G., and P. W. Daly (1998), Analysis Methods for Multi-Spacecraft Data. ISSI Scientific Reports Series SR-001, ESA/ISSI, Vol. 1. ISBN 1608-280X, 1998, *ISSI Sci. Rep. Ser.*, **1**.

Paul, J. M. (1971), The rate of energy loss and intrinsic resolution of silicon detectors, *Nucl. Inst. & Meth.*, **94**(2), 275–283, 10.1016/0029-554X(71)90579-9.

Pulupa, M. P., S. D. Bale, C. Salem, and K. Horaites (2014), Spin-modulated spacecraft floating potential: Observations and effects on electron moments, *J. Geophys. Res.*, **119**, 647–657, 10.1002/2013JA019359.

Reames, D. V. (2017), *Solar Energetic Particles*, *Lecture Notes in Physics*, vol. 932, Springer International Publishing AG, 10.1007/978-3-319-50871-9.

Rösler, M., and W. Brauer (1988), Theory of Electron Emission from Solids by Proton and Electron Bombardment, *Phys. Stat. Sol. B*, **148**(1), 213–226, 10.1002/pssb.2221480119.

Schecker, J. A., M. M. Schauer, K. Holzscheiter, and M. H. Holzscheiter (1992), The performance of a microchannel plate at cryogenic temperatures and in high magnetic fields, and the detection efficiency for low energy positive hydrogen ions, *Nucl. Inst. & Meth. in Phys. Res. A*, **320**, 556–561, 10.1016/0168-9002(92)90950-9.

Skoug, R. M., W. C. Feldman, J. T. Gosling, D. J. McComas, and C. W. Smith (2000), Solar wind electron characteristics inside and outside coronal mass ejections, *J. Geophys. Res.*, **105**, 23,069–23,084, 10.1029/2000JA000017.

Skyrme, D. J. (1967), The passage of charged particles through silicon, *Nucl. Inst. & Meth.*, **57**, 61–73, 10.1016/0029-554X(67)90498-3.

Sternglass, E. J. (1957), Theory of Secondary Electron Emission by High-Speed Ions, *Phys. Rev.*, **108**(1), 1–12, 10.1103/PhysRev.108.1.

Stone, E. C., A. M. Frandsen, R. A. Mewaldt, E. R. Christian, D. Margolies, J. F. Ormes, and F. Snow (1998), The Advanced Composition Explorer, *Space Sci. Rev.*, **86**, 1–22, 10.1023/A:1005082526237.

Štverák, v., M. Maksimovic, P. M. Trávníček, E. Marsch, A. N. Fazakerley, and E. E. Scime (2009), Radial evolution of nonthermal electron populations in the low-latitude solar wind: Helios, Cluster, and Ulysses Observations, *J. Geophys. Res.*, **114**, 5104, 10.1029/2008JA013883.

Turner, D. L., L. B. Wilson III, T. Z. Liu, I. J. Cohen, S. J. Schwartz, A. Osmane, J. F. Fennell, J. H. Clemmons, J. B. Blake, J. Westlake, B. H. Mauk, A. N. Jaynes, T. Leonard, D. N. Baker, R. J. Strangeway, C. T. Russell, D. J. Gershman, L. A. Avanov, B. L. Giles, R. B. Torbert, J. Broll, R. G. Gomez, S. A. Fuselier, and J. L. Burch (2018), Autogenous and efficient acceleration of energetic ions upstream of Earth's bow shock, *Nature*, **561**(7722), 206–210, 10.1038/s41586-018-0472-9.

von Rosenvinge, T. T., L. M. Barbier, J. Karsch, R. Liberman, M. P. Madden, T. Nolan, D. V. Reames, L. Ryan, S. Singh, H. Trexel, G. Winkert, G. M. Mason, D. C. Hamilton, and P. Walpole (1995a), The

Energetic Particles: Acceleration, Composition, and Transport (EPACT) investigation on the WIND spacecraft, *Space Sci. Rev.*, **71**, 155–206, 10.1007/BF00751329.

von Rosenvinge, T. T., L. M. Barbier, J. Karsch, R. Liberman, M. P. Madden, T. Nolan, D. V. Reames, L. Ryan, S. Singh, H. Trexel, G. Winkert, G. M. Mason, D. C. Hamilton, and P. Walpole (1995b), The Energetic Particles: Acceleration, Composition, and Transport (EPACT) investigation on the WIND spacecraft, *Space Sci. Rev.*, **71**, 155–206, 10.1007/BF00751329.

Whipple, E., and H. Lancaster (1995), International Coordination of Solar Terrestrial Science, *Space Sci. Rev.*, **71**(1-4), 41–54, 10.1007/BF00751325.

Wilson III, L. B. (2010), The microphysics of collisionless shocks, Ph.D. thesis, University of Minnesota *lynn.b.wilsoniii@gmail.com*, publication Number: AAT 3426498; ISBN: 9781124274577; Advisor: Cynthia Cattell.

Wilson III, L. B. (2021), Space plasma missions idl software library, 10.5281/zenodo.6141586.

Wilson III, L. B. (2023), *Wind* waves tdsf dataset, 10.5281/zenodo.10107360.

Wilson III, L. B., C. A. Cattell, P. J. Kellogg, K. Goetz, K. Kersten, J. C. Kasper, A. Szabo, and M. Wilber (2010), Large-amplitude electrostatic waves observed at a supercritical interplanetary shock, *J. Geophys. Res.*, **115**, A12104, 10.1029/2010JA015332.

Wilson III, L. B., C. A. Cattell, P. J. Kellogg, J. R. Wygant, K. Goetz, A. Breneman, and K. Kersten (2011), The properties of large amplitude whistler mode waves in the magnetosphere: Propagation and relationship with geomagnetic activity, *Geophys. Res. Lett.*, **38**, L17107, 10.1029/2011GL048671.

Wilson III, L. B., A. Koval, A. Szabo, A. Breneman, C. A. Cattell, K. Goetz, P. J. Kellogg, K. Kersten, J. C. Kasper, B. A. Maruca, and M. Pulupa (2012), Observations of electromagnetic whistler precursors at supercritical interplanetary shocks, *Geophys. Res. Lett.*, **39**, L08109, 10.1029/2012GL051581.

Wilson III, L. B., A. Koval, A. Szabo, A. Breneman, C. A. Cattell, K. Goetz, P. J. Kellogg, K. Kersten, J. C. Kasper, B. A. Maruca, and M. Pulupa (2013a), Electromagnetic waves and electron anisotropies downstream of supercritical interplanetary shocks, *J. Geophys. Res.*, **118**(1), 5–16, 10.1029/2012JA018167.

Wilson III, L. B., A. Koval, D. G. Sibeck, A. Szabo, C. A. Cattell, J. C. Kasper, B. A. Maruca, M. Pulupa, C. S. Salem, and M. Wilber (2013b), Shocklets, SLAMS, and field-aligned ion beams in the terrestrial foreshock, *J. Geophys. Res.*, **118**(3), 957–966, 10.1029/2012JA018186.

Wilson III, L. B., D. G. Sibeck, A. W. Breneman, O. Le Contel, C. Cully, D. L. Turner, V. Angelopoulos, and D. M. Malaspina (2014a), Quantified Energy Dissipation Rates in the Terrestrial Bow Shock: 1. Analysis Techniques and Methodology, *J. Geophys. Res.*, **119**(8), 6455–6474, 10.1002/2014JA019929.

Wilson III, L. B., D. G. Sibeck, A. W. Breneman, O. Le Contel, C. Cully, D. L. Turner, V. Angelopoulos, and D. M. Malaspina (2014b), Quantified Energy Dissipation Rates in the Terrestrial Bow Shock: 2. Waves and Dissipation, *J. Geophys. Res.*, **119**(8), 6475–6495, 10.1002/2014JA019930.

Wilson III, L. B., D. G. Sibeck, D. L. Turner, A. Osmane, D. Caprioli, and V. Angelopoulos (2016), Relativistic electrons produced by foreshock disturbances observed upstream of the Earth's bow shock, *Phys. Rev. Lett.*, **117**(21), 215101, 10.1103/PhysRevLett.117.215101, editors' Suggestion.

Wilson III, L. B., A. Koval, A. Szabo, M. L. Stevens, J. C. Kasper, C. A. Cattell, and V. V. Krasnoselskikh (2017), Revisiting the structure of low Mach number, low beta, quasi-perpendicular shocks, *J. Geophys. Res.*, **122**(9), 9115–9133, 10.1002/2017JA024352.

Wilson III, L. B., M. L. Stevens, J. C. Kasper, K. G. Klein, B. Maruca, S. D. Bale, T. A. Bowen, M. P.

Pulupa, and C. S. Salem (2018), The Statistical Properties of Solar Wind Temperature Parameters Near 1 au, *Astrophys. J. Suppl.*, **236**(2), 41, 10.3847/1538-4365/aab71c.

Wilson III, L. B., L.-J. Chen, S. Wang, S. J. Schwartz, D. L. Turner, M. L. Stevens, J. C. Kasper, A. Osmane, D. Caprioli, S. D. Bale, M. P. Pulupa, C. S. Salem, and K. A. Goodrich (2019a), Electron energy partition across interplanetary shocks: I. Methodology and Data Product, *Astrophys. J. Suppl.*, **243**(8), 10.3847/1538-4365/ab22bd.

Wilson III, L. B., L.-J. Chen, S. Wang, S. J. Schwartz, D. L. Turner, M. L. Stevens, J. C. Kasper, A. Osmane, D. Caprioli, S. D. Bale, M. P. Pulupa, C. S. Salem, and K. A. Goodrich (2019b), Electron energy partition across interplanetary shocks: II. Statistics, *Astrophys. J. Suppl.*, **245**(24), 10.3847/1538-4365/ab5445.

Wilson III, L. B., L.-J. Chen, S. Wang, S. J. Schwartz, D. L. Turner, M. L. Stevens, J. C. Kasper, A. Osmane, D. Caprioli, S. D. Bale, M. P. Pulupa, C. S. Salem, and K. A. Goodrich (2020), Electron energy partition across interplanetary shocks: III. Analysis, *Astrophys. J.*, **893**(22), 10.3847/1538-4357/ab7d39.

Wilson III, L. B., A. L. Brosius, N. Gopalswamy, T. Nieves-Chinchilla, A. Szabo, K. Hurley, T. Phan, J. Kasper, N. Lugaz, I. G. Richardson, C. H. K. Chen, D. Verscharen, R. T. Wicks, and J. M. TenBarge (2021a), A Quarter Century of *Wind* Spacecraft Discoveries, *Rev. Geophys.*, **59**(2), e2020RG000,714, 10.1029/2020RG000714.

Wilson III, L. B., L.-J. Chen, and V. Roytershteyn (2021b), The discrepancy between simulation and observation of electric fields in collisionless shocks (invited), *Front. Astron. Space Sci.*, **7**(592634), 14, 10.3389/fspas.2020.592634.

Wilson III, L. B., C. S. Salem, and J. W. Bonnell (2023a), Spacecraft floating potential measurements for the *Wind* spacecraft, *Astrophys. J. Suppl.*, **269**(52), 10, 10.3847/1538-4365/ad0633.

Wilson III, L. B., M. L. Stevens, J. C. Kasper, K. G. Klein, B. Maruca, S. D. Bale, T. A. Bowen, M. P. Pulupa, and C. S. Salem (2023b), Erratum: "The Statistical Properties of Solar Wind Temperature Parameters Near 1 au", *Astrophys. J. Suppl.*, **269**(62), 12, 10.3847/1538-4365/ad07de.

Wilson III, L. B., et al. (2021c), *Wind* lz calibration and decommutation software, 10.5281/zenodo.4451304.

Wüest, M., D. S. Evans, J. P. McFadden, W. T. Kasprzak, L. H. Brace, B. K. Dichter, W. R. Hoegy, A. J. Lazarus, A. Masson, and O. Vaisberg (2007), Review of Instruments, *ISSI Sci. Rep. Ser.*, **7**, 11–116.

Wüest, M., Evans, D. S., & von Steiger, R. (Ed.) (2007), *Calibration of Particle Instruments in Space Physics*, ESA Publications Division, Keplerlaan 1, 2200 AG Noordwijk, The Netherlands.